(2)

ANNUAL REPORT

Office of Naval Research

Contract No. N00014-90-J-1300

December 1, 1989–December 31, 1992

MATERIALS

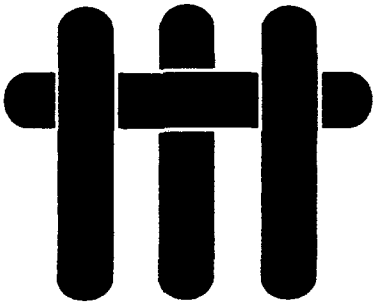

EFFECT OF MICROSTRUCTURE ON THE STRENGTH AND FRACTURE ENERGY OF BIMATERIAL INTERFACES

by

A.G. Evans
Materials Department
College of Engineering
University of California
Santa Barbara, California 93106–5050

Sponsored by: Office of Naval Research

REPORT DOCUMENTATION PAGE

Form Approved
OMB No. 0705–0188

1. AGENCY USE ONLY (Leave blank)	2. REPORT DATE	3. REPORT TYPE AND DATES COVERED
	921231	ANNUAL REPORT 900101 TO 921231

4. TITLE AND SUBTITLE

Effect of Microstructure on the Strength and Fracture Energy of Bimaterial Interfaces

5. FUNDING NUMBERS

N00014-90-J-1300

6. AUTHOR(S)

Evans, Anthony G.

7. PERFORMING ORGANIZATION NAME(S) AND ADDRESS(ES)

MATERIALS DEPARTMENT
COLLEGE OF ENGINEERING
UNIVERSITY OF CALIFORNIA
SANTA BARBARA, CA 93106-5050

8. PERFORMING ORGANIZATION REPORT NUMBER

9. SPONSORING/MONITORING AGENCY NAME(S) AND ADDRESS(ES)

OFFICE OF NAVAL RESEARCH
MATERIALS DIVISION
800 NORTH QUINCY STREET
ARLINGTON, VA 22217-5000

10. SPONSORING/MONITORING AGENCY REPORT NUMBER

11. SUPPLEMENTARY NOTES

12A. DISTRIBUTION/AVAILABILITY STATEMENT

~~See Distribution List~~

12B. DISTRIBUTION CODE

13. ABSTRACT (Maximum 200 words)

The annual report of the Office of Naval Research grant at UCSB on Strength and Fracture Energy of . Bimaterials Interfaces includes three sections: Mechanics of Interfaces, Coating Design for Composite Systems, and Mechanics of Brittle Matrix Composites. For more details see Executive Summary.

14. SUBJECT TERM

Effect, Microstructure, Strength, Fracture Energy, Bimaterial Interfaces

15. NUMBER OF PAGES

350

16. PRICE CODE

17. SECURITY CLASSIFICATION OF REPORT	18. SECURITY CLASSIFICATION OF THIS PAGE	19. SECURITY CLASSIFICATION OF ABSTRACT	20. LIMITATION OF ABSTRACT
UNCLASSIFIED	UNCLASSIFIED	UNCLASSIFIED	

Section 1 EXECUTIVE SUMMARY

Section 2 MECHANICS OF INTERFACES

Section 3 COATING DESIGN FOR COMPOSITE SYSTEMS

Section 4 MECHANICS OF BRITTLE MATRIX COMPOSITES

	TITLE	AUTHOR
Article 20.	The Fracture Resistance of Directionally Solidified Dual-Phase NiAl Reinforced With Refractory Metals	F.E. Heredia M.Y. He G.E. Lucas A.G. Evans H.E. Dève D. Konitzer
Article 21.	The Mechanics of Crack Growth in Layered Materials	M.Y. He F.E. Heredia D.J. Wissuchek M.C. Shaw A.G. Evans

Section 1: EXECUTIVE SUMMARY

The research is concerned with the mechanical properties of ceramic/metal bonded systems and with establishing criteria for interface decohesion, sliding and for cracking across interfaces. The research is closely coordinated with other DARPA/ONR programs at UCSB concerned with advanced composites. The research has application to the mechanical performance of biphasic systems, including metal matrix composites, layered materials and refractory metal toughened ceramics. It is also relevant to the adhesion of ceramic coatings on alloy substrates, the joining and brazing of metals to ceramics as well as the mechanical integrity of multilayer capacitors and ceramic packages for electronic devices. A central issue concerns the elucidation of relationships between the interface fracture energy Γ_i and the properties and dimensions of the constituents and interphases, as well as the influence of plasticity in the metal. One eventual objective is to provide models that allow Γ_i to be predicted from constituent properties.

The basic information about Γ_i, as well as the sliding resistance τ, is necessary for interpretation of the mechanical performance of biphasic systems. The interface results will be used to manipulate the properties of these materials by choosing material combinations that exhibit wide ranges of Γ_i and τ. The debonding and sliding of interfaces also influence the mechanisms that dominate stress redistribution in composites (MMCs, CMCs, IMCs). Mechanism transitions have substantial import for structural performance. The creation of mechanism maps and their dependence on Γ_i and τ represents another important objective.

The basic interface studies have established the central role of either reaction products or interphases on the interface fracture energy. When such interlayers develop upon forming the bond, Γ_i is typically *lower* than the magnitude achievable when a *direct* bond develops between the metal and ceramic. In the absence of an interlayer, plastic dissipation is encouraged in the metal adjacent to the interface, leading to Γ_i in the range, $10\text{-}10^3 Jm^{-2}$, dependent upon the metal yield strength, σ_O, etc. When interlayers form, they are usually brittle and decohesion occurs, either within this layer or at one of the interfaces. Consequently, Γ_i has magnitude typical of the interphase material itself, $1\text{-}50 Jm^{-2}$. As a result, when defect-free bonds can be generated without reaction products, superior properties are achievable. However, in some cases, bonds can only be created when a reaction product is induced, such as Si_3N_4/Ni. Then, it is important to maximize the fracture energy of the reaction product.

Few interfaces have a sufficiently low Γ_i to permit controlled debonding in biphasic composite systems. Among the few are interfaces between certain refractory metals (particularly Mo, Cr, W) and either oxides or intermetallics. Usually, these systems develop oxide interphases (MoO_2, Cr_2O_3, etc.) and decohesion occurs (at $\Gamma_i \approx 1 Jm^{-2}$) between the refractory metal and its own oxide. While the underlying principles are not yet understood, the observation may be exploited. Two phenomena have been explored, based on the low Γ_i for certain refractory metal biphasic systems. (i) The fracture resistance of layered systems between NiAl and Mo(Cr) alloys produced by directional solidification (DS). (ii) Debonding and sliding in Al_2O_3/Al_2O_3 CMCs with refractory metal fiber coatings.

Crack growth has been monitored in the layered DS NiAl/Mo(Cr) system. Controlled debonding occurred at the interfaces, consistent with a small Γ_i. Stress redistribution effects associated with debonding have been calculated. The results have been correlated with the high fracture resistances found in these materials, relative to NiAl.

Composites consisting of thin Mo coatings on sapphire fibers in a polycrystalline Al_2O_3 matrix have been produced. It has been demonstrated that the Mo coatings protect the fiber upon composite consolidation. It has also been shown that debonding occurs at the interface in these composites, consistent with the low Γ_i. However, the sliding resistance τ is relatively high ($\approx$ 120 MPa) and controlled by the shear yield strength of the Mo. Smaller values of τ would be preferred for optimal composite performance.

Section 2

MECHANICS OF INTERFACES

Composites Science and Technology **42** (1991) 3–24

The Role of Interfaces in Fiber-Reinforced Brittle Matrix Composites

A. G. Evans, F. W. Zok & J. Davis

Materials Department, College of Engineering,
University of California, Santa Barbara, California 93106, USA

(Received 8 November 1990; accepted 25 January 1991)

ABSTRACT

The dominant influence of fiber coatings on the mechanical performance of brittle matrix composites is addressed. These effects are described in terms of two independent mechanical parameters, the debond energy, Γ_i, and the sliding resistance along the debond, τ. Complications associated with mode mixity, roughness and coating microstructure are emphasized. A mechanics of composite behavior based on these parameters is described, together with measurement approaches that allow Γ_i and τ to be evaluated either in situ *or in model composites. Key problems associated with fiber coatings are identified and discussed.*

NOMENCLATURE

a	Matrix flaw radius
d	Debond length
D	Matrix crack spacing
E	Longitudinal modulus of composites, $fE_f + (1-f)E_m$
E_f	Young's modulus of fiber
E_m	Young's modulus of matrix
f	Fiber volume fraction
$\mathcal{G}_{tip}$	Energy release rate at crack tip
h	Fiber pull-out length
H	Roughness amplitude
J	J integral

J_R Material resistance
l Wavelength of roughness
L_b Bridging zone length
L_c Roughness related contact zone size
L_0 Scale parameter
m Shape parameter
p Longitudinal residual stress in matrix
P Load
q Residual stress normal to interface
R Fiber radius
S_b Fiber bundle strength
S_0 Scale parameter for fiber strength
u Crack opening displacement
α Elastic mismatch parameter
Γ 'Composite' fracture energy, $\Gamma = f\Gamma_f + (1-f)\Gamma_m$
Γ_f Fracture energy of fibers
Γ_i Interface fracture energy
Γ_m Fracture energy of matrix
Γ_o Mode I fracture energy of interface
δ Displacement
ε_T Misfit strain
μ Friction coefficient
ν Poisson's ratio
$\bar{\sigma}_i$ Debond interaction stress on fiber
σ_o Matrix cracking stress
$\bar{\sigma}_p$ Peak stress on fiber
σ_u Ultimate tensile strength
τ Interface sliding stress

1 INTRODUCTION

Interfaces have a dominant effect on the mechanical properties of brittle matrix composites, such as fiber-reinforced ceramics, glasses and intermetallics. Generally, for enhanced crack growth resistance, the interface between the fiber and the matrix must be 'weak'. Indeed, 'weak' interfaces are a prerequisite for attainment of fracture resistances that appreciably exceed those of the matrix, whereupon frictional dissipation along the debonded interfaces becomes the primary source of enhanced 'toughness'. Conversely, creep resistance is enhanced by having a 'strong' interface. Consequently, a *rigorous* definition of 'weak' and 'strong' needs to be established for interfaces of interest. Thermochemical and thermomechanical consider-

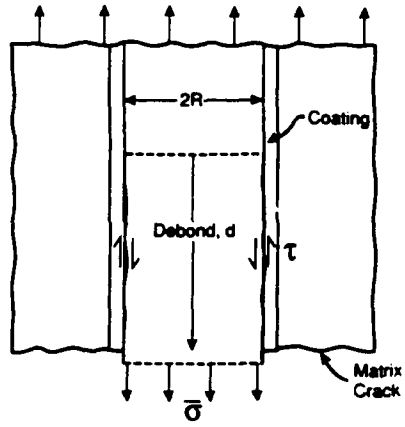

Fig. 1. A typical 'interface' in a brittle matrix composite: (a) schematic illustration showing a debond crack formed following matrix cracking; (b) the LAS/Nicalon system, with debonding within the carbon layer caused by thermal expansion misfit.

ations usually dictate that the 'interface' consists of one or more thin coatings between the fiber and matrix. Also, in some cases, a reaction product layer forms during processing. A typical 'interface' is depicted in Fig. 1. The intent of the present article is to provide a framework for expressing and characterizing the mechanical response of interfaces and relating these to the properties of brittle matrix composites. With this objective, various nondimensional parameters are identified and their role described. These include (Table 1): an elastic mismatch parameter, α; debond parameter, $\mathscr{D}$; matrix cracking parameters, $\mathscr{M}$ and $\mathscr{R}$; a pull-out parameter, $\mathscr{H}$; and an interface roughness parameter, χ.

The fracture properties of brittle matrix composites are governed by *matrix cracking*, followed by interaction of these cracks with the fibers and interfaces.[1-4] Such interactions have been found to involve two independent interface mechanical parameters: the *debond fracture energy*, Γ_i, and the *sliding resistance along the debond*, τ.[4-6] The role of these parameters in

TABLE 1
A Summary of Prominent Non-dimensional Parameters

Initial debonding	$\mathscr{D} = \Gamma_i/\Gamma_f$
Thermal cracking	$\mathscr{R} = RE_m\varepsilon_T^2/\Gamma_m$
Matrix cracking	$\mathscr{M} = \sigma_c/fS_b$
Pull-out	$\mathscr{H} = (\tau f\bar{h}/R)\sqrt{L_b/\Gamma_m E_m}$
Interface roughness	$\chi = EH^2/\Gamma_o$
Elastic mismatch	$\alpha = (E_f - E_m)/(E_f + E_m)$
Debond propagation	$G = \Gamma_i/ER\varepsilon_T^2$
Interface separation	$\Sigma_p = \sigma_p/E\varepsilon_T$

composite behavior is emphasized and relationships between Γ_i, τ, and the microstructure of the interfaces are described. A specific focus of this article will be on the longitudinal properties of unidirectional composites. While such properties are only a small subset of the array of properties that govern the performance of the composite, they represent a *prerequisite* for brittle matrix composites having attractive structural characteristics. Notably, brittle matrix composites are only of structural interest when unidirectional material exhibits relative insensitivity to the presence of notches and holes.

The use of Γ_i as a characterizing parameter for the interface is predicated on the mechanics of interface cracks.[7] It has been demonstrated that such cracks can be represented by a combination of two parameters, an energy release rate, $\mathcal{G}$, and a mode mixity angle, ψ (defined such that $\psi = 0$ for opening, mode I, cracks and $\psi = \pi/2$ for shear, mode II, cracks). These parameters are, in turn, influenced by elastic mismatch parameters: the more important mismatch parameter α, is defined as[7,8]

$$\alpha = (\bar{E}_1 - \bar{E}_2)/(\bar{E}_1 + \bar{E}_2) \tag{1}$$

where $\bar{E}$ is the plane strain modulus, $E/(1-\nu^2)$, with E being Young's modulus and ν the Poisson ratio; the subscripts 1 and 2 refer to the two materials. Given the mismatch α, both $\mathcal{G}$ and ψ relate explicitly to the stress and displacement fields near the crack tip and can be calculated for any loading and geometry by well-established numerical procedures.[9-11] With this capability for determining $\mathcal{G}(\psi)$, it has been found that interface debonding occurs when $\mathcal{G}$ reaches a critical value, designated the debond fracture energy, Γ_i. An important complication, however, is that Γ_i usually depends on ψ, through various crack/microstructure interactions.[7,12,13]

The sliding resistance of a debonded interface has not been rigorously studied, but progress has been made by using friction concepts to establish a phenomenological basis for progress. The sliding resistance has thus been expressed as[14]

$$\begin{aligned} \tau &= \tau_0 - \mu q \qquad (q < 0) \\ \tau &= \tau_0 \qquad\qquad (q \geq 0) \end{aligned} \tag{2}$$

where q is the stress normal to the interface, μ is the friction coefficient and τ_0 is the sliding resistance when q is positive (tensile).

2 COMPOSITE BEHAVIOR

Unidirectional brittle matrix composites have characteristics that generally fit into three classes, as distinguished by their tensile load/deflection

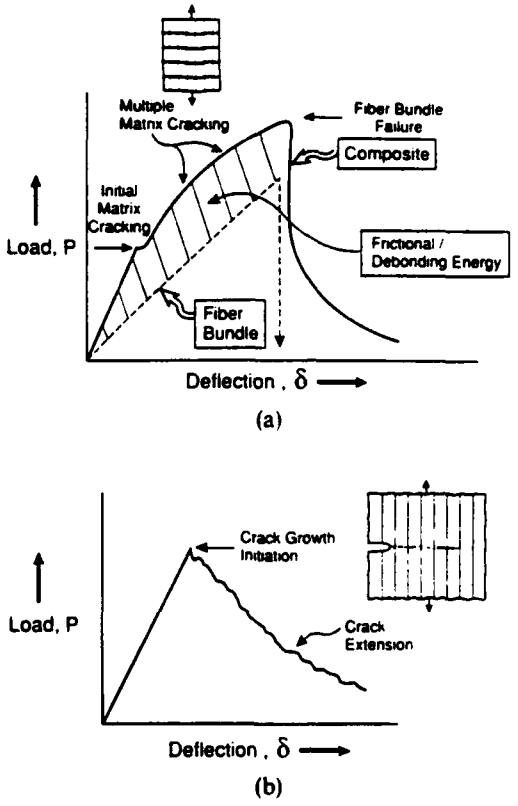

Fig. 2. Load/deflection curves and fracture behavior of unidirectional ceramic matrix composites: (a) Class I materials; (b) Class II materials. The cross-hatched area represents the energy per unit volume that goes into multiple matrix cracking, interface debonding and frictional sliding; the latter is typically the major contribution.

response and their fracture behavior (Fig. 2). Class I materials are deemed 'tough' and exhibit nonlinear behavior up to an ultimate load, which occurs at tensile strains of ~0·5–1%. A load drop occurs at the ultimate, followed by a long 'tail'. Such materials exhibit damage in the form of multiple matrix cracking and their behavior up to the ultimate load can be described through continuum damage mechanics (CDM), which is based on the mechanics of matrix cracking.[1,5,15,16] Class II materials are linear up to a load maximum, followed by a monotonically decreasing load upon continued deformation. Such behavior arises from domination by a single mode I crack.[17] The distinction between Class I and Class II materials is shown to be primarily governed by the sliding properties of the interface and the resulting effects on fiber failure. Class III materials are also linear up to a load maximum, but fail catastrophically. In these materials, the fiber/matrix interface is sufficiently 'strong' that debonding during matrix cracking is precluded.

2.1 Debonding

The first interface property of importance is the ratio[6]

$$\mathscr{D} = \Gamma_i/\Gamma_f \tag{3}$$

where Γ_i is the mixed-mode interfacial fracture energy (at $\psi \approx \pi/4$) and Γ_f is the mode I fracture energy of the fiber. This ratio dictates whether cracks that first form in the matrix either cause interface debonding (Class I/II) or propagate through the interface into the fiber (Class III). Plane strain calculations and experiments have demonstrated that debonding occurs provided that $\mathscr{D}$ is less than a critical value $\mathscr{D}_c$.[6,18] This critical value depends on both the elastic mismatch, α, and the inclination between the matrix crack and the interface. Trends in $\mathscr{D}_c$ with α are summarized in Fig. 3a. (The debonding calculations have been conducted for small putative cracks subject to plane strain. They then apply with equal facility to debonding in laminates, as well as the debonding of fibers in a matrix.)[6] A typical debonding observation when $\mathscr{D} < \mathscr{D}_c$ is presented in Fig. 3b. When the debonding condition is satisfied, the composite exhibits 'toughness', in accordance with the load/deflection characteristics depicted in Fig. 2a and b. Conversely, when the debonding condition is not satisfied, composite fracture occurs catastrophically. Consequently, for brittle matrix composites, a 'weak' interface is defined as one for which $\mathscr{D} < \mathscr{D}_c$.

2.2 Matrix cracking

While interface debonding is a prerequisite for obtaining high toughness in brittle matrix composites, the debonding can either adversely or beneficially influence the evolution of matrix cracks. Other important variables in this connection are the fracture energy of the matrix, Γ_m, and the mismatch strain between fiber and matrix, ε_T (as governed by the thermal expansion mismatch and by matrix phase transformations).

When debonding does not occur, $\mathscr{D} > \mathscr{D}_c$, the cracking stress in a composite subject to longitudinal tension is given by

$$\sigma_o = \sqrt{\frac{\Gamma E}{\pi a}} \tag{4}$$

where $2a$ is the diameter of the largest matrix flaw and Γ is the fracture energy. A typical fracture surface of such a composite material (Fig. 4) indicates that the fracture is coplanar, with no beneficial effect imparted by the fibres (unless $\Gamma_f \gg \Gamma_m$). The above result is obtained when the matrix flaws are large relative to the fiber spacing. Such behavior is similar to that

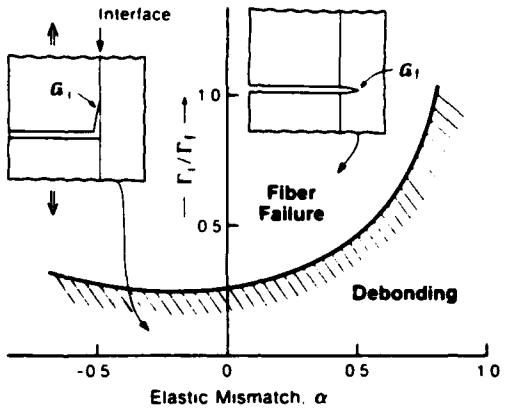

(a)

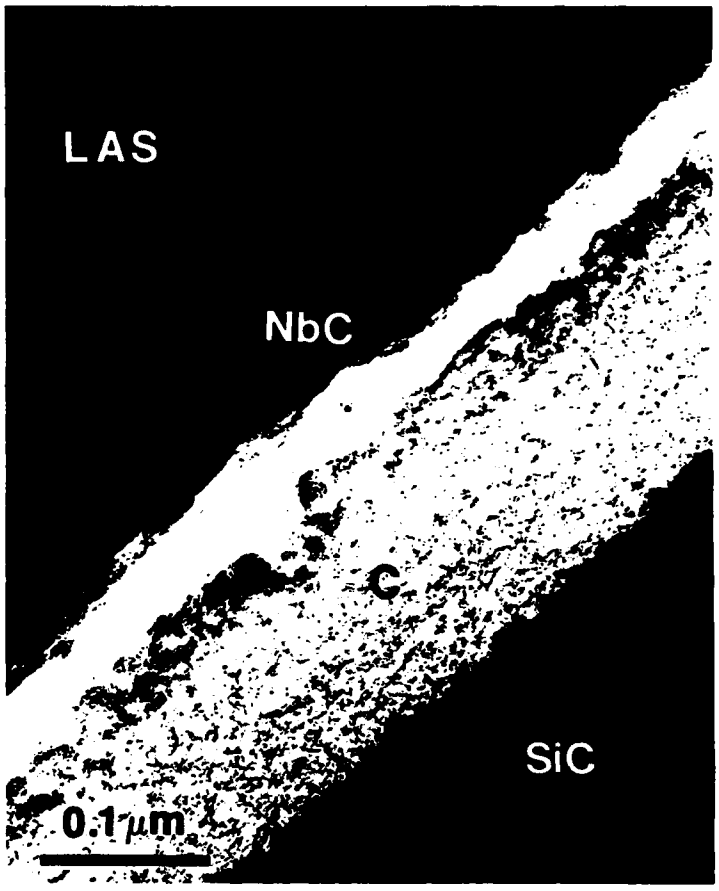

(b)

Fig. 3. Debonding in fiber-reinforced brittle matrix composites: (a) debond diagram, (b) debonding in a carbon coating between a Nicalon fiber and an aluminosilicate matrix.

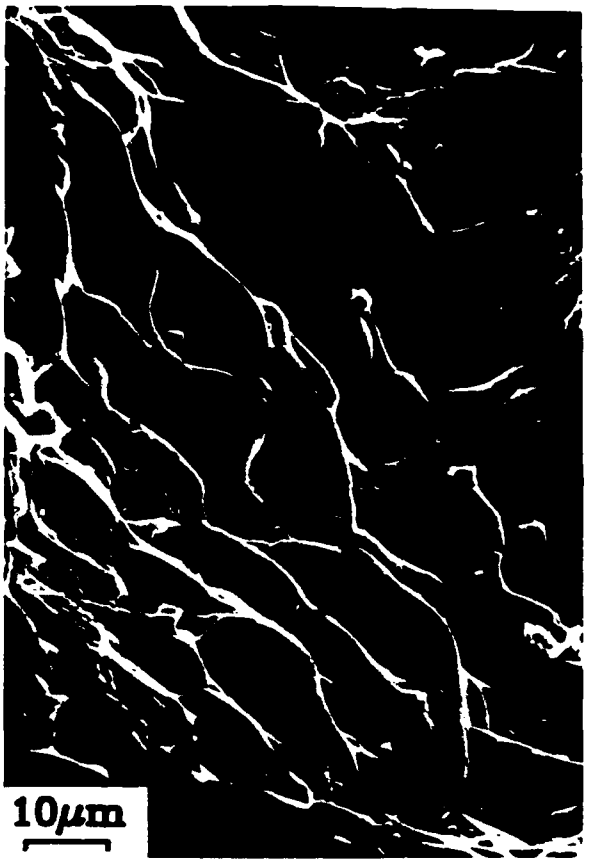

Fig. 4. A fracture surface for the case $\mathscr{D} > \mathscr{D}_c$: silica matrix with Nicalon fibers.

encountered in monolithic ceramics and intermetallics, in the sense that toughness is still low and the cracking stress is sensitive to flaw size.

When debonding occurs ($\mathscr{D} < \mathscr{D}_c$), the matrix cracking stress depends on both the interface sliding stress, τ, and the debond energy, Γ_i. A lower bound to the steady-state matrix cracking stress is given by,[5]

$$\sigma_o = \left[\frac{6\tau\Gamma_m f^2 E_f E^2}{(1-f)E_m^2 R}\right]^{1/3} - pE/E_m \tag{5}$$

where R is the fiber radius and p is the longitudinal residual tension in the matrix. Equation (5) applies in the limit $\mathscr{D} \to 0$, as well as when the matrix crack length exceeds a critical length (typically about 5–10 fiber spacings) and when $\sigma_o \gtrsim fS_b$. The first requirement, $\mathscr{D} \to 0$, ensures that Γ_i is sufficiently small that it does not contribute to σ_o;[14] the second requirement dictates that the matrix crack be large enough to interact with many fibers before becoming unstable;[15] and the third requirement ensures that only a

small fraction of the fibers fail as the matrix crack extends, resulting in Class I behavior.

A range of glass and ceramic matrix composites reinforced with SiC fibers[3] that have either carbon or BN fiber coatings exhibit longitudinal properties in good accordance with eqn (5). Specifically, the first matrix cracks, as well as nonlinearities in the stress/strain curves are observed at stresses about equal to σ_o. At stresses above σ_o multiple matrix cracking proceeds and eventually saturates at a spacing, d. Final fracture occurs at a stress, $\sigma_u \approx fS_b$, leading to the stress/strain characteristics depicted in Fig. 2(a). Both carbon and BN coatings seemingly have the attribute that $\mathscr{Q} \approx 0$ and τ is small (mostly in the range 2–20 MPa, depending on q), such that the conditions needed for eqn (5) to operate are satisfied. When other fiber coatings are used, such as oxides or metals, τ tends to be larger, often leading to a Class II behavior.[17]

The preceding analysis suggests that a distinction between Class I and Class II behavior can be made in terms of a matrix cracking parameter,

$$\mathscr{M} = \frac{\sigma_o}{fS_b} \tag{6}$$

Notably, Class I behavior is obtained when $\mathscr{M} < \mathscr{M}_c$. For this case, $\mathscr{M}_c$ is of order unity for unnotched specimens. In the presence of notches, $\mathscr{M}_c$ decreases with an increase in notch length. When τ is large, such that $\mathscr{M} > \mathscr{M}_c$, Class II behavior prevails, wherein a single mode I matrix crack propagates and simultaneously induces fiber failure.[17,19] However, fiber failure does not normally occur at the matrix crack plane (Fig. 5). Consequently, fiber pull-out occurs, leading to a corresponding increase in fracture resistance with crack extension (Fig. 6).

The important issues pertaining to the resistance curve include the effects of large-scale bridging (LSB) and the fiber pull-out length, $\bar{h}$.[19,20] In materials that have attractive mechanical properties ($\bar{h}/R \gtrsim 5$), the following considerations usually pertain. For short cracks ($\gtrsim 1$ mm), the crack opening displacements are small compared with $\bar{h}$.[17] Consequently, the tractions σ_b on the crack are approximately

$$\sigma_b \approx \frac{2\tau f\bar{h}}{R} \tag{7}$$

These tractions can be used to simulate the nominal resistance curve, taking account of the finite specimen geometry and associated LSB effects, as illustrated in Fig. 6. The enhancement of fracture resistance due to pull-out is characterized by the parameter

$$\mathscr{H} = \frac{\tau f\bar{h}}{R}\sqrt{\frac{L_b}{\Gamma_m E_m}} \tag{8}$$

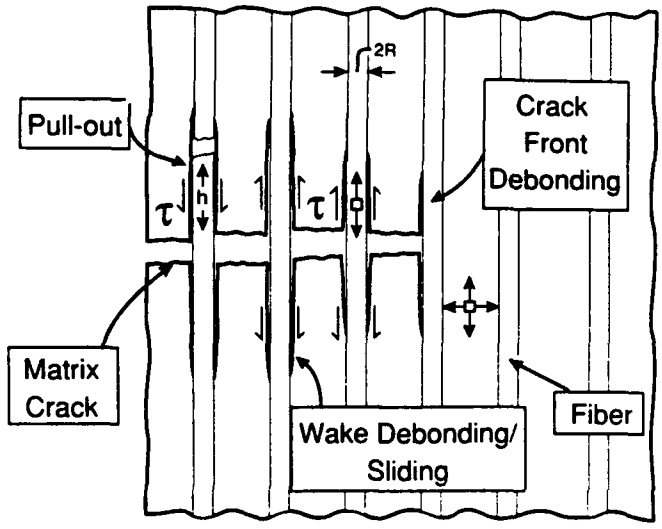

(a)

(b)

Fig. 5. A mode I crack in a brittle matrix composite subject to fiber failure and pull-out: (a) schematic; (b) observations on a LAS/Nicalon composite for two different crack extensions. The arrows identify the fiber failure sites.

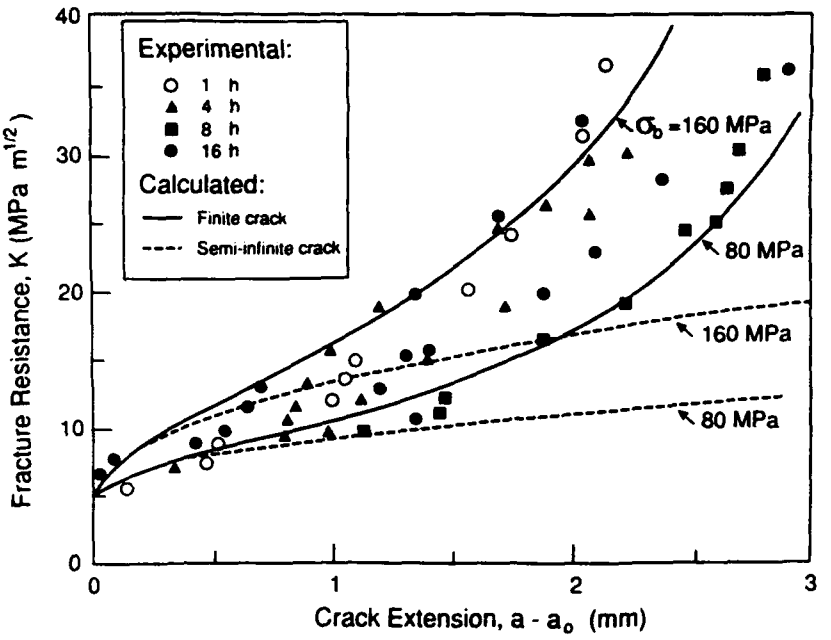

Fig. 6. Mode I fracture resistance curves for a LAS/Nicalon composite following heat treatment at 800°C for times indicated in the legend. Also shown are the simulated curves.

where L_b is the bridging zone length. The magnitude of $\mathscr{H}$ can be related to either the resistance curve or the load/displacement curve, in accordance with the procedure indicated in Fig. 7. An important question concerns the dependence of $\bar{h}$ on material properties. An analysis based on weakest link statistics predicts the scaling[19]

$$\bar{h} \approx [S_0 R L_0^{1/m}/\tau]^{m/(m+1)} \tag{9}$$

where m is the shape parameter, and S_0 and L_0 are scale parameters for the fiber strength distribution, such that $\mathscr{H}$ takes the form

$$\mathscr{H} = f\left(\frac{L_0\tau}{R}\right)^{1/(m+1)} \sqrt{\frac{L_b}{\Gamma_m E_m}}\, S_0^{m/(m+1)} \tag{10}$$

The notable feature is that $\mathscr{H}$ increases with τ at a rate determined by m. However, for typical values of m ($\sim$2 to 4), the sensitivity to τ is small. This trend has been tentatively validated by experiments on glass ceramic matrix composites,[17] but the analysis requires additional experimental assessment.

An additional consequence of eqn (5) occurs when q is sufficiently large that $\sigma_o \to 0$. Matrix cracks then form *during processing*, as a result of thermal

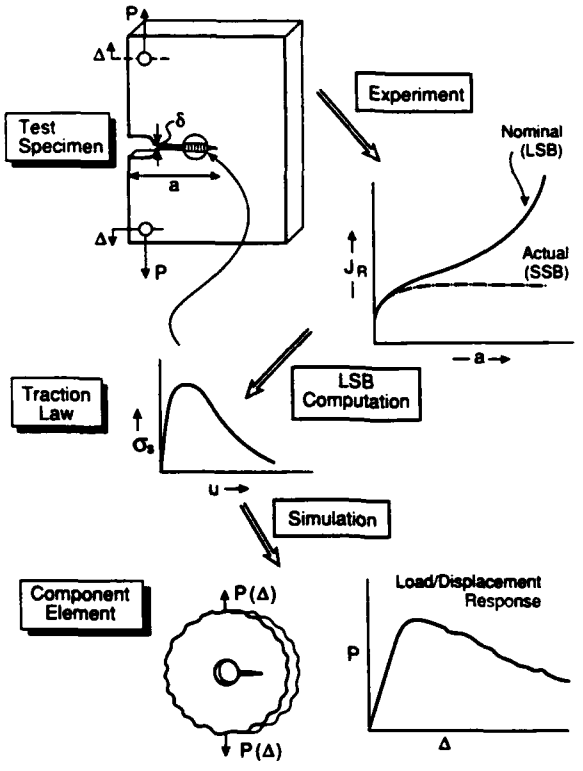

Fig. 7. Procedure for measuring the crack surface tractions and relating to the load/deflection properties of composite structures.

expansion mismatch. The allowable misfit can be expressed through a parameter $\mathscr{R}$, defined as[20]

$$\mathscr{R} = RE_m\varepsilon_T^2/\Gamma_m \tag{11}$$

such that *longitudinal* matrix cracks (also referred to as z-cracks) occur in the absence of applied loads when $\mathscr{R}$ is greater than a critical value $\mathscr{R}_c$. The magnitude of $\mathscr{R}_c$ depends on both the fiber volume fraction and the interface friction coefficient, μ, but is typically of order unity.

3 INTERFACE PROPERTIES

As already described, the 'interface' in brittle matrix fiber composites consists of one or more thin coatings and/or matrix reaction product layers (Fig. 1). The first role of the fiber coating is *thermochemical.* This objective requires that the coating prevent reactions with the fibers from occurring

during composite processing. The second role of the coating is *thermomechanical*. The coating must allow debonding to occur ($\mathscr{D} < \mathscr{D}_c$), control τ (such that the pull-out length, $\bar{h}$, is in a useful range for high toughness) and must also prevent fiber degradation. The thermomechanical issues are addressed in this article. To limit the scope of the discussion, it is noted that there are only two commercially-available fiber materials that satisfy matrix cracking requirements ($\mathscr{R} < \mathscr{R}_c$) in viable ceramic, glass and intermetallic matrix composites. These are Al_2O_3 and SiC. For these fibers, observations have indicated that the coatings can be classified into four groups:[13] (i) ductile coatings that do not debond; (ii) ductile coatings that debond; (iii) brittle coatings that debond at one interface, and (iv) brittle coatings that debond within the coating. The emphasis here is on the latter two, because these are most representative of the coatings that have application at elevated temperatures, although a combination of coatings may prove to be more effective in some cases.

3.1 Mechanics of debonding and sliding

The debonding problem of most interest in brittle matrix composites involves mixity in the range, $\pi/4 < \psi \lesssim \pi/2$. In this range, when brittle coatings are used, sliding and debonding are typically interrelated. For elastic systems, the criterion used to characterize debonding is $\mathscr{G}_{tip} = \Gamma_o$, where Γ_o is the critical value of the crack tip strain energy release rate.[7,21,22] This premise is also used here, but it is emphasized that there has been no direct experimental validation for fiber coatings. For $\psi > 0$, the apparent interface fracture energy $\Gamma_i > \Gamma_o$, because of shielding. The most likely shielding mechanism for brittle coatings on brittle fibers in a brittle matrix involves asperity contact when the debond is non-planar.[23] Analysis of such shielding identifies a nondimensional roughness parameter

$$\chi = EH^2/l\Gamma_o \tag{12}$$

where H is the amplitude and l the wavelength of the roughness.

A comprehensive mechanics of debonding and sliding in fiber composites resides in knowledge of the size of the roughness induced contact zone, L_c, compared with the debond length, d. For cases wherein $L_c \ll d$, small-scale contact conditions apply and debonding can be addressed as an elasticity problem, which entails evaluating $\mathscr{G}(\psi)$ and equating to $\Gamma_i(\psi)$.[21] Conversely, for large-scale contact, $L_c \to d$, the mechanics are nonlinear and are addressed by allowing sliding over the contact zone, while also requiring that $\mathscr{G}_{tip} = \Gamma_o$.[14] For brittle matrix composites, the latter approach is usually more appropriate and has been used to model the sequential phenomena of

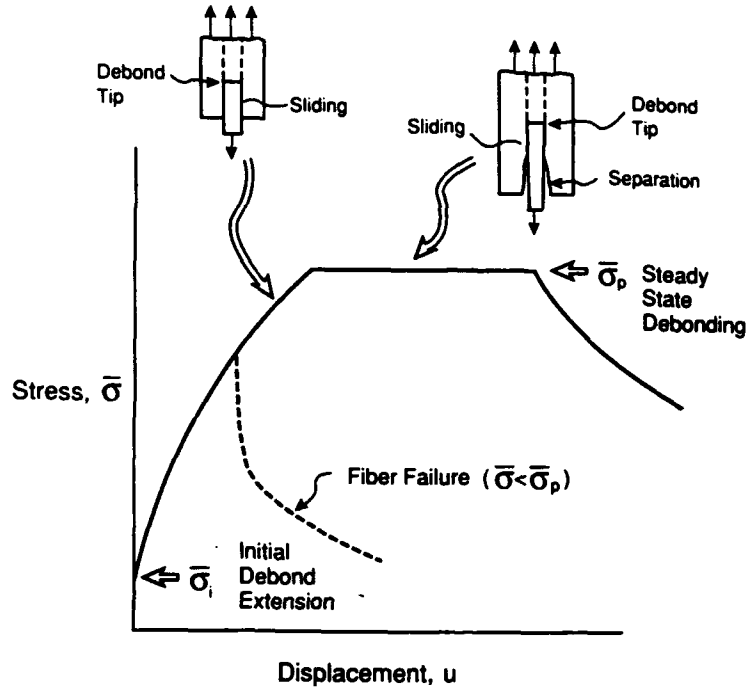

Fig. 8. A schematic fiber pull-out curve indicating the various nondimensional parameters that govern the process.

wake debonding and sliding, followed by fiber failure and pull-out. The basic characteristics are summarized in Fig. 8 for a composite in which the misfit causes the interface to be in residual compression. The details are governed by six nondimensional parameters: $\Sigma = \bar{\sigma}/E\varepsilon_T$, $\Sigma_p = \bar{\sigma}_p/E\varepsilon_T$, $\Sigma_i = \bar{\sigma}_i/E\varepsilon_T$, $G = \Gamma_i/ER\varepsilon_T^2$, $T = \tau/E\varepsilon_T$, $\nabla = u/R\varepsilon_T$, where $\bar{\sigma}$ is the stress on the fiber between the crack faces, with the subscript i referring to debond initiation and p to the peak stress, as illustrated in Fig. 8. These nondimensional parameters characterize the debond initiation stress, $\bar{\sigma}_i$, the peak stress, $\bar{\sigma}_p$, and the crack opening, u. These quantities in turn, can be used to determine complete expressions for the matrix cracking stress, σ_o (the magnitude of σ_o given in eqn (5) applies for $\mathscr{D} \to 0$), as well as the pull-out contribution to the crack extension resistance. Explicit formulae applicable when $E = E_m = E_f$ are:

$$\Sigma_p = f/v \tag{13a}$$

$$\Sigma_i = G^{1/2}/c_1 - c_2/c_1 \tag{13b}$$

$$\nabla = b_2\left\{\frac{(1-f)G^{1/2}\Sigma_p}{(f)c_1c_2T} + \frac{\Sigma_p^2}{4f^2T} + \frac{(1-f)}{2fc_3}\left[\frac{\Sigma}{T} - \frac{\Sigma_i}{T}\right]\left[\Sigma_p\left(\frac{1}{f} - a_1\right) + a_2\right]\right\} \tag{13c}$$

where c_i, b_i and a_i are coefficients of order unity tabulated by Hutchinson and Jensen.[14]

The physical picture that underlies these formulae is as follows. As the load is applied to the fibers, debonding proceeds in conjunction with frictional sliding, such that a nonlinear stress/displacement relation is obtained. The initial debond stress (at zero displacement) is determined by Γ_i, whereas the slope of the curve is governed primarily by τ. At a stress $\bar{\sigma}_p$, Poisson contraction of the fiber causes the interface to separate near the matrix crack and further debonding and sliding occur at constant load. For most brittle matrix composites, fiber cracks occur before σ_p is reached, as indicated by the dashed curve in Fig. 8. Fiber cracking is followed by a load drop and a pull-out tail. The latter is governed by τ and the pull-out length, $\bar{h}$, as discussed earlier. It is noted here that, for purposes of simulating the mode I fracture resistance of Class I composites, the behavior at small crack opening displacements is found to be most important.

3.2 Measurement methods

3.2.1 In situ

The properties of interfaces within actual composites have been assessed by several different approaches, with the objective of separately determining τ and Γ_i. Each method relies on measurements of load and displacements and then uses a model to infer the interface properties. Experience has identified those approaches which provide information most consistent with the overall mechanical properties of the composite. These approaches are emphasized here.

For Class I materials, τ can be estimated from the saturation crack spacing, D, using [1,3]

$$\tau \approx (1-f)[\Gamma_m E_f E_m R^2/fED^3]^{1/2} \tag{14}$$

Some typical values of τ obtained with this approach are summarized in Table 2. The table also provides a comparison between the values of the matrix cracking stress, σ_o, predicted by using τ in eqn (4) and the measured values. Confidence in the method is provided by this consistency check. For these materials, a more rigorous evaluation of τ involves measuring the matrix crack opening displacement, u, as a function of applied stress, whereupon τ is uniquely related to the hysteresis in u between loading and unloading.[2,4] These measurements can also be used to obtain the residual stresses. Finally, τ can be obtained on individual fibers from push-through measurements.[22,24] Evaluation of Γ_i is more difficult; in principle, Γ_i can be determined from the load/displacement measurements obtained following

TABLE 2
Properties of Typical Unidirectional Class I Ceramic and Glass Matrix Composites (All with Nicalon Fibers and C Interfaces)

Matrix	τ (*MPa*)	σ_0 (*MPa*)	
		Calculated	*Measured*
LAS (ceramic)	2·0	270–310	290 ± 20
LAS (glass)	7·0	240–300	240 ± 20
CAS	9·0	140–160	160 ± 20
Aluminosilicate	9·0	240–290	240 ± 20
Soda lime glass	12·0	-30 to -70	<0

matrix cracking (eqn 13(c)), as well as from push-through tests. However, this capability has not been verified.

For Class II materials, a more sophisticated measurement capability is needed to obtain τ and Γ_i. In some cases, push-through tests can be used, but a limitation is imposed by the size of the indentation compared with the fiber diameter. More generally, τ could be evaluated from the opening profile of a model I matrix crack, subject to a measurement method that provides sufficient displacement resolution (in the order 0·01 μm). An estimate of τ can also be obtained from the distribution of fiber pull-out lengths.[25] A good in-situ method for evaluating Γ_i has not been devised. Tests conducted on 'model composites' have been used to infer this information.

3.2.2 Model systems

Experiments to obtain τ and Γ_i have been conducted by using relatively large diameter Al_2O_3 or SiC fibers ($R \gtrsim 50\,\mu$m) embedded in various matrices. Fiber coatings and appropriate heat treatments, which can drastically alter the interface morphology, may be used to approximate the interfaces present in actual composites. In this case, single fiber pull-out and push-through tests can be used (Fig. 9(a) and (b)), wherein the load on the fiber and the relative displacement between the fibers and matrix are measured. Subject to independent knowledge of the residual stress and the elastic properties, the pull-out analysis[14] allows both τ and Γ_i to be determined for $\Psi \approx \pi/2$. Both τ and Γ_i can be determined from a single test. However, there are major difficulties associated with producing the specimens and successfully introducing sharp precracks at the interface. The major limitation of the push-through test arises because the interface is axially compressed during loading and large loads are needed, especially when τ becomes large (> 10 MPa).[4]

Other test methods can be used to determine Γ_i at $\Psi \approx \pi/4$ (a phase angle

of importance for establishing $\mathcal{Q}$, as outlined in Section 2.1). A mixed-mode flexure test[26] and a modified Hertzian indentation test (Fig. 9(c) and (d))[27] are particularly useful in that the samples are easily produced and the tests are relatively simple to perform. In addition, these tests are not restricted to interfaces with small τ. Thus, the fracture resistance of a greater number of interfaces can be obtained. These specimens can be produced by a method which includes coating planar matrix and fiber substrates and diffusion bonding in a sandwich geometry. Each of these tests has the obvious disadvantage that it cannot be used to determine τ. However, both are good screening tests to establish debonding in systems of interest and to identify useful fiber coatings. To date, much of the information pertaining to fracture properties of interfaces, shown in Fig. 10 and Table 3, has been obtained using such tests.

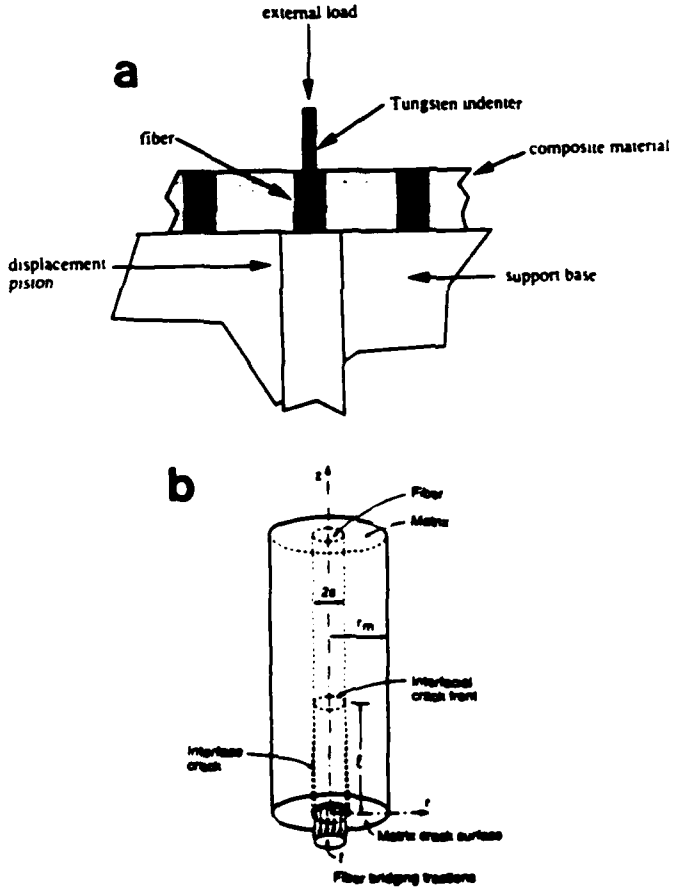

Fig. 9. Schematics of test specimens used to evaluate the mechanical properties of interfaces: (a) fiber push-through; (b) fiber pull-out.

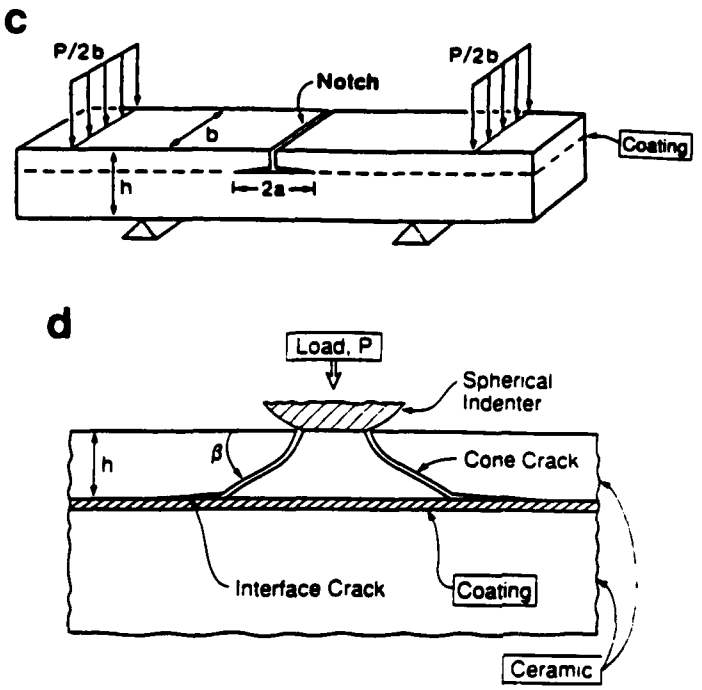

Fig. 9—*contd.* (c) mixed-mode flexure; (d) interfacial cone crack.

TABLE 3
Summary of Sapphire Fiber Coatings and Their Observed Properties

Coating	*Debonding*	*Stability*	*Interphase reaction with Al_2O_3*
ZrO_2	possibly	good	no
Y_2O_3	possibly	good	yes
NiAl	no	poor	yes
TiAl	no	poor	yes
Mo	yes	poor	no
Nb	no	fair	no
Zr	yes	fair	yes
Cr	yes	fair	yes

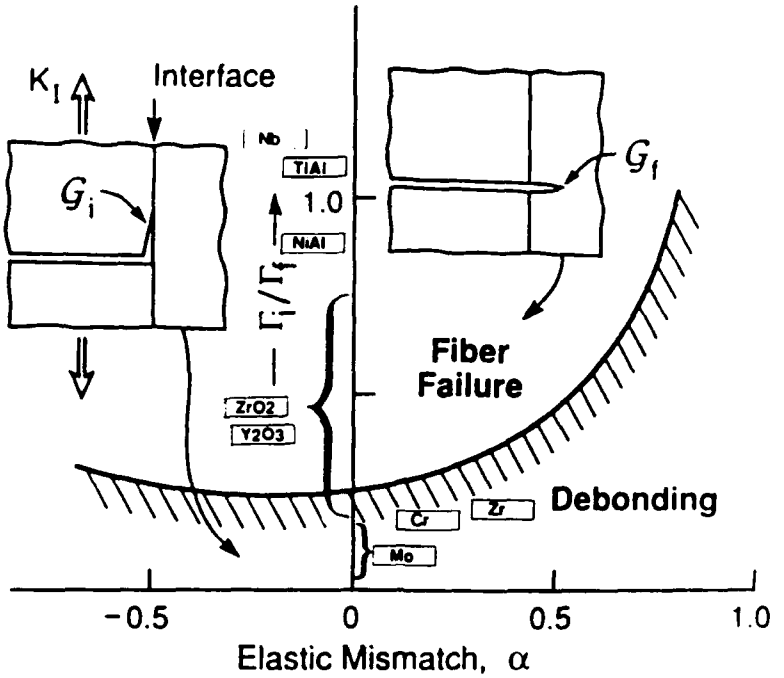

Fig. 10. Results of interface fracture energy measurements of various coatings on basal plane sapphire. The results are presented in terms of the coating's ability to satisfy the debond criterion.

3.3 Microstructural effects

For either SiC or Al_2O_3 fibers, relatively few coatings are known to satisfy debonding requirements, $\mathscr{D} < \mathscr{D}_c$, after the system has been subjected to the temperatures and pressures experienced upon composite processing. Interface debonding has only been definitely found for certain refractory metal coatings on Al_2O_3, especially molybdenum. These interfaces have a fracture energy $\Gamma_i \approx 2$–$5\,Jm^{-2}$ for $\psi \approx \pi/4$. Debonding within the coating has been found for carbon and BN coatings on SiC (Fig. 3(b)) with $\Gamma \approx 0{\cdot}1\,Jm^{-2}$, as well as for various highly-porous oxide coatings on Al_2O_3 (Fig. 11(a)). The latter requires porosities of $\sim 30\%$, whereupon $\Gamma \approx 3$–$16\,Jm^{-2}$, reflecting effects of porosity on the fracture energy of oxides. However, at sites where grains of the oxide coating are bonded to the Al_2O_3, thermal expansion misfit and/or phase transformations induce appreciable residual stress in the fiber (Fig. 11(b)), which can seriously degrade the fiber strength. Some glass coatings ($\Gamma = 4$–$8\,Jm^{-2}$) also allow debonding with both SiC and Al_2O_3 fibers.[18] The surface morphology of the fibers represents another important microstructural variable.[4] Surface roughness appears to have primary importance for the magnitude of the sliding stress.

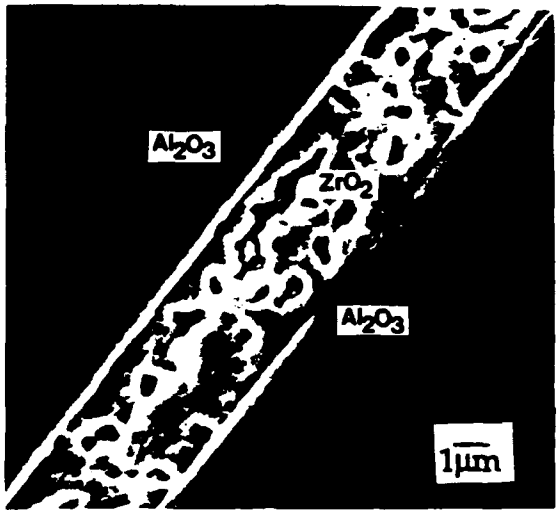

(a)

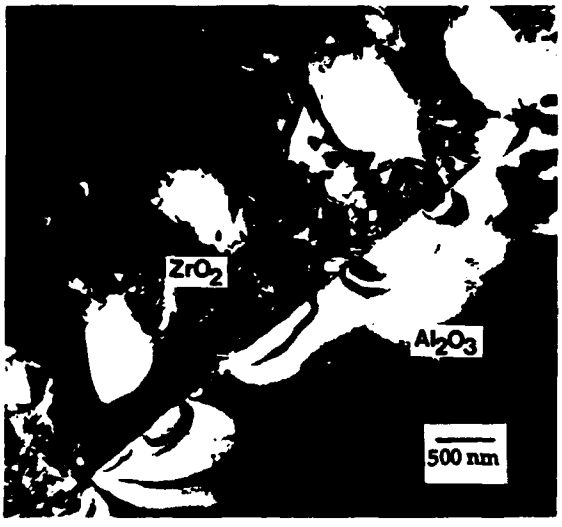

(b)

Fig. 11. (a) A porous ZrO_2 coating on Al_2O_3: debonding occurs within the coating. (b) A TEM view revealing residual stress in the Al_2O_3.

4 REMARKS

The basic role of interfaces in brittle matrix composites has been defined in a consistent manner, based on a mixity dependent debond energy, $\Gamma_i(\psi)$, and a sliding stress, τ. A fundamental mechanics of interface behavior in composites has been devised in terms of these parameters, including the

effects of interfaces on both distributed damage and discrete cracking. However, a number of important problems have yet to be solved by this approach: particularly, multiple matrix cracking in composites with complex architecture subject to multiaxial loads. Systematic progress on this issue is expected in the next several years.

The major problem in brittle matrix composites concerns fiber coatings that provide acceptable values of τ and Γ_i, subject to thermochemical compatibility requirements and the avoidance of fiber degradation. The material choices *known* to satisfy these requirements (carbon, BN, molybdenum) are *all* subject to oxidative degradation at high temperatures. Some porous oxide coatings that obviate this problem appear to provide an opportunity, but further research is needed concerning their influence on fiber strength and degradation, coupled with a study of their microstructural stability.

A fundamental chemical understanding that guides fiber coating development is lacking. Indeed, it seems ironic that the *avoidance* of debonding is a problem when coatings are deposited at low homologous temperatures, whereas the encouragement of debonding is a problem at elevated temperatures. The implication is that kinetic issues are of major importance, such that all fiber coatings which debond are non-reactive, *refractory* materials (C, BN, W, Mo) that only experience moderate homologous temperatures upon composite processing. Additional research is needed to explore this rationale for selecting fiber coatings.

The basic mechanics of interface debonding has been established, leading to an understanding that mixity effects are important and that plasticity as well as roughness has a central role in mixity effects. However, there is still no appreciation of the mechanisms whereby mode II debonding occurs and how this relates to material properties. Given that mode II debonding is a dominant phenomenon in brittle matrix composites, the mechanisms involved require systematic study. Finally, frictional sliding along debonded interfaces *within composites* needs to be more comprehensively addressed.

REFERENCES

1. Aveston, J., Cooper, G. A. & Kelly, A., The properties of fibre composites. *IPC Science and Technology Press*, London, 1971.
2. Marshall, D. B. & Evans, A. G., *J. Am. Ceram. Soc.*, **68** (1985) 225.
3. Cao, H. C., Bischoff, E., Sbaizero, O., Rühle, M., Evans, A. G., Marshall, D. B. & Brennan, J. J., *J. Am. Ceram. Soc.*, **73** (1990) 1691.
4. Evans, A. G. & Marshall, D. B., *Acta Metall.*, **37** (1989) 2567.
5. Budiansky, B., Hutchinson, J. W. & Evans, A. G., *J. Mech. Phys. Solids*, **2** (1986) 167.

6. He, M. Y. & Hutchinson, J. W., *Intl Jnl Solids Structures*, **25** (1989) 1053.
7. Hutchinson, J. W., *Metal/Ceramic Interfaces*, Pergamon Press, 1990, pp. 295–307.
8. Dundurs, J., *J. Appl. Mech.*, **36** (1969) 650.
9. Rice, J. R., *J. Appl. Mech.*, **55** (1988) 98.
10. Charalambides, P. G., Lund, J., McMeeking, R. M. & Evans, A. G., *J. Appl. Mech.*, **111** (1989) 77.
11. Charalambides, P. G. & Evans, A. G., *J. Am. Ceram. Soc.*, **72** (1989) 746.
12. Cao, H. C. & Evans, A. G., *Mech. Mtls*, **7** (1989) 295.
13. Evans, A. G., Rühle, M., Dalgleish, B. J. & Charalambides, P. G., *Mat. Sci. Eng.*, **A126** (1990) 53.
14. Hutchinson, J. W. & Jensen, H. M., *Mech. Mtls*, **9** (1990) 139.
15. Marshall, D. B., Cox, B. N. & Evans, A. G., *Acta Metall.*, **33** (1985) 2013.
16. McCartney, L. N., *Proc. Roy. Soc.*, **A409** (1987) 329.
17. Zok, F. W., Sbaizero, O., Hom, C. L. & Evans, A. G., *J. Am. Ceram. Soc.*, **74** (1991) 187.
18. Evans, A. G., He, M. Y. & Hutchinson, J. W., *J. Am. Ceram. Soc.*, **72** (1989) 2300.
19. Thouless, M. D. & Evans, A. G., *Acta Metall.*, **36** (1988) 517.
20. Lu, M. C., Suo, Z., Mehrabian, R., Hecht, R. J. & Evans, A. G., *Acta Metall. Mater.*, in press.
21. Jensen, H., Hutchinson, J. W. & Kim, K. S., *Intl J. Solids Structures*, **26** (1990) 1099.
22. Marshall, D. B. & Oliver, W., *J. Am. Ceram. Soc.*, **70** (1987) 542.
23. Evans, A. G. & Hutchinson, J. W., *Acta Metall.*, **37** (1989) 909.
24. Wiehs, T. P., Dick, C. M. & Nix, W. D., *Mat. Res. Soc. Proc.*, **120** (1988) 267.
25. Thouless, M. D., Sbaizero, O., Sigl, L. S. & Evans, A. G., *J. Am. Ceram. Soc.*, **72** (1989) 525.
26. Charalambides, P. G., Cao, H. C., Lund, J. & Evans, A. G., *Mech. Mtls*, **8** (1990) 269.
27. Davis, J. B., Cao, H. C., Bao, G. & Evans, A. G., *Acta Metall.*, (in press).

Acta metall. mater. Vol. 40, No. 6, pp. 1251–1257, 1992
Printed in Great Britain.

0956-7151/92 $5.00 + 0.00

EFFECTS OF FIBER ROUGHNESS ON INTERFACE SLIDING IN COMPOSITES

T. J. MACKIN, P. D. WARREN and A. G. EVANS

Materials Department, College of Engineering, University of California, Santa Barbara, CA 93106, U.S.A.

(Received 7 October 1991)

Abstract—The presence of asperities at the fiber–matrix interface is noted experimentally as a load rise during the initial stages of push-out and as a reseating load drop during push-back. These effects are modelled by considering the elastic deformation of asperities at the interface. During fiber sliding, the decorrelation of initially matching fiber and matrix geometries results in an asperity pressure at the interface. Fractal models of interface roughness are incorporated into an equation of fiber sliding that is found to accurately reproduce experimental observations. Additionally, an asperity wear mechanism must be introduced to explain the effects of fatigue, the variation of fiber reseating with sliding distance, and the rapid decay in sliding stress during pristine fiber push-out.

Résumé—La présence d'aspérités à l'interface fibre/matrice est constatée expérimentalement comme une élévation de charge pendant les stades initiaux de la poussée et comme une chute de charge pendant la poussée inverse. Ces effets sont modélisés en considérant la déformation élastique des aspérités à l'interface. Pendant le glissement des fibres, la décorrélation des géometries initialement assorties des fibres de la matrice conduisent à une pression d'aspérité à l'interface. Des modèles fractaux de la rugosité de l'interface sont incorporés dans l'équation du glissement des fibres qui reproduit avec précision les observations expérimentales. De plus, un mécanisme d'usure des aspérités doit être introduit pour expliquer les effets de la fatigue, la variation de remise en place de la fibre avec la distance de glissement, et la rapide décroissance de la contrainte de glissement pendant la première poussée sur la fibre.

Zusammenfassung—Rauhigkeiten an der Grenzfläche zwischen Faser und Matrix machen sich im Experiment als Anstieg der Last während der Anfangsphase des Ausziehens und als Lastabfall durch Wiedereinrasten während des Zurückschiebens bemerkbar. Diese Effekte werden modellhaft beschrieben, indem die elastische Verformung der Rauhigkeiten an der Grenzfläche beschrieben werden. Während des Gleitens der Faser führt das "Ausrasten" der ursprünglich passenden Faser- und Matrixgeometrien zu einem Druck durch die Rauhigkeiten an der Grenzfläche. Fraktale Modelle der Grenzflächenrauhigkeit werden in eine Gleichung der Fasergleitung eingebaut; es ergibt sich, daß diese die experimentellen Beobachtungen genau wiedergibt. Zusätzlich muß win Rauhigkeits-Abriebmechanismus eingeführt werden, um die Effekte der Ermüdung, der Variation des Einrastens der Faser mit dem Gleitweg und den raschen Abfall in der Gleitspannung während des vorausgegangenen Ausziehens der Faser erklären zu können.

1. INTRODUCTION

Fiber-reinforced composites gain much of their toughening from the frictional sliding of fibers [1–4]. Most descriptions of sliding have employed a sliding stress, τ, that does not incorporate the microscopic roughness of the sliding surfaces [5–7]. Recent experimental evidence, however, has elevated the role of interface roughness. In particular, certain features of fiber push-out and pull-out cannot be explained by the frictional sliding of smooth fibers. For example, after a fiber has been pushed through [Fig. 1(a)] or pulled out and returned to its original location, it experiences a reseating load drop [Fig. 1(b)] [8–11]. This load drop arises from the geometric memory of the fiber–matrix debond surface: the fiber and matrix geometries re-correlate in their original orientation. Furthermore, fiber push-out is often accompanied by an increasing load during the early stages of sliding [Fig. 1(a)] [7, 11]: a phenomenon which is also attributed to geometric decorrelation during fiber displacement. Additional evidence for roughness arises from effects associated with cyclic sliding during fatigue (Fig. 2) [11]. This article develops a simple model of fiber sliding that incorporates fiber roughness, which may be used to simulate and interpret fiber push-out and pull-out measurements. The model shows that the decorrelation of initially matching fiber and matrix geometries is seemingly responsible for many of the observed phenomena.

Jero *et al.* [8, 9] first noted the importance of fiber roughness and modelled its effect as an addition to the interfacial clamping pressure. They assumed that the fiber and matrix geometries, once removed from their original position, would create a uniform asperity pressure that simply adds to any existing clamping pressure. A more detailed analysis of asperity interactions was presented by Carter *et al.* [10] wherein asperity roughness is modelled as Hertzian contacts,

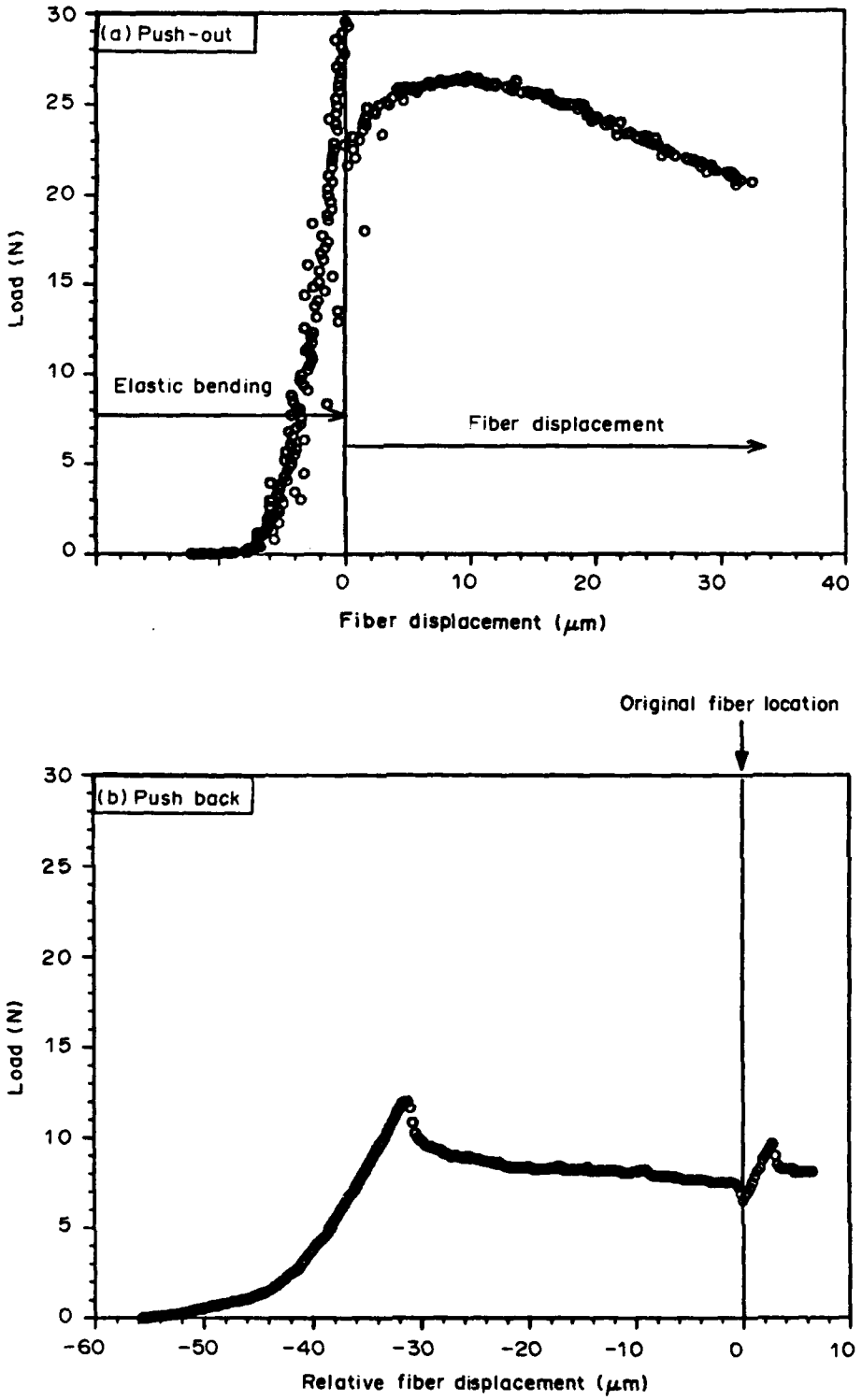

Fig. 1. Fiber push-out (a) and push-back (b) in a Ti(15-3)–SCS-6 composite. During fiber push-out, there is a notable increase in the sliding stress associated with the first few microns of fiber sliding. Note the reseating load drop associated with fiber push-back ($h = 410\ \mu m$).

leading to a sinusoidal modulation of the sliding stress. Kerans and Parthasarathy [12] include asperity pressure in a detailed treatment of fiber debonding and sliding during both push-out and pull-out experiments. They note that asperity pressure, due to roughness, plays an important role in fiber sliding. Additionally, Kerans and Parthasarathy [12] introduce discussion of abrasion during fiber sliding that would have implications during the sliding of fatigued fibers.

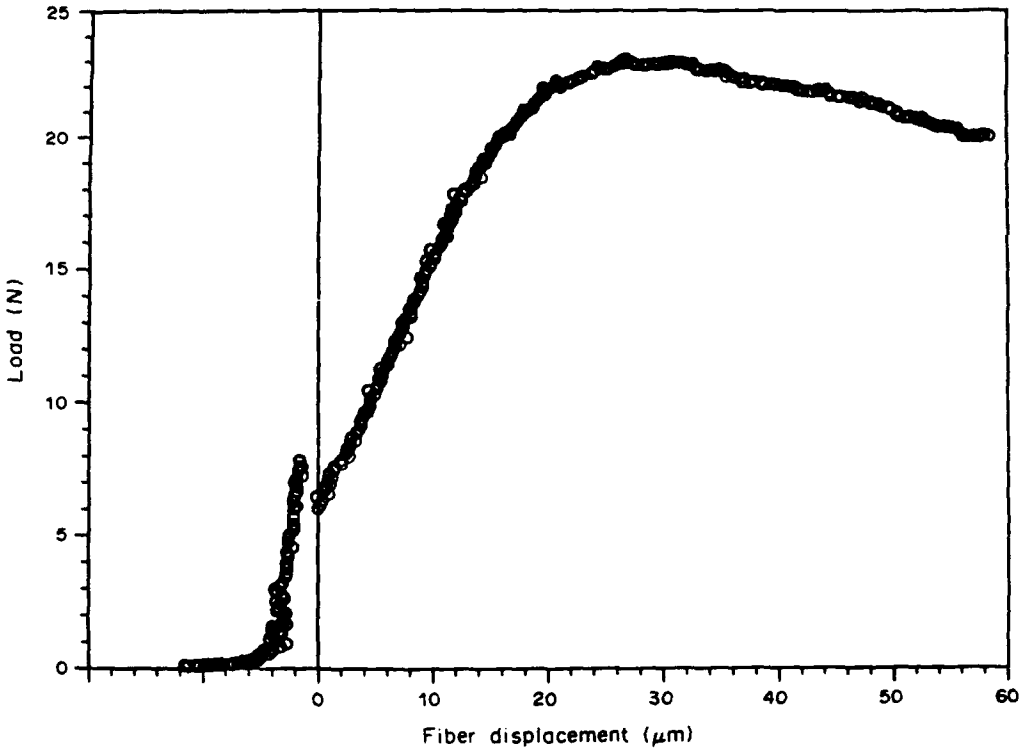

Fig. 2. Push-out for fatigued fibers ($h = 450\ \mu$m).

The present model considers an elastic asperity mismatch akin to that of Jero *et al.* [8, 9] but includes a full spectrum of fiber roughness, represented using fractal geometry. As such, computer simulations using this model illustrate all of the fundamental aspects of sliding along a rough, debonded interface, and directly demonstrate asperity effects during the sliding of both pristine and fatigued fibers.

2. SLIDING MECHANICS

Fiber sliding, in the absence of roughness, has been analyzed using a generalized sliding law [5, 13]

$$\tau = \tau_0 - \mu\sigma_r \tag{1}$$

where τ is the sliding stress, μ is a friction coefficient, σ_r is the compressive stress normal to the interface, and τ_0 is a constant sliding stress. When τ_0 and ϵ_T, the mismatch strain between fiber and matrix, are independent of location along the fiber, z, the push-out stress on the fiber, σ_u, is [5, 13]

$$\sigma_u = \frac{\sigma_0[\exp(2\mu Bt/R) - 1](1-f)}{[f(E_f/E_m)\exp(2\mu Bt/R) + 1 - f]} \tag{2}$$

where f is the fiber area fraction, E is Young's modulus, R the fiber radius, and t is the embedded length of the fiber (Fig. 3), with the subscripts f and m referring to fiber and matrix, respectively, and

$$B = vE[E_f(1+v) + E(1-v)]^{-1}$$

$$\sigma_0 = \frac{E_f\epsilon_T}{v} + \left(\frac{\tau_0}{\mu}\right)\frac{E}{BE_m(1-f)}$$

$$t = h - d$$

with v being Poisson's ratio (assumed to be the same for fiber and matrix), E is the composite modulus, h is the specimen thickness and d is the sliding distance of the fiber.

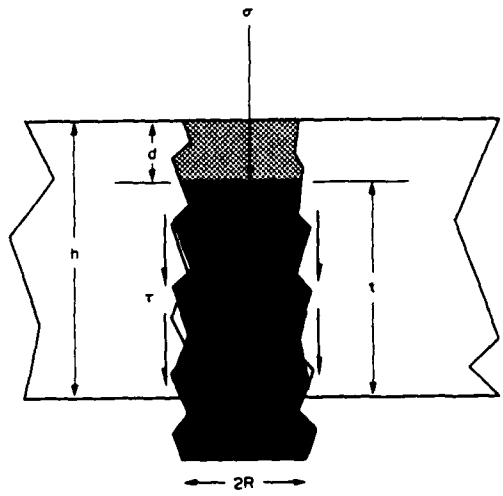

Fig. 3. Schematic of fiber sliding and the associated geometry.

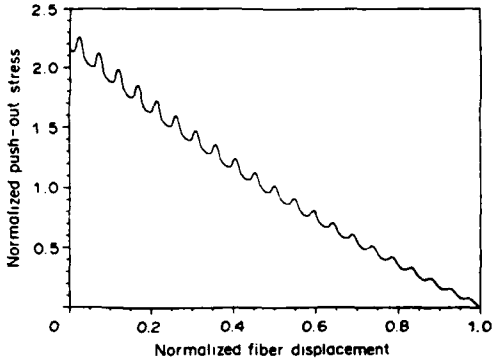

Fig. 4. A sinusoidal interface surface results in a similar modulation of the sliding stress.

When the misfit is *dependent* upon z, because of roughness along the debonded interface, the push-out stress is modified. For this purpose, ϵ_T is re-expressed as

$$\epsilon_T = \epsilon_a + \delta(z)/R \tag{3}$$

where ϵ_a is the thermal expansion misfit and $\delta(z)$ is the asperity mismatch between fiber and matrix along the embedded length of the fiber (Fig. 3). If the asperities are axisymmetric, the roughness leads to a local misfit strain, $\delta(z)/R$, at locations where asperities in the fiber and matrix slide past each other. In essence, the asperity induces an additional pressure, p, that determines τ_0: mechanistically arising from the geometric decorrelation of fiber and matrix during fiber sliding. As such, the interfacial shear stress presented in equation (1) is entirely Coulombic

$$\tau = \mu(\sigma_r + p) \tag{4}$$

with, $\tau_0 = -\mu p$. (Note that, because p is compressive, τ_0 is positive.)

For simplicity of presentation, roughness effects are demonstrated for the case of single fiber push-out with $\nu_f = \nu_m$ and small f, such that equation (2) reduces to

$$\sigma_u = \sigma_0 \exp(2\mu Bt/R - 1). \tag{5}$$

The integral of the asperity mismatch over the embedded length of the fiber provides the asperity pressure. Hence, the push-out stress given by equation (5) becomes

$$\sigma_u(d) = \frac{E\epsilon_a}{2B}[\exp(2\mu Bt/R(1 - d/t)) - 1] + (2E\mu/R^2)\exp(-2\mu Bd/R) \times \int_d^h [\exp(2\mu Bz/R)]\delta(z)\,dz \tag{6}$$

where d is the push-out distance (Fig. 3). Consequently, by specifying an interface roughness, $\delta(z)$, the push-out stress can be computed from equation (6).

3. SIMULATIONS

Fiber push-out simulations are conducted that address the push-out force *after the debonding load drop*. The roughness of the debonded interface is modelled using fractal algorithms with identical fractal profiles assigned to both sides of the debond. Once assigned, the profiles are compared at each sliding distance to determine a diametral mismatch, $\delta(z)$, at increments along the fiber length. Using equation (6), the resulting push-out stress is determined. The simulation methodology was tested by computing the push-out behavior of a fiber that has a single wavelength, axisymmetric, sinusoidal profile. For such roughness, a sinusoidal form is demonstrated in a push-out simulation (Fig. 4). More realistic fiber profiles were simulated using a fractal geometric technique known as fractional Brownian motion (*fBm*) [14–17], a technique that has found widespread use in the simulation of natural geometries. Evidence for the utility of *fBm* modelling is presented in Fig. 5, which compares the profile of an (SCS-6)SiC fiber, taken using a profilometer [Fig. 5(a)] with a fractal representation [Fig. 5(b)]. The use of fractal modelling enables controlled simulation of fiber "roughness," and, consequently, demonstrates the role of roughness in fiber sliding.

The following simulations relate to push-out curves measured on Ti alloy/(SCS-6)SiC fiber metal–matrix composite. These simulations, using known values of elastic moduli and roughness, are compared directly with experimental results [11]. The elastic constant, B in equation (6) was computed from the formulae of Hutchinson and Jensen [5]. Fiber roughness simulations were based upon a fractal analysis of SCS-6 fiber profiles, providing a profile fractal dimension of $D = 1.12$. The fiber and matrix surfaces were modelled as axisymmetric surfaces of revolution, resulting in a fiber surface dimension of 2.12. Profilometry of (SCS-6)SiC fibers indicated a roughness with a maximum amplitude of tenths of microns [Fig. 5(a)] and the fractal representations were scaled accordingly.

At the onset of fiber sliding, the fiber and matrix geometries are in perfect registry. Consequently, the roughness term vanishes from equation (6), resulting in an equation for smooth fiber push-out. Thus, a coefficient of friction was determined by matching theory and experiment at the point of initial sliding. This matching for the results on Ti/SiC (SCS-6) indicated that $\mu = 0.26$.

A typical set of simulations is illustrated in Fig. 6. Various behaviors are apparent, dependent on the roughness amplitude distribution sampled within the specimen section thickness. Most relevant is the frequent appearance of rising load portions of the push-out curve. This feature is observed experimentally (Fig. 1) and is at variance with the behavior expected for smooth fibers. Furthermore, the extent of the rise is consistent with that found by experiment, as illustrated in Fig. 7. After rising to a

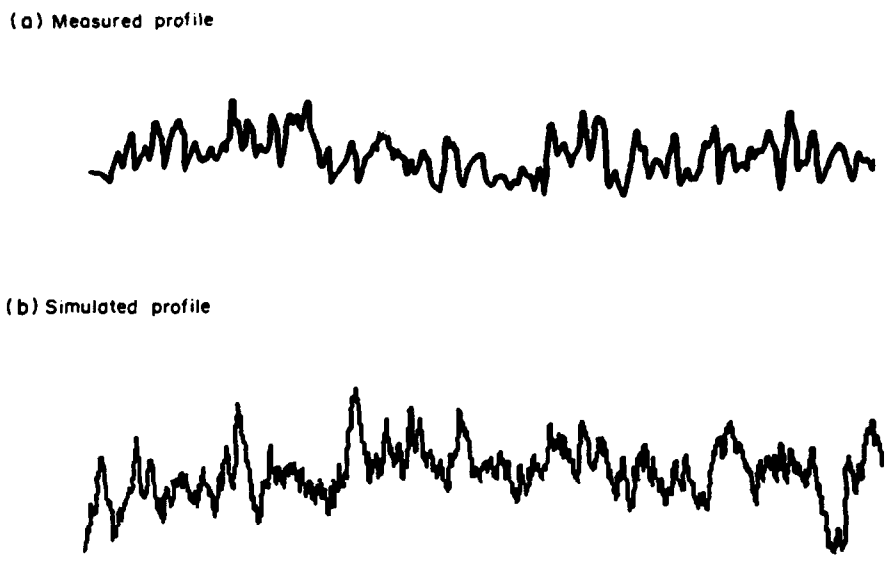

Fig. 5. Comparison of actual (a) and simulated (b) SCS-6 fiber profiles.

maximum, experimental push-outs experience a rapid decrease in the applied load. As shown in Fig. 7, simulated push-outs are found to consistently remain higher than experimental results. Such a rapid decrease in push-out load cannot be modelled without the introduction of interface wear, a process that will be discussed in connection with fiber reseating and fatigue. As expected, fibers having an interface roughness amplitude greater than that for SCS-6 fibers exhibit push-out curves with larger oscillations (Fig. 8).

Consistent with previous studies of push-out and pull-out, the push-out force is found to be strongly influenced by the friction coefficient over the full

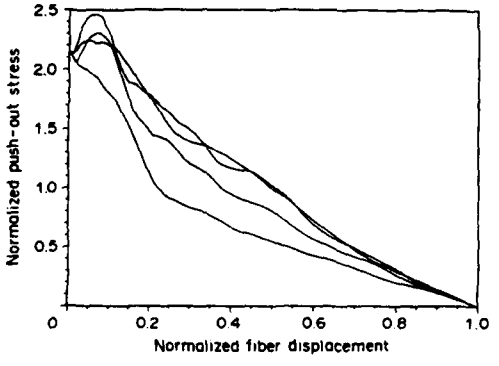

Fig. 6. Push-out simulations exhibit the same qualitative behavior as experimental push-outs. Each curve represents a random sampling from the roughness distribution.

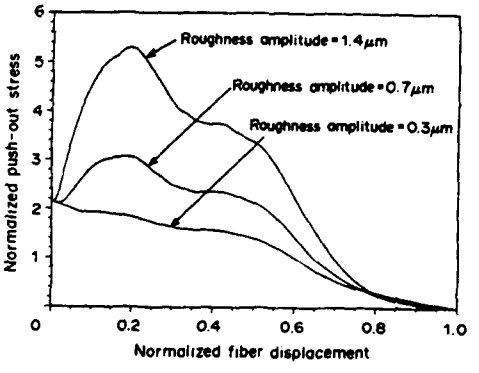

Fig. 8. An increase in roughness amplitude has a pronounced effect on fiber sliding.

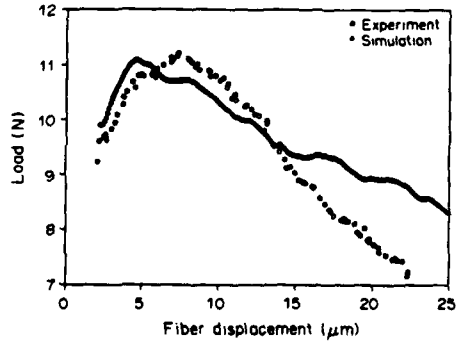

Fig. 7. Rough fiber push-out simulations resemble experimental results ($h = 210\ \mu m$).

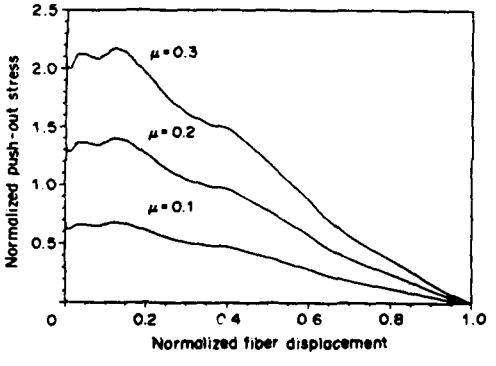

Fig. 9. An increase in the coefficient of friction, μ, increases fiber sliding stress.

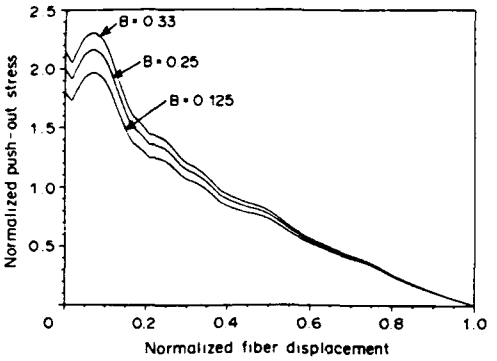

Fig. 10. An increase in the Poisson's ratio increases fiber sliding stress: B is a composite Poisson's ratio [equation (2)].

push-out distance (Fig. 9), but only moderately dependent on Poisson's ratio at initial push-through (Fig. 10). The effects of thermal expansion misfit are of particular interest (Fig. 11). As expected, the push-out force is reduced when the misfit is reduced, but is still finite when the misfit is reduced to zero. For zero misfit, the push-out curve is dependent *entirely on the roughness distribution*. Consequently, the shape of the curve changes when different segments of the roughness distribution are included in the specimen section (Fig. 11). The behavior, in essence, governs τ_0 in equation (1).

4. INTERFACE FATIGUE

Experiments on interfaces subject to cyclic siding in fatigue have revealed push-out behavior that departs significantly from that of their pristine counterparts [11] (Figs 1 and 2). The initial sliding stress of pre-fatigued fibers was much lower and, during subsequent push-out, was followed by substantial load increase, even though the embedded fiber length is decreasing as push-out proceeds. The low initial sliding stress is attributed to interface degradation during fatigue, while the subsequent increase in fiber stress arises from an asperity mismatch pressure. Thus, in addition to roughness, the simulation of fatigued fiber sliding requires interface wear.

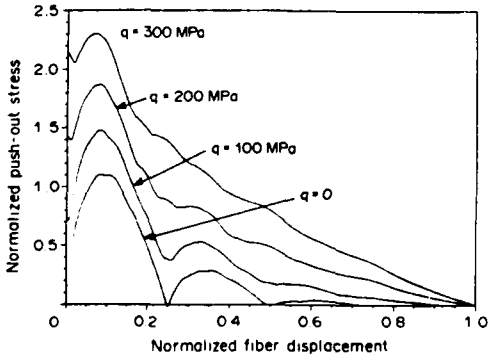

Fig. 11. A change in the thermal misfit at identical roughness changes both the character and magnitude of the sliding stress: q is the thermal expansion misfit stress, $q = E\epsilon_a$.

Fatigue degradation of the fiber–matrix interface was modelled in two ways: smoothing and fragmentation. The first simulation technique employs a low pass filter to eliminate chosen scales of roughness, akin to asperity wear. Profile filtering is performed on the Fourier spectrum of the profile, wherein a low pass cut-off frequency is chosen and the profile is reconstructed using only those wavelengths below the cut-off. In these simulations, only the fiber profile is smoothed, indicative of preferential wear at the fiber side of the interface. Consequently, the fiber and matrix no longer afford a perfect match, and small gaps form between the fiber and matrix. Asperity filtering, however, did not simulate the fatigued fiber push-out features found by experiment.

The second approach entails removing a thin shell of interface material from around the fiber, somewhat equivalent to relaxing the residual thermal stress, but permitting small gaps at the interface. The fragments formed by cyclic sliding are assumed to be removed from the interface and become relocated between the matrix crack surfaces. The results of these simulations (Fig. 12) exhibit correspondence with the experimental curves (Fig. 2). A reduction in interface sliding stress upon cyclic sliding caused by coating fragmentation thus appears to be the more plausible degradation mechanism.

5. FIBER RESEATING

Perhaps the most telling evidence of fiber geometry is that of fiber reseating [8–11]. This occurs when a fiber has been displaced within the matrix and then returned to its original location. As the fiber moves back into position, the reseating is accompanied by a considerable load drop. This phenomenon has been witnessed in at least two matrices containing (SCS-6)SiC fibers: Ti(15-3) and glass. The present simulation procedure is inherently reversible and *always* produces fiber reseating. Yet, experimental evidence suggests that the fiber is worn during sliding and that subsequent reseating is affected by the extent of sliding [11]. This effect can be simulated by introducing a wear mechanism that relaxes the clamping

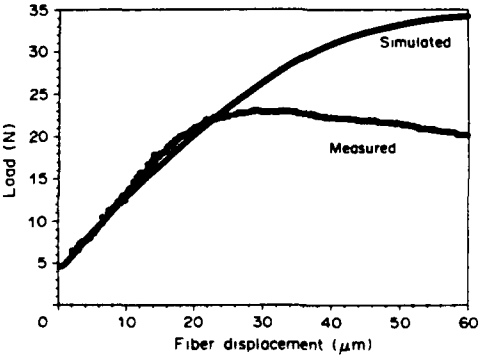

Fig. 12. Fatigue simulated by relaxing the misfit resembles experimental results.

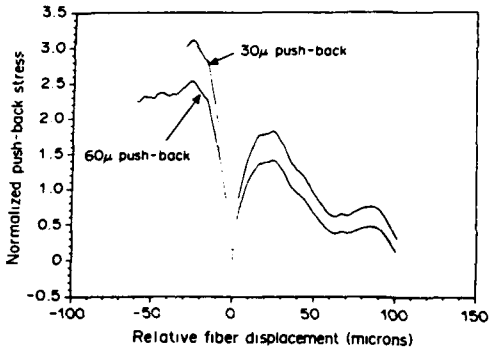

Fig. 13. Push-back reseating load drop is modelled by implementing a wear process during fiber sliding.

pressure on the fiber surface. For simplicity, the wear mechanism was modelled as a linear function, reducing the asperity pressure in direct proportion to the fiber sliding distance. Simulated push-back curves for two push-out distances (Fig. 13) exhibit the same features found in the experiments [11].

6. SUMMARY

A model of fiber sliding that incorporates the effect of interface roughness has been presented. The effect is analogous to an elastic shrink-fit due to geometric decorrelation of initially matching surfaces as asperities slide past each other. The subsequent asperity pressure contributes perturbations to the clamping pressure at the interface and generates sliding phenomena in general accordance with experimental observations. One important phenomenon is the increase in initial sliding stress, after debonding, often encountered in the presence of interface roughness. This increase is influenced by the amplitude of the roughness and its fractal characteristics. Such behavior could have a substantial effect on the incidence and location of fiber failure and hence, on the frictional contribution to the fracture resistance.

Another significant finding is the change in interface properties caused by cyclic sliding in fatigue. The push-out simulations are found to have the same form as the experimental measurements when the fiber coating is assumed to fragment and relax the thermal expansion misfit between fiber and matrix. Such fragmentation has been observed experimentally. This reduction in sliding stress would have the detrimental effect of accelerating fatigue crack growth [18].

REFERENCES

1. B. Budiansky, J. C. Amazigo and A. G. Evans, *J. Mech. Phys. Solids* **36**, 167 (1988).
2. L. R. F. Rose, *J. Mech. Phys. Solids* **35**, 383 (1987).
3. A. G. Evans and R. M. McMeeking, *Acta metall.* **34**, 2435 (1986).
4. D. B. Marshall and A. G. Evans, *J. Am. Ceram. Soc.* **68**, 225 (1985).
5. J. W. Hutchinson and H. M. Jensen, *Mech. Mater.* **9**, 139 (1990).
6. Y.-C. Gao, Y.-W. Mai and B. Cotterell, *J. appl. Math. Phys. (ZAMP)* **39**, 550 (1988).
7. J. D. Bright, S. Danchaivijit and D. K. Shetty, *J. Am. Ceram. Soc.* **74**, 115 (1991).
8. P. D. Jero and R. J. Kerans, *Scripta metall. mater.* In press.
9. P. D. Jero, R. J. Kerans and T. A. Parthasarathy, *J. Am. Ceram. Soc.* In press.
10. W. C. Carter, E. P. Butler and E. R. Fuller, *Scripta metall. mater.* **25**, 579 (1991).
11. P. D. Warren, T. J. Mackin and A. G. Evans, *Acta metall. mater.* **40**, 1243 (1992).
12. R. J. Kerans and T. A Parthasarathy, *J. Am. Ceram. Soc.* **74**, 1585 (1991).
13. J. W. Hutchinson, private communication.
14. B. B. Mandelbrot, *The Fractal Geometry of Nature*. W. H. Freeman, San Francisco, Calif. (1983).
15. *The Science of Fractal Images* (edited by H.-O. Peitgen and D. Saupe). Springer, Berlin (1988).
16. M. Barnsley, *Fractals Everywhere*. Academic Press, New York (1988).
17. J. Feder, *Fractals*. Plenum Press, New York (1988).
18. D. Walls, G. Bao and F. Zok, *Scripta metall. mater.* **25**, 911 (1991).

Acta metall. mater. Vol. 40, No. 6, pp. 1243–1249, 1992
Printed in Great Britain.

0956-7151/92 $5.00 + 0.00
Pergamon Press Ltd

DESIGN, ANALYSIS AND APPLICATION OF AN IMPROVED PUSH-THROUGH TEST FOR THE MEASUREMENT OF INTERFACE PROPERTIES IN COMPOSITES

P. D. WARREN, T. J. MACKIN and A. G. EVANS

Materials Department, College of Engineering, University of California, Santa Barbara, CA 93106-5050, U.S.A.

(Received 7 October 1991)

Abstract—An improved fiber push-through test has been designed and used to obtain new information about interfaces in composites consisting of matrices of a Ti alloy and a borosilicate glass, both reinforced with SiC fibers. Interpretation of these results is accomplished through an analysis of coupled debonding and push-through, followed by push-back. The sliding stress is found to vary with push-out distance and to be substantially reduced in the vicinity of a fatigue crack in the Ti matrix composite. These effects are attributed to asperity wear, matrix plasticity and fragmentation of the fiber coating around the debonded interface. Reseating effects on push-back have been demonstrated, but have been found to diminish as the relative fiber–matrix displacement increases. Fiber roughness has been identified as an important aspect of interface sliding.

Résumé—Un essai amélioré d'enfoncement des fibres est proposé et utilisé pour obtenir de nouvelles informations sur les interfaces dans des composites formés de matrices en alliage de titane et en verre au borosilicate, toutes deux renforcées par de fibres de SiC. L'interprétation de ces résultats est effectuée par une analyse de la séparation et de l'enfoncement couplés, suivi d'une poussée en sens inverse. On trouve que la contrainte de glissement varie avec la distance d'enfoncement et qu'elle est rèduite considérablement au voisinage d'une fissure de fatigue dans le composite à matrice de titane. Ces effets sont attribués à l'usure des aspérités, à la plasticité de la matrice et à la fragmentation du revêtement des fibres autour de la surface de séparation. Des effets de remise en place lors de la poussée en sens inverse sont observés, mais ils diminuent lorsque le déplacement relatif fibre/matrice augmente. On montre que la rugosité de la fibre est un aspect important du glissement interfacial.

Zusammenfassung—Ein verbesserter Faser-Durchstoß-Test wird entworfen und angewandt, um neue Informationen über Grenzflächen in Verbundwerkstoffen zu erhalten. deren Matrix entweder aus einer Ti-Legierung oder einem Borsilikat-Glas, beide verstärkt mit SiC-Fasern, besteht. Mit einer Analyse der gekoppelten Prozesse Ablösen und Durchstoßen, gefolgt von Zurückschieben, werden diese Ergebnisse interpretiert. Die Gleitungsspannung ändert sich mit der Ausziehlänge und ist in der Nähe eines Ermüdungsrisses in dem Werkstoff mit Ti-Matrix beträchtlich verringert. Diese Einflüsse werden dem Abrieb, der Plastizität in der Matrix und dem Bruch des Faserüberzugs im abgelösten Grenzflächenbereich zugeschrieben. Effekte der Wiedereinlagerung beim Zurückschieben werden gefunden, sie verschwinden aber mit steigender relativer Verschiebung zwischen Faser und Matrix. Es wird gezeigt, daß die Faserrauhigkeit ein wichtiger Aspekt der Grenzflächengleitung ist.

1. INTRODUCTION

Fiber push-through tests have been widely exploited as an approach for measuring the sliding properties of fiber–matrix interfaces in composite materials [1–5]. The advantages of this method include relative simplicity in testing and a capability for conducting experiments at elevated temperatures [6]. The disadvantages are concerned with interpretation of the measurements, because of relatively complex deformations that occur during the loading and sliding processes. The first intent of the present study is to provide a further development of the push-through test, in conjunction with an analysis that allows determination of the interface sliding stress, τ. The second objective is to apply the technique to interfaces between SiC (SCS-6) fibers and a β-Ti (15-3-3) alloy matrix, before and after fatigue crack growth [7], as well as interfaces between SiC (SCS-6) fibers and a borosilicate–glass matrix.

Previous studies on the push-through test have relied primarily on the peak load for initial push-through as a measure of "debonding." Push-back has been used to provide a measure of the sliding stress, τ, along the debonded interface. The magnitude of τ has been calculated from the force, P, and displacement, d, from the expression

$$\tau = P/2\pi R(h - d) \quad (1)$$

where R is the fiber radius and h is the section thickness. More comprehensive analysis of coupled debonding and sliding [8, 9] during push-through allows substantial additional information to be gained from push-through and push-back tests when appropriately modified and instrumented. Solutions for pull-out [8] and push-through [9] for coupled debonding and sliding have been characterized by a debond energy, Γ_i, a sliding stress, τ, and a thermal expansion misfit strain, ϵ_T. Some of the salient results are summarized, as needed to relate the push-through force, P, to the displacement, d, in terms of τ and ϵ_T. The basic solutions are described in terms of a friction law

$$\tau = \tau_0 - \mu\sigma_r \tag{2}$$

where μ is the friction coefficient and σ_r is the compressive stress normal to the interface. During initial push-through, stable debonding proceeds with frictional sliding occurring behind the debond tip. This is followed by a load drop and push-out resisted by friction. Results are presented for the following conditions: (i) the Poisson's ratio of the fiber and matrix are the same, (ii) the misfit strain in the axial and radial directions are the same and, (iii) the radial stress is zero at the outer boundary (Type I conditions) [8, 9].

The load–displacement behavior during debonding is sensitive to the *initial* debond length which, in turn, is affected by the sectioning process and the misfit strain. However, after the debond has propagated completely along the interface, since there is no contribution from debonding, the load, P, becomes

$$\frac{P}{\pi R^2} = \frac{\hat{\sigma}_0[\exp(2\mu Bt/R) - 1]}{1 + \left[\frac{f}{(1-f)}\frac{E_f}{E_m}\right]\exp\left(\frac{2\mu Bt}{R}\right)} \tag{3}$$

where

$$\hat{\sigma}_0 = \frac{E_f\epsilon_T}{\nu} + \frac{\tau_0}{\mu}\frac{E/E_m}{B(1-f)}$$

$$B = \nu E/[(1+\nu)E_f + (1-\nu)E]$$

with E being Young's modulus, ν Poisson's ratio and $t = h - d$,† with the subscripts m and f referring to matrix and fiber, respectively. For the special case, $\mu = 0$, equation (4) reduces to equation (1) with $\tau = \tau_0$, whereupon P decreases linearly with d. However, when $\mu \neq 0$, P is slightly non-linear. This general solution has been implemented in a companion paper [10] to predict the effect of fiber roughness and of misfit on the push-out force. The results will be invoked in this article to interpret some of the experimental measurements.

†It should be noted that f in these formulae is *not* the fiber volume fraction, but rather the ratio

$$f = \frac{\text{area of fiber}}{\text{total area of composite}}.$$

This implies that f is always small (typically 10^{-4}).

2. PUSH-THROUGH TEST

2.1. Design

For fibers having either a relatively large diameter or large values of Γ_i and/or τ, substantial forces are needed to displace the fibers. In such cases, the indenter design and the loading arrangement needed to obtain useful information are particularly important. Many previous studies have used sharp indentors that penetrate the fiber. Two problems arise: (i) at high loads, cracks are introduced into the fibers that can influence the measurements; (ii) at moderate displacements, the indentor comes into contact with the matrix, curtailing further measurements. To obviate these problems, cylindrical indentors are preferred and used in conjunction with the apparatus schematically illustrated in Fig. 1. The test is performed by preparing a thin section of the composite. This section is located on an Al alloy base containing a 220 μm diameter hole, with the fiber of interest placed over the hole. A small SiC cylinder, 100 μm diameter, is emplaced on the fiber *ex situ* in an optical microscope. A small rod located within the hole is maintained in intimate contact with the fiber and connected to a cantilever beam with an attached strain gauge. This device measures the displacement at the bottom of the fiber during push-through. Loads are applied to the indentor through a flat Al_2O_3 plate connected to a load cell, which monitors the force, P. This system can be located within a furnace for high-temperature measurements. Two additional features of this design are noted. The use of a relatively small diameter hole minimizes bending stresses. However, loads are limited to ~40N, because at larger loads, either cone cracks form in the SiC fibers or the SiC indentor fractures.

2.2. Materials and specimens

Tests were conducted on composites consisting of (SCS-6, CVD) SiC fibers in either a Ti alloy (Ti–15V–3 Al) or a borosilicate glass (Corning 7741) matrices. The elastic and thermal properties of the specimens are listed in Table 1. In both cases, specimens were ground and polished with a final 1 μm diamond finish. Two different specimen thicknesses

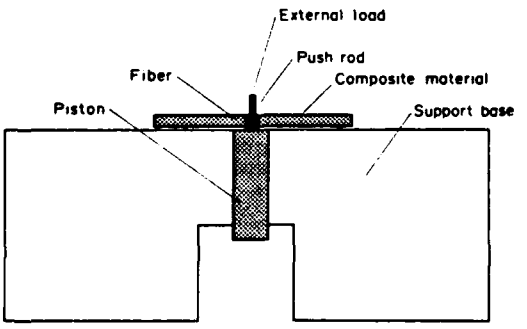

Fig. 1. Schematic diagram of the fiber push-through apparatus.

Table 1. Properties of the two matrices

	Ti-15-3/SiC	Glass/SiC
Modulus, E_m	115 GPa	70 GPa
Composite modulus, E	196 GPa	70 GPa
Poisson's ratio, ν_m	0.33	0.20
Thermal expansion coefficient, α_m	7.6×10^{-6}°C^{-1}	3.25×10^{-6}°C^{-1}
Thermal mismatch strain, ϵ_T	4.5×10^{-3}	7.0×10^{-4}
Radial thermal mismatch stress, σ_R	−300 MPa	−60 MPa
Volume fraction of fibers, ρ	0.35	6.8×10^{-4}
Area of fiber/area of specimen, f	4.5×10^{-4}	6.8×10^{-4}
Fiber properties		
Modulus E_f	360 GPa	
Poisson's ratio, ν_f	0.17	
Thermal expansion coefficient, α_f	2.6×10^{-6}°C^{-1}	

were used for each composite: 210 and 410 μm for the Ti alloy, 1.5 and 2.1 mm for the glass. Fibers were pushed out to a range of displacements up to 80 μm and then pushed back. The loads and deflections were continuously monitored. Some tests were conducted on the Ti alloy matrix composite which had been subjected to fatigue cracking at a stress amplitude $\Delta\sigma = 300$ MPa and an R ratio = 0.1 [7]. This fatigue schedule lead to matrix crack-growth without fiber failure. A push-through specimen was prepared from a 450 μm thick section of material parallel to the matrix fatigue crack (Fig. 2). Tests were conducted on fibers at different locations relative to the fatigue crack front.

3. RESULTS

3.1. Pristine materials

A variety of experimental results have been obtained. Typical results obtained on pristine material are presented in Figs 3 and 4. An increase in load occurs associated with elastic bending and stable debonding. A load drop, ΔP, often accompanies debond pop-through. The magnitude of ΔP increases as the section thickness increases (Table 2). This load drop may be used to estimate the intefacial debond energy (see Appendix). Frequently, an initial rise in load is found following pop-through, for the first 2–3 μm of fiber displacement. This is followed by a load that usually diminishes as the push-through displacement increases. Upon push-back, the load at which fiber displacements resume, P_s (Fig. 4), is usually somewhat smaller than the termination load upon push-through, P_1. Thereafter, the load remains essentially constant until the fiber reaches the original location. At that location, there is a small load drop, ΔP_d, associated with the fiber reseating into its initial position, as observed in previous studies [3, 4]. The relative load drop, $\Delta P_d/P$. usually decreases as the initial push-through distance increases (Table 2).

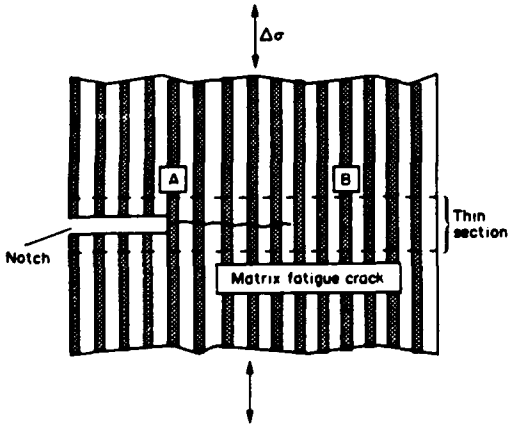

Fig. 2. Schematic of the fatigue specimen showing the notch root and fatigue crack growing from the root. The fibers are perpendicular to the fatigue crack, with a center–center spacing ≈250 μm.

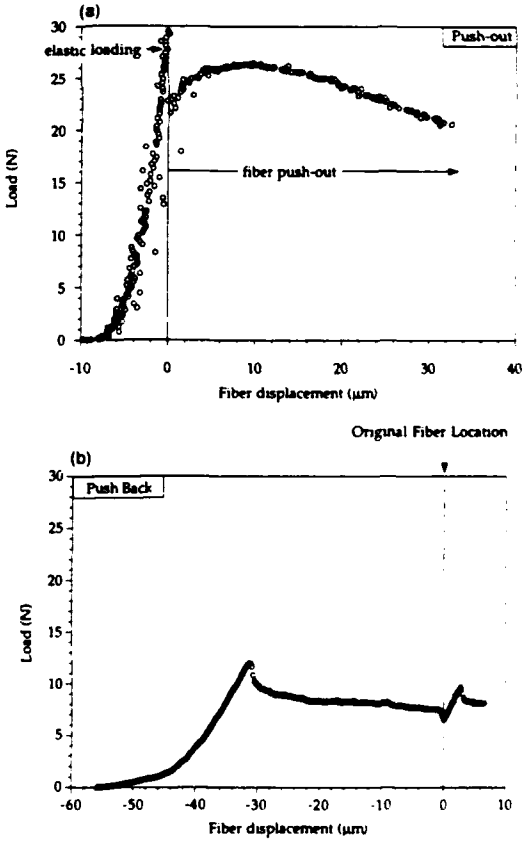

Fig. 3. Two examples of force–displacement results for push-through and push-back on the Ti-15-3/SiC material (specimen thickness 410 μm).

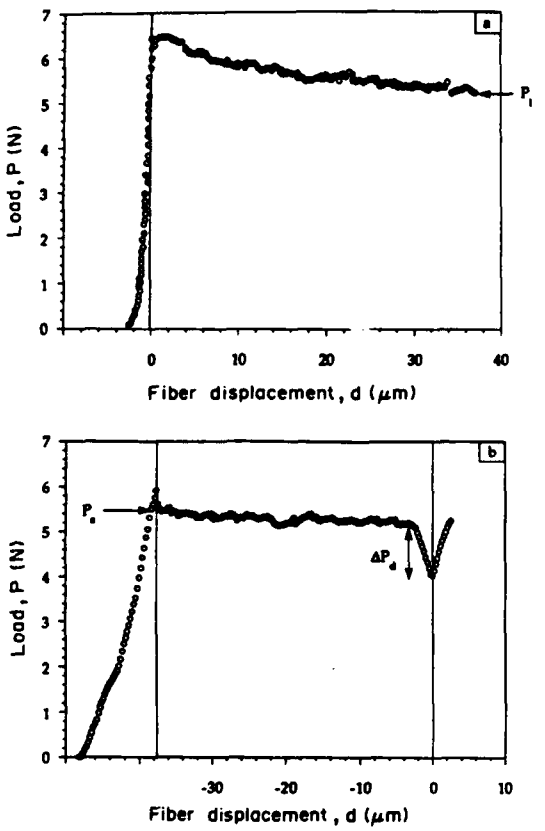

Fig. 4. Force–displacement results for push-through and push-back of the glass/SiC material (specimen thickness 1.5 mm).

A comparison of the results for the two different matrices reveal important differences. The Ti matrix composite exhibits, (i) consistently larger value of the push-out force, (ii) a substantially larger push-through load drop, ΔP, and (iii) greater differences in the relative push-back force, P_s/P_i. Also, the relative load decrease that occurs as the push-out process proceeds is larger for the Ti matrix composite. Conversely, the relative reseating load drop, $\Delta P_d/P$, is larger for the glass matrix system.

Observations of fibers following initial push-through using scanning electron microscopy (SEM) indicated that sliding in the Ti matrix system occurs at the interface between the fiber coating and the reaction product which forms at the interface [Fig. 5(a)], whereas in the borosilicate matrix system, debonding and sliding proceeds at the fiber-coating/matrix interface [Fig. 5(b)].

Table 2. (a) Reseating load drop

Push-out distance (μm)	Relative load drop, ΔP_d (N)
	Ti matrix
5	0.55
10	0.36
20	0.13

(b) Push-through load drop

Section thickness (μm)	Load-drop, ΔP (N)
	Ti matrix
410	7.3
210	5.1

3.2. *Fatigued material*

The specimens prepared following fatigue crack propagation exhibited different push-out characteristics. At fiber locations ahead of the fatigue crack-tip (B in Fig. 2), the push-through characteristics are essentially the same as these on pristine specimens. However, adjacent to the notch (A in Fig. 2), the push-through force–displacement curves have the form depicted in Fig. 6. Subsequent to elastic deflection and a small load drop, push-out commences at a relatively low load but the push-through load *increases* for push-through displacements of the order of 30 μm. Thereafter, the load decreases with increasing displacement.

Push-back tests have the same features exhibited by pristine specimens: an essentially constant load, similar in magnitude to that reached upon termination of

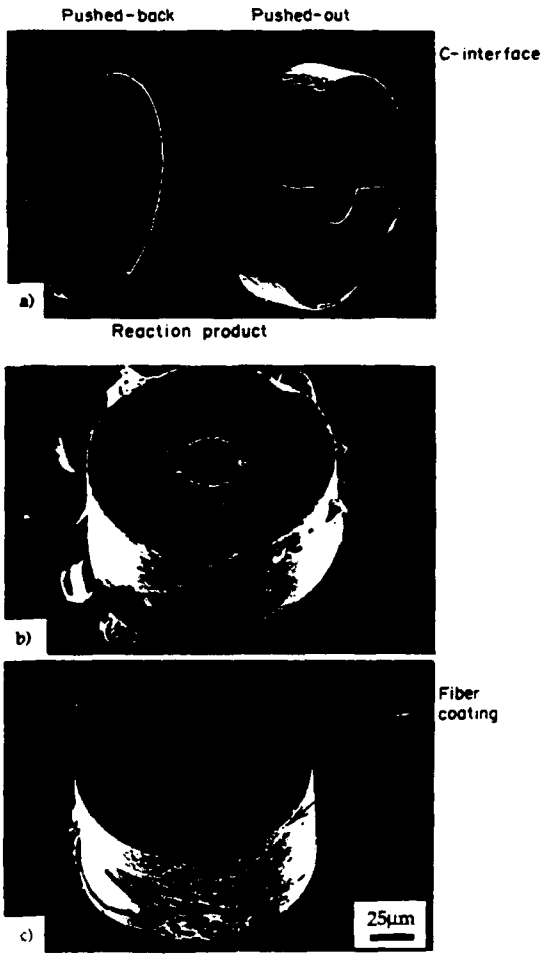

Fig. 5. SEM micrographs of fibers after push-through, (a) the Ti–15–3/SiC composite, (b) the glass/SiC composite—note the glass fragments adhering to the fiber, (c) fatigued Ti matrix sample—note the extensive damage to the coating.

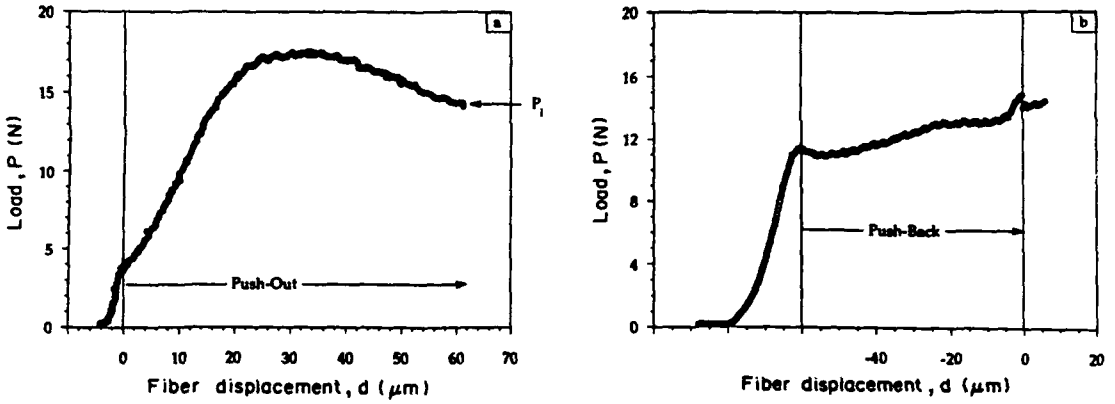

Fig. 6. Force–displacement results for push-through and push-back in the fatigued Ti–15–3/SiC material.

push-through. However, there was no load drop associated with reseating. Observations of the sliding interface indicate extensive fragmentation of the fiber coating [Fig. 5(c)].

4. ANALYSIS

Preliminary representation of the sliding behavior is made using equation (1), as plotted on Fig. 7. The Ti matrix system has a sliding stress about an order of magnitude larger than that for the glass matrix material. Also, the decrease in τ with sliding displacement is much larger for the Ti system. Attempts to fit the load–displacement results to equation (3) with consistent τ_0 and μ have yielded unacceptable correlations. The problem is illustrated *for the glass matrix system* in Fig. 8. First, by using the misfit ϵ_T and the elastic properties for this composite (from Table 1),

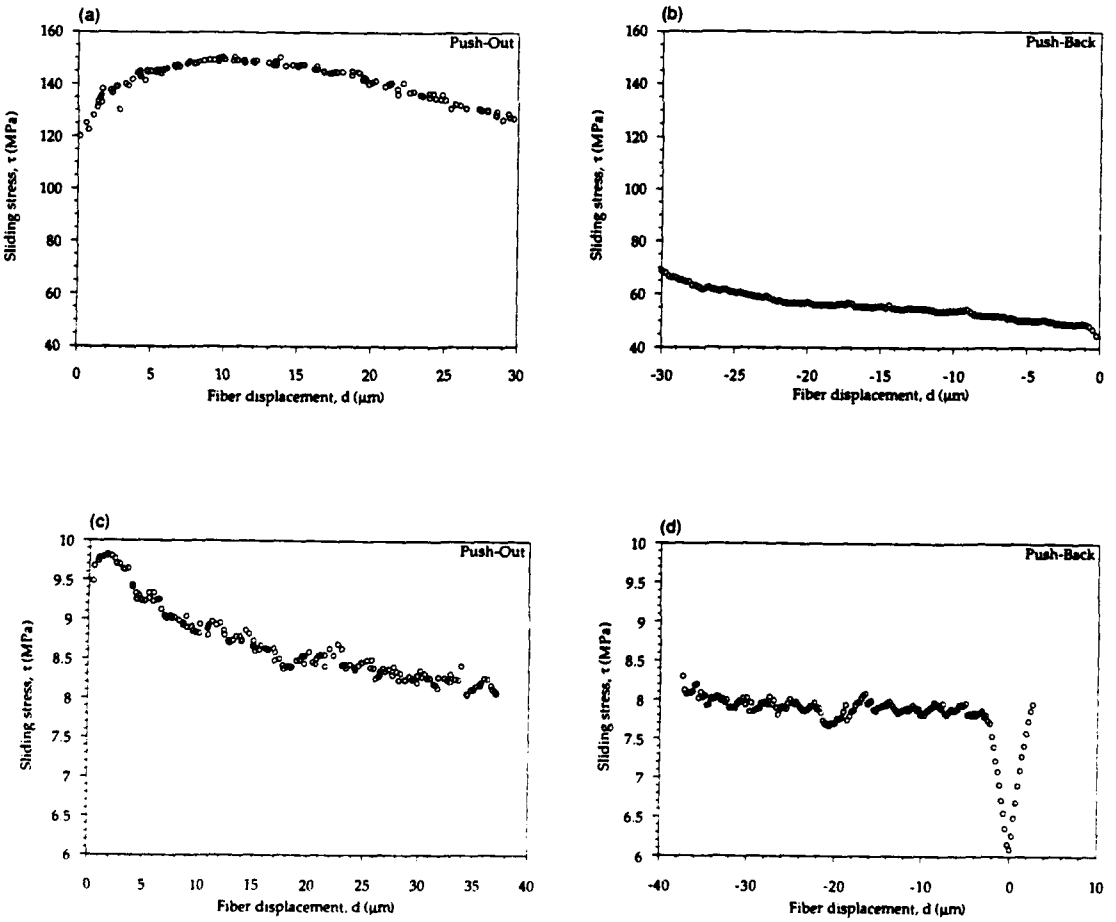

Fig. 7(a–d). *Caption overleaf.*

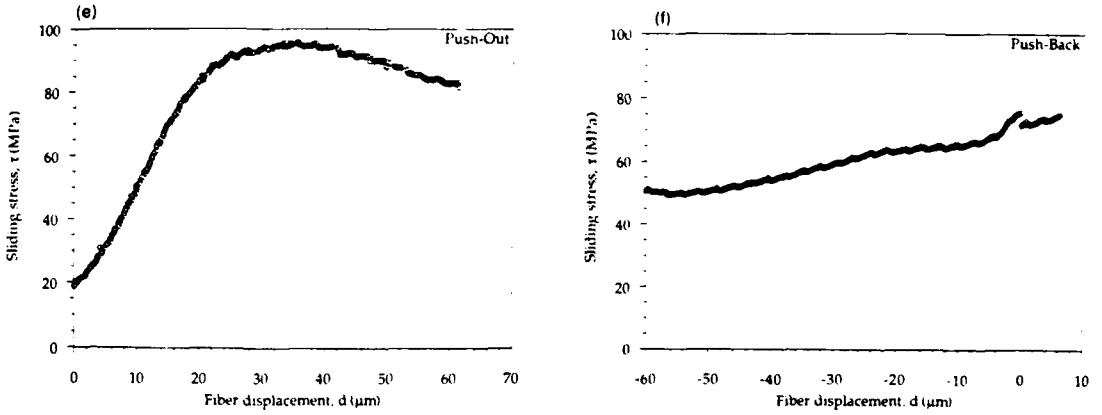

Fig. 7(e,f)

Fig. 7. Values of the sliding stress τ as a function on push-through and push-back: (a,b) Ti matrix composite, (c,d) glass matrix composite, (e,f) Ti matrix after fatigue.

a fit of equation (3) to the initial push-through force indicates that $\mu \approx 0.2$ and $\tau_0 \approx 2$ MPa. Then, by maintaining μ and τ_0 at these levels, equation (3) predicts a substantially smaller load reduction upon push-out than indicated by the experiments. This situation differs from that found when initial push-through measurements are made as a function of embedded lengths (Fig. 9), wherein all measurements involve small displacements ($< 2\,\mu$m). The inference is that either μ or τ_0 or both are diminishing as push-out proceeds. An assessment of the degradation is made (Fig. 10) by either regarding μ as constant and evaluating the reduction in τ_0 or vice versa. Based on an analysis elaborated in a companion paper [10], the preferred interpretation is that τ_0 decreases. This analysis relates τ_0 to fiber *roughness*. It explains various unexpected phenomena, such as the frequently found rise in initial push-out stress (Fig. 3) in terms of a geometric decorrelation. It also demonstrates that τ_0 decreases as the amplitude of the roughness decreases. The implication regarding the results presented for the glass matrix system in Fig. 10 is that wear of the interface asperities occurs as the interface slides during push-out, causing τ_0 to diminish. Direct measurements of asperity amplitudes would be needed to verify this interpretation.

The much larger reduction in τ in the Ti matrix system cannot be explained by the same asperity wear mechanism, because the extent of asperity wear that would be needed to correlate with the experiments is unacceptably large [10]. The interpretation most consistent with the measurements [Fig. 7(a)], is a reduction in misfit strain with push-out, probably caused by plastic expansion of the matrix around the fiber, as asperities slide over each other.

The large reduction in initial push-out stress induced upon fatigue crack growth (Fig. 6) has also been related to a diminished misfit strain [10]. In this case, fragmentation and removal of the fiber coating [Fig. 5(c)] is regarded as the major source of the reduced misfit. The subsequent increase in push-out load is qualitatively consistent with this interpretation, but the magnitude is larger than this mechanism could predict. Further study is needed to understand these details.

The reseating effect on push-back has been noted and explained [3, 4] in terms of asperities on the debonded interface. One notable addition provided

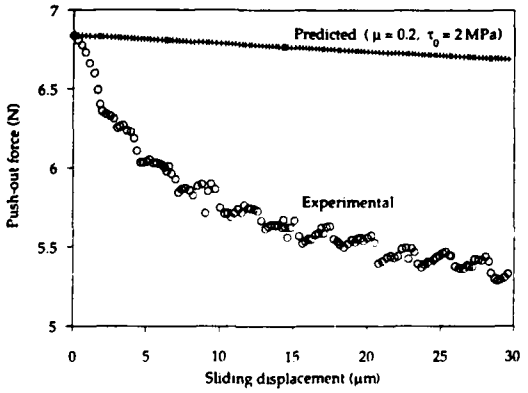

Fig. 8. A comparison of push-through measurements for the glass matrix system with prediction based on equation (4) with μ and τ_0 held constant.

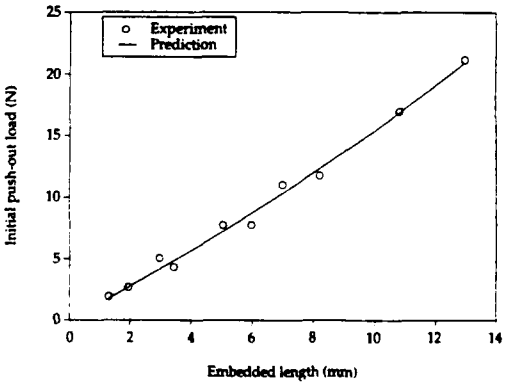

Fig. 9. A comparison of push-out data as a function of embedded length with the prediction of equation (3) [5] ($\tau_0 = 0$, $\mu = 0.2$).

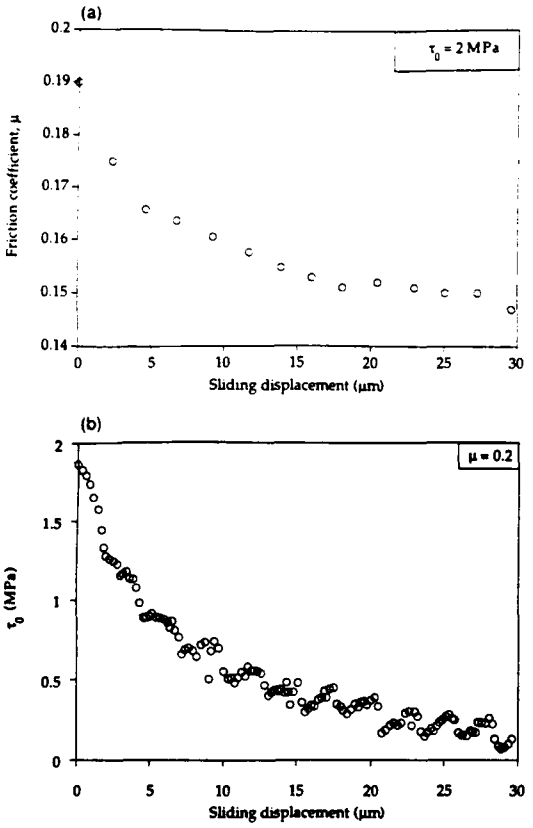

Fig. 10. Change in sliding parameters with push-out for a glass matrix system: (a) fixed, τ_o, (b) fixed μ.

by the present study concerns the reduction in the associated load drop with increase in the push-through displacement in the Ti–15–3 matrix material (Table 2). This observation is consistent with the above speculations that the matrix in this material is being plastically deformed during push-through.

5. CONCLUDING REMARKS

Based on the development of an improved push-through test, some important sliding characteristics of interfaces in metal and glass matrix composites have been identified. In particular, changes in sliding behavior caused by monotonic and cyclic sliding displacements have been revealed. Qualitative comparison with a sliding model based on fiber roughness and friction [10] have provided some insight about the origin of these effects. Changes in monotonic sliding resistance τ are larger for metal (MMC) than glass (GMC) matrix composites, suggesting that release of misfit by matrix plasticity is important for MMCs whereas asperity wear dominates for GMCs. The effects of fatigue seem to involve fragmentation of the fiber coating that also reduces the thermal expansion misfit and reduces τ.

Some of the changes are substantial and have important implications for matrix cracking in composites, subject to either monotonic or cyclic loading: processes that have high sensitivity to τ. The details that govern the sliding induced changes in τ have not been elucidated and require further study.

Acknowledgement—Funding for this work was supplied by the Defense Advanced Research Projects Agency through the University Research Initiative Program of UCSB under the Coatings contract No. MDA972-90-K-0001.

REFERENCES

1. D. B. Marshall, *J. Am. Ceram. Soc.* **67**, 259 (1984).
2. D. B. Marshall and W. C. Oliver, *J. Am. Ceram. Soc.* **70**, 542 (1987).
3. P. D. Jero and R. J. Kerans, *Scripta metall. mater.* In press.
4. W. C. Carter, E. P. Butler and E. R. Fuller, *Scripta metall. mater.* **25**, 579 (1991).
5. J. D. Bright, S. Danchaivijit and D. K. Shetty, *J. Am. Ceram. Soc.* **74**, 115 (1991).
6. G. Morscher, P. Pirouz and A. H. Heuer, *J. Am. Ceram. Soc.* **73**, 713 (1990).
7. D. Walls, G. Bao and F. Zok, *Scripta metall. mater.* **25**, 911 (1991).
8. J. W. Hutchinson and H. M. Jensen, *Mech. mater.* **9**, 139 (1990).
9. C. Liang and J. W. Hutchinson. To be published.
10. T. J. Mackin, P. D. Warren and A. G. Evans. To be published.

APPENDIX

Estimating the Interface Debond Energy, Γ_i

Liang and Hutchinson [9] have shown that a load drop, ΔP, occurs after the debond has propagated completely along the interface (for $\tau_o = 0$),

$$\frac{\Delta P}{\pi R^2} = \left[A_1 \epsilon_T + A_2 \sqrt{\frac{E_m \Gamma_i}{R}}\right] \exp\left(\frac{2\mu B h}{R}\right) \qquad \text{(A1)}$$

where

$$A_1 = \frac{E_f + E}{(1+\nu) + (1-\nu)E/E_f}$$

$$A_2^2 = \frac{4EE_f[(1+\nu)E_f + (1-\nu)E]}{(1-f)(1+\nu)E_m^2[E_f + (1-2\nu)E]}$$

In (A1), the first term in parentheses reflects the release of residual stress when the debond propagates completely along the interface while the second term reflects the contribution to the load induced by the bond.

Measurements of ΔP enable Γ_i to be estimated provided that ϵ_T is independently known. As a first approximation, we assume that the axial mismatch strain is entirely relieved when the thin composite sections are sliced: $\epsilon_T = 0$. Values of Γ_i are then estimated for the Ti matrix composite in which debonding occurs within the fiber coating. For this case [Fig. 7(a)], $\tau = 90$ MPa and the mismatch stress $\sigma_0 = 300$ MPa (Table 1) giving $\mu = 0.3$. With this value for μ, the measured push-through load drops (Table 2) give Γ_i in the range 4–7 Jm^{-2}. A more complete analysis awaits a numerical solution that includes the influence of sectioning presently under development [9].

Int. J. Solids Structures Vol. 29, No. 21, pp. 2639–2648, 1992
Printed in Great Britain.

0020–7683/92 $5.00+.00

THIN FILM CRACKING AND THE ROLES OF SUBSTRATE AND INTERFACE

T. YE†, Z. SUO and A. G. EVANS
Materials Department, University of California, Santa Barbara, CA 93106-5050, U.S.A.

(*Received* 6 *August* 1991; *in revised form* 13 *March* 1992)

Abstract—Cracks in thin films caused by residual tension are examined. Attention is focused on film cracking, subject to either interface debonding or substrate cracking. For crack channeling along the film, the driving force is found to depend on the channel cross-section, as governed by the fracture properties of the interface and the substrate, in addition to known effects of film thickness, residual stress and elastic moduli. The critical film thickness needed to avoid cracking is determined to be lower if the crack extends into the substrate. Conditions for thin film spalling and constrained debonding are prescribed. Finally, the *T*-stress is used to account for crack branching in substrates.

1. INTRODUCTION

Thin films deposited on a substrate are usually subject to residual stress, with a misfit strain ε_0. For example, if the thermal expansion coefficient of the film differs from that of the substrate, the misfit strain is biaxial, having magnitude

$$\varepsilon_0 = (b_f - b_s)\Delta T, \tag{1}$$

where ΔT is the temperature drop and b the thermal expansion coefficient; the subscripts f and s indicate film and substrate, respectively. The misfit stress in the film is also biaxial, with magnitude

$$\sigma_0 = \varepsilon_0 E_f/(1-\nu_f), \tag{2}$$

where E_f is the Young's modulus and ν_f the Poisson's ratio. The residual stress is tensile when the thermal expansion coefficient for the film is larger than for the substrate, and is given explicitly by eqn (2) when the film is much thinner than the substrate. Thin films in residual tension are considered in this paper.

Many cracking patterns in film–substrate systems have been observed and analysed (Evans *et al.*, 1988; Hutchinson and Suo, 1992). A crack nucleates from a flaw either in the film or at the edge, and propagates both towards the interface and laterally through the film. Depending on the material, the crack may stop at the interface (Fig. 1a), penetrate into the substrate (Fig. 1b), or bifurcate onto the interface (Fig. 1c). These cracks then channel laterally. After the channel length exceeds a few times the film thickness h, a *steady state* is reached, wherein the entire front and the cross-section in the wake maintain their shape as the crack advances. When the steady-state channel extends by unit length, the potential energy decreases by (Suo, 1990; Ho and Suo, 1991)

$$\mathcal{G} = \frac{\sigma_0}{2}\int_0^h \delta(x)\,dx, \tag{3a}$$

† Now at Stewart & Stevenson Services, Inc., Gas Turbine Products Division, 164 15 Jacintport Blvd, Houston, TX 77015, U.S.A.

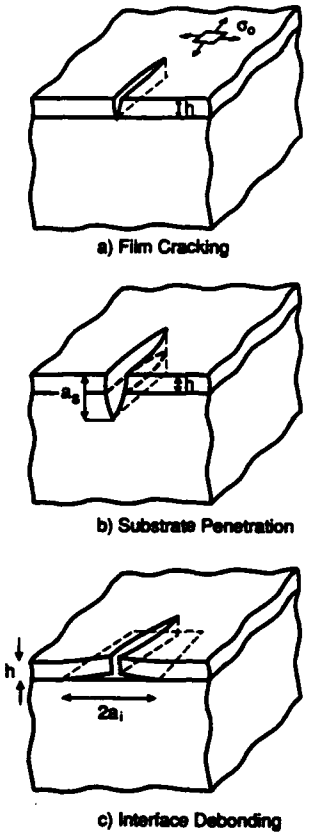

Fig. 1. (a) A channeling crack within a thin film. (b) A channeling crack penetrating into the substrate. (c) A channeling crack with interface debonding.

or by (Gille, 1985; Hu and Evans, 1988)

$$\mathscr{U} = \int \mathscr{G}(a)\,\mathrm{d}a, \tag{3b}$$

where $\delta(x)$ is the separation of the cracked film in the wake, $\mathscr{G}(a)$ is the energy release rate of a plane strain crack, and the integration in eqn (3b) is over all cracks in the cross-section of the wake.

Previous studies have assumed that the channel bottom is a sharp crack front lying on the interface (Fig. 1a). However, in practice a film crack may either extend into the substrate (Fig. 1b) or bifurcate along the interface (Fig. 1c), depending upon the relative fracture energies of thin film, substrate and interface. Such microscopic features relax the constraint of the system and increase the separation $\delta(x)$ which, in turn, increases the driving force $\mathscr{U}$. Consequently, the loss of constraint lowers the critical residual stress needed to drive the channel crack. Explicit determination of these effects is the subject of this article.

Consider an ideally constrained channel in the film (Fig. 1a). The potential energy decrease for the channel to extend unit length, $\mathscr{U}$, equals the energy released at the channel front, $h\,\mathscr{G}_{ss}$. Dimensional arguments lead to

$$h\mathscr{G}_{ss} = \mathscr{U} = (\sigma_0^2 h^2/\bar{E}_f)\Sigma, \tag{4}$$

where $\bar{E}_f = E_f/(1-\nu_f^2)$, and Σ is dimensionless and depends on elastic mismatch, as calculated by Beuth (1992) for the channel confined in the film.

Table 1. Fracture energies for typical film/substrate combinations

Material	Fracture energy (Jm^{-2})	Film/substrate†
Si	6	F, S
GaAs	2–4	F, S
SiO_2	6	F
SiC	20	F
Si_3N_4	10–40	F
Al_2O_3	10–30	S
Cu	10^4	F
Al	10^4	F
Ni	10^4	F,S
Polyimide	10^3	F

† F refers to film, S refers to substrate.

Let Γ_f be the fracture energy of the film, and define a non-dimensional cracking number, Ω_c, as

$$\Omega_c = \sigma_0^2 h/\bar{E}_f\Gamma_f. \tag{5}$$

The channel grows if $\mathcal{G}_{ss} = \Gamma_f$. Consequently, for the ideally constrained channel to grow, $\Omega_c = 1/\Sigma$. Once Ω_c has been established, it defines a critical film thickness below which film cracking is prohibited

$$h_c = \Omega_c(\bar{E}_f\Gamma_f/\sigma_0^2). \tag{5a}$$

Determination of Ω_c is the principal objective of this paper.

The material properties that dominate the conditions for film cracking, through their influence on the magnitude of Ω_c, are the system fracture energies and the elastic mismatch parameters. The relevant fracture energies Γ are Γ_i/Γ_f and Γ_i/Γ_f, where the subscripts i, f and s refer to the interface, film and substrate, respectively. Typical values for Γ_f and Γ_s are indicated in Table 1 for substrate and film combinations of technological interest. The interface fracture energy Γ_i is sensitive to details regarding the substrate surface, as well as the film deposition and post annealed processes. Values in the range 01–100 JM^{-2} have been measured for various systems (Reimanis *et al.*, 1991; Evans *et al.*, 1990).

2. PLANE STRAIN PROBLEMS

The elastic mismatch is characterized by the two Dundurs' parameters

$$\alpha = \frac{(1-\nu_s)/\mu_s-(1-\nu_f)/\mu_f}{(1-\nu_s)/\mu_s+(1-\nu_f)/\mu_f}, \quad \beta = \frac{1}{2}\frac{(1-2\nu_s)/\mu_s-(1-2\nu_f)/\mu_f}{(1-\nu_s)/\mu_s+(1-\nu_f)/\mu_f}, \tag{6}$$

where μ is the shear modulus and ν the Poisson's ratio. For typical film/substrate combinations, α and β tend to be interrelated, such that $\beta \approx \alpha/4$ (Evans *et al.*, 1990) with α ranging between 0 and 0.7. In the computational results reported below, $\nu_f = \nu_s = \frac{1}{3}$ (equivalently, $\beta = \alpha/4$).

The plane strain problems pertaining to the *wake of the channel*, shown in the insets of Fig. 2, provide the information needed to determine the potential energy decrease for channel cracking, $\mathcal{U}$. Each material is taken to be isotropic and linearly elastic, the substrate is semi-infinite and, by using Eshelby arguments, the stress intensity induced by the misfit stress must equal that induced by an applied traction of the magnitude.

For linear elastic problems, the plane strain energy release rate $\mathcal{G}$ is quadratic in the residual stress and dimensional considerations show that

$$\mathcal{G} = (\sigma_0^2 h/\bar{E}_f)\omega, \tag{7}$$

where ω is a dimensionless number depending on a/h, α and β. A few mathematical considerations capture the main features of the solution, as follows.

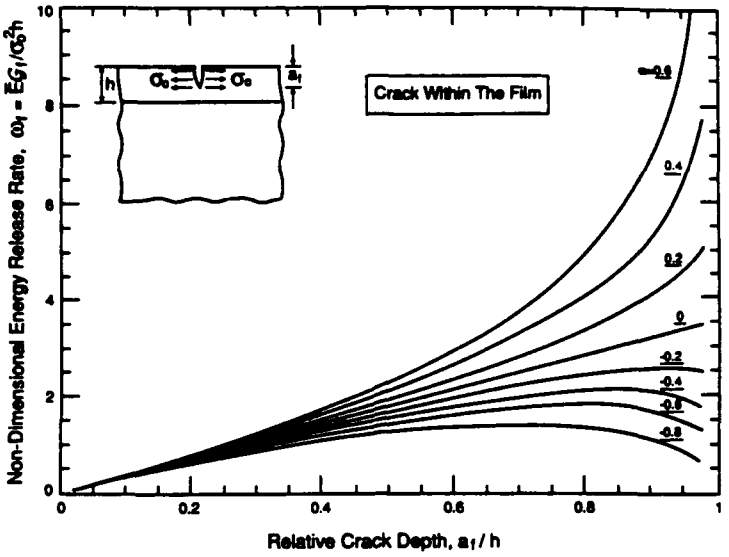

(a)

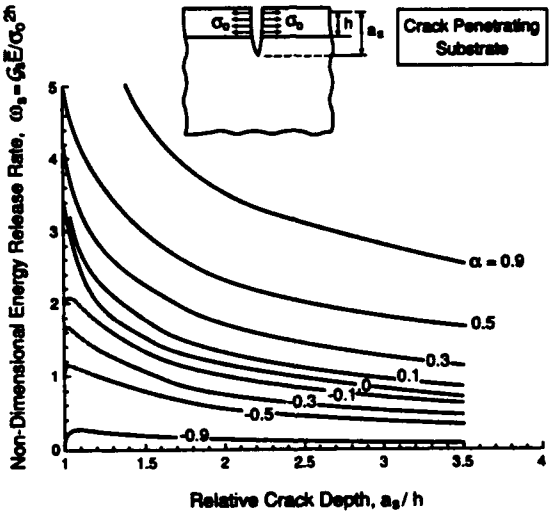

(b)

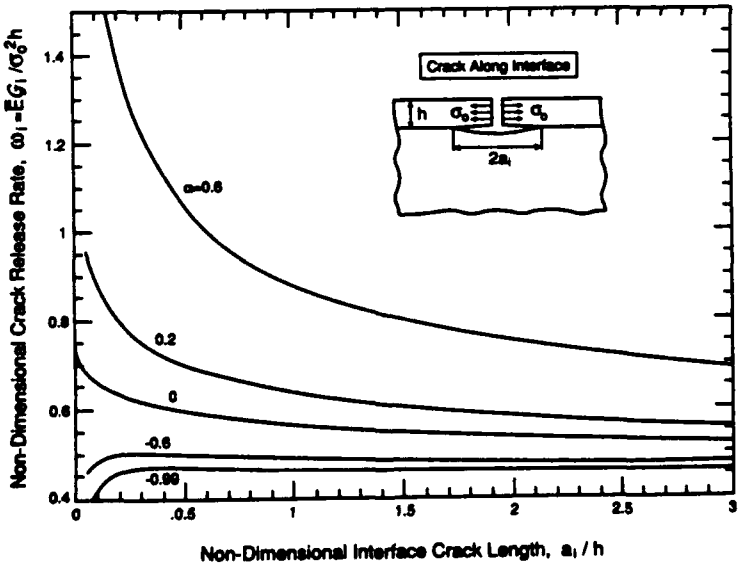

(c)

Fig. 2. Energy release rate for cracks under plane strain conditions. (a) Crack tip in the film. (b) Crack tip in the substrate. (c) Interface crack.

The stress field for a crack perpendicular to the interface, with the tip at the interface, is given by Zak and Williams (1963). The singular term is

$$\sigma_{ij} \sim \tilde{K} r^{-s} f_{ij}(\theta), \tag{8}$$

where (r, θ) is the polar coordinate centered at the tip, and f_{ij} are dimensionless angular distributions. The scaling factor, $\tilde{K}$, is analogous to the regular stress intensity factor, but having different dimensions [stress] [length]^s. The exponent s $(0 < s < 1)$ is the root to

$$\cos(s\pi) - 2\left[\frac{\alpha-\beta}{1-\beta}\right](1-s)^2 + \left[\frac{\alpha-\beta^2}{1-\beta^2}\right] = 0. \tag{9}$$

Table 1 lists s for given values of α. Dimensionality and linearity require that

$$\tilde{K} \sim \sigma h^s, \tag{10}$$

with the pre-factor dependent on α and β only.

Now consider a crack perpendicular to the interface, but with the crack tip either in the film or in the substrate (Figs 2a, b). As $a/h \to 1$, the stress field far from the small ligament $|h-a|$ behaves as if the crack tip were on the interface and is governed by $\tilde{K}$. At the crack tip, however, the stress field is square root singular and is scaled by the regular stress intensity factor K. Linearity requires that

$$K \sim \tilde{K} |h-a|^{1/2-s}. \tag{11}$$

Combination of eqns (10) and (11) gives

$$K/\sigma_0\sqrt{h} \sim \begin{cases} (1-a/h)^{1/2-s}, a/h \to 1^- \\ (1-h/a)^{1/2-s}, a/h \to 1^+. \end{cases} \tag{12}$$

2.1. *Crack tip in the film*

For a crack tip in the film (Fig. 2a), Beuth (1991) has shown that, subject to $\mathcal{G}_f = K^2/\bar{E}_f$,

$$\omega_f = 3.951\eta_f(1-\eta_f)^{1-2s}(1+\lambda_1\eta_f)^2, \tag{13}$$

where ω_f is the dimensionless number defined in eqn (7), $\eta_f = a_f/h$ and λ_1 is a fitting parameter to the full numerical solution (Table 2). The pre-factor is chosen such that, as $\eta_f \to 0$, eqn (13) approaches the classical solution of an edge crack in a semi-infinite homogeneous plane. Notice that the normalized energy release rate ω_f increases with α, confirming the known behavior that a compliant substrate attracts cracks more than a stiff substrate.

2.2. *Crack tip in the substrate*

For a crack that penetrates into the substrate (Fig. 2b) by using $\mathcal{G}_s = K^2/\bar{E}_s$, our finite element results can be expressed as

$$\omega_s = \frac{4\pi}{\pi^2-4}(\bar{E}_f/\bar{E}_s)\eta_s[\sin^{-1}(1/\eta_s)(1-\eta_s^{-1})^{1/2-s}(1+\lambda_2/\eta_s)]^2, \tag{14}$$

Table 2. ($\nu_f = \nu_s = \frac{1}{3}$, or $\beta = \alpha/4$)

α	−0.99	−0.8	−0.6	−0.4	−0.2	0	0.2	0.4	0.6	0.8	0.99
s	0.312	0.350	0.388	0.425	0.462	0.500	0.542	0.591	0.654	0.744	0.940
λ_1	−0.0894	−0.0784	−0.0627	−0.0437	−0.0224	0	0.0215	0.0389	0.0465	0.0335	−0.0257
λ_2	1.087	0.711	0.429	0.211	0.0201	−0.136	−0.296	−0.440	−0.584	−0.708	−0.962
λ_3	2.220	1.951	1.615	1.282	0.957	0.496	0.660	0.666	0.796	1.268	
λ_4	2.391	2.570	2.594	2.392	2.017	1.336	1.217	0.918	0.694	0.521	

where ω_s is the dimensionless number defined in eqn (7), $\eta = a_s/h$, and the fitting parameter λ_2 is listed in Table 2. The pre-factor ensures that, as $\eta_s \to \infty$ eqn (14) approaches the solution of an edge crack in a semi-infinite plane loaded by a pair of point forces (Tada *et al.*, 1985). Since the residual stress is localized in the film, the energy release rate decreases rapidly as the plane strain crack extends into the substrate.

2.3. *Interface crack*

When the crack extends along the interface (Fig. 2c), even though stresses are oscillatory at an interface crack tip, the energy release rate $\mathcal{G}_i$ still has the usual interpretation. Finite element calculation provides the following approximation:

$$\omega_i = \frac{1}{2}\left(\frac{\eta_i}{1+\eta_i}\right)^{1-2s}\left[1+\lambda_3 \exp\left(-\lambda_4\sqrt{\eta_i}\right)\right], \tag{15}$$

where ω_i is the dimensionless number defined in eqn (7) and $\eta_i = a_i/h$. The two parameters, λ_3 and λ_4, used to fit the finite element solutions are listed in Table 2. The pre-factor ensures that the solution is exact as $\eta_i \to \infty$. For systems having films stiffer than substrates ($\alpha > 0$), ω_i monotonically decreases to a constant level, $\omega_i = 0.5$. For such systems, the interface debonds, unless the crack can either blunt or extend into the substrate. For more compliant films ($\alpha < 0$), a maximum ω_i exists, suggesting a condition wherein debonding could not occur provided that the interface toughness exceeds a critical level.

3. CHANNEL CRACKS

3.1. *Brittle substrates*

When the substrate is brittle, the crack in the film may penetrate into the substrate (Fig. 1b). Thus, $\mathcal{U}$ can be obtained by substituting eqns (13) and (14) into eqn (3b) to give

$$\frac{\mathcal{U}\bar{E}_f}{\sigma_0^2 h^2} \equiv \Sigma = \int_0^1 \omega_f \, d\eta_f + \int_1^{a_s/h} \omega_s \, d\eta_s. \tag{16}$$

For a unit advance of the channel, the potential energy is balanced by the energy needed to create crack surfaces

$$\mathcal{U} = h\Gamma_f + (a_s - h)\Gamma_s, \tag{17}$$

where Γ_f and Γ_s are fracture energies for the film and substrate, respectively. At the bottom of the channel, the energy release rate must equal the fracture energy of the substrate,

$$\mathcal{G} = \Gamma_s. \tag{18}$$

Equations (17) and (18) can be rewritten in nondimensional forms

$$\Omega_c = [1 + (\Gamma_s/\Gamma_f)(\eta_s^* - 1)]/\Sigma \tag{19a}$$

and

$$\omega_s \Omega_c = \Gamma_s/\Gamma_f, \tag{19b}$$

where Ω_c is defined by eqn (5). Equations (19a, b) can be solved to give the channel depth *into the substrate*, $\eta_s^*[= (a_s/h)^*]$, and the critical cracking number, Ω_c, as a function of both Γ_s/Γ_f and the Dundurs' parameter, α. Both equations are nonlinear in η_s, since Σ and ω_s depend on η_s.

It is apparent from Fig. 3a that the crack depth into the substrate increases either as the relative substrate fracture energy, Γ_s/Γ_f, decreases or as α increases. The cracking

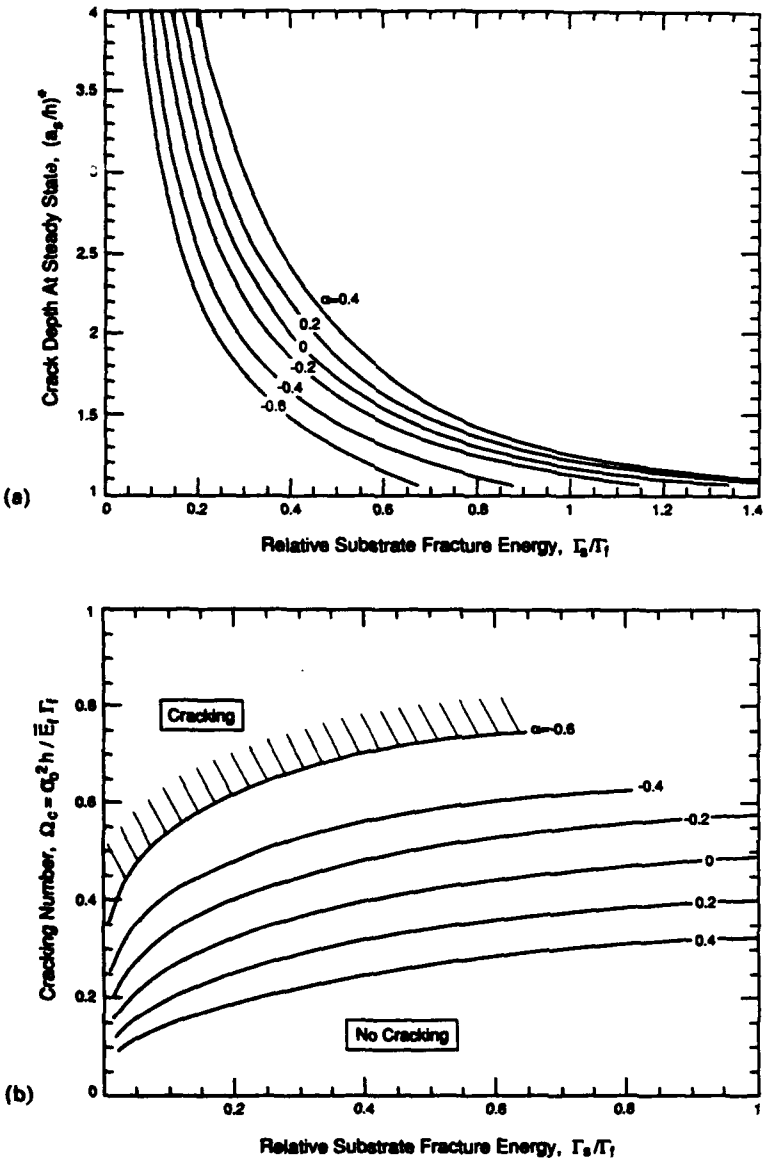

Fig. 3. The effect of substrate fracture energy and elastic mismatch on (a) the steady-state crack depth and (b) the film cracking and non-cracking regimes, expressed through the cracking number, Ω_c.

number Ω_c decreases as small Γ_s/Γ_f (Fig. 3b), reducing the critical film thickness, h_c. However, it is also of importance to note that Ω_c is essentially invariant when $\Gamma_s/\Gamma_f \gtrsim 1$. This is consistent with the prediction that crack penetration into film is negligible when $\Gamma_s/\Gamma_f \gtrsim 1$ (Fig. 3a). Consequently, the substrate fracture properties are *only important when the substrate has appreciably less toughness than the film.*

3.2. *Weak interfaces*

Denote Γ_i as the fracture energy of the interface at the phase angle pertinent to interface debonding [52° when film and substrate have similar elastic constraints; see Fig. 53 in Hutchinson and Suo (1992)]. The non-dimensional energy release rate for an interface crack quickly approaches an asymptotic value, $\omega_i = 0.5$ (Fig. 2c). For practical purposes, this prescribes the critical cracking number defined in eqn (5) as

$$\Omega_c = 2\Gamma_i/\Gamma_f. \tag{20}$$

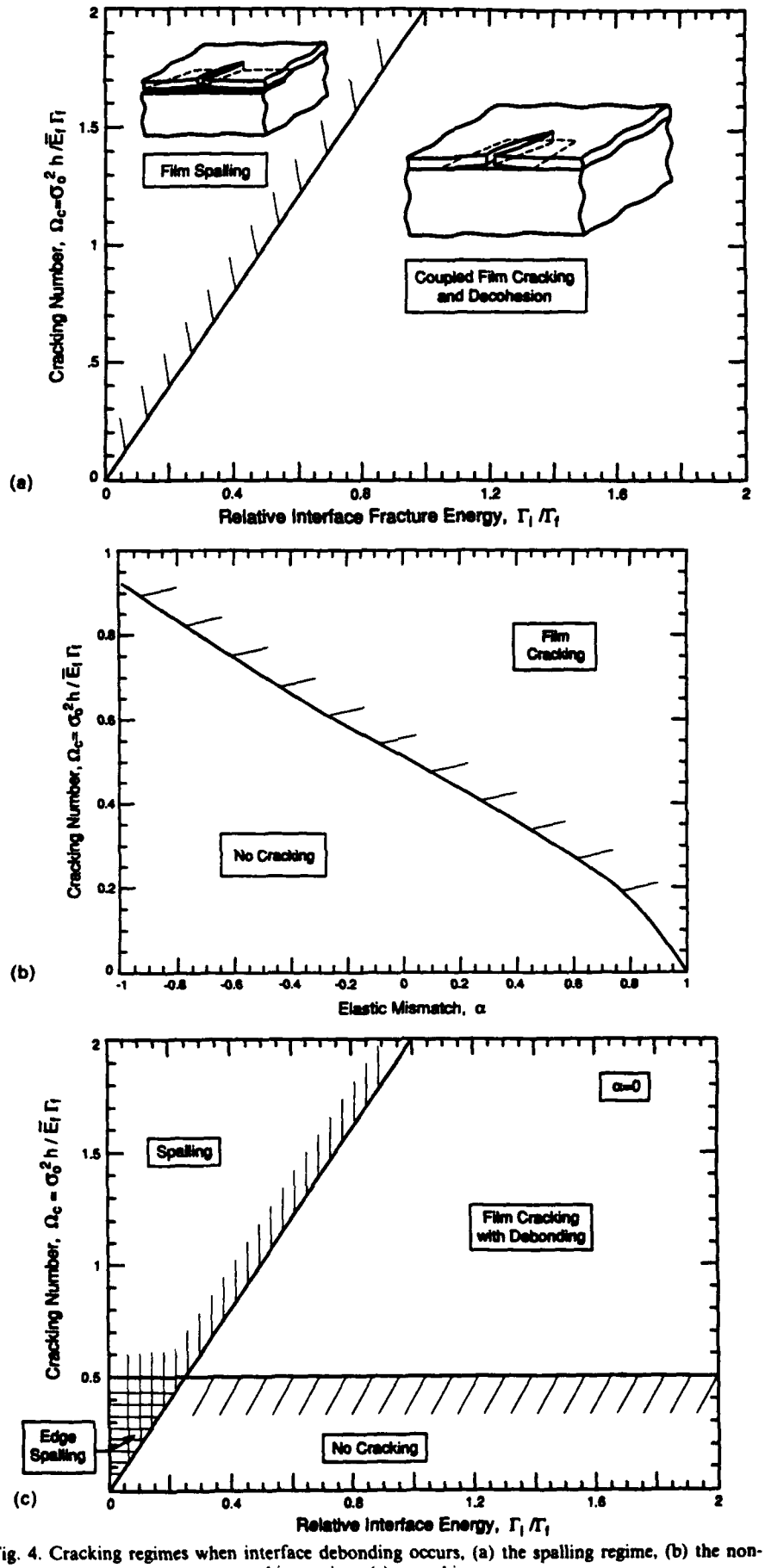

Fig. 4. Cracking regimes when interface debonding occurs, (a) the spalling regime, (b) the non-cracking regime, (c) a cracking map.

The interpretation of this result is as follows. For $\Omega_c > 2\Gamma_i/\Gamma_f$, the debond extends without limit and the entire film spalls off *as the crack extends across the film*, (Fig. 4a). This condition does not depend on the Dundurs' parameter, α.

Another limit coincides with the condition for the *avoidance of cracking*. This limit arises when $\eta_i = 0$ (Beuth, 1992)

$$\Omega_c = \frac{1}{\int_0^1 \omega_f \, d\eta_f}. \tag{21}$$

This condition depends on α (Fig. 4b). A map that combines the above information is shown in Fig. 4c for the case $\alpha = 0$. The area indicated by edge cracking indicates that thin film cracking is avoided, but Γ_i is so low that interface debonds from the edge of the film. It is noted that constrained debonding does not reduce Ω_c appreciably, so that Fig. 4b is sufficient for practical purposes.

4. CRACK BRANCHING IN THE SUBSTRATE

After a crack penetrates into a brittle substrate, it bifurcates (Drory and Evans, 1990) (Fig. 5). To account for this phenomenon, the concept of the T-stress is used. For a mode I crack, the Williams expansion defines T-stress as

$$\sigma_{ij}(r,\theta) = \frac{K}{\sqrt{2\pi r}} f_{ij}(\theta) + T\delta_{1j}, \tag{22}$$

where T is the stress acting parallel to the crack. A crack in an isotropic, homogeneous, brittle solid normally selects a trajectory with mode I loading. The crack perpendicular to the interface, with tip in the substrate, is indeed under mode I. According to Cotterell and Rice (1980), a mode I crack is directionally stable if $T < 0$, but unstable if $T > 0$. With this concept in mind, the T-stress after a crack penetrates into the substrate was computed using finite elements (Fig. 5). It is apparent that conditions exist near the interface with $T > 0$. Cracks in the substrate near the interface thus appear to be unstable. The observed bifurcation may be plausibly explained by this effect. Noticing that the singular term in (22) vanishes in crack flanks and, in particular, $f_{xx}(\pm\pi) = 0$, we compute σ_{xx} using finite element along the flanks, near the crack tip, which approaches T. Fine meshes at the crack tip are

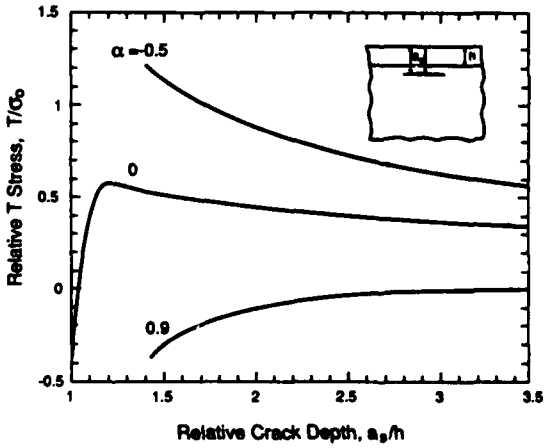

Fig. 5. The T-stress as a function of substrate crack depth for various levels of elastic mismatch. The crack branches when $T > 0$.

used which are varied and refined to ascertain mesh insensitivity [see Sham (1991) for more sophisticated methods for computing T-stress].

Acknowledgements—This investigation is supported by the ONR/URI contract 8-482491-25910-3. ZS is in addition supported by NSF grant MSS-9011571. The finite element computations were performed using ABAQUS. We thank the reviewers for several suggestions.

REFERENCES

Beuth, J. L. (1992). Cracking of thin bonded films in residual tension. *Int. J. Solids Structures* **29**, 1657–1675.
Cotterell, B. and Rice, J. R. (1980). Slightly curved or kinked cracks. *Int. J. Fract.* **16**, 155–169.
Drory, M. D. and Evans, A. G. (1990). Experimental observation of substrate fracture caused by residual stressed films. *J. Am. Ceram. Soc.* **73**, 634–638.
Evans, A. G., Drory, M. D. and Hu, M. S. (1988). The cracking and decohesion of thin films. *J. Mater. Res.* **3**, 1043–1049.
Evans, A. G., Rühle, M., Dalgleish, B. J. and Charalambides, P. G. (1990). The fracture energy of bimaterial interface. *Mat. Sci. Engng* **A126**, 53–64.
Gille, G. (1985). Strength of thin films and coatings. In *Current Topics in Materials Science* (*Edited by E. Kaldis*), Vol. 12. North Holland, Amsterdam.
Ho, S. and Suo, Z. (1991). Tunnelling cracks in constrained layers (submitted).
Hutchinson, J. W. and Suo, Z. (1992). Mixed mode cracking in layered materials. *Adv. Appl. Mech.* **29**, 63–191.
Hu, M. S. and Evans, A. G. (1988). The cracking and decohesion of thin films on ductile substrates. *Acta metall.* **37**, 917–259.
Reimanis, I. E., Dalgleish, B. J. and Evans, A. G. (1991). The fracture resistance of a model metal/ceramic interface. *Acta Metall. Mater.* **39**, B133–B3142.
Sham, T.-L. (1991). The determination of the elastic T-term using higher order weight functions. *Int. J. Fract.* **48**, 81–102.
Suo, Z. (1990). Failure of brittle adhesive joints. *Appl. Mech. Rev.* **43**, S276–S279.
Tada, H., Paris, P.C. and Irwin, G. R. (1985). *The Stress Analysis of Cracks Handbook*. Del. Research, St Louis, Mo.
Zak, A. R. and Williams, M. L. (1963). Crack point stress singularities at a bi-material interface. *Appl. Mech.* **30**, 142–143.

Acta metall. mater. Vol. 39, No. 12, pp. 3133–3141, 1991
Printed in Great Britain.

0956-7151/91 $3.00 + 0.00

THE FRACTURE RESISTANCE OF A MODEL METAL/CERAMIC INTERFACE

I. E. REIMANIS, B. J. DALGLEISH and A. G. EVANS
Materials Department, College of Engineering, University of California, Santa Barbara, CA 93106, U.S.A.

(Received 25 March 1991)

Abstract—Crack propagation has been measured for the Al_2O_3/Au interface subject to conditions that exclude stress corrosion. Crack growth has been shown to occur with a rising resistance, governed by intact metal ligaments in the crack wake. The level of resistance also increases as the metal layer thickness increases. Crack extension occurs by a combination of plastic void growth and interface debonding. The fracture energies are much larger than the work of adhesion, but appreciably smaller than those expected for ductile interface fracture. The fracture energy is nevertheless dominated by plastic dissipation, which increases at larger metal layer thicknesses.

Résumé—On mesure la propagation des fissures pour l'interface Al_2O_3/Au soumise à des conditions qui excluent la corrosion sous contrainte. On montre que la croissance d'une fissure se produit avec une résistance croissante, contrôlée par les ligaments métalliques intacts dans le sillage de la fracture. Le niveau de résistance croît aussi lorsque l'épaisseur de la couche métallique augmente. L'extension de la fissure se produit par une combinaison de croissance plastique des cavités et de décollement de l'interface. Les énergies de rupture sont beaucoup plus grandes que le travail d'adhérence, mais beaucoup plus petites que celles que l'on attendait pour une rupture ductile d'interface. L'énergie de rupture est néanmoins dominée par la dissipation plastique qui augmente pour les grandes épasseurs de la couche métallique.

Zusammenfassung—Die Rißausbreitung wird an der Grenzfläche Al_2O_3/Au unter Bedingungen gemessen, die Spannungskorrosion ausschließen. Sie geht mit steigendem Widerstand einher und ist geprägt von intakten Metallbrücken im Spalt. Die Größe des Widerstandes nimmt auch zu, wenn die Dicke der Metallschicht zunimmt. Die Ausbreitung des Risses läuft über eine Kombination von plastischem Porenwachstum und von Ablösungen in der Grenzfläche ab. Die Bruchenergien übersteigen die Adhäsionsarbeit erheblich, sind aber merklich kleiner als diejenigen, welche für duktilen Bruch an der Grenzfläche erwartet werden. Trotzdem ist die Bruchenergie beherrscht von plastischer Dissipation, die mit dickerer Metallschicht größer wird.

1. INTRODUCTION

The fracture of metal/ceramic interfaces may involve irreversible processes such as phonon dissipation, plasticity and phase transformations [1, 2, 4–7] and can occur by either brittle or ductile mechanisms [1, 7]. Brittle mechanisms involve atomic decohesion at the crack tip [6], whereas ductile mechanisms involve void nucleation and growth [7, 8] usually ahead of the tip. Brittle fracture can be environmentally assisted [5, 7], although the associated fracture energy still involves an appreciable contribution from plastic dissipation that occurs in the metal as the brittle crack extends along the interface [5, 7].

The intent of the present study is to investigate explicit effects of plasticity on the fracture of a metal/ceramic interface. A model system of gold bonded to sapphire is used. This system has the attributes that the properties of the constituents have been thoroughly characterized, and that a discrete interface can be produced by diffusion bonding without the formation of interphases and without dissolution of Al_2O_3 in the Au [7]. Finally, the transparency of the sapphire allows *in situ* observation of crack propagation along the interface [7].

2. EXPERIMENTAL PROCEDURES

2.1. Diffusion bonding

As described previously [7], interfaces between Au and Al_2O_3 can be created by the diffusion bonding of high purity polycrystalline Au foil to single crystal Al_2O_3 discs having basal plane (0001) orientation. The bonding was done in vacuum ($\sim 10^{-6}$ torr) at 1040°C for 48 h and subjected to a normal stress of about 5 MPa. The diffusion bonded discs consisted of thin Au layers of 100, 25 or 10 μm thickness between two thick Al_2O_3 layers: one having 1 mm thickness and other 3.5 mm thickness. The Au foil was polycrystalline after bonding, but highly textured such that the foil plane has a (001) orientation [7]. Residual porosity remains at the interface [7, 9] in the form of isolated facetted pores in the Au, approx. 3–10 μm wide and about 1 μm deep, with a mean spacing of about 20–50 μm. The thinnest foil exhibited tearing in some locations (Fig. 1).

Fig. 1. Optical micrograph of 10 μm thick Au foil diffusion bonded between plates of sapphire, showing tears in the Au (arrowed).

2.2. Mechanical testing

Most bimaterial interface fracture problems occur under mixed-mode loading conditions [1]. A flexural configuration (Fig. 2) which has a mode mixity angle, $\psi \approx \pi/4$, is thus particularly appropriate for the investigation of interface fracture [10]. Furthermore, the relative ease of introducing a stable precrack facilitates use of this specimen. Subsequent to diffusion bonding, beams were diamond machined with overall dimensions, 45 × 3.5 × 4.2 mm. In some cases, side faces were polished to facilitate optical observation during testing. A precrack was established in the following way. Knoop indentations, loaded to ~50 N, were placed on the center of the tensile side of the beam. The sample was then loaded in 3-point bending until the crack from the indents grew unstably through the sapphire. Following precracking, three- and four-point bend tests were carried out *in situ* in an inverted optical microscope [7]. The load was measured using a high-resolution, button-type load cell consisting of semiconductor strain gages. Tests were performed in a dry N_2 environment which was achieved by enclosing the apparatus and maintaining a positive pressure outflow of dry, high purity N_2. To fully suppress subcritical crack growth, high purity grade N_2 (3 ppm H_2O) was necessary. The chamber was flushed with N_2 for at least 20 min prior to testing.

2.3. Characterization

After the crack had been propagated to a length ~5 mm, fracture surfaces were prepared for microscopic investigation using the following procedure. Water was introduced into the crack front and the specimens loaded in 3-point bending, whereupon the H_2O debonded intact regions by stress corrosion. This process occurred at sufficiently low load levels that the fracture surface remained essentially undamaged. Thereafter, the specimens were embedded in epoxy to ensure that the mating fracture surfaces were not damaged during subsequent cutting. Following diamond sawing into the desired shape, the specimens were removed from the epoxy by soaking in acetone, and the top sapphire layer separated from the Au foil to allow characterization of the fracture surfaces. These surfaces were investigated in the SEM in conjunction with X-ray spectroscopy (EDS) to determine possible chemical differences.

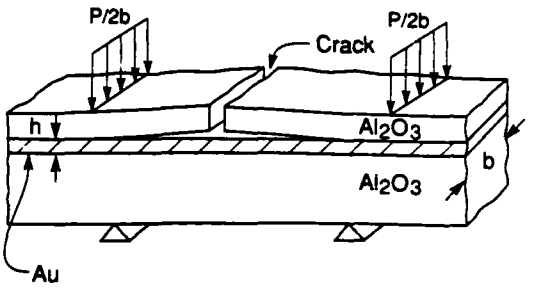

Fig. 2. Flexure specimen geometry used for interface fracture energy measurements.

3. RESULTS

3.1. Measurements and observations

Four-point flexure tests conducted in a dry N_2 atmosphere revealed resistance behavior, manifest in loads that increased as the interface cracks extended. The resistance Γ_R determined from the loads has the characteristics indicated in Fig. 3. Both the initiation resistance Γ_0 and the subsequent growth resistance appear to increase as the metal layer thickness increases. Explicit trends in Γ_0 with metal layer thickness are presented in Fig. 4.

The crack growth mechanisms, which were ascertained from *in situ* observations, revealed some dependence on the metal layer thickness, although generic characteristics exist. In particular, alternate debonding usually occurred on both interfaces, as illustrated schematically in Fig. 5(a). This behavior was elucidated by matching top and bottom interfaces, wherein the region which remained intact on the top interface [Fig. 5(b)] debonded on the bottom interface [Fig. 5(c)]. Consequently, ductile ligaments bridge the crack, even after crack extensions of 5 mm. Slip lines visible on the perimeter of the intact area (Fig. 6(a)], which delineate the plastically deformed ligaments, are continuous through the metal

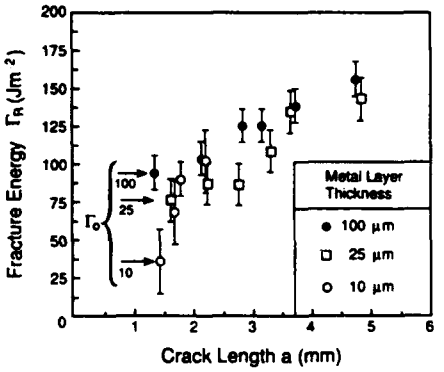

Fig. 3. Interface fracture energy Γ_R as a function of crack length a, for 10, 25 and 100 μm thick Au layers.

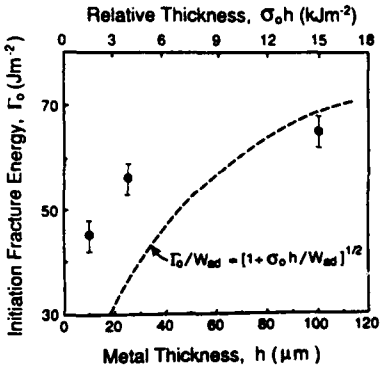

Fig. 4. Initiation fracture energy as a function of actual and relative metal layer thickness.

[Fig. 6(a), (b)]. The intact areas begin to debond ~3 mm behind the crack tip and continue to debond as the crack extends (Fig. 7). The debonding behind the crack tip occurred by continuous decohesion with no obvious interaction with interface porosity. For Au layers having intermediate and larger thickness, the crack front extended primarily on the upper interface, but for the thinnest layers the crack preferentially selected the lower interface.

Subsequent to crack extension of several millimeters in dry N_2, some samples were unloaded and reloaded in 3-point bending in air, thereby causing the intact ligaments between crack faces to debond by stress corrosion. When all of the intact ligaments had been debonded, the sample was again unloaded and reloaded in 4-point bending in dry N_2. The crack was found to resume growth at an energy release rate comparable to the initiation resistance Γ_0, and to further extend subject to a resistance curve having the same characteristics as the original curve (Fig. 8). These experiments explicitly relate the rising fracture resistance to the presence of metal ligaments across the interface crack faces, consistent with previous studies on the Cu/glass system [5].

The initial growth mechanisms were most readily visualized from experiments wherein the crack had been previously extended by stress corrosion, resulting in a ligament-free crack. The crack in the thicker Au layers was observed to extend by abrupt increments of order 200 μm in width, occurring at distinct sites along the crack front (Fig. 9), with no evident interaction with the interface porosity. The contrast which developed along the fracture surface delineates the grain boundaries in the Au and indicates that the increments of crack growth typically encompass several grains. For Au layers of intermediate thickness, voids nucleated ahead of the crack front (Fig. 10). The nucleation sites are pre-existing pores on the interface within ~30 μm of the crack front. Voids within about 10 μm of the crack extend back and coalesce with the crack, whereas voids greater than about 10 μm from the crack grow, but do not necessarily interact with the crack. The associated plastic deformation, which extends approx. 1 pore diameter, was ~0.1 μm deep, as measured using an electron damage technique [7]. Finally, in the thinnest Au layer, the crack extends continuously on the lower interface by direct growth from the crack front, with some isolated debonding in the form of void growth, on the upper interface, reminiscent of the crack growth process subject to stress corrosion [7].

Subsequent to initial growth, continued crack extension was accompanied by periodic debonding at the second interface. Interfacial pores were located at the centers of each debond, suggesting that pores are the preferred nucleation sites. The nature of void growth ahead of the crack and thus, the size of the intact ligaments, was noted to depend on the metal layer thickness: the intact ligaments being smallest for the thinnest layers. A characterization of the size

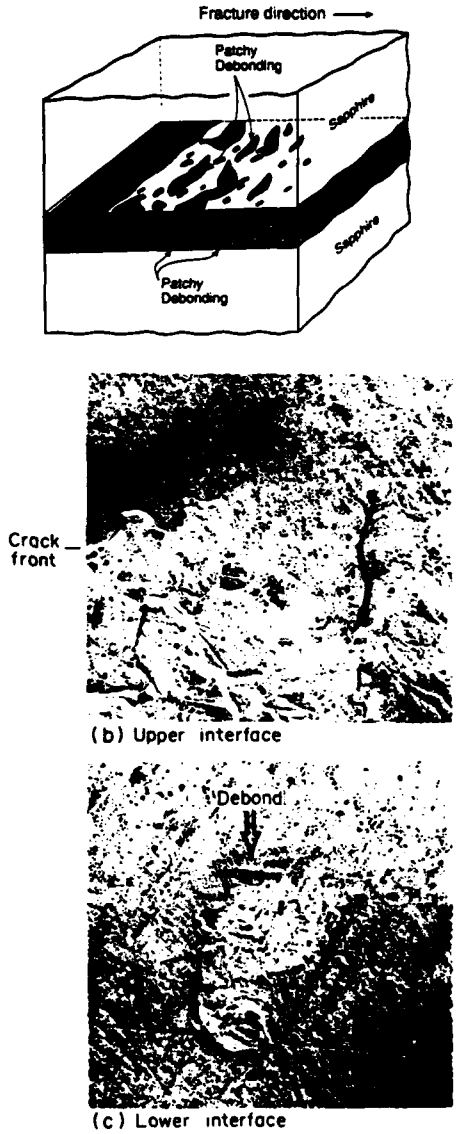

Fig. 5. Debonding along alternate interfaces. (a) Schematic illustration. (b) The intact depression along the crack front on the top interface corresponds to debonded area on the bottom interface (c).

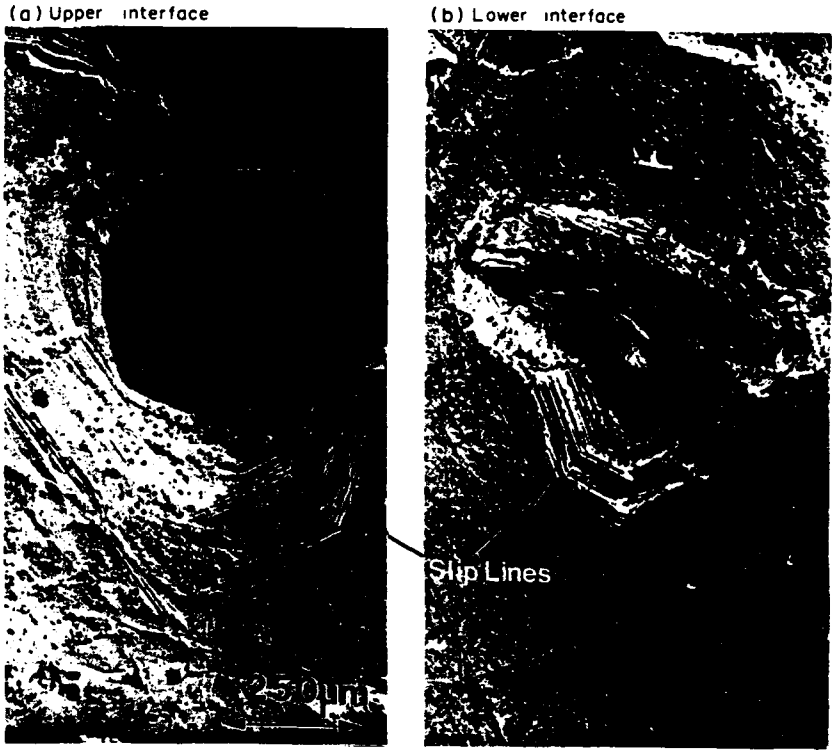

Fig. 6. (a) Intact ligament on top interface with slip lines visible at the perimeter. (b) Debonded area on bottom interface corresponding to (a), also showing slip lines.

and distribution of intact areas is summarized in Table 1.

The annulus of plastic distortion at the perimeter of intact ligaments also depended on the metal layer thickness. Typically, the annuli had widths of ~ 50 and $\sim 150\,\mu$m for the 25 and 100 μm Au layer thicknesses, respectively. Intact regions smaller than about 20 μm in diameter exhibited no detectable deformation. An estimate of the plastic strain in the ligaments was obtained from measurements of the difference in height between the intact and the debonded regions, using the electron beam damage technique. This height difference was observed to depend on the metal layer thickness, but typically had maximum values in the range of 1–2 μm, which corresponds with a plastic shear strain of $\sim 5 \times 10^{-3}$.

Finally, the uniaxial flow stress of the Au was estimated *in situ* by emplacing Vicker's indentations into the Au side of the fracture surfaces, using loads of 0.01 N. The indent size was less than about one-third the Au layer thickness to ensure that the

Fig. 7. (a) Intact ligament region behind crack tip. (b) The same region as in (a) for a larger crack length: intact area is commencing to debond in (b).

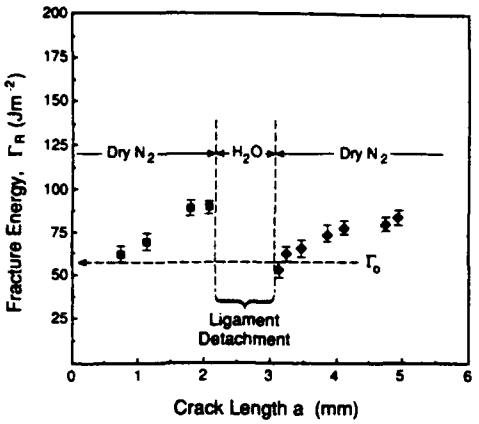

Fig. 8. Interface fracture energy as a function of crack length before and after removing intact ligaments by stress corrosion.

Al_2O_3 substrate did not have an effect. By regarding that the hardness, $H \approx 3\sigma_0$ [11], the flow stress was estimated as $\sigma_0 = 130$ MPa for all three layer thicknesses. This strength is larger than that for bulk annealed Au.

3.2. Interface characterization

Following crack growth in dry N_2, surfaces separated by stress corrosion in water were observed in the SEM. X-ray analysis in the SEM revealed no evidence of Au on the sapphire and no evidence of Al on the Au, even in the regions where crack propagation occurred in dry N_2 by a void growth mechanism. It is thus concluded that fracture proceeded along the interface plane.

An estimate of the work of adhesion, W_{ad}, was obtained from measurements of angle θ between the pore wall and the Au fracture surface (Appendix), as measured on Au fracture surfaces created by subcritically growing the crack in the presence of water. About 30 such angles were measured giving $\theta = 135° \pm 8°$. The work of adhesion was calculated from θ [12] by using a surface energy for Au, given by $\gamma_m = 1.3\ \mathrm{J\,m^{-2}}$ [13, 14]. This gave, $W_{ad} \approx 0.38 \pm 0.12\ \mathrm{J\,m^{-2}}$.

4. MICROMECHANICS OF METAL/CERAMIC INTERFACES

4.1. Initial crack extension

Analysis of ductile fracture mechanisms associated with stationary cracks in a thin metal foil between two elastic plates [15] recognizes that the plastic constraint in a thin metal layer causes the stress to attain values substantially larger than that possible in a homogeneous elastic/plastic solid (Fig. 11). Furthermore, a stress maximum occurs at a distance ahead of the crack governed by the metal layer thickness. One ductile fracture mechanism involves the unstable plastic cavitation which occurs when the mean stress at the interface, σ_m, reaches a critical value. This instability has been shown to occur when the ratio of the mean stress to the uniaxial yield stress, σ_0, is given by

$$\sigma_m/\sigma_0 \approx 5.5. \quad (1)$$

Fig. 9. Crack initiation and growth for 100 μm thickness at three different levels of energy release rate. (a) 63, (b) 96 and (c) 131 J m^{-2}.

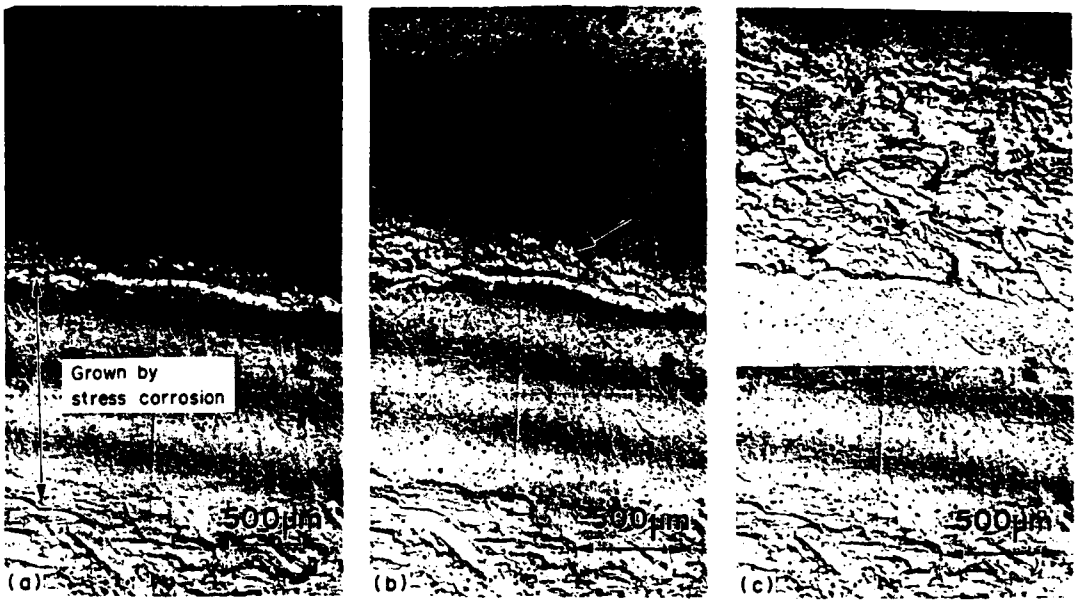

Fig. 10. Crack initiation and growth for 25 μm thickness at three different levels of energy release rate. (a) 53, (b) 62 and (c) 77 J m^{-2}.

In mode I loading, the preceding analysis predicts a distance between the location of this maximum stress and the crack tip given by [15]

$$d \approx 2.2\,h \tag{2}$$

where h is the metal layer thickness. The corresponding critical energy release rate for initial mode I crack growth is [15]

$$\Gamma_0 = 0.2\,\sigma_0 h. \tag{3}$$

A second ductile mechanism obtains when the pore spacing is sufficiently small that the pores near the crack tip nucleate voids which grow plastically and coalesce with the crack tip. The mode I fracture energy for this process is given by [6]

$$\Gamma_0 = 2.0\,\sigma_0 \delta_t \tag{4}$$

where δ_t is the critical crack tip opening displacement. Initial crack growth is presumed to occur when δ_t is on the order of the pore spacing, χ_0 [17], such that

$$\Gamma_0 \approx 2.0\,\sigma_0 \chi_0. \tag{5}$$

Consequently, the ratio of the flaw spacing χ_0 to the metal layer thickness h is an important quantity in controlling the ductile fracture mechanism that dominates initial crack growth. Specifically, for $\chi_0/h < 0.1$ the energy for ductile fracture by void coalescence is below that for cavitation, and vice versa, as indicated on Fig. 12.

Table 1

Au layer thickness h (μm)	Area fraction of debond on lower interface f_c	Width of intact area (μm)
10	0.8-0.9	< 50
25	0.4-0.6	50-100
100	0.2-0.4	100-200

When interface fracture involves debonding, as well as plastic void growth, equations (3) and (5) represent upper bounds for the fracture energy. Explicit relations between Γ_0 and either the plastic flow strength or the work of adhesion when debonding occurs are unknown. Some possibilities suggested by the experiments, with the insight given by equations (3) and (5), are discussed in Section 5.

4.2. *The fracture resistance*

The rising resistance behavior can be rationalized by examining the effect of crack surface tractions caused by the intact metal ligaments on the energy release rate. Analysis of this phenomenon for mixed-mode cracks indicates that such tractions reduce the mode I crack tip stress intensity but increase the mode

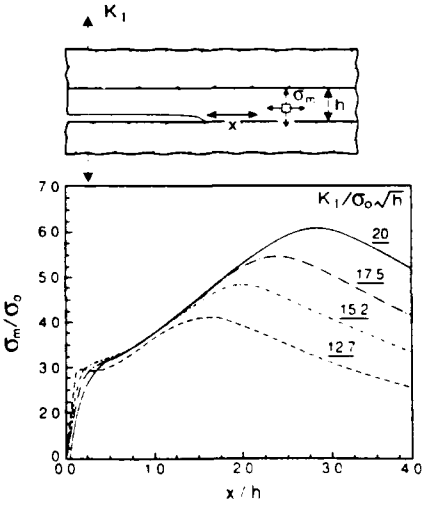

Fig. 11. Plot of normalized mean stress as a function of distance from crack tip [15].

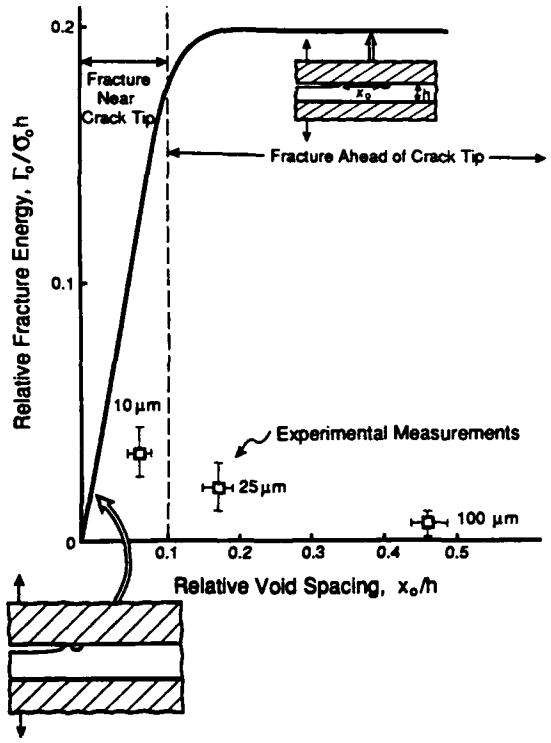

Fig. 12. Plot of normalized Mode I fracture energy for crack extension by ductile fracture as a function of the non-dimensional quantity h/χ_0: the experimental data obtained from Fig. 3 are superposed.

II stress intensity [18]. Consequently, the fracture energy Γ_R varies sensitively with the mode mixity dependence of the underlying interface crack extension mechanism. Expressions for this mixity effect are needed before resistance curves can be calculated [18]. An expression for the mixity effect that appears to conform with typical experimental data is given by [19]

$$\Gamma_R/\Gamma_0 = [1-(1-\lambda)\sin^2\psi]^{-1} \quad (6)$$

where ψ is the mixity angle (zero for mode I and $\pi/2$ for mode II) and λ is a parameter between 0 and 1. Specifically, the fracture energy of a material with $\lambda \to 1$ has little sensitivity to mixity angle, whereas $\lambda \to 0$ refers to strong effects of mixity. Experimental results are mostly in the range $\lambda \approx 0.1$–0.3 [19]. With this background, the calculations [18] reveal that the resistance Γ_R can be characterized by the non-dimensional parameter

$$\sum = ph/E_c\Gamma_0 \quad (7)$$

where E_c is the Young's modulus for the ceramic and p is the traction exerted by the ligaments on the crack surfaces. For metal ligaments

$$p = \sigma_0 f_p \quad (8)$$

where f_p is the area fraction of Au which contributes to the bridging given in Table 1. Resistance curves predicted for a range of Σ and λ are plotted on Fig. 13.

5. THE CRACK GROWTH RESISTANCE

In the presence of H_2O, stress corrosion occurs at the interface with a low fracture energy [7], suggestive of brittle bond rupture at the interface. Such a brittle mechanism occurs despite the incidence of plastic flow and some crack blunting. In dry N_2, interface fracture by plastic void growth is the prevalent mechanism, but this is accompanied by interface debonding. In an attempt to correlate the fracture energy trends, it is first recalled that the initiation fracture resistance, Γ_0, is smaller than the level expected for ductile interface fracture (Fig. 12). Another notable feature is that the non-dimensional fracture energy, $\Gamma_0/\sigma_0 h$, increases as the metal layer thickness decreases, indicative of a corresponding increase in the relative contribution of plasticity to the fracture energy. This effect is the origin of the non-linearity apparent in Fig. 4. However, the absolute contribution of plasticity to Γ_0 must decrease as the metal layer thickness decreases and approach zero as $h \to 0$. Furthermore, since fracture involves interface decohesion, it is reasonable to suppose that $\Gamma_0 \to W_{ad}$ as $h \to 0$. With this background, plus the insights provided by Section 4.1, it has been possible to identify a simple non-dimensional expression for Γ_0, which includes the role of W_{ad}, given by (Fig. 4),

$$\Gamma_0 \approx W_{ad}[1+\sigma_0 h/W_{ad}]^{1/2}. \quad (9)$$

While this expression has no fundamental basis, it appears to be useful for correlating experimental information and should provide guidance for the development of crack growth models.

The subsequent resistance, Γ_R, above Γ_0, may be rationalized using the ligament model presented in Section 4.2 in conjunction with the information on Table 1, plus the uniaxial yield strength obtained from hardness measurements. Then, with Γ_0 from Fig. 3, the experimental data can be transposed onto Fig. 13. It is apparent from this construct that the

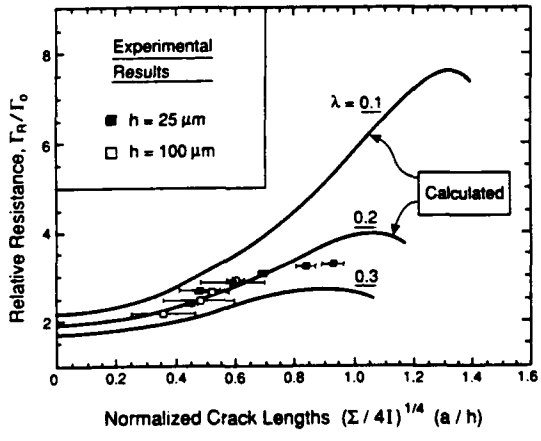

Fig. 13. Resistance curves predicted for interface cracks with bridging tractions [18]. Experimental data points from Fig. 3 are also shown: I is the moment of inertia of the beam and Σ is given by equation (7).

normalization suggested by the models brings the data onto a single curve, consistent with the curve calculated for a mixity parameter, $\lambda \approx 0.2$. Values of λ in this range are typical for interfaces [19]. It is thus concluded that the resistance behavior ($\Gamma_R > \Gamma_0$) is explicable in terms of the bridging associated with intact metal ligaments. It is recalled that such bridging effects are specimen geometry dependent [18] and consequently, Γ_R should not be construed as an unique resistance characteristic of the interface.

6. CONCLUDING REMARKS

This study has demonstrated several characteristics of crack propagation along a metal/ceramic interface. The fracture resistance is sensitive to moisture through a stress corrosion mechanism. In the absence of stress corrosion, the interface cracks extend subject to a rising resistance curve, governed by intact metal ligaments in the crack wake. Additionally, the resistance increases as the metal layer thickness increases. These changes in resistance with crack extension are fully explicable interms of crack shielding caused by the bridging ligaments.

Crack extension occurs by a combination of plastic void growth (that typically initiates at interface pores) accompanied by brittle interface debonding. The measured fracture energies are substantially greater than the work-of-adhesion, but less than the values expected for ductile interface fracture. It has not been possible to use existing models of the plastic dissipation to correlate the experimental fracture energy data. Instead, a semi-empirical function has been identified that seemingly correlates the present data. The development of the associated understanding is an important topic for further research.

REFERENCES

1. A. G. Evans, M. Rühle, B. J. Dalgleish and P. G. Charalambides, *Mater. Sci. Engng* **A126**, 53–64 (1960).
2. R. M. Cannon, R. M. Fisher and A. G. Evans, *Mater. Res. Soc. Proc.* **54**, 799 (1986).
3. B. J. Dalgleish, M. C. Lu and A. G. Evans, *Acta metall.* **36**, 2029 (1988).
4. R. M. Cannon, V. Jayaram, B. J. Dalgleish and R. M. Fisher, *Mater. Sci. Res.* **21**, 959 (1986).
5. T. S. Oh, J. Rodel, R. M. Cannon and R. O. Ritchie, *Acta metall.* **36**, 2083 (1988).
6. P. M. Anderson, J. S. Wang and J. R. Rice, *34th Sagamore Army Materials Research Conference*, Lake George, N.Y. (1987).
7. I. E. Reimanis, B. J. Dalgleish, M. Brahy, M. Rühle and A. G. Evans, *Acta metall. mater.* **38**, 2645 (1990).
8. B. J. Dalgleish, K. P. Trumble and A. G. Evans, *Acta metall.* **37**, 1923 (1989).
9. B. Derby and E. R. Wallach, *Metall. Sci.* **18**, 427 (1984).
10. P. G. Charalambides, J. Lund, A. G. Evans and R. M. McMeeking, *J. appl. Mech.* **56**, 77 (1989).
11. D. Tabor, *Hardness of Metals*. Clarendon Press, Oxford (1951).
12. E. D. Hondros, *Inst. Phys. Conf.*, Ser. No. 75, Conf. Science of Hard Materials, Chap. II (1986).
13. A. R. Miedema, *Metallkde* **69**, 287 (1978).
14. R. M. Pilliar and J. Nutting, *Phil. Mag.* **16**, 181 (1967).
15. A. G. Varias, Z. Suo and C. F. Shih. To be published.
16. R. M. McMeeking, *J. Mech. Phys. Solids* **25**, 357. (1977).
17. J. R. Rice and M. A. Johnson, *Inelastic Behavior of Solids* (edited by M. F. Kenninen *et al.*), p. 641. McGraw–Hill, New York (1970).
18. G. Bao, B. Fan and A. G. Evans, *Mech. Mater.* In press.
19. H. Jensen, J. W. Hutchinson and K. S. Kim, *Int. J. Solids Struct.* **26**, 1099 (1990).
20. R. A. Hoover, *J. Phys. E. Scient. Instrum.* **4**, 747 (1971).

APPENDIX

The equilibrium angle θ between the Au and Al_2O_3 at an interface and the pore depth can be measured in the following way. First, an electron beam damage line is induced in the SEM across the void with the surface normal to the beam. Tilting by Ψ about an axis parallel to the deposition line, the depth of the void d is reflected in the displacement Δa, (Fig. A1): $d = \Delta a / \sin \Psi$ [20]. The angle θ obtained by geometry in terms of the rotation angles θ_R and Ω (Fig. A1), such that

$$\tan \vartheta = \frac{d \cos \beta \tan \vartheta_r}{d \sin \Psi - \Delta h \tan \vartheta_r} \qquad \text{(A1)}$$

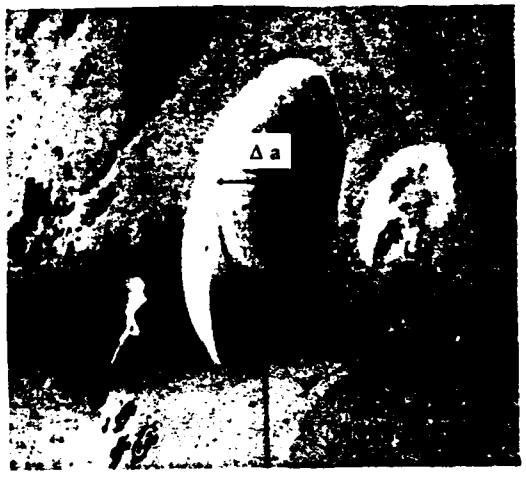

(a)

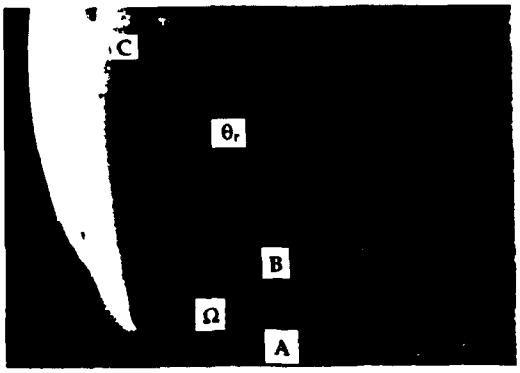

(b)

Fig. A1. (a) Scanning electron micrograph of pore with damage line made apparent by titling, $\Psi = 70^\circ$. (b) Higher magnification SEM of edge of pore in (a).

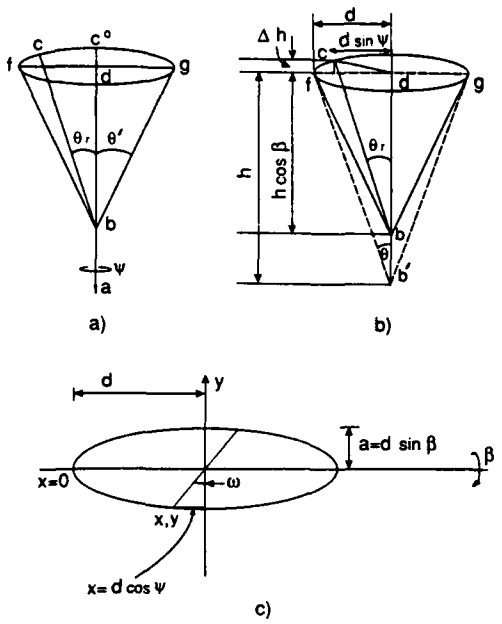

Fig. A2. (a) Cone rotated by Ψ around axis *bd*. (b) Cone rotated by Ψ around axis *bd* and by β around axis *fg*. (c) Ellipse showing rotations Ψ and β (see text).

where

$$\Delta h = d \cos \Psi \sin \beta. \tag{A2}$$

For the ellipse in Fig. A1

$$y = d \sin \Psi \sin \beta, \tag{A3}$$

$$\equiv \frac{d \cos \Psi}{\tan \Omega}. \tag{A4}$$

Consequently, equating (A3) and (A4),

$$\beta = \sin^{-1}\left[\frac{1}{\tan \Psi \tan \Omega}\right]. \tag{A5}$$

Placing (A5) and (A2) into (A1) gives

$$\tan \vartheta = \frac{\cos\left\{\sin^{-1}\left[\frac{1}{\tan \Psi \tan \Omega}\right]\right\} \tan \vartheta_r}{\sin \Psi \tan \Omega - \frac{\cos^2 \Psi \tan \vartheta_r}{\sin \Psi \tan \Omega}}. \tag{A6}$$

Thus, ϑ is obtained from knowledge of the SEM tilting angle, Ψ, and from measurements of Ω, and ϑ_r in Fig. A2.

Acta metall. mater. Vol. 39, No. 7, pp. 1587–1593, 1991
Printed in Great Britain.

0956-7151/91 $3.00 + 0.00

THE STRENGTH AND FRACTURE OF METAL/CERAMIC BONDS

M. Y. HE and A. G. EVANS
Materials Department, College of Engineering, University of California, Santa Barbara, CA 93106, U.S.A.

(Received 30 November 1990)

Abstract—The fracture strength of ceramics bonded with metals is limited by the presence of stress concentrations that arise around the bond, especially near edges. Yet, in some cases, fracture can be induced to occur in the ceramic away from the bond. Analysis of the combined effect of elastic mismatch, plasticity and thermal expansion misfit is presented in this paper, to provide understanding of the trends in bond strength. Important influences of plastic relaxation and thermal expansion misfit are identified and some general fracture characteristics are described.

Résumé—La résistance à la rupture des céramiques liées à des métaux est limitée par la présence de concentrations de contraintes qui se produisent autour de la liaison, spécialement prés des arêtes. Cependant dans certains cas, la rupture peut survenir dans la céramique loin de la liaison. Dans cet article, on présente une analyse de l'effet combiné du desaccord élastique, de la différence de plasticité et de la dilatation thermique sur la résistance à la rupture. On montre les influences importantes de la relations plastique et de la différence de dilatation thermique et on décrit quelques caractéristiques générales de la rupture.

Zusammenfassung—Die Bruchfestigkeit von metallkeramischen Verbindungen wird durch Spannungskonzentrationen um die Verbindung herum, inbesondere an den Kanten, eingeschränkt. Es kann aber doch in einigen Fällen Bruch im keramischen Material, also außerhalb der metallkeramischen Grenzfläche, erzeugt werden. In dieser Arbeit wird der gesamte Einfluß von Fehlpassung, Plastizität und thermische induzierter Fehlpassung analysiert, um die zusammenhänge bei der Bindungsfestigkeit versethen zu können. Einige allgemeine Charakteristika des Bruches werden beschrieben; hingewiesen wird auf den wichtigen Einfluß der plastischen Relaxation und der thermisch induzierten Fehlpassung.

1. INTRODUCTION

There are several reported instances in which the fracture of ceramic/metal bonds originates in the ceramic *near the interface*, rather than *at the interface* [1–4]. Such behavior is most likely when (i) the bond is relatively thin, such that the limit load is substantially higher than the yield strength of the metal[4] and (ii) when the bond is relatively devoid of flaws [1]. When these conditions are achieved, it is of interest to understand the behavior of flaws near the interface. Three important factors are involved in the behavior of these flaws: the mismatch in elastic properties, plastic flow in the metal and residual strain caused by thermal expansion mismatch. Each of these factors is included in the present study. Testing experience indicates that fracture typically originates from flaws near the interface, especially at the edge of the bond. The emphasis of the analysis will thus be on stress concentrations and flaws in this locale. In some cases, fracture occurs in the ceramic well away from the bond, suggesting that stress concentrations can be supressed when the system has the appropriate properties.

Previous studies have given an indication of some of the salient issues [1–6]. The elastic mismatch causes the energy release rate G at edge flaws near the interface to become larger than that expected for an elastically homogenous material [1, 2]. This elevation in G at edge flaws is mitigated by the development of a plastic zone in the metal layer. Residual stress also exerts an influence on fracture and can, indeed, cause fracture in the absence of applied loads. Some aspects of the residual stress have been analyzed [5, 6], but there has been no attempt at *combining the effects of residual and applied loads in the presence of plasticity in the metal*. Analysis of this coupled problem is needed to provide a comprehensive understanding of the overall behavior.

2. STATEMENT OF THE PROBLEM

The geometry (Fig. 1) consists of a thin metal bond between two ceramics with a crack in the ceramic near the interface. Initially, the crack is considered to be parallel to the interface, but effects of crack orientation are also addressed. The materials are

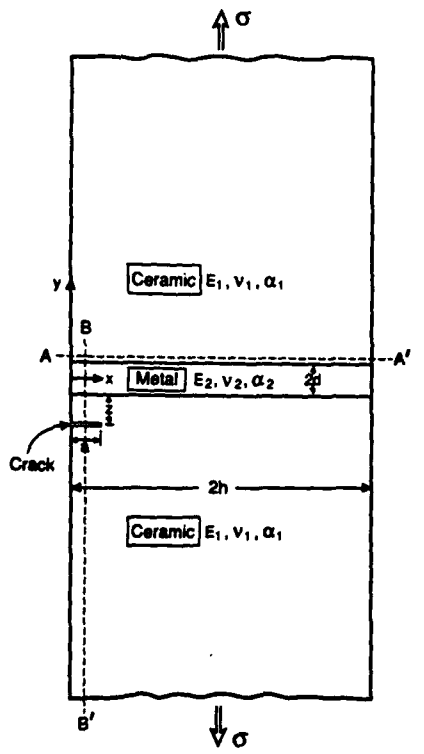

Fig. 1. The thin bond geometry used to conduct the calculations.

chosen to have elastic properties representative of many metal/ceramic systems with the Young's modulus E of the metal being substantially less than that of the ceramic. The metal is considered to yield and work harden such that the uniaxial stress-strain curve satisfies,

$$\epsilon = \sigma/E + A\epsilon_0(\sigma/\sigma_0)^n \qquad (1)$$

where ϵ_0 is the yield strain, σ_0 the uniaxial yield strength, n is a work hardening parameter and A is a coefficient of order unity. Residual strain in the system is motivated by a mismatch in thermal expansion coefficient, between the metal α_2 and the ceramic, α_1 ($\Delta\alpha = \alpha_2 - \alpha_1$) and a cooling temperature, ΔT.

The problem is solved using the following approach. A mismatch strain $\Delta\alpha\Delta T$ is imposed on the bond to simulate cooling and the resultant development of residual stress calculated. In most cases, the mismatch strain is taken to be sufficiently large compared with the yield strain that the metal has fully yielded during this process. Subsequently, loads are applied and the energy release rate, G, as well as the phase angle of loading, ψ, associated with cracks in the ceramic are calculated by finite elements, using the ABAQUS code. The finite element meshes used to conduct the calculations are summarized in Fig. 2. Eight-node biquadratic plane strain elements were used with nine integration points for each element.

3. RESULTS

3.1. Stresses for bonds without a crack

The stress field characteristics of interest to the above cracking phenomenon occur in the ceramic either on a plane near the interface (AA' in Fig. 1) or on a plane near the edge (BB' in Fig. 1). The stresses of particular importance are σ_{yy} and σ_{xy}, which govern the mode I and mode II components of the energy release rate. Some preliminary results for a bond without a crack, summarized in Fig. 3, indicate the general trends in σ_{yy} when the expansion misfit is positive ($\alpha_2 > \alpha_1$). In particular, the σ_{yy} residual stresses exhibit a tensile boundary layer in the ceramic

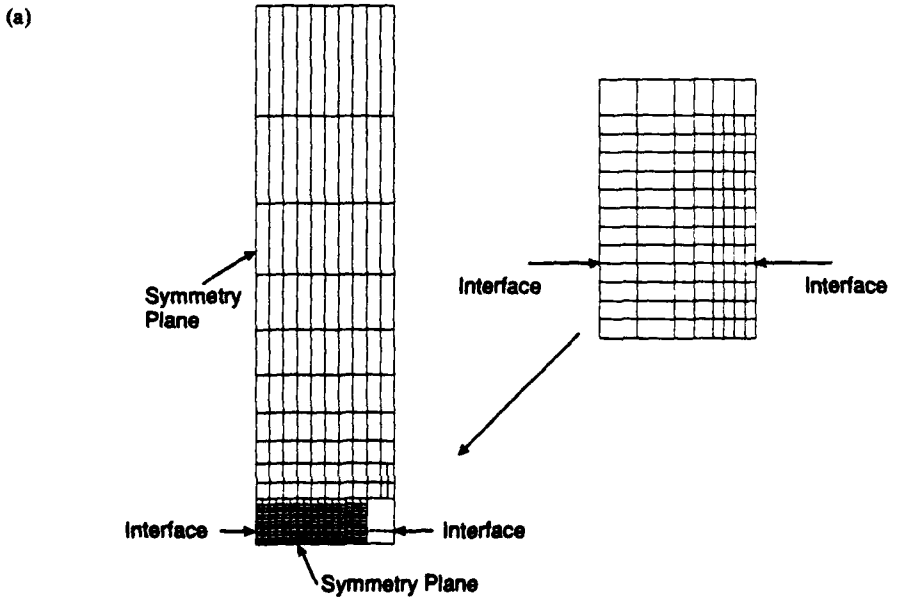

Fig. 2. (a) *Caption on facing page.*

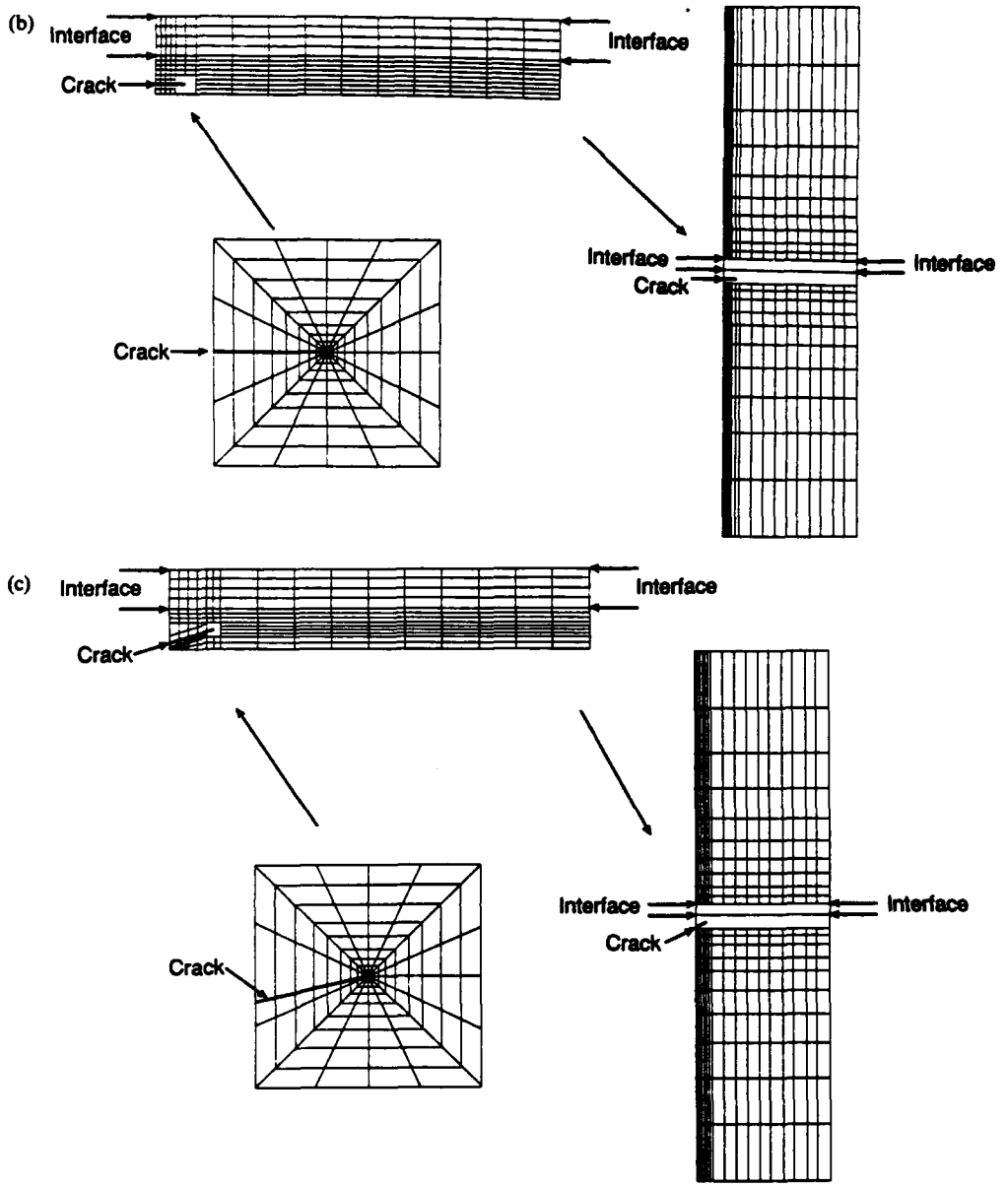

Fig. 2. Typical finite element meshes (a) without a crack (b) with a crack parallel to the interface (c) with a crack inclined to the interface.

along the edge [Fig. 3(a)]. This layer often dominates the formation of *edge* cracks in the ceramic [7]. Under applied loading in the absence of thermal mismatch, contours of this σ_{yy} stress near the interface [Fig. 3(b)] reveal that a new deformation field becomes established which eventually eliminates the residual field and results in a concentrated σ_{yy} stress near the corner. The explicit effects of yield strain ϵ_0 and of the mismatch strain, $\Delta\alpha\Delta T$, can be expressed through the parameter

$$\lambda = \Delta\alpha\Delta T/\epsilon_0. \tag{2}$$

Notably, the width of the σ_{yy} tensile boundary layer (Fig. 4) diminishes as λ increases, confirming the beneficial role of yielding (lower ϵ_0) on the tensile residual stresses in the ceramic. These effects are further illustrated from plots of the residual stresses along BB′ in the non-dimensional form σ_{yy}/σ_0 (Fig. 5), which reveal that the stress amplitudes for two substantially different values of λ are similar upon using σ_0 as the normalizing stress. Consequently, the magnitudes of the tensile stresses in the boundary layer also *diminish* as the yield strength decreases.

The stress along AA′ near the interface which is primarily of interest with regard to cracking in the ceramic is the principal stress σ_1, and its orientation with respect to the interface, ϕ. A plot of the stress (Fig. 6) indicates that it is tensile near the center of the bond and almost normal to the interface. Cracks

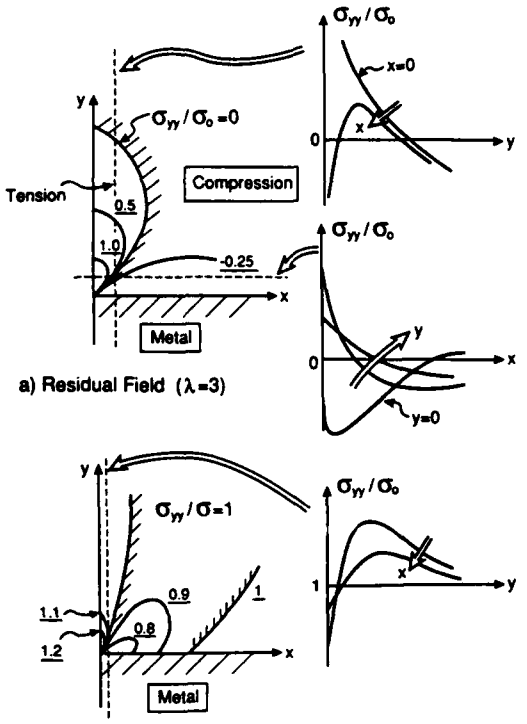

Fig. 3. A schematic indicating the general characterization of the σ_{yy} stress (a) residual stress caused by positive misfit (b) applied loads.

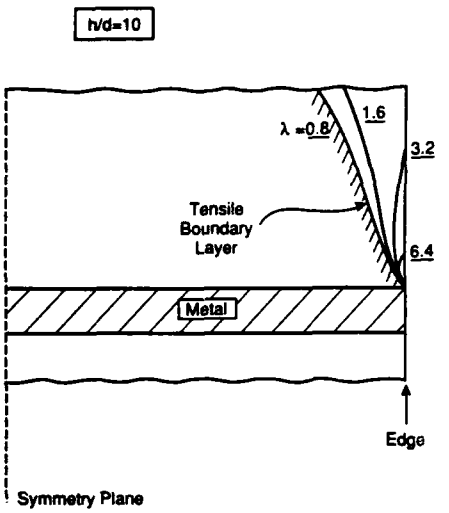

Fig. 4. The σ_{yy} tensile boundary layer caused by the residual field and the effect of the expansion misfit coefficient, $\lambda = \Delta\alpha\Delta T/\epsilon_0$.

that form in response to this stress are observed in metal/ceramic bonds [7].

3.2. Energy release rates

Aspects of the bond strength manifest in the energy release rate for cracks near the interface are best expressed in terms of the non-dimensional energy release rate, G/G_h, where G_h is the energy release rate for homogeneous material (i.e. no bond layer). Furthermore, since only those bonds having high strength are of technological interest, the calculations emphasize stresses σ/σ_0 in the range 1–6.† The general trends that have become apparent from the calculations are schematically illustrated in Fig. 7. It is first noted that at small σ/σ_0, G/G_h increases as σ/σ_0 increases, followed by a behavior at large σ/σ_0 wherein G/G_h then decreases with further increase in the stress. The rising segment is attributed to *elastic* mismatch across the interface which increases the relative elastic energy between the crack and the interface as the stress increases, as indicated by the dotted line in Fig. 7. At larger σ/σ_0, the elasticity effect is counteracted by plasticity in the metal which, as noted above, tends to suppress the tensile boundary layer in the ceramic near the interface (Figs 4 and 5). Plastic relaxation tends to diminish G/G_h as σ/σ_0 increases, as indicated by the second dotted line in Fig. 7. The net effect in the presence of both *elastic mismatch and plasticity* is a curve wherein G/G_h initially increases and then decreases as σ/σ_0 increases.

The thermal expansion misfit and the relative crack length also have an important influence on G/G_h. As already noted, positive misfit suppresses the tensile boundary layer and thus at smaller values of σ/σ_0, when the misfit is important, G/G_h systematically *reduces, provided that the cracks are relatively long* ($a/h \gtrsim 0.1$). However, when the cracks are short ($a/h \lesssim 0.1$) and located within the boundary layer, *misfit tends to increase* G/G_h at small stresses. Consequently, misfit may have either detrimental or beneficial effects on bond strength, depending on the crack size.

Specific results obtained for G/G_h, summarized in Figs 8, 9 and 10, elaborate on these trends. For *short cracks*, it is apparent that *plastic relaxation* is the most important factor (Figs 8 and 9) such that, at high stress level ($\sigma/\sigma_0 \gtrsim 4$–5), G can be less than G_h when the dominant flaws in the ceramic are not immediately adjacent to the interface. However, a complete understanding of bond strength and of the benefits of plastic relaxation would require a full statistical analysis in the presence of a distribution of edge flaws near the interface. Conversely, for *large cracks*, *expansion misfit* has the greatest effect on fracture suppression, such that G can be less than G_h at large λ, but only when the stresses are low (Fig. 10). This behavior may be important for *crack arrest* in some cases, such as thermal loading.

Calculations of the phase angle of loading ψ associated with cracks parallel to the interface (Fig. 11) indicate that, in the absence of misfit, the phase angle is *negative* at all stress levels and the cracks would tend to deviate *toward* the interface. However, for significant positive misfit, the phase angle changes sign and becomes positive, especially at

†Bonds fail by ductile rupture at stresses $\sigma \gtrsim 6\sigma_0$ [8].

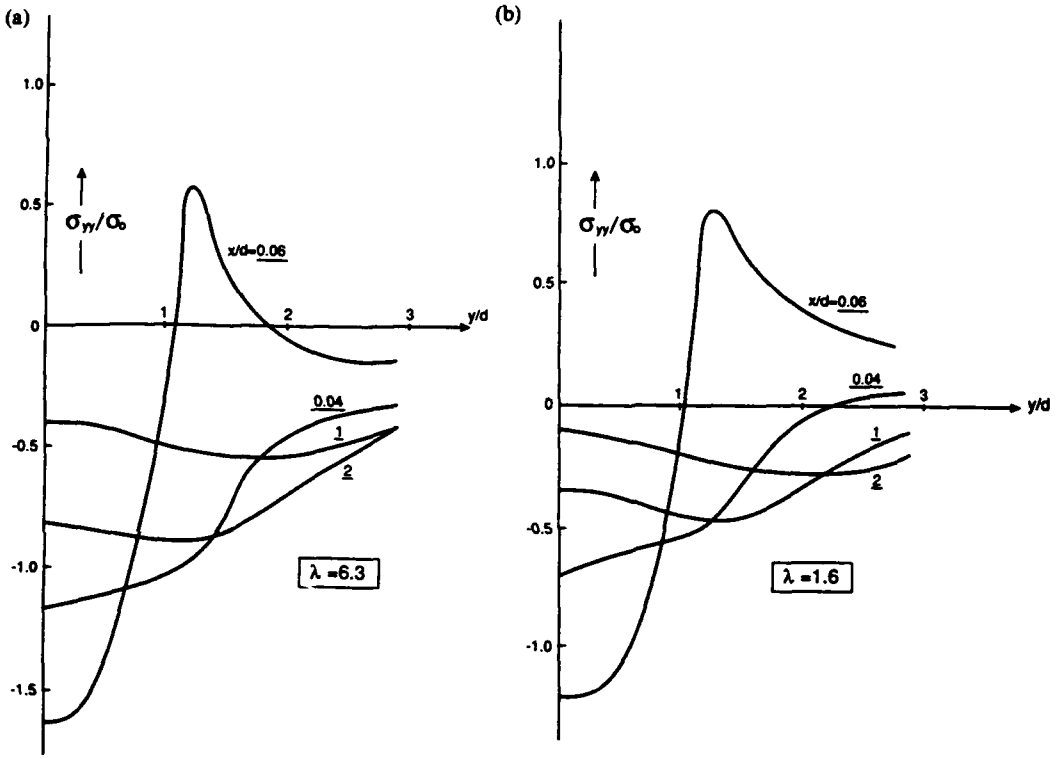

Fig. 5. The residual σ_{yy} stresses near the edge (a) $\lambda = 6.3$, (b) $\lambda = 1.6$.

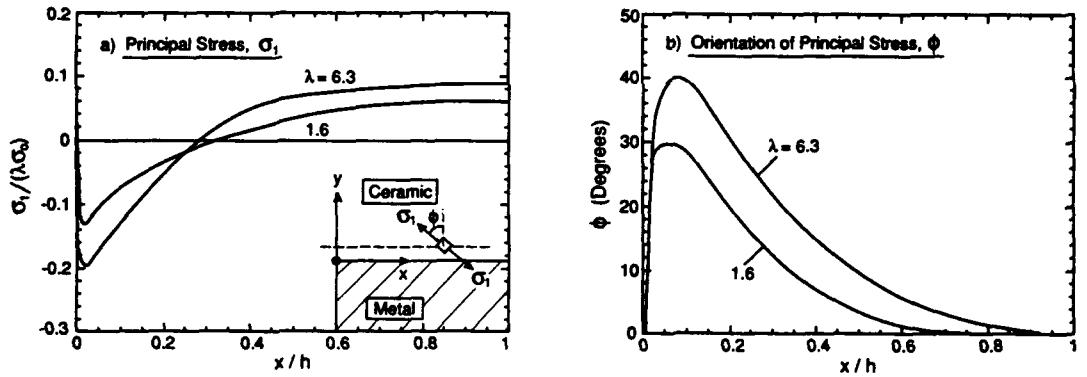

Fig. 6. (a) The principal stress, σ_1, in the ceramic near the interface. (b) The orientation of the most positive principal stress, σ_1.

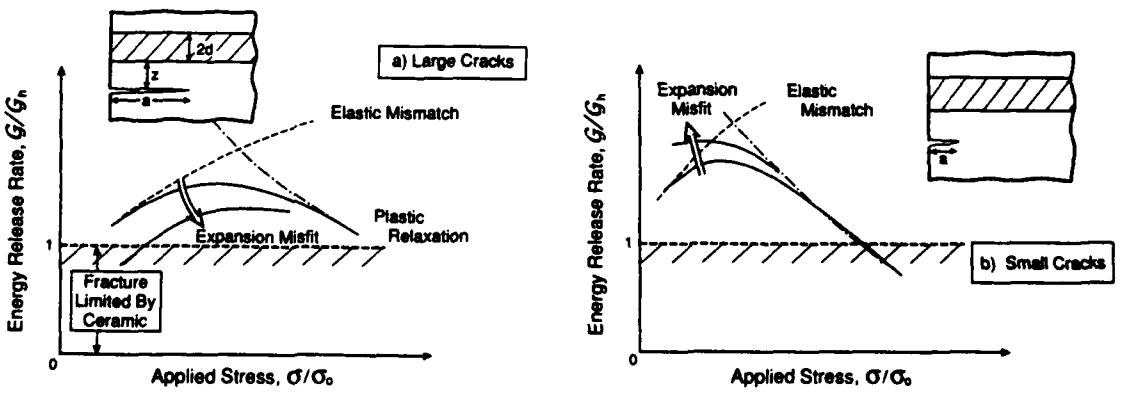

Fig. 7. A schematic indicating trends in the energy release rate with applied stress (a) large cracks (b) small cracks, $a/h \lesssim 0.1$.

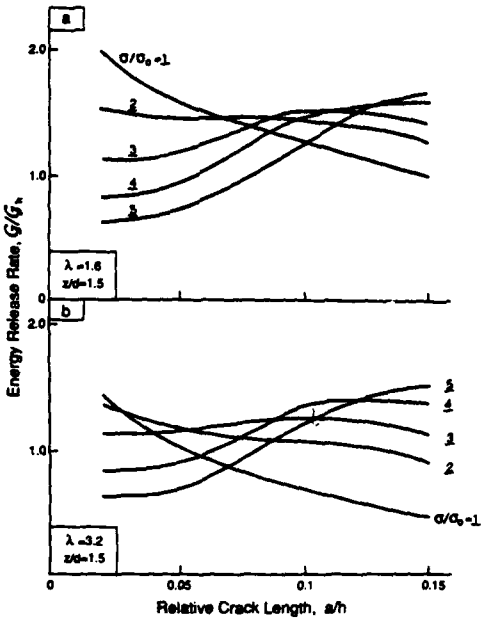

Fig. 8. Variation in the normlized energy release rate with crack length for various stresses (a) $\lambda = 1.6$, $z/d = 1.5$, (b) $\lambda = 3.2$, $z/d = 1.5$.

smaller σ/σ_0, indicative of a tendency for cracks to direct *away* from the interface, as found experimentally [7].

The general mixed-mode nature of cracks parallel to the interface suggests that the energy release rate may be larger for edge flaws inclined to the interface.

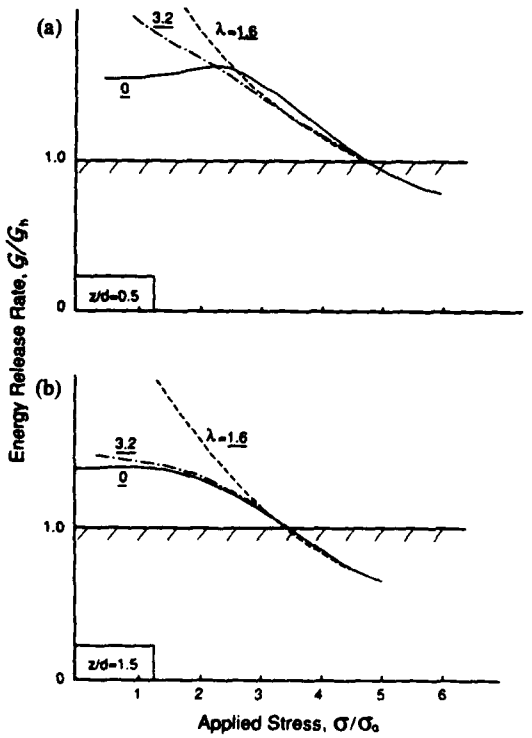

Fig. 9. Effects of stress and expansion misfit on the energy release rate for *short cracks* ($a/h = 0.02$), (a) $z/d = 0.5$, (b) $z/d = 1.5$.

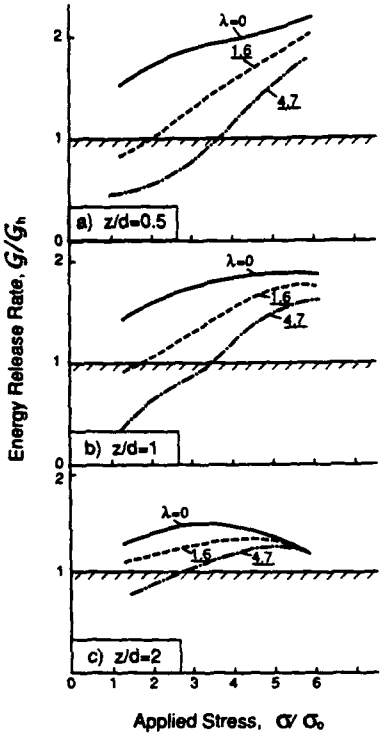

Fig. 10. Effect of stress and expansion misfit on the energy release rate for *long cracks* ($a/h = 0.2$), (a) $z/d = 0.5$, (b) $z/d = 1.0$, (c) $z/d = 2.0$.

To address this possibility, G has been calculated for flaws having various inclinations θ (Fig. 12), within a range around the $K_{II} = 0$ plane suggested by the phase angle calculations. The results reveal that G is relatively orientation insensitive, especially at lower stresses, provided that the crack is defined in terms of the length projected parallel to the interface (Fig. 12).

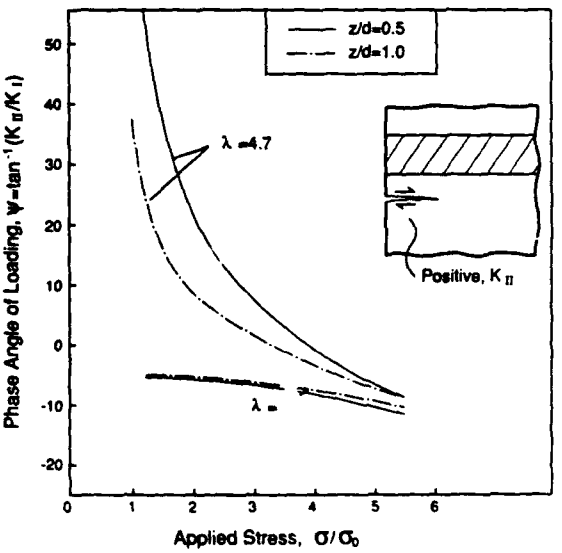

Fig. 11. Effects of stress and expansion misfit on the phase angle of loading for a long crack near the interface ($a/h = 0.2$).

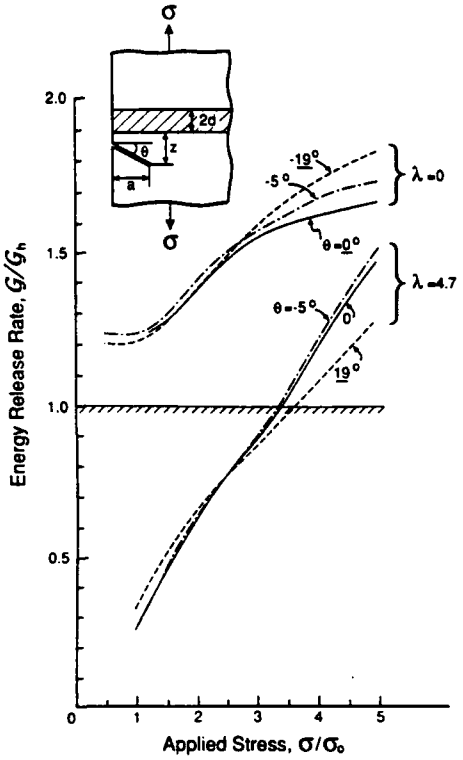

Fig. 12. Effects of crack orientation on the energy release rate.

4. IMPLICATIONS AND CONCLUSIONS

The preceding calculations have the following principal implications for the strength of ceramics bonded with thin metal layers, when the metal has the larger thermal expansion coefficient (positive misfit).† When the interface has a sufficiently high fracture energy that failure does not occur at the interface, the major limitation on the strength concerns stress concentrations in the ceramic near the edge. These stress concentrations arise because of elastic mismatch between the metal and the ceramic. The magnitude of the stress and of the energy release rate at edge flaws is modified by thermal expansion misfit and by plastic relaxation. Two basic behaviors have been identified. For *strong bonds*, wherein the edge *flaws are small* and the *stresses are large*, plastic relaxation effects dominate. Notably, edge failures in the ceramic near the bond can be supposed by using a metal with a low yield strength. In this regime, expansion misfit effects, although small, are detrimental.

Very different characteristics obtained when the cracks are relatively large and the stress small, as appropriate for the assessment of *crack arrest*, e.g. when the loadings are displacement dominated. In this regime, the energy release rate is diminished by having large (positive) expansion misfit, because of the compressive residual stresses generated near the interface.

†Negative misfit induces edge cracking along the interface [5].

Acknowledgements—This work was supported by the DARPA University Research Initiative (Sub agreement P.O. No. UB38639-0 with the University of California, Santa Barbara, ONR Prime Contract No. N00014-86-K-0753). Provision of the ABAQUS finite element code by Hibbitt, Karlsson and Sorensen, Inc. of Providence, Rhode Island is gratefully acknowledged. The calculations on the FPS 500 EA computer were made possible by FPS Computing through the UCSB Industrial Liaison Program.

REFERENCES

1. B. J. Dalgleish, M. C. Lu and A. G. Evans, *Acta metall.* **36**, 2029 (1988).
2. A. G. Evans, M. C. Lu, M. Rühle and S. Schmauder, *Acta metall.* **34**, 1643 (1986).
3. W. Mader and M. Rühle, *Acta metall.* **37**, 853 (1989).
4. B. J. Dalgleish, K. P. Trumble and A. G. Evans, *Acta metall.* **37**, 1923 (1989).
5. H. C. Cao, M. D. Thouless and A. G. Evans, *Acta metall.* **36**, 2037 (1988).
6. A. G. Evans, M. Rühle and M. Turwitt, *J. Physique* **C4**, C4-613 (1985).
7. A. Bartlett, M. Rühle and A. G. Evans, *Acta metall. mater.* **39**, 1579 (1991).
8. V. Tvergaard and J. W. Hutchinson. To be published.

Scripta METALLURGICA et MATERIALIA
Vol. 25, pp. 1003-1010, 1991
Printed in the U.S.A.

VIEWPOINT SET No. 16

THE FRACTURE RESISTANCE OF METAL/CERAMIC/INTERMETALLIC INTERFACES

A. G. Evans, A. Bartlett, J. B. Davis, B. D. Flinn, M. Turner and I. E. Reimanis
Materials Department, College of Engineering
University of California, Santa Barbara, California 93106

(Received February 28, 1991)

Introduction

A concerted effort on the mechanics of interface cracks (1–3), coupled with the development of test methods for measuring the interface fracture resistance (4, 5), has provided a framework for characterizing the mechanical properties of interfaces. There appear to be four governing issues (4, 6, 7). i) Interface fracture can be either brittle or ductile. ii) The fracture resistance is strongly influenced by the loading mixity, primarily through its influence on the crack path. iii) Crack growth by stress corrosion and by fatigue are commonly encountered. iv) The fracture resistance is substantially larger than the work of adhesion and is affected by plastic dissipation, as well as by interface non-planarity and by segregation. There are also appreciable geometric effects, such as the thickness of the metal present in laminates, adhesive bonds and fiber composites. In addition, residual stresses are typically involved and often provide an appreciable contribution to the energy release rate (8), as well as influencing the loading mixity (6).

There are major differences in interface fracture with the homologous temperature, T/T_m, used to produce the interface. Low homologous temperatures ($T/T_m < 0.3$) processes such as evaporation result in interface mechanical properties dominated by impurities, especially organics present on the original surface prior to deposition (9). Consequently, thin bond layers, such as Cr and Ti, are often used to enhance the fracture resistance. The presence of these layers apparently results in the formation of carbides and hydrides that 'clean' the surface. The use of high homologous temperatures ($T/T_m > 0.5$) generally results in 'strong' bonding for a wide range of metals, ceramics, intermetallics and glasses. Such diffusion bonds are emphasized in this article.

The fracture resistance of diffusion bonds can be influenced by the presence of reaction products. It is thus convenient to catagorize interfaces in terms of their susceptibility to reaction product formation. An incomplete list of diffusion bonded interfaces that have been subject to *mechanical characterization* are summarized in Table I, together with the known incidence of reaction products. When reaction products form, cases have been found wherein cracks propagate within the product phase (10). and other cases wherein interface cracks extend between this phase and the parent material (11, 12), dependent on the system and the loading mixity.

A comprehensive review of the interface fracture processes associated with each system is not attempted here. Rather, the range of effects that can occur are illustrated from some of the systems presented in Table I. Consequently, the following sections are organized in accordance with present understanding of the dominant fracture mechanisms: ductile void growth, brittle debonding and decohesion, as well as combined void growth and debonding.

Ductile Interface Fracture

Two systems are known to the authors in which fracture occurs by ductile void growth and coalescence in the metal near the interface. These are Al/Al_2O_3 (13, 14) and $Ti/Ti_3Al/Al_2O_3$ (15). This mechanism involves void nucleation in the metal, typically at interface sites (Fig. 1a). For example, in Al/Al_2O_3, voids preferentially form at grain junctions in the Al_2O_3 (14) (Fig. 1b). When this mechanism applies, there are several profound geometric effects on the mechanical fracture resistance: especially with regard to the metal layer thickness, h, and the loading mixity, ψ. The metal layer thickness enters through its influence on the stresses at the interface ahead of the crack (16) (Fig. 2). The trend is for these stresses to increase as h decreases, causing the fracture resistance Γ_R to diminish at small h. An extreme case is illustrated in Fig. 3 which demonstrates ductile void growth in a thin α_2-Ti_3Al layer formed between Ti(Ta)

0036-9748/91 $3.00 + .00

and Al_2O_3 (15). For this thin layer ($h \approx 0.15\ \mu m$), the fracture resistance $\Gamma_R \approx 25\ Jm^{-2}$ is smaller than that for brittle interface fracture in many systems, as elaborated below. The spacing between void nucleation sites along the interface is also important and may dominate when this spacing is appreciably less than h (16).

The loading mixity is important because of the influence on the crack path (6). In particular, the loading that encourages the crack to deviate from the interface may induce cracking into the ceramic and prevents measurement of Γ_R. Measurements of Γ_R require careful consideration of test specimens having mixities that constrain the crack to remain at the interface, as exemplified by the flexure specimen depicted in Fig. 4 (17).

Brittle Debonding and Decohesion

Brittle debonding of metal/ceramic interfaces formed by diffusion bonding has rarely been observed. The only example known to the authors is the Al_2O_3/Mo interface, which has a fracture energy, $\Gamma_R \approx 3\text{-}4\ Jm^{-2}$ (Fig. 5) (18). There is also circumstantial evidence that Al_2O_3/W interfaces have a similarly low fracture resistance. However, even in these systems, Γ_R is appreciably larger than the thermodynamic work of adhesion, W_{ad}, indicating that dissipation mechanisms accompany interface fracture. The only other known example of brittle interface debonding occurs in the Ti(Ta)/Al_2O_3 system, when a γ-TiAl reaction product forms (12). In this case, fracture occurs at the interface between the parent Al_2O_3 and the γ-TiAl reaction product (Fig. 6a), with a fracture energy, $\Gamma_R \equiv 17\ Jm^{-2}$. This result contrasts with the behavior of diffusion bonded interfaces between γ-TiAl and Al_2O_3 which are resistant to debonding (19) (Fig. 6b). Essentially all other interface fractures that involve debonding are accompanied by appreciably plastic dissipation in the metal, as elaborated below.

When brittle reaction products form and when thin brittle interlayers are used, brittle decohesion within the layer has been frequently observed. Examples include the σ-phase reaction product between γ-TiAl and Nb (10), as well as porous oxide interlayers between Al_2O_3 and other materials (20). In such cases, Γ_R is dominated by the microstructure of the layer and the associated fracture resistance. The effects are exemplified by porous oxide interlayers, wherein Γ_R varies with the level of the porosity. The phenomenon is illustrated for ZrO_2 interlayers in Al_2O_3 (Fig. 7). For the porous interlayers (porosity ~ 30%) fracture occurs *within the layer*, with a fracture energy, $\Gamma_R \approx 3\text{–}5\ Jm^{-2}$. However, for the dense ZrO_2 interlayer, fracture can be induced *at the interface* with a fracture energy, $\Gamma_R \approx 15\text{–}20\ Jm^{-2}$.

Debonding with Plasticity

Many of the interfaces summarized in Table I involve debonding accompanied by plastic dissipation. These systems include Al_2O_3/Au, Al_2O_3/Pt and Al_2O_3/Nb. Furthermore, the behavior is complicated by the incidence of stress corrosion (7), as well as by crack face bridging caused by metal ligaments (21, 22). The latter results in an interface fracture resistance that rises with crack extension (Fig. 8a). The rising resistance is well-described by plastic bridging models (23) (Fig. 8b). In the absence of stress corrosion caused by moisture, direct observations of interface crack extension (22) have revealed that the crack advances by the nucleation of debonds at the interface ahead of the crack (Fig. 9). These debonds grow by combined brittle debonding of the interface with plastic deformation and then coalesce to cause crack extension. This process occurs at a fracture resistance substantially lower than that expected for ductile fracture by plastic void growth. Models of this process have yet to be developed.

Moisture induced stress corrosion substantially reduces Γ_R, whereupon interface cracks grow with a characteristic growth rate that increases as Γ_R increases (7). This behavior is presumed to be analogous to that found in monolithic bodies. Furthermore, the nominal interface fracture resistance decreases as the metal layer thickness decreases (22) (Fig. 10), reflecting an important role of plastic dissipation in fracture, even through stress corrosion is occurring (7).

Remarks

Some of the interface fracture phenomena evident in both metal/ceramic and metal/intermetallic interfaces have been briefly outlined. It is apparent that a rich spectrum of effects is involved, analogous to fracture in monolithic materials. While a start has been made, a systematic experimental effort is needed to characterize the range of fracture behaviors, along with the development of models that relate to each important fracture mechanism. Important issues that have not been addressed in this brief survey include effects of mode mixity on Γ_R and fatigue crack growth at interfaces.

TABLE I

Interfaces That Have Been Subject to Mechanical Characterization

METAL	CERAMIC-INTERMETALLIC	KNOWN REACTION PRODUCTS
Al	Al_2O_3	None
Au	Al_2O_3	None
Nb	Al_2O_3	None
Mo	Al_2O_3	None
W	Al_2O_3	None
Ti	Al_2O_3	γ-TiAl α_2-Ti_3Al
Al	SiC	Al_4C
Al(Si)	SiC	None
Al(Mg)	Al_2O_3	Spinel
Ti(Ta)	Al_2O_3	γ-TiAl α_2-Ti_3Al σ-phase
Pt	Al_2O_3	Pt_3Al
Nb	γ-TIAL	T2, σ-phase
TiNb	γ-TIAL	α_2-Ti_3Al
Nb	$MoSi_2$	$(NbMo)_5Si_3$
Cu	SiO_2	None

References

1. J. W. Hutchinson, *Metal/Ceramic Interfaces* (Ed., M. Rühle *et al.*) Pergamon (1990).
2. Z. Suo, this volume.
3. J. W. Hutchinson and Z. Suo, *Advances in Applied Mech.*, vol. 28 (1991).
4. A. G. Evans, B. J. Dalgleish, P. G. Charalambides and M. Rühle, *Mtls. Sci. and Engr.*, A R6 (1990) 53.
5. J. S. Wang and Z. Suo, *Acta Metall.*, 38 (1990) 1279.
6. A. G. Evans, M. Y. He and J. W. Hutchinson, *Acta Metall.*, 37 (1989) 3249.
7. I. E. Reimanis, B. J. Dalgleish, M. Brahy, M. Rühle and A. G. Evans, *Acta Metall. Mater.*, in press.
8. P. G. Charalambides, H. C. Cao, J. Lund and A. G. Evans, *Mech. of Mtls.*, 8 (1990) 269.
9. R. M. Cannon, R. Fisher and A. G. Evans, *MRS Proceedings* (1986) 799.
10. H. E. Dève, A. G. Evans, G. R. Odette, R. Mehrabian, M. L. Emiliani and R. J. Hecht, *Acta Metall. Mater.*, 38 [8] (1990).
11. A. Bartlett, M. Rühle and A. G. Evans, *Acta Metall. Mater.*, in press.
12. M. Y. He, A. Bartlett and J. W. Hutchinson, *J. Am. Ceram. Soc.*, in press.
13. B. J. Dalgleish, K. P. Trumble and A. G. Evans, *Acta Metall.*, 37 [7] (1989).
14. B. D. Flinn, F. W. Zok, F. F. Lange and A. G. Evans, *Proc. 1990 ASM/TSM Fall Meeting*, in press.
15. A. Bartlett and A. G. Evans, to be published.
16. A. G. Varias, Z. Suo and C. F. Shih, *Mechanics and Phys. of Solids*, in press.
17. P. G. Charalambides, J. Lund, R. M. McMeeking and A. G. Evans, *Jnl. Appl. Mech.*, 56 (1989) 77.
18. J. B. Davis, G. Bao, H. C. Cao and A. G. Evans, *Acta Metall. Mater.*, in press.
19. M. L. Emiliani, R. J. Hecht, H. E. Dève, J. B. Davis and A. G. Evans, to be published.
20. J. B. Davis, E. Bischoff and A. G. Evans, to be published in *Proceedings of the Symposium on Ceramic, Polymer and Metal Matrix Composites*, Am. Cer. Soc. (Nov. 1990).
21. T. S. Oh, R. M. Cannon and R. O. Ritchie, *J. Am. Ceram. Soc.*, 70 [12] C-352– C-355 (1987).
22. I. E. Reimanis and A. G. Evans, *Acta Metall. Mater.*, to be published.
23. G. Bao, B. Fan and A. G. Evans, *Mech. of Mtls.*, in press.

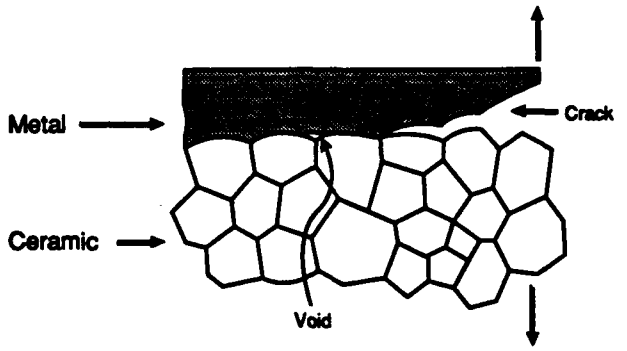

Fig. 1. a) A schematic of interface fracture by void growth.

b) A fracture surface of an Al/Al_2O_3 specimen indicating Al ridges formed by plastic void coalescence. Note that virtually all of the ridges surround three-grain junctions in the Al_2O_3 which act as void nuclei.

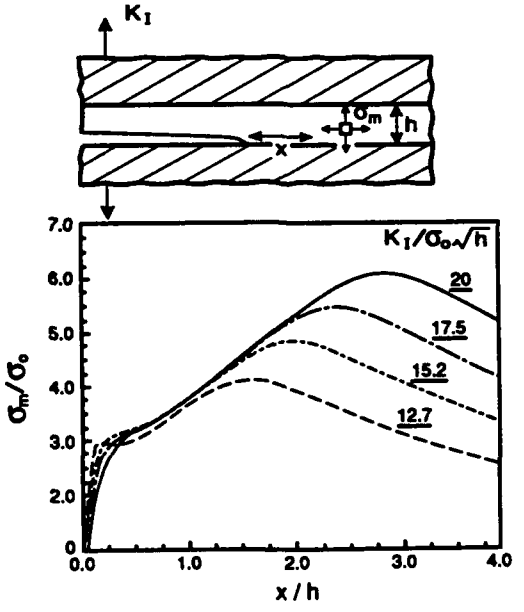

Fig. 2. Stresses at the interface ahead of a crack for a thin metal layer between two brittle solids.

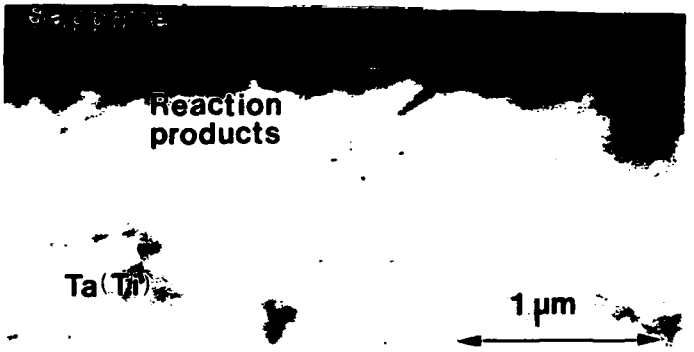

Fig. 3. Fracture by ductile void growth within a thin α_2-Ti_3Al reaction product layer found between Al_2O_3 and Ti(Ta).

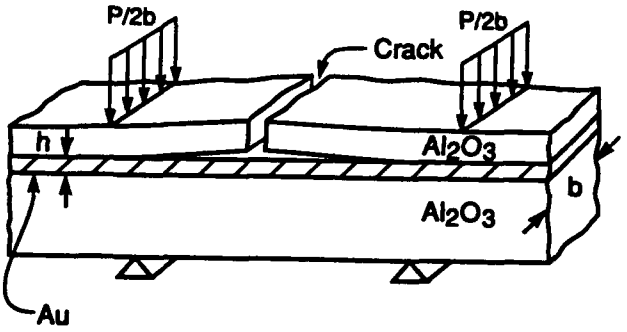

Fig. 4. A mixed mode flexure specimen for measuring the interface fracture resistance that constrain crack extension to occur along the interface.

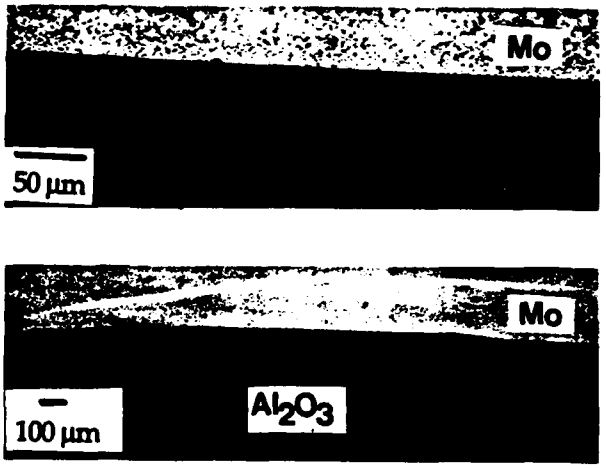

Fig. 5. An interface debond between Mo and Al_2O_3.

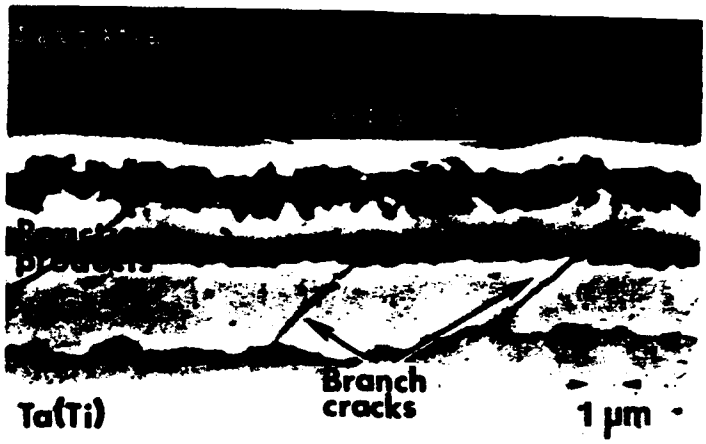

Fig. 6. a) Interface debonding between a γ-TiAl reaction product layer and Al_2O_3: note the branch cracks in the reaction layer.

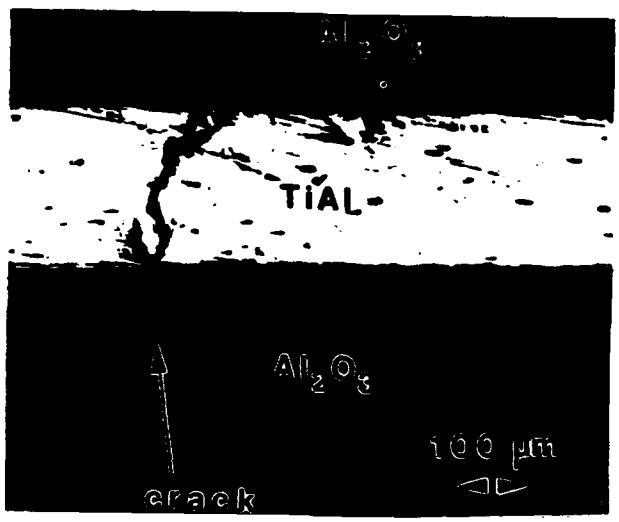

b) Crack extension across the interface, without debonding, in a diffusion brittle γ-TiAl/Al_2O_3

Fig. 7. SEM micrograph of ZrO_2 interfaces on Al_2O_3 (a) porous interlayer that fractures through the layer with $\Gamma_R \approx 4\ Jm^{-2}$ (b) dense interlayers that fracture at the interface with $\Gamma_R \approx 20\ Jm^{-2}$.

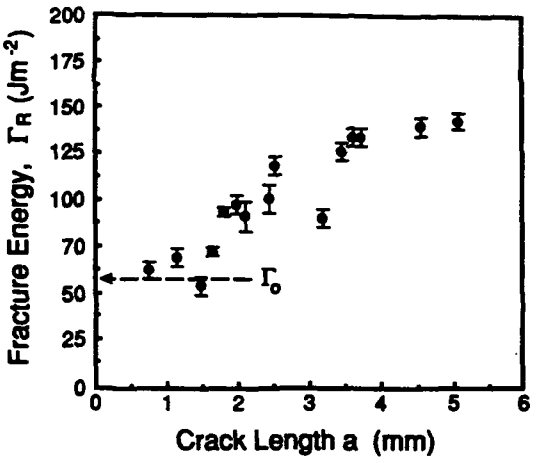

Fig. 8. a) A resistance curve for the Au/Al_2O_3 interface measured in a dry atmosphere.

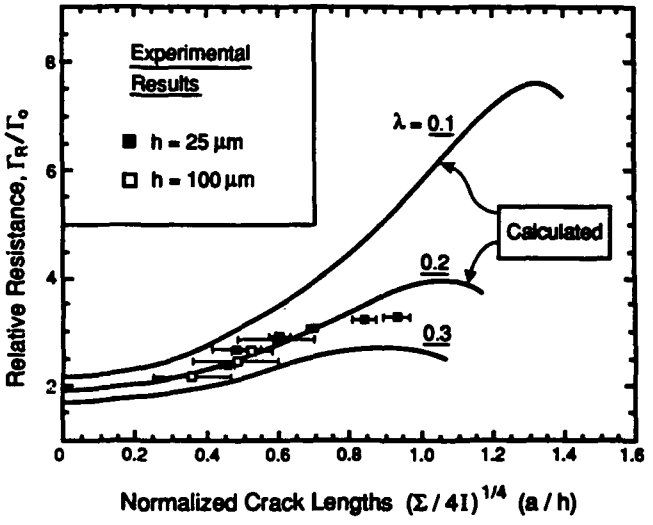

Fig. 8. b) A comparison of the measured resistance curve for Au/Al_2O_3 with calculations based on a ligament model.

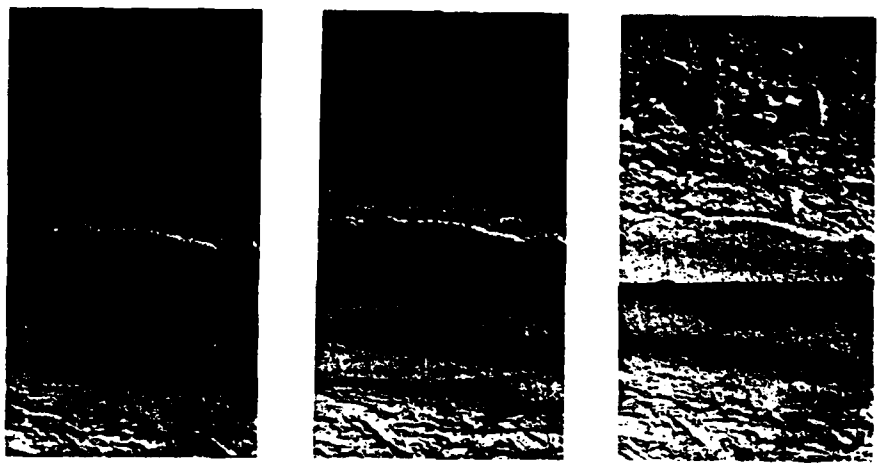

Fig. 9. A sequence showing the crack advance mechanism at the Au/Al_2O_3 interface tested in a dry atmosphere.

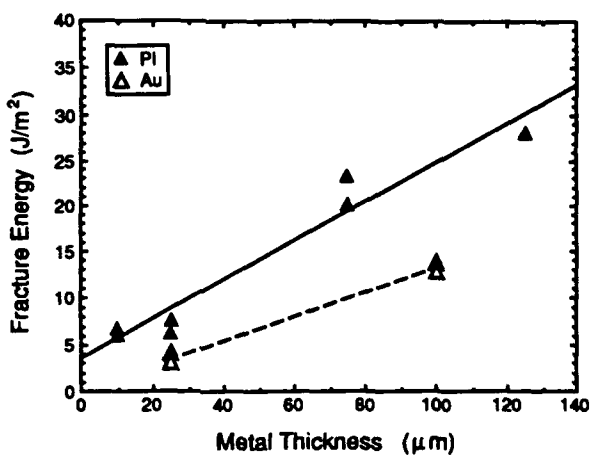

Fig. 10. Trends in the nominal fracture resistance with metal layer thickness for tests conducted in air.

Acta metall. mater. Vol. 38. No. 12. pp. 2645–2652. 1990
Printed in Great Britain

0956-7151/90 $3.00 + 0.00
Pergamon Press plc

EFFECTS OF PLASTICITY ON THE CRACK PROPAGATION RESISTANCE OF A METAL/CERAMIC INTERFACE

I. E. REIMANIS†, B. J. DALGLEISH, M. BRAHY, M. RÜHLE† and A. G. EVANS
Materials Department, College of Engineering, University of California, Santa Barbara, CA 93106, U.S.A.

(*Received* 21 *March* 1990)

Abstract—Fracture experiments have been conducted on a gold/sapphire interface. The interface is found to fail by interface separation in a nominally "brittle" manner with a critical strain energy release rate, $\mathcal{G}_c \approx 50\,\mathrm{Jm}^{-2}$, substantially larger than the work of adhesion, $W_{ad} \approx 0.5\,\mathrm{Jm}^{-2}$. Evidence of plastic deformation on the gold fracture surface, such as blunting steps and slip steps, suggest that plastic dissipation is the primary contribution to the measured $\mathcal{G}_c$. Calculations suggest that the majority effect occurs in the plastic zone through the crack wake. The interface is also found to be susceptible to slow crack growth.

Résumé—On effectue des expériences de rupture sur une interface or/saphir. On trouve que l'interface se rompt par séparation de celle-ci d'une manière "fragile" avec un taux critique pour la libération de l'énergie de déformation, $\mathcal{G}_c \cong 50\,\mathrm{Jm}^{-2}$, beaucoup plus grand que le travail d'adhérence, $W_{ad} \cong 0.5\,\mathrm{Jm}^{-2}$. La mise en évidence d'une déformation plastique sur la surface de rupture de l'or, par exemple de marches émoussées et de marches de glissement, suggère que la dissipation plastique est la principale contribution à la valeur de $\mathcal{G}_c$ mesurée. Des calculs suggèrent que l'effet prépondérant se produit dans la zone plastique par l'intermédiaire du sillage de la fissure. On trouve aussi que l'interface est susceptible de ralentir la croissance d'une fissure.

Zusammenfassung—Bruchexperimente wurden an Gold-Saphir-Grenzflächen durchgeführt. Die Grenzfläche bricht durch Trennung an der Grenzfläche nominal "spröd". Die kritische Energie-Freisetzungsrate $\mathcal{G}_c$ beträgt $\approx 50\,\mathrm{Jm}^{-2}$, welches deutlich höher ist als die Adhäsionsarbeit W_{ad} von $\approx 0{,}5\,\mathrm{Jm}^{-2}$. Hinweise auf plastische Verformung an der Gold-Bruchfläche, wie abstumpfende Stufen und Gleitstufen, legen nahe, daß plastische Dissipation der wesentliche Beitrag zum gemessenen $\mathcal{G}_c$ ist. Rechnungen legen nahe, daß der überwiegende Effekt von der plastischen Zone in der Spur des Risses herrührt. Auch neigt die Grenzfläche zu langsamem Rißwachstum.

1. INTRODUCTION

Metal/ceramic interfaces exhibit a wide range of fracture energies, dependent on bonding, interface morphology, plasticity in the metal and on the presence of interphases [1–3]. Detailed understanding of the fracture energy requires a systematic experimental study in conjunction with calculations of crack tip fields, using continuum [4, 5] as well as dislocation level calculations. One aspect of this problem is addressed in this article; notably an experimental study of the effect of plasticity. To investigate this issue, the sapphire/gold system has several attributes. In particular, test specimens can be produced by diffusion bonding without the formation of interphases. Furthermore, bonding occurs without dissolution of Al_2O_3 in the Au and consequently, the flow stress of the Au is well-behaved. Finally, the transparency of the sapphire allows *in situ* observation of crack propagation along the interface, as needed to elucidate the dominant fracture mechanism.

The fracture energy of bimaterial interfaces can be measured with good precision by using a mixed mode four-point bending specimen [6]. This specimen has the dual advantage that precracking can be conducted with good control and that, when the interface crack is between the inner loading points, the energy release rate is essentially crack length independent [6]. In addition, the crack orientation in this specimen facilitates the *in situ* observations of crack growth.

2. DIFFUSION BONDING

Diffusion bonded plates are produced by carefully polishing basal plane oriented sapphire discs having 2-in. diameter. Polishing is conducted mechanically using diamond media. Gold foil, cold rolled to thicknesses in the range 10–250 μm, is inserted between the sapphire plates and the system subjected to a normal stress of about 5 MPa, within a resistance furnace. The temperature is raised to 1040°C either in air or in vacuum and maintained at that temperature for 1–48 h. The system is then slowly cooled to room temperature. Inspection of the interfaces in the optical microscope reveals the progression of the bonding

†Present address: MPI für Metallforschung, Stuttgart, F.R.G.

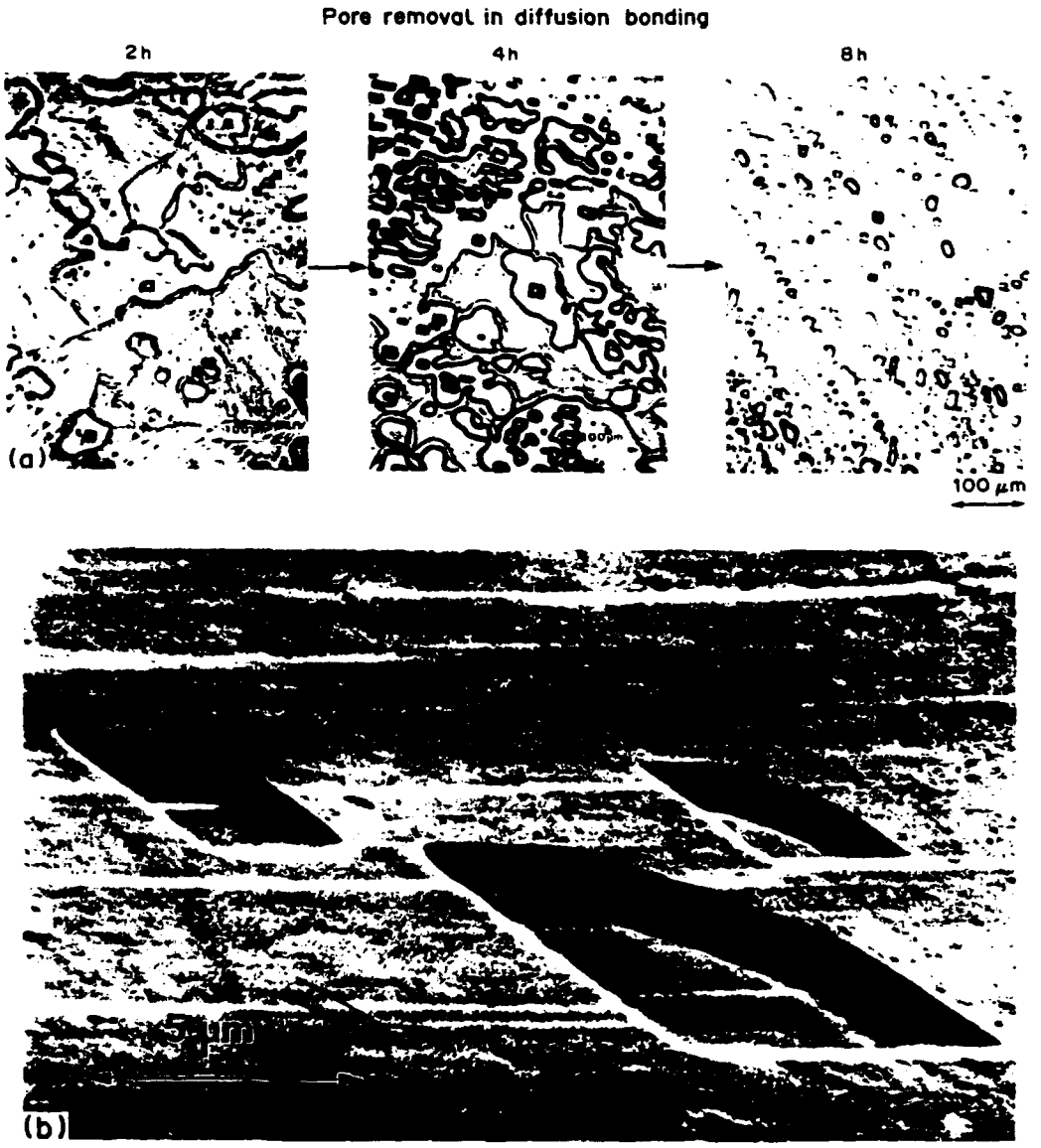

Fig. 1. (a) The evolution of interface voids observed during diffusion bonding at 1040°C. (b) Scanning electron micrograph of residual interface voids observed on the gold surface after fracture: slip steps formed during fracture are also visible.

process [Fig. 1(a)] from large planar voids to small, isolated, facetted voids in the Au. Such behavior is typical of void elimination processes at interfaces involving diffusion. Furthermore, the process was essentially the same for bonding conducted in air and in vacuum. After 48 h, some small isolated voids remain, corresponding to an area fraction of interface of ~10%. The same voids can also be identified on fracture surfaces [Fig. 1(b)]. The pores are typically about 1 μm deep and 3–10 μm wide.

3. EXPERIMENTAL

Beams with overall dimensions 40 × 3 × 3 mm are cut from the diffusion bonded plates and polished to facilitate optical observation during testing Experience has indicated that testing is expedited by having a sapphire layer on the tensile side with thickness of ~0.5–1.0 mm while the sapphire on the compression side has a thickness of ~2.5–4.0 mm. Subsequent to cutting and polishing, a Knoop indentation, loaded to ~100 N, is emplaced in the thinner sapphire layer, with axis normal to the beam axis, as needed to initiate a surface crack. Thereafter, the specimens are precracked by loading in three-point bending, using an outer span of 33 mm. During this process, the surface crack extends through the sapphire layer to the sapphire/gold interface and also extends symmetrically along the interface on both sides of the precrack to a length of ~0.5 mm [Fig. 2(a)].

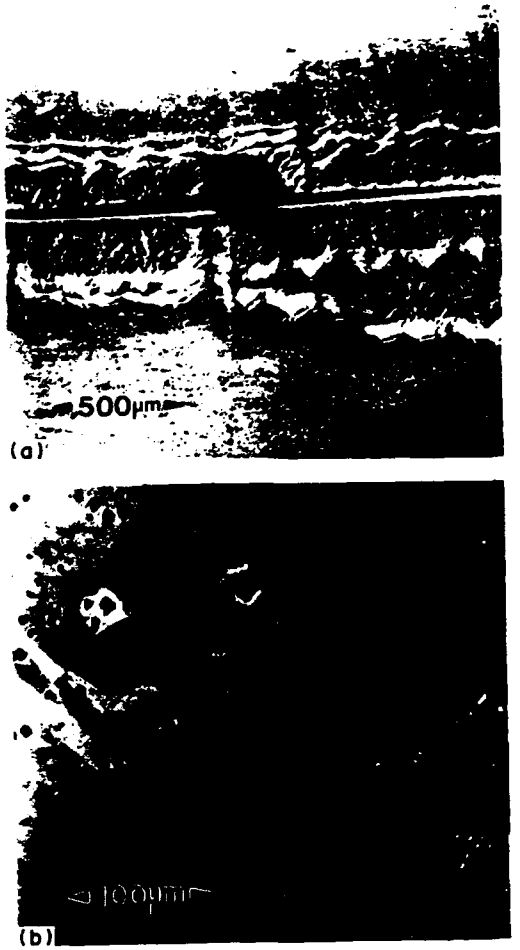

Fig. 2. (a) A precracked specimen viewed through the sapphire layer revealing the symmetrical cracks at the interface (specimen unloaded). (b) Also visible at higher magnification is the facetted nature of the apparent (closure) crack front and the residual opening around voids.

Subsequent to precracking, the specimen is loaded in a four-point bending (inner and outer spans of 33 and 19 mm, respectively) located in an inverted optical microscope (Fig. 3), as needed to permit *in situ* observation of cracking. Surfaces of the specimens and of the loading rods are carefully polished to negate effects of friction. The microscope is operated using Nomarski interference, such that fine topographic variations on the order of the wavelength of light are apparent, facilitated by the high reflectivity of gold. The Nomarski mode is also sensitive to changes of index of refraction, and thus the boundary between the debonded and bonded region (ie. the crack front) can be located precisely.

A high degree of precision in load application is achieved through micrometer sensitivity (0.0001 cm resolution) and the high stiffness of the hardened steel parts. As crack propagation proceeds, load/crack length data are generated by recording crack front profiles. In some cases, intermittent unloading is conducted in conjunction with optical observation of the interface.

Following mechanical testing, the fracture surfaces are investigated in the scanning electron microscope (SEM), with the objective of both characterizing morphological features of the fracture process and investigating possible chemical differences using energy dispersive X-ray procedures (EDS). In addition, electron backscattering channeling patterns are obtained and used to characterize crystallographic orientations. Finally, transmission electron microscopy (TEM) of cross sections is used to provide further information about the chemical and atomistic characteristics of the interface.

4. MEASUREMENTS AND OBSERVATIONS

Preliminary observations of crack growth reveal that subcritical crack extension occurs. However,

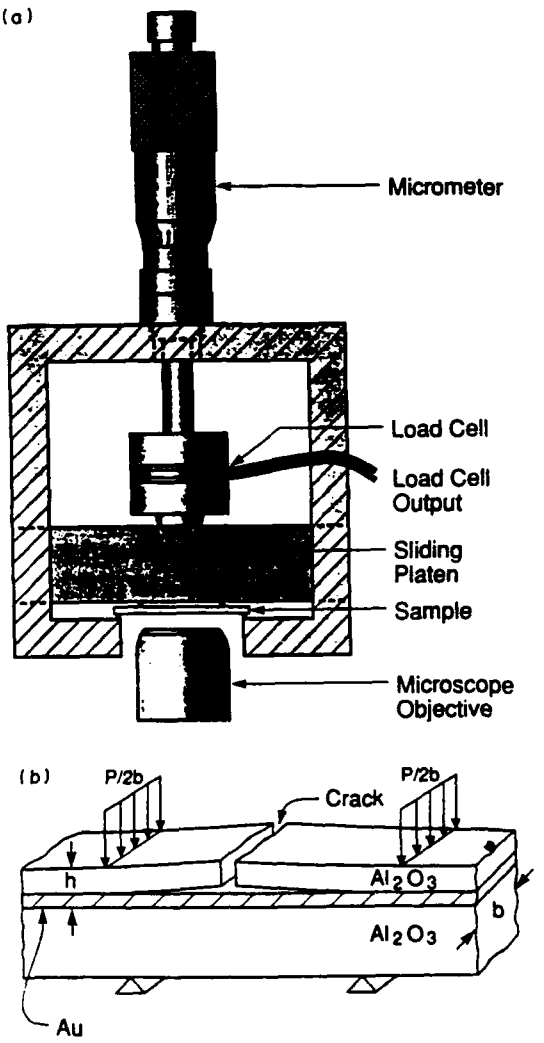

Fig. 3. (a) A schematic of the test fixture used for *in situ* measurements of crack growth of the interface. (b) A schematic of the test specimen.

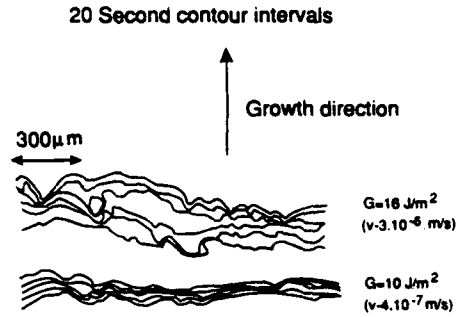

Fig. 4. Sequences of crack front profiles that illustrate the intermittent nature of crack extension at two different $\mathcal{G}$ levels.

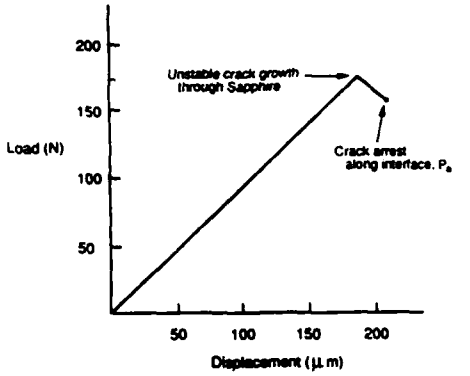

Fig. 5. Load, deflection characteristics associated with precracking during three-point bending. The crack arrest load, P_a, is used to estimate $\mathcal{G}_c$.

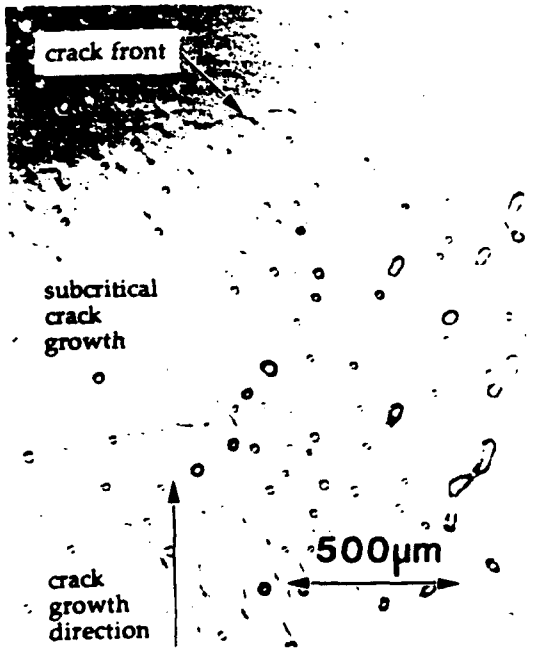

Fig. 6. Optical view through the sapphire of blunting steps formed upon load changes and of the featureless surface formed upon uniform, slow crack growth.

crack extension is intermittent and erratic, as illustrated by the crack front sequences depicted in Fig. 4(a). Nevertheless, the crack extends at an essentially uniform mean velocity when a constant load is applied and furthermore, the mean velocity increases when the load is increased. It is also notable that there is no apparent correlation between the crack front shape and the pore distribution along the interface. The subcritical growth behavior is seemingly characterized by a relationship between the crack velocity $\dot{a}$ and the energy release rate $\mathcal{G}$. The corresponding value of the phase angle of loading [6] ψ is 52°. The range in velocity at fixed $\mathcal{G}$ reflects the intermittent nature of crack growth which, in turn, may depend on the spatial non-uniformity of the "bonding".

The magnitude of the critical energy release rate $\mathcal{G}_c$ can be estimated from the precracking experiments.

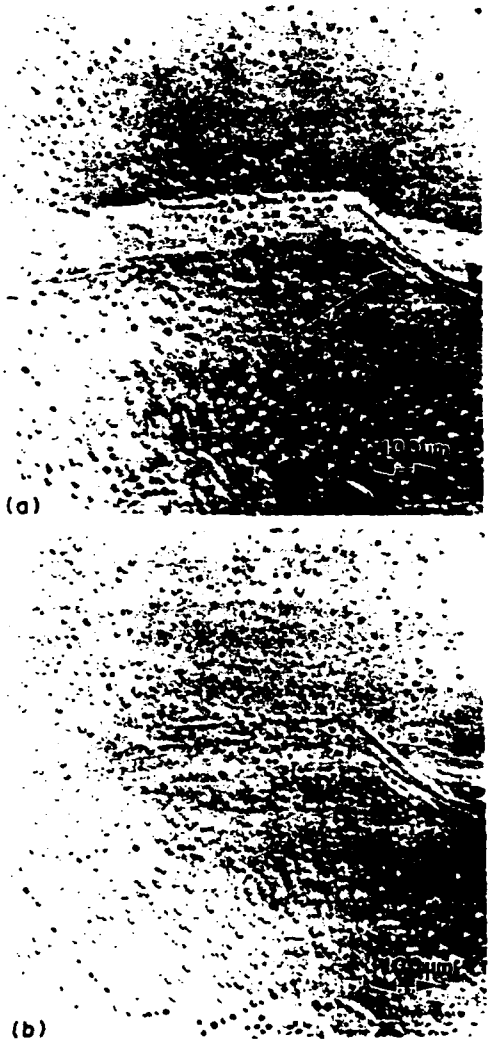

Fig. 7. (a) A crack front following slow crack growth at $\mathcal{G} \approx 20\ \mathrm{Jm}^{-2}$. A slip step (arrowed) is also visible (specimen loaded). (b) After unloading, closure occurs over $\sim 100\ \mu\mathrm{m}$, but the original crack front is also still visible.

During precracking, the load is increased until the Knoop indentation crack in the sapphire is induced to extend unstably across the specimen. This event coincides with a load drop (Fig. 5), to a load P_a, at which the crack bifurcates along the interface, arrests and then slowly extends (Fig. 2). Interface crack extension during this sequence occurs quite rapidly and consequently, the magnitude of $\mathcal{G}$ deduced from P_a is regarded as an approximate measure of $\mathcal{G}_c$. Estimates of $\mathcal{G}_c$ can be obtained from solutions generated by Charalambides *et al.* [6] extrapolated into the short crack range. This procedure indicates that $\mathcal{G}_c$ is about 50 Jm^{-2}.

Upon constant-load crack growth at $\mathcal{G} < \mathcal{G}_c$, the fracture surface is found to be relatively featureless at optical resolutions (Fig. 6). However, a change in load generates a step in the gold along the crack front (Fig. 6). The steps are indicative of crack blunting, as elaborated below. Slip steps that emanate from the crack front are also evident in some cases. During unloading, crack closure occurs over dimensions of order 100 μm (Fig. 7). However, the original crack front is still visible as a small trough, again indicative of a blunt crack.

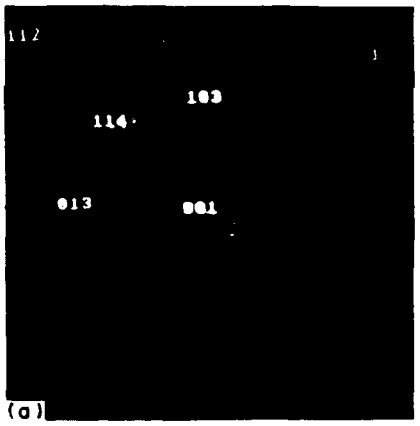

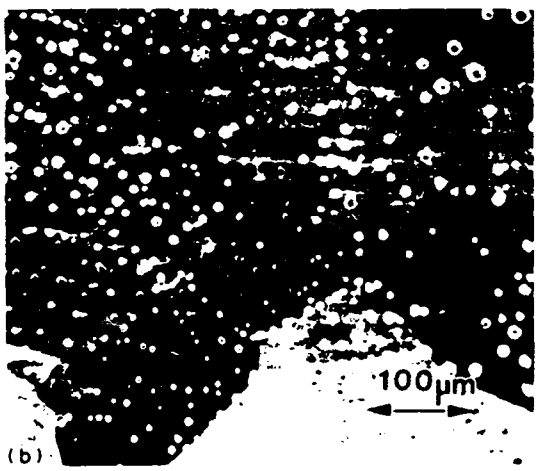

Fig. 8. (a) Channeling patterns obtained on a gold surface revealing the (001) orientation. (b) A view of the sub-grains in the gold obtained in the SEM.

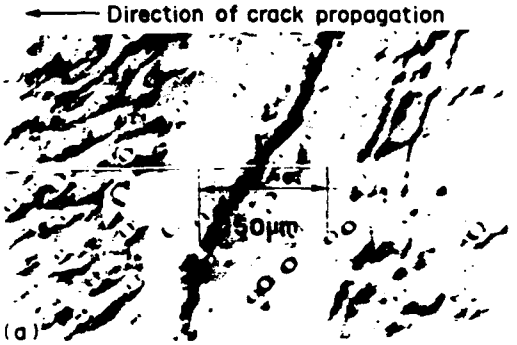

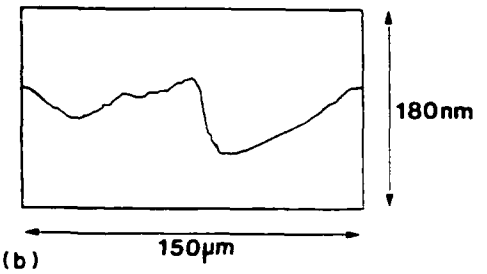

Fig. 9. Profilometer measurements on the Au fracture surface. (a) An optical view of a plastic trough passing over a blunting step. (b) A profilometer amplitude trace over blunting steps.

5. CHARACTERIZATION

5.1. Scanning electron microscopy

The fracture surfaces have been examined by scanning electron microscopy. Within the resolution limits of EDS, there is no evidence of Au on the sapphire fracture surface and no evidence of Al on the Au. Channeling patterns obtained on the Au surface [Fig. 8(a)] reveal that the Au has recrystallized during diffusion bonding into a highly textured foil with a {100} interface plane. The grain size is approximately 100–200 μm [Fig. 8(b)]. Furthermore, patterns obtained on both sides of slip steps reveal small lattice rotations of up to 5°. The oriented nature of the Au allows determination of the facet and slip step directions from the channelling patterns. In all cases, the facets and slip steps are along ⟨110⟩, consistent with slip in the Au occurring on {111}.

Observations of the sapphire surface reveal that it is featureless and essentially the same as the original surface prepared prior to bonding. It is thus concluded that there have been minimal morphological changes in the sapphire during bonding and mechanical testing, consistent both with the low diffusivities in the sapphire at the bonding temperature and with its high resistance to slip at room temperature.

The topography of the Au fracture surface has been examined using two techniques. In one case, a profilometer was scanned over the surface, to create a narrow plastic trough of uniform width. The profilometer readings gave one measure of the topography (Fig. 9). Secondly, lines of electron beam damage

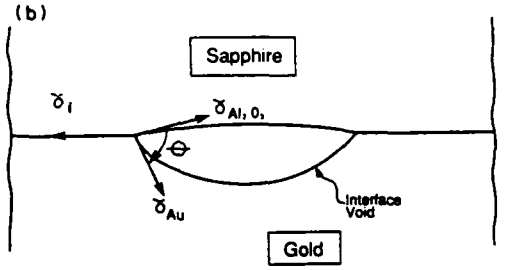

$$\gamma_i = \gamma_{Al_2O_3} + \gamma_{Au} \cos\Theta$$
$$W_{ad} = \gamma_{Au} + \gamma_{Al_2O_3} - \gamma_i$$
$$= \gamma_{Au}(1-\cos\Theta)$$

Fig. 10. (a) An electron damage line across an interface void, tilted to determine the void profile. (b) Schematic of the approach used to estimate the work of adhesion W_{ad}.

have been created while the fracture surface was oriented normal to the incident beam. This was achieved by imposing a high voltage, in line profile mode, while the beam scanned the specimen in one direction [7]. The specimens were then tilted by 60–80° to allow the shapes of the features to be deduced from the line profiles [7] (Fig. 10).

These techniques indicated that the crack front *blunting* steps were typically $<0.1\ \mu$m in height and that all such steps had the same sign (Fig. 9). Investigation of the residual voids (Fig. 10) was of primary interest for estimation of the work of adhesion W_{ad} from the void surface inclination at the interface. These measurements gave, $W_{ad} \approx 0.5\ \mathrm{Jm}^{-2}$, consistent with previous estimates [5].

5.2. *Transmission electron microscopy*

Thin foils normal to the interface have been made by mechanical dimpling followed by ion beam milling. Preliminary TEM analysis indicates the following characteristics. An atomic resolution image [Fig. 11(a)] shows that the Au/sapphire interface is incoherent and that there is no intervening phase. Analytical TEM indicates that there is no Al in the Au and no Au in the Al_2O_3 at the detectability limits of the EDS system (about 1 at.%). Furthermore, no other elements were noted in the EDS spectrum. In some places, the interface is non-planar [Fig. 11(b)], reflecting roughness associated with the original sapphire surface before bonding.

6. THE FRACTURE ENERGY

The seeming absence of gold on the sapphire fracture surface and of sapphire on the gold, coupled with the relatively low values of $\mathcal{G}_c$ compared with the fracture energy expected for a soft ductile metal ($\mathcal{G}_c > 10^4\ \mathrm{Jm}^{-2}$), suggests that the crack progresses by brittle bond rupture at the interface. In support of this contention, it is noted that ductile interface fracture occurs by hole growth in the metal, leaving metal ligaments attached to the ceramic side of the fracture surface [8] (Fig. 12). The proposed "brittle" mode of failure at the Al_2O_3/Au interface occurs despite the incidence of plastic flow in the Au and of crack blunting.

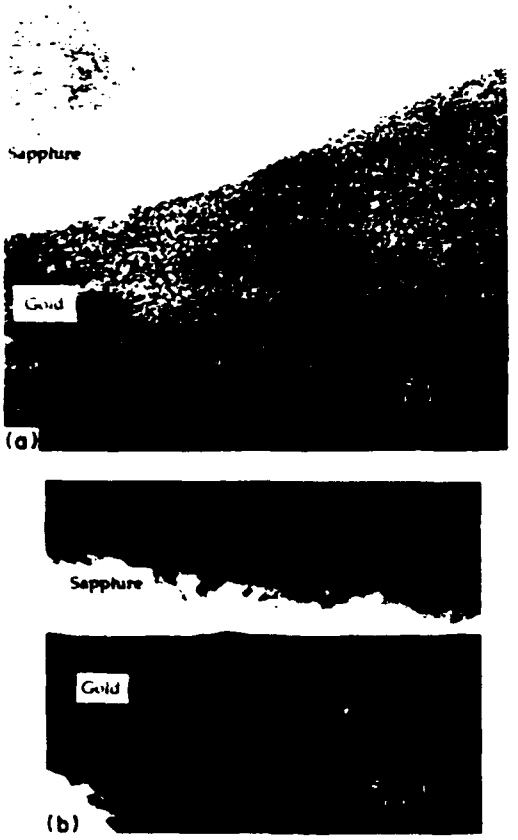

Fig. 11. (a) An atomic resolution image of the interface. (b) A conventional TEM view revealing interface non-planarity.

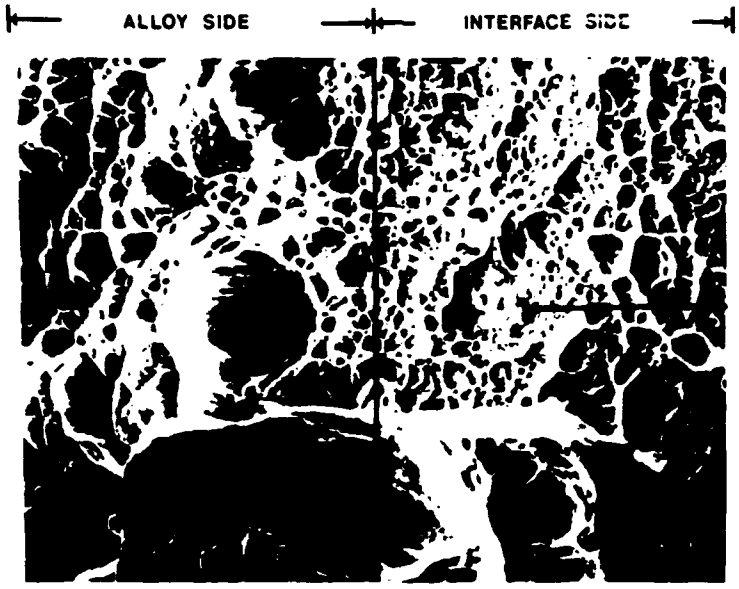

Fig. 12. A fracture surface of a ductile interface fracture between Al_2O_3 and Al.

The plastic dissipation associated with a crack growing along an interface can be addressed by invoking comparison with the behavior of cracks in isotropic elastic/plastic solids. For such materials, the energy release rate at the tip of a growing crack is strictly zero, such that the measured energy release rate equates entirely with the plastic dissipation [9]. Consequently, within the framework of continuum analysis, it has not been possible to relate the dissipation within the plastic zone to the dissipation within the fracture process zone. Yet, for the present problem, it is important to develop a basic expression that allows the plastic dissipation $\mathcal{G}_p$ to be related to such variables as the metal layer thickness, the work of adhesion, etc. A preliminary attempt, described in the Appendix, considers the admissible dissipation outside the blunting width, δ, and yields a dissipation

$$\mathcal{G}_p \approx \mathcal{G}_0(h/\delta) \qquad (1)$$

where h is the metal layer thickness and $\mathcal{G}_0$ is the dissipation within the fracture process zone. If $\mathcal{G}_0$ is regarded as being W_{ad}, then for the present case ($h = 25\,\mu m$, $\delta \approx 0.1\,\mu m$), $\mathcal{G}_p \approx 100\,Jm^{-2}$. This level of dissipation is of the same order as the measured value ($\mathcal{G}_c \approx 50\,Jm^{-2}$). Qualitatively, therefore, the measured fracture energy is consistent with a dominant contribution from plastic dissipation.

The presence of slow crack growth indicates that rupture is chemically assisted and occurs in accordance with stress corrosion concepts [10]. These concepts typically invoke a brittle fracture process zone at the crack tip and a maximum stress-based fracture criterion in this zone [10]. However, for a thin metal layer between two elastic plates, the maximum normal stress of the interface exists at an appreciable distance ahead of the crack, governed by the layer thickness [11]. An interface decohesion criterion based strictly on the normal stress would thus predict a fracture mechanism that operates ahead of the crack front: at variance with present observations. Consequently, this topic also requires additional investigation.

7. CONCLUDING REMARKS

The relatively large fracture energy measured for the gold/sapphire interface reflects an influence of plasticity. Yet, the fracture process itself is brittle and seemingly occurs by "brittle" bond rupture. For such a process, it is qualitatively appreciated that the fracture energy should be a multiple of the work of adhesion, W_{ad}, and the metal layer thickness, h. Consequently, variations in fracture energy with metal layer thicknesses should provide further insight into the appropriate relations. However, ultimately, it will be necessary to couple the continuum level analysis of fracture to the atomistic bond rupture criterion through the use of discrete dislocation configurations.

The incidence of stress corrosion has been noted in other metal/ceramic interfaces [12] and could be analyzed phemnologically using conventional expressions between crack velocity $\dot{a}$ and energy release rate $\mathcal{G}$ [10]. However, appreciable additional research is needed to understand the underlying mechanism.

Acknowledgement—The authors are grateful for financial support provided by the Office of Naval Research under Contract No. N00014-85-K-0883.

REFERENCES

1. A. G. Evans, B. J. Dalgleish, P. G. Charalambides and M. Rühle, *Metall. Trans.* In press.

2. R. M. Cannon, R. M. Fisher and A. G. Evans, *MRS Proc.* **54**, 799 (1986).
3. B. J. Dalgleish, M. C. Lu and A. G. Evans, *Acta metall.* **36**, 2029 (1988).
4. C. F. Shih and R. J. Asaro, *J. appl. Mech.* **55**, 312 (1988).
5. C. F. Shih, R. J. Asaro and N. P. O'Dowd, *Metal/Ceramic Interfaces* (edited by M. Rühle and A. G. Evans). Pergamon Press, Oxford. In press.
6. P. G. Charalambides, J. Lund, R. M. McMeeking and A. G. Evans, *J. appl. Mech.* **111**, 77 (1989).
7. R. A. Hoover, *J. Phys. E. Scientific Instruments* **4**, 747 (1971).
8. B. J. Dalgleish, K. P. Trumble and A. G. Evans, *Acta metall.* **37**, 1923 (1989).
9. J. W. Hutchinson, *Non-Linear Fracture Mechanics*, Technical Univ. of Denmark, Monograph (1979).
10. S. M. Wiederhorn, *Fracture Mechanics of Ceramics* (edited by R. C. Bradt *et al.*), Vol. 4, p. 549. Plenum, New York (1977).
11. Z. Suo and J. W. Hutchinson. To be published.
12. T. S. Oh, J. Rödel, R. M. Cannon and R. O. Ritchie, *Acta metall.* **36**, 2083 (1988).

APPENDIX

Preliminary Analysis of Plastic Dissipation Associated with Crack Growth in Steady-State†

The basic features associated with plastic dissipation can be explored by considering the behavior of strips, dy, within the metal layer (Fig. A1). The dissipation within each layer, dW_p, for a non-hardening metal is given approximately by

$$dW_p \approx \tau_0 \gamma_p \, dy \tag{A1}$$

where τ_0 is the shear yield strength and γ_p is the maximum plastic strain experienced within that strip element as the crack extends. The plastic strain associated with the growing crack at the interface with a thin metal layer is unknown. However, for a homogeneous elastic/plastic solid, the plastic strain for a non-hardening material has the form [9]

$$\gamma_p \approx \gamma_0 \ln(\alpha h/y) \tag{A2}$$

where γ_0 is the yield strain and α is a coefficient. Assuming that equation (A2) also applies to the thin strip, but with α unknown, integration of equation (A1) over the metal layer with γ_p taken from equation (A2) gives

$$W_p = \int_0^h \tau_0 \gamma_0 \ln(\alpha h/y) \, dy = \tau_0 \gamma_0 h[1 + \ln \alpha]. \tag{A3}$$

The magnitude of α for the metal strip can now be estimated by appreciating that, for the growing crack within a plastically deforming medium, the energy release rate at the crack tip is zero [9] and consequently the energy release rate and W_p are identical, i.e.

$$\mathcal{G}_c = W_p. \tag{A4}$$

†The treament used in this Appendix was suggested and developed by J. W. Hutchinson.

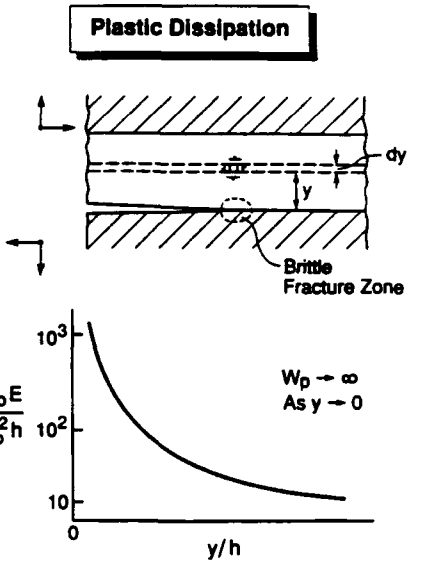

Fig. A1. Trends in the non-dimensional plastic dissipation density with distance from the crack plane, y.

Consequently, from equations (A3) and (A4)

$$\ln \alpha = \mathcal{G}_c/\tau_0 \gamma_0 h - 1. \tag{A5}$$

The preceding result is only useful in the present context if some choice is made regarding the relative dissipation that occurs in the plastic zone and in the fracture process zone, respectively. In a preliminary attempt to address this issue, the fracture process mechanism is considered to operate within a zone of width, δ, and that this process occurs subject to a dissipation, $\mathcal{G}_0$. Then, plastic dissipation occurs within the range δ to h and has magnitude $\mathcal{G}_p$. Thereupon, equation (A3) can be reexpressed as

$$\mathcal{G}_p \equiv W_p - \mathcal{G}_0 = \int_\delta^h \tau_0 \gamma_0 \ln(\alpha h/y) \, dy. \tag{A6}$$

Integration of equation (A6) with α given by equation (A5) gives

$$\mathcal{G}_p = \mathcal{G}_0\left(\frac{h}{\delta} - 1\right) - h\tau_0 \gamma_0 \ln(h/\delta). \tag{A7}$$

Then, for small δ/h and subject to the inequality

$$\mathcal{G}_0 \tau_0 \gamma_0 \delta \gg \ln(h/\delta).$$

Equation (A7) reduces to the simple results

$$\mathcal{G}_p \approx \mathcal{G}_0(h/\delta).$$

This result, which is used in the text to provide an initial estimate of the plastic dissipation, indicates that $\mathcal{G}_p$, for a non-hardening metal, is proportional to the energy dissipation involved in bond rupture process and also to the metal layer thickness. These features are amenable to experimental evaluation. However, the ambiguity with this formulation is the choice and the significance of the rupture process zone cut-off dimension, δ. Further basic understanding of the fields very close to the crack tip is needed to address this issue.

Acta metall. mater. Vol. 39, No. 7, pp. 1579–1585, 1991
Printed in Great Britain.

0956-7151/91 $3.00 + 0.00

RESIDUAL STRESS CRACKING OF METAL/CERAMIC BONDS

A. BARTLETT and A. G. EVANS
Materials Department, College of Engineering, University of California, Santa Barbara, CA 93106, U.S.A.

and

M. RÜHLE
Max Planck Institut für Metallforschung, Stuttgart, Deutschland

(Received 30 November 1990)

Abstract—Metal/ceramic bonds subject to residual stress caused by thermal expansion misfit have been investigated in an Al_2O_3/Ta(Ti) system. The residual stresses cause cracking of either the Al_2O_3 or the interface, dependent on the magnitude and sign of the residual stress. The observed locations, orientations, and trajectories of the cracks have been rationalized on the basis of residual stress fields, energy release rates and fracture energies for the ceramic and the interface.

Résumé—On étudie les liaisons métal/céramique soumises à une contrainte résiduelle due à la différence de dilatation thermique dans un système Al_2O_3/Ta(Ti). Les contraintes résiduelles provoquent une fissuration soit de Al_2O_3, soit de l'interface suivant la grandeur et le signe de la contrainte résiduelle. La situation, l'orientation et la trajectoire des fissures observées sont rationalisées à partir des champs de contrainte résiduelle, de la vitesse de libération de l'énergie et des énergies de rupture de la céramique et de l'interface.

Zusammenfassung—In dem System Al_2O_3/Ta(Ti) werden metallkeramische Verbindungen, die einer Restspannung wegen der thermischen Fehlpassung unterworfen sind, untersucht. Die Restspannung führt je nach Höhe und Vorzeichen zu Rißbildung entweder im Al_2O_3 oder in der Grenzfläche. Die beobachteten Orte, Orientierungen und Trajektorien der Risse werden anhand der Restspannungsfelder, der Energiefreisetzungsraten und der Bruchenergien der Grenzfläche. Die beobachteten Orte, Orientierungen und Trajektorien der Risse werden anhand der Restspannungsfelder, der Energiefreisetzungsraten und der Bruchenergien der Keramik und der Grenzfläche erklärt.

1. INTRODUCTION

Most metal/ceramic bonds are subject to residual stress. This stress can cause cracking of either the ceramic or the interface. The residual stresses may also degrade the mechanical strength of the bonded system. Some aspects of residual stress induced cracking have been analyzed previously [1–3], but a comprehensive description of this phenomenon has not yet been presented. The intent of the present investigation is the experimental characterization of cracking and correlation with the results of stress analysis and of fracture mechanics.

A model system consisting of sapphire diffusion bonded to Ta(Ti) alloys is used for the experimental study. This system has several attributes. The alloy compositions used in this study (20–50% Ti) show solid solubility, such that the coefficient of thermal expansion, α, can be continuously varied between $\approx 10 \times 10^{-6}\,K^{-1}$ (pure Ti) to $\approx 7 \times 10^{-6}\,K^{-1}$ (pure Ta), compared with $\approx 8 \times 10^{-6}\,K^{-1}$ for sapphire.† Consequently, alloys can be prepared that have either smaller or larger thermal expansions than sapphire. It will be shown that a second advantage of this system is that a thin multiphase reaction product layer forms during diffusion bonding having composition relatively insensitive to the original alloy composition within the range of interest. The "interface" thus has relatively consistent mechanical characteristics.

The fracture behavior can be rationalized by invoking various solutions for residual stresses and for stress intensity factors associated with bonds. To facilitate interpretation, it is also noted that, within homogeneous brittle solids, crack propagation occurs along a trajectory in which the mode II stress intensity factor, K_{II}, is zero [4, 5]. However, cracks on interfaces can extend subject to mixed mode conditions with fracture energy Γ, influenced by the phase angle, Ψ [6, 7].

†The coefficient of thermal expansion is a function of temperature.

2. EXPERIMENTS

2.1. Diffusion bonding

Sapphire discs having random orientation were mechanically polished to provide surfaces with good

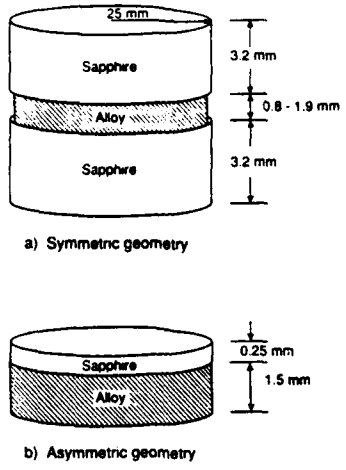

Fig. 1. Schematic of the geometries used in the experiments.

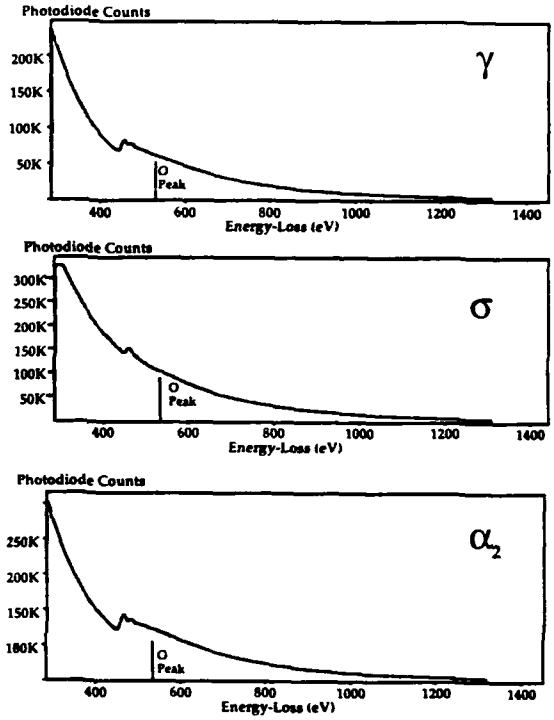

Fig. 2. PEELS spectra for the metal and reaction product layers revealing the absence of oxygen *within detectable limits*.

planarity. Foils of Ta(Ti) alloys 0.8–1.9 mm thick were placed between two of the sapphire discs and located within a compression loading fixture in a vacuum furnace. A normal compression of 3–5 MPa was applied and the system heated to 1100°C, held at that temperature for $\frac{1}{2}$ h and cooled at a rate of 5°C/min. Both symmetric and asymmetric specimens were produced (Fig. 1).

2.2. *Interface properties*

In all bonds, reaction products were formed, as elaborated elsewhere [8] and summarized here. In general, three distinct reaction products formed, as established by cross-section TEM. A PEELS spectrum revealed that *within detectable limits* ($\approx 5\%$) no oxygen was present in any of the reaction products (Fig. 2).

Consequently, use of a preliminary Ta–Ti–Al ternary phase diagram [9] (Fig. 3) suggests that the phases are: γ, α_2, and σ. Electron diffraction results (Fig. 4) combined with EDS and with lattice parameters obtained from X-ray data confirm the identity of these phases.

Asymmetric specimens with one thin layer of sapphire allowed measurement of the interface fracture energy [10–12]. Alloy compositions giving zero residual stress were chosen in order to simplify measurements. These samples were prepared by careful diamond sawing of the diffusion bonded discs into flexural beams having dimension $\approx 28 \times 1 \times 1$ mm. A precrack was introduced into the thin sapphire layer using a Knoop indentor. Thereafter, loading in three-point bending extended the precrack to the interface. Subsequent fracture energy measurements on the precracked specimens were conducted in four-point bending [10, 11]. *In situ* testing in the SEM allowed detailed observations of crack evolution. These observations revealed that the precrack propagated unstably through the sapphire and reaction product layers and then arrested at the reaction product/alloy interface, accompanied by blunting [Fig. 5(a)]. Upon subsequent loading the crack extended along the sapphire/reaction product interface. In addition, periodic branch cracks were observed in the reaction layer [Fig. 5(b)]. The load at which the crack extended gave a fracture energy for the interface between the sapphire and reaction layer, $\Gamma_i = 17 \pm 3\ \mathrm{Jm}^{-2}$ ($\Psi \approx 50°$). For comparison, the fracture energy of the σ-phase reaction product [13] $\Gamma \approx 40\ \mathrm{Jm}^{-2}$, and that for sapphire on non-basal planes [14] $\Gamma \approx 12\ \mathrm{Jm}^{-2}$.

2.3. *Cracking observations*

A general observation is that positive misfit systems ($\alpha_{alloy} > \alpha_{Al_2O_3}$ made with alloys having < 67 at.%

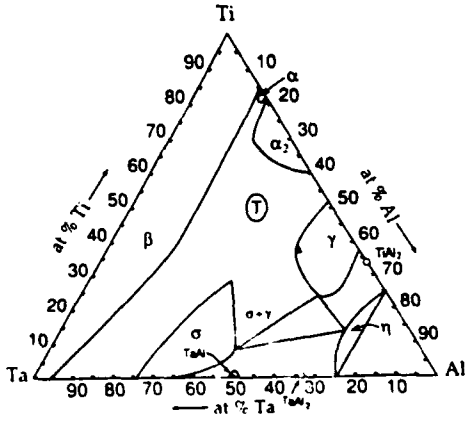

Fig. 3. Ternary Ti–Ta–Al phase diagram.

Ta at 1100°C) crack predominantly within the sapphire, although the details depend on sample geometry and history. Conversely, systems subject to negative misfit ($\alpha_{alloy} < \alpha_{Al_2O_3}$) crack along the interface. Systems with *positive* misfit when inspected with light microscopy revealed continuous *perimeter cracks* with no sign of internal cracking. In order to observe the trajectory of these cracks in detail, the samples were sectioned, polished and characterized by SEM, revealing the morphology detailed in Fig. 6. (The bonding geometry was such that the sapphire extended beyond the edge of the metal.) Crack initiation did not occur at the ceramic/metal interface, but instead *nucleated in the ceramic* at a distance $\approx 15\ \mu m$ from the interface. The crack angle ϕ with respect to the interface was consistently in the

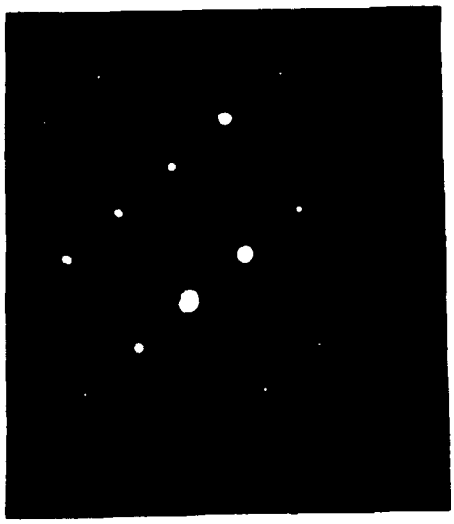

Experimental

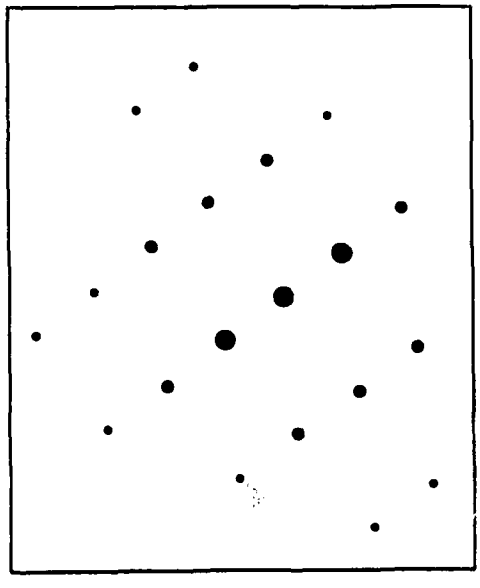

Calculated $\bar{1}21$ zone

Fig. 4. (a) Calculated and observed electron diffraction pattern: γ phase.

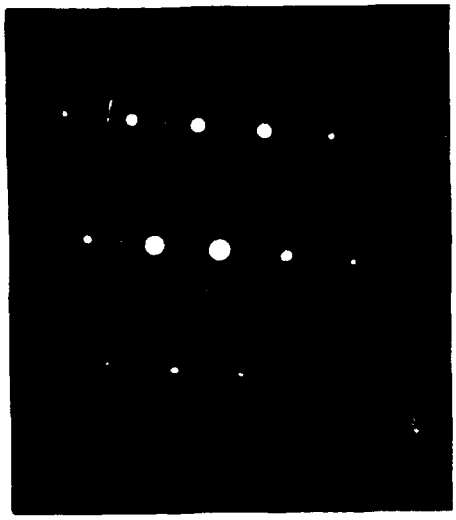

Experimental

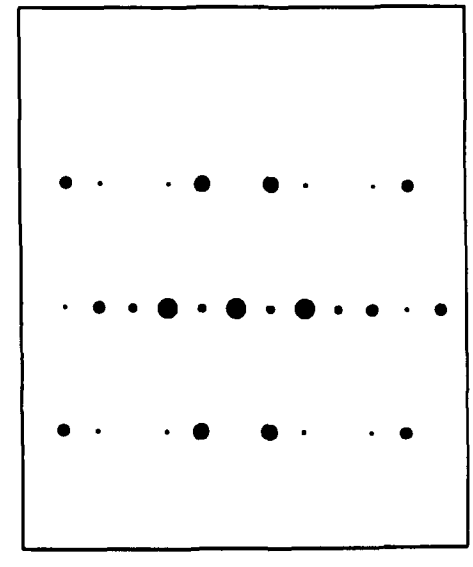

Calculated $\bar{1}2\bar{1}2$ zone

Fig. 4. *Continued.* (b) Calculated and observed electron diffraction pattern: α_2 phase. (*Continued overleaf.*)

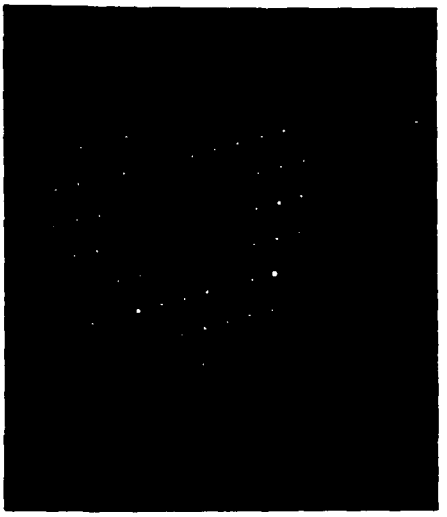

Experimental

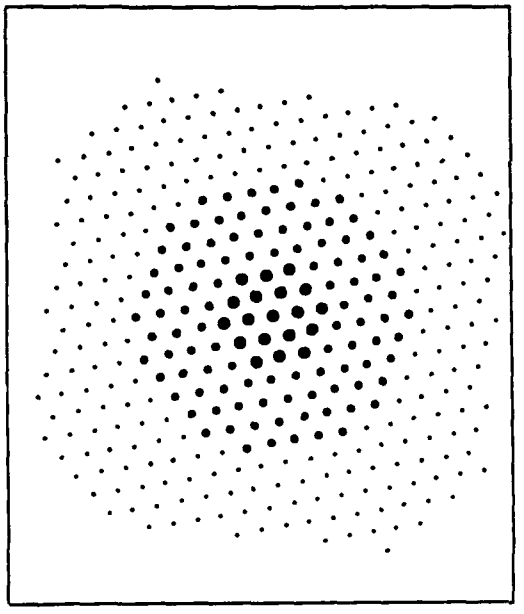

Calculated $1\bar{1}\bar{1}$ zone

Fig. 4. *Continued.* (c) Calculated and observed electron diffraction pattern: σ phase.

range 62–64°. Following initiation, the cracks curved in a continuous trajectory, turning parallel to the interface at a distance on the order of the metal layer thickness, before arresting.

Sectioning and polishing led to additional cracking having the features illustrated in Fig. 6. Two types of cracks were present. Periodic small *zone cracks* were apparent near the interface (within 10 μm), but did not extend into the reaction product layer. The initial inclination ϕ of these cracks decreased with distance from the specimen edge. *Edge cracks* occurred in the ceramic parallel to the interface at distances of 50–100 μm from the interface and extended almost continuously over the cross-section. Further sectioning and polishing revealed that these cracks, which are traces of new perimeter cracks, formed at the new surface introduced by sectioning and initiated at a "stand off" distance from the interface $\approx 50\,\mu$m.

For systems having *negative* misfit (misfit strain, $\epsilon_T \approx 5 \times 10^{-4}$) no cracking was observed in the as-cooled samples. However, sectioning introduced flaws that, in some cases, initiated visible cracks. These cracks formed near the edge and propagated *along both interfaces* (Fig. 7). *No cracking was observed in the ceramic.* The cracks propagate on a variety of interface paths: within the reaction product layer, along the reaction product/sapphire interface, and along the reaction product/alloy interface.

3. SOME RELATED MECHANICS

Information about the *initiation* of cracks can be gained from the principal tensile stress. Crack *trajectories* are addressed by evaluation of the crack path along which the mode II stress intensity factor is zero. The stress field information [1, 15] is summarized in Fig. 8. In the ceramic close to the interface, the *principal tensile stress* is essentially normal to the interface near the center but around the perimeter is

Fig. 5. (a) A precrack that penetrates the reaction product layer and blunts at the alloy interface. (*Continued on facing page.*)

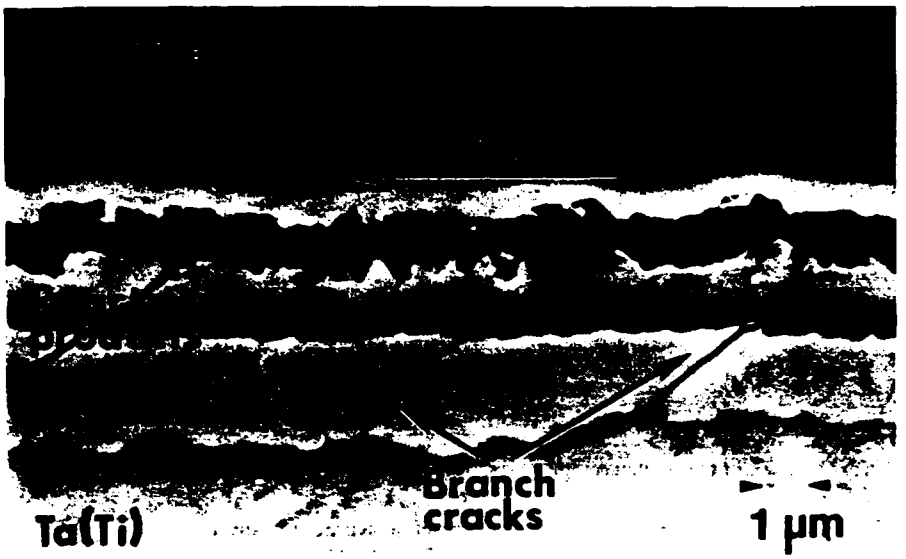

Fig. 5. *Continued.* (b) Crack trajectory when testing to obtain the fracture energy: note the periodic branch cracks in the reaction product layer and the roughness of the interface.

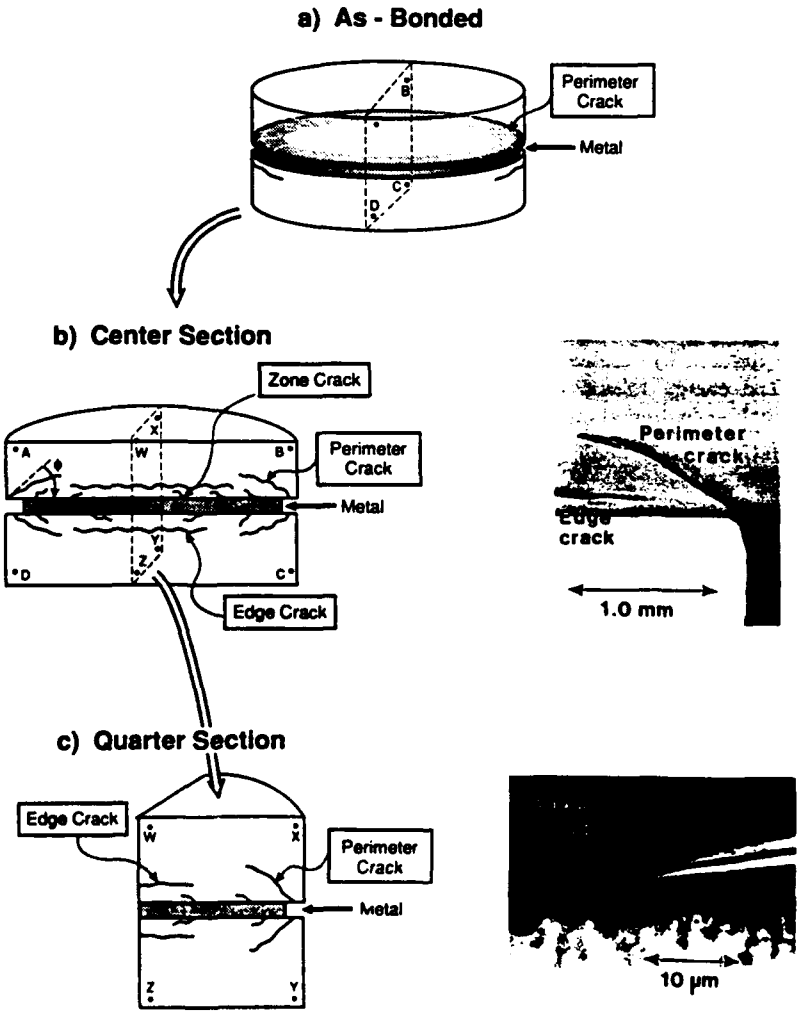

Fig. 6. A summary of cracking patterns observed in the sapphire for systems with positive misfit.

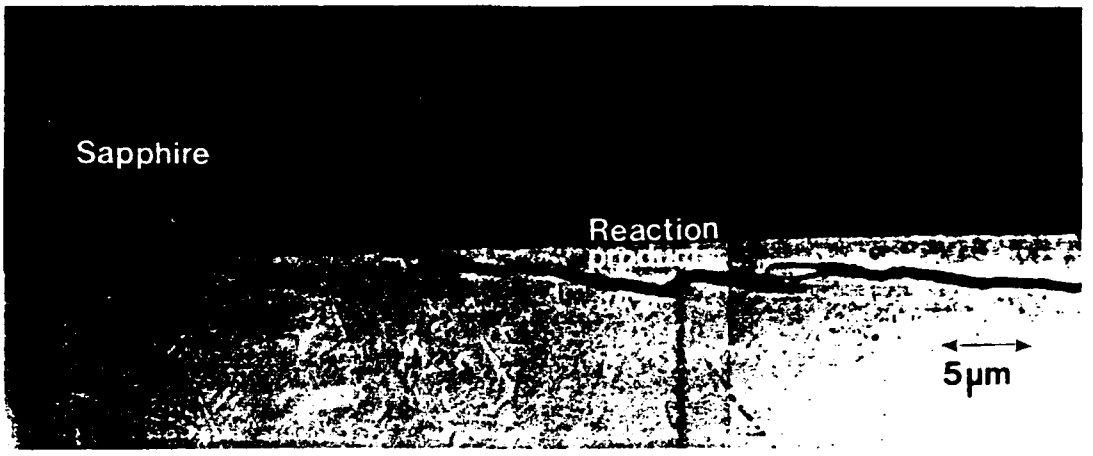

Fig. 7. Crack in the reaction product layer for a system with negative misfit ($\epsilon_T \approx 5 \times$)$^{-4}$)

inclined at $\beta \approx 30^\circ$. Along the periphery, the principal stresses are tensile within a narrow boundary layer near the interface. This stress is high but the stress gradient is also large. A crack in this layer experiences an energy release rate G that reflects both the stress amplitude and gradient (Fig. 9). Consequently, G exhibits a maximum at a characteristic stand-off distance proportional to the metal layer thickness.

When cracks develop into a length comparable to a characteristic specimen dimension (such as either the metal or ceramic layer thickness) interaction with the boundaries occurs [4, 16, 17, 19]. These interactions tend to deflect the crack into a $K_{II} \approx 0$ path parallel to the relevant boundary, at a distance proportional to the layer thickness. The most comprehensively analyzed examples involve cracks in a brittle substrate induced by residually stressed thin films [16, 17]. The energy release rate G for the example of a crack extending along *both* interfaces of a symmetric specimen has the non-dimensional form [1, 18]

$$G\,\bar{E}\epsilon_T^2 d = \Omega \qquad (1)$$

where 2d is the metal layer thickness, ϵ_T is the misfit strain, $\bar{E}$ is a composite modulus and Ω is a cracking number ≈ 1.

4. ANALYSIS OF CRACKING

The general cracking features can be related to the sign of the misfit strain. *Positive* misfit ($\alpha_{alloy} > \alpha_{Al_2O_3}$) leads to a *negative* K_I for interfacial edge cracks [1]. Such cracks are thus suppressed and fracture would occur preferentially in the sapphire. Conversely, for *negative* misfit ($\alpha_{alloy} < \alpha_{Al_2O_3}$), edge cracks experience a *positive* K_I along the interface [1] and interface failure would be encouraged. Further details are sensitive to the overall geometry and the crack location. For *positive* misfit the initiation of the crack

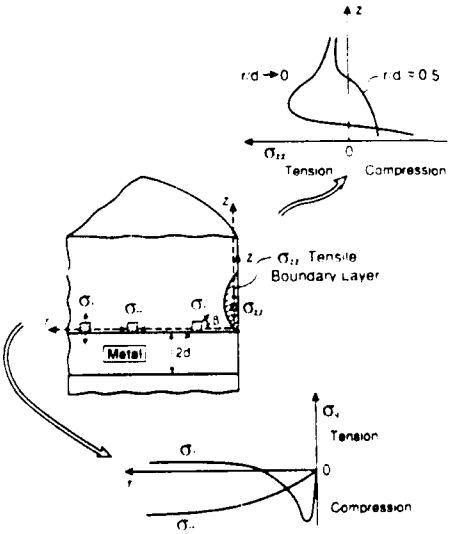

Fig. 8. Principal tensile stress fields for a system subject to positive misfit

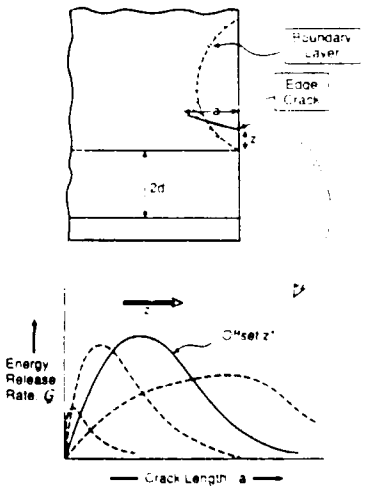

Fig. 9. A schematic of trends in the energy release rate for cracks in the sapphire near the interface. The stand-off distance is given by the location at which G attains its maximum value

in the sapphire reflects the above stress field and energy release rate information. The *perimeter* and *edge* cracks appear to be dominated by the stress in the tensile boundary layer (Fig. 8), whereupon their nucleation at a stand-off distance from the interface is in accordance with energy release rate considerations (Fig. 9). The subsequent extension of these cracks into a trajectory parallel to the interface is consistent with the known characteristics of $K_{II} = 0$ trajectories [16, 17].

The formation of the *zone* cracks reflects the characteristics of the principal tensile stress in the sapphire, near the interface (Fig. 8). The variation in the orientation of these cracks with distance from the edge is consistent with the principal tensile stress trajectories. However, the absence of such cracking into the interface is not understood, given the comparable values of the fracture energies of the interface and the sapphire. It is presumed that the σ_{rr} compression in the sapphire near the interface (Fig. 8) prevents the zone cracks from reaching the interface.

For *negative* misfit, the interface near the edge experiences residual tension and cracking would be expected to occur preferentially at the edge. The available energy release for this process, based on equation (1) is $G \approx 25\,\mathrm{Jm}^{-2}$. Comparison with the measured value of the interface fracture energy $\Gamma_i \approx 17\,\mathrm{Jm}^{-2}$, confirms that this G is sufficient to induce interface cracks. Undulating cracks paths within the reaction product layer suggest detailed interactions involving elastic mismatch and residual stress due to the presence of the reaction layer [19].

5. CONCLUDING REMARKS

Residual stresses have been shown to lead to cracking of a metal/ceramic bonded system. Systems subject to a positive misfit ($\alpha_{alloy} > \alpha_{Al_2O_3}$) crack in the ceramic, while those with negative misfit ($\alpha_{alloy} < \alpha_{Al_2O_3}$) fail along the interface. Based on information about the residual stress field, as well as the fracture energies of the sapphire and the interface, most of the cracking features have been rationalized. The effects of specimen boundaries on crack trajectories within the sapphire have also been shown to be in agreement with existing understanding.

REFERENCES

1. H. C. Cao, M. D. Thouless and A. G. Evans, *Acta metall.* **36**, 2037 (1988).
2. K. Burger, W. Schulte and G. Petzow, *Z. Zähn. Implant.* **4**, 22 (1988).
3. K. Suganuma, T. Okamoto, M. Koizumi and M. Shimaoa, *J. Am. Ceram. Soc.* **68**, C334 (1985).
4. M. D. Thouless, A. G. Evans, M. F. Ashby and J. W. Hutchinson, *Acta metall.* **35**, 1333 (1987).
5. M. D. Drory, M. D. Thouless and A. G. Evans, *Acta metall.* **36**, 2019 (1988).
6. J. R. Rice, *J. appl. Mech.* **55**, 98 (1988).
7. J. W. Hutchinson, *Metal/Ceramic Interfaces, Acta/Scripta Metall. Proc.* (edited by by M. Rühle *et al.*), Vol. 4, p. 295. Pergamon Press, Oxford (1990).
8. A. Bartlett and A. G. Evans. To be published.
9. C. McCullough, J. J. Valencia, C. G. Levi and R. Mehrabian. To be published.
10. P. G. Charalambides, J. Lund, R. M. McMeeking and A. G. Evans, *J. appl. Mech.* **111**, 77 (1989).
11. I. E. Reimanis, B. J. Dalgleish and A. G. Evans. To be published.
12. A. G. Evans, *Acta/Scripta Metall. Proc.* (edited by M. Rühle *et al.*), Vol. 4, p. 345. Pergamon Press, Oxford (1990).
13. H. Dève, A. G. Evans, G. R. Odette, R. Mehrabian, R. Emiliani and R. Hecht, *Acta metall. mater.* **38**, 1491 (1990).
14. S. M. Wiederhorn, *J. Am. Ceram. Soc.* **52**, 485 (1969).
15. M. Y. He and A. G. Evans. To be published.
16. Z. Suo and J. W. Hutchinson, *In. J. Solids Struct.* **25**, 1337 (1989).
17. M. D. Drory and A. G. Evans, *J. Am. Ceram. Soc.* **73**, 634 (1990).
18. Z. Suo, *Appl. Mech. Rev.* **43**, 5276 (1990).
19. N. Fleck, Z. Suo and J. W. Hutchinson, *Int. J. Solids Struct.* (1991).

Acta metall. mater. Vol. 39, No. 5, pp. 1019–1024, 1991
Printed in Great Britain

0956-7151/91 $3.00 + 0.00
Pergamon Press plc

THE FRACTURE ENERGY OF INTERFACES: AN ELASTIC INDENTATION TECHNIQUE

J. B. DAVIS, H. C. CAO, G. BAO and A. G. EVANS

Materials Department, College of Engineering, University of California, Santa Barbara, CA 93106, U.S.A.

(Received 22 June 1990)

Abstract—Debonding of thin refractory coatings between two oxides has been investigated by developing a new, simple indentation test technique. The method is based on a Hertzian indentation approach, modified to incorporate crack propagation down an interface plane beneath and parallel to the indented surface. The test method has been analyzed using finite elements and the results validated by experiments on homogeneous solids. Test materials have been selected to distinguish coatings capable of debonding from those immune from debonding. The implications for fiber coatings suitable for use in high temperature oxide based composites have been discussed.

Résumé—Nous avons étudié la décohésion de revêtements réfractaires, de faible épaisseur entre deux oxydes, en développant une technique nouvelle et simple d'essais d'indentation. Cette méthode, basée sur une approche d'indentation hertzienne, a été modifiée pour tenir compte de la propagation des fissures le long d'un plan d'interface parallèle et sous-jacent à la surface indentée. Cette méthode d'essais a été analysée en utilisant les éléments finis et les résultats expérimentaux obtenus sur des solides homogènes. Les matériaux testés ont été choisis en distinguant tant des revêtements capables de se décoller que d'autres qui ne le sont pas. Nous discutons l'importance de nos résultats par le choix des revêtements de fibre utilisables dans les composites de haute température à base d'oxydes.

Zusammenfassung—Das Ablösen dünner überzüge aus Refraktormaterialien zwischen zwei Oxiden wird mittels der Entwicklung eines neuen, einfachen Endrückversuches analysiert. Die Methode baut auf einer Hertzschen Näherung des Stempeleindrucks auf und wird modifiziert, um die Rißausbreitung entlang einer Grenzfläche unterhalb undparallel zur eingedrückten Oberfläche zu erfassen. Diese Method wird mit finiten Elementen analysiert; Experimente an homogenen Festkörpern bestätigen den Ansatz. Untersuchungsmaterialien wurden ausgewählt, um zwischen überzügen unterscheiden zu können, die sich ablösen und die dem Ablösen widerstehen. Die Bedeutung für Faserüberzüge, die für die Verwendung in Hochtemperaturmaterialien auf Oxidbasis geeignet sind, werden diskutiert.

1. INTRODUCTION

A basic mechanics framework for characterizing the fracture resistance properties of bimaterial interfaces has been established, based on the critical strain energy release rate G_c (or equivalently the fracture energy, Γ_i) and the phase angle of loading, Ψ [1–3]. The latter is a measure of the fracture mode mixity, between shear and opening. Furthermore, the formulism whereby $\Gamma_i(\Psi)$ data may be used for the interpretation of such phenomena as fiber debonding in composites [4, 5] and coating decohesion [5–7] has been established. A suite of test methods has also been developed that allows measurement of $\Gamma_i(\Psi)$ over a range of Ψ [2, 8, 9]. Some Γ_i data on interfaces have been generated using these techniques. However, the preparation and testing of specimens typically involves several intricate steps. Consequently, it has not been possible to quickly evaluate the fracture properties of interfaces and thereby identify classes of interface that exhibit debonding, resist decohesion, etc. The intent of the present article is to describe an indentation test that can be used to quickly and accurately explore the fracture energy of interfaces (Fig. 1).

Other attempts have been made to devise indentation tests to measure Γ_i for interfaces [10, 11]. These have been based primarily on elastic/plastic indentation procedures, such as a Vickers indenter. However, the elastic/plastic fields are complex and, consequently, relationships between Γ_i and the indentation load P are approximate. These methods have thus had limited applicability. Superior accuracy in relating Γ_i and P should be possible when indentation is conducted with a spherical indenter in the elastic range: analogous to Hertzian fracture in homogeneous brittle solids [12] (Fig. 1).

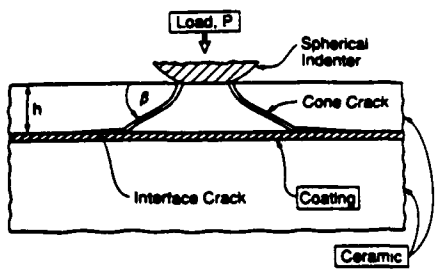

Fig. 1. A schematic of the test geometry and the cracking patterns associated with the elastic indentation technique.

As a prelude to studies that examine interface crack growth, a summary of the Hertzian fracture problem is appropriate. Hertzian cracks initially propagate normal to the surface and then rotate into a trajectory having constant cone angle, β (Fig. 1). The behavior at small crack lengths is complex. However, dimensional analysis indicates that, for cracks in the constant cone angle range [3]

$$E\Gamma_c R^3/P^2 = \alpha(\nu)\cos\beta(\nu) \qquad (1)$$

where P is the load, R is the cone crack radius (Fig. 8), E is Young's modulus, Γ_c is the fracture energy, ν is Poisson's ratio and α is a coefficient. Experimental results for glass, with $\nu \approx 0.25$, coupled with stress analysis, have suggested that [13] $\alpha \approx 2.2 \times 10^{-3}$. However, detailed effects of ν on α and β have not been specifically addressed. A preliminary feature of the present analysis is thus the application of finite element methods to clarify the Hertzian cone crack problem. The ensuing insights establish a basis for finite element analysis of crack extension along the interface, in accordance with the geometry indicated in Fig. 1.

The present calculations and most previous analyses [14] are based on the premise that elasticity prevails throughout the indentation cycle. However, other parameters enter the problem when elastic response at the contact zone is violated. Important inelastic effects include frictional tractions at the contact induced by elastic property differences between the indenter and the indented surface [15], as well as plasticity either within the indented material or in the coating. Usually, such non-linearities are manifest in crack extension as the indentor load is removed [15]. Consequently, *in situ* observations of cracking provide one check on the utility of the elastic analysis.

The experimental approach is described and illustrated for test specimens consisting of either glass or sapphire, in conjunction with a variety of diffusion bonded interfaces, involving oxides, refractory metals and intermetallics (Table 1). Comparison between the numerical solutions and the experimental results provides a calibration of the test specimen and also generates fracture energy data on interfaces of practical interest.

To facilitate such interpretations, it is noted that sapphire exhibits anisotropy in the fracture energy. Consequently, the experiments are conducted with {0001} as the indented surface, in order to minimize effects of anisotropy in Γ_c. However, the anisotropy still influences the crack trajectory and the associated value of Γ_c. Prior research [16] has indicated that the relatively weak planes in sapphire [16], ($\{10\bar{1}0\}$ and $\{\bar{1}012\}$), have $\Gamma_c \approx 12$–$20\ \mathrm{Jm}^{-2}$. Conversely, fracture on the basal planes {0001} is prohibitively difficult: $\Gamma_c > 80\ \mathrm{Jm}^{-2}$.

Table 1

Coating material	Bonding temperature (°C)	Homologous temperature (T/T_m)	Compositional changes
Y_2O_3[a]	1300	0.54	Yes
t-ZrO_2 (Y_2O_3)	1300	0.48	—
m-ZrO_2[a]	1300	0.48	No
Mo	1450	0.56	No
TiAl	1050	0.69	Yes

[a] Denotes that both sputtered and sol gel coatings were used.

2. EXPERIMENTAL

2.1. Specimen preparation

Specimens suitable for indentation testing of interfaces are produced by diffusion bonding. To create these bonds, thin discs of either sapphire or glass are mechanically polished on one face to achieve good planarity. Coatings of the second material are then produced on the polished surfaces either by physical vapor deposition or by sol gel, as elaborated elsewhere [17]. The coatings have thickness in the range 0.4–6 μm. The coated surfaces are put in contact and emplaced in the bonding fixture, subject to a pressure of $\sim$1 MPa. The bonding fixture is then subjected to a diffusion bonding cycle that depends largely on the melting temperature of the coating material (Table 1). The diffusion bonding is conducted in vacuum ($< 10^{-6}$ torr).

2.2. Coating characteristics

The *sputtered coatings* have a characteristic columnar microstructure [Fig. 2(A)]. However, after diffusion bonding, various microstructural changes are apparent [17]. The *sol gel* coatings have a very different initial microstructure, but yield essentially

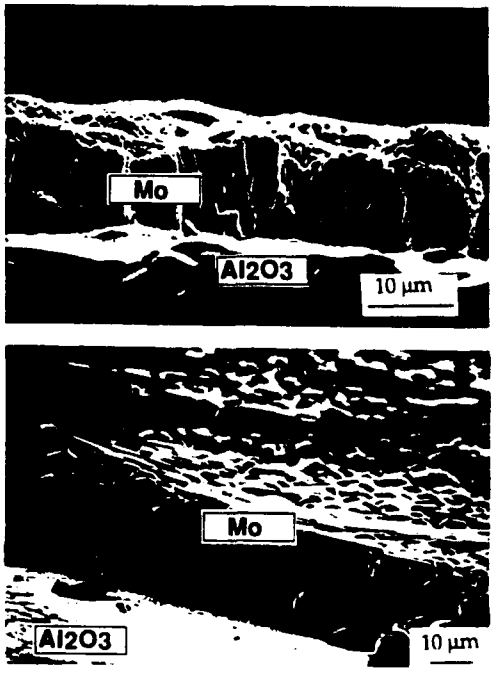

Fig. 2. Coating microstructures revealed by scanning electron microscopy (A) after physical deposition (Mo coating); (B) after diffusion bonding (Mo coating).

Fig. 3. A cone crack in glass revealed by optical microscopy with oblique incident illumination.

the same post-bonding microstructural characteristics, except that they have greater porosity. In some cases, reactions occur. Notably, the Y_2O_3 and TiAl coatings react with the sapphire to form various aluminate and aluminide reaction products. In particular, Y_2O_3 reacts with the Al_2O_3 to form YAG, as determined by X-ray analysis. Conversely, the pure ZrO_2 and Mo coatings are non-reactive. Furthermore, the pure ZrO_2 coating is monoclinic at room temperature whereas ZrO_2 (3% Y_2O_3) coatings are tetragonal: a feature that may offer insight into their different fracture behaviors. All coatings are also subject to substantial grain growth during bonding. The resultant coating microstructure typically consists of equiaxed grains having dimensions comparable to the coating thickness, often with substantial interspersed porosity [Fig. 2(B)].

2.3. Test procedure

The indentation tests are conducted with a 12.5 mm diameter WC sphere. The surfaces to be indented are lightly abraded to introduce surface flaws that allow ready nucleation of cone cracks beneath the indented surface. A thin Teflon film is placed between the surface and the indenter to minimize non-linear effects associated with frictional sliding within the contact area. Also, a die penetrant is used to highlight the crack features. In the present experiments, the transparency of the glass and sapphire allow *in situ* optical observation of the cracks. Through such observations, it is found that cone cracks nucleate in the indented material and propagate stably toward the interface as the load is increased. Upon reaching the interface, two extremes of behavior are encountered. In some cases, the cone crack continues through the coating into the lower substrate material. In other cases, the crack jumps along the interface, then arrests and thereafter propagates steadily as the load on the indenter is further increased. The analysis for evaluating the fracture energies of coated interfaces applies only when the second behavior obtains. Debond crack growth upon unloading has not been observed when the above test procedure is implemented.

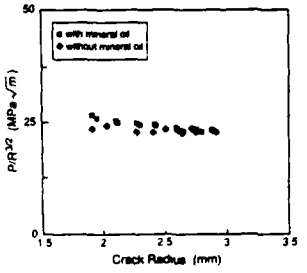

Fig. 4. Trends in cone crack radius R with load P obtained for glass, plotted in accordance with the parameter $P/R^{3/2}$ suggested by equation (1).

2.4. Results

A series of cone crack experiments has first been conducted on soda lime glass and (0001) sapphire. In these experiments, the crack diameter $2R$, is monitored *in situ* using a low magnification optical microscope (Fig. 3). In some cases, the surfaces are also immersed in oil to limit access of hydroxyl ions to the crack and thus minimize effects of stress corrosion. Some typical results for the soda lime glass are plotted on Fig. 4, using the normalization suggested by equation (1), $P/R^{3/2}$. For the glass experiments, the cone angle achieved subsequent to initial crack formation is symmetric and constant, such that $\beta = 22°$ (Fig. 3). For sapphire, some asymmetry exists and the cone angle is larger: on average $\beta \cong 30°$. This angle tends to increase as the crack approaches the bottom surface of the indented plate.

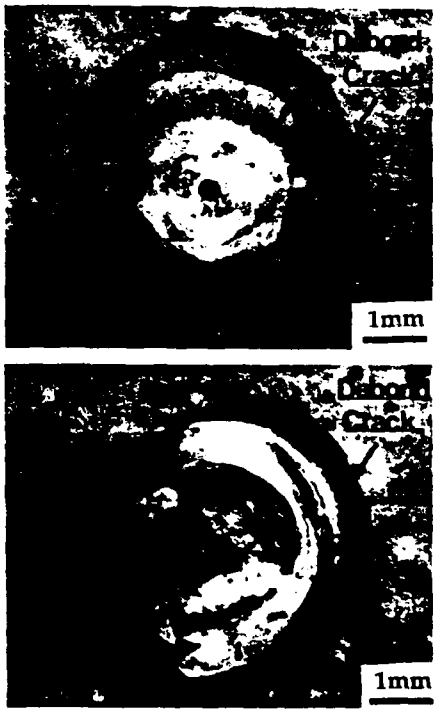

Fig. 5. Optical micrographs of debond cracks obtained with a sol gel m-ZrO_2 coating viewed from beneath the indentation.

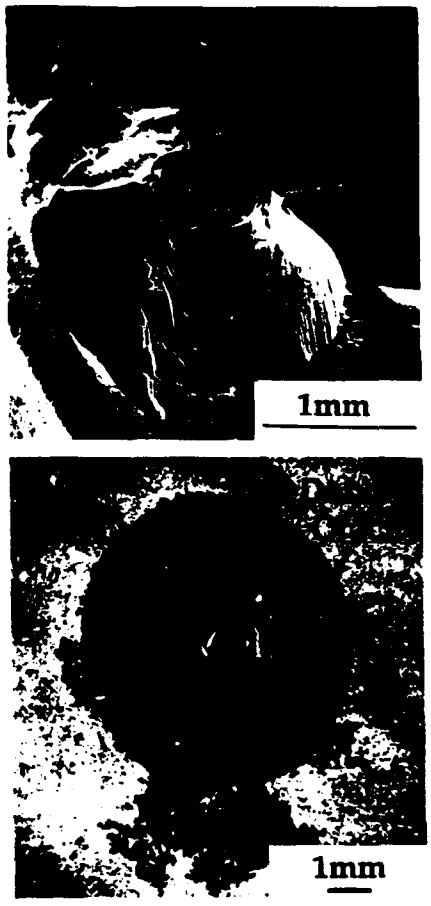

Fig. 6. (A) A SEM view of an exposed cone obtained with a Mo coating; (B) an optical micrograph of debond crack of Mo coating viewed from beneath the indentation.

Experiments have also been conducted for interfaces between sapphire and the four refractory coatings described in Table 1. The tests revealed that the cone crack extends through the coatings into the substrate when either Y_2O_3 (sputtered and sol gel), sputtered γ-TiAl, sol gel partially stabilized ZrO_2 and sputtered pure ZrO_2 coatings are used. Conversely, the crack extends down the interface when either sol gel pure ZrO_2 or sputtered Mo coatings are present. In some cases, the debond cracks obtained with the sol gel ZrO_2 coatings are not symmetrical (Fig. 5), indicating that the bonds are subject to local variability, perhaps due to microstructural variations (i.e. porosity) across the bonded surfaces.

To provide a vivid visualization of the cone crack and the interface debond, a section around an indent from a specimen of a Mo coating on sapphire has been detached and examined in the scanning electron microscope (Fig. 6). This view of the indent fracture reveals several features. Debonding along the Al_2O_3/Mo interface has clearly occurred. Cone cracking in the sapphire has attained a near constant trajectory state, similar to that obtained in homogeneous sapphire, with $\beta \approx 30$. However, upon interaction with the "weak" interface, the cone angle increases and the crack seemingly extends into the interface with a cone angle $\beta \to \pi/2$.

3. ANALYSIS OF THE INDENTATION SPECIMEN

The elastic indentation test has been analyzed using a finite element procedure, based on the ABAQUS code. The finite element mesh is illustrated in Fig. 7. The first problem to be addressed concerns the cone crack in a homogeneous, isotropic elastic half space. To facilitate the analysis, the cone crack is considered to have attained a *constant* cone angle configuration. Consequently, the initial growth of the cone, which occurs subject to a larger cone angle, is not simulated. The error introduced in this step is negligible when the cone crack is fully developed: i.e. when R is appreciably greater than the radius of the contact area.

The analysis is conducted by calculating both the mode I and mode II stress intensity factors and the calculation iterated for different cone angles, until that angle which gives $K_{II} \approx 0$ is identified. This procedure is used because cracks in isotopic brittle solids occur along trajectories having $K_{II} \approx 0$ [1, 7]. The results of this analysis reveal that the preferred cone angle, β, changes with the Poisson's ratio ν of the material. The importance of Poisson's ratio had been implied in previous studies [14]. The non-dimensional energy release rate, $\chi = EGR^3/P^2$, is evaluated and plotted as a function of crack size R for various cone angles β (Fig. 8) to verify that χ is independent of R. These trends in χ with cone angle provide a basis for connecting with other studies [13] [equations (1) and (2)]. The present analysis indicates an explicit connection between the non-dimensional energy release rate and β, such that

$$\chi \equiv EGR^3/P^2 \approx \frac{1.30}{\pi^2} \tan^2 \beta. \qquad (2)$$

A substantial effect of the cone crack angle β on the energy release rate is apparent. Moreover, for glass

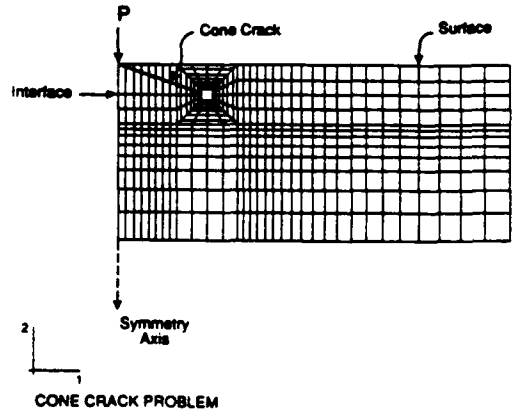

Fig. 7. The finite element mesh used to compute the energy release rate G and the phase angle of loading, Ψ.

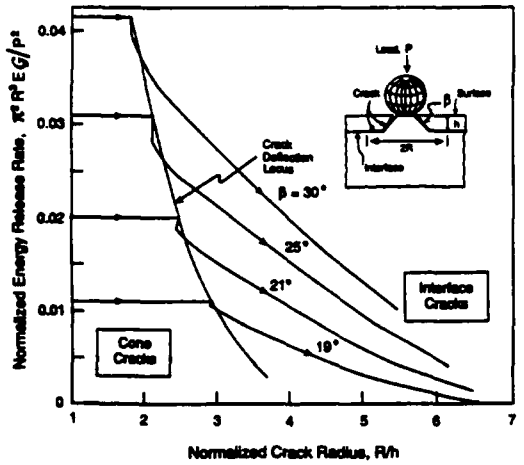

Fig. 8. The non-dimensional energy release rate as a function of crack radius for several values of cone angle.

($\beta = 22°$) the values of χ from equation (2) and from equation (1) are comparable.

Further analysis considers the cone crack expanding radially outward along a "weak" interface parallel to the surface. The specific problem of interest concerns a thin coating between two like materials and, consequently, to first order, the energy release rate G and the phase angle of loading Ψ can be calculated as if the system were an isotropic elastic body [6]. Then, the small correction to Ψ caused by the thin coating layer can be made based on the elastic mismatch with the coating, as well as the coating thickness. These calculations have been conducted for cone angles applicable to the present materials ($\beta \approx 20$–$30°$). The results reveal (Fig. 8) that after the cone crack intersects the interface, the non-dimensional strain energy release rate diminishes as the crack extends, while Ψ increases. Again, the non-dimensional G depends strongly on the cone angle, β. These curves may be used to determine interface fracture energies when the crack propagates down the coating interface and when elastic contact conditions operate, as described below.

4. INTERPRETATION OF RESULTS

Based on the above energy release rate solutions, load/crack radius data may be used to determine critical energy release rates (or fracture energies). The results obtained for glass (Fig. 4) provide fracture energies (Γ_c of 8–10 Jm^{-2}) compared with literature values, $\Gamma_c \approx 8\ Jm^{-2}$.† Interpretation of the results for sapphire is somewhat complicated by its elastic and fracture anisotropy. Nevertheless, values of Γ_c evaluated using the measured cone angle, β, and assuming elastic isotropy indicate values in the range 25–30 Jm^{-2}, comparable with literature values for $\{10\bar{1}0\}$ and $\{10\bar{1}2\}$ [16]. Results obtained for the coatings, interpreted using Fig. 8, indicate that for Mo, $\Gamma_i = 3$–5 Jm^{-2} and for sol gel, m-ZrO_2, $\Gamma_i = 15$–$20\ Jm^{-2}$.

5. IMPLICATIONS FOR FIBER COATINGS

The present interface fracture energy results have immediate implications for oxide matrix composites reinforced with sapphire fibers, based on the debonding diagram [18] summarized in Fig. 9. Specifically, sol gel m-ZrO_2 and Mo are viable coatings, whereas Y_2O_3, TiAl, and t-ZrO_2 are unacceptable and should not be used. More specifically, when basal plane (c-axis) oriented sapphire fibers are used, having a fracture energy, $\Gamma_f \approx 25\ Jm^{-2}$, both sol gel m-$ZrO_2$ and Mo coatings have fracture energies in the debonding range (Fig. 9). However, for sol gel m-ZrO_2 coatings, debonding may only occur when the fibers are inclined to the crack plane normal, and are probably unsuitable for other fiber orientations, since $\Gamma_f \approx 12$–$20\ Jm^{-2}$. The m-ZrO_2 and Mo coatings are also thermochemically and morphologically stable at elevated temperature and thus have high temperature potential. One obvious limitation of Mo coatings concerns the tendency toward formation of a volatile oxide. However, other refractory metals less prone to oxidation degradation (such as Ta, W, Nb) may also prove viable.

Another notable feature of the preceding results is that the fiber coatings that give debonding are expected to be in residual compression. The Mo should be compressed because it has a smaller thermal expansion coefficient than Al_2O_3. The m-ZrO_2 is in compression because of the dilation that accompanies the martensite transformation. This feature may be important because residual compression in coatings

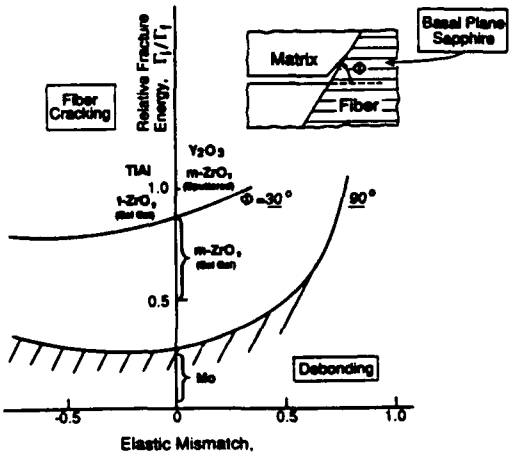

Fig. 9. Debond diagram for sapphire fiber reinforced composites with various fiber coatings.

†Elastic mismatch between the indenter and indented material appears to lead to systematic errors in the measurement of Γ, the sign and magnitude of which depend on the materials used. This error arises primarily from friction in the contact region [15] and idealizations of point loading in the analysis. If necessary, this source of error can be minimized by experimental calibration.

tends to trap cracks in the interface by suppressing crack kinking into the coating [19]. Porosity in the coating may also be important, because the only apparent difference between the sputtered m-ZrO_2 which does not debond and the sol gel in m-ZrO_2 that does debond is the existence of appreciable porosity in the latter.

6. CONCLUDING REMARKS

A simple, elastic-indentation procedure capable of measuring the fracture energy of thin embedded coatings has been devised, analyzed and calibrated. A diffusion bonding procedure for preparing test specimens has also been described and used to produce specimens containing several refractory coatings: including oxides, intermetallics and metals. Application of this test to these coating systems has demonstrated the utility of the approach. In particular, Y_2O_3 and TiAl coatings have been shown to both react with and to bond well with Al_2O_3 and thus are unacceptable for Al_2O_3 fibers and composites. Conversely, Mo and porous m-ZrO_2 satisfy the basic thermochemical and thermomechanical requirements for Al_2O_3 composites and have potential as debond coatings.

REFERENCES

1. J. W. Hutchinson, *Acta Scripa Metall. Proc.* (edited by A. G. Evans and M. Rühle), p. 295. Pergamon Press, Oxford (1990).
2. A. G. Evans, M. Rühle, B. J. Dalgleish and P. G. Charalambides, *Mater. Sci. Engng* **A126**, 53 (1990).
3. J. R. Rice, *J. appl. Mech.* **55**, 98 (1988).
4. P. G. Charalambides and A. G. Evans, *J. Am. Ceram. Soc.* **72**, 746 (1989).
5. A. G. Evans, M. Y. He and J. W. Hutchinson, *J. Am. Ceram. Soc.* **72**, 2303 (1989).
6. Z. Suo and J. W. Hutchinson, *Mater. Sci. Engng* **A107**, 135 (1989).
7. M. D. Drory, M. D. Thouless and A. G. Evans, *Acta metall.* **36**, 2019 (1988).
8. H. C. Cao and A. G. Evans, *Mech. Mater.* **7**, 295 (1989).
9. P. G. Charalambides, J. Lund, R. M. McMeeking and A. G. Evans, *J. appl. Mech.* **56**, 77 (1989).
10. D. B. Marshall and A. G. Evans, *J. appl. Phys.* **56**, 2632 (1984).
11. J. E. Ritter, L. G. Rosenfeld, M. R. Lin and T. S. Lardner, in *Thin Films: Stresses and Mechanical Properties, MRS Symp. Proc.*, p. 130, Material Research Society (1989).
12. F. C. Frank and B. R. Lawn, *Proc. R. Soc.* **A299**, 291 (1967).
13. J. E. Field, *The Properties of Diamond.* Academic Press, New York (1979).
14. I. Finnie and Vaidyanathan, in *Fracture Mechanics of Ceramics*, p. 231. Plenum Press, New York (1974).
15. K. L. Johnson, J. J. O'Connor and A. C. Woodward, *Proc. R. Soc.* **A334**, 95 (1973).
16. S. M. Weiderhorn, *J. Am. Ceram. Soc.* **52**, 485 (1969).
17. J. Davis, A. G. Evans, M. L. Emiliani and R. Hecht. To be published.
18. M. Y. He and J. W. Hutchinson, *J. appl. Mech.* **56**, 270 (1989).
19. M. Y. He, A. Bartlett and J. W. Hutchinson, *J. Am. Ceram. Soc.* In press.

journal

Reprinted from the Journal of the American Ceramic Society, Vol. 74, No. 4, April 1991

J. Am. Ceram. Soc., 74 [4] 767-71 (1991)

Kinking of a Crack out of an Interface: Role of In-Plane Stress

Ming-Yuan He, Andrew Bartlett,* and Anthony G. Evans*

Materials Department, College of Engineering, University of California, Santa Barbara, California 93106

John W. Hutchinson*

Division of Applied Sciences, Harvard University, Cambridge, Massachusetts 02138

A crack lying in the interface between two brittle elastic solids can advance either by continued growth in the interface or by kinking out of the interface into one of the adjoining materials. This competition can be assessed by comparing the ratio of the energy release rates for interface cracking and for kinking out of the interface to the ratio of interface toughness to substrate toughness. The stress parallel to the interface, σ_0, influences the energy release rate of the kinked crack and can significantly alter the conditions for interface cracking over substrate cracking if sufficiently large. This paper provides the dependence of the energy release rate ratio on the in-plane stress. The nondimensional stress parameter which emerges is, $\sigma_0(a/E_* \Gamma_i)^{1/2}$, where a is the initial length of the kink into the substrate, E_* is a modulus quantity, and Γ_i is the fracture energy of the interface. An experimental observation of the cracking of reaction product layers in bonds between Ti(Ta) and Al_2O_3 is rationalized by the theory. [Key words: crack growth, interfaces, kinking, stress, fibers.]

I. Introduction

In an earlier paper (He and Hutchinson,[1] hereafter designated by HH), a study was made of the tendency of a crack in an interface to either remain in the interface or kink out (Fig. 1). The ratio $\mathcal{G}_i/\mathcal{G}_s^{max}$ was determined where $\mathcal{G}_i$ is the energy release rate for crack advance in the interface and $\mathcal{G}_s^{max}$ is the energy release rate for the crack kinking into the substrate maximized with respect to the kink angle ω. The competition between interface cracking and substrate cracking then depends on whether $\mathcal{G}_i/\mathcal{G}_s^{max}$ is greater or less than the toughness ratio, Γ_i/Γ_s, where Γ_i and Γ_s are the interface and substrate toughnesses, respectively.

The analysis in HH is an asymptotic one in which the prediction of $\mathcal{G}_i/\mathcal{G}_s^{max}$ is accurate when the length a of the kinked crack segment is very small compared to all other lengths in the problem, including the length of the parent interface crack itself. If there is a stress σ_0 in the substrate parallel to the interface (Fig. 1) due to either residual stress or applied loads, then an additional nondimensional length parameter, not considered in HH, becomes important:

$$\eta = \sigma_0\sqrt{a}/(E_*\mathcal{G}_i)^{1/2} \tag{1}$$

where E_* is a modulus quantity defined below. The role of this parameter in the competition between kinking and continued interface cracking is the subject of this paper. An experimental observation of the cracking at the reaction product layer formed upon bonding Ti(Ta) to Al_2O_3 is used to illustrate the phenomenon.

II. Stress Intensity Factors and Energy Release Rates for a Kinked Crack

As in HH, it will be assumed that the putative length a of the kinked crack is very small compared with all other geometric length quantities and, in particular, small compared with the length of the parent interface crack. Under these circumstances, an asymptotic problem can be posed, as depicted in Fig. 1(B). Notably, a semi-infinite interface crack is loaded remotely by the singular crack tip field associated with the interface crack of Fig. 1(A), with stress intensity factors K_1 and K_2 and by the stress σ_0 parallel to the interface located in the material into which the crack kinks.† In an application, the stress intensity factors K_1 and K_2 are regarded as the applied stress intensities and are determined for the interface crack in the actual geometry.

Plane strain cracks are considered, and the two materials bonded at the interface (Fig. 1) are assumed to be isotropic and elastic. The two elastic mismatch parameters of Dundurs governing plane strain problems are

$$\alpha = (\bar{E}_1 - \bar{E}_2)/(\bar{E}_1 + \bar{E}_2) \tag{2}$$

$$\beta = \frac{1}{2}[\mu_1(1 - 2\nu_2) - \mu_2(1 - 2\nu_1)]/[\mu_1(1 - \nu_2) + \mu_2(1 - \nu_1)] \tag{3}$$

†Only the stress component in the material into which the kink extends has any effect on the change in energy release rate.

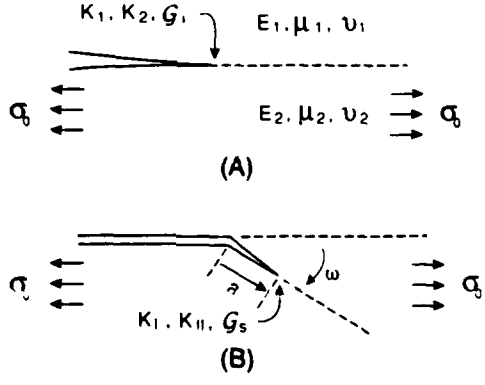

Fig. 1. Notation and conventions: (A) interface crack, (B) kinked crack.

R. F. Cook – contributing editor

Manuscript No. 197664. Received April 4, 1990; approved December 12, 1990.
*Member, American Ceramic Society.

where E, μ, and ν denote Young's modulus, shear modulus, and Poisson's ratio, respectively, and $\bar{E} = E/(1 - \nu^2)$. The condition $\alpha = \beta = 0$ refers to a homogeneous system. An "oscillation index" ε, which appears below, depends only on β according to

$$\varepsilon = \frac{1}{2\pi} \ln\left(\frac{1-\beta}{1+\beta}\right) \tag{4}$$

A general discussion of elastic interface cracks has been given by Rice.[2] For a specific problem, the complex interface stress intensity factor necessarily has the dimensional form (with $i = (-1)^{1/2}$)

$$K \equiv K_1 + iK_2 = (\text{applied stress}) \cdot L^{1/2} L^{-i\varepsilon} F \tag{5}$$

where L is a length (e.g., the parent crack length or layer thickness) and F is a dimensionless function of parameters characterizing the in-plane geometry and of α and β. The tractions on the interface ahead of the interface crack tip (still with $a = 0$) are given by

$$\sigma_{22} + i\sigma_{12} = K(2\pi x_1)^{-1/2} x_1^{i\varepsilon} \tag{6}$$

When $\beta = 0$, and thus $\varepsilon = 0$ so that $x_1^{i\varepsilon} = 1$, K_1 and K_2 can be regarded as conventional mode 1 and mode 2 stress intensity factors, i.e.,

$$\sigma_{22} = K_1(2\pi x)^{-1/2}$$
$$\sigma_{12} = K_2(2\pi x_1)^{-1/2} \tag{7}$$

As emphasized in Ref. 3, the clarity in interpretation achieved by taking β to be zero is often worth the small sacrifice in accuracy.

It will be useful for later purposes to introduce the "phase" ψ of the stress intensity factors. With L defined in Eq. (5),

$$K \equiv K_1 + iK_2 = |K| e^{i\psi} L^{-i\varepsilon} \tag{8a}$$

or

$$\tan\psi = I_m[KL^{i\varepsilon}]/R_e[KL^{i\varepsilon}] \tag{8b}$$

In particular, when $\beta = 0$

$$\psi = \tan^{-1}(K_2/K_1) \tag{9}$$

and ψ provides a measure of the relative amount of mode 2 to mode 1 of the loading on the interface crack.

The energy release rate for advance of the crack in the interface is

$$\mathcal{G}_i = (K_1^2 + K_2^2)/E_* \tag{10}$$

where

$$\frac{1}{E_*} = \frac{1}{2}\left[\frac{1}{\bar{E}_1} + \frac{1}{\bar{E}_2}\right]\frac{1}{\cosh^2 \pi\varepsilon} = \left(\frac{1-\beta^2}{1+\alpha}\right)\frac{1}{\bar{E}_2} \tag{11}$$

The stress component σ_0 has no effect on $\mathcal{G}_i$, since it acts parallel to the advancing crack.

The tip of the putative crack kinking into the substrate in Fig. 1(B) experiences conventional mode I/mode II stressing characterized by stress intensity factors K_I and K_{II}. The relationship between the intensity factors of the kinked crack and those of the parent interface crack is expressed compactly as

$$K_I + iK_{II} = cKa^{i\varepsilon} + \bar{d}\bar{K}a^{-i\varepsilon} + b\sigma_0 a^{1/2} \tag{12}$$

where $(^-)$ denotes the complex conjugate. Here c, d, and b are dimensionless complex functions of ω, α, and β. The argument leading to the K terms in Eq. (12) is based primarily on simple dimensional considerations given in HH. The σ_0 term can be justified solely on the grounds that K_I and K_{II} depend linearly on σ_0 and that the only length quantity in the elasticity problem is a.

The calculations of $b \equiv b_1 + ib_2$ use the integral equation formulation of HH. The present results were obtained using the previous numerical scheme simply by changing the "loading on the crack" to be that associated with σ_0. Curves of b_1 and b_2 as functions of ω for various α, all with $\beta = 0$, are shown in Fig. 2. There is virtually no dependence of b_1 and b_2 on β. For example, the values computed with $\beta = \alpha/4$ differ from those computed with $\beta = 0$ by no more than about 1%. (The connection $\beta = \alpha/4$ corresponds with $\nu_1 = \nu_2 = 1/3$, typical for many material combinations.)[4] An approximate solution for the case of no elastic mismatch is readily obtained from the formulas given in Ref. 5. That approximation is

$$b_1 = 2(2/\pi)^{1/2} \sin^2\omega$$
$$b_2 = (2/\pi)^{1/2} \sin 2\omega \tag{13}$$

and, as shown by the dashed curve in Fig. 2, gives a good approximation for $\alpha = \beta = 0$ when ω is less than about 60°.

The real and imaginary parts of $c = c_R + ic_I$ and $d = d_R + id_I$ have been tabulated as functions of ω for a wide range of combinations of α and β.[6] When $\beta = 0$, Eq. (12) can be written as

$$K_I = (c_R + d_R)K_1 - (c_I + d_I)K_2 + b_1\sigma_0 a^{1/2} \tag{14}$$

$$K_{II} = (c_I - d_I)K_1 + (c_R - d_R)K_2 + b_2\sigma_0 a^{1/2} \tag{15}$$

The energy release rate of the kinked crack is

$$\mathcal{G}_s = (K_I^2 + K_{II}^2)/\bar{E}_2 \tag{16}$$

such that, with Eq. (12)

$$\mathcal{G}_s = (\mathcal{G}_s)_{\eta=0} + 2\sigma_0 a^{1/2} R_e[\bar{b}(cKa^{i\varepsilon} + \bar{d}\bar{K}a^{-i\varepsilon})]/\bar{E}_2 + (b_1^2 + b_2^2)\sigma_0^2 a/\bar{E}_2 \tag{17}$$

where

$$(\mathcal{G}_s)_{\eta=0} = \{(|c|^2 + |d|^2)K\bar{K} + 2R_e(cdK^2 a^{2i\varepsilon})\}/\bar{E}_2 \tag{18}$$

This last quantity is the energy release rate when $\sigma_0 = 0$. The ratio of the two release rates is obtained from Eqs. (10) and (17) using Eq. (8) as

$$\mathcal{G}_s/\mathcal{G}_i = f^{(0)}(\omega_1, \tilde{\psi}) + \eta f^{(1)}(\omega_1, \tilde{\psi}) + \eta^2 f^{(2)}(\omega) \tag{19}$$

where η is defined in Eq. (1) and

$$f^{(0)} = ((1+\alpha)/(1-\beta^2))\{|c|^2 + |d|^2 + 2R_e[cde^{2i\tilde{\psi}}]\}$$
$$f^{(1)} = 2((1+\alpha)/(1-\beta^2))R_e\{\bar{b}[ce^{i\tilde{\psi}} + \bar{d}e^{-i\tilde{\psi}}]\}$$
$$f^{(2)} = ((1+\alpha)/(1-\beta^2))(b_1^2 + b_2^2)$$

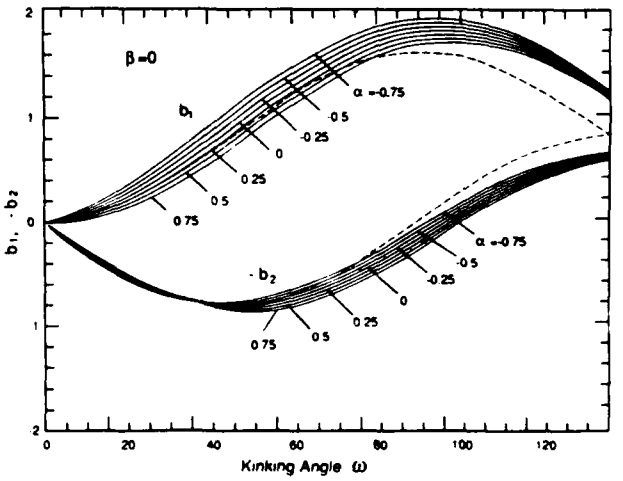

Fig. 2. Curves of b_1 and b_2 as a function of ω for various α. The dashed line curve is the approximation (13).

with

$$\tilde{\psi} = \psi + \varepsilon \ln (a/L)$$

The functions $f^{(i)}$ are independent of the magnitude of K but depend on the phase ψ of the interface stress intensity factors, as well as on the kink angle ω. If $\beta = 0$, these functions are independent of the putative crack length a, and therefore $\mathcal{G}_s/\mathcal{G}_i$ depends on a only through η. When $\beta \neq 0$, there is an additional *very weak* dependence on a through term $\varepsilon \ln (a/L)$ in $f^{(0)}$ and $f^{(1)}$. In what follows, the focus is on material mismatches with $\beta = 0$, either exactly or approximately. This choice averts the (usually nonessential) complications associated with the weak $\varepsilon \ln (a/L)$ dependence. Some assessment of the effect of nonzero β values can be obtained from the results presented below by simply accounting for the contribution $\varepsilon \ln (a/L)$ to $\tilde{\psi}$. This term amounts to a phase shift in ψ. Some further discussion of how this dependence affects the behavior when σ_0 vanishes is given in HH.

III. Interface Cracking versus Kinking

The role played by σ_0 on the competition between continued interface cracking and kinking into the substrate is illustrated in Figs. 3 and 4. The ratio $\mathcal{G}_i/\mathcal{G}_s$, as calculated from Eq. (19), is plotted in Fig. 3 as a function of the kink angle ω for the case $\alpha = \beta = 0$. The parent interface crack is loaded with equal amounts of mode 1 and mode 2 ($\psi = 45°$). The stress σ_0 begins to have an appreciable effect on the release rate ratio when $|\eta|$ is about 1/10; furthermore, when $|\eta|$ is 1/4, the $\mathcal{G}$ ratio is increased or decreased by about 50%, depending on the sign of σ_0.

The ratio $\mathcal{G}_i/\mathcal{G}_s^{max}$ is plotted as a function of ψ in Fig. 4, again for the case $\alpha = \beta = 0$. Here, $\mathcal{G}_s^{max}$ is the value of $\mathcal{G}_s$ maximized with respect to the kink angle ω. As detailed in HH for the limit $\eta = 0$, the value of ω at which $\mathcal{G}_s$ is maximized usually corresponds very closely (but not exactly) to the direction of the kink corresponding to $K_{II} = 0$. A significant difference between these two directions occurs only when the material into which the crack kinks is substantially stiffer than the other material, and then only when the loading on the interface crack is heavily mode 2.

Consider the role of *in-plane tension* ($\eta > 0$) with the aid of Fig. 4. Determine $\mathcal{G}_i/\mathcal{G}_s^{max}$, given the mode of loading as specified by ψ and the value of η based on estimates of initial flaw size a and σ_0. Let $\Gamma_i(\psi)$ be the mode-dependent interface toughness and $\Gamma_s = K_{IC}^2/E_2$, the mode I toughness of the substrate material. If

$$\Gamma_i/\Gamma_s < \mathcal{G}_i/\mathcal{G}_s^{max} \tag{20}$$

the interface crack meets the condition for continuing advance in the interface at an applied load too low to advance the flaw into the substrate. Conversely, if the inequality in Eq. (20) is reversed, the flaw initiates a kink at an applied load lower than that necessary to advance the crack in the interface. The *transition toughness ratio* separating interface cracking from substrate kinking is given by

$$(\Gamma_i/\Gamma_s)_{TRANSITION} = \mathcal{G}_i/\mathcal{G}_S^{max} \tag{21}$$

The curves in Fig. 4 thus provide the transition toughness ratio for a given mode of loading and a given η. Note that at the transition, $\mathcal{G}_i$ can be replaced by Γ_i in the expression (1) for η. For this case, once substrate cracking is initiated, η increases as the crack grows, further increasing the driving force on the tip of the crack, and the kink becomes unstable.

In-plane compression in the substrate ($\eta < 0$) leads to very different behavior. In this case, $\mathcal{G}_s$ decreases with increasing a, and cracks which kink into the substrate tend to arrest. To further examine this phenomenon, let

$$\Delta = \Gamma_i/\Gamma_s - (\mathcal{G}_i/\mathcal{G}_S^{max})_{\eta=0} \tag{22}$$

If $\Delta < 0$, *interface cracking* occurs and substrate cracks will not be initiated. If $\Delta > 0$, sufficiently small flaws will initiate kink cracks but, because η decreases (as a increases), these will subsequently arrest when

$$\mathcal{G}_S^{max} = \Gamma_s \tag{23}$$

Now imagine a three-dimensional interface crack front encountering small flaws in the substrate. When σ_0 is compressive and $\Delta > 0$, *it is possible to have interface cracking* (with $\mathcal{G}_i = \Gamma_i$) *and still initiate small cracks which kink into the substrate and then arrest upon growth to a length governed by Eq. (23).*

The effect of elastic mismatch on $\mathcal{G}_i/\mathcal{G}_s^{max}$ is shown in Figs. 5 and 6 for ($\alpha = 0.5$, $\beta = 0$) and ($\alpha = -0.5$, $\beta = 0$), respectively. All other things being equal, increasing the relative compliance of the material into which the crack kinks increases the energy release rate of the kinked crack, and thus increases the tendency for substrate cracking.

To facilitate estimation of the effects of in-plane stress, the lowest order influence of η on the release rate ratio is expressed as

$$\mathcal{G}_i/\mathcal{G}_S^{max} \cong (\mathcal{G}_i/\mathcal{G}_S^{max})_{\eta=0} - \eta f(\alpha, \psi) \tag{24}$$

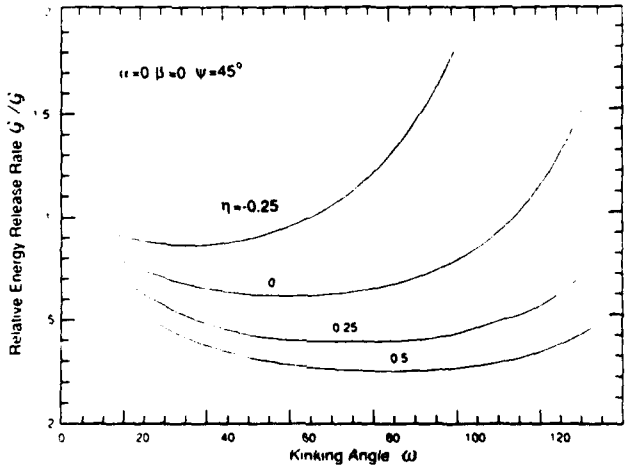

Fig. 3. Energy release rate ratio as a function of the kinking angle ω for various values of the residual stress parameter η; $\psi \equiv \tan^{-1}(K_2/K_1) = 45°$ and $\alpha = \beta = 0$.

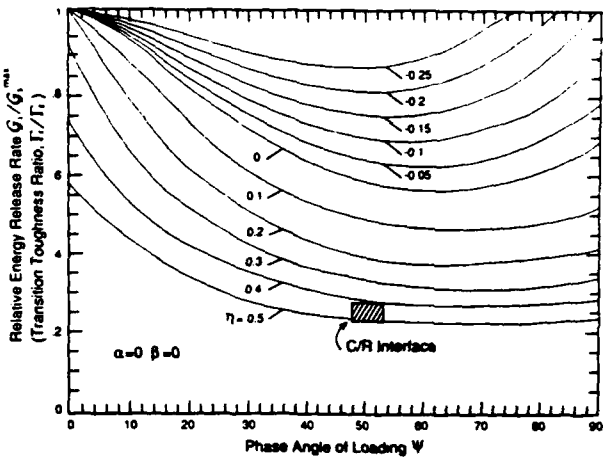

Fig. 4. Ratio of interface energy release rate to maximum energy release rate of kinked crack as a function of the phase of loading $\psi \equiv \tan^{-1}(K_2/K_1)$ for various values of the in-plane stress parameter η. $\alpha = \beta = 0$. The interpretation as the transition toughness ratio, Γ_i/Γ_s, applies only for $\eta > 0$. The datum is discussed in Section IV.

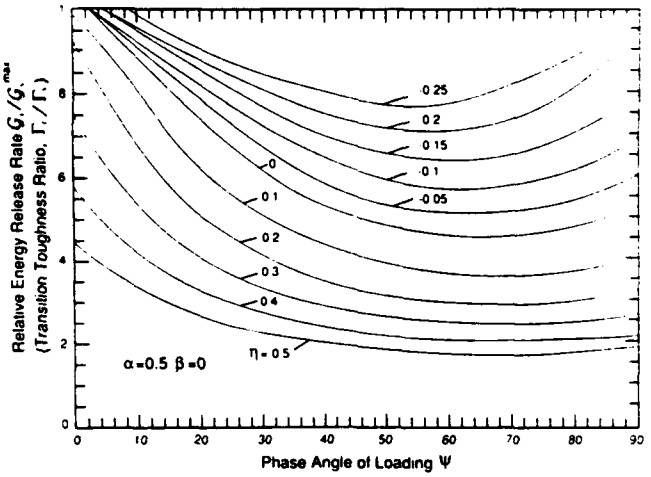

Fig. 5. Energy release rate ratio versus ψ for $\alpha = 0.5$, $\beta = 0$

This result is obtained from Eq. (19) with

$$(\mathcal{G}_i/\mathcal{G}_s^{max})_{\eta=0} = 1/f^{(0)}(\omega^*,\psi)$$

$$f = f^{(1)}(\omega^*,\psi)/f^{(0)}(\omega^*,\psi)^2 \quad (25)$$

where ω^* is the value of ω which maximizes $f^{(0)}(\omega,\psi)$. Curves of $(\mathcal{G}_i/\mathcal{G}_s^{max})_{\eta=0}$ and f as functions of ψ for various α (with $\beta = 0$) are shown in Figs. 7(A) and (B). Comparison of Eq. (24) with the full numerical results in Figs. 4 to 6 reveals that the approximation retains accuracy to within about 10% for $|\eta| \lesssim 0.2$.

Based on this approximation, the transition toughness ratio shifts with tensile in-plane stress according to

$$(\Gamma_i/\Gamma_s)_{TRANSITION} \cong (\mathcal{G}_i/\mathcal{G}_s^{max})_{\eta=0} - \eta f(\alpha,\psi) \quad (26)$$

When σ_0 is compressive, the length of the arrested kink cracks can also be estimated using Eq. (24) when $|\eta| \lesssim 0.2$. Suppose, as discussed earlier, that Δ in Eq. (22) is positive. Using Eq. (24) with the arrest condition (Eq. (23)) gives

$$-\eta = (-\sigma_0)(a/(E_*\Gamma_i))^{1/2} \cong \Delta/f \quad (27)$$

IV. Experimental Illustration

An experimental illustration of the importance of the above calculations concerns cracking in a diffusion bonded system between Ti(Ta) and Al_2O_3. Upon diffusion bonding, brittle reaction products form in this system, consisting of various intermetallics,[7,8] including the γ, α_2, and σ phases in the Ti, Al, Ta ternary. These layers are typically 3 μm thick

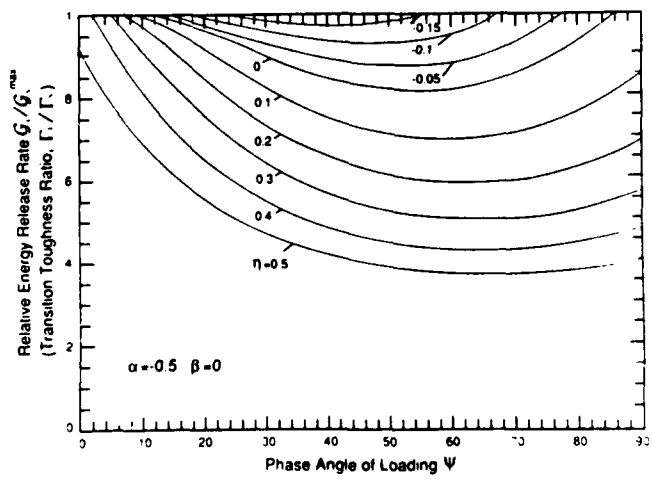

Fig. 6. Energy release rate ratio versus ψ for $\alpha = -0.5$, $\beta = 0$

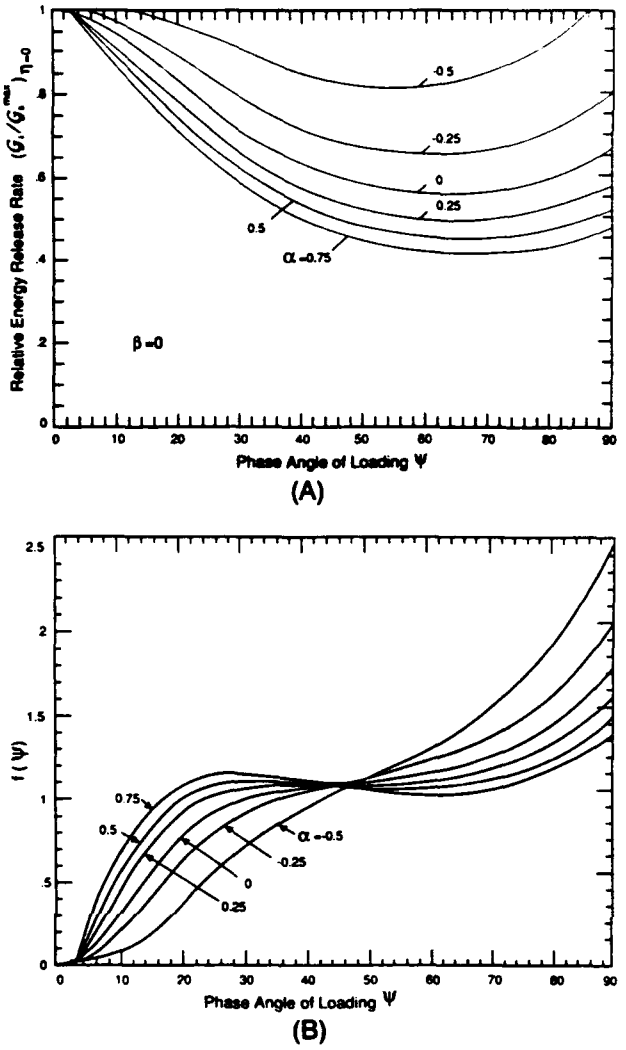

Fig. 7. (A) Energy release rate ratio versus $\psi \equiv \tan^{-1}(K_2/K_1)$ for $\eta = 0$. (B) Coefficient of lowest order contribution of η to energy release rate ratio in Eq. (24). In both cases, $\beta = 0$.

(Fig. 8). Interface fracture energy measurements have been made on this system using a notched flexural specimen.[7] Two observations and measurements are relevant. When precracking is conducted in three-point flexure, the crack introduced into the Al_2O_3, which extends normal to the interface, penetrates the reaction product layer and arrests at the reaction product/Ti interface (Fig. 8(A)), referred to as the R/M interface. Subsequent to precracking, when the specimen is loaded in four-point bending, cracks nucleate at the Al_2O_3/reaction product interface, referred to as the C/R interface, and propagate along that interface (Fig. 8(B)). The associated propagation load[7] indicates a fracture energy for this interface of $\Gamma_i \approx 17\ J \cdot m^{-2}$. Also, periodic branch cracks are emitted into the reaction product layer as the primary crack extends along the interface. These branch cracks arrest at the R/M interface (Fig. 8(B)). Cross sections suggest that the branch cracks tunnel across the reaction product layer, starting from the free edge. It is apparent from these results that the R/M interface has a relatively high fracture energy and is not a factor in the fracture process. Independent measurements of the fracture energy of reaction products in Ti/Al, refractory metal ternary systems, such as the σ phase,[9] indicate values in the range $\Gamma_R \approx 40$ to $50\ J \cdot m^{-2}$. This multiplicity of fracture behaviors can be rationalized using the preceding calculations.

During precracking, with the mode I crack in the Al_2O_3 normal to the interface, the fracture energy ratio between the

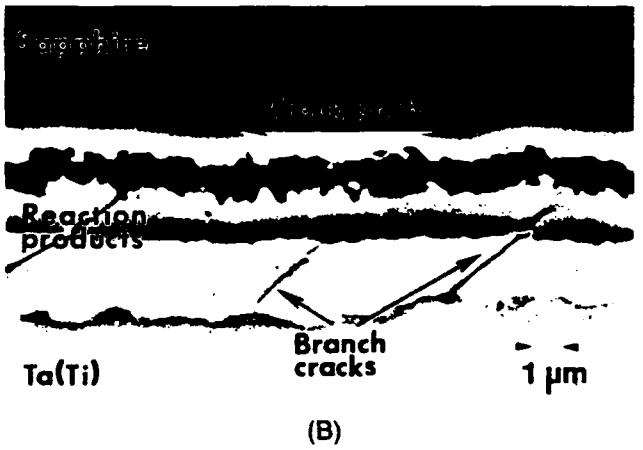

Fig. 8. (A) A precrack that extended in the Al_2O_3 normal to the interface and propagated through the reaction product interface in a Ti(Ta)/Al_2O_3 bond. (B) A mixed-mode crack extending along the Al_2O_3/reaction product layer interface. Also shown are periodic, inclined branch cracks in the reaction product layers formed upon interface crack extension.

reaction products and the C/M interface is $\Gamma_i/\Gamma_R \approx 1/3$. This ratio is in a range consistent with the observed crack penetration into the reaction products.[10] Upon subsequent loading, when crack extension occurs along the C/R interface, the phase angle ψ is approximately 50°.[11] For this case, with $\eta = 0$ and $\Gamma_i/\Gamma_R \approx 1/3$, Fig. 4 would indicate that the crack *should remain at the C/R interface.* However, if a tensile misfit stress exists within the reaction product layer, Fig. 4 indicates that $\eta \approx 0.5$ *would allow the formation of branch cracks.* Based on the elastic properties of the Ti/Al_2O_3 system,[7] the requirement for branch cracking becomes, $\sigma_0(c)^{1/2} \approx 1$ MPa · $m^{1/2}$. Since the branch cracks tunnel in from the edge, c should be about equal to the reaction product layer thickness (~3 μm), whereupon the misfit stress should be $\sigma_0 > 600$ MPa. Such levels of misfit stress arise from the thermal expansion mismatch between either the γ-TiAl or the σ reaction layer with either the Al_2O_3 or the Ta(Ti).

V. Conclusion

In-plane stresses can have a major influence on the behavior of interface cracks. In particular, tensile in-plane stress acts in conjunction with flaws near the interface to destabilize interface cracks and causes them to depart from the interface. Conversely, compressive in-plane stresses stabilize interface cracks and essentially deactivate flaws around the interface. Such issues are important in the failure of bonds when either reaction layers or coatings subject to misfit stresses are present, and in fiber fracture from interface debonds in brittle matrix composites. The calculations are illustrated by observations of branch cracks within a reaction product layer formed in the Ti(Ta)/Al_2O_3 system.

References

[1]M.Y. He and J.W. Hutchinson, "Kinking of a Crack out of an Interface," *J. Appl. Mech.*, **56** [2] 270–78 (1989).

[2]J. R. Rice, "Elastic Fracture Mechanics Concepts for Interfacial Cracks," *J. Appl. Mech.*, **55** [1] 98–103 (1988).

[3]J.W. Hutchinson, "Mixed Mode Fracture Mechanics of Interfaces"; in *Metal/Ceramic Interfaces.* Edited by M. Rühle, A. G. Evans, M. F. Ashby, and J. P. Hirth. Pergamon Press, Elmsford, NY, 1990.

[4]T. Suga, E. Elssner, and S. Schmauder, "Composite Parameters and Mechanical Compatibility of Material Joints," *J. Comp. Mater.*, **22**, 917–34 (1988).

[5]B. Cotterell and J. R. Rice, "Slightly Curved or Kinked Cracks," *Int. J. Fract.*, **16** [2] 155–69 (1980).

[6]M.Y. He and J.W. Hutchinson, "Kinking of a Crack out of an Interface: Tabulated Solution Coefficients," Harvard University Report MECH-113A (available for a limited period from Marion Remillard, Pierce Hall 314, Division of Applied Sciences, Harvard University, Cambridge, MA 02138).

[7]A. Bartlett, M. Rühle, and A. G. Evans, "Residual Stress Cracking in Metal/Ceramic Bonds," *Acta Metall.*, in press.

[8]J. Kennedy and G. Geshwind, "Interfacial Reactions in Potential Titanium Matrix Composites"; p. 2299 in *Titanium Science and Technology.* Edited by R. I. Jaffee and H. M. Burte. Plenum Press, New York, 1973.

[9]H. E. Dève, G. R. Odette, R. Mehrabian, and A. G. Evans, "Ductile Reinforcement Toughening of γ-TiAl," *Acta Metall.*, **38**, 1491 (1990).

[10]M.Y. He and J.W. Hutchinson, "Crack Deflection at an Interface between Dissimilar Elastic Materials," *Intl. J. Solids Struct.*, **25**, 1053–67 (1989).

[11]P. G. Charalambides, J. Lund, R. M. McMeeking, and A. G. Evans, "A Test Specimen for Determining Fracture Resistance of Bimaterial Interfaces," *J. Appl. Mech.*, **56**, 77–82 (1989). □

Acta metall. mater. Vol. 40, Suppl., pp. S333–S344, 1992
Printed in Great Britain.

0956-7151/92 $5.00 + 0.00

INTERFACES BETWEEN ALUMINA AND PLATINUM: STRUCTURE, BONDING AND FRACTURE RESISTANCE

M. DE GRAEF[1]†, B. J. DALGLEISH[2], M. R. TURNER[1] and A. G. EVANS[1]

[1]Materials Department, College of Engineering, University of California, Santa Barbara, CA 93106-5050 and [2]Materials and Mineral Engineering Department, Hearst Mining Building, University of California, Berkeley, CA 94710, U.S.A.

Abstract—Various diffusion bonded interfaces have been produced between Pt and either sapphire or polycrystalline Al_2O_3. The structure, bonding and fracture resistance of these interfaces have been examined, as well as the infuence of intervening silicate phases, both amorphous and crystalline. It is found that the intrinsic fracture resistance Γ_i of the Pt/sapphire interface is high, especially when Pt has an epitaxial orientation with respect to the sapphire. The fracture resistance is substantially degraded by amorphous silicate phases at the interface, even when discontinuous, but is not adversely influenced by crystalline silicates. By contrast, the silicate phase enhances the diffusion bonding and facilitates formation of void-free bonds. This duality in the role of silicates is a major feature of this article.

Résumé—Diverses interfaces liées par diffusion sont élaborées entre du platine et soit du saphir, soit de l'alumine polycristalline. La structure, la liaison et la résistance à la rupture de ces interfaces sont étudiées, de même que l'influence des phases silicatées qui se produisent, tant amorphes que cristallisées. On trouve que la résistance intrinsèque a la rupture Γ_i de l'interface Pt/saphir est élevée, spécialement lorsque Pt a une orientation epitaxique par rapport au saphir. La résistance à la rupture est considérablement dégradée par les phases silicatées amorphes à l'interface, même lorsqu'elles sont discontinues, mais elle n'est pas défavorablement influence par les silicates cristallisés. Au contraire, le phases silicatées renforcent la liaison par diffusion et facilitent la formation de liaisons exemptes de cavités. Cette dualité du rôle des silicates est un aspect majeur de ce travail.

Zusammenfassung—Verschiedene diffusionsgefügte Grenzflächen werden zwischen Pt und Saphir oder polykristallinem Al_2O_3 hergestellt. Struktur, Bindung und Bruchwiderstand dieser Grenzflächen werden untersucht, ebenso der Einfluß eingelagerter Silikatphasen, amorph oder kristallin. Es ergibt sich, daß der intrinsische Bruchwiderstand Γ_i der Pt/Saphir-Grenzfläche hoch ist, insbesondere wenn Pt epitaktisch zum Saphir orientiert ist. Der Bruchwiderstand wird beträchtlich verringert durch eine amorphe Silikatphase an der Grenzfläche, auch wenn sie diskontinuierlich ist, jedoch nicht gegenteilig beeinflußt wird durch kristallines Silikat. Dagegen verstärkt die Silikatphase die Diffusionshaftung und erleichtert die Bildung porenfreier Verbindungen. Diese Dualität der Rolle des Silikates ist wichtigstes Anliegen dieser Arbeit.

1. INTRODUCTION

Attention has been given to the structure and the thermodynamics of the interface between aluminum oxide and platinum [1]. However, there have been no reported attempts at measuring the fracture resistance of such interfaces and relating these resistances to the structure, chemistry and microstructure. The principal intent of the present article is to address this issue. The emphasis is on interfaces generated at elevated temperatures by a diffusion bonding process. Both sapphire and a commercial polycrystalline alumina are used, in conjunction with polycrystalline Pt. Since commercial polycrystalline Al_2O_3 contains silicates, insight regarding their effect on bonding and fracture is gained by conducting experiments with a layer of silica deposited onto sapphire prior to diffusion bonding with Pt.

Previous studies on comparable interfaces [2–5] have indicated strong effects on the fracture energy, Γ_i of plasticity, of reaction products and of the atmosphere, coupled through the interface fracture mechanism [4, 5]. Crack extension along interfaces without reaction products may occur either by ductile void growth, by brittle debonding or by coupled debonding with plasticity [6]. Interface cracking involving plasticity often occurs by a debonding mechanism operating at interfacial defects ahead of the interface crack front, whereas brittle debonding occurs by direct bond rupture at the crack front itself. The dominant mechanism (among these possibilities) governs the role of such parameters as yield strength, work of adhesion, metal thickness, environment and interface defect

†On leave from the Department of Metallurgy and Materials Engineering, K. U. Leuven, de Croylaan 2, B-3001 Belgium.

population. The present experimental study provides new information about the relative importance of some of these variables.

2. MATERIALS

Basal plane oriented sapphire was acquired and carefully polished. High purity platinum foils were obtained from Johnson-Matthey (99.99%) and Engelhard (99.95%) having thickness 25–250 μm. Polycrystalline Al_2O_3 was obtained from Coors: this material was ~99.5% Al_2O_3, with the remaining phases consisting of silicates, generally in the amorphous state. Diffusion bonds between either the sapphire or polycrystalline alumina and the Pt foils were made in a sandwich geometry, wherein the foil was placed between the two polished alumina plates [5]. Prior to bonding, the sapphire and Al_2O_3 plates were dry pre-annealed at 1000°C for 2 h and the Pt foil was dry pre-annealed for 2 h at 1200°C. Two different furnaces were used for this purpose. One furnace, designated A, had been used only for diffusion bonding. The other, designated B, was a multipurpose air annealing furnace. As demonstrated below, the choice of annealing furnace had a profound effect both on the diffusion bonding and the resultant interface fracture energy. Consequently, hereafter the bonds are designated A or B, according to the furnace used for pre-annealing. Following pre-annealing, a small load was applied to the sandwich layer, the system placed within a vacuum furnace and the temperature raised to 1450°C. At this temperature, an additional load corresponding to a stress of ~5 MPa was applied for 12 h to achieve the diffusion bonding. Thereafter, the system was cooled to room temperature, with the load still applied.

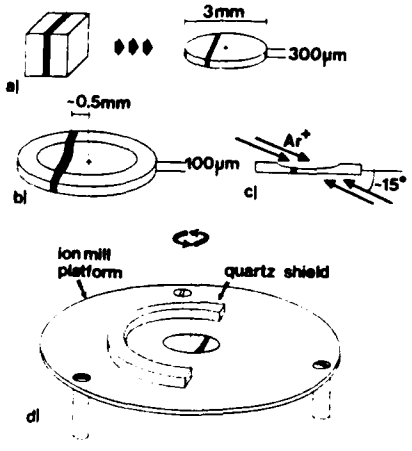

Fig. 1. Successive stages of the sample preparation procedure: (a) cutting geometry; (b) position of dimple, relative to the interfaces; (c) incident ion beams graze along the metal layer; and (d) geometry of the semi-circular quartz shields on the ion-mill platform.

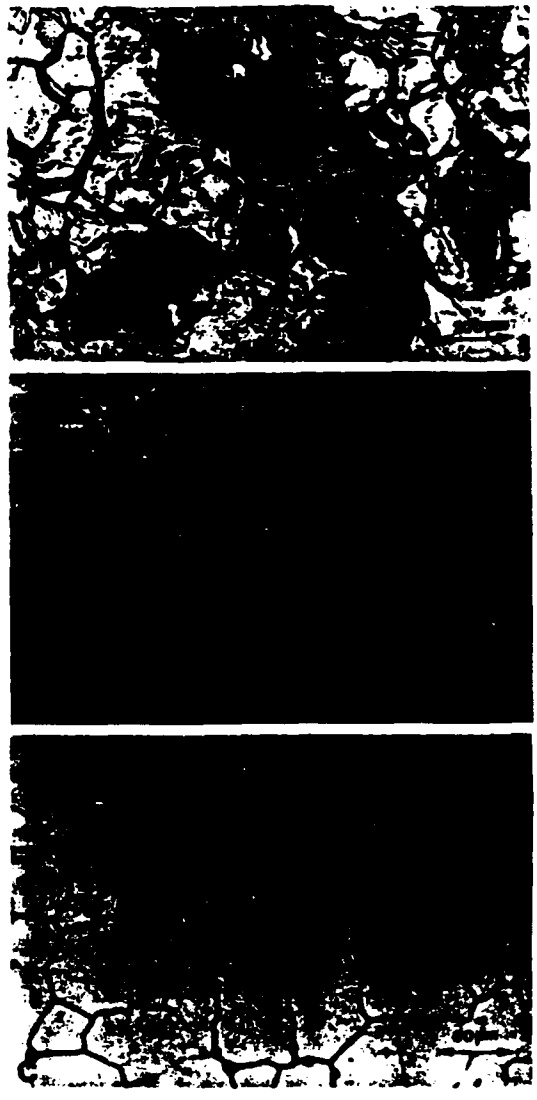

Fig. 2. Optical observation of Pt–sapphire interfaces. (a) A bonds, (b) A bonds coated with a 100 nm thin SiO_2 layer and (c) B bonds.

Subsequently, diamond sawing and grinding were used to prepare test specimens from the bonded plates. Some bonded materials were produced by first depositing a thin (approximately 100 nm) silica layer onto basal plane sapphire by reaction sputtering and then diffusion bonding with Pt.

3. PROCEDURES

Mechanical measurements were made primarily with the mixed mode flexure specimen [2–5]. The basic test procedures, elaborated elsewhere [4], are briefly described. A row of Vickers indentations was placed along the center line of the thinner Al_2O_3 layer. The specimen was loaded in three-point flexure with the indentation on the tensile surface. Loading

was continued until a crack formed and propagated to the interface. The crack arrest load was recorded. Following this precracking step, further testing was conducted in four-point flexure, with the loading performed within an optical microscope to allow *in situ* observation of interface crack growth. These tests were conducted in air. In some cases, mode I tests were conducted on notched beams (wherein the notch was prefabricated into the bonded structure) and the specimen tested to fracture.

Specimens fractured in accordance with either of the above test procedures were examined in the scanning electron microscope (SEM). Emphasis was placed on the interfacial fracture surfaces, wherein both the morphological and chemical characteristics were examined. In some cases, Pt and sapphire fracture surfaces were examined by atomic force microscopy (AFM) on a Nanoscope II from Digital Instruments. In other cases, XPS was used to investigate fracture surfaces. When interface fracture could not be induced, some aspects of the interface were studied by using HF dissolution to separate the layers and expose the as-bonded Pt interface.

Transmission electron microscopy (TEM) has emphasized sections *normal* to the interface. Because of the very different ion-milling rates of Al_2O_3 and Pt, a new thinning method was developed for preparing samples suitable for transmission electron microscopy observations. Cross section samples were cut from the as-bonded plates using a low speed diamond saw. Circular samples (3 mm diameter) were cut from these beams, using an ultrasonic cutter

[Fig. 1(a)]. The samples were ground (3–4 at a time) down to about 80–100 μm using 30 or 15 μm paste. One side was polished with 1 μm diamond paste. The unpolished side was dimpled on a Dimple Grinder, using 6 and 3 μm diamond pastes with $\frac{1}{4}$ μm paste used for final polishing. The dimple was displaced relative to the top of the metal layer. The distance between the center of the dimple and the interface is crucial for later success in the ion-milling step; a distance of about 0.5–0.8 mm is optimum. The geometry of the sample after dimpling is shown in Fig. 1(b). The final thickness of the sample at the dimple center was 10–15 μm. For ion thinning, the off-center position of the metal-ceramic interface is oriented with respect to semi-circular shields [Fig. 1(d)] such that ions only graze the metal layer [Fig. 1(c)]. The ion milling conditions are: 5 kV, 1 mA, at 13–17°, two-sided milling.

All TEM observations were carried out on a JEOL 4000FX analytical transmission electron

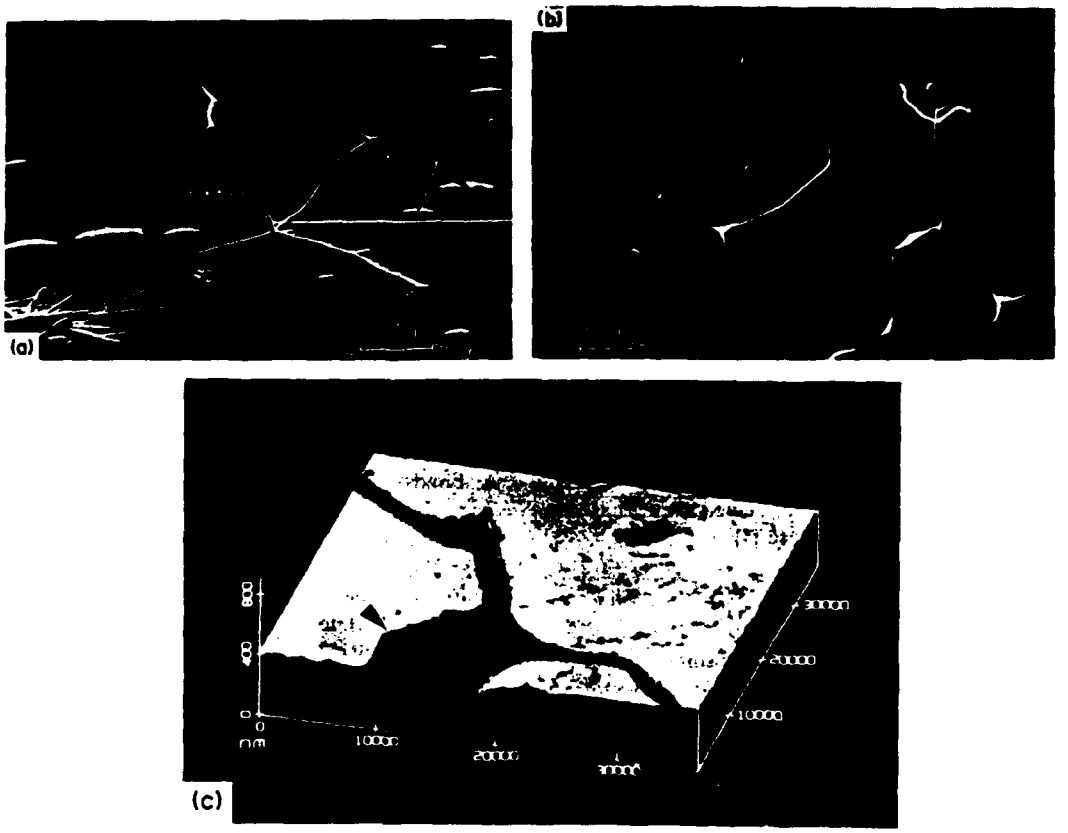

Fig. 3. SEM of Pt–sapphire fracture surfaces produced from B bonds. (a) Sapphire side, (b) Pt side, (c) an AFM trace across one of the ridges on the sapphire fracture surface.

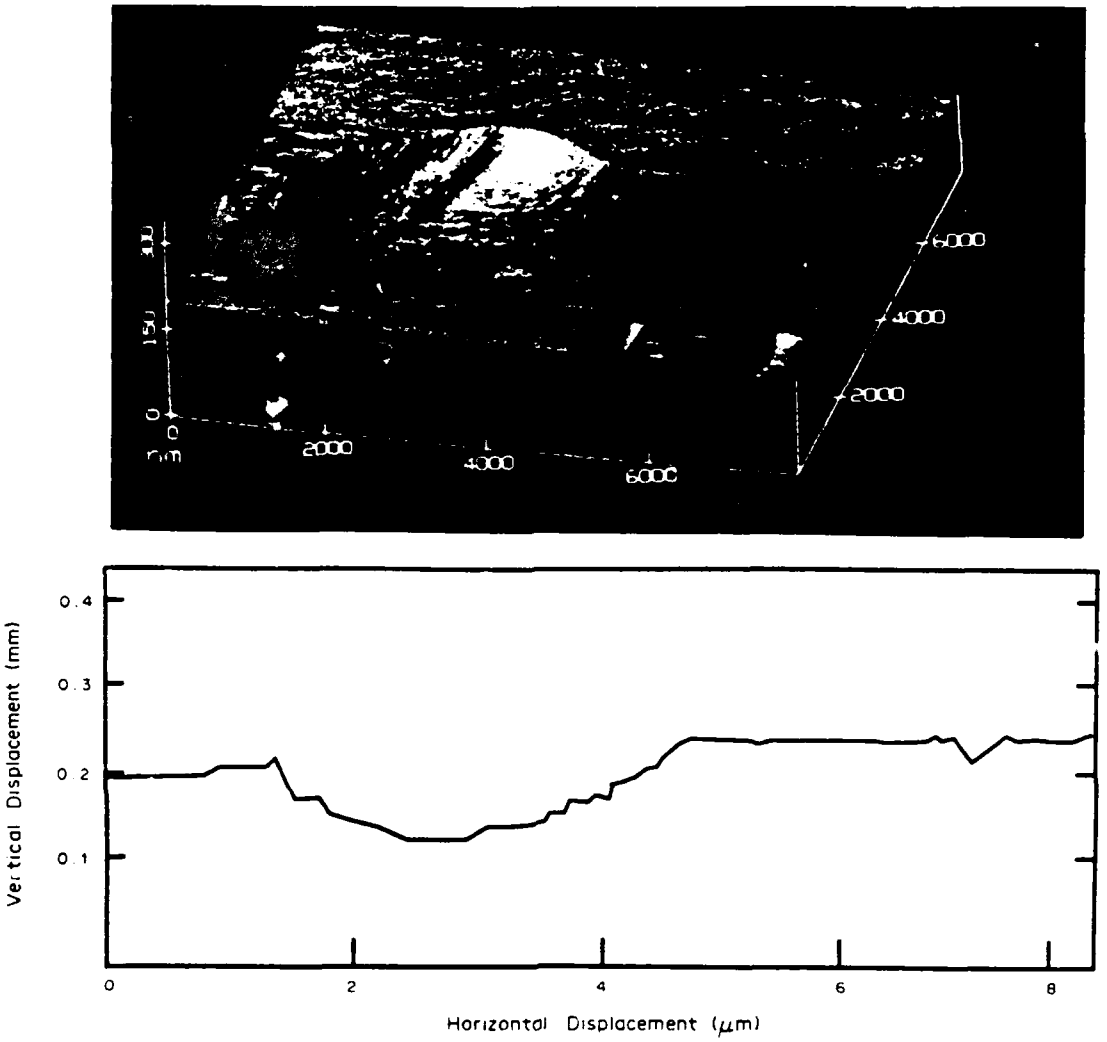

Fig. 4. AFM trace of a "void" on the interface of a Pt–sapphire B bond.

microscope, operated at 350 and 400 kV. This microscope is equipped with high angle X-ray (Tracor) and parallel EELS (GATAN) detectors with an optical fiber imaging system. Some electron diffraction was performed on a JEOL 200CX, operated at 200 kV. All crystallographic computations and diffraction pattern simulations were conducted on a Vaxstation 3200 with the EMS-software [7].

4. OBSERVATIONS

The diffusion bonds produced using *sapphire* were amenable to preliminary observation in the *optical microscope*. Fracture surfaces in B bonds, which were susceptible to interface fracture, could also be studied by SEM and AFM. However, interface fracture could not be induced in A bonds and SEM information could only be obtained on the Pt interface after separation of the bond by HF dissolution. The results of optical observations are summarized in Fig. 2. The A bonds† exhibit three basic types of contrast [Fig. 2(a)]. (i) Linear features outline those regions that did not bond during the diffusion bonding cycle‡ [Fig. 2(a)]. (ii) Within the area that bonded, a continuous network delineates the grain boundaries in the Pt (and defines the grain size). (iii) Finally, faint lines within the network may relate to facetting on the sapphire. Similar regions appear in the A bonds formed with the silica layer [Fig. 2(b)], except that the area fraction of debonded interface was substantially smaller, and the grain structure in the Pt less visible. The B bonds† [Fig. 2(c)] exhibit only one form of contrast. There is no evidence of unbonded regions. The observed contrast relates to ridges that form on the sapphire in the bonding process, at the location

†Recall that A and B refer to the designation of the pre-annealing furnace.

‡Prior experience with sapphire–Au interfaces [4, 5] has facilitated explicit definition of these features

of the grain boundaries in the Pt. Note that this "grain boundary" contrast is more distinct than that in A bonds [Fig. 2(a)]. Furthermore, the contrast is more evident in the B bonds produced using the thicker (100 μ) Pt foils. The average grain size of the Pt in B bonds is smaller than in A.

A direct visualization of the continuous network delineating the Pt grains in B bonds is provided by SEM observations of the *fracture surfaces* [Fig. 3(a, b)], which reveal ridges on the sapphire side of the fracture surface that coincide with depressions at the grain boundaries in the Pt. That the linear features are ridges rather than depressions on the sapphire and vice versa is established by AFM traces across the fracture surface [Fig. 3(c)]. Such studies also established that the maximum height of the ridges was approximately 450 nm. Some of these ridges were determined by EDX to contain appreciable quantities of Ca and Si. No evidence of these species could be detected on the interface *between* the ridges. These impurities must arise from the pre-annealing furnace, by deposition of either vapor or particulate Ca, Si, O species originating from the furnace walls. Similar furnace effects have been found in other studies performed with Al_2O_3 [8].

There were no indications of species other than Pt on the *metal side* of the fracture surface (either as adhering particles or from EDX determinations). The Pt interface produced in A bonds revealed after dissolution with HF, provided another visualization of the regions that did not bond during the diffusion bonding cycle. Based on these observations, there appear to be three principal differences between A and B bonds. (i) Bonding is more complete in B than in A. (ii) The Pt grain size is smaller in B than in A. (iii) Impurities (especially Ca and Si) are involved in the bonding achieved with B.

An additional characteristic of B bonds revealed by AFM is of significance. On both fracture surfaces, features that appear to be "voids" that remain after diffusion bonding are evident (Fig. 4).

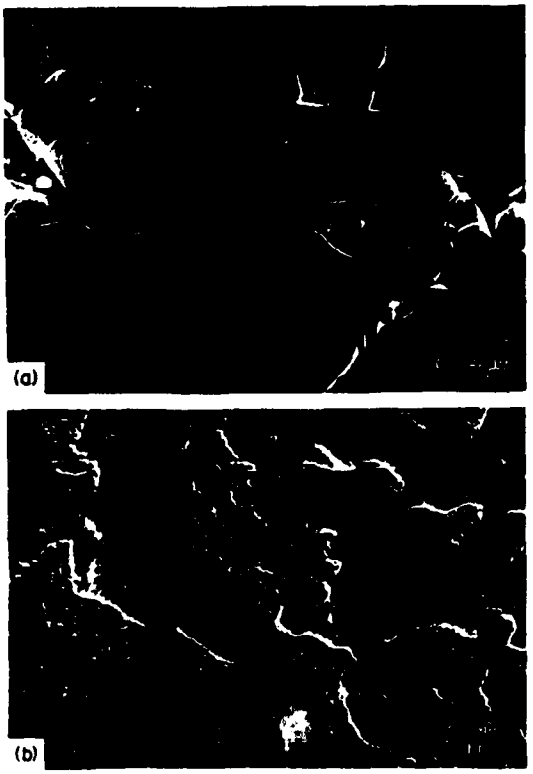

Fig. 5. SEM of fracture surface of interface produced with polycrystalline Al_2O_3: (a) Al_2O_3 side showing the outline of the amorphous interphase; (b) Pt side.

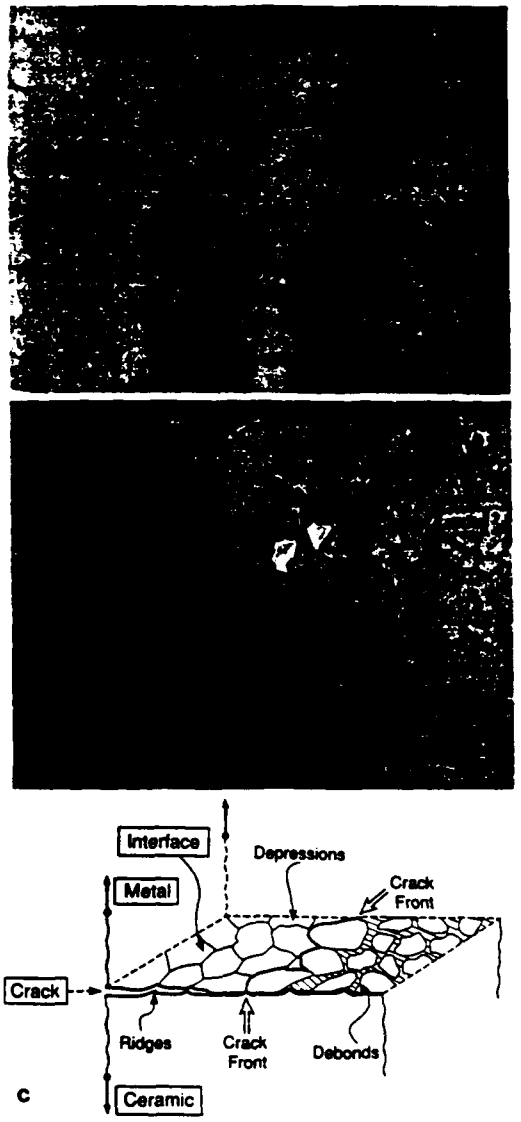

Fig. 6. Direct observations of the fracture mechanism at the Pt–sapphire B interface. (a) Initial interface, (b) debond (arrowed) forming at the silicate ridges, (c) schematic of the crack growth mechanism.

Such "voids" are also visible in the optical images (Fig. 2). However, AFM traces across these features indicate that they are depressions in the Pt (Fig. 4) but hillocks in the sapphire. Furthermore, by using EDX, Si and some Ca could be detected at the hillocks on the sapphire side of the fracture surface, suggesting that a lenticular silicate phase exists at these locations.

The *polycrystalline* Al_2O_3 is opaque and not amenable to optical observation. Reliance has thus been placed on SEM observations of fracture surfaces. The key observation is that the Al_2O_3 side of the fracture surface has a smooth appearance with frequently occurring outlines that circumvent voids and other defects at the interface [Fig. 5(a)]. These features suggest that a thin amorphous layer exists at the interface. A study of this surface by XPS has established the presence of Si, consistent with an amorphous silicate layer having formed during diffusion bonding. On the Pt side of the fracture surface, there is evidence of adhering particles [Fig. 5(b)], but otherwise, there are no EDX indications of species other than Pt. Interface decohesion thus appears to have occurred at the Pt–silicate interface.

5. FRACTURE RESISTANCE

Attempts at measuring the Pt–sapphire interface fracture resistance using the mixed mode flexure specimen were only successful for B bonds. The fracture resistance was obtained from the measured propagation load and the specimen dimensions [2]. Results obtained for 25 and 100 μm thick Pt layers are, $\Gamma_i = 40$ and 20 Jm^{-2}, respectively. Most notable is the lower fracture energy measured for the Pt with the larger metal layer thickness. This is contrary to a trend found for bonds between sapphire and Au [5], as well as for layer thickness effects described below for interfaces between Pt and polycrystalline Al_2O_3.

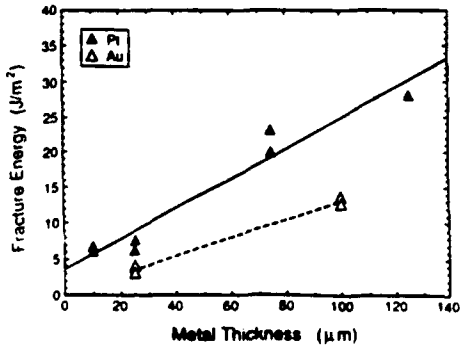

Fig. 7. Effects of Pt thickness on the mode I nominal interface fracture energy for Pt–polycrystalline Al_2O_3. Results for Au–Al_2O_3 bonds are also shown.

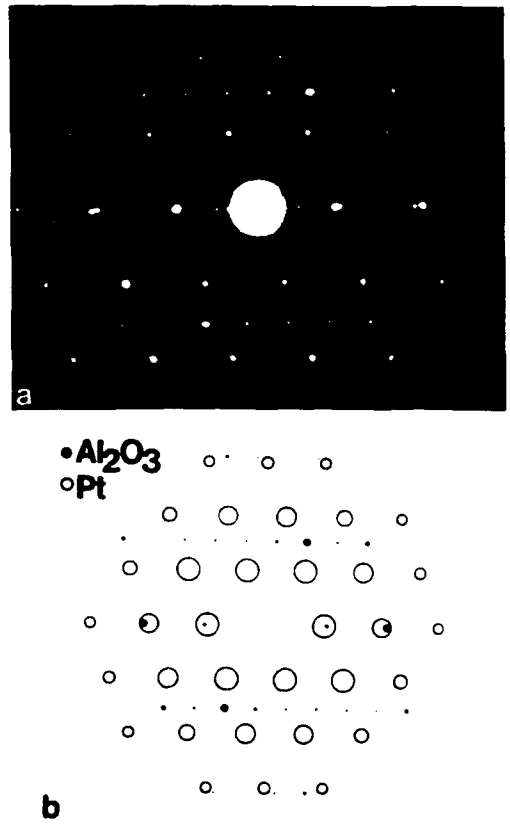

Fig. 8. (a) Experimental $[101]_{Pt}$–$[\bar{4}5.0]_S$ zone axis pattern and (b) computation of this geometry for a $[00.1]_S \| [111]_{Pt}$, $(2\bar{1}0)_S \| (1\bar{2}1)_{Pt}$ orientation relation.

For A bonds, following precracking, further cracking renucleated in the lower Al_2O_3 layer, and only a lower bound of 100 Jm^{-2} could be assigned to the interface fracture resistance.

Direct observation of crack growth in B bonds in the optical microscope revealed that crack extension involved debonding events that originated *ahead of the crack front* (Fig. 6). The debonding commenced at the silicate ridges along the Pt grain boundaries and proceeded to decohere the intervening interface. Such debonding was most extensive in the B bonds produced with the thicker (100 μm) Pt foil. Little time-dependent crack extension was detectable, contrasting with the strong effects found in the Au–Al_2O_3 system [4].

Experimental information obtained on bonds between Pt and polycrystalline Al_2O_3 consisted of prenotched mode I flexure tests. While these are not valid fracture resistance tests (because precracks were not introduced along the interface) the trends with the Pt layer thickness are of interest (Fig. 7). Notably, the nominal mode I fracture resistance increases as the metal layer thickness increases and extrapolates to $\Gamma_i \approx 4\ Jm^{-2}$ at zero thickness. Mode I results obtained on interfaces between Au and polycrystalline Al_2O_3 are included for comparison.

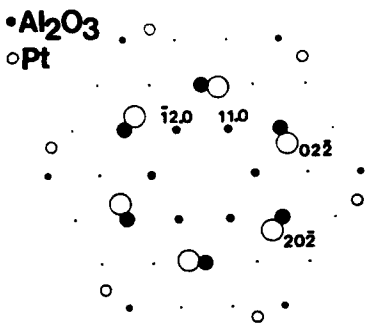

Fig. 9. Computed zone axis pattern for a $[00.1]_S = [111]_{Pt}$ zone axis in the same orientation relation as in the previous figure.

6. TRANSMISSION ELECTRON MICROSCOPY OF INTERFACE

6.1. Sapphire/Pt interfaces

Electron diffraction analysis of A bonds revealed epitaxial growth of Pt on the substrate. The observed orientation relationship is $[00.1]\|[111]$ and $(2\bar{1}.0)\|(1\,\bar{2}1)$. The experimental diffraction pattern and a computer simulation (kinematical approximation) are shown in Fig. 8. This orientation relation corresponds to a 19.1° rotation of the close packed directions in the Pt-layer with respect to the underlying close packed oxygen plane. This rotation angle is reminiscent of a frequently occurring orientation relationship in systems with intercalant layers, wherein the intercalant layer has an effective in-plane lattice parameter $\sqrt{7}$ times that of the substrate† and rotated by 19.1°. Furthermore, a similar rotation was previously observed for epitaxial Cu and Pt on basal sapphire [1]. Superposition of the [0001] and [111] zone axis patterns results in the geometry of Fig. 9. The slightly different in-plane lattice parameter represents a lattice mismatch of 1%. This causes strain contrast observed at several locations along the interface. The sapphire surface also shows multiple surface steps with a step-height of approximately 3 nm. The Pt-layer follows the steps perfectly. *Occasionally*, amorphous regions were observed about 150 nm thick and up to about 600 nm in extent along the interface. In such regions, the epitaxy between metal and sapphire was locally imperfect. Energy dispersive X-ray analysis (EDS) of the amorphous regions reveals Ca, Si and Al; parallel electron energy loss spectroscopy (PEELS) shows the presence of oxygen. The relative concentrations of Ca, Si and Al indicate that this amorphous phase is related to anorthite.

In one sample, an intermetallic reaction zone exhibiting a domain structure was found (Fig. 10); different orientation variants alternate with Pt regions. EDS-analysis suggested a composition close to Pt_2Al. Electron diffraction analysis of this phase resulted in the zone axis patterns shown in Fig. 11(a, b). Pt_2Al is orthorhombic, having a space group *Pmma*, $a = 1.629$ nm, $b = 0.392$ nm, $c = 0.543$nm, with 24 atoms per unit cell [9]. This structure is shown in Fig. 11(c), in a [010]-projection. Note the wavy character of the (001)-planes. Based on these unit cell data, the experimental patterns [Fig. 1(a, b)] were successfully simulated, using kinematical diffraction theory [Fig. 11(d, e)]. Pattern 11(d) is obtained by superimposing two orientation variants of the Pt_2Al structure. There are a total of 3 different variants with respect to the perfect Pt-structure: two obtained by rotating the original cell by 90° around the *b*-axis, the third has the long axis perpendicular to the plane [Fig. 11(e)]. PEELS observations did not reveal O in the intermetallic. EDS measurements in the Pt away from the intermetallic indicated a solid solution of up to 10 at % Al.

Observations of B bonds indicated that the majority of Pt grains are randomly oriented, although some grains are in epitaxial orientation with respect to the sapphire. A thin amorphous interlayer, with composition similar to that of the amorphous region in A, was frequently identified at junctions between two or more Pt grains and the interface (Fig. 12). This phase is believed to coincide with the ridges found in the SEM and AFM (Fig. 4). High-resolution microscopy suggests that the amorphous phase is confined to the junction and is not continuous.

A new epitaxial relationship was also found in some cases. A diffraction pattern (Fig. 13) of the [2$\bar{1}$.0] sapphire zone axis with a slightly misoriented [100] Pt zone axis suggests the following orientation relationship: $[2\bar{1}.0]_S\|[100]_{Pt}$ and $(0\,\bar{3}.0)_S\|(0\,\bar{1}1)_{Pt}$. Hence, the $(011)_{Pt}$-plane is parallel to the basal plane of sapphire. The lattice mismatch in this orientation is small: the mismatch parameters are 0.98% for the $[100]_{Pt}$ direction and 1.06% for the perpendicular

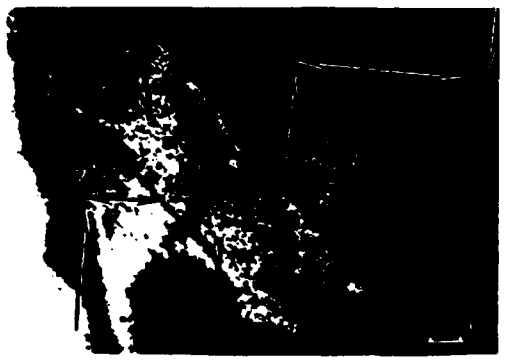

Fig. 10. Low magnification micrograph of a Pt_2Al reaction zone close to the Pt–sapphire interface; different orientation variants are indicated with arrows.

†In the Pt–sapphire system, this occurs even though there is no simple $\sqrt{7}$ relation between the two in-plane lattice parameters: 0.2747 nm for sapphire and 0.2774 nm for Pt [1].

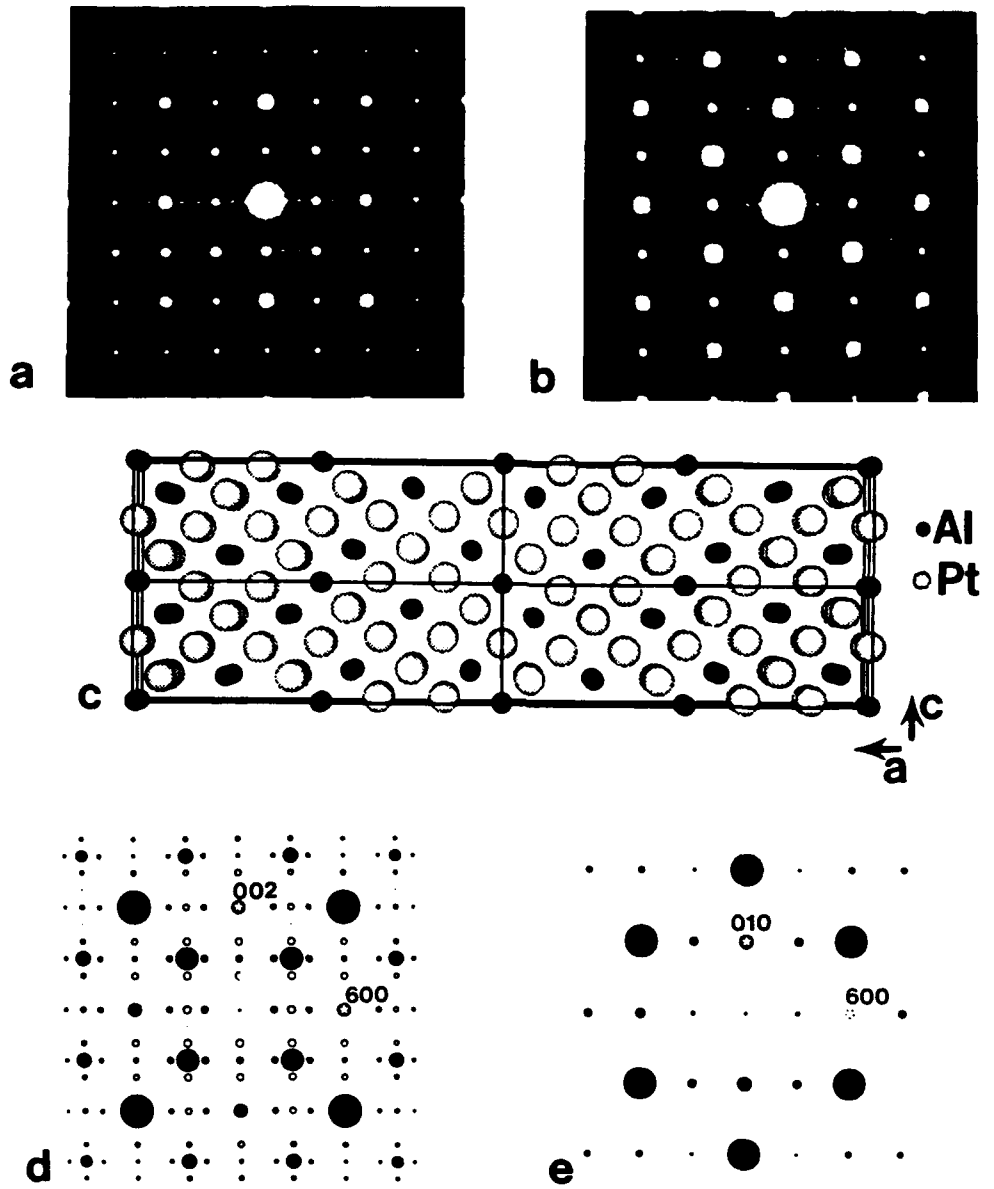

Fig. 11. (a) [010] and (b) [001] experimental diffraction patterns for the Pt_2Al intermetallic (orthorhombic, *Pmma*); (c) structure drawing projected along the [010] axis, (d) and (e) computed zone axis patterns corresponding to (a) resp. (b). Open and filled circles in (d) refer to two orientation variants.

direction. This mismatch can be accommodated either by misfit dislocations or a misorientation of the metal layer, as apparent from the diffraction pattern (Fig. 13).

6.2. *Sapphire–silica–Pt interfaces*

Electron diffraction observations of the interface formed with a thin layer of silica indicate that the silica layer has become crystalline and that the three materials (Pt, silica and sapphire) are single crystals over distances of several millimeters. Diffraction patterns indicate that the $[2\bar{1}.0]$ sapphire zone axis is parallel to the [111] zone axis of low crystobalite: a tetragonal form of silica, with lattice parameters, $a = 0.497$ nm and $c = 0.693$ nm, and space group $P4_12_12$. The [111] crystobalite zone axis is, in turn, parallel to the [123] Pt zone axis. The orientation relation is completed by the indices of the parallel lattic planes: $(11\bar{1})_{Pt} \| (10\,\bar{1})_{LC} \| (00.1)_S$. Computed electron diffraction patterns and experimental zone axis patterns for the two interfaces, as well as the orientation relations [Fig. 14(a–d)] reveal that the rotation for the close packed oxygen and metal planes is again 19.1°. As illustrated in the micrograph of Fig. 15, the interfaces of crystobalite with both sapphire and Pt

Fig. 12. Low magnification micrograph of a Pt-grain boundary (G.B.) close to the interface; there is an amorphous layer filling the triangular opening. The mottled contrast in the Pt regions is caused by ion milling damage.

are flat and well defined. The crystobalite layer is about 60–70 nm thick. There is no evidence of either Al or Ca in the layer at the resolution limits of the EDS system. The absence of such elements probably accounts for the formation of the crystalline SiO_2 phase, rather than the amorphous phase formed with the polycrystalline Al_2O_3. Several twins were observed in the crystobalite. The twin plane is of the $(01\bar{1})_{LC}$-type and is perpendicular to the interface. Occasionally, twins parallel to the interface were observed. Low crystobalite is extremely radiation sensitive. After approximately 20 s in a focussed 200 kV beam, the illuminated region becomes completely amorphous.

7. DISCUSSION

7.1. *Diffusion bonding*

Differences observed in the diffusion bonding characteristics in the Pt–sapphire system found between A and B bonds, as well as between A bonds with and without SiO_2, provide important insights. The complete diffusion bonding evident with B bonds suggests more rapid diffusion induced by the amorphous silicate phase created by the Ca, Si impurities. This could occur by a liquid phase mechanism, assuming some solubility of the Pt (and/or Al_2O_3) in the silicate [8]. In support of this hypothesis is the occurrence of the silicate phase at the interface "voids" (Fig. 4).† One paradox with the liquid phase mechanism that needs further investigation is the apparent absence of a continuous phase at the interface, which would be needed as a rapid transport medium for the Pt, throughout the bonding sequence.‡

An amorphous silicate having similar composition also appears to be involved in the diffusion bonding of Pt with polycrystalline Al_2O_3, implying a liquid phase mechanism. However, in this instance, a *continuous* amorphous phase has been identified at the interface. The apparent difference in amorphous phase continuity may be related either to compositional differences or to orientation effects (associated with the basal plane in Al_2O_3 having a lower interface energy with Pt than other planes).

The enhanced sintering of A bonds induced by the *crystalline* SiO_2 layer may also be caused either by a greater diffusivity of the Pt (in either the SiO_2 layer or at the SiO_2–Pt interface) or by a relatively smaller Pt–SiO_2 interface energy compared with Pt–Al_2O_3. The present experimental results are unable to distinguish between these possibilities. However, the absence of alkali impurities, such as Ca, which allow this phase to remain crystalline,

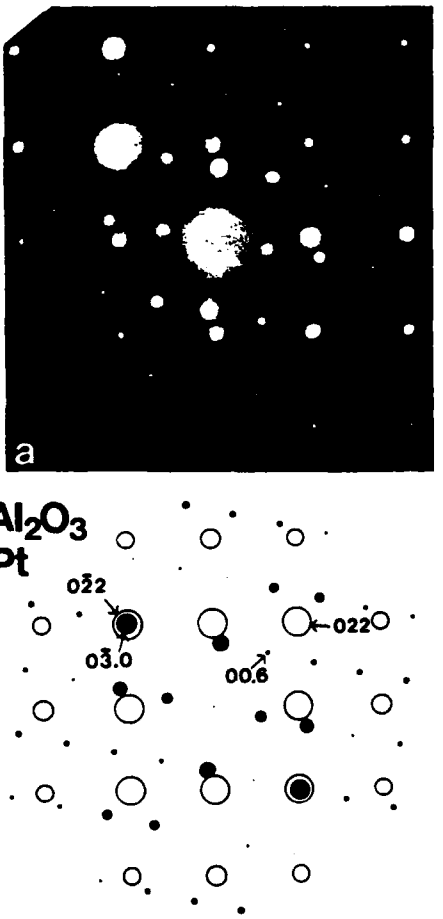

Fig. 13. (a) Experimental and (b) computed zone axis patterns for the $[2\bar{1}.0]\|[100]_{Pt}$ orientation relation. Note that the Pt crystal is slightly misaligned in the experimental pattern.

†This observation only appears explicable if precipitation occurred at interface voids during cooling, by exsolution from the Pt: a phenomenon documented in the Nb–Al_2O_3 system [10].

‡A continuous phase present *at the bonding temperature* is not precluded by the TEM conducted at room temperature.

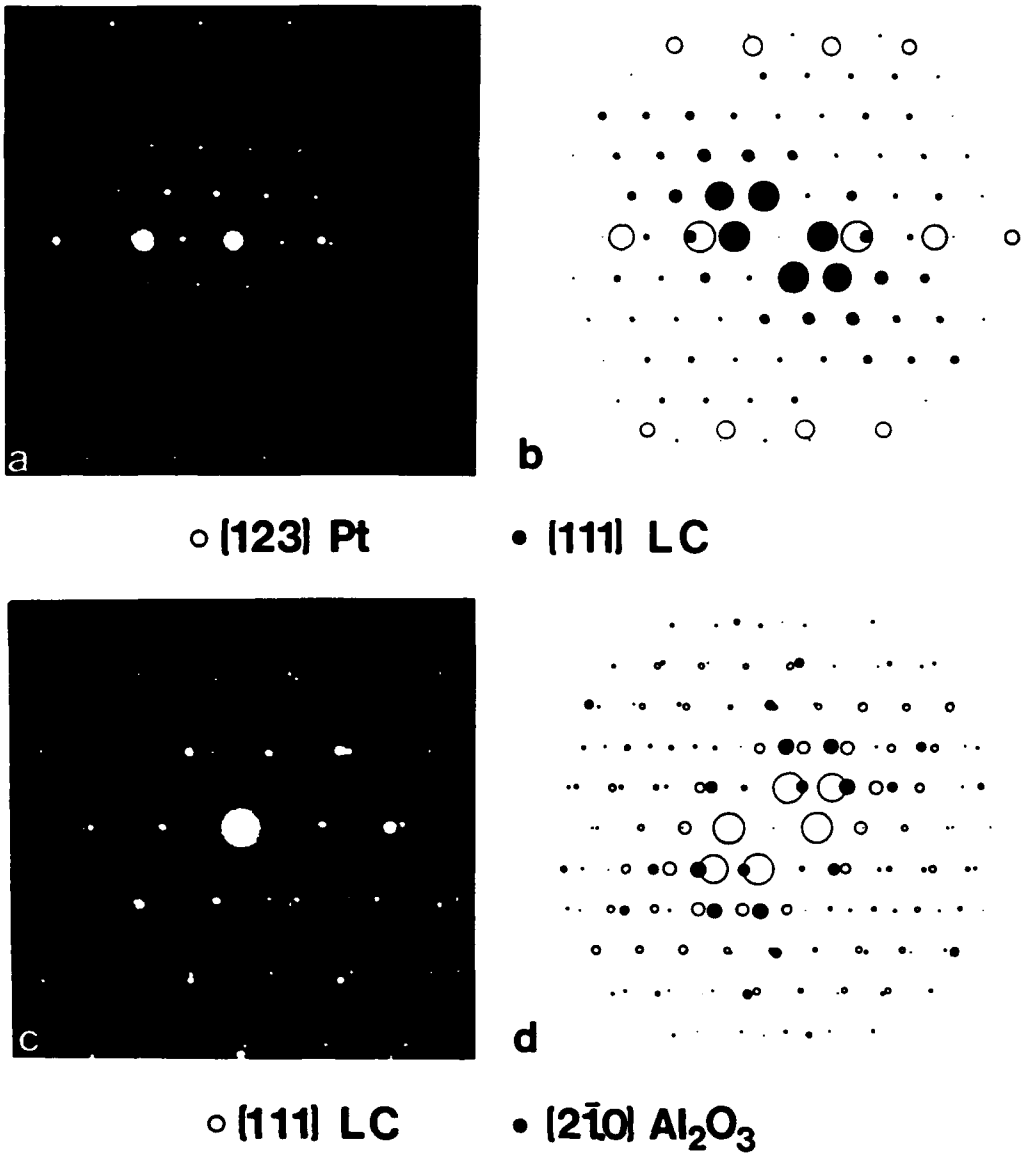

Fig. 14. (a, c) Experimental and (b, d) computed zone axis patterns for respectively the Pt–crystobalite and the crystobalite–sapphire interfaces.

would diminish the diffusivity compared with the amorphous silicates.

7.2. Fracture resistance

The overall comparisons between the measurements of fracture resistance and the characteristics of interface structure have revealed some important trends. The interfaces formed with polycrystalline Al_2O_3 resulted in a lower fracture resistance than those formed with sapphire. The thin, amorphous silicate layer present at the interface with polycrystalline Al_2O_3 appears to have a key influence on the fracture resistance. This assertion is consistent with the magnitude of the fracture resistance as extrapolated to zero Pt layer thickness ($\Gamma_i \approx 4\ Jm^{-2}$), which is about equal to the bulk fracture resistance of oxide glasses [11]. Furthermore, the linear increase in fracture energy with increase in Pt layer thickness infers an influence of plasticity on Γ_i in qualitative accordance with models of the effects of plastic dissipation [4].

The consistently larger Γ_i obtained for Pt–sapphire bonds than for Pt–Al_2O_3 indicates that this interface has an intrinsically greater fracture resistance than that associated with the amorphous layer. However, the differing fracture characteristics for the A and B bonds indicate important effects of *impurities* on the fracture resistance. Present evidence suggests that the effect relates to debond nucleation in the crack tip field, at the silicate ridges formed by the Ca, Si impurities [Fig. 6(c)], rather than by homogeneous segregation. Since these ridges are amorphous, they

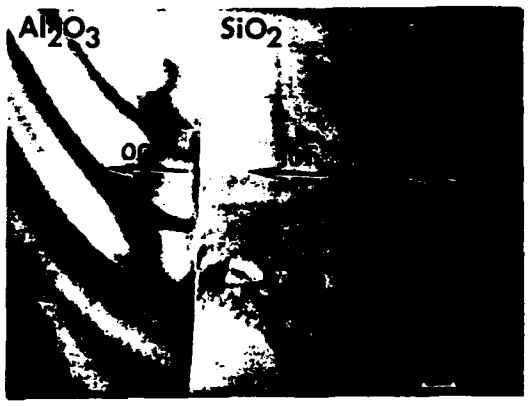

Fig. 15. Low magnification micrograph of the crystobalite layer at the interface. The arrows and indices indicate the normals to the planes parallel to the interface (close packed planes in both sapphire and Pt).

would be expected to decohere at fracture energies characteristic of that noted above for the amorphous interface formed with the polycrystalline Al_2O_3. Furthermore, the high density of such ridges found in B bonds produced with the thicker (100 μm) Pt foils is qualitatively consistent with the important influence of the ridges. Otherwise, the thicker layer would be expected to have the higher Γ_i, as found for bonds between Au and sapphire [5], as well as the bonds between Pt and polycrystalline Al_2O_3.

The interface fracture mechanism in B bonds, compared with A, must also reflect differences in interface orientation. The essentially random Pt–Al_2O_3 interface orientation exhibited by B is presumed to cause the interface *between* ridges to have a lower work of adhesion relative to the epitaxial interfaces prevalent in A. Consequently, the debonds that originate at the silicate ridges are able to extend and coalesce along the Pt–Al_2O_3 interface, resulting in crack growth [Fig. 6(c)]. Interface crack growth by debonding ahead of the crack previously has been found for the Au–Al_2O_3 system [5], provided that stress corrosion is suppressed by excluding moisture from the test environment. The apparent absence of time dependent crack growth in Pt–Al_2O_3 bonds suggests that this system is less susceptible to stress corrosion, consistent with the fracture occurring by debonding *ahead* of the crack front.

The inability to debond the interface with the intervening crystobalite phase contrasts with the relatively low Γ_i found when an amorphous silicate phase forms at the interface. The epitaxial nature of the bond from Pt to SiO_2 to Al_2O_3 undoubtedly accounts for the good bonding. It remains to be determined whether a high fracture energy occurs between Pt and polycrystalline SiO_2.

7.3. Interface structure and bonding

The [0001]‖[111]; $(\bar{2}\bar{1}.0)$‖$(1\,\bar{2}1)$ (19.1° or 10.9°) orientation relation between Pt and basal sapphire found in the A bonds has previously been reported for both Cu and Pt on sapphire [1]; the lattice mismatch was 66:65 for Cu and 120:121 for Pt. However, contrary to previous assertions, these lattice mismatch ratios should not be used as "explanations" for the observed orientation relations. When two hexagonal networks with different lattice parameters are superimposed in an arbitrary orientation, it is always possible to find three atoms of the top lattice which coincide with three atoms of the substrate. This coincidence only requires a rigid translation and an arbitrarily small change in lattice parameter of one of the two lattices. Such a change effectively results in a lattice mismatch parameter of unity, when computed with respect to these atom positions. Therefore, this parameter is not a good indicator of possible orientation relationships. The locations of the three coinciding atoms define two vectors, which can be used as the base vectors for a coincidence lattice. All distortions and modulations at the interface must be periodic within this superlattice (introduced as the "0"-lattice [12]).

A first principles approach is not possible with the current state-of-the-art algorithms. The number of atoms required for such a computation far exceeds capacities. Most of these techniques require an input structure for which the total energy is minimized with respect to the lattice parameter. The introduction of imperfections along the interface would then require *a priori* knowledge of the atomistic equilibrium structure of the interface.

An alternative approach [13, 14] uses the reciprocal base vectors corresponding to the coincident site superlattice, plus a model interaction potential, and computes the interface energy as a function of misorientation angle. The necessary input for such a calculation is the potential energy of a top layer atom as a function of its location above the substrate. For the Pt–sapphire system, such a potential might be derived from a self-consistent cluster molecular-orbital model [15] for contact between the transition/noble metals and sapphire. This potential function could be used to minimize the energy across the interface plus elastic energy due to the distortions in both materials with respect to the Fourier components of the distortion parameters. Again, the rotation angle between the two materials cannot be treated as a variational parameter, because the superlattice size depends on this angle. This approach will be pursued in future studies in an attempt to provide a rationale for the observed orientation relationship.

8. IMPLICATIONS

A major finding of the present research has been the duality associated with the presence of an amorphous phase between ceramic–metal interfaces. The amorphous phase accelerates diffusion bonding and results in an interface with a small area fraction of

defects and voids. However, this phase leads to a reduced interface fracture energy, Γ_i. When the amorphous phase is continuous, as with polycrystalline Al_2O_3, Γ_i is similar to that for amorphous oxides, but increases as the metal layer thickness increases. When discontinuous, Γ_i is larger, but still much less than that for the "clean" interface, and the interface fracture mechanism involves debonding at amorphous phase ridges ahead of the crack front.

The key influence of impurities on the bonding and fracture behavior of this model metal–ceramic interface provides an incentive to conduct systematic studies of these effects. Additionally, new interface fracture techniques will need to be devised in order to measure the relatively large values of Γ_i that apparently obtain for "clean" interfaces.

Acknowledgements—The authors would like to thank M. E. Hedberg for the TEM specimen preparation and the Office of Naval Research for financial support. M. De Graef is Research Associate with the Belgian National Science Foundation (NFWO).

REFERENCES

1. C. A. M. Mulder and J. T. Klomp, *J. Physique* **46**, C4-111 (1985).
2. P. G. Charalambides, J. Lund, R. M. McMeeking and A. G. Evans, *J. appl. Mech.* **111**, 77 (1989).
3. A. G. Evans, B. J. Dalgleish, P. G. Charalambides and M. Rühle, *Mater. Sci. Engng A* **126**, 53 (1990).
4. I. E. Reimanis, B. J. Dalgleish, M. Brahy, A. G. Evans and M. Rühle, *Acta metall. mater.* **38**, 2645 (1990).
5. I. E. Reimanis, B. J. Dalgleish and A. G. Evans, *Acta metall. mater.* **40**, 3133 (1992).
6. A. G. Evans, I. E. Reimanis, A. Bartlett, B. D. Flinn, J. B. Davis and M. Turner, *Scripta metall. mater.* **25**, 1003 (1991).
7. P. A. Stadelman, *Ultramicrosc.* **21**, 131 (1987).
8. B. Derby and E. R. Wallach, *Metal Sci.* **18**, 427 (1980).
9. T. Chattopadhyay and K. Schubert, *J. less-common Metals* **45**, 79 (1976).
10. M. Rühle, K. Burger, W. Mader and A. G. Evans, *Fundamentals of Diffusion Bonding* (edited by Y. Ishida), p. 43 (1987).
11. S. M. Weiderhorn, *J. Am. Ceram. Soc.* **52**, 485 (1969).
12. W. Bollmann, *Phil. Mag.* **7**, 1513 (1962); *Discuss. Faraday Soc.* **38**, 26 (1964); *Phil. Mag.* **16**, 363, 383 (1967).
13. N. H. Fletcher and P. L. Adamson, *Phil. Mag.* **14**, 99 (1966).
14. N. H. Fletcher, *Phil. Mag.* **16**, 159 (1966).
15. K. H. Johnson and S. V. Pepper, *J. appl. Phys.* **53**, 6634 (1982).

MATERIALS

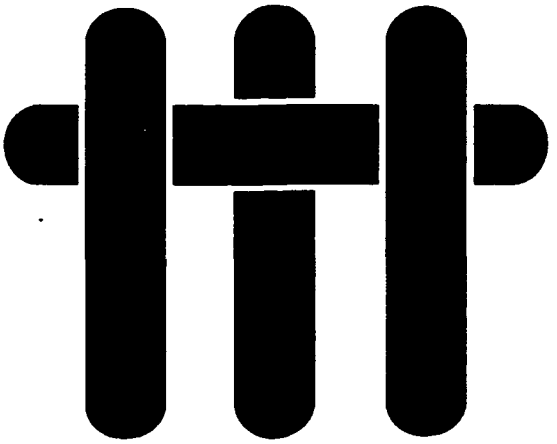

ENVIRONMENTALLY COMPATIBLE DOUBLE COATING CONCEPTS FOR SAPPHIRE FIBER-REINFORCED γ-TiAl

by

T.J. Mackin, J. Y. Yang, C.G. Levi and A.G. Evans
High Performance Composites Center
Materials Department
College of Engineering
University of California
Santa Barbara, California 93106–5050

KJS-Evans-15•E•TA-Envm Cmptlb 92/05/07•2:15 PM•6/9/92

ABSTRACT

Fiber push-out tests were used to evaluate environmentally compatible double coating concepts for sapphire fibers in γ-TiAl. The double coatings consisted of an inner debond coating, followed by an outer coating of alumina that serves as a diffusion barrier. Each double coating is found to permit debonding and sliding of the sapphire fibers. The inner coatings are allowed to oxidize at elevated temperatures and change the interfacial properties. However, the coating design still allows the oxidized system to debond and slide with desirable fiber pull-out characteristics.

1. INTRODUCTION

The mechanical properties of fiber-reinforced materials are known to be strongly influenced by the fiber/matrix interface. [1-3] Optimum longitudinal properties, for both brittle and ductile matrix materials, require that the interface debond and slide with a relatively low shear resistance, τ, relative to fiber strength, S. Small values of τ /S are needed to achieve a "rule-of-mixtures" composite tensile strength, by ensuring that a global load sharing (GLS) condition obtains: generally, τ /S must be smaller than ~ 0.05.[3-6] A high composite fracture resistance also requires small values of τ /S as needed to achieve large fiber pull-out lengths and hence, a substantial contribution of frictional dissipation to the work of rupture.[3,7,8] The attainment of suitably small values of τ requires fiber coatings.[1] The intent of this study is to devise a fiber coating concept that provides appropriate values of τ for an intermetallic matrix composite (IMC) consisting of sapphire fiber-reinforced γ-TiAl.

Direct bonded interfaces between Al_2O_3 and γ-TiAl are "strong" and do not satisfy the debonding requirements for IMCs. [9,10] Furthermore, while there is no reaction product between these systems, Al_2O_3 dissolves slowly in γ-TiAl at high temperatures.[9] This information suggests a fiber coating[1,11] to protect the fiber from reaction with the matrix. If the chosen coating reacts with the matrix, it can be protected by the addition of a second coating (Fig. 1). According to this concept, the inner coating would be a material that debonds from either the fiber or the outer coating (or both), while the outer coating would consist of an oxide (either Al_2O_3 or Y_2O_3), which acts as a diffusion/reaction barrier. Moreover, to impart stability in oxidizing environments, the inner coating should have one of two characteristics. It should either be fugitive or oxidation resistant.[11,12] Both approaches are explored in this study. In the former approach, a gap would be left between the fiber and outer oxide coating upon oxidation, such that the sliding resistance is then governed exclusively by fiber

roughness.[13] To implement the latter approach, oxidation resistant inner coatings that debond and slide readily (as well as minimize fiber strength degradation) would need to be identified. One potential concept involves the use of a highly porous oxide.[11]

Sapphire fibers have a sinusoidal surface roughness that exerts an important influence on coating design.[13] Specifically, when the inner coating is chosen to have a thickness less than the peak-to-peak amplitude of the fiber roughness, the debond surfaces would mimic the underlying fiber geometry, leading to explicit roughness effects on τ. Conversely, coating thicknesses many times the fiber roughness would tend to obviate effects of the underlying fiber geometry. Various thicknesses of inner coating are used to explore these effects.

2. MATERIALS

The sapphire fibers were double coated *before consolidation into the* γ-TiAl matrix. The outer coating provided a barrier to reaction with the matrix, both upon consolidation and during high-temperature exposure. The inner coating was used to ensure debonding during mechanical testing and also protects the fiber from damage during consolidation. The choice for the outer coating was a dense Al_2O_3, which dissolves slowly in γ-TiAl at high temperatures,[9] but otherwise acts as a barrier to Ti diffusion.** The inner coating was either carbon or a carbon/Al_2O_3 mixture. This choice was made because C does not react with Al_2O_3 below ~ 1200°C and thus protects the fiber during consolidation and also provides a debond capability. Furthermore, it will be demonstrated that the C can be removed by oxidation after consolidation, resulting in an oxidatively stable composite interface, having well-controlled sliding characteristics.

** Dissolution of the Al_2O_3 coating is not expected, however, at the anticipated service temperatures of γ-TiAl composites.

The inner coating was of three types: carbon black, colloidal graphite and a highly porous alumina. Carbon black was deposited by passing fibers through an acetone flame, resulting in a sub-micron coating thickness. A dipping procedure was used with both the colloidal graphite and the porous alumina systems, resulting in a continuous coating, having thickness ranging from 1–3 μm. In the former, fibers were dipped into a colloidal graphite solution. In the latter, fibers were dipped into a mixture of colloidal graphite and 10% Al_2O_3 sol to create a highly porous alumina network, within the colloidal graphite coating. After coating, the fibers were air dried. The outer coating was produced by dipping into an alumina sol containing 40 wt % α-Al_2O_3 seeds,‡ air dried and then sintered at 1350°C in Argon.

The coated fibers were mixed in a γ-TiAl slurry,* vacuum canned and HIPed for four hours at 1066°C in a pressurized Ar atmosphere at 276 MPa. Typical cross sections of the coated fibers in the γ-TiAl matrix (Fig. 2) indicate that the inner coating of carbon black has sub-micron thickness, whereas both the colloidal graphite and C/alumina coatings are ~ 1-3 μm thick. The outer Al_2O_3 coating is several microns thick in all cases.

To simulate anticipated service, exposures to high-temperature, oxidizing environments were used to eliminate the inner carbon coating and change the nature of the interface. Specifically, some materials were exposed to air at either 800°C for one hour or 1000°C for 24 hours, and the interface characteristics re-evaluated.

3. TESTING PROCEDURES AND ANALYSIS

Push-out tests were conducted to determine the interfacial characteristics associated with these coatings. The apparatus, described elsewhere,[14] employs a flat cylindrical indenter to apply loads to the fibers. The fiber is pushed into a

‡ AKP-50, 0.18 μm diameter.
* 120 μm Ti-48Al-2.3Nb-0.5Ta particles in deionized water.

220 μm-diameter hole in the support base with a transducer used to monitor displacement. For testing purposes, thin wafers of the composite were cut perpendicular to the fiber axis. Each side of the wafer was polished to a 1 μm diamond finish, so that the sides were nearly parallel.

Push-out curves show a linear elastic loading region, followed by stable debond propagation down the fiber/matrix interface. Subsequently, the debond crack becomes unstable at ~ 1.5 fiber radii from the bottom side of the specimen, resulting in a load drop, ΔP. Thereafter, the fibers slide relative to the matrix. The debond load drop, ΔP, is related to the debond energy, Γ, by[15]

$$\Delta P = \left[2\sqrt{\frac{\Gamma E_f}{B_2 R}}e^{3\mu B_1} + \frac{(\tau_0 + \mu n_R)}{\mu B_1}\left(e^{-3\mu B_1} - 1\right) + p_R\right]e^{2\mu B_1 h} \qquad (1)$$

where

$$B_1 = \frac{\nu_f E}{(1-\nu_f)E + (1+\nu)E_f}$$

and

$$B_2 = 1 - 2\nu_f B_1$$

E is the Young's modulus, ν is Poisson's ratio, subscripts *f* and m refer to fiber and matrix, respectively, h is the section thickness, μ is a coefficient of friction, R is the fiber radius, p_R is the residual axial compressive stress in the fiber, n_R is the residual radial compressive stress at the interface, τ_0 is the shear strength at zero normal stress (mechanistically related to an asperity pressure that arises during fiber sliding).[16] The

nominal sliding strength τ at push-out displacement d is obtained from the instantaneous load, P, using

$$\tau = \frac{P}{2\pi R(h - d)} \tag{2}$$

In general, the sliding stress is not constant, because of asperity effects and wear processes.[13,16-19] Consequently, the sliding stress just after the debond load drop is used for comparing coatings. It is also useful to compare the coefficients of friction for each of the sliding interfaces. For this purpose, since the fiber/matrix asperities are in near perfect registry at the onset of sliding ($\tau_0 \approx 0$), μ is given by

$$\mu \approx \frac{R}{2B_1 h} \ln\left(\frac{P}{n_R - B_1 p_R}\right) \tag{3}$$

The stresses p_R and n_R are evaluated from the thermal expansion mismatch, using the formulae summarized in reference [20]. For this study, it is assumed that the axial mismatch pressure, p_R, is relieved by debonding. The relevant material properties used in equations (1) through (3) are included in Table I.

4. RESULTS AND ANALYSIS

Typical push-out curves for the as-HIPed specimens accompanied by SEM micrographs (Fig. 3) reveal correspondences between surface texture and sliding stress. The *carbon black* interface (Fig. 3a) exhibits a very small debond load drop and a relatively high sliding stress. Recall that this is the *thinnest* of the three inner coating systems and will be most affected by the underlying fiber geometry. This feature is clearly demonstrated in Fig. 4, where the sinusoidal modulations in the load

displacement trace have a wavelength identical to that of the fiber surface roughness. Push-outs for the *colloidal graphite* inner coatings (Fig. 3b) indicate a small debond load drop (though larger than that of the carbon black coating) and a low sliding stress. The low τ arises because the relatively thick C coating behaves as a compliant zone that mediates the mismatch pressure and also provides a debond propagation path that differs from that of the underlying fiber geometry. The C/Al_2O_3 inner coating (Fig. 3c) has the largest debond load drop, because the associated alumina network provides a bonded framework between the fiber and outer alumina coating (apparent from the rough appearance of the debonded interface). However, once sliding commences, the sliding stress has intermediate magnitude.

The range of push-out curves obtained after high-temperature oxidation exposure (Fig. 5) provide several insights. These exposures eliminate the carbon inner layers and may also modify the outer Al_2O_3 coating. The system with C/Al_2O_3, which was converted into a porous alumina inner coating (Fig. 5a), experienced no significant changes upon heat treatment. Such consistency arises because this coating has a stable, interconnected porous alumina network that had fully developed during consolidation. The interfacial characteristics are dominated by the presence of this network. In the *carbon black* system, oxidation slightly relieves the mismatch pressure, such that the 1 h heat treatment at 800°C reduces the sliding stress (Fig. 5b). However, further heat treatment at 1000°C for 24 h increased variability in the sliding behavior, attributed to some sintering of the outer Al_2O_3 coatings to the fiber. The *colloidal graphite* system exhibited similar characteristics (Fig. 5c), consistent with a decrease in the clamping pressure. The sliding stress is always *below* that of the as-HIPed specimens.

Values of the debond and sliding parameters for each system, Γ, τ and μ, obtained from Eqns. (1–3) are summarized in Table II. A bar chart comparison of τ before and after heat treatment (Fig. 6) facilitates comparisons and validates the features outlined above. For this purpose, τ was computed at the peak load, in order to emphasize effects

of interfacial sintering during heat treatment. A statistical comparison of the results demonstrates that heat treatment at 800°C for 1 h significantly affects the sliding stress for both *carbon* coatings, but has no effect for the C/Al_2O_3 coating. However, continued heat treatment, at 1000°C for 24 h, introduces substantial variability, resulting in similar sliding behavior for all systems.

Finally, fracture tests conducted on beam specimens, both before and after heat treatment, revealed substantial fiber pull-out (Fig. 7) and a corresponding enhancement in fracture resistance.[21]

5. CONCLUDING REMARKS

Double coating systems for sapphire fibers in γ-TiAl were compared using fiber push-out tests. These double coating systems employ an inner, debond coating of either carbon or carbon/alumina that provides a path for interfacial crack propagation and also protects the fiber during consolidation. These inner coatings are, in turn, protected from the matrix by a second, diffusion barrier of dense alumina. Each coating system was found to permit debonding and sliding, in accordance with accepted criteria for strengthening and toughening. Thus, the double coating concept had been demonstrated as a viable methodology for composite systems.

Results from an oxidation study of the interface show distinct differences associated with removal of the carbon. One effect, which is beneficial, concerns reduction of the mismatch strain, which causes τ to decrease. Then, fiber roughness exerts an important influence on the sliding characteristics. The second effect is deleterious. It involves sintering of the outer Al_2O_3 coating to the sapphire fiber. It has been demonstrated that this effect can be controlled by creating a highly porous Al_2O_3 network within the inner coating. Alternately, the outer coating may be replaced by another oxide (such as YAG), less prone to sintering with sapphire.[22]

ACKNOWLEDGEMENTS

This work was supported by the Defense Advanced Research Projects Agency through the University Research Initiative under Office of Naval Research contract no. N–00014–86–K–0753.

TABLE I

Material Properties

PROPERTY	COMPOSITE	SAPPHIRE FIBER
E (GPa)	173	434
Poisson's Ratio, ν	0.33	0.27
Coefficient of Thermal Expansion, α	$13 \times 10^{-6}/°C$	$9 \times 10^{-6}/°C$

TABLE II

Comparison of Interfacial Properties For Each Coating

SAMPLE	Γ_i (J/m^2)	τ (MPa)	μ
Carbonblack/Alumina	0.01	100	0.23
Colloidal Graphite/Alumina	0.01	40	0.09
Porous Alumina/Alumina	0.05	75	0.09

REFERENCES

[1] A.G. Evans, F.W. Zok and J. Davis, "The Role of Interfaces in Fiber-Reinforced Brittle Matrix Composites," *Composites Sci. and Tech.*, **42**, pp. 3–24, 1991.

[2] R.J. Kerans, R.S. Hay, N.J. Pagano and T.A. Parasarathay, "The Role of the Fiber-Matrix Interface in Ceramic Composites," *Cer. Bull.*, Vol. 68, No. 2, 1989.

[3] W. Curtin, "Theory of Mechanical Properties of Ceramic-Matrix Composites," *J. Am. Cer. Soc.*, **74**(11), 2837 (1991).

[4] S. Ochai and K. Osamura, *Met. Trans.*, **21A** (1991) 971.

[5] M.-Y. He, A.G. Evans and W.A. Curtin, "The Ultimate Tensile Strength of Metal and Ceramic-Matrix Composites," to be published.

[6] S. Jansson, H.E. Dève and A.G. Evans, "The Anisostropic Mechanical Properties of a Ti Matrix Composite Reinforced with SiC Fibers," *Met. Trans. A*, Vol. 22A, pp. 2973–2984, 1991.

[7] M.D. Thouless and A.G. Evans, *Acta Metall.*, **36**, 517 (1988).

[8] M. Sutcu, *Acta Metall.*, **37**, 651 (1989).

[9] J. Porter, private communication.

[10] A.G. Evans, A. Bartlett, J. Davis, B. Flinn, M. Turner and I. Reimanis, *Scripta Met. et Mat.*, **25** (1991) 1003.

[11] J.B. Davis, J.P.A. Löfvander, A.G. Evans, E. Bischoff and R.L. Emiliani, "Fiber Coating Concepts for Brittle Matrix Composites," submitted to *J. Am. Cer. Soc.*

[12] T. Mah, K. Keller, T.A. Parthasarathy and J. Guth, "Fugitive Interface Coatings in Oxide-Oxide Composites: A Viability Study," *Ceram. Eng. Sci. Proc.*, **12**[9–10] pp. 1802–1815 (1991).

[13] T.J. Mackin, J.Y. Yang and P.D. Warren, "The Influence of Fiber Roughness on the Sliding Behavior of Sapphire Fibers in Glass and TiAl Matrices," submitted to the *J. Amer. Cer. Soc.*, April 1992.

[14] P.D. Warren, T.J. Mackin and A.G. Evans, "Design, Analysis and Application of an Improved Push-Through Test for the Measurement of Interface Properties in Composites," *Acta Metall. Mater.*, **40**[6], pp. 1243–49, 1992.

[15] C. Liang and J.W. Hutchinson, "Mechanics of the Fiber Pushout Test," to be published.

[16] T.J. Mackin, P.D. Warren and A.G. Evans, "Effects of Fiber Roughness on Interface Sliding in Composites," *Acta Metall. Mater.*, 40[6], pp. 1251–57, 1992.

[17] P.D. Jero and R.J. Kerans, "The Contribution of Interfacial Roughness to Sliding Friction of Ceramic Fibers in a Glass Matrix," *Scripta Met.*, **25** (1991) 2457.

[18] P.D. Jero , R.J. Kerans and T.A. Parthasarathy, "Effect of Interfacial Roughness on The Frictional Stress Measured Using Push-out Tests," *J. Am. Cer. Soc.*, **74**(11), 2793, 1991.

[19] W.C. Carter, E.P. Butler and E.R. Fuller, Jr., "Micro-Mechanical Aspects of Asperity-Controlled Friction in Fiber Toughened Ceramic Composites," *Scripta Met et Mat.*, Vol. 25, pp. 579–584, 1991.

[20] B. Budiansky, J.W. Hutchinson and A.G. Evans, *J. Mech. Phys. Solids*, **2** (1986) 167.

[21] C.H. Weber, J.P.A. Löfvander, C.G. Levi and A.G. Evans, to be published.

[22] R. Kerans, private communication.

FIGURE CAPTIONS

Fig. 1. Schematic representation of a double coating concept for sapphire fibers in γ-TiAl.

Fig. 2. Representative cross sections of double coated sapphire fibers. a) composite overview, b) carbon black followed by alumina, c) colloidal graphite followed by alumina and d) colloidal graphite with 10% alumina sol, followed by alumina.

Fig. 3. A comparison of representative push-out curves and associated micrographs of pushed fibers with a) a carbon black inner coating, b) a colloidal graphite inner coating and c) a carbon/alumina inner coating.

Fig. 4. Fiber roughness appears as a sinusoidal modulation in the push-out curve.

Fig. 5. Range of results for push-out tests, comparing heat treated and as-HIPed specimens a) carbon/alumina inner coating, b) carbon black inner coating, c) colloidal graphite inner coating.

Fig. 6. Comparison of the peak sliding stress for each coating and each heat treatment condition.

Fig. 7. Fiber pull-out exhibited after fracture testing (courtesy C. Weber)

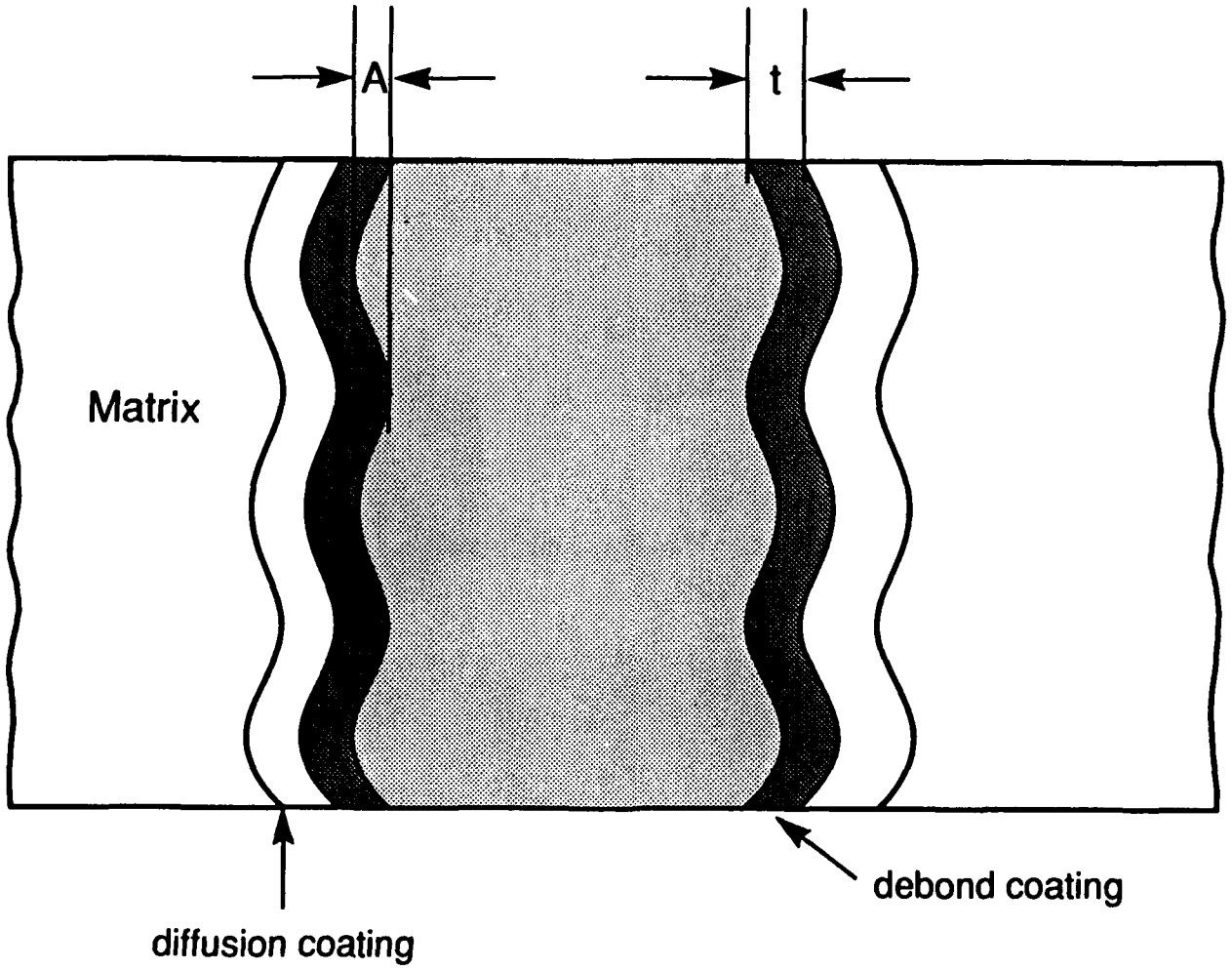

Figure 1

Figure 1

MATERIALS

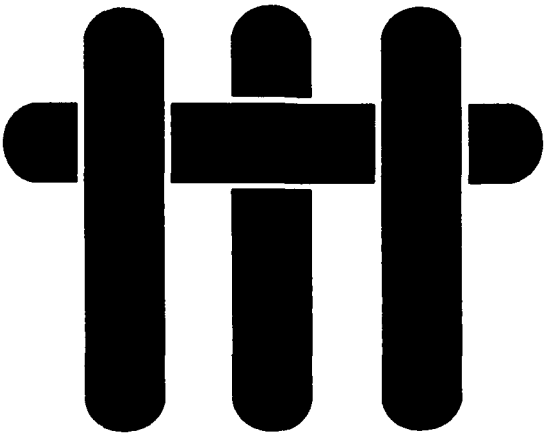

THE EFFECT OF REACTION PRODUCTS ON THE FRACTURE RESISTANCE OF A METAL/CERAMIC INTERFACE

by

A. Bartlett and A. G. Evans

Materials Department
College of Engineering
University of California
Santa Barbara, California 93106–5050

KJS-Evans-16-Q-R-TA-Rctn Prdct 91/07/11-1:35 PM-5/8/92

ABSTRACT

Solid state diffusion bonds between a Ta(Ti) alloy and Al_2O_3 have been used to study the effect of reaction products on the fracture resistance of a metal/ceramic interface. The reaction layer consists of brittle intermetallics, consistent with the Ti-Ta-Al ternary phase diagram. The interface fracture energy Γ_i was found to be dominated by periodic tunnel cracking of the reaction products, and was relatively insensitive to layer thickness, because of the self-similar nature of the periodic cracking. The contribution to Γ_i from plastic dissipation within the alloy was minimal because the intervening reaction layer inhibited yielding. A sequence of cracking observations was used to bound the unknown values of the fracture energy of the reaction products, the residual stress within the layer and the fracture energy of the reaction product/sapphire interface.

1. INTRODUCTION

Many metal/ceramic bonds form reaction products.[1,2] The effects of these reaction layers on interface fracture are disparate, as illustrated by two examples. i) In the system Ni/Al_2O_3, the formation of a $NiAl_2O_4$ spinel layer *decreases* interface tensile strength.[3] ii) Conversely, in the NiO/Pt system, the formation of a NiPt interlayer *increases* the interface shear strength.[4] The morphology and mechanical properties of the reaction products are expected to be responsible for such diverse behavior.

Interface fracture has been observed to proceed in one of three ways: i) within the reaction product layer itself, ii) at either of the interfaces, iii) on an alternating path between the interface and the reaction zone. These observations have been on the systems, TiAl/Nb,[5] Ti/Al_2O_3,[6] and Hf/Si_3N_4,[7] respectively. However, there is little understanding of the relationships between the properties of the reaction products and the interface fracture mechanisms. To provide new insight, the present study has been conducted on interfaces in the Al_2O_3/Ta(Ti) system that forms intermetallic reaction products consistent with the Ti-Al-Ta phase diagram (Fig. 1).[8] Measurements and observations of interface decohesion in this system will be used to establish the dominant parameters affecting fracture, including the fracture energy of the reaction products and the residual stress within the layer.

The existence of a variety of fracture paths at metal/ceramic interfaces containing reaction products has analogies in the failure of brittle adhesive joints.[9-11] In particular, the occurrence of either interface or adhesive failure, as well as the energy required for crack propagation, have been shown to depend on phase angle of loading (the relative shear at the crack tip), the modulus mismatch and the relative fracture energies of the constituents. Such analogies will be used to facilitate interpretation of the behavior found at metal/ceramic interfaces containing reaction products.

2. EXPERIMENTAL PROCEDURES

The Ta(Ti) alloy was produced in an argon atmosphere arc melter, with composition 0.67 Ta-0.33 Ti, chosen in order to minimize thermal misfit between the alloy and the sapphire.[12] After homogenization, the material was cold rolled to 1 mm in thickness and mechanically polished. The sapphire plates were 250 μm in thickness, having random crystallographic orientation. Bonds were fabricated in the geometry indicated on Fig. 2a. The bonding temperature was 1100°C. Bonding was conducted subject to a compressive stress of 3 MPa for 1/2 hr. at an ambient pressure of 10^{-6} Torr. The cooling rate was 5°C/min. In addition, some of the bonds were heat treated at 1100°C for 120 hours in order to increase the reaction product layer thickness.

Specimens for mechanical testing were prepared by careful diamond sawing and polishing to dimensions ~ 25 x 1 x 1 mm (Fig. 2b). A precrack was introduced in the sapphire perpendicular to the interface by first indenting with a Knoop indenter and extending the associated radial crack to the interface by loading in three-point bending. The sample was subsequently loaded in four-point bending, causing the crack to propagate along the interface. The *mixed mode* interface fracture resistance Γ_i at a phase angle $\psi \approx 50°$, was then obtained from the load required to extend the crack.[13] *In situ* observation in the SEM allowed detailed study of the cracking mechanisms. Finally, in order to explore the effect of the loading mode on the fracture mechanism, in some cases, *mode I* cracks ($\psi \approx 0$) were introduced at the interface, by emplacing 200N Vickers indents in the Al_2O_3, near the interface.

3. EXPERIMENTAL RESULTS

3.1 Reaction Products

Bonds produced at 1100°C for 1/2 hour had reaction products with a thickness of ~ 5 μm (Fig. 3a). Energy loss spectroscopy (PEELS) measurements in the TEM indicated an absence of oxygen within the reaction layer, at the detectability limits of the technique, consistent with the reaction products being intermetallics. The formation of intermetallic (rather than oxide) reaction products reflects rapid oxygen diffusion through the layer into solution in the alloy, which acts as an oxygen sink. Electron diffraction and energy dispersive X-ray (EDS) measurements in the TEM, plus X-ray diffraction results in conjunction with the Ti-Al-Ta ternary (Fig. 1), identified a sequence of three phases: γ, α_2 and σ. The γ-TiAl was adjacent to the Al_2O_3, and σ adjacent to the alloy.

The bonds subsequently heat treated for 120 hours at 1100°C had a reaction product layer ≈ 20 μm thick. The γ phase was again continuous and adjacent to the sapphire, but its thickness had increased to ≈ 3 μm. The remainder of the reaction zone consisted of intermixed layers of the σ and α_2 phases (Fig. 3b). Prior to testing, no cracking was visible in the reaction layers.

3.2 Mechanical Characteristics

Precracks in the sapphire were found to penetrate the reaction product layers and arrest at the reaction product/metal interface (Fig. 4). Subsequent loading in four-point flexure caused cracks to propagate along the interfacial zone. Crack growth occurred subject to a *mixed mode* fracture energies, $\Gamma_i \approx 18\ Jm^{-2}$ at $\psi \approx 50°$. Two types of cracking were observed i) The main interface crack propagated along the γ / Al_2O_3 interface. ii) Periodic branch cracks formed in the reaction product layer.

In the specimens with the *thinner* reaction layer, the branch cracks were spaced approximately 9 μm apart, inclined at an angle, $\theta \approx 40°$, to the main crack (Fig. 5) and always formed in association with the interface crack tip. Removal of the sapphire layer after testing showed that these were surface traces of cracks that *tunneled* in from the free surface (Fig. 6). For the specimens with the *thicker* reaction products, the branch cracks were spaced ~ 30 μm apart and inclined at $\theta \approx 60°$. Furthermore, their formation was disassociated from the parent interface crack (Fig. 8), being manifest as a discrete damage zone. One end of these cracks terminated at the reaction product/alloy interface, but at the other end often deflected along the reaction product/Al_2O_3 interface.

The *mode I* interface cracks produced by indentation propagated along the γ / Al_2O_3 interface (Fig. 7). Such fractures were not accompanied by periodic branch cracking in the reaction products. A precise determination of the mode I fracture energy could not be obtained because of the distortion of the indentation. However, use of the indentation toughness formulae[14] combined with the observation of extensive interface cracking inferred a low value, $\Gamma_i < 10\ Jm^{-2}$.

4. ANALYSIS

The measured interface fracture energies may be rationalized in terms of the mechanisms depicted in Fig. 9. The principal contributions to the fracture energy arise from three terms: a) the energy dissipated by periodic cracking of the reaction products; b) cracking of the γ / Al_2O_3 interface; c) the residual strain energy released by the cracking of the reaction products. The first and second terms are *positive*, while the third term is *negative*. These three contributions to the fracture energy Γ_i may be expressed as:

$$\Gamma_i = (h/d\sin\theta)\bar{\Gamma} + \Gamma_I - \sigma_R^2 h/2E \qquad (1)$$

where h is the reaction layer thickness, d the periodic crack spacing, θ the periodic crack angle with respect to the interface, $\bar{\Gamma}$ the fracture energy of the reaction products, σ_R the residual stress in the reaction product layer, E the plane strain Young's modulus of the layer, and Γ_I the fracture energy of the γ / Al_2O_3 interface. Plastic dissipation is assumed to be negligible because the intervening reaction product layer inhibits yielding of the alloy, by reducing the Mises stress below its yield strength.†

The fracture energy given by Eqn. (1) is dependent upon *three unknown factors*: i) the fracture energy of the γ / Al_2O_3 interface, ii) the fracture energy of the reaction products, and iii) the residual stress in the reaction product layer. Several independent observations and analyses of both interface and reaction product cracking may be used to provide information about these factors. This information may then be used to rationalize the measured values of Γ_i.

The observation that tunnel cracks in the thick reaction zone *deflect along* the γ / Al_2O_3 interface (Fig. 8) provides an *upper* bound on the interface fracture energy, Γ_I. This bound is obtained by using the criterion for crack deflection along an interface.[15,16] This criterion may be expressed in terms of the fracture energy ratio, Γ_I / Γ_s, relating the γ / Al_2O_3 interface fracture energy Γ_I to that of sapphire, Γ_s, as a function of the crack inclination, θ. For the measured crack inclination, $\theta = 60°$, this criterion requires that the following inequality applies, $\Gamma_I / \Gamma_s \leq 0.6$. Consequently, since $\Gamma_S = 7\ Jm^{-2}$ on rhombohedral and prismatic planes,[17] it is required that the γ / Al_2O_3 interfaces have a fracture energy, $\Gamma_I \leq 4\ Jm^{-2}$.

The incidence of tunnel cracking provides *combined* information about the fracture energy of the reaction products, $\bar{\Gamma}$, *and* the residual stress, σ_R. One bound on the $\bar{\Gamma}/\sigma_R$ relationship is provided by the *occurrence of crack kinking* in the thinner reaction layer

---

† The Mises stress in the alloy [$\sigma_e \approx (E\Gamma_i/6\pi h)^{1/2}$] is about 250 MPa, compared with a yield strength, $\sigma_O \approx 700$ MPa

during interface crack growth. Another bound can be derived from the *absence of residual stress cracking* in the thicker bond. Interface crack kinking is governed by the magnitude of the parameter, η, defined as[16]

$$\eta = \sigma_R [x/E\Gamma_I]^{1/2} \quad (2)$$

where x is the incipient flaw size in the reaction product, at the interface. For kinking to occur, η must exceed a critical value, dependent on the ratio of the fracture energy of the reaction products to that of the interface, $\bar{\Gamma}/\Gamma_I$ and the loading phase angle, ψ (Fig. 10). By assuming that the undulations along the interface are the incipient flaws ($x \approx 1\ \mu m$), the kinking criterion provides the *upper* bound relationship between $\bar{\Gamma}$ and σ_R, plotted on Fig. 11.

Residual stress induced tunnel cracking in a reaction product layer occurs when the residual stress, σ_R, exceeds a critical value, σ_c, given by[18]

$$\sigma_c = 1.12\sqrt{\bar{\Gamma}E/\pi h} \quad (3)$$

Consequently, the *absence* of spontaneous tunnel cracking in the *thicker* layer ($h \approx 20\ \mu m$) provides the *lower* bound relationship between $\bar{\Gamma}$ and σ_R, plotted on Fig. 11.

Yet another relationship between $\bar{\Gamma}$ and σ_R is provided by Eqn. (1). The independently *measured* values of Γ_i, h, d and θ are used in conjunction with Γ_I, evaluated above, to give the relation plotted as an overlay in Fig. 11. The *allowed* values of $\bar{\Gamma}$ and σ_R *must be located on this line and lie within the above bounds*, such that the *required* magnitudes are: $\bar{\Gamma} \approx 18\ Jm^{-2}$ and $\sigma_R \approx 450$ MPa (Table I). Consequently, the

preceding description of interface fracture is self-consistent if the inferred values of $\bar{\Gamma}$ and σ_R are compatible with available information about Ti intermetallics.

The inferred fracture energy of the reaction products, $\bar{\Gamma} \approx 18\ Jm^{-2}$, is of the order expected for brittle solids, but lower than reported values for the bulk γ and σ phases.[5,19] Relatively low values may be expected in the presence of dissolved oxygen, which has been shown to substantially reduce the room temperature ductility of γ.[20]

Residual stress arising solely from thermal expansion misfit would require a thermal expansion coefficient for the reaction products to be in the range, $\alpha_R \approx 10 \times 10^{-6}\ C^{-1}$, to provide consistency with the inferred, $\sigma_R \approx 450$ MPa. Values of thermal expansion in this range are typical for Ti intermetallics.[21]

It thus appears that the interface cracking phenomena represented by Eqns. (1)–(3) and Fig. 10, provide a consistent description of reaction product effects in the Al_2O_3/Ta(Ti) system. However, independent measurements of $\bar{\Gamma}$ and σ_R would be needed to fully validate the preceding phenomenology. This has not been possible in the present study, because of the experimental difficulties involved in unambiguous measurements of these quantities in thin reaction product layers.

5. REMARKS

Fracture of the Al_2O_3/Ta(Ti) interface in *mixed mode* is found to be dominated by periodic cracking of the reaction products, despite the low fracture energy of the parent interface crack. The periodic nature of the cracking is similar to that observed in thin films.[22] For bonds with a thin reaction layer, multiple cracking occurs by kinking of the interface crack into the reaction products. For thicker layers, a damage zone of tunnel cracks forms ahead of the parent crack. The conditions that distinguish these behaviors are discussed in the Appendix. Reaction layer thickness is found to have little effect on the interface fracture energy, because an increase in layer thickness results in a self-

similar increase in periodic crack spacing. This behavior contrasts with the thickness effect found in adhesive layers.[23,24] However, whereas failure of adhesive layers can occur on *either* interface, the high fracture energy of the alloy/reaction product interface prevents decohesion along that plane, causing branch cracks to terminate at one interface.

The *mode I* crack shows no periodic cracking in the reaction products. The fracture energy should then be dependent only on Γ_I, consistent with the sharply reduced value inferred from indentation. A discontinuous change in Γ_i with phase angle is implied. This discontinuous behavior arises because kinking of the interface crack into the reaction products only occurs when the loading is mixed-mode. Notably, for the Al_2O_3Ta(Ti) system, the interface parameters (Table I) dictate that $\eta \approx 0.45$, and $\Gamma_I / \bar{\Gamma} \approx 0.2$. Consequently, Fig. 10 predicts that kinking should commence only when the loading phase angle, $\psi \gtrsim 30°$. This prediction is consistent with the occurrence of kinking in mixed mode ($\psi \approx 50°$) and the absence of kinking in mode I ($\psi \approx 0$). Once kinking occurs, Γ_i increases from a low value dominated by the γ / Al_2O_3 interface, Γ_I, to a higher value governed by the fracture energy of the reaction products, $\bar{\Gamma}$. A similar discontinuous change in Γ_i has been observed for Al/epoxy bonds.[25]

The low value of Γ_I for the γ / Al_2O_3 interface differs from values reported for diffusion-bonded/sapphire interfaces.[26] Indeed, sapphire fiber-reinforced TiAl composites require fiber coatings to provide the low interface fracture energy suitable for interface debonding and subsequent composite toughening. The presence of Ta and oxygen in the γ-phase reaction product formed in this system are probably responsible for this difference.

In summary, interface fracture in the presence of a reaction product layer has been shown to depend upon the relative fracture energies of the interfaces and reaction products, the residual stress within the layer and the mode of loading. In general, it is prohibitively difficult to access independent information about all of the necessary

properties of the reaction products. However, a variety of cracking observations, in conjunction with simple models, may be used to understand and rationalize interface cracking phenomena and associated fracture energies. Finally, it is apparent that there is no *single* criterion for predicting interface failure, when reaction products exist.

ACKNOWLEDGEMENTS

This work was supported by the Office of Naval Research. The authors would like to thank D. Doherty for TEM specimen preparation.

TABLE I

Summary of Interface Properties

Residual Stress, $\sigma_R \approx 450$ MPa

Interface Fracture Energy ($TiAl/Al_2O_3$) $\Gamma_I \approx 4\ Jm^{-2}$

Reaction Product Fracture Energy, $\bar{\Gamma} \approx 18\ Jm^{-2}$

Incipient Interface Flaw Size, $x \approx 1\ \mu m$

Crack Kinking Parameter, $\eta \approx 0.45$

Plane Strain Young's of Intermetallics, $E \approx 180$ GPa

APPENDIX

Periodic Cracking of Reaction Products

The observed transition with reaction layer thickness in the periodic cracking mechanism—from a frontal damage zone to crack front kinking—can be addressed by examining the stress field in the reaction layer ahead of an interface crack. A frontal damage zone is expected when the net stress in the layer (residual plus applied) at a finite distance ahead of the crack exceeds the tunnel cracking requirement, given by Eqn. (3). For a simplified situation, represented by an elastically homogeneous solid, the average stress $\bar{\sigma}$ caused by the interface crack, along the normal to a tunnel crack trajectory, can be readily obtained from standard elastic formulae. This stress $\bar{\sigma}$, when combined with σ_R (Table I), indicates the distance, y, ahead of the interface crack at which a tunnel crack may form, as a function of layer thickness and residual stress. The result is plotted on Fig. A1 for an interface crack experiencing $\mathcal{G} = 4\,\mathrm{Jm}^{-2}$.

REFERENCES

[1] K.P. Trumble, Ph. D. Thesis, University of California, Santa Barbara, CA (1990).

[2] R.E. Tressler, T.L. Moore and R.L. Crane, *J. Mater. Sci.*, **8**, 151 (1973).

[3] K.P. Trumble and M. Rühle, *Acta Metall.*, **39**, 1915 (1991).

[4] F.-S. Shieu, R. Raj and S.L. Sass, *Acta Metall. Mater.*, **38**, 2215 (1990).

[5] H.E. Dève, A.G. Evans, G.R. Odette, R. Mehrabian, M.L. Emiliani and R.J. Hecht, *Acta Metall. Mater.*, **38**, 1491 (1990).

[6] M. Rühle, Unpublished Research.

[7] G. Elssner, T. Suga and M. Turwitt, *J. Physique*, **46**, C4-597 (1985).

[8] C. McCullough, J.J. Valencia, C.G. Levi and R. Mehrabian, *Acta Metall. Mater.*, 1992, in press.

[9] J.-S. Wang and Z. Suo, *Acta Metall. Mater.*, **38**, 1279 (1990).

[10] H. Chai, *Int. J. Frac.*, **32**, 211 (1987).

[11] M.D. Thouless, *Acta Metall. Mater.*, **38**, 1135 (1990).

[12] A. Bartlett, A.G. Evans and M. Rühle, *Acta Metall. Mater.*, **39**, 1579 (1991).

[13] P.G. Charalambides, J. Lund, R.M. McMeeking and A.G. Evans, *J. Appl. Mech.*, **456**, 77 (1989).

[14] R.F. Cook and G.M. Pharr, *J. Am. Ceram. Soc.*, **73**, 787 (1990).

[15] M.-Y. He and J.W. Hutchinson, *Int. J. Solids Str.*, **25**, 1053 (1989).

[16] M.-Y. He, A. Bartlett, J.W. Hutchinson and A.G. Evans, *J. Am. Ceram. Soc.*, **74**, 767 (1991).

[17] S. M. Weiderhorn, *J. Am. Ceram. Soc.*, **52**, 485 (1969).

[18] J.W. Hutchinson and Z. Suo, *Advances in Applied Mech.*, **29**, 63 (1992).

[19] Y.-W. Kim, *Journal of Metals*, **41**, 24 (July 1989).

[20] M.J. Blackburn and M.P. Smith *AFWAL Technical Report No. AFWAL-TR-80-4175* (1980).

[21] T.C. Lu, J. Yang, R. Hecht, Z. Suo, R. Mehrabian and A.G. Evans, *Acta Metall. Mater.*, **39**, 1883 (1991).

[22] M.S. Hu and A.G. Evans, *Acta Metall.*, 37, 917 (1989).

[23] W.R. Zdaniewski, J.C. Conway and H.P. Kirchner, *J. Am. Ceram. Soc.*, 70, 110 (1987).

[24] J.J. Bikerman, *The Science of Adhesive Joints*, 2nd ed., Academic Press, New York (1968).

[25] H.-C. Cao and A.G. Evans, *Mech. of Mtls.*, 7, 295 (1989).

[26] A.G. Evans, F.W. Zok and J.B. Davis, *Composites Science and Technology*, 42, 3 (1991).

FIGURE CAPTIONS

Fig. 1. Ti-Ta-Al ternary phase diagram.

Fig. 2. a) Schematic of geometry used for diffusion bonding.
b) Test specimen geometry for measuring mixed-mode interface fracture resistance.

Fig. 3. Micrographs showing reaction product morphology a) TEM of 1/2 hour bond. The intermetallic γ-TiAl adjoins the sapphire, the σ-phase is formed adjacent to the alloy, with α_2-Ti_3Al intervening b) TEM of 120 hour bond. γ is continuous and adjacent to the Al_2O_3, with intermixed σ and α_2 comprising the remainder of the layer.

Fig. 4. Precrack penetrating the reaction product layers and terminating at the reaction product/alloy interface.

Fig. 5. A mixed-mode crack propagating along the sapphire/reaction product interface, 1/2 hour bond. Note the appearance of periodic branch cracks.

Fig. 6. Plan view of the reaction product layer subsequent to the removal of the sapphire, showing tunnel cracks in the reaction products (thin layer, 1/2 hour bond).

Fig. 7. Mode I interface crack, propagated by an indent at the interface (thin layer, 1/2 hour bond).

Fig. 8. Interface fracture path, for the thicker layer (120 hour bond). Tunnel cracks form a damage zone ahead of the interface crack.

Fig. 9. Schematic of cracking mechanisms.

Fig. 10. Predicted kinking diagram when residual stresses exist: η is defined in Eqn. (2). Kinking occurs when $\Gamma_I / \bar{\Gamma}$ lies above the curve.

Fig. 11. Upper and lower bounds on the relationship between $\bar{\Gamma}$ and σ_r established by crack kinking and tunnel cracking requirements. The allowable $\sigma_r / \bar{\Gamma}$ line governed by the fracture mechanism is superimposed. The admissible values of σ_r and $\bar{\Gamma}$ are identified

Fig. A.1 Distance ahead of crack at which stress exceeds critical tunneling stress, as a function of layer thickness.

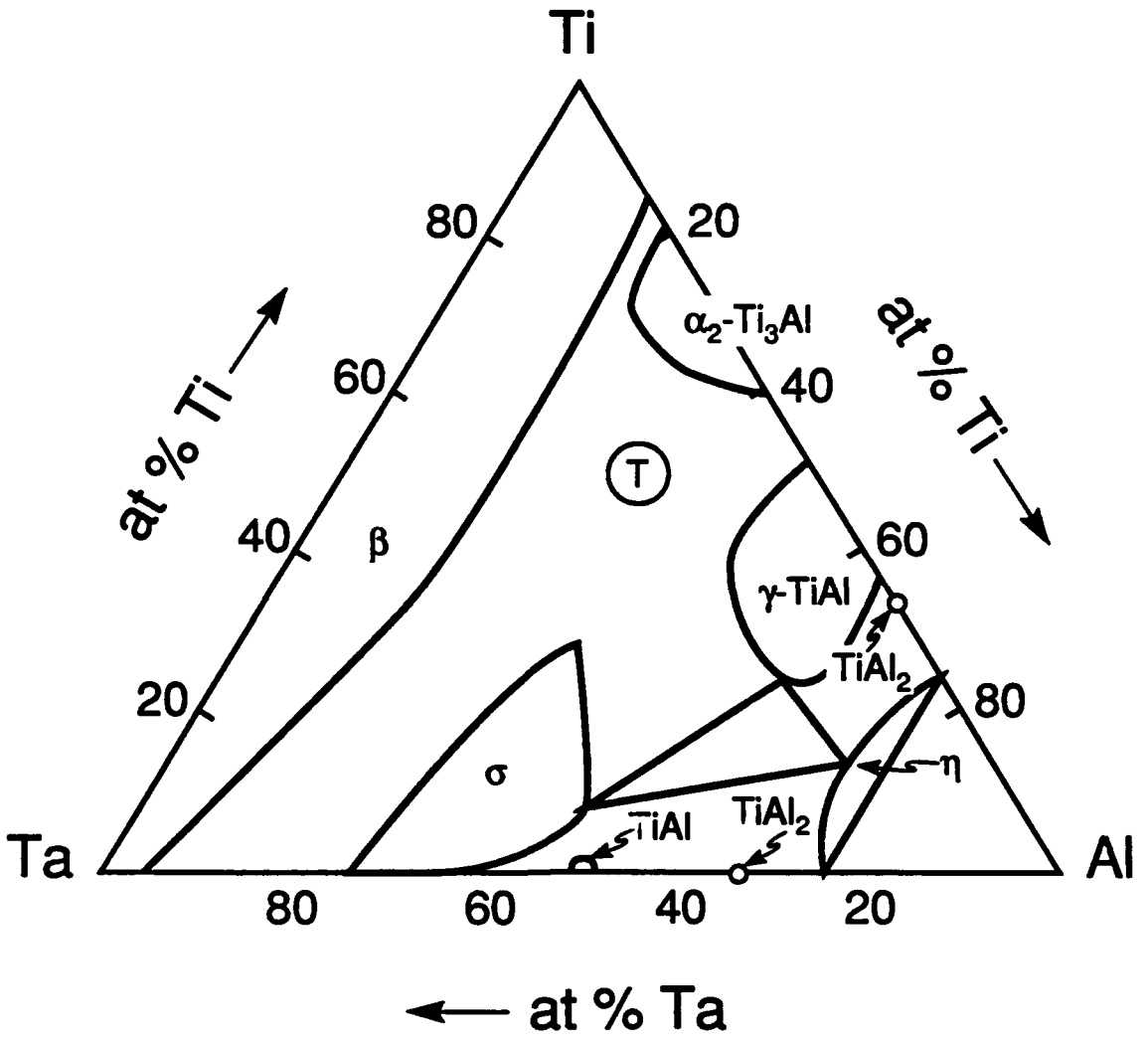
Ti
80
20
α_2-Ti_3Al
at % Ti
60
40
at % Ti
T
40
β
60
γ-TiAl
$TiAl_2$
20
80
σ
η
TiAl
$TiAl_2$
Ta
Al
80
60
40
20
at % Ta

Figure 1

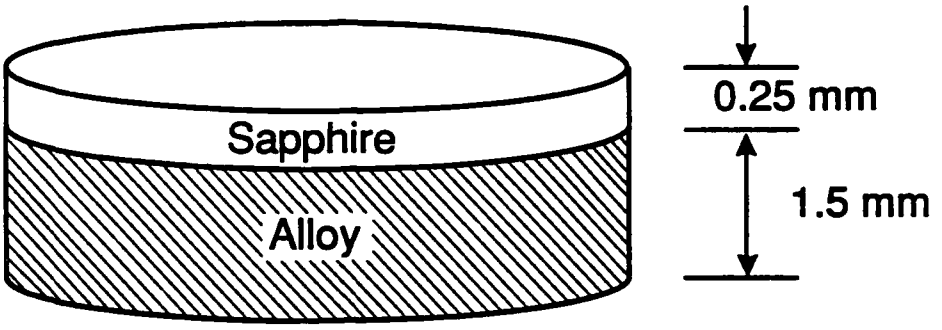
Sapphire
Alloy
0.25 mm
1.5 mm

(a)

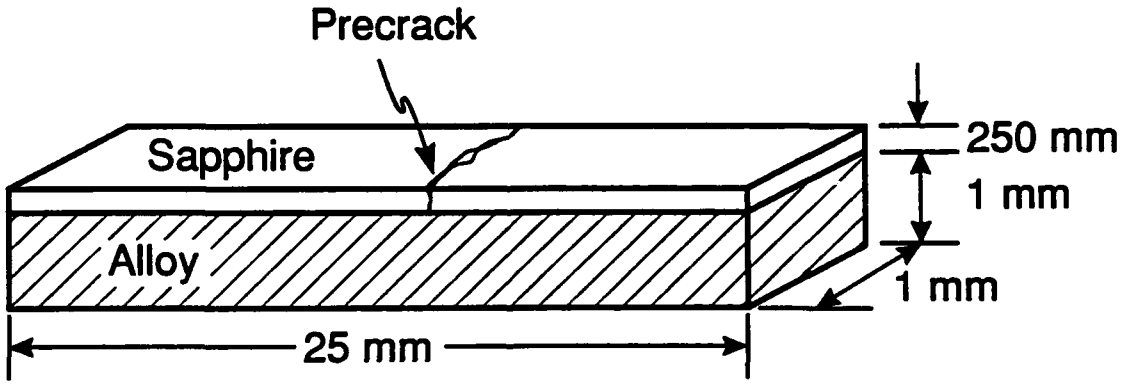
Precrack
Sapphire
Alloy
250 mm
1 mm
1 mm
25 mm

(b)

Figure 2

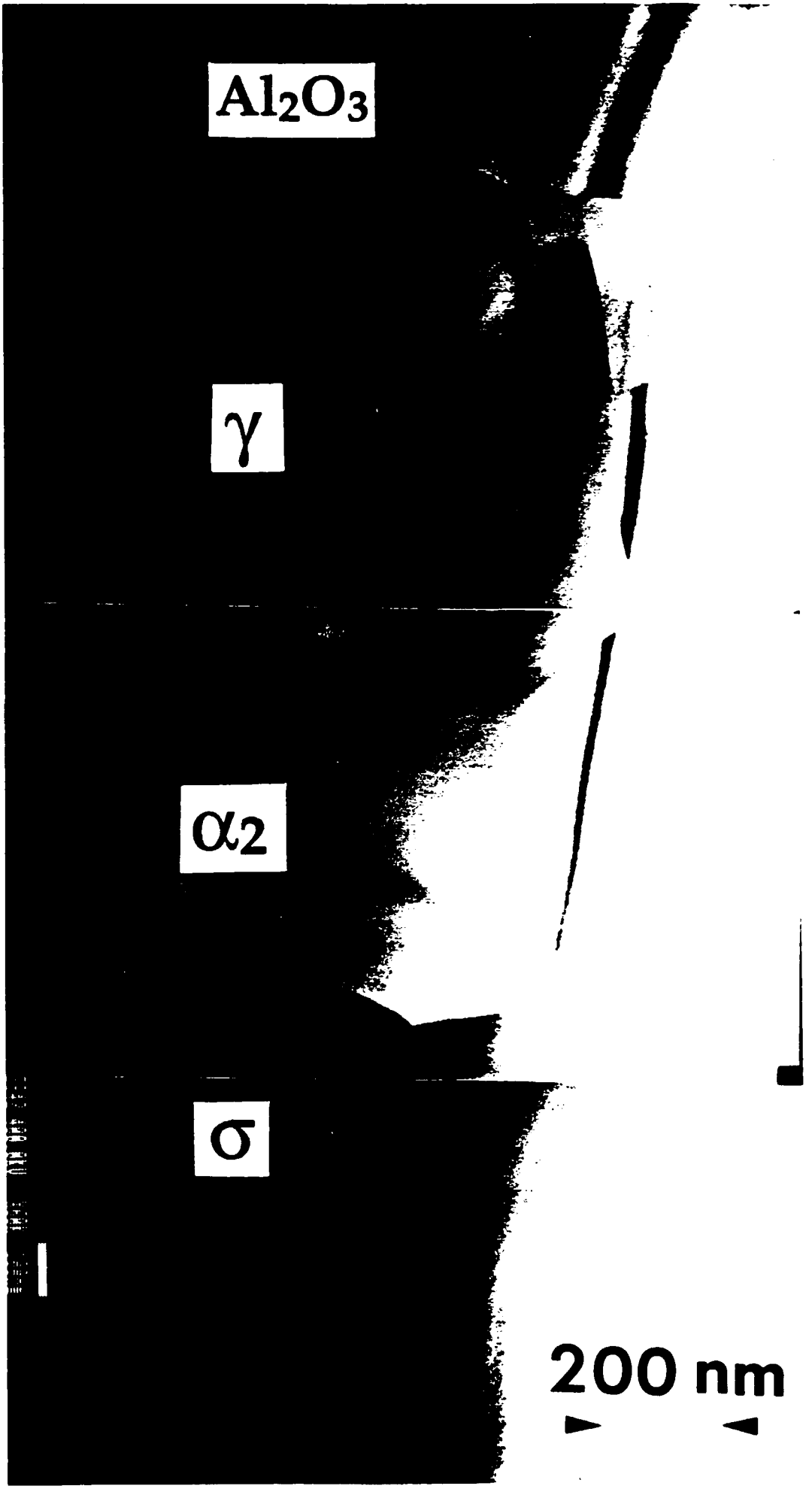

Figure 3a

Figure 3b

Figure 4

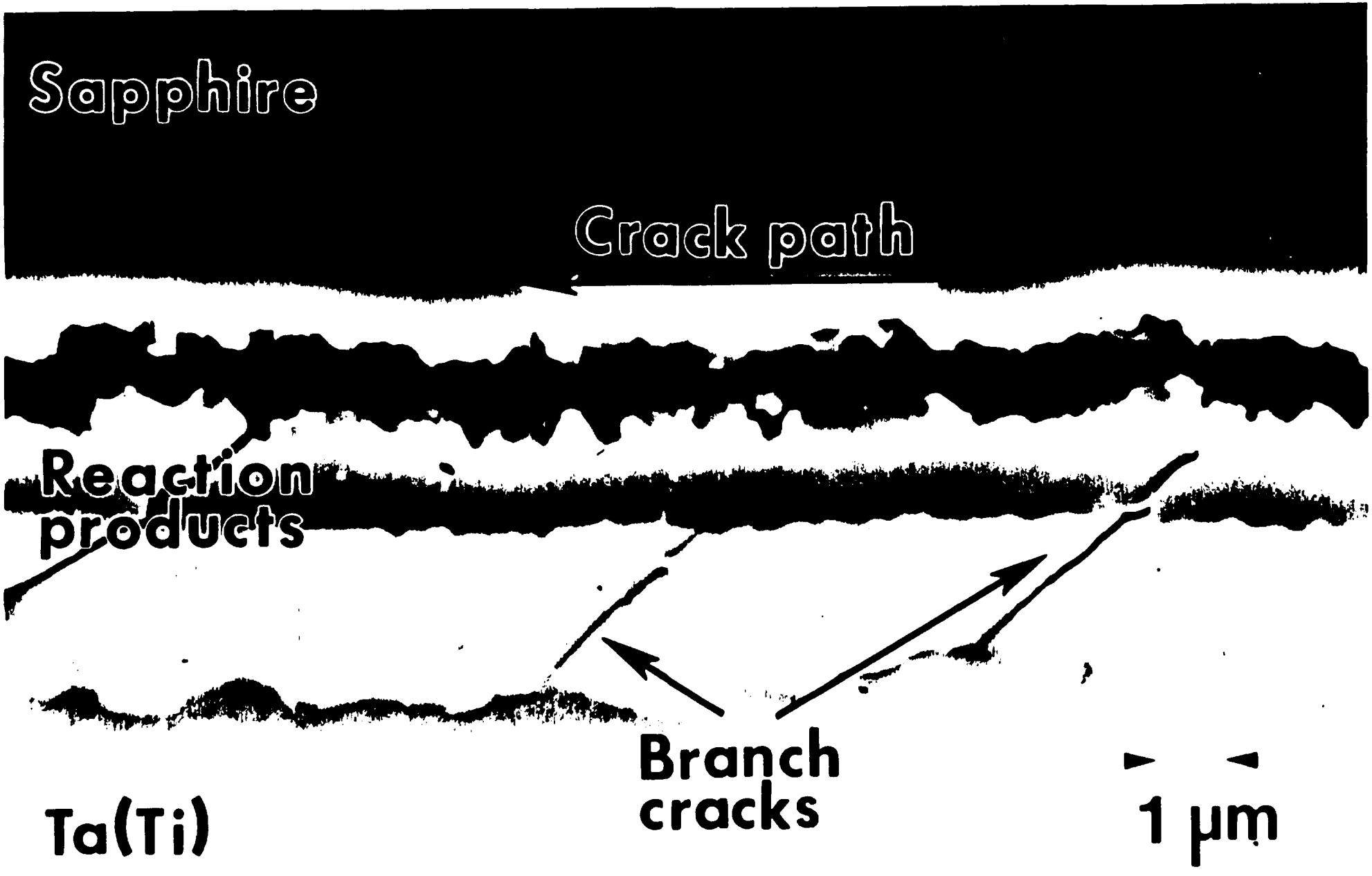
Sapphire
Crack path
Reaction products
Branch cracks
Ta(Ti)
1 μm

Figure 5

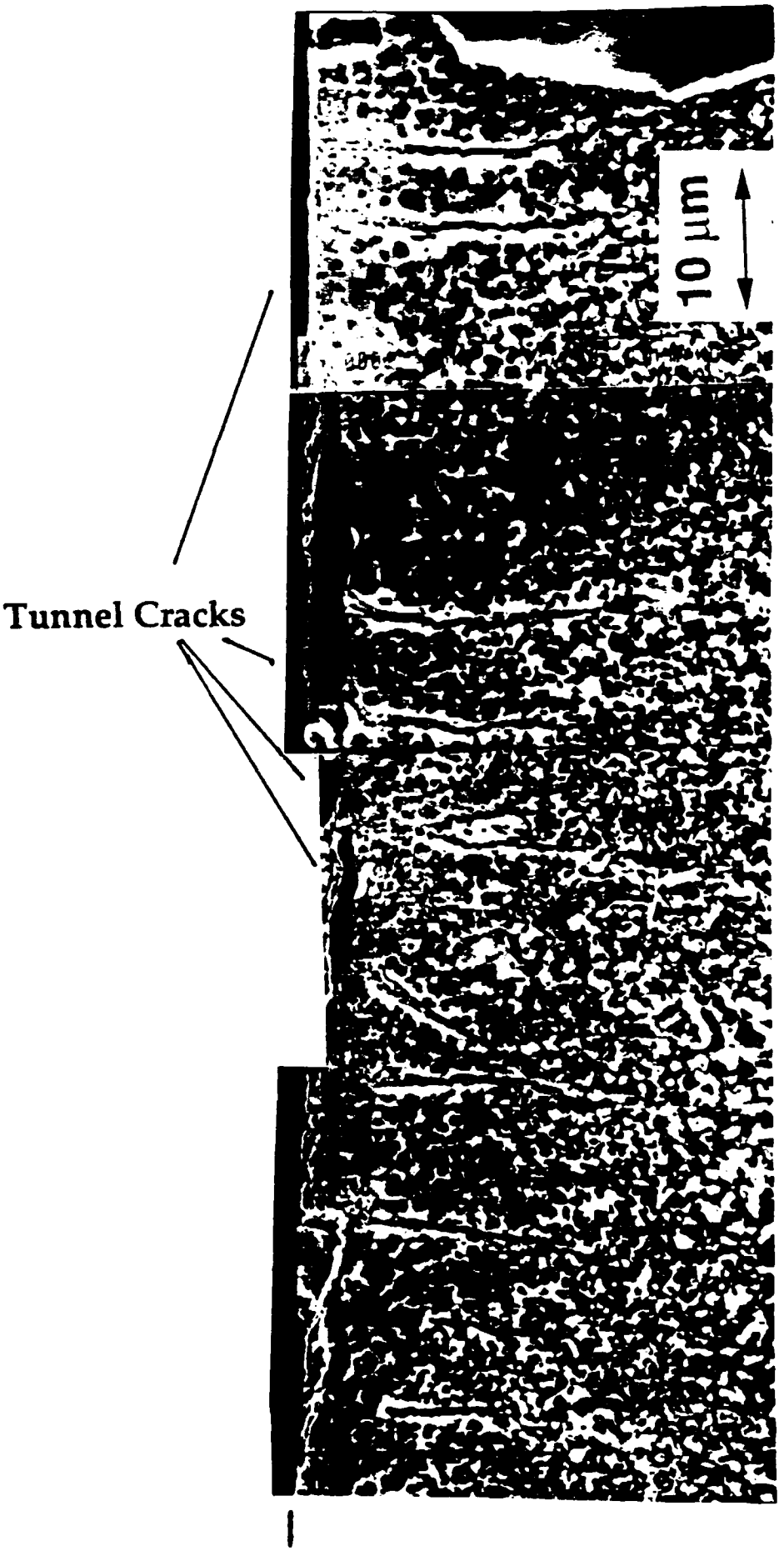

Figure 6

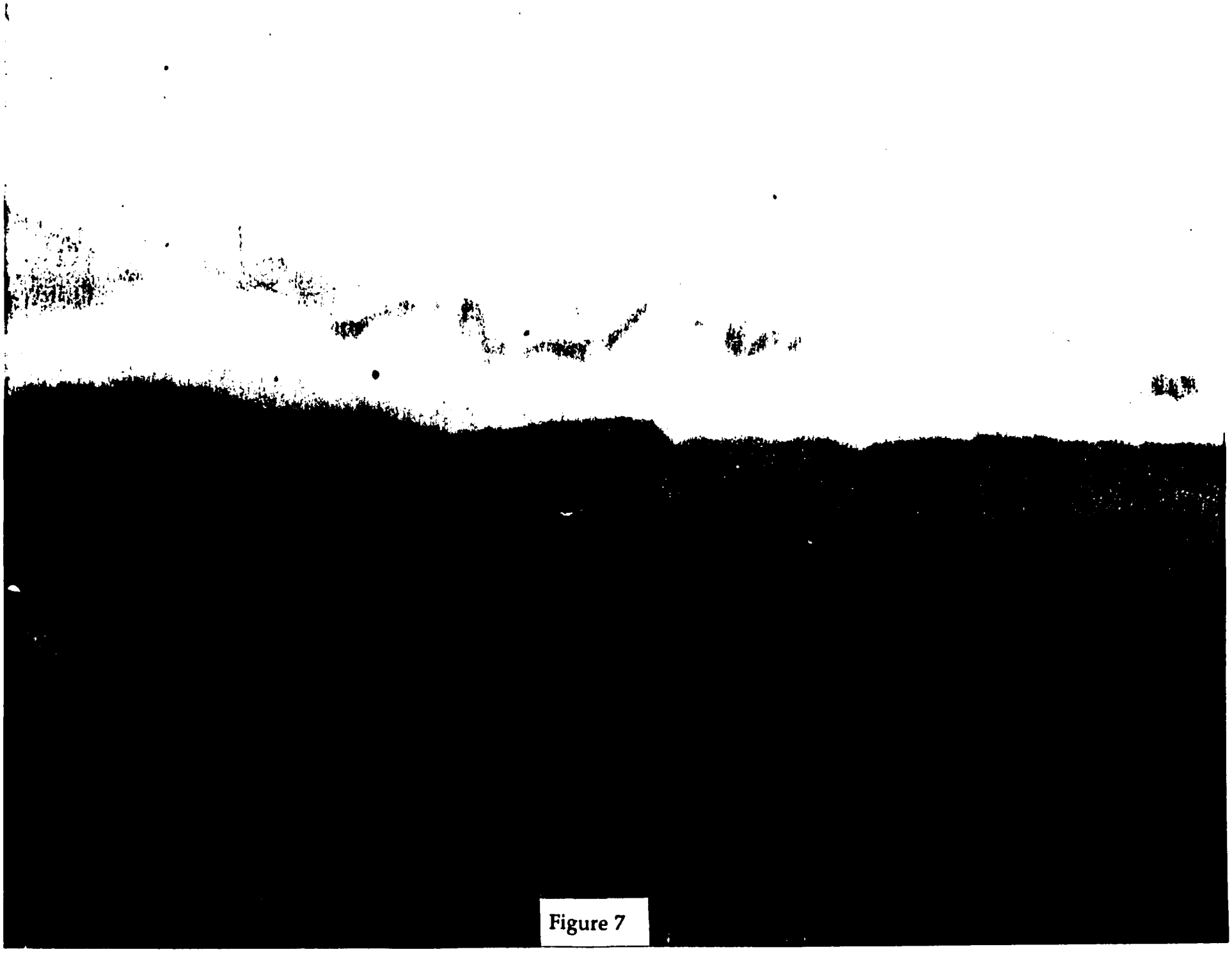

Figure 7

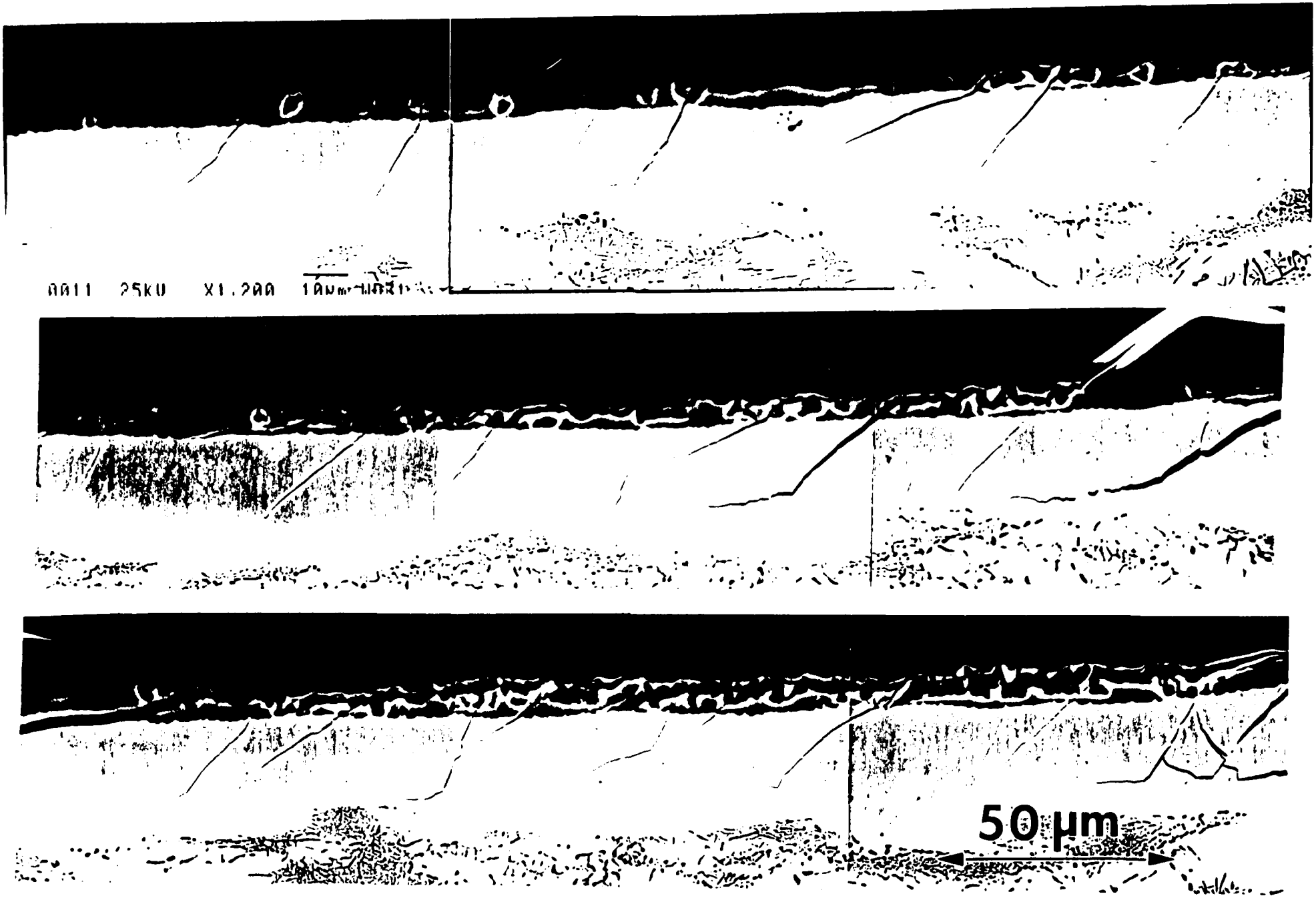

Figure 8

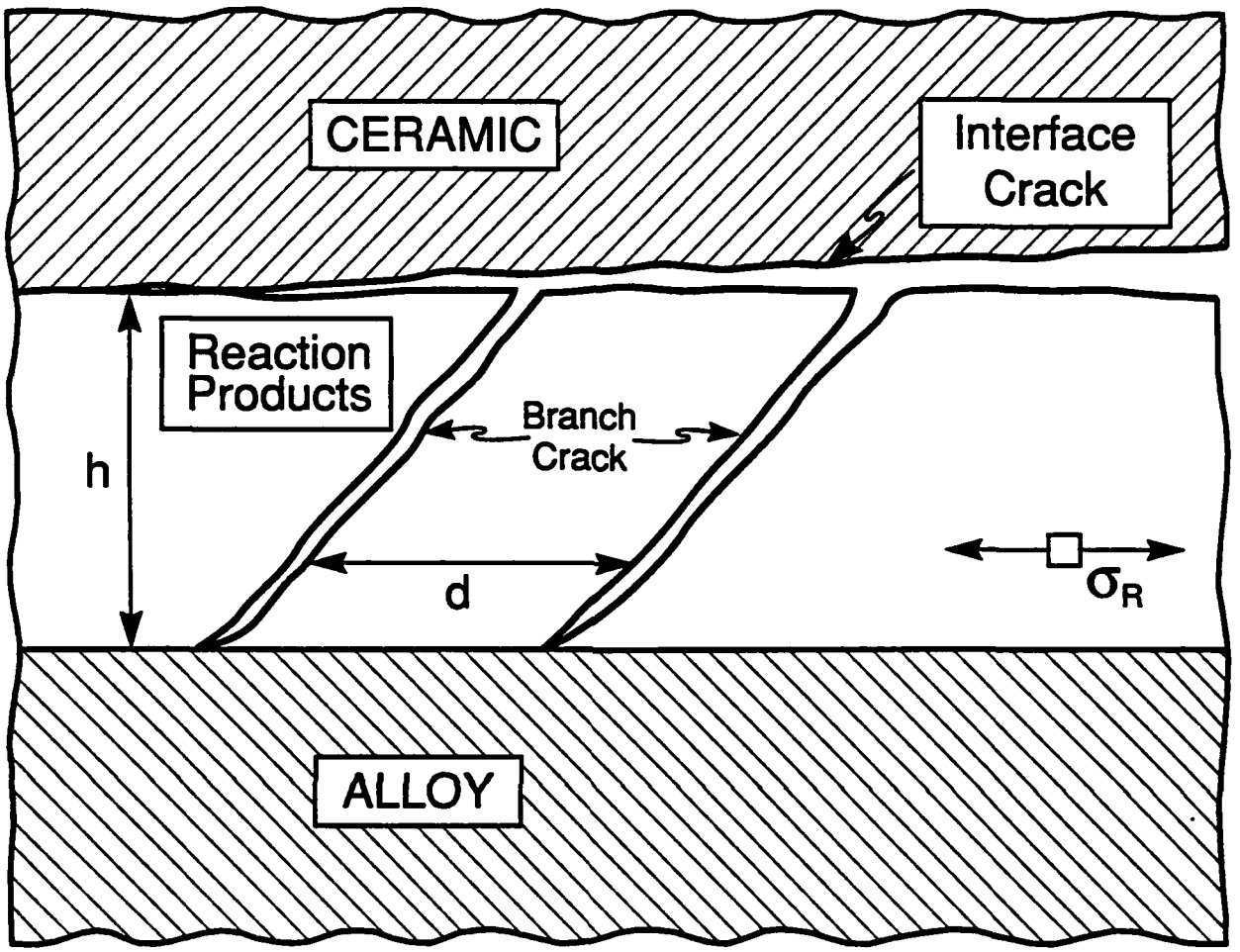
CERAMIC
Interface
Crack
Reaction
Products
h
Branch
Crack
d
σ_R
ALLOY

Figure 9

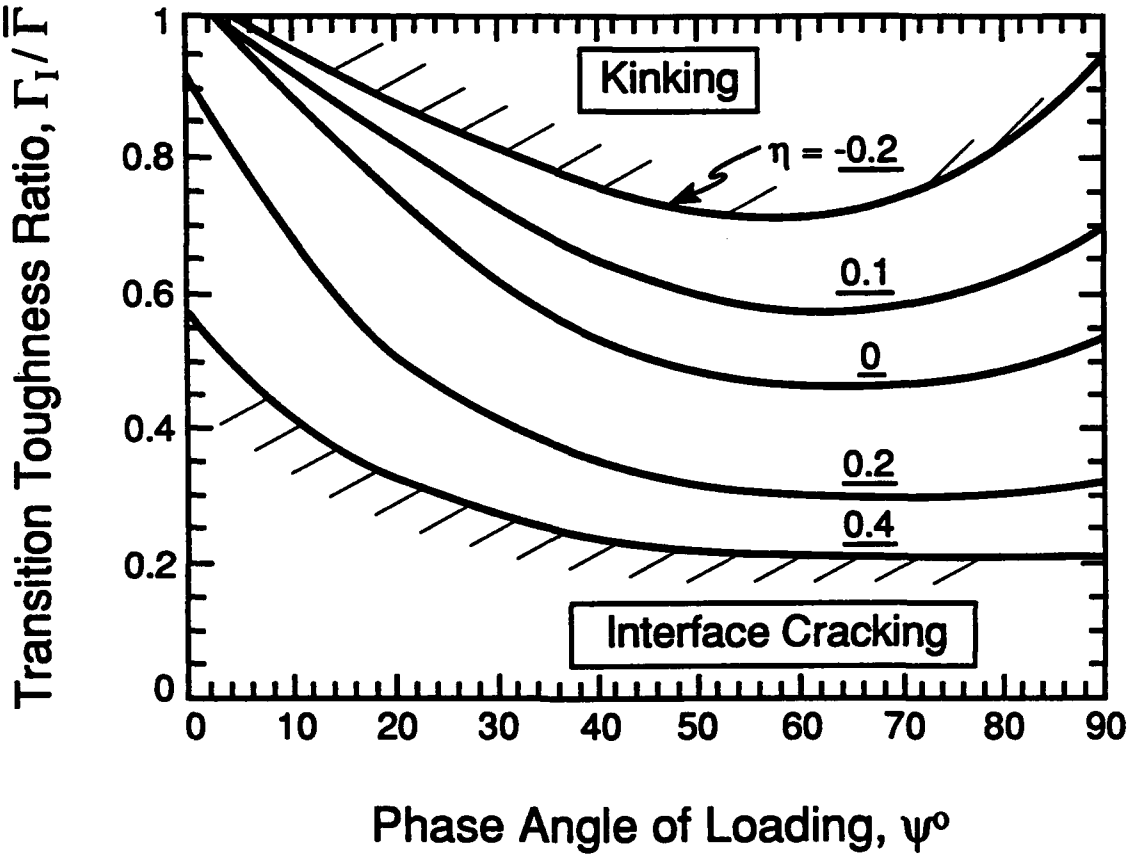
Transition Toughness Ratio, $\Gamma_I / \bar{\Gamma}$
1
0.8
0.6
0.4
0.2
0
0
10
20
30
40
50
60
70
80
90
Kinking
η = -0.2
0.1
0
0.2
0.4
Interface Cracking
Phase Angle of Loading, ψ°

Figure 10

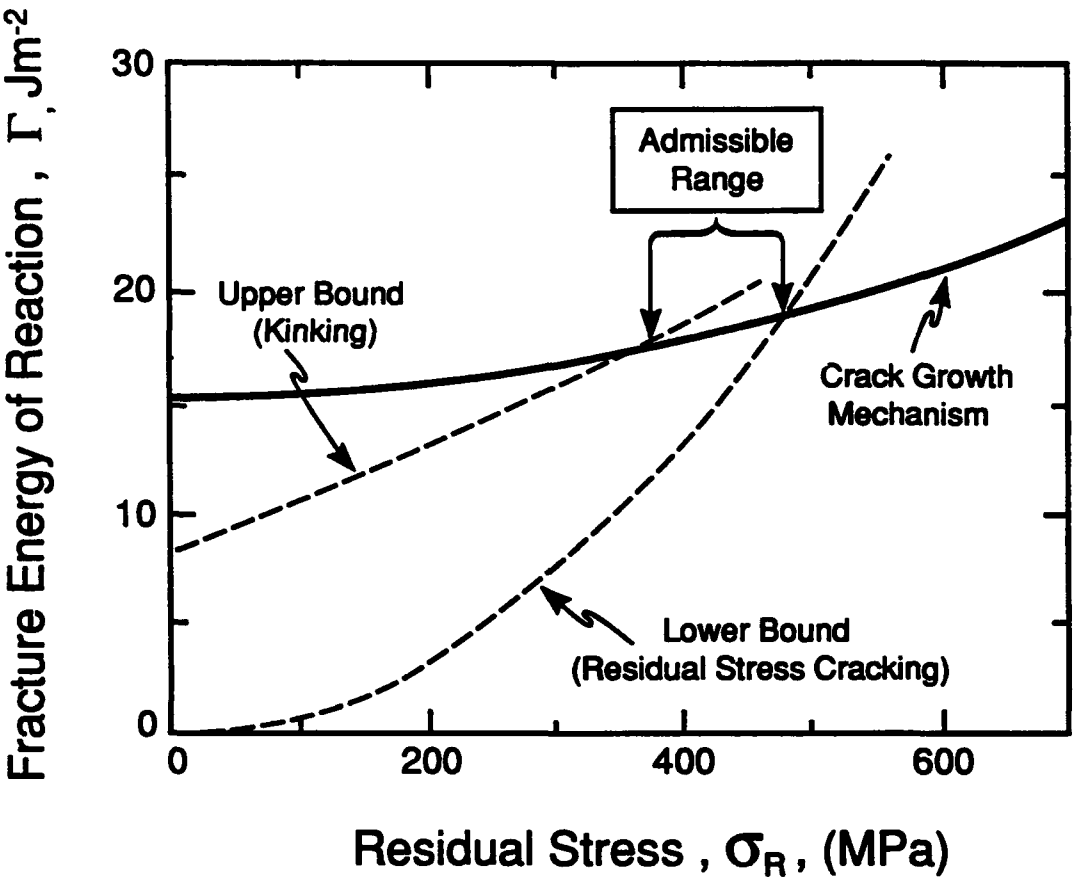
Fracture Energy of Reaction , $\overline{\Gamma}$, Jm^{-2}
30
20
10
0
0
200
400
600
Admissible Range
Upper Bound (Kinking)
Crack Growth Mechanism
Lower Bound (Residual Stress Cracking)
Residual Stress , σ_R, (MPa)

Figure 11

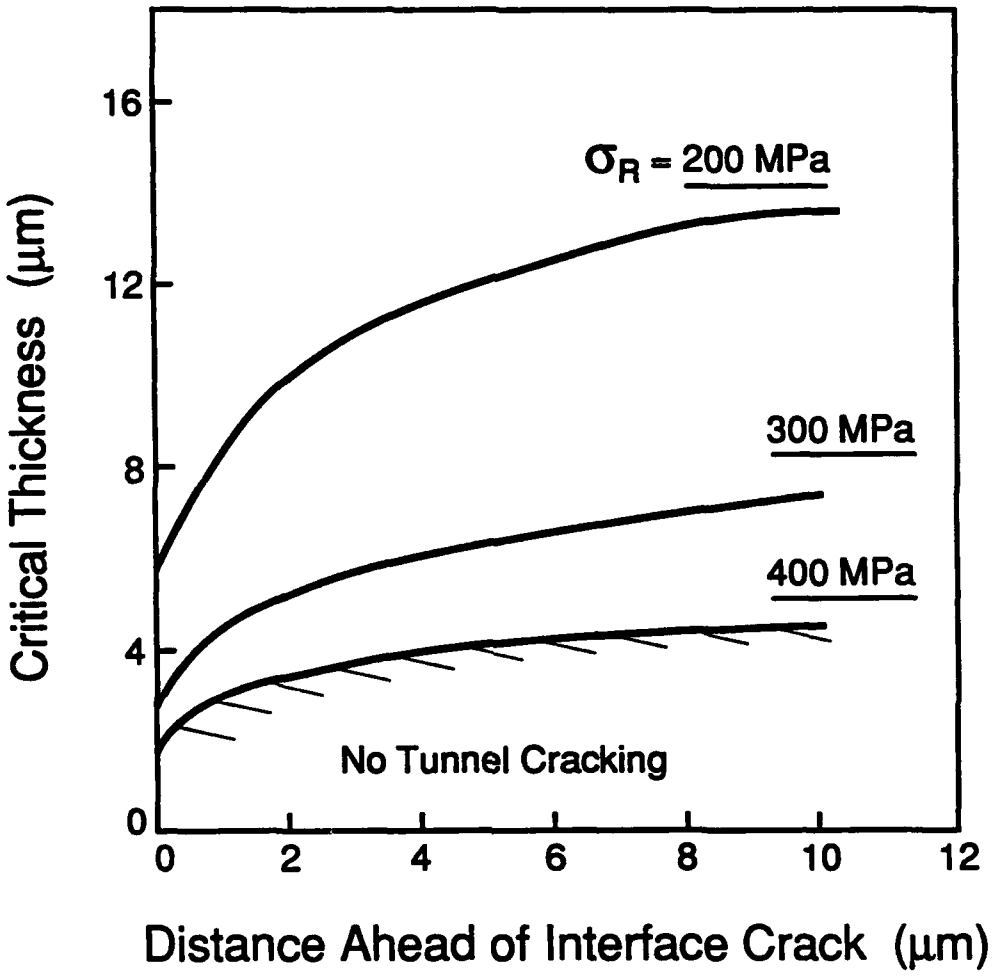
16
12
8
4
0
Critical Thickness (μm)
σ_R = 200 MPa
300 MPa
400 MPa
No Tunnel Cracking
0
2
4
6
8
10
12
Distance Ahead of Interface Crack (μm)

Figure A.1

MATERIALS

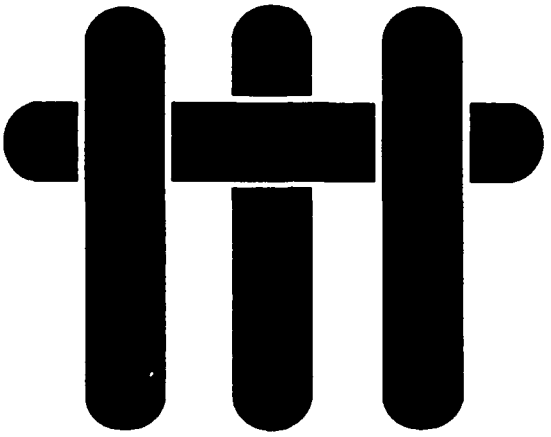

THE FRACTURE RESISTANCE OF METAL/CERAMIC INTERFACES

by

A.G. Evans and B.J. Dalgleish
Materials Department
College of Engineering
University of California
Santa Barbara, California 93106–5050

KJS-Evans-29•Frc N-Fz•TA-Frct Rst M/C 91/10/08•11:31 AM•11/21/91

ABSTRACT

The effects of interface structure and microstructure on the fracture energy, Γ_i, of metal/ceramic interfaces are reviewed. Some systems exhibit a ductile fracture mechanism and others fail by brittle mechanisms. In the absence of either interphases or reaction products, Γ_i is dominated by plastic dissipation (for both fracture mechanisms), leading to important effects of metal thickness, h, and yield strength, σ_o. Additionally, Γ_i is larger when fracture occurs by ductile void growth (for the same h and σ_o). A fundamental understanding now exists for the ductile fracture mechanism. However, some basic issues remain to be understood when fracture occurs by brittle bond rupture, particularly with regard to the role of the work of adhesion, W_{ad}.

Interphases and reaction products have been shown to have an important effect on Γ_i. A general trend found by experiment is that Γ_i scales with the fracture energy of the interphase itself, wherein Γ_i tends to increase for the interphase sequence: amorphous oxides > crystalline oxides > intermetallics. However, there also appear to be important effects of the residual stresses in the interface (which influences the fracture mechanism) and the layer thickness.

1. INTRODUCTION

There have been many studies concerned with the formation of metal/ceramic bonds and bond strength. These investigations have established that the overall mechanical response of interfaces resulting from such bonds involves considerations of several factors: including the fracture resistance Γ_i and the magnitude of the interfacial flaws, a, as well as mismatches in elastic, plastic and thermal properties, which cause stress concentrations at edges and discontinuities. The appropriate interconnections have been addressed in previous reviews.[1-5] The focus of this article is on *the most basic mechanical property of the interface: the fracture resistance,* Γ_i. A framework for discussing this property is presented in Fig. 1, reflecting both the mechanisms of crack growth and the incidence of either reaction products or interphases. Notably, crack extension can proceed either by ductile void growth in the metal adjacent to the interface[5,6] or by brittle debonding along the interface,[7,8] perhaps accompanied by a zone of plastic deformation in the adjoining metal. The presence of either reaction products or interphases introduces additional mechanisms, such as microcrack coalescence within the interphase,[9,10] and also encourages brittle modes of failure. In this article, the fundamental ductile and brittle fracture mechanisms are addressed for interfaces that form without reaction products (some of these systems are summarized in Table I), followed by consideration of changes in behavior that arise when either crystalline or amorphous interphases are present.

To provide perspective, several pervasive issues that must be rigorously addressed in order to obtain accurate measurements of Γ_i are briefly reviewed: residual stresses, crack trajectories, pre-cracking. *Residual stresses caused by thermal expansion misfit* can induce an appreciable energy release rate $\mathcal{G}_R$ at interface cracks.[11] These stresses are difficult to measure and predict, especially when plasticity occurs in the metal upon cooling after bonding. Test specimen geometries that minimize $\mathcal{G}_R$ are desirable and, in

some cases, essential. This objective may be achieved by using a sandwich geometry, consisting of a relatively thin metal layer bonded within the ceramic (Fig. 2). Then, only a small fraction of the residual energy is released upon interface cracking, because the metal remains bonded to the thicker ceramic.[12] Furthermore, the magnitude of $\mathcal{G}_R$ can often be computed for this geometry, because bending effects on cooling are minimal. The specimen design, as well as the expansion misfit can also affect the Γ_i measurement by influencing the *crack trajectory*. Notably, when the interface crack is subject to shear loadings that result in a negative phase angle, ψ (as defined in Fig. 3), the crack may deviate from the interface into the ceramic, thereby preventing measurements of Γ_i.[2,13,14] Specimens that provide *positive* ψ on interface cracks are thus preferred. Furthermore, ψ must be known (from calculations) because there can be appreciable effects of ψ on the magnitude of Γ_i.[15-17] Introducing a *sharp pre-crack* along the interface is another necessary step in the measurement of Γ_i. Attempts to accomplish this by locally contaminating the interface during bonding have usually led to inconsistent results. Mechanical pre-cracking procedures after bonding are preferred and specimens that facilitate this procedure are expected.

The preceding considerations have resulted in a number of test specimen choices, depicted in Fig. 2. Many of the data presented in this article have been obtained using the flexural specimen shown in Fig. 2c, primarily because it has attributes that address each of the above issues.[2,18] In particular, the phase angle ($\psi \approx \pi/4$) encourages interface cracking. Also stable pre-cracking along the interface can be achieved in three-point loading. Moreover, upon loading in four-point bending (after pre-cracking), a steady-state energy release rate applies:[18] a condition that facilitates the acquisition of *accurate and consistent* fracture resistance data. Moreover, when the ceramic is transparent (e.g., single crystals), direct observations of crack growth can be made *in situ* in an optical microscope,[7,8] leading to vitally important information about the crack growth mechanism.

Most metal/oxide interfaces have been found to exhibit a relatively high fracture energy compared with the thermodynamic work of adhesion, W_{ad}, provided that the bonding has been conducted at relatively high homologous temperatures ($T/T_m > 1/2$, with T_m referring to the lowest melting constituent). In fact, it has been difficult to identify the low Γ_i interfaces needed for reinforcement debonding in composites.[19] Nevertheless, W_{ad} is still expected to have major relevance to interface failure. Estimates of this quantity may be obtained from measurements of the dihedral angle ϕ associated with the residual voids on diffusion-bonded interfaces.* A convenient procedure for obtaining ϕ, when the interface fails by a brittle mechanism, is to make measurements on the fracture surface using the atomic force microscope (Fig. 4). Then, W_{ad} is obtained from[8,20]

$$W_{ad} = \gamma_m(1-\cos\phi) \tag{1}$$

where γ_m is the surface energy of the metal. An important objective of interface fracture studies is to ascertain relationships between Γ_i and W_{ad}. It will be demonstrated that such a relationship may exist for interfaces that fail by brittle debonding, but is not to be expected when failure occurs by ductile mechanisms.

2. DUCTILE INTERFACE FRACTURE

A limited number of metal/ceramic bonds are found not to be susceptible to brittle debonding at the interface. The most extensively studied have been Al_2O_3 bonded to either Al or Cu.[5] In such systems, interface fracture may proceed by the nucleation, growth and coalescence of voids, occurring by plastic flow in the metal adjacent to the

* One objective of atomistic calculations is to determine the work of adhesion.

interface (Fig. 5).[5,6] The mechanism has the classical features of ductile fracture, modified by two factors: constraint and void nucleation.

The *constraint* arises when the metal exists as a *thin layer between two ceramics*. This situation is manifest within metal matrix composites, as well as layered materials and in certain metal/ceramic bonds. In thin layers, high hydrostatic stress $\bar{\sigma}$ is developed due to inherent limitations on slip. This component of the stress tensor is important because it dominates the plastic void growth rate $\dot{V}$, in approximate accordance with an exponential expression,[22] $\dot{V}/V \sim \exp(\bar{\sigma}/\sigma_o)$, where σ_o is the uniaxial yield strength. Consequently, by understanding trends in $\bar{\sigma}/\sigma_o$, factors affecting ductile fracture can be addressed. One useful limit for interface ductile fracture is associated with an instability that occurs at large $\bar{\sigma}/\sigma_o$,[23] which arises when this stress reaches a critical level. This critical stress, $\bar{\sigma}_c$ (while having some dependence on the work hardening coefficient) is of order[23]

$$\bar{\sigma}_c/\sigma_o \approx 5.5 \tag{2}$$

Of particular relevance is the elevation of hydrostatic tensile stress $\bar{\sigma}$ that occurs *ahead of an interface crack* (Fig. 6).[24] These stresses attain a maximum at a distance ahead of the crack a few times the layer thickness. This maximum $\bar{\sigma}_{max}$ can be expressed in the form

$$\bar{\sigma}_{max}/\sigma_o \approx F\left[E\mathcal{G}/\sigma_o^2 h, \psi, N\right] \tag{3}$$

where $\mathcal{G}$ is the energy release rate associated with the applied loads, σ_o is the uniaxial yield strength of the metal, h is the metal layer thickness, N is the work hardening coefficient and F is a function evaluated by Varias *et al.*[24] Because the stresses $\bar{\sigma}_{max}/\sigma_o$ can attain large values, the void growth instability condition (Eqn. 2) can be reached. A

useful bound is thus identified by allowing crack extension to occur when σ_{max}/σ_o satisfies Eqn. (2), whereupon the interface fracture resistance becomes

$$\Gamma_i = (\sigma_o \varepsilon_o h) H(\psi) \tag{4}$$

where ε_o is the yield strain and H is a function given by Varias *et al.*[24] A simplified interpretation of Eqn. (4) is that the fracture energy is exclusively governed by plastic dissipation, occurring at flow strength σ_o, fully contained within the metal layer of thickness h. Furthermore, the layer experiences a plastic strain somewhat in excess of the yield strain ε_o. Consequently, the dissipation per unit area of crack extension must scale as, $\Gamma_i \sim \sigma_o h \varepsilon_o$. This trend in fracture energy with metal layer thickness and yield strength provides a simple framework for interpreting experimental results.

The above bound is only applicable when the metal layer thickness is small. For thicker layers, the number density of nucleation sites becomes important. In this case, the ductile fracture criterion is found to be essentially the same as that of the homogeneous metals[25]

$$\Gamma_i \approx 2\sigma_o X_o \tag{5}$$

where X_o is the spacing between nucleation sites. This mode of fracture dominates when $X_o/h \lesssim 0.1$[24] (Fig. 7). In this case, the majority of the plastic dissipation is confined to the metal ligaments *between the voids:* hence, the key length scale becomes the spacing X_o, rather than the metal layer thickness, h. One observation suggests that the voids originate at the interface (Fig. 5): analogous to void nucleation at hard particle interfaces in alloys. Hence, the interface *microstructure* can have an important influence on the fracture energy. The preferred interfacial sites for nucleation are three-grain junctions[6] in the ceramic at the interface (Fig. 5b). Consequently, in this range of metal thickness,

the grain size of the ceramic D has an important influence on Γ_i, with D replacing X_o in Eqn. (5). The most vivid illustration of this grain size effect is in interface debonding in Al_2O_3 toughened by Al alloys.[6] When the Al_2O_3 grain size is small ($D \lesssim 2\ \mu m$), extensive debonding occurs during crack growth (Fig. 8a) and the composite has a high work of rupture. Conversely, when the grains are large ($D > 10\ \mu m$), the interface does not debond (Fig. 8b) and the composite has a reduced work of rupture. Similar trends in void nucleation with ceramic grain size have been found in transverse testing of Al alloys reinforced with Al_2O_3 fibers.[26]

In summary, when interface fracture occurs by a ductile mechanism, the debond energy satisfies some simple rules. The dominant length scales are the metal layer thickness, h, and the ceramic grain size D, as well as the length ratio, D/h. At small D/h, D is the important length and vice versa. In all cases, the stress scaling parameter is the uniaxial yield strength σ_o.

3. BRITTLE DEBONDING

A number of systems have been found in which no reaction products form and fracture occurs by brittle debonding. Such debonding differs morphologically from ductile interface fracture in that there is no metal attached to the ceramic side of the fracture surface (Fig. 1). Furthermore, there is no ceramic attached to the metal, clearly indicating that the crack extends by brittle bond rupture at the interface plane. These interfaces are characterized by a well-defined interface plane, when imaged at atomic revolution in the transmission electron microscope.[20] The interface is typically faceted and there may be some of the ceramic in solution in the metal and vice verse, resulting from interdiffusion during diffusion bonding. The systems that have been most extensively studied consist of Al_2O_3 bonded to Au,[7,8] Pt[27] or Nb[20,28] and SiO_2 bonded to Cu.[29] A coherent model that characterizes the interface fracture resistance when this

mechanism occurs has yet to be devised. However, certain general characteristics are apparent. i) The fracture energies are appreciably larger than the work of adhesion, because plastic dissipation in the metal accompanies interface crack extension, leading to effects of metal layer thickness and yield strength. ii) The interface can be embrittled by environments that induce stress corrosion, suggestive of a scaling between Γ_i and W_{ad} analogous to that in homogeneous oxides and in liquid metal embrittlement. iii) The interface microstructure is important through its effect on the density of debond nucleation sites. iv) The fracture energies are considerably smaller than those obtained when the interface fails by ductile fracture. v) Interface crack growth can be subject to resistance curve behavior associated with intact ligaments that remain in the wake of the propagating crack. Each of these points will be illustrated by examples taken from the above systems.

Stress corrosion effects have been most vividly demonstrated for the Cu/SiO_2 [29] and Au/Al_2O_3 [7] system, but are probably widespread when interface fracture occurs by brittle debonding. The responsible environmental species is water, as demonstrated by dramatic effects that occur upon excluding moisture manifest in the fracture energy and the morphology of the fracture surface.[7] When moisture is present, Γ_i is low (but still larger than W_{ad}) and the metal side of the fracture surface is relatively undistorted (Fig. 9c). When moisture is excluded, Γ_i is substantially larger and the metal fracture surface experiences substantial plastic distortion[8] (Fig. 9b). Furthermore, interface crack growth subject to stress corrosion appears to have the classical dependence of the crack growth rate, $\dot{a}$, on the energy release rate, $\mathcal{G}$.[30] By analogy with the behavior of oxides and metals, the inference is that the crack growth rate in stage I has the form,

$$\dot{a} = \dot{a}_o \left(\mathcal{G}/\Gamma_i^o\right)^n \qquad (6)$$

where Γ_i^o is the interface fracture energy when stress corrosion is absent and the scale velocity $\dot{a}_o$ depends on relative humidity. Further measurements are needed to validate this behavior.

When stress corrosion is excluded, crack growth involves several additional features, including resistance curve behavior[8,29] with large associated values of the fracture energy, Γ_R (Δa) (Fig. 10). Crack extension proceeds by debonding from voids on the interface ahead of the crack (Fig. 9b), leading to the incidence of alternating debonding on both interfaces (Fig. 11). In turn, this causes intact ligaments in the crack wake. These ligaments are subject to extensive plastic distortion (Fig. 12), implying that they are the source of the rising resistance curve behavior noted in Fig. 10. Verification of this premise is achieved by removing the ligaments through exposure to a wet atmosphere under stress in order to stress corrode the ligament interfaces.[8] When this has been accomplished and testing is continued in a dry atmosphere, the fracture resistance reverts to its original level and the initial resistance curve is duplicated as new ligaments develop upon further crack growth (Fig. 13). With this confirmation that the rising resistance is governed by plastic dissipation in the ligaments, the resistance effect can be readily simulated.[8,31] The salient non-dimensional parameters are Γ_R/Γ_i^o and $[(\sigma_o f_A)^2 H/2E\Gamma_i^o]^{1/4}$, (a/H) where f_A is the fraction of interface area subject to intact ligaments and H is the beam thickness. Numerical simulations for large-scale bridging (Fig. 14) are consistent with experimental measurements, including independently obtained information about f_A and σ_o. Based on this understanding, it should be possible to design interfaces that have high fracture resistance. One interesting approach, demonstrated for Cu/SiO_2, is to introduce morphological features on the interface that increase the ligament area, f_A.[29]

The most basic interface fracture resistance is that occurring upon initial crack extension ($\Delta a \rightarrow 0$), designated Γ_i^o. Limited data on Al_2O_3/Au indicate that Γ_i^o increases as the metal layer thickness increases, indicative of an influence of plastic dissipation,

but is much smaller than the resistance expected when fracture is ductile (Fig. 7). Furthermore, results for Al_2O_3/Nb[28] suggest important effects of yield strength. These measurements, coupled with observations of extensive plastic distortion (Fig. 9b), imply an important role of plastic dissipation. Dimensional analysis based on a brittle debonding mechanism with plasticity identifies the following basic parameters: Γ_i^o/W_{ad}, $\sigma_o h/W_{ad}$, N. An empirical fit to limited experimental data for Al_2O_3/Au based on these parameters (neglecting N) suggests the approximate relationship[8]

$$\Gamma_i^o \approx W_{ad}\left[\sigma_o h/W_{ad} + 1\right]^{1/2} \tag{7}$$

Such empirical relationships based on non-dimensional parameters provide guidance for basic studies of interface fracture in accordance with this mechanism.

A key fundamental problem in modelling and predicting relationships between Γ_i and W_{ad} is illustrated in Fig. 15. Atomistic calculations of bond separation indicate that stresses of order $\mu/100$ (or > 10 GPa) are needed at the crack front to cause rupture. However, continuum elastic/plastic calculations indicate that the stresses cannot exceed ~ 3–5 σ_o,[24] (or < 1 GPa for Au, Pt, Nb). The missing feature is an intervening zone, not described by existing continuum formulations, having radius of order $10^2 - 10^3$b (where b is the Burger's vector).[32] This zone contains a distribution of dislocations that allows the stress to build up to that needed for bond rupture. A representation for this zone compatible with the boundary conditions associated with the surrounding continuum elastic/plastic material has yet to be provided.

4. EFFECT OF INTERPHASES

Two types of interphases have been identified: i) Crystalline reaction products formed by interdiffusion that can be rationalized from phase equilibria and kinetics.

ii) Amorphous phases formed either by viscous flow of a phase that pre-exists in the ceramic or by reaction. A simple conclusion based on various measurements of interface fracture in interphase dominated interfaces is that Γ_i is often closely related to the fracture energy of the interphase material itself. Notably, amorphous interfaces lead to Γ_i in the range 5–10 Jm^{-2}, crystalline oxide interphases, 10-20 Jm^{-2}, and intermetallic interphases, 20–40 Jm^{-2}. This ranking has important exceptions elaborated below, but generally seems to apply despite considerable complexity in the local details of interface fracture. The basic phenomena are discussed with reference to results for the following systems: a) Al_2O_3 bonded to Ti/Ta alloys which form intermetallic reaction products,[9,10] b) Pt and Au bonded to commercial grade Al_2O_3 which forms an amorphous oxide interphase during bonding and c) Pt bonded to sapphire with interphases consisting of either crystalline SiO_2 (cristobalite) or an amorphous Ca silicate.[27] A preliminary observation is that interphases typically facilitate diffusion bonding, leading to diminished residual voids and defects, as exemplified in Fig. 16 for the Pt/sapphire system, with and without interphases. Enhanced diffusivities within the interphase are probably responsible for this phenomenon. However, the fracture energies of bonds with interphases are typically lower than those found for directly bonded metal/ceramic interfaces.

Fracture energy results obtained for either Au or Pt bonded to commercial grade Al_2O_3 (Fig. 17) indicate that fracture energies Γ_i approach ~ 6 Jm^{-2} as the metal layer thickness tends to zero, where plastic dissipation effects become negligible. Observations on these systems reveal that an amorphous layer is present on the Al_2O_3 side of the fracture surface (Fig. 18) and occasional oxide particulates on the metal side. Thus, while fracture appears to occur predominantly at the metal/glass *interface*, nevertheless, the fracture energies are similar to that for the *glass itself*. Furthermore, Γ_i is considerably lower than that for either Au or Pt directly bonded to Al_2O_3, described above.

When Pt is bonded to sapphire with an intermediate SiO_2 layer, this layer is found to be crystalline and epitaxial (Fig. 19), resulting in a high fracture energy, $\Gamma_i > 40$ Jm^{-2}. However, when Ca is also present, amorphous ridges form during diffusion bonding, located at intersections between the sapphire and grain boundaries in the Pt. These ridges are evident on fracture surfaces (Fig. 20) and also dictate the contrast observed by optical microscopy (Figs. 16c and 21a). This interface has a relatively low fracture energy, $\Gamma_i \approx 15$ Jm^{-2}, and fracture occurs by decohesion at the amorphous ridges (Fig. 21b), followed by progressive debonding of the intervening interface (Fig. 21c). Again, therefore, the presence of an amorphous interface has a *detrimental* effect on Γ_i.

Intermetallic interphases formed by reaction in the Al_2O_3/Ti(Ta) system illustrate a rich array of phenomena, including effects of layer thickness and of residual strain within the reaction products. The reaction products in this system are intermetallics formed by diffusion of the oxygen from the Al_2O_3 into the Ti alloy, accompanied by interdiffusion of Ti, Ta and Al. The phases that form are rationalized by the Ti, Ta, Al ternary diagram (Fig. 22). Notably, α_2-Ti_3Al, γ-TiAl and σ-phase form, with the TiAl adjacent to the Al_2O_3. All of these phases have a larger thermal expansion coefficient than either Al_2O_3 or the Ti(Ta) alloy and are thus subject to residual tension of about 600 MPa.[10] This residual stress causes periodic microcracks to form *within the layers* during interface failure (Fig. 23). In consequence, the interface fracture energies, $\Gamma_i \approx$ 20–30 Jm^{-2}, are found to be comparable to those for the (oxygen saturated) intermetallic reaction products. Observations of periodic microcracks within the reaction products indicate that they have characteristics typical of tunnelling cracks,[33] which propagate across the layers when the tensile stress, σ_T, in the layer (residual plus applied) exceeds, σ_c, given by

$$\sigma_c = \sqrt{E_s \Gamma_s / h} \qquad (8)$$

where h is the layer thickness, Γ_s is the fracture energy of the layer material and E_s its Young's modulus. Furthermore, the cracks form with a spacing, $\ell \approx 4\text{–}8h$. Consequently, when residual tensile stresses exist and the layer is relatively thick (small σ_c, Eqn. 8), these microcracks can be activated by the tensile field associated with the interface crack. The interface fracture mechanism then consists of the formation and coalescence of these microcracks, as sketched in Fig. 24. The microcrack coalescence mechanism could, in principle, be suppressed either if the reaction product layer is very thin (large σ_c, Eqn. 8) or the residual stresses are compressive. In such cases, the fracture energy should be related to that for the interface itself, which (in the one case investigated) appears to be lower than that for the reaction products.[10] This speculation requires experimental validation. It is also noted that there appears to be no contribution of plastic dissipation to Γ_i when the reaction product layer is thick, but such a contribution may arise for thin layers, as suggested by the data presented in Fig. 17.

Finally, it is noted that two systems (Al_2O_3/Mo, Al_2O_3/Cr) have been identified that form interphases and have exceptionally low fracture energies (substantially smaller than for the reaction products themselves).[19,34] In both cases, oxygen in solution in the refractory metal is responsible for the formation of an oxide that grows epitaxially on the Al_2O_3 during diffusion bonding (Fig. 25). Also, fracture occurs *at the oxide/metal interface.* It is not yet clear whether there is a fundamental reason for "weak" interfaces between either Mo or Cr and their own oxides (MoO_2 and Cr_2O_3, respectively), i.e., governed by a low work of adhesion. An alternate possibility is that the oxygen in solution in the refractory metal sufficiently elevates its flow strength‡ that minimal plastic dissipation accompanies interface fracture.[35]

---

‡ The flow strength of b.c.c. metals is strongly influenced by dissolved oxygen.

5. CONCLUDING REMARKS

Some of the basic issues associated with the fracture energy Γ_i of metal/ceramic interfaces are now clear, through elucidation of some key crack growth mechanisms: ductile void growth, brittle debonding and microcrack coalescence. For each mechanism, some understanding has been developed, leading to preliminary models that relate Γ_i to the separate properties of the adjoining materials, the interphases (when present) and the interfaces. The limitations of the models have also been described in order to identify a focus for further research.

When fracture occurs by ductile mechanisms, the relevant length scales have been identified as either the metal thickness, h, or the ceramic grain size, D, depending upon the magnitude of D/h. The other important parameter is the uniaxial yield strength of the metal. While this understanding now exists, it is not clear why brittle debonding is suppressed, causing ductile void growth to become the preferred failure mechanism.

Interfaces that form without interphases can also fail by brittle interface debonding. Such interfaces have relatively large Γ_i, because of a major role of plastic dissipation in the metal, as evident from effects of metal thickness and yield strength. It is hypothesized that W_{ad} is still an important quantity governing Γ_i, but this has yet to be verified. A fundamental effort is needed to address this issue that couples atomistic calculations with elastic/plastic continuum mechanics. A complicating factor is the existence of a resistance curve, caused by metal ligament bridging, but a good understanding of this effect seems to exist. Another complication is that these systems are susceptible to stress corrosion cracking, caused by moisture.

Interphases and reaction products have a major effect on Γ_i. A general trend is that Γ_i increases as the fracture energy Γ_s of the interphase increases, but there are important exceptions. Studies of crack extension when interphases are present have identified a microcrack coalescence mechanism that rationalizes the importance of Γ_s. This

understanding has highlighted a potentially key role of residual stress in the interphases. Appreciable plastic dissipation in the metal also appears to be suppressed when relatively thick interphases are present. This has an important effect on lowering Γ_i and needs to be explored in further detail, especially the relationship with layer thickness.

Two refractory metal systems with interphases that have particularly low fracture energies have been identified: these are Al_2O_3 bonded to either Mo or Cr. In both cases, oxygen in solution in the metal leads to oxide interfaces and fracture occurs between the metal and its own oxide. Further research is needed to establish whether these systems are unusual by virtue of a low work of adhesion between the metal and its oxide interphase or whether oxygen in the metal inhibits significant plastic dissipation.

TABLE I

Interfaces to be Considered in This Article

SYSTEM	INTERPHASES	COMMENTS
Al_2O_3/Au	None	Au Texture[7,8]
Al_2O_3/Nb	None	Al, O in solution in Nb[20,28]
Al_2O_3/Pt	None	Epitaxial[27]
	Pt_2Al	
Al_2O_3/SiO_2/Pt	Cristobalite	Epitaxial[27]
Al_2O_3/Silicate/Pt	Amorphous Ridges	Low Γ_i[27]
Al_2O_3/Al	None	Ductile[5,6]
Al_2O_3/Al(Mg)	Mg spinel	Ductile[5]
Al_2O_3/Ti(Ta)	γ-TiAl α_2-TiAl σ	Residual Tension In Reaction Products[9,10]

REFERENCES

[1] See *Metal-Ceramic Interfaces* (Ed. M. Rühle *et al.*) Pergamon Press, Exeter, 1990.

[2] A.G. Evans, B.J. Dalgleish, P.G. Charalambides and M. Rühle, *Mat. Sci. Eng.*, **A126** (1990) 53.

[3] M.-Y. He and A.G. Evans, *Acta Metall. Mater.*, in press.

[4] B.J. Dalgleish, M.C. Lu and A.G. Evans, *Acta Metall.*, **36** (1988) 2029.

[5] B.J. Dalgleish, K.P. Trumble and A.G. Evans, *Acta Metall.*, **37** (1989) 1923.

[6] B.D. Flinn, F.W. Zok and A.G. Evans, to be published.

[7] I.E. Reimanis, B.J. Dalgleish, M. Brahy, M. Rühle and A.G. Evans, *Acta Metall. Mater.*, **38** (1990) 2645.

[8] I.E. Reimanis, B.J. Dalgleish and A.G. Evans, *Acta Metall. Mater.*, in press.

[9] M.-Y. He, A. Bartlett, A.G. Evans and J.W. Hutchinson, *J. Am. Ceram. Soc.*, **74** (1991) 187.

[10] A. Bartlett and A.G. Evans, to be published.

[11] P.G. Charalambides, H.C. Cao, J. Lund and A.G. Evans, *Mech. of Mtls.*, **8** (1990) 269.

[12] Z. Suo and J.W. Hutchinson, *Appl. Mech. Reviews*, **28** (1991) in press.

[13] M.-Y. He and J.W. Hutchinson, *J. Appl. Mech.*, **56** (1989) 270.

[14] A.G. Evans, M.-Y. He, B.J. Dalgleish and J.W. Hutchinson, *Acta Metall.*, **37** (1989) 3249.

[15] H.C. Cao and A.G. Evans, *Mech. of Mtls.*, **7** (1989) 295.

[16] K.M. Liechti and .'.S. Chan, *J. Appl. Mech.*, (1991) in press.

[17] H. Jensen, J.W. Hutchinson and K.S. Kim , *Intl. Jnl. Solids Structures*, **26** (1990) 1099.

[18] P.G. Charalambides, J. Lund, A.G. Evans and R.M. McMeeking, *J. Appl. Mech.*, **111** (1989) 77.

[19] A.G. Evans and F.W. Zok, *Composite Science and Technology*, **42** (1991) 3.

[20] M. Rühle and A.G. Evans, Mater. Research Society, Proc **120** (1988) 293.

[21] R. Hill, *The Mattematerial Theory of Plasticity*, Clarendon Press, Oxford (1950).

[22] B. Budiansky, J.W. Hutchinson and S. Slutsky, *Mechanics of Solids* (Eds., H.G. Hopkins and M.J. Sewell), Pergamon, Oxford (1982) p. 1.

[23] Y. Huang, J.W. Hutchinson and V. Tvergaard, *J. Mech. Phys. Solids*, **39** (1991) 223.

[24] A. Varias, Z. Suo and F. Shih, *J. Mech. Phys. Solids*, **39** (1991) 963.

[25] R.M. McMeeking, *J. Mech. Phys. Solids*, **25** (1977) 357.

[26] M.S. Hu, H.C. Cao, J. Yang and A.G. Evans, to be published.

[27] M. De Graef, B.J. Dalgleish, M. Turner and A.G. Evans, *Acta Metall. Mater.*, this volume.

[28] H.F. Fischmeister, W. Mader, M. Gibbesch and S. Elssner, *Mat. Res. Soc. Proc.*, **122** (1988) 529.

[29] R.O. Ritchie, R.M. Cannon and B.J. Dalgleish, *Acta Metall. Mater.*, this volume.

[30] S.M. Weiderhorn, *J. Am. Ceram. Soc.*, **52** (1969) 485.

[31] G. Bao, B. Fan and A.G. Evans, *Mech. of Mtls.*, in press.

[32] J.R. Rice, to be published.

[33] Z. Suo and J.W. Hutchinson, *Applied Mech. Reviews* (1991) in press.

[34] J.B. Davis, E. Bischoff, J.P.A. Löfvander and A.G. Evans, to be published.

[35] R.M. Cannon, private communication.

FIGURE CAPTIONS

Fig. 1. A schematic indicating the various fracture mechanisms that occur in metal/ceramic interfaces.

Fig. 2. A diagram indicating the region in which cracks deviate from the interface, using fracture energy/phase angle space.

Fig. 3. Sandwich test specimens suitable for interface fracture energy measurements.

Fig. 4. A void on the fracture surface between Pt and Al_2O_3 and the AFM trace that can be used to obtain the dihedral angle.

Fig. 5. Fracture surfaces formed when the interface fails by a ductile mechanism, obtained for the Al/Al_2O_3 system: a) matching fracture surfaces at low magnification b) a high resolution view of the Al_2O_3 side of the fracture surface indicating a network of Al attached to this surface caused by void coalescence (see Fig. 1): note that each element in the network forms around a three-grain junction in the Al_2O_3, suggesting that these are the void nucleating features.

Fig. 6. Variations in the hydrostatic stress ahead of the crack for a range of metal layer thicknesses.

Fig. 7. Trends in interface fracture energy with metal layer thickness when fracture occurs by a ductile mechanism.

Fig. 8. Incidence of ductile debonding between Al alloy-reinforced Al_2O_3 a) extensive debonding in materials with a 2 μm grain size b) absence of debonding in a material with 20 μm grain size.

Fig. 9. Fracture surfaces observed *in situ* in the optical microscope for cracks extending at the Au/Al_2O_3 interface a) moist air (RH 100%); b) dry air indicating plastic distortion.

Fig. 10. Interface fracture resistances for the Al_2O_3/Au interface.

Fig. 11. Alternating debonding at the two interfaces formed in a thin layer between Au and Al_2O_3.

Fig. 12. Slip steps on Au fracture surface associated with ligaments that bridge the crack surface, indicative of extensive plastic strain.

Fig. 13. The effect of removing the ligaments by stress corrosion on the resistance curve. Note that after the ligaments have been removed, the original resistance curve is duplicated.

Fig. 14. Simulated resistance curves based on large-scale bridging by metal ligaments: experimental results are superposed.

Fig. 15. A schematic of the features around an interface crack that fails by brittle debonding.

Fig. 16. Diffusion bonded interface in the Pt/Al_2O_3 system a) no interphase with extensive unbonded area b) crystalline SiO_2 interphase with some residual voids c) amorphous silicate interphase that forms a network at the junction between the Pt grain boundaries and the Al_2O_3 (see Fig. 20).

Fig. 17. Trends in Γ_i with metal layer thickness for interface between Au or Pt and commercial grade Al_2O_3.

Fig. 18. The ceramic side of a fracture interface between Pt and commercial grade Al_2O_3.

Fig. 19. TEM cross section of Pt/Al_2O_3 bond with SiO_2 (cristobalite) interphase.

Fig. 20. Ridges of amorphous Ca-silicate on the Al_2O_3 side of a fracture surface of Pt/Al_2O_3 bond.

Fig. 21. Interface debonding mechanism in Pt/Al_2O_3 interface. Decohesion of amorphous phase ridges (a) and (b). Progressive debonding of the intervening interface is schematically represented in (c).

Fig. 22. The Ti-Ta-Al ternary phase diagram.

Fig. 23. Periodic microcracks formed within the intermetallic reaction product layer during interface fracture in the $Al_2O_3/Ti(Ta)$ system.

Fig. 24. The microcrack mechanism of interface fracture with brittle reaction products subject to residual tensile stress.

Fig. 25. Oxide interphase formation in Al_2O_3 refractory metal bonds a) Mo/Al_2O_3 with MoO_2 interphase b) Cr/Al_2O_3 with Cr_2O_3 interphase: the oxygen needed to form the oxide comes from solution in the refractory metal. Debonding occurs at the oxide/metal interface.

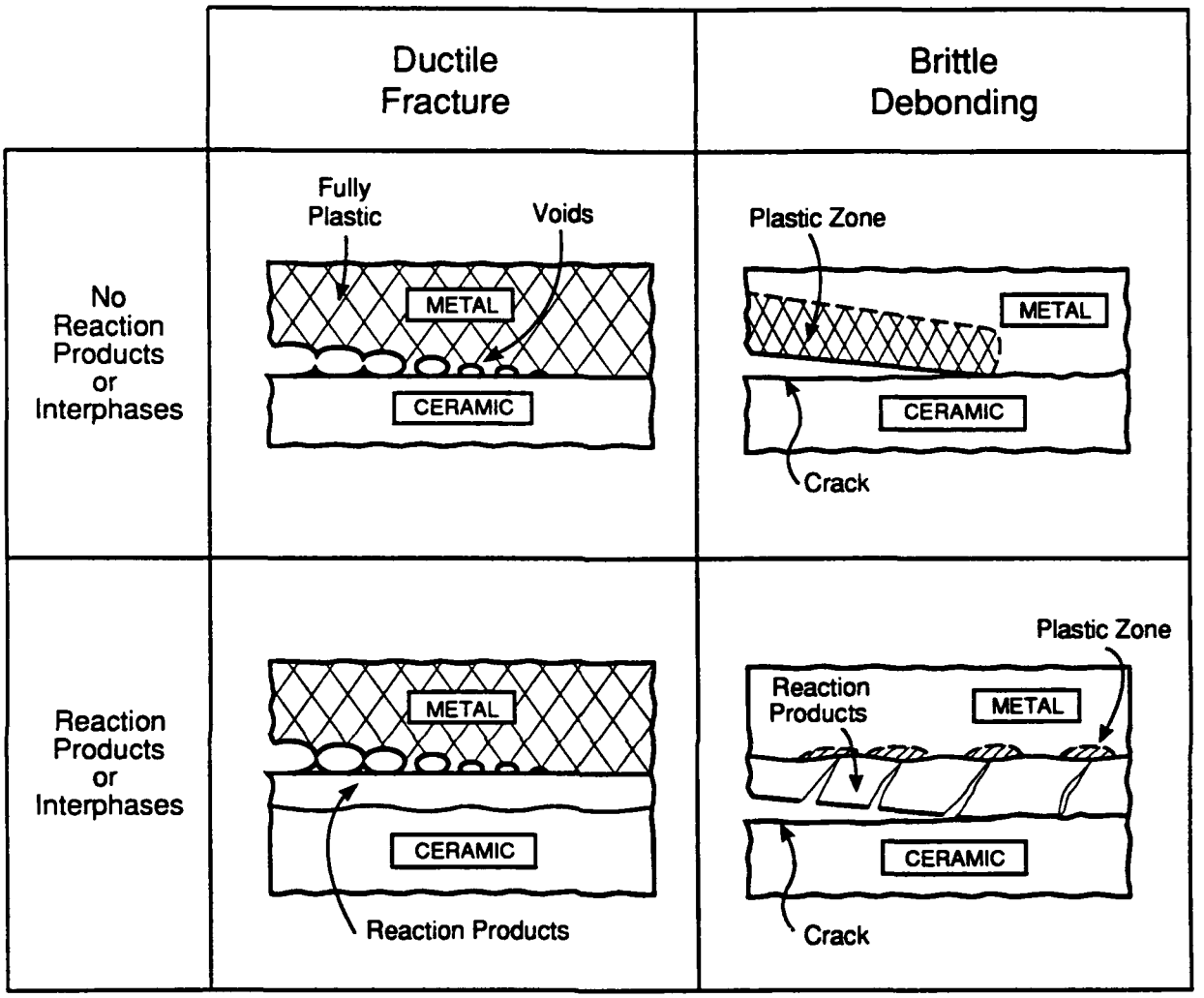

Fig. 1. A schematic indicating the various fracture mechanisms that occur in metal/ceramic interfaces.

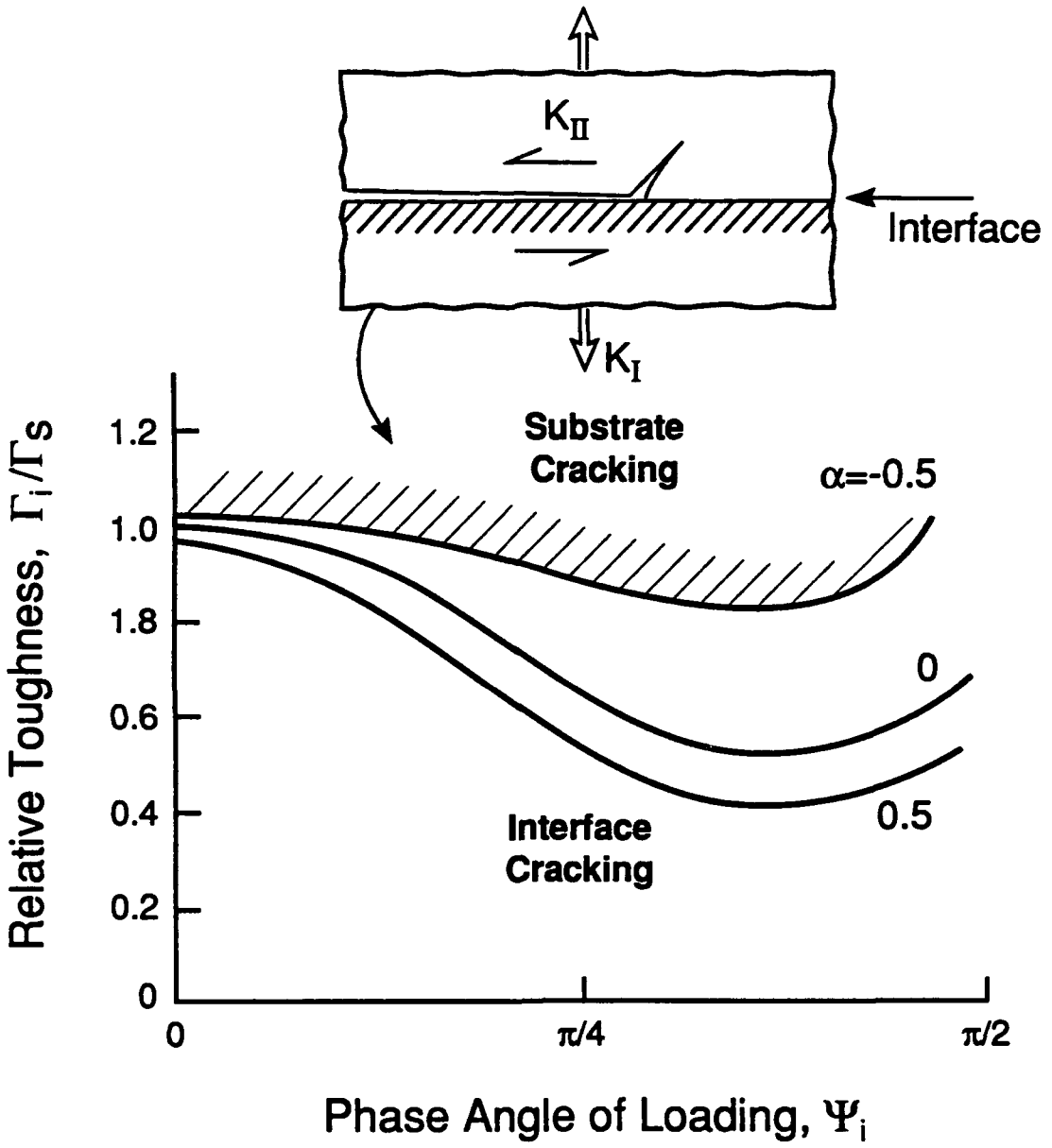

Fig. 2. A diagram indicating the region in which cracks deviate from the interface, using fracture energy/phase angle space.

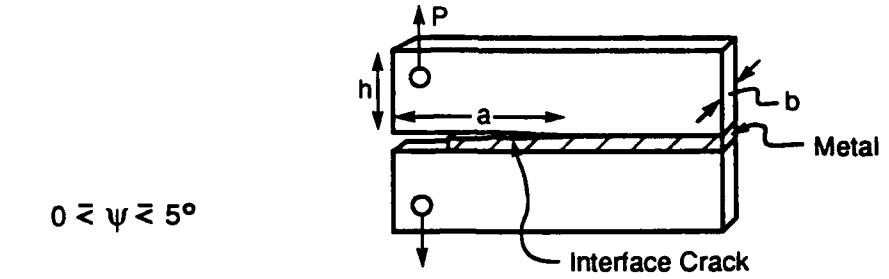

$0 \lesssim \psi \lesssim 5°$

a) **Double Cantilever Beam**

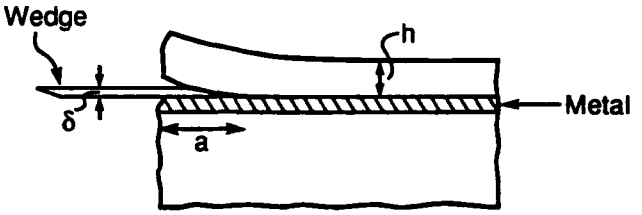

$\psi \approx -50°$

b) **Wedge Loaded Peel Test**

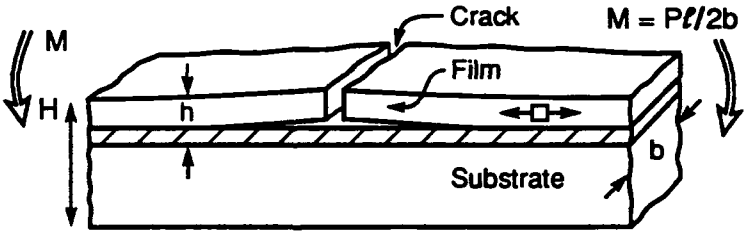

$\psi \approx 50°$

c) **Mixed Mode Flexure**

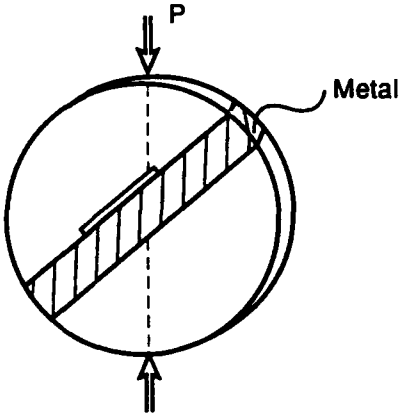

$0 \lesssim \psi \lesssim 90°$

c) **Brasil Specimen**

Fig. 3. Sandwich test specimens suitable for interface fracture energy measurements.

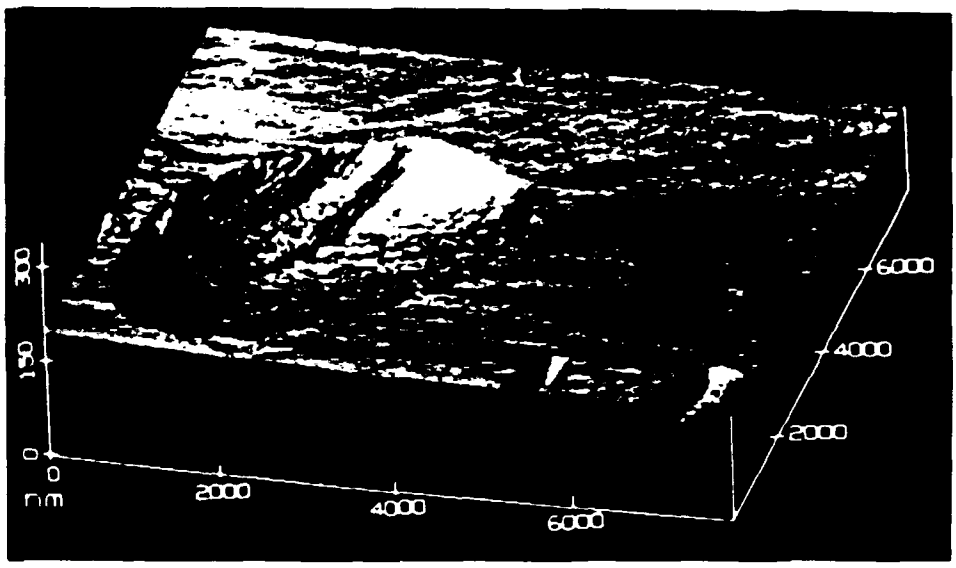

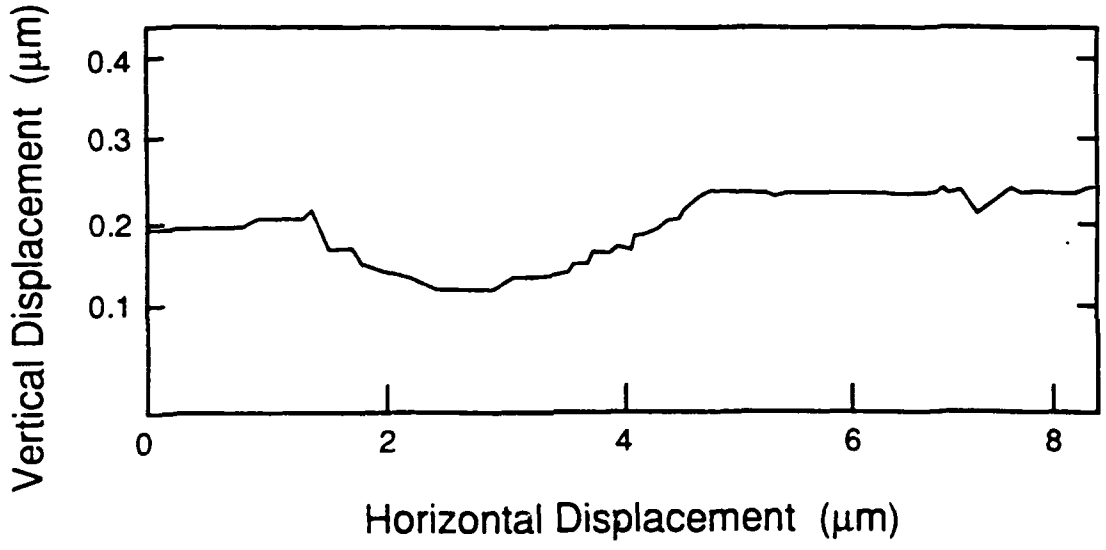

Fig. 4. A void on the fracture surface between Pt and Al_2O_3 and the AFM trace that can be used to obtain the dihedral angle.

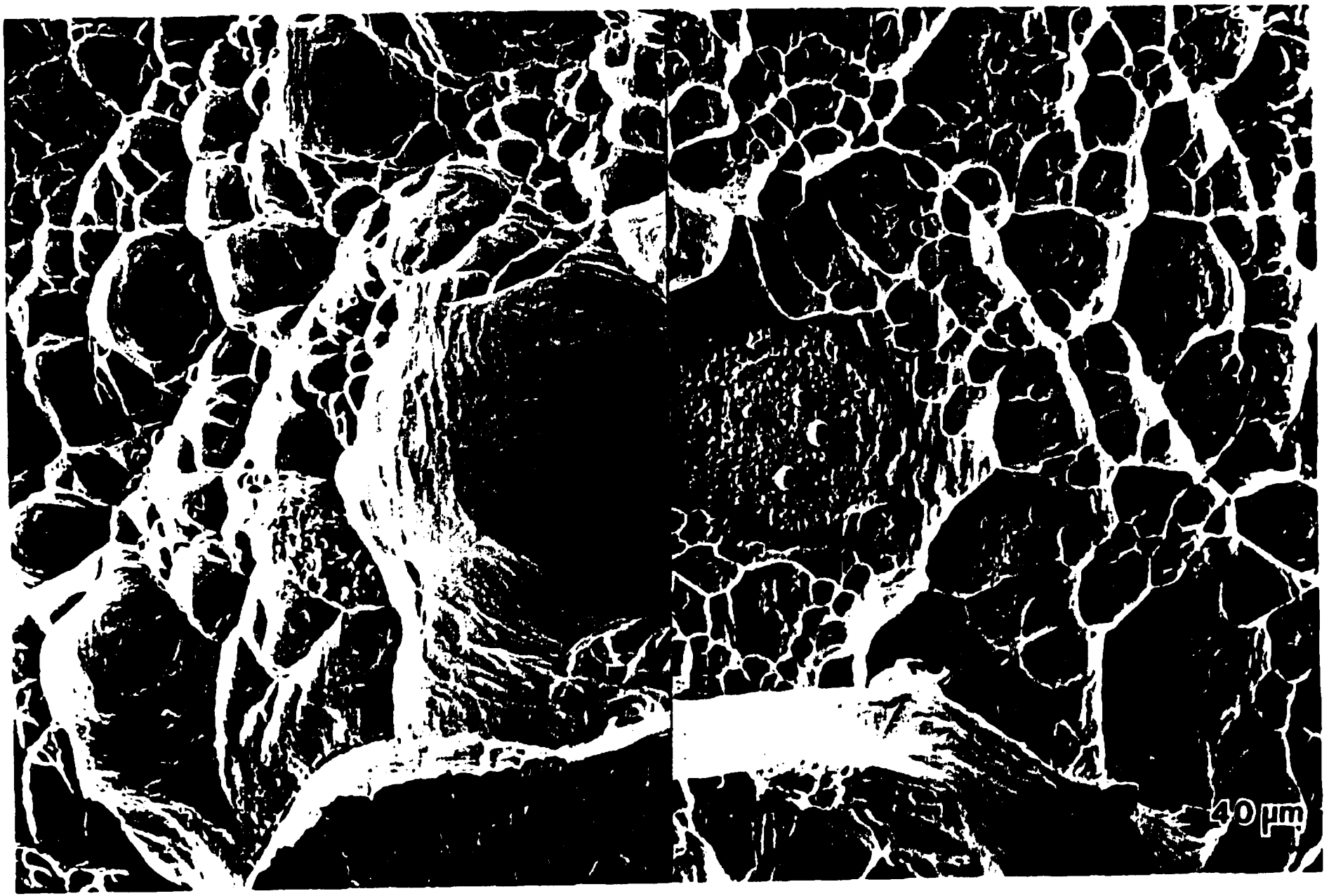

Fig. 5. Fracture surfaces formed when the interface fails by a ductile mechanism, obtained for the Al/Al_2O_3 system: a) matching fracture surfaces at low magnification

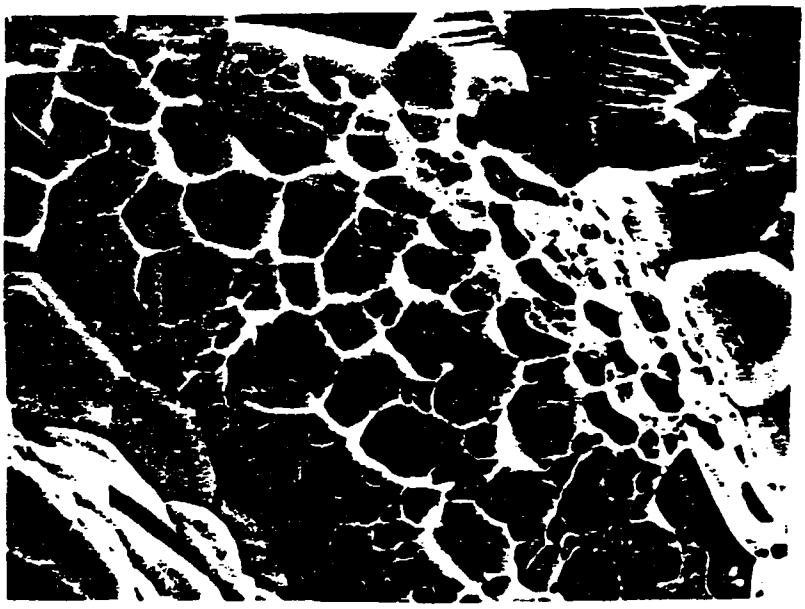

Fig. 5. Fracture surfaces formed when the interface fails by a ductile mechanism, obtained for the Al/Al_2O_3 system: b) a high resolution view of the Al_2O_3 side of the fracture surface indicating a network of Al attached to this surface caused by void coalescence (see Fig. 1): note that each element in the network forms around a three-grain junction in the Al_2O_3, suggesting that these are the void nucleating freatures.

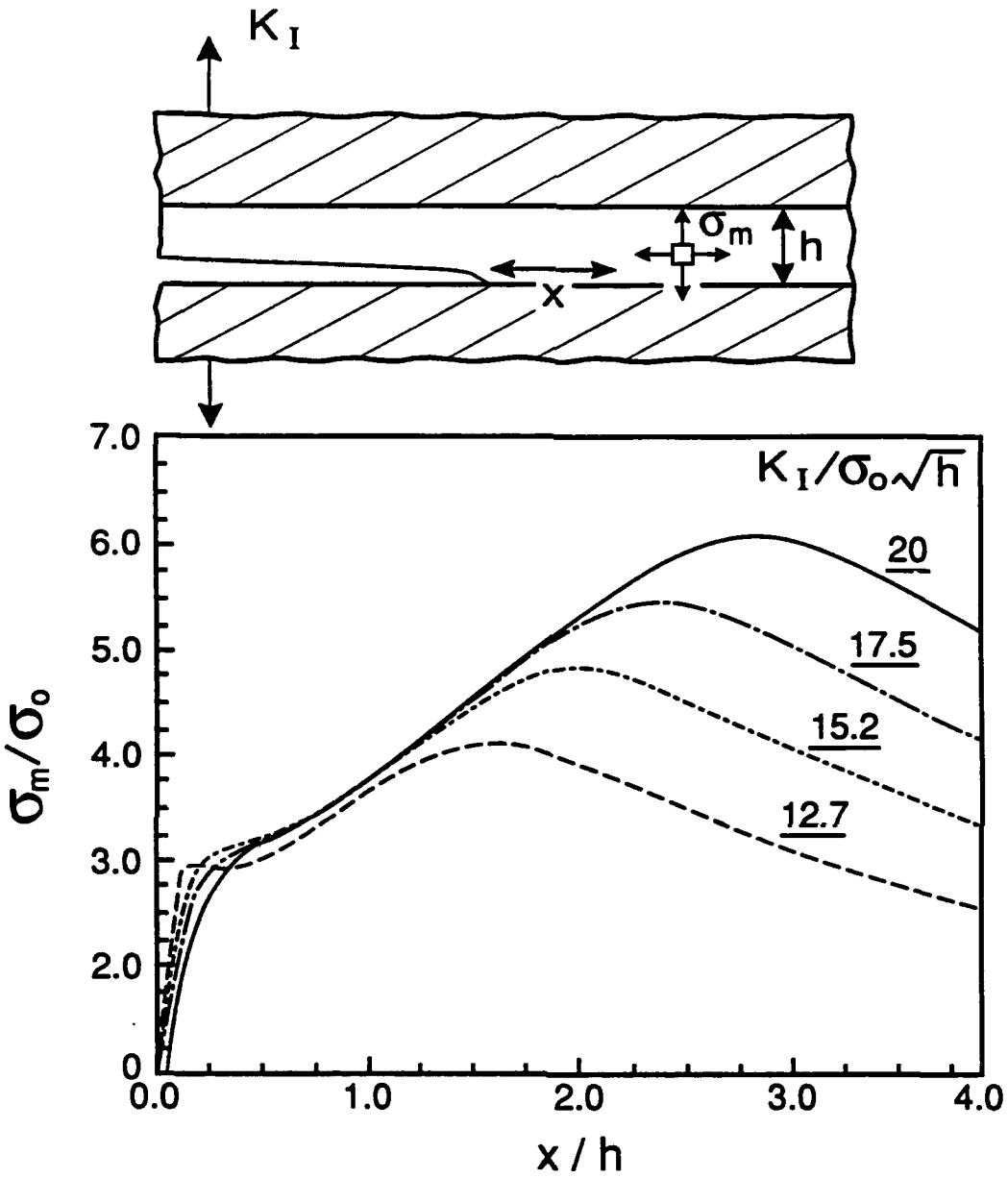

Fig. 6. Variations in the hydrostatic stress ahead of the crack for a range of metal layer thicknesses.

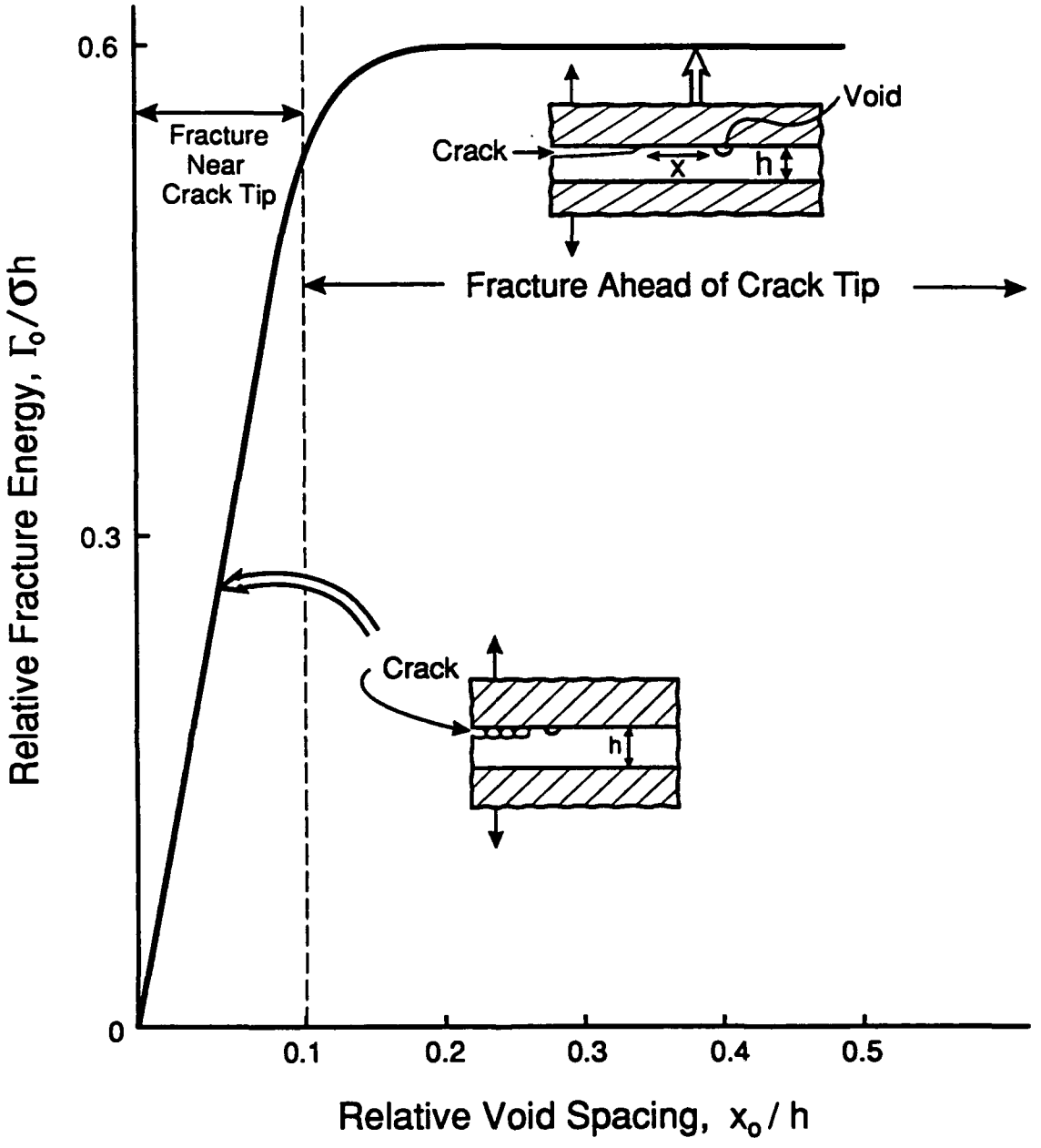

Fig. 7. Trends in interface fracture energy with metal layer thickness when fracture occurs by a ductile mechanism.

Fig. 8. Incidence of ductile debonding between Al allov-reinforced Al_2O_3 a) extensive debonding in materials with a 2 μm grain size.

Fig. 8. Incidence of ductile debonding between Al alloy-reinforced Al_2O_3 b) absence of debonding in a material wityh 20 μm grain size.

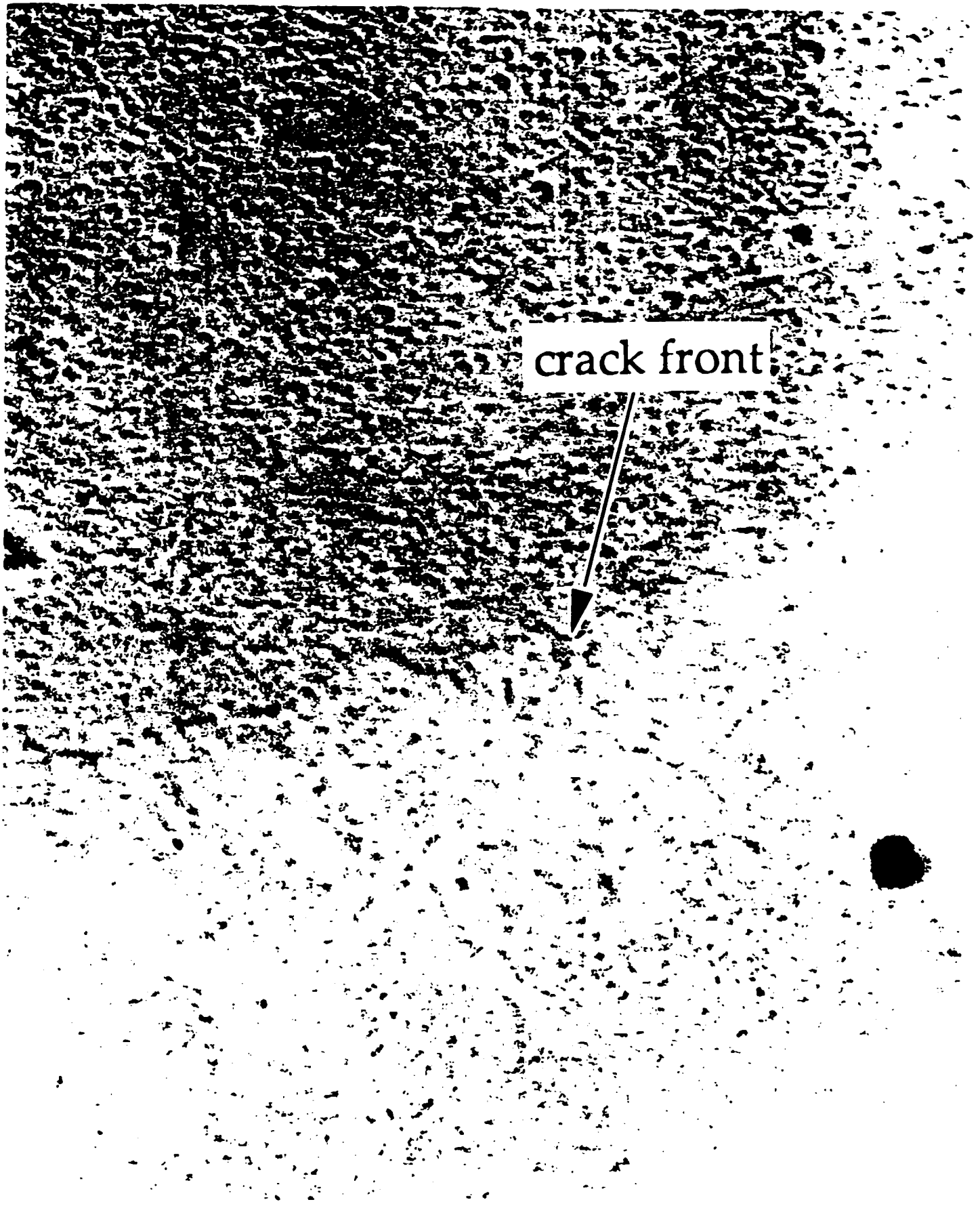

Fig. 9. Fracture surfaces observed *in situ* in the optical microscope for cracks extending at the Au/Al_2O_3 interface a) moist air (RH 100%);

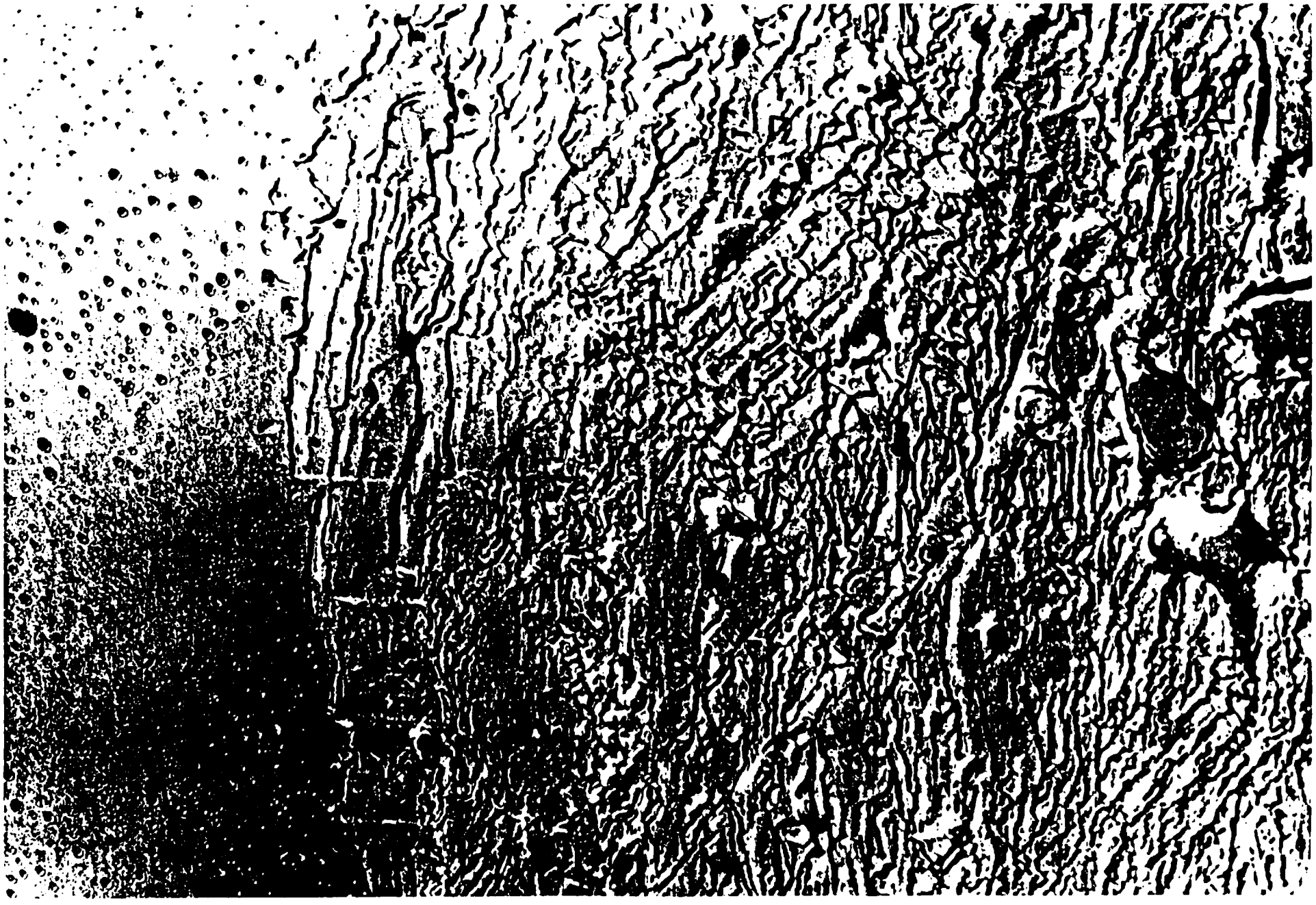

Fig. 9. Fracture surfaces observed *in situ* in the optical microscope for cracks extending at the Au/Al_2O_3 interface b) absence of debonding in a material with 20 μm grain size

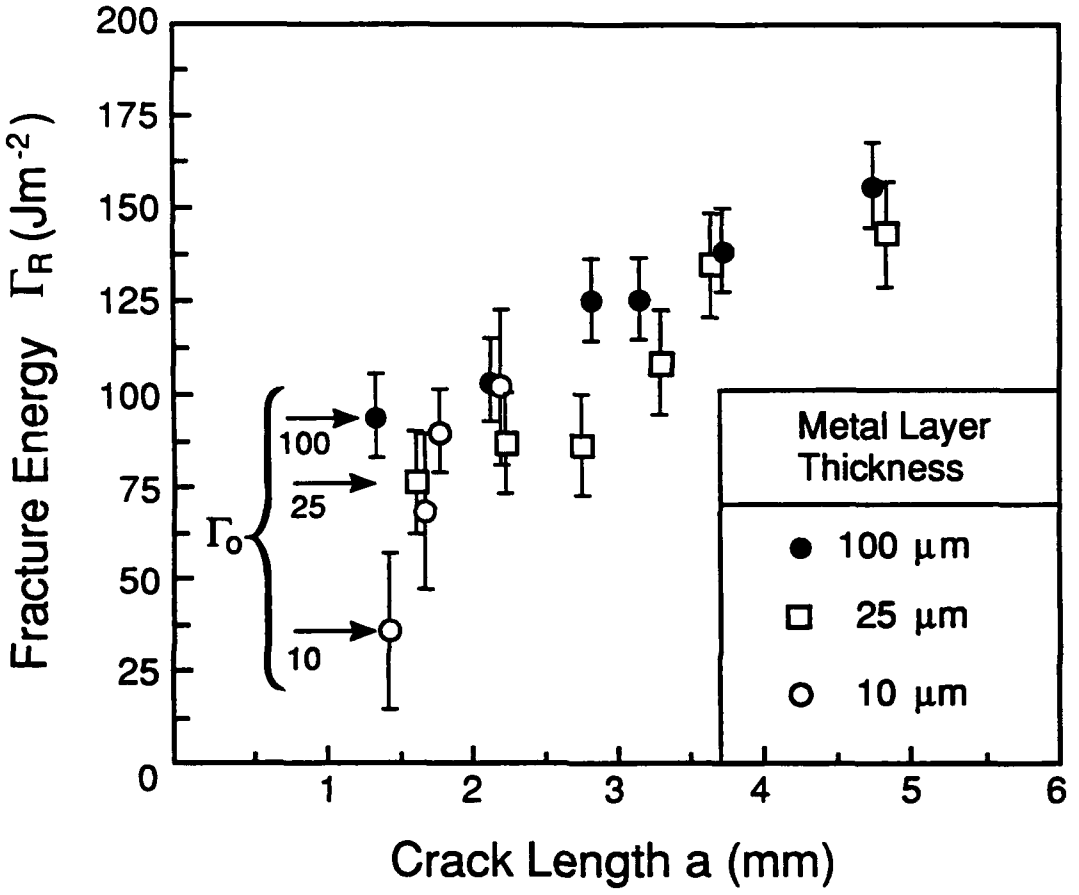

Fig. 10. Interface fracture resistances for the Al_2O_3/Au interface.

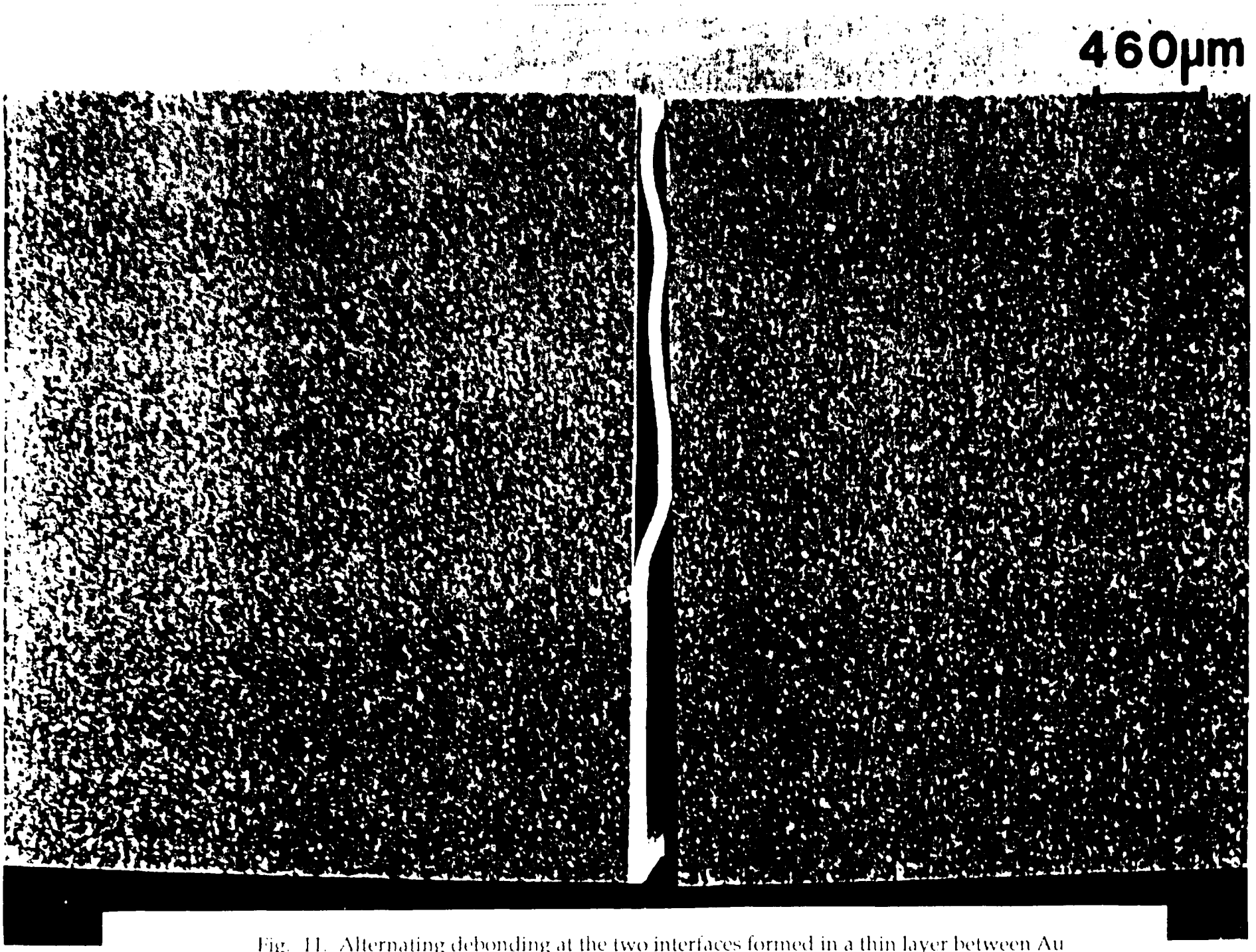

Fig. 11. Alternating debonding at the two interfaces formed in a thin layer between Au and Al

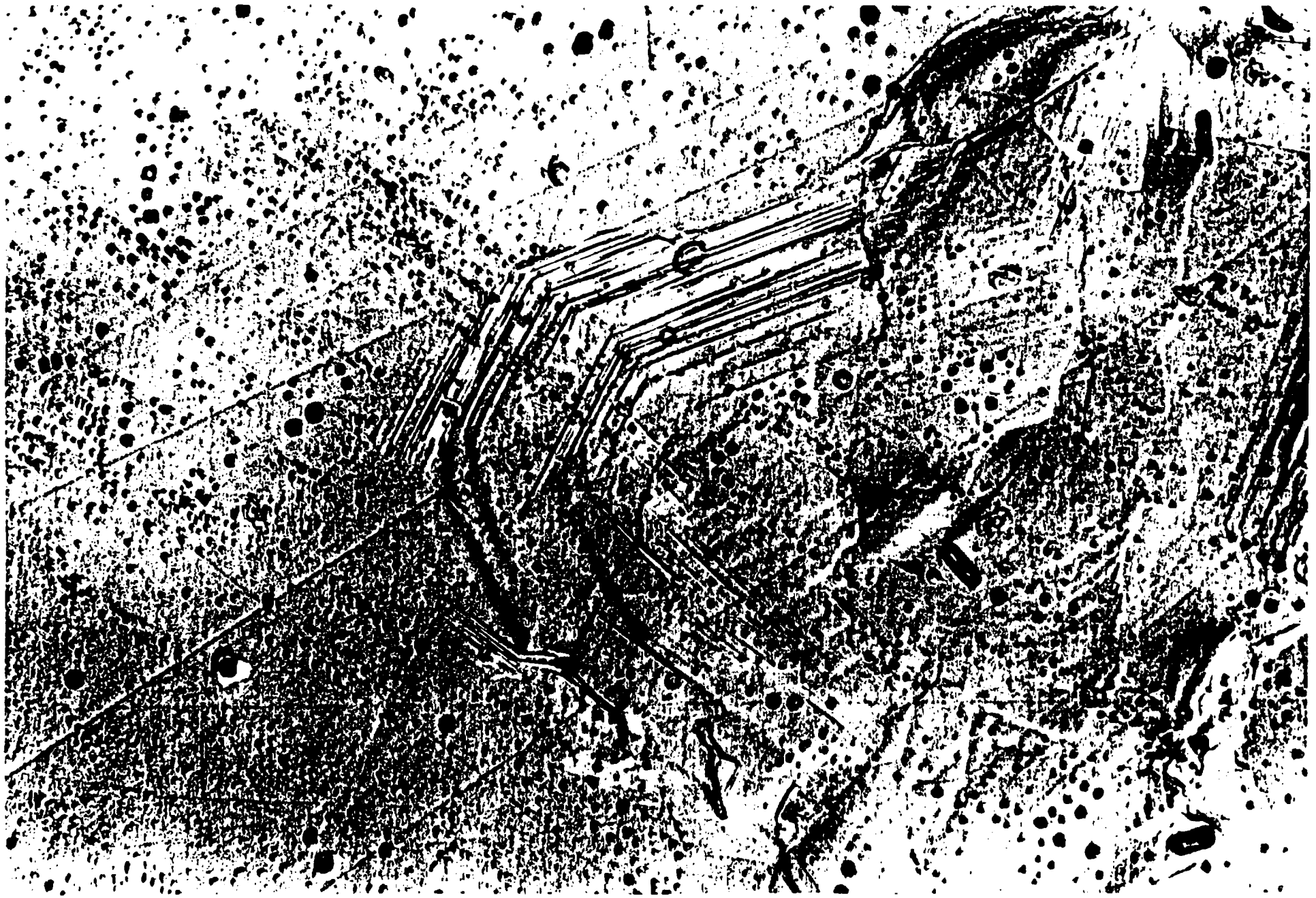

Fig. 12. Slip steps on Au fracture surface associated with ligaments that bridge the crack surface, indicative of extensive plastic strain.

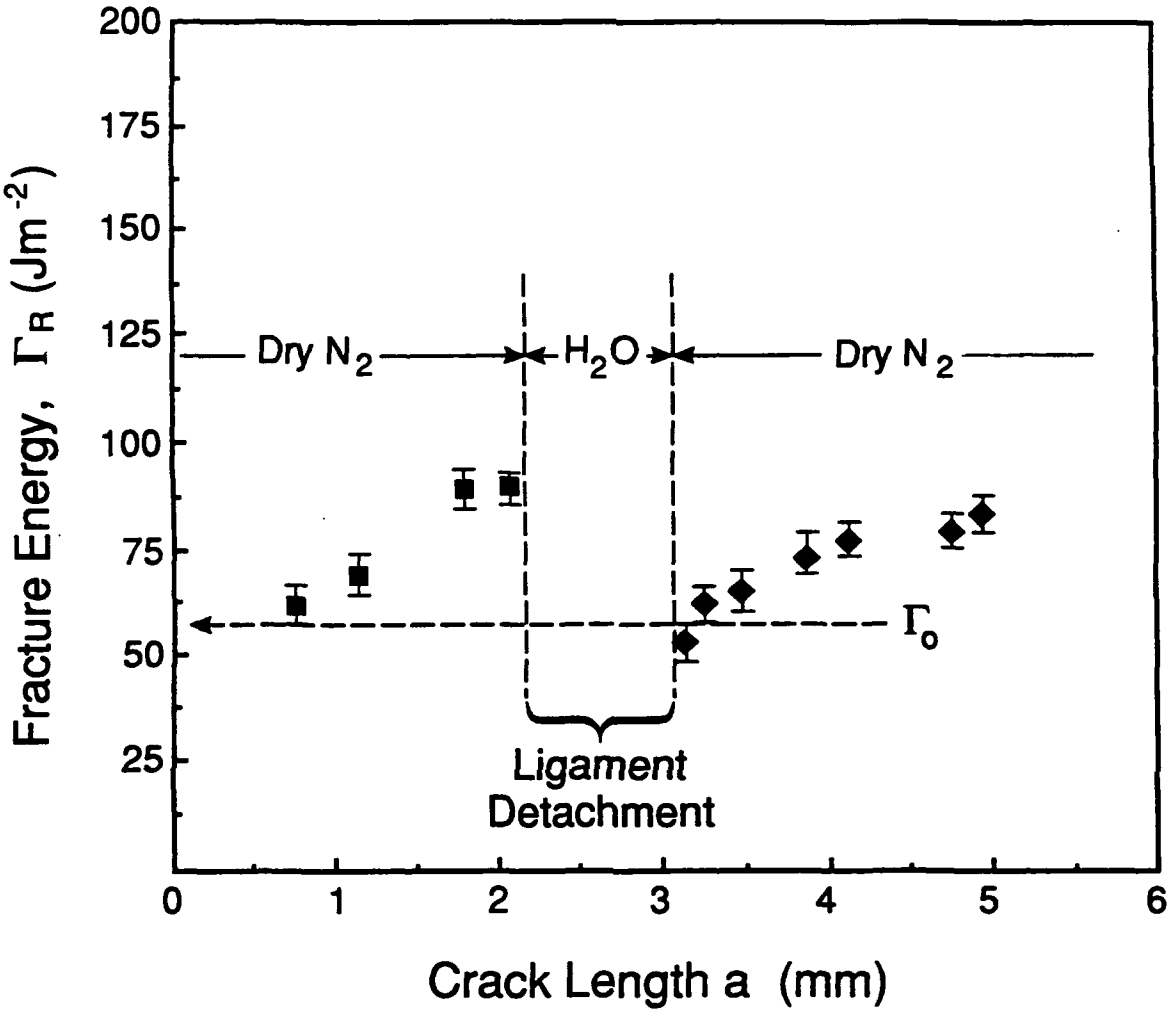

Fig. 13. The effect of removing the ligaments by stress corrosion on the resistance curve. Note that after the ligaments have been removed, the original resistance curve is duplicated.

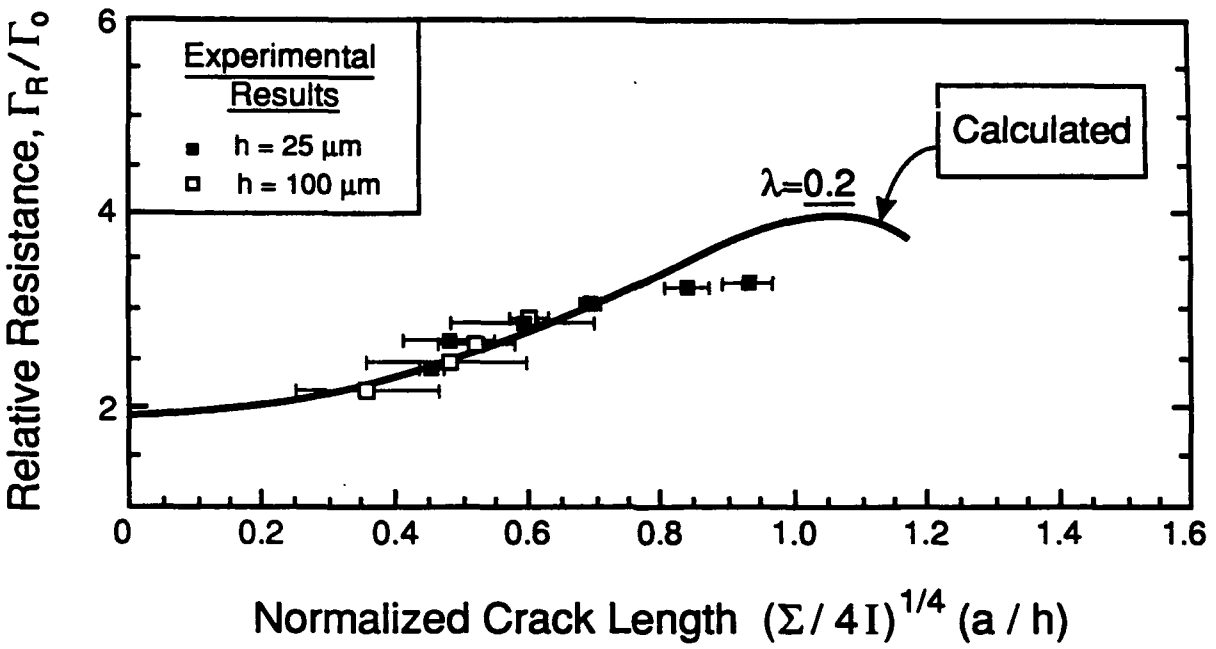

Fig. 14. Simulated resistance curves based on large-scale bridging by metal ligaments: experimental results are superposed.

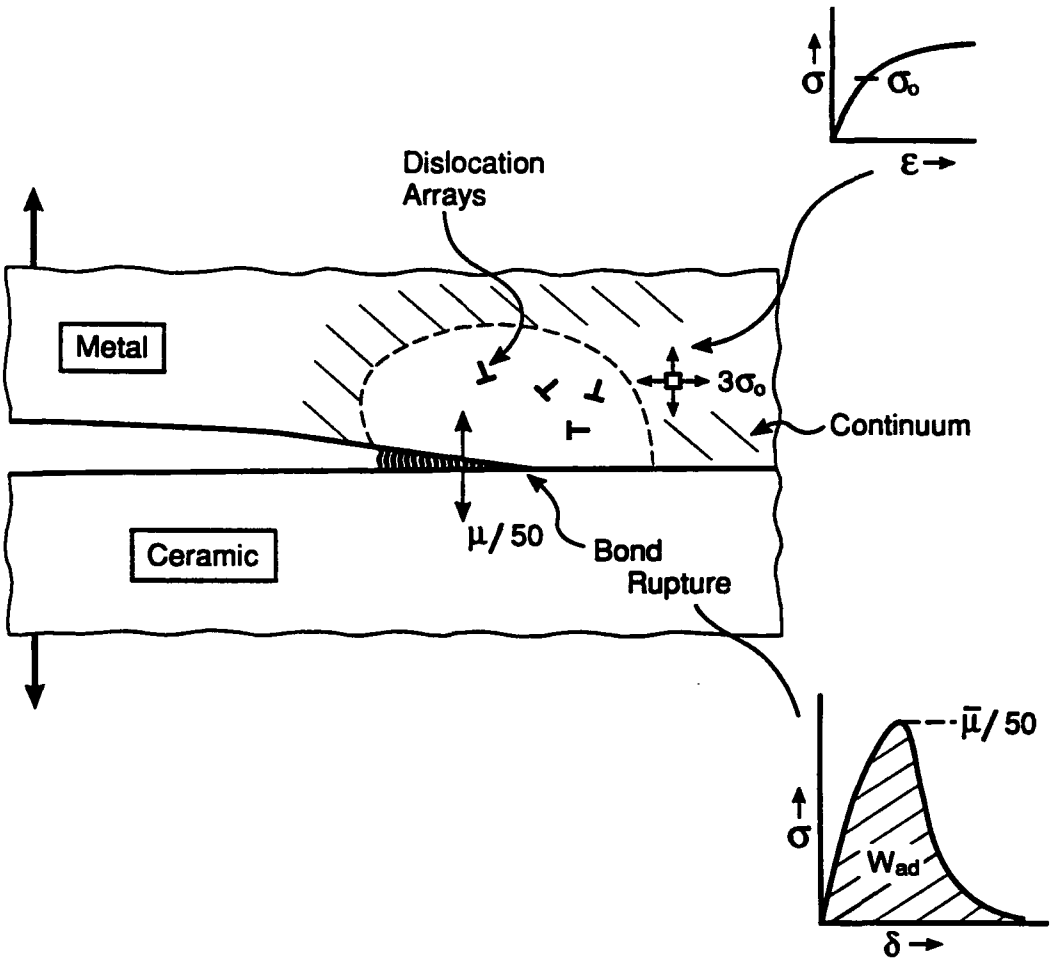

Fig. 15. A schematic of the features around an interface crack that fails by brittle debonding.

Fig. 16. Diffusion bonded interface in the Pt/Al_2O_3 system a) no interphase with extensive unbonded area.

Fig. 16. Diffusion bonded interface in the Pt/Al_2O_3 system b) crystalline SiO_2 interphase with some residual voids.

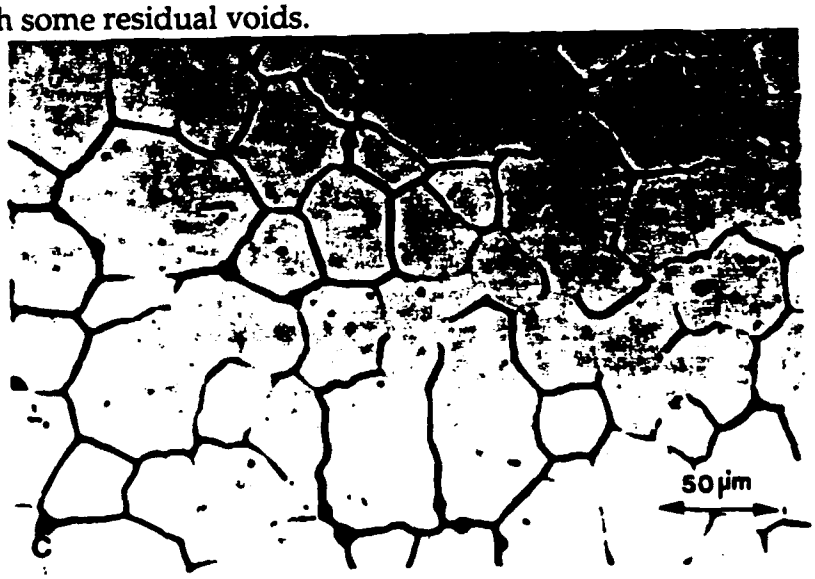

Fig. 16. Diffusion bonded interface in the Pt/Al_2O_3 system c) amorphous silicate interphase that forms a network at the junction between the Pt grain boundaries and the Al_2O_3 (see Fig. 20).

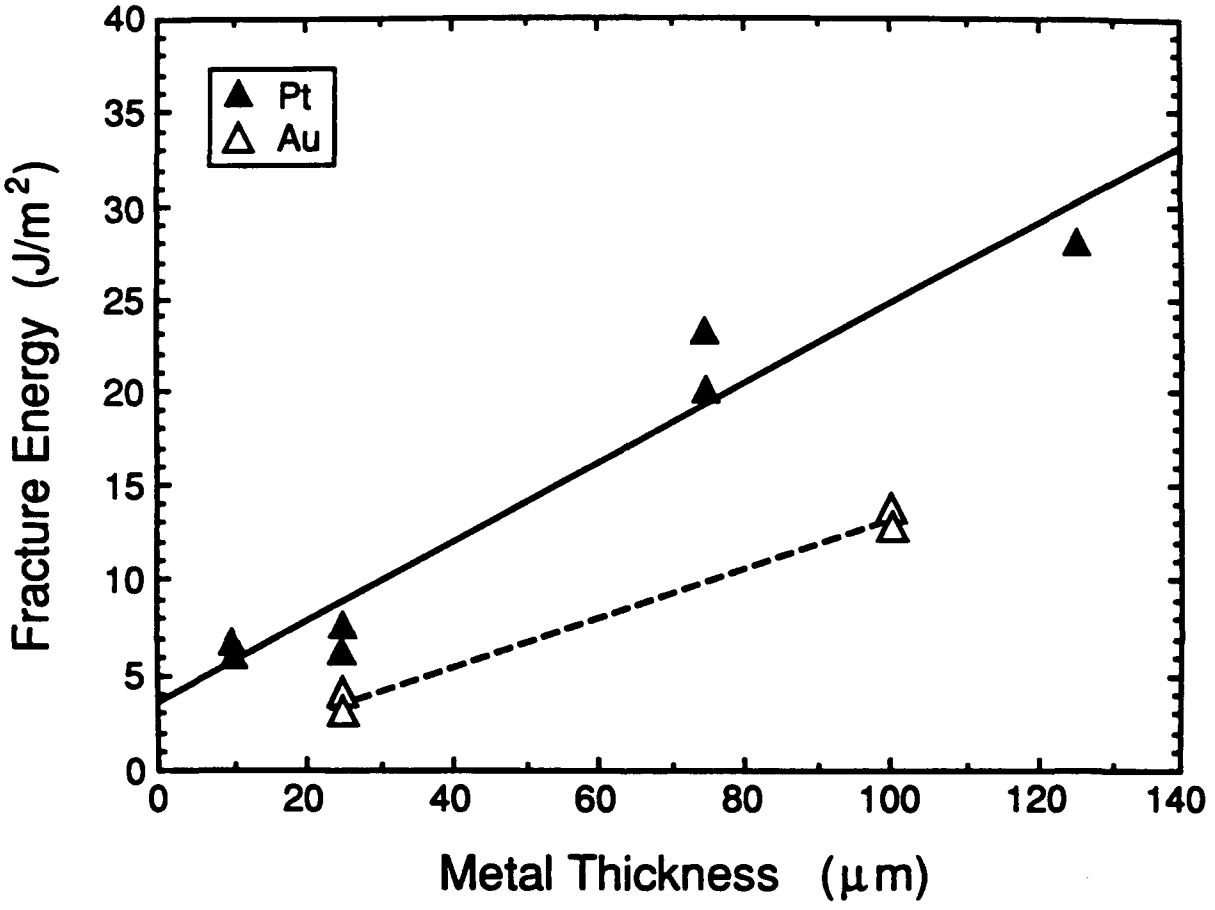

XBL 916-1215

Fig. 17. Trends in γ_i with metal layer thickness for interface between Au or Pt and commercial grade Al_2O_3.

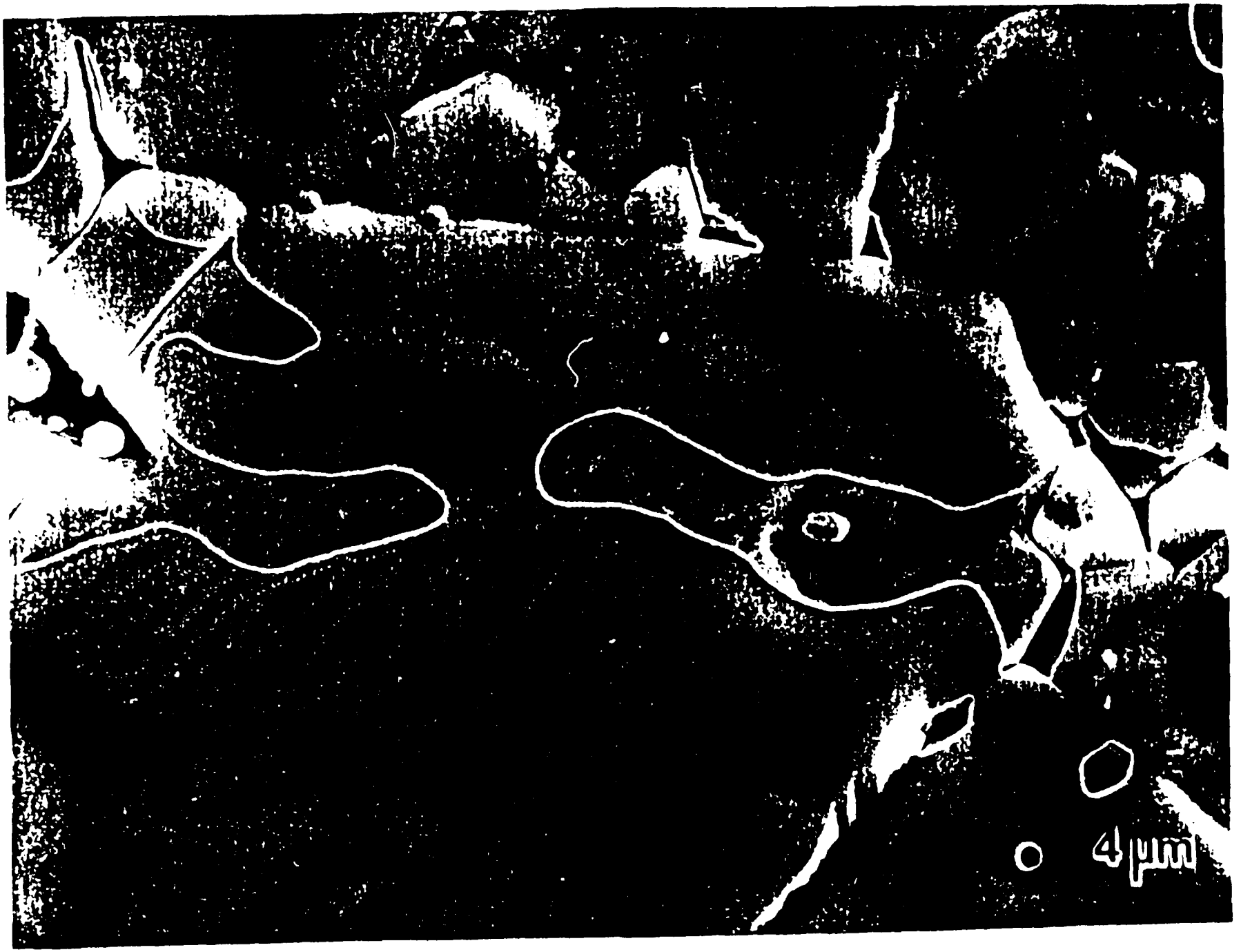

Fig. 18. The ceramic side of a fracture interface between Pt and commercial grade Al_2O_3.

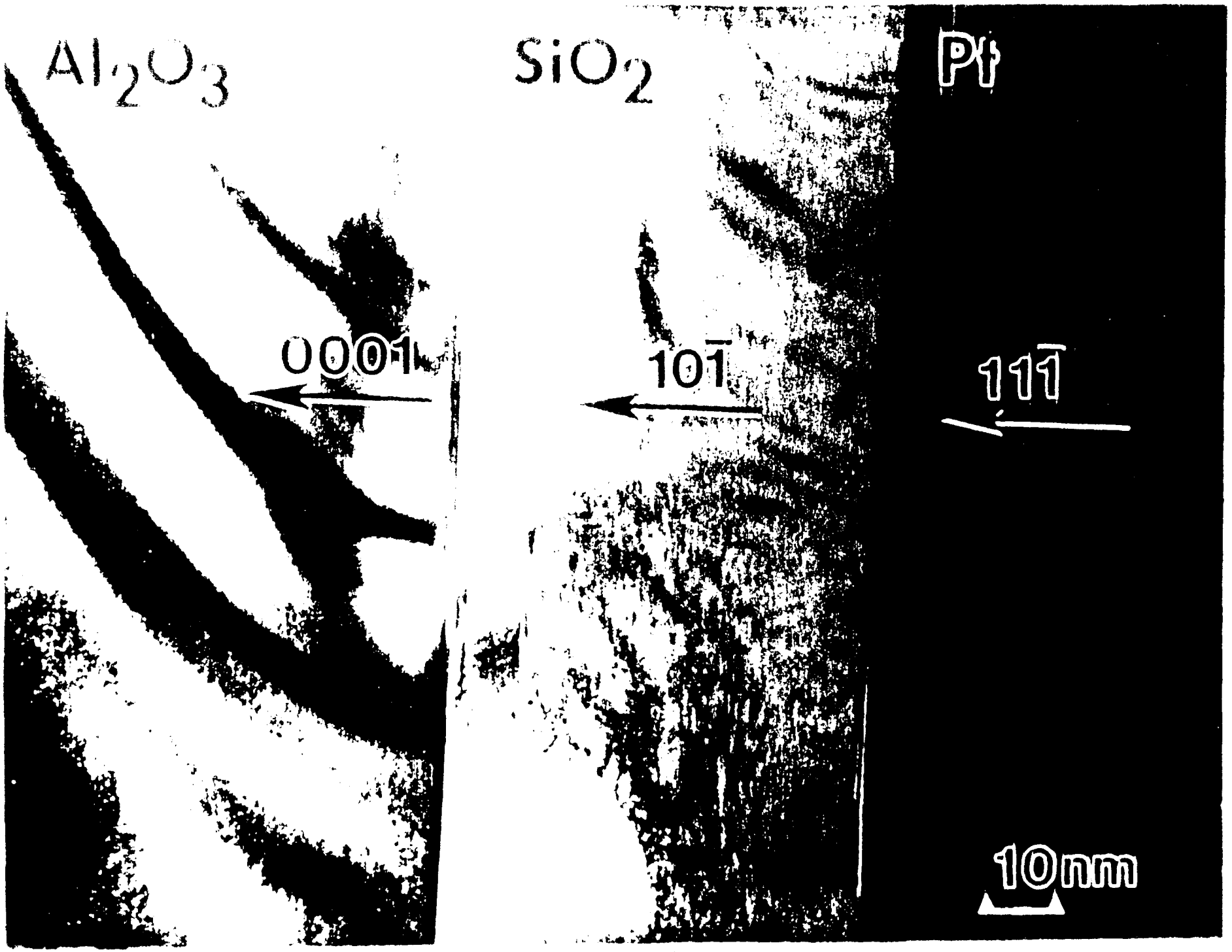
Al_2O_3
SiO_2
Pt
0001
$10\bar{1}$
$11\bar{1}$
10nm

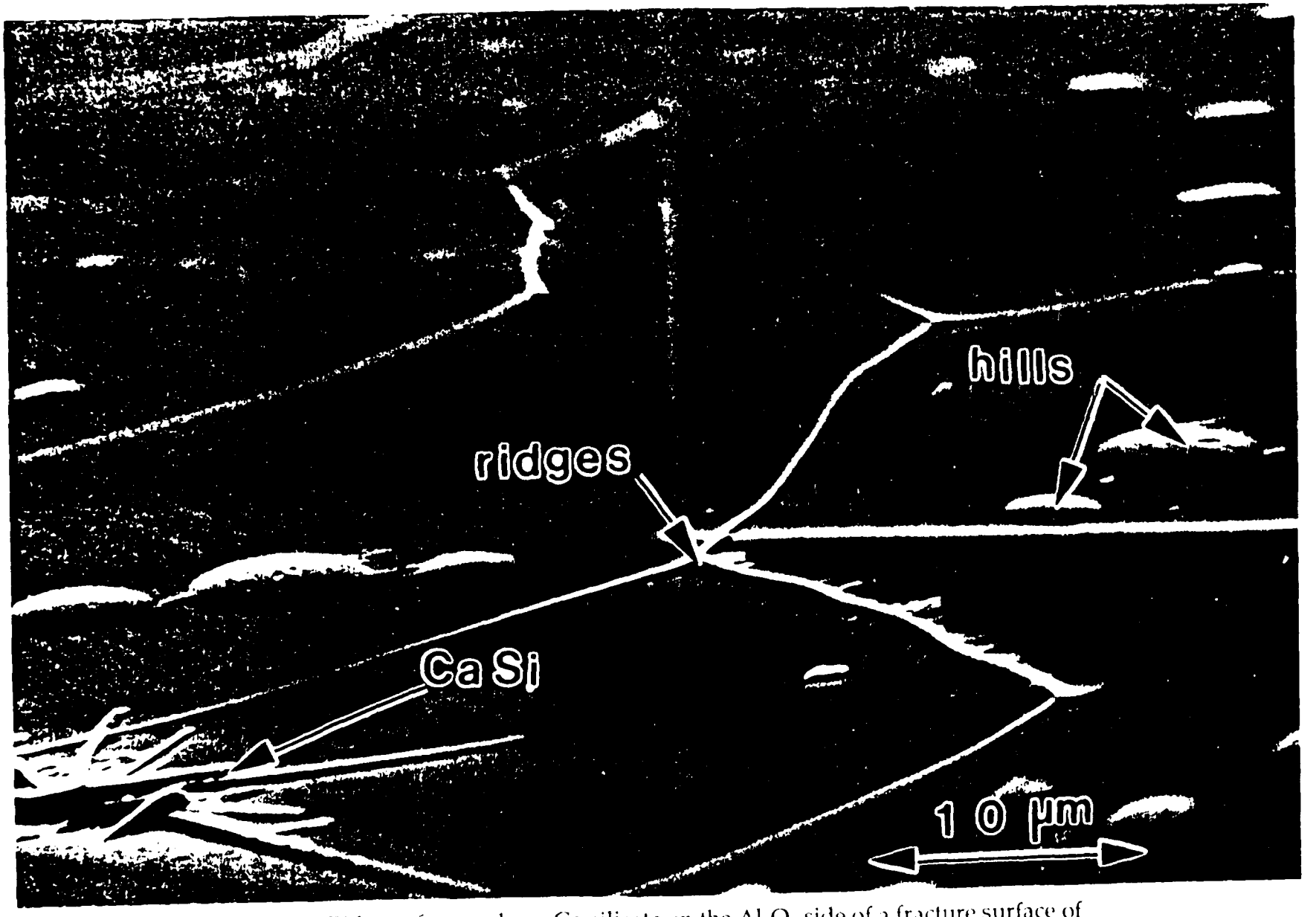

Fig. 20. Ridges of amorphous Ca-silicate on the Al_2O_3 side of a fracture surface of Pt/Al_2O_3 bond.

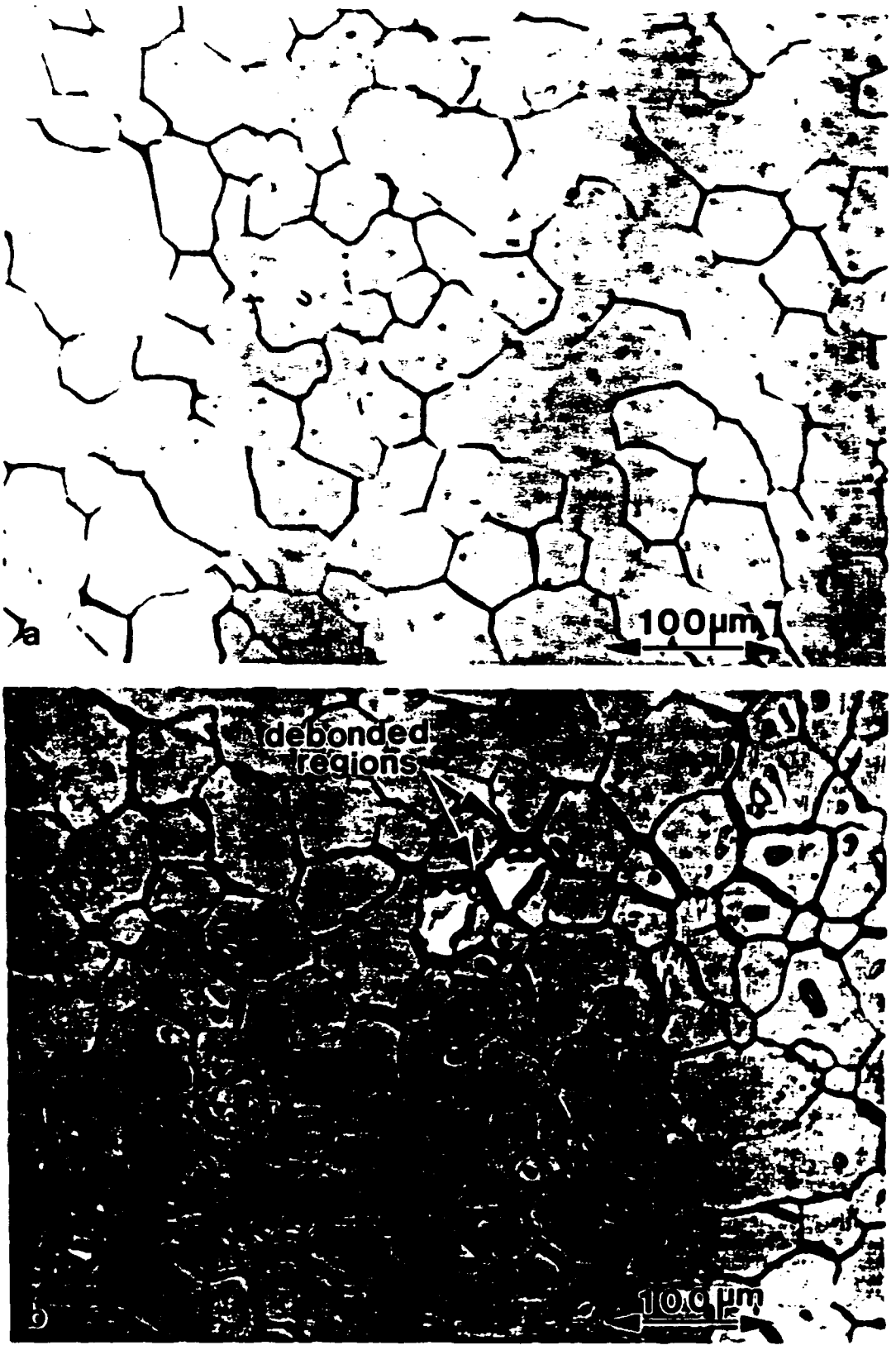

Fig. 21. Interface debonding mechanism in Pt/Al_2O_3 interface. Decohesion of amorphous phase ridges (a) and (b). Progressive debonding of the intervening interface is schematically represented in (c).

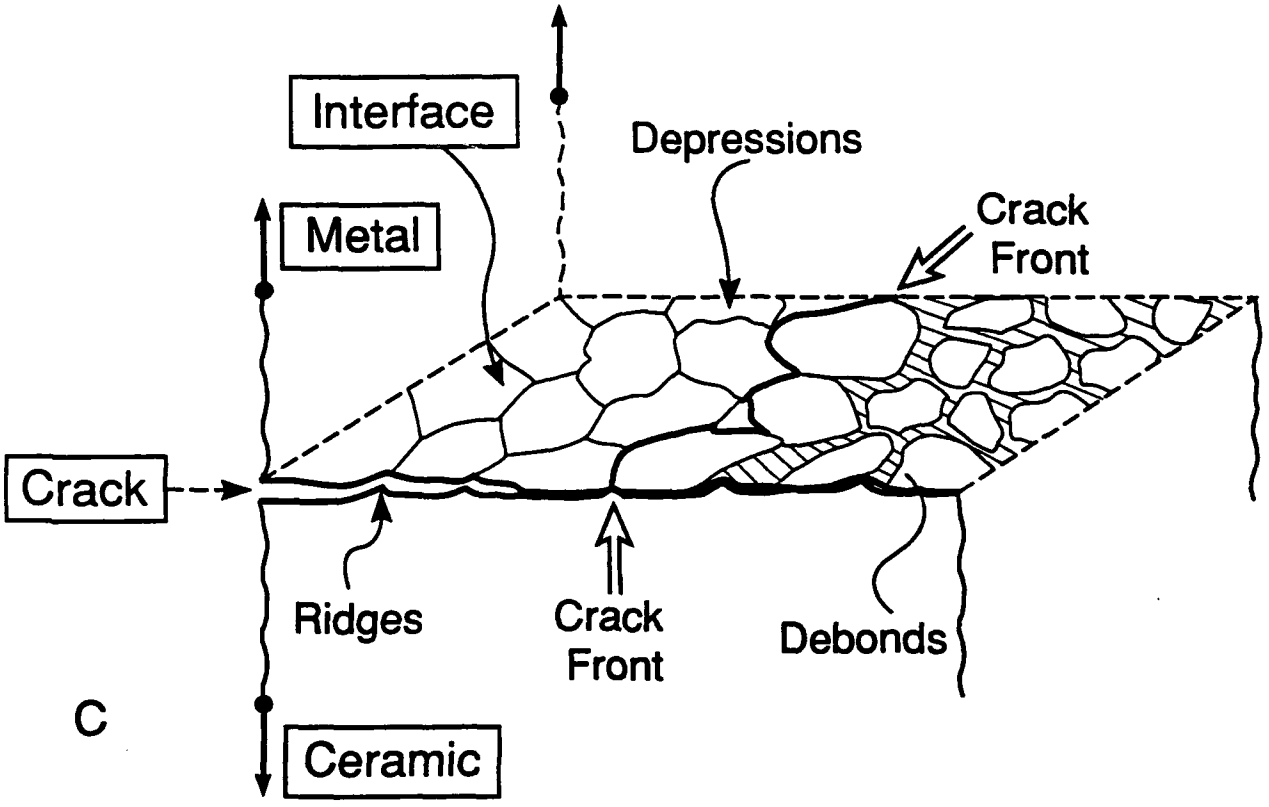

Fig. 21. Interface debonding mechanism in Pt/Al_2O_3 interface. Decohesion of amorphous phase ridges (a) and (b). Progressive debonding of the intervening interface is schematically represented in (c).

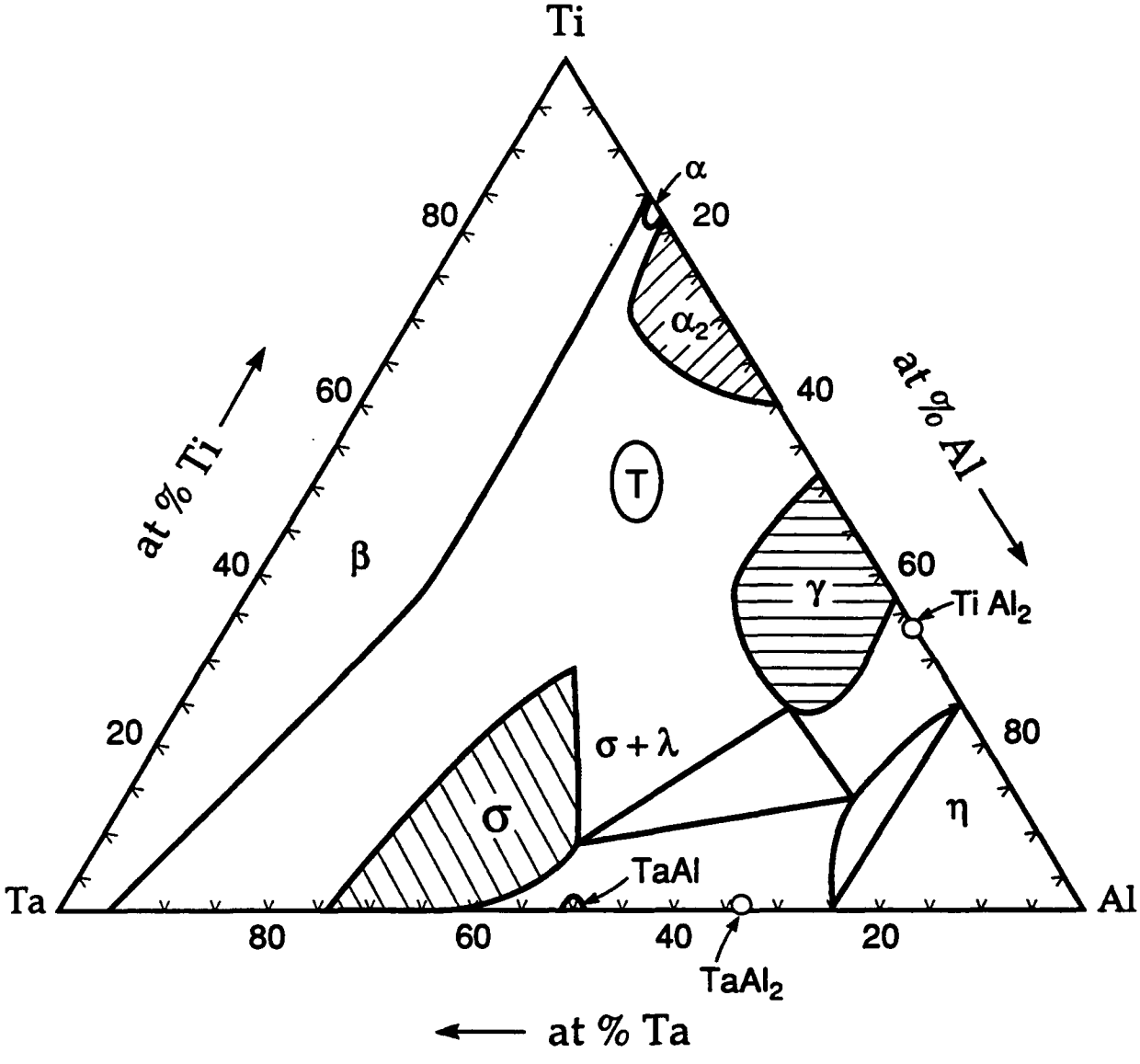

Fig. 22. The Ti-Ta-Al ternary phase diagram.

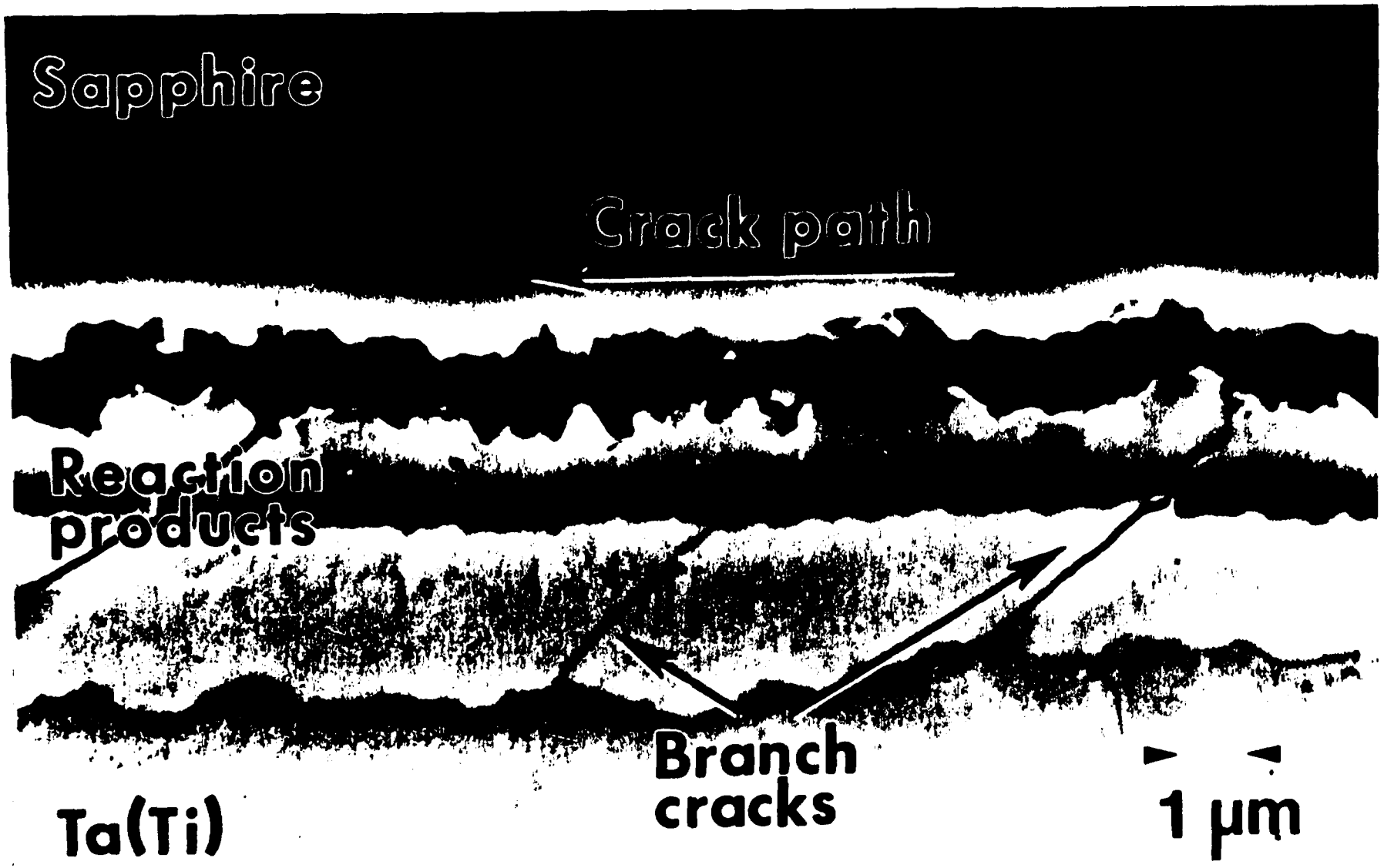

Fig. 23. Periodic microcracks formed within the intermetallic reaction prduct layer during interface fracture in the Al_2O_3/Ti(Ta) system.

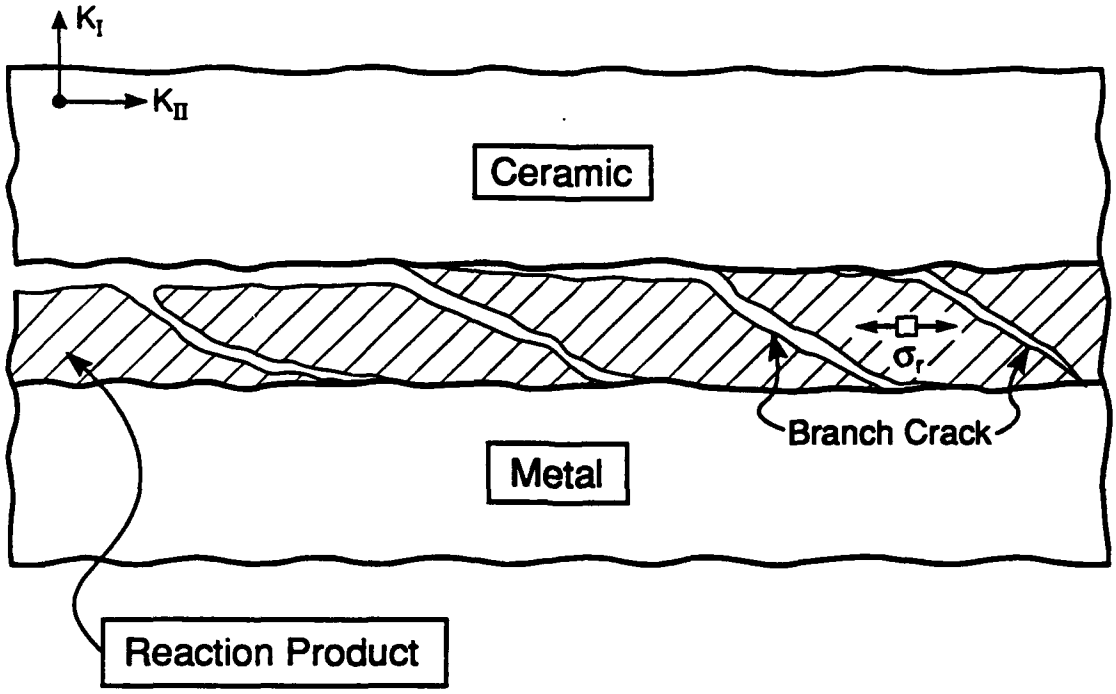

Fig. 24. The microcrack mechanism of interface fracture with brittle reaction products subject to residual tensile stress.

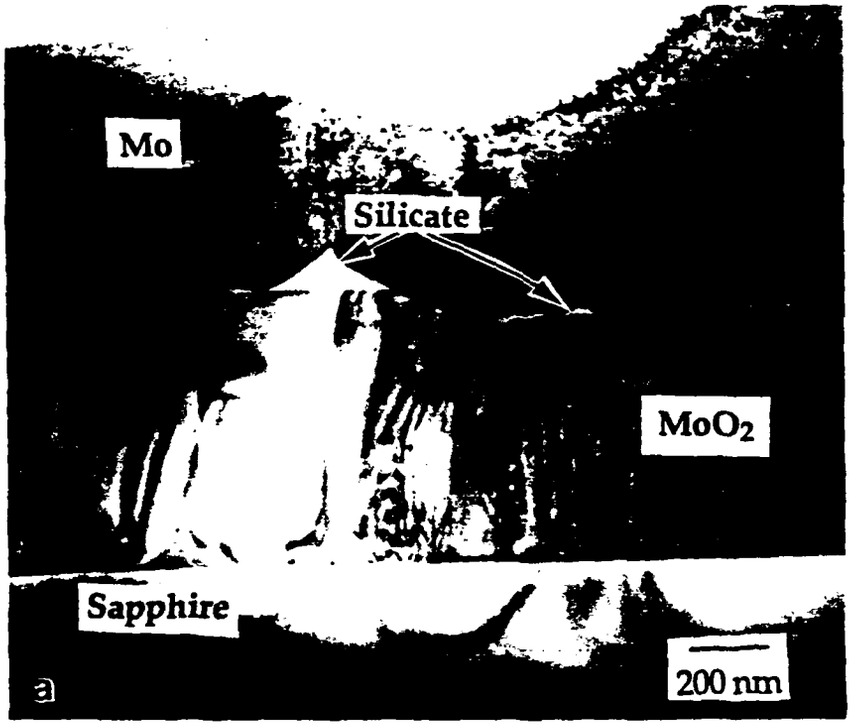

Fig. 25. Oxide interphase formation in Al_2O_3 refractory metal bonds a) Mo/Al_2O_3 with MoO_2 interphase

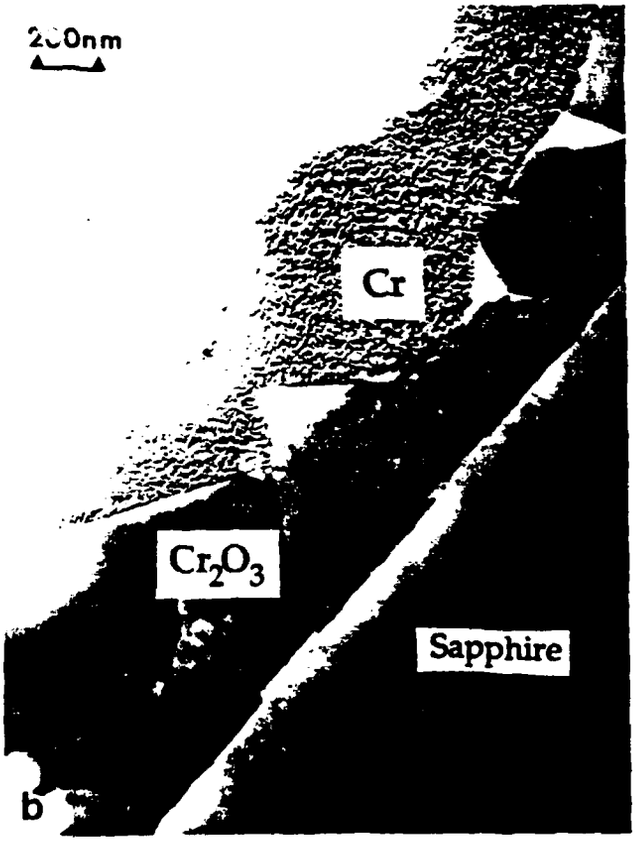

Fig. 25. Oxide interphase formation in Al_2O_3 refractory metal bonds b) Cr/Al_2O_3 with Cr_2O_3 interphase: the oxygen needed to form the oxide comes from solution in the refractory metal. Debondin occurs at the oxide/metal interface.

Section 3

COATING DESIGN FOR COMPOSITE SYSTEMS

ZIRCONIA COATINGS FOR SAPPHIRE FIBER-REINFORCED COMPOSITES

J. B. Davis, E. Bischoff and A. G. Evans
Materials Department
University of California, Santa Barbara, CA 93106

ABSTRACT

Sapphire fibers are promising reinforcements for both ceramic and intermetallic matrices because of their high specific strength and stiffness as well as their superior creep resistance. These attributes can be utilized only if fiber coatings are identified to control the interfacial properties. The feasibility of employing ZrO_2 coatings, which are thermochemically compatible with sapphire, was determined on the basis of fiber debonding requirements. In general, two types of behavior are observed: coatings which promote debonding, and coatings which permit fiber failure. These characteristics are explained in terms of microstructural differences between the coatings which result from variations in the coating deposition method and subsequent processing.

INTRODUCTION

Requirements for high temperature, oxidation resistant materials necessitate the development of ceramic and intermetallic matrices reinforced with strong brittle fibers such as sapphire. To achieve acceptable toughnesses in such brittle matrix composites, it is imperative that criteria be satisfied for debonding of the fiber from the matrix at the crack tip as well as further debonding and fiber pullout in the crack wake. Hence, the fiber/matrix interface behavior determines the overall toughness of brittle matrix composites. The debonding criterion is governed by the ***relative fracture energies of the interface and fiber***[1]. The pullout characteristics are governed by the ***interfacial sliding resistance***[2]. Recognizing that interfacial properties can be manipulated with fiber coatings has led to numerous investigations to identify coatings which are thermochemically compatible with typical fiber and matrix materials and also satisfy the mechanical property requirements outlined above. The present study emphasizes coatings for sapphire fibers in an Al_2O_3 matrix. This system has been selected because matrix cracking problems, which arise from thermal expansion differences between the fiber and matrix, are minimized. However, the results of this study may also be applicable when intermetallic matrices such as γ-TiAl and $MoSi_2$ are used. The coating material selected for this study was ZrO_2, which is both chemically stable with sapphire at temperatures of interest, 1000°C to 1200°C, and oxidation resistant.

An important concept from interfacial fracture mechanics investigations[1-5] concerns the critical interface-to-fiber fracture energy ratio which must be satisfied for fiber debonding to occur in preference to fiber failure. This concept can best be illustrated with the "debond

map" for bimaterial interfaces shown in Figure 1.[1] Plotted is the fracture energy ratio for two values of matrix crack inclination, Φ, as a function of the elastic mismatch between the two materials, represented by the Dundurs' parameter α.[6] The identification of two regimes separated by the locus of fracture energy ratios makes it possible to predict the maximum allowable interfacial fracture energy for a composite with fibers of known fracture energy. As an example, assuming an elastically homogeneous system (ie., $\alpha = 0$) and noting that for sapphire[7,8] $\Gamma \approx 25\text{-}30\ Jm^{-2}$, debond coatings on sapphire fibers must have interfacial fracture energies less than $\sim 7\ Jm^{-2}$ if the system is to lie in the debonding regime for ***all matrix crack inclinations***. Residual stresses and the intrinsic size of flaws in the fiber and coating may shift the position of the debond loci when debonding occurs either within the coating or at the matrix/coating interface.[9]

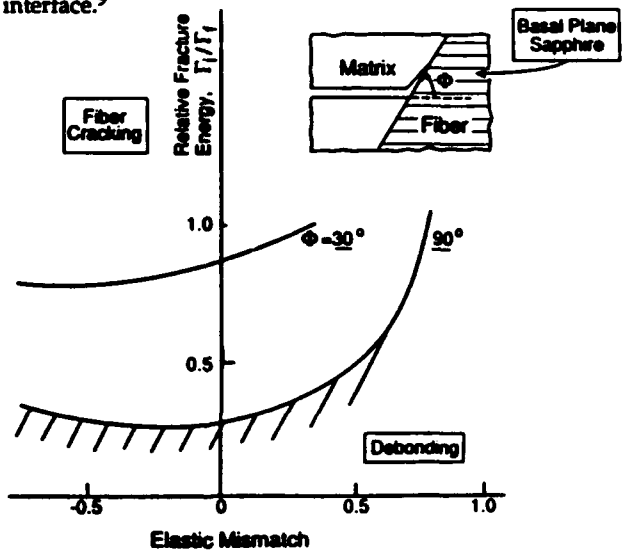

Figure 1. Debond map for bimaterial interfaces.

EXPERIMENTAL PROCEDURE

Sample Preparation

ZrO_2 coatings were deposited onto basal-plane, optical-quality sapphire discs (2-4 cm diameters) using either sputtering or liquid precursors (sol gel) which were pyrolyzed following deposition. The sputter coatings were ~1-2 μm thick, whereas the sol gel coatings were ~ 0.25-0.5 μm. In all cases, the as-deposited films were porous. Two such discs, with coating placed against coating, were diffusion bonded into the sandwich geometry

schematically shown in Figure 2. For these experiments, sapphire has been used to represent both the matrix and fiber, as elaborated above. The bonding conditions involve heating in vacuum (<10^{-6} torr) to 1300° C (~1/2 T_m for ZrO_2) under a small applied load (1-3 MPa) for times of 12 and 48 hours. The processing temperatures thus *exceed* the range of projected use temperatures, ensuring the evaluation of microstructurally stable interfaces.

Mechanical Testing

The diffusion bonded samples were used to produce two types of mechanical test specimens.[7,10] The phase angle of loading for both techiniques is similar and comparable to that associated with crack front debonding in actual composites. [1,4] Furthermore, the fracture energies obtained from analysis of these specimens are unaffected by residual stress in the thin coatings, since such stresses are not relieved by the propagation of the interface crack.

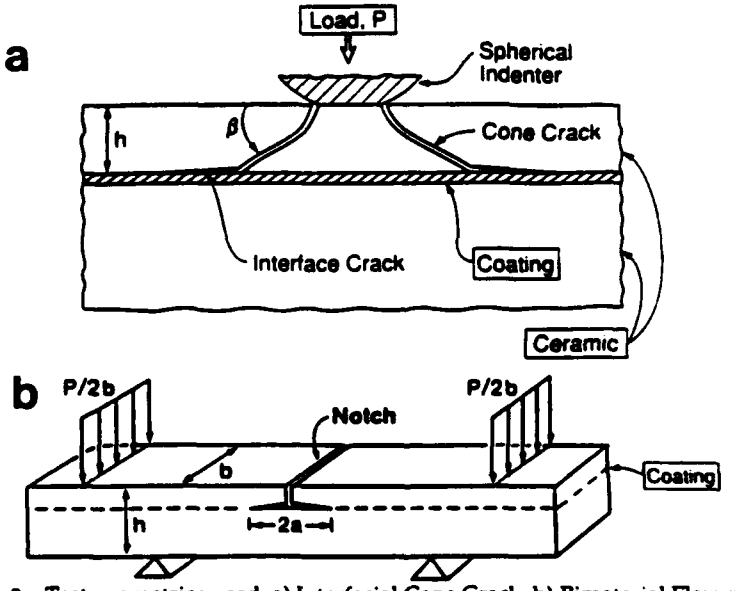

Figure 2. Test geometries used a) Interfacial Cone Crack b) Bimaterial Flexure Beams

The Interfacial Cone Crack Test[7], illustrated in Figure 2a, employs an elastic indentation technique to simulate the behavior of a composite containing a matrix crack. The advantages of this test include small sample size (~2cm diameter) and simple sample preparation, making it an ideal initial test for debond coatings. A spherical WC indenter is used to produce a Hertzian cone crack in the upper "matrix" layer, which can be stably

grown through this layer until it reaches the coated interface. Furthermore, the choice of a transparent sapphire matrix facilitates direct crack growth observation. The cone crack produced is inclined to the interface at an angle which depends on matrix properties (crystallographic anisotropy and Poisson's ratio). For sapphire, $\Phi = 30°$, whereupon the debond map indicates that debonding occurs in systems for which $\Gamma_i < 0.8\,\Gamma$. For coatings on sapphire fibers, this corresponds to a maximum interfacial fracture energy of ~20 Jm^{-2}. Debonding in the Interfacial Cone Crack Test is a necessary, but not sufficient condition for fiber coating selection. Consequently, coatings which debonded were also evaluated using a flexure test[10] in which the crack plane is perpendicular to the coated interface ($\Phi = 90°$). Beams (Figure 2b) which had dimensions 3.5mm x 4mm x 40mm were tested in four point flexure in a jig affixed to the stage of an optical microscope.

RESULTS AND DISCUSSION

Three types of ZrO_2 coatings were examined: sol gel and sputter coatings diffusion bonded for 12 hours, and sputter coatings subject to bonding for 48 hours. The mechanical test results for these coated interfaces are shown in Figure 3. The samples produced with sol

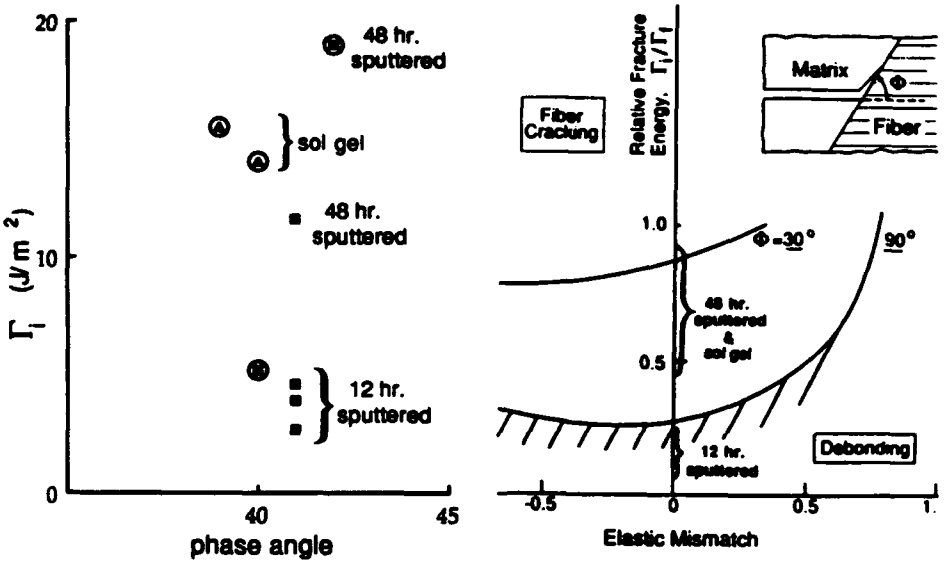

Figure 3. *Results of mechanical tests on ZrO_2 coated interfaces.* (Interfacial Cone Crack test results are circled)

gel coatings bonded for 12 hours, and sputter coatings bonded for 48 hours, had interfacial fracture energies in the "fiber failure" regime of the debond map and are unsuitable for composite use. However, the sputter coated interfaces bonded for 12 hours exhibited relatively low interfacial fracture energies and the debond map predicts that such coatings may be satisfactory for sapphire fibers.

The difference in the observed fracture behaviors for coated interfaces of identical chemical composition can be explained in terms of the coating microstructures. TEM micrographs reveal that the sapphire/sol gel ZrO_2/sapphire interface (Figure 4a) is much thinner than those produced by sputtering (Figures 4b and 4c.) Furthermore, when debonding is induced by using inclined matrix cracks, this system is found to fracture at the *interface*. Similar fracture characteristics were exhibited by the sputter coated samples bonded for 48 hours (Figure 5). In this case, the fracture path deviated from the interface over small isolated areas, possibly because of inhomogeneities. In contrast, the sputter coated samples bonded for 12 hours contained significantly more porosity (Figure 4). This *inter-coating porosity provides an alternate fracture path, through the coating rather than at* the interface (Figure 6) which accounts for the relatively low fracture energy. The implication of this study is that the fracture energy of the interface between ZrO_2 and sapphire is too high to satisfy the debonding criterion for all matrix crack inclinations. However, debonding can be encouraged through the development of a porous microstructure which provides a lower energy fracture path ***through the coating.***

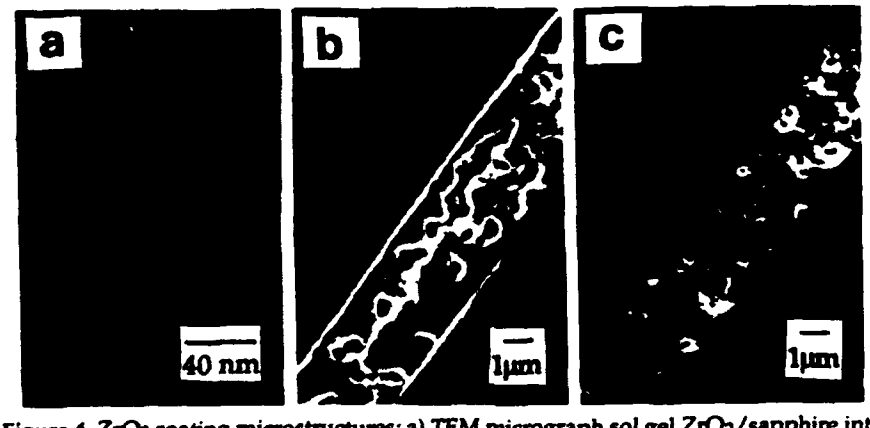

Figure 4. ZrO_2 coating microstructures; a) TEM micrograph sol gel ZrO_2/sapphire interface
b) SEM micrograph 12 hour sputter ZrO_2 /sapphire interface
c) SEM micrograph 48 hour sputter ZrO_2 /sapphire interface.

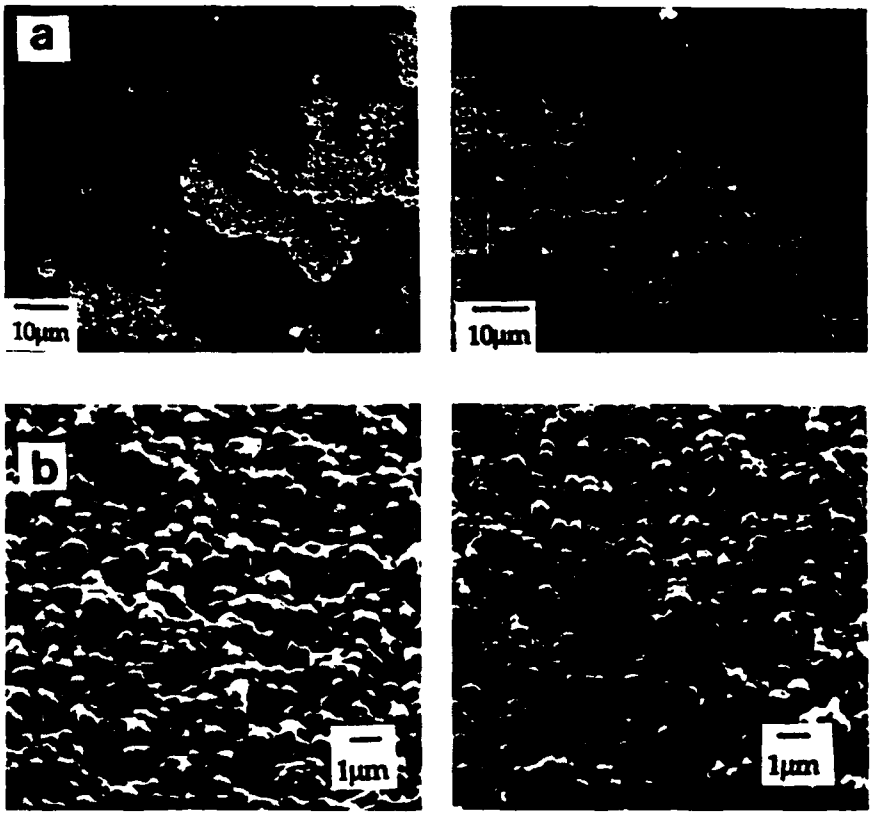

Figure 5. Mating fracture surfaces for sputter coated samples a) bonded for 48 hours b) bonded for 12 hours

The use of ZrO_2 debond coatings for sapphire may be limited by factors other than the interfacial fracture energy. Pure ZrO_2 is known to transform, on cooling, from a tetragonal to a monoclinic crystal structure. The effect of this phase transformation and the thermal expansion mismatch between ZrO_2 and sapphire, can be seen in TEM micrographs (Figure 7.) Microcracks in the ZrO_2 coating and at the coating/sapphire interface, as well as bend contours associated with localized strain in the sapphire were observed. Both of these factors may ***degrade the strength*** of sapphire reinforcements and reduce the utility of ZrO_2 debond coatings.

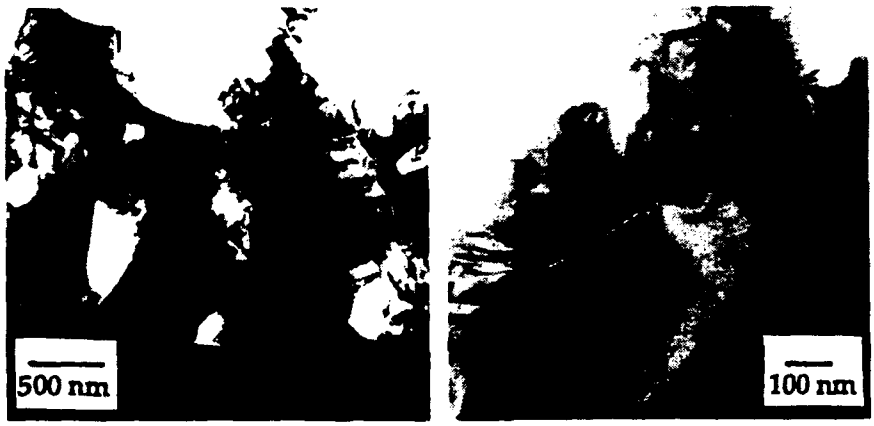

Figure 6. Microcracks and interfacial strain revealed by TEM.

CONCLUSIONS

The fracture energies of several ZrO_2 coating/sapphire interfaces were measured. The interface fracture energy was found to be prohibitively high for fiber debonding to occur over all matrix crack/ fiber inclinations. However, when the inter-coating porosity is substantial, the porosity is found to provide a low energy fracture path through the coating rather than at the interface, such that fiber debonding in sapphire fiber-reinforced composites can be achieved. Interfacial microcracking and residual strain in the sapphire caused by the coating may degrade the fiber strength and limit the usefulness of ZrO_2 coatings.

ACKNOWLEDGEMENTS

The authors wish to acknowledge the support of the Defence Advanced Research Projects Agency for financial support under contract MDA 972-90-K-001, and the contributions of M.L. Emiliani and R. Hecht at United Technologies, Pratt & Whitney for providing sputtered coatings.

REFERENCES

1) M.Y. He and J.W. Hutchinson, A Crack Kinking Out of an Interface, *Jnl. Appl. Mech.*, 56 270-278 (1989).
2) M.D. Thouless, O. Sbaizero, L.S. Sigl, and A.G. Evans, Effect of Interface Mechanical Properties on Pullout in a SiC-Fiber-Reinforced Lithium Aluminum Silicate Glass-Ceramic, *J. Am. Ceram. Soc.*, 72 [4] 525-32 (1989).

3) J.R. Rice, Elastic Fracture Mechanics for Interfacial Cracks, *Jnl. Appl. Mech.*, 55 98 (1988).
4) D.B. Marshall and A.G. Evans, Overview No. 85, The Mechanical Behavior of Ceramic Matrix Composites, *Acta. Metall.*, 37 [10] 2567-2583 (1989).
5) Z. Suo and J.W. Hutchinson, Sandwich Test Specimens for Measuring Interface Crack Toughness, *Mater. Sci. Eng.*, A107,135-43 (1989).
6) J. Dundurs, Discussion, *Jnl. Appl. Mech.*, Trans. ASME 91 Ser. E, 650-652 (1968).
7) J.B. Davis,H.C. Cao, G. Bao and A.G. Evans, Fracture Energies of Interfaces: An Elastic Indentation Technique,*Acta. Metall.*, in press.
8) S.M. Weiderhorn,Fracture of Sapphire, *J. Am. Ceram. Soc.*, 52, (1969) 485.
9) M.Y. He, A. Bartlett and J.W. Hutchinson, *J. Am. Ceram. Soc.*, in press.
10) P.G. Charalambides, H.C. Cao, J. Lund and A.G. Evans, Development of a Test Method for Measuring the Mixed Mode Fracture Resistance of Bimaterial Interfaces, *Mech. Mater.* 8 269-283 (1990).

MATERIALS

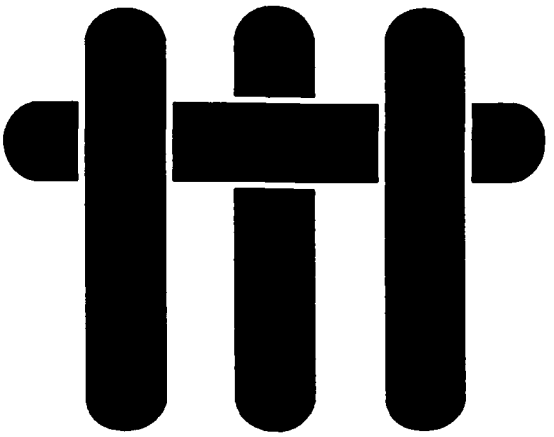

FIBER COATING CONCEPTS FOR BRITTLE MATRIX COMPOSITES*

by

J. B. Davis, J. P. A. Löfvander and A. G. Evans
Materials Department
College of Engineering
University of California
Santa Barbara, California 93106–5050

E. Bischoff
Max-Planck-Institut für Metallforschung
Seestraße 92, D–7000 Stuttgart 1, Germany

M.L. Emiliani
Pratt and Whitney, Materials Engineering
P.O. Box 109600
West Palm Beach, Florida 33410

*Supported by the Defense Advanced Research Projects Agency
under Contract No. MDA 972-90-K-001

ABSTRACT

The current interest in tough, high-temperature materials has motivated fiber coating development for brittle matrix composites with brittle reinforcements. The system investigated in this study was sapphire fiber-reinforced alumina. This system is thermochemically stable for severe use conditions, exhibits little thermal expansion mismatch and utilizes the excellent strength and creep resistance of sapphire reinforcements. Porous oxide and refractory metal coatings which satisfy requirements for toughness improvement in these composites were identified by employing a variety of newly-developed mechanical testing techniques for determining the interfacial fracture energies and sliding resistances.

1. INTRODUCTION

The mechanical requirements for fiber coatings in brittle matrix composites are reflected in two properties[1-3]: debonding and sliding. These properties are manifest as an interface debond energy, Γ_i, and a sliding stress along the debonded interface, τ. A prerequisite for good composite strength and toughness is that a debond criterion be satisfied, wherein the debond energy relative to the fiber fracture energy, Γ_f, satisfy $\Gamma_i/\Gamma_f < 1/4$.[4] Control of sliding is needed to ensure a notch-resistant material, such that $\tau \lesssim 100$ MPa. Coatings of C and BN provide these properties, but both are susceptible to oxidation. Consequently, when SiC fibers are used, and when matrix cracks are present, oxidation embrittlement is encountered because the fiber oxidizes to form a silicate layer that violates debonding requirements.[5] Other coatings are thus desirable for high temperature applications. The present study examines some alternative fiber coating concepts, with emphasis on coatings for oxide fibers, such as sapphire.

Debonding of sapphire fibers* requires coatings with a debond energy, $\Gamma_i \lesssim 5$ Jm^{-2}. Few high-temperature materials have *intrinsic fracture energies* small enough to satisfy such a requirement. Potential options are oriented micas,[7] ‡ some amorphous oxides,[8] and fugitive coatings which are removed after composite consolidation.[9] However, the amorphous coatings have limitations governed by viscous flow at elevated temperatures, plus reaction with Al_2O_3. Two alternative concepts are explored in this article: i) porous oxide coatings and ii) coatings that form 'weak' interfaces with Al_2O_3. The first concept recognizes that *porosity* generally decreases the fracture energy of brittle materials, such as oxides.[10] Consequently, certain porous oxide coatings may be able to satisfy debonding requirements for sapphire fibers, by allowing debonding *within the coating* itself. The second concept is based on the expectation that certain non-

---

* Γ_f = 12–20 Jm^{-2}, depending on the fracture plane.[6]
‡ This concept is being explored at Corning, by K. Chyung.

oxide coatings may allow *interface debonding*.[11] While most such interfaces have relatively high fracture energies ($\Gamma_i > 10$ Jm^{-2}),[11-13] larger than that required for the debonding of sapphire fibers, preliminary evidence has suggested that certain refractory metals provide suitably low values.[11]

An effective coating should have the attribute that it does not degrade the strength of the fibers. Consequently, coatings that either react with or dissolve the fibers are usually unacceptable. This thermochemical requirement further limits the potential set of coating materials. Various refractory materials that exhibit known thermochemical compatibility with Al_2O_3 at 1500°C have been evaluated (Table I), plus C, Y_2O_3 and the refractory metals, Mo, W, Cr and Zr.

2. APPROACH

The overall approach used to identify viable fiber coating concepts is illustrated in Fig. 1. Planar geometries readily amenable to processing and testing are used to screen candidate coating materials. The associated test procedures include a Hertzian indentation technique[14] and a mixed-mode flexure test[15] (Figs. 1a, 1b). For coatings that exhibit debonding, the fracture energy, Γ_i, may also be determined from these tests. The subset of coating materials that satisfy fiber debonding requirements is then used to address composite performance. For this purpose, sapphire fibers are coated and incorporated into a brittle matrix. Beam specimens are cut from the consolidated plate (Fig. 1c), with the fibers oriented along the beam axis. Tensile and/or flexural tests are then used to assess the interaction of a crack with the coated fibers and to obtain information about the sliding stress, τ. The magnitude of τ is ascertained from a measurement of the crack opening displacement as a function of the applied load.[16] Such tests also permit measurement of the fiber pull-out length, h, and the fiber fracture mirror radii.[17-19] The latter yield a direct estimate of the *in situ* strengths of fibers, S.[19]

The magnitudes of S and h, in turn, give another estimate of τ, and thus provide a useful consistency check. In addition, τ can be obtained from fiber push-through tests (Fig. 1d).[20-22] In the present study, a combination of the above tests is used to assess coating concepts for sapphire fibers in polycrystalline Al_2O_3.

3. EXPERIMENTAL PROCEDURES

3.1 Processing

The coatings were deposited either by evaporation, sputtering, chemical vapor deposition or by sol gel methods. For the *planar geometry*, coatings were deposited on two surfaces, each representing either the fiber or matrix component of the composite. Bonding was then conducted by hot pressing at homologous temperatures (for the coating material) in the range $0.4 < T/T_m < 0.7$. Consequently, the system experienced a thermal cycle analogous to that expected for composite processing. *Specimens containing fibers* were produced by sputter or evaporation coating sapphire fibers and incorporating them into matrices by powder processing, using either hot pressing or HIPing to achieve consolidation.

3.1.1 Coating Deposition

Oxide "sol gel" coatings were produced from liquid precursor materials. A spin coating apparatus was used to deposit the coatings onto the planar substrates used for diffusion bonding. The coated substrates were then heat treated in air to temperatures suitable for pyrolysis of the precursor, typically below 1000° C. During pyrolysis, the film is converted to an oxide. Subsequent iterations were used to increase the thickness of the coating.

Sputtered coatings were deposited onto sapphire *discs* and *fibers* in an R.F. diode sputtering unit. The sputtering targets used in most cases were high purity (≥ 99.9%):

only the W target had a lower purity (~ 99.5%). Oxide coatings were deposited by reactive sputtering using a 50%-50% mixture of research grade argon and oxygen at a total working gas pressure of 6 millitorr. The intermetallic compounds were produced from dual opposed targets of the pure elements. Both the refractory metal and intermetallic coatings were deposited in an atmosphere comprised of research grade argon at 6 millitorr working gas pressure. The top and bottom target voltages were maintained at 3kV and 0.5kV, respectively. Fibers were rotated during coating at ~ 1 rpm.

Submicron thick Mo coatings were deposited onto sapphire fibers using an electron beam evaporator and a high purity target. A glow discharge cleaning procedure was used prior to coating the fibers. Deposition was carried out at relatively high vacuum (< 10^{-6} torr), with the fibers rotated at ~ 10 rpm.

The carbon coatings were produced by a low pressure chemical vapor deposition technique in which methane was mixed with research grade argon carrier gas in a tube furnace. Flow rates of 10 cc/min, for the methane, and 100 cc/min, for the argon, were used. Throughout deposition, the furnace temperature was maintained at 1200°C to 1300°C.

3.1.2 Bonding and Consolidation

For experiments to be conducted with planar configurations, three different Al_2O_3 materials were used: i) (0001) sapphire; ii) a high purity (99.5%) polycrystalline material; and iii) a low purity (96%) material.* The test specimens were produced by diffusion bonding, using a procedure described elsewhere.[14] Bonding at $T/T_m \approx 0.5$ allowed coatings to be produced with relative density levels in the range 0.65 to 1.

* Coors AD-995 and Coors AD-96 Substrates.

Tests on coated sapphire fibers were conducted after incorporating into a high-purity (99.9%) polycrystalline Al_2O_3 matrix. For this purpose, submicron Al_2O_3 powder[**] was isostatically cold pressed into two thin discs ~ 5 cm in diameter. These discs were then sintered in air at 1500° C for two hours. A row of coated fibers and loose powder were placed between the discs, the assembly inserted between dies and vacuum hot pressed at 1500°C for 2hr subject to an axial pressure of ~ 2 MPa. These consolidation conditions resulted in an essentially fully dense matrix.

3.2 Testing and Analysis

3.2.1 *Mechanical Behavior*

The Hertzian indentation and mixed-mode flexure testing procedures used with planar specimens have been described elsewhere.[14-15] The flexural tests required precracking. This step was conducted in three-point flexure, using a row of Knoop indentations along the tensile surface to control the crack pop-in load and hence, the extent of the precrack along the interface.

The tests used with the specimens containing fibers have been performed using a combination of fiber push-out and pull-out techniques. The fiber push-out technique has been described previously.[20] The fiber pull-out tests required that chevron notches were machined into beams containing single fibers (Fig. 1). This notch geometry ensured stable crack growth through the beam upon flexural loading. The crack was grown until the crack front passed below the fiber. This occurred with a small crack opening, which induced some fiber debonding and sliding. After precracking, the beam was supported and the remaining matrix ligament mechanically removed. This procedure created a specimen consisting of two blocks of matrix material bridged by a single fiber, amenable to tensile testing. Tests were conducted *in situ* in a Hitachi 2100

[**] AKP-50 with a particle size ~ 0.5 μm obtained from Sumitomo Chemical.

scanning electron microscope (SEM) to permit measurement of the crack opening displacement and the corresponding tensile loads. These measurements may be used to evaluate the sliding resistance, τ.[16]

3.3 *Analytical Techniques*

Specimens for scanning electron microscopy were prepared using standard metallographic techniques. Carbon-coated samples were examined in a JEOL SM 848 SEM in secondary mode. The microscope was equipped with a Tracor Northern TN 5500 system. Samples for transmission electron microscopy (TEM) were prepared by grinding wafers to a final thickness of approximately 100 μm before cutting 3 mm specimens. These were subsequently dimple-ground and ion milled to electron transparency with Ar at 5kV and lmA at 14° incidence angle. The samples were examined at 200kV in a JEOL 2000FX TEM equipped with a LINK eXL high take-off angle energy dispersive spectroscopy system. Computer simulations and indexing of selected area diffraction (SAD) patterns were facilitated by the Diffract software package (Microdev Software, Hillsboro, Oregon 97124).

4. COATING CHARACTERIZATION

4.1 Oxides

For the oxide coatings, a range of porosities was generated, as illustrated in Fig. 2. At the equivalent bonding cycle, the thinner, sol gel coatings had lower *intracoating* porosity than the sputtered coatings, whereas the porosity at the interface was similar for both. In all cases, the grain size was about equal to the coating thickness. The most notable features found by TEM were bend contours in the sapphire caused by residual strains[23] (Fig. 3). For unstabilized ZrO_2 coatings, extensive straining in the sapphire was apparent, as well as microcracks within the coating (Fig. 3a). This effect diminished with

decreasing coating thickness (Fig. 3b). Selected area diffraction indicated that the ZrO_2 was monoclinic and the strains are attributed to the tetragonal to monoclinic phase transformation. For ZrO_2 coatings partially stabilized with 3 mol % Y_2O_3, the tetragonal phase was retained and the intensity of the strain contours diminished (Fig. 3c). However, some residual strain persisted, attributed to the thermal expansion mismatch between ZrO_2 and Al_2O_3. Such strains appear to be an inherent problem with oxide coatings, potentially leading to fiber strength degradation (Appendix).

4.2 Refractory Metals

For the refractory metal coatings, thin foil cross sections for TEM were difficult to produce, because of debonding. However, for Mo, results have been obtained in two cases: a) a thin (0.7 μm) *evaporated* coating with the high purity Al_2O_3 matrix and b) a thicker (> 3 μm) *sputtered* coating with the lower purity Al_2O_3 matrix. For the former, the coating appeared to have some discontinuity (Fig. 4a), but otherwise survived the consolidation. These discontinuities, which are induced by diffusion, are typical for thin, polycrystalline films.[24] EDS analysis was unable to detect either Mo in the Al_2O_3 or Al in the Mo. For the latter, a relatively thick (~ 300 nm) dense polycrystalline MoO_2 phase found at the sapphire interface (Fig. 4b). In addition, an amorphous silicate phase was observed at the MoO_2/Mo interface that presumably resulted from viscous flow of the silicate from the polycrystalline Al_2O_3 into porosity at this interface.

The Mo coatings were also investigated by SEM, *after debonding*. For *sputtered* coatings, oxide particles (identified as MoO_2) were found to be attached to the sapphire in regions where debonding occurred between the Mo and sapphire. X-ray diffraction of the debond surface confirmed the presence of MoO_2 on the sapphire. Shallow ridges were also apparent on the sapphire side of the debond surface, having spacings comparable to the grain size in the metal (Fig. 5a). These ridges are believed to form at

grain boundaries, by diffusion, during the bonding process, as equilibrium dihedral angles are established. Small impressions were evident on the Mo side of the debonded surface between Mo and the *higher purity* Al_2O_3 (Fig. 6), having dimensions which coincide with the Al_2O_3 grain size. These are believed to have formed by deformation of the Mo during diffusion bonding.

The *sputtered* Cr coatings exhibited similar features. A thin polycrystalline Cr oxide (~ 200 nm thick) was attached to the sapphire (Fig. 7), with the remainder of the coating being Cr. Analysis by EDS indicated no Cr in the Al_2O_3 and only trace amounts of Al in the Cr oxide. Selected area diffraction patterns established that the Cr oxide was Cr_2O_3, and significant porosity existed at the metal/oxide interface. Debonding was evident, occurring between the metal and its oxide layer.

The *sputtered* W coatings on sapphire exhibited pronounced ridges on the sapphire side of the debond surface (Fig. 5b). These have been associated with Fe and Cr rich grain boundary impurity phases, originating in the sputtering target. The resulting degradation of the sapphire, evident in Fig. 5b, illustrates the importance of selecting chemically stable coatings. Similar features were observed at C/Al_2O_3 interfaces diffusion bonded at high temperatures (> 1400°C) in high vacuum (> 10^{-6} torr). For this system, the ridges are attributed to the formation of an Al_4C_3 reaction product.

Studies of the *as-sputtered* Mo and Cr films, using WDS and X-ray diffraction, revealed an oxide surface layer. In addition, there was an oxide layer adjacent to the sapphire, identified by peeling the coating from the substrate. These findings indicate that the oxide phase is initially deposited on the sapphire substrate during sputtering and that a surface oxide forms subsequent to deposition, prior to diffusion bonding.

5. MECHANICAL MEASUREMENTS

5.1 Debonding

Preliminary experiments conducted on planar specimens with a spherical indenter provided information about the incidence of debonding at a 30° crack inclination to the interface. From such experiments, it was established that most diffusion bonded coatings formed high fracture energy interfaces. Only the coatings consisting of Mo, W, Cr, Zr and C debonded consistently. Coatings of ZrO_2 and $Y_3Al_5O_{12}$* were found to exhibit variable debonding tendencies. Coatings of Nb, γ-TiAl and NiAl did not debond. Furthermore, from the list of promising coating materials, several were observed to chemically react with the sapphire during diffusion bonding. The only coating materials from this set which were found to be *chemically stable* with sapphire above 1300°C and to *reliably debond* were: Mo, Cr, porous ZrO_2 and porous Al_2O_3. Further studies were confined to these materials.

The debonding propensity of the *refractory metal* coatings was observed to vary with the purity of the Al_2O_3. When either sapphire or sapphire plus *high purity* polycrystalline Al_2O_3 were used, debonding occurred consistently, with $\Gamma_i \approx 4\ Jm^{-2}$ for Mo and 2–3 Jm^{-2} for Cr. Furthermore, as already noted, the debonding occurred at the interfaces between either Mo/Al_2O_3 or Mo/MoO_2 and Cr/Cr_2O_3. Conversely, when the *impure* Al_2O_3 was used, debonding was not observed in the Hertzian indentation test, implying a *lower bound* for Γ_i of ~ 16 Jm^{-2}.‡ This behavior is attributed to the silicate phase found at the Mo/MoO_2 interface, which seemingly forms a strong bond[25,26] and increases Γ_i for that interface. In addition, as already noted, MoO_2 appears to bond well with sapphire.

---

* Formed by chemical reaction during bonding with Y_2O_3 coatings.

‡ This lower bound is, $\Gamma_i = 0.8\,\Gamma_f$, corresponding to a crack/interface inclination of 30°, with $\Gamma_f \approx 20\ Jm^{-2}$.

The results for the *oxide coatings* were found to be sensitive to the coating porosity. The *dense* coatings, which have a relatively high interfacial fracture energy, debond along the *interface*. But debonding only occurred when the crack approached the interface at a shallow inclination. Conversely, the coatings having the *lowest relative density* ($\rho \approx 0.65$), exhibited a relatively low interfacial fracture energy, $\Gamma_i \approx 5\ Jm^{-2}$, and debonded *within the coating, at all crack inclinations*. Such debonds exhibit fracture surface features typical of those for porous ceramics.[10] These debonding tendencies are rationalized by using the coating density, ρ, as a plotting variable against the ratio of the interfacial fracture energy to sapphire fracture energy Γ_i / Γ_f, (Fig. 8a).

The debonding results obtained *for all of the above coatings* can be displayed on a debond diagram, relevant to sapphire fiber-reinforced brittle matrix composites (Fig. 8b).

5.2 Sliding Resistance

For *porous oxide coatings* on sapphire fibers in a polycrystalline Al_2O_3 matrix, single fiber tests revealed small fiber pull-out (Fig. 9). Debonding resulted in a monolayer of the oxide particles attached to the fiber that remained throughout the sliding process (Fig. 9). These particles are believed to act as asperities that resist sliding, resulting in a relatively large sliding stress, τ. This stress was estimated from the pull-out length and the fracture[16-18] mirror radius to be ~ 140 MPa (Table II). A similar value was obtained from fiber push-out measurements. This value of τ is larger than that required for optimum composite strength and toughness.

The refractory metal coatings debond readily during single fiber pull-out tests, but the coating is plastically deformed. This deformation occurs because the coating conforms to both the matrix and fiber during consolidation and results in prohibitively high sliding resistances, such that little fiber pull-out occurs (Fig. 10). Similar behavior is

found during push-out tests (Fig. 11a), which also indicate a high sliding resistance, $\tau \approx 120$ MPa (Fig. 13).

A reduction in the sliding resistance for Mo coated fibers has been achieved by *removing the coating*, after composite consolidation, to leave a gap between the fiber and matrix. This has been accomplished by heating the composite in air* (1000°C for 2 hours). The surface roughness of the fiber and the matrix then provide the sliding resistance. For coatings somewhat thicker than the asperity amplitude on the fiber (~ 1 μm), the sliding resistance obtained from crack opening displacement measurements in single fiber pull-out tests is found to be small ($\tau < 1$ MPa), with large associated pull-out lengths (Fig. 12). This sliding resistance is too low for the requisite combination of strength and toughness in the composite. For thinner (~ 0.7 μm) coatings, push-out tests indicate a sliding resistance within the requisite range, $\tau \approx 20$ MPa (Fig. 13), with no evidence of wear mechanisms on the fiber surface (Fig. 11b).

6. CONCLUDING REMARKS

The debonding and sliding properties of various coating materials on sapphire fibers have been evaluated. In general, most materials bonded well to sapphire. The notable exceptions were certain *refractory metals* (such as Mo, Cr, and W) which formed low fracture energy interfaces with sapphire. Several factors may be responsible for the low debond energies: porosity at the interfaces, oxygen dissolved in the metal (that suppresses plastic dissipation)[13] and the formation of a metal oxide (MoO_2 or Cr_2O_3).[27,28] A systematic study would be needed to identify the critical factor(s).

---

* Because Mo forms volatile oxides.

Oxide coatings, which form strong interfaces with sapphire, can also be useful debond coatings, provided that they contain a significant amount of porosity subsequent to composite consolidation. The porosity in these coatings provides a low fracture energy path causing debonding within the coating.

The sliding characteristics of the various interfaces were also investigated. The sliding resistances obtained on interfaces produced with refractory metal coatings is apparently too high for significant fiber pull-out, because the coating deforms during sliding. However, for coatings such as Mo, which form volatile oxides, the interfacial sliding resistance can be significantly reduced through coating removal by heat treatment in air. Fugitive carbon coatings also have this attribute,[9] but were not used in this study because the carbon reacted with the sapphire in the diffusion bonding experiments. It is recognized, however, that altering the processing conditions could eliminate this problem. Once the coating has been removed, the fiber surface and matrix roughness provide the sliding resistance needed for load transfer. The resultant system is also oxidatively stable. The coating thickness relative to the fiber and matrix roughness amplitude is now a key parameter.[22] An optimization study is in progress.

The *sliding resistances* of oxide coatings examined in this study were also unacceptably high, because of the undulating debond trajectory. It is believed that τ can be reduced if the grain size and porosity of the coating are carefully controlled. Further studies of the effect of debond surface irregularities on the sliding behavior are needed to address this issue.

Fiber strength degradation is another concern for oxide coatings. When reaction products with the fiber coating are avoided, potential sources of fiber strength degradation persist, including residual strain (Fig. 3) and undulations produced on the fiber surface by diffusion (Fig. 5). Some basic characteristics are amenable to analysis (Appendix). The predictions (Fig. 14) indicate that m-ZrO_2 coatings are unacceptable because, for typical coating thicknesses ($h \approx 0.1 - 1\ \mu m$), the large mismatch stresses

caused by the transformation lead to fiber strengths below the acceptable limit for high performance applications ($S < 1$ GPa). Furthermore, coatings such as YAG with a mismatch governed by thermal expansion are also predicted to cause an unacceptably low fiber strength ($S < 2$ GPa), unless the coatings are thin ($h < 3\ \mu m$). A general implication is that oxide coatings, which typically bond well to sapphire, are a possible source of fiber strength degradation. The extent of degradation is diminished by thin coatings and small thermal expansion mismatch. Also, porosity in the coating tends to alleviate the degradation problem.

TABLE I

Some Materials Thermochemically Stable with Al_2O_3 at 1500°C

Material	References	Remarks
γ-TiAl	29	Al_2O_3 dissolves
Nb	30	Al_2O_3 dissolves
NiAl	31	
ZrO_2	32	

TABLE II

Sliding Stress with Porous Alumina Interface

Fracture Mirror Radius, a_m (μm)	*In Situ* Fiber Strength, S* (GPa)	Pullout Length, h (μm)	Sliding stress, τ # (MPa)
27	1.68	193	142

*$S = 3.5\left(\frac{K_c}{\sqrt{a_m}}\right)$, where K_c is the fiber toughness (~ 2.5 MPa)[17]

#$\tau = S\left(\frac{r}{2h}\right)$, where r is the fiber sapphire radius[17]

APPENDIX

FIBER DEGRADATION

When the coating is in residual tension caused by thermal expansion misfit, the coating cracks prior to fiber failure and may cause a degradation in fiber strength. When this crack penetrates into the fiber, the stress intensity factor, for a crack of depth, a, associated with the residual field from the coating is[33]

$$K_R = 1.1E_c\varepsilon_T h/\sqrt{\pi a}\,(1-\nu) \equiv 1.1\sigma_o h/\sqrt{\pi a} \qquad \text{(A1)}$$

where ε_T is the misfit strain, h the coating thickness, E_c its Young's modulus and σ_o the misfit stress. The applied stress σ also induces a stress intensity[33]

$$K = 1.1\sigma\sqrt{\pi a} \qquad \text{(A2)}$$

By adding the K's and equating to the fracture resistance of the fiber, the stress/crack length relation becomes

$$\sigma = 0.9\sqrt{\frac{E_f\Gamma_f}{\pi a}} - \frac{\sigma_o h}{\pi a} \qquad \text{(A3)}$$

Differentiating Eqn. (A3) and setting $d\sigma/da = 0$ for the maximum, σ_{max}, gives a fiber strength,

$$S \equiv \sigma_{max} = 0.2\left(E_f\Gamma_f/\sigma_o h\right) \qquad \text{(A4)}$$

This result applies when S is smaller than the strength S_0 of the uncoated fibers. Fiber strengths as a function of coating thickness for a range of dense and porous oxide coatings are plotted on Fig. 14.

ACKNOWLEDGEMENTS

The authors wish to acknowledge Dr. M. De Graef for helpful discussions and the TEM micrograph shown in Figure 4a.

REFERENCES

[1] J. Aveston, G.A. Cooper and A. Kelly, "Properties of Fibre Composites," *IPC Science and Technology Press*, London, (1971).

[2] D.B. Marshall and A.G. Evans, Overview No. 85, "The Mechanical Behavior of Ceramic Matrix Composites," *Acta Metall. Mater.*, **37** [10] 2567–2583 (1989).

[3] D.B. Marshall, B.N. Cox and A.G. Evans, "The Mechanics of Matrix Cracking in Brittle-Matrix Fiber Composites," *Acta Metall. Mater.*, **33** [11] 2013–2021 (1985).

[4] M.Y. He and J.W. Hutchinson, "A Crack Kinking Out of an Interface," *Jnl. Appl. Mech.*, **56**, 270–278 (1989).

[5] H.C. Cao, E. Bischoff, O. Sbaizero, M. Rühle, A.G. Evans, D.B. Marshall and J.J. Brennan, "Effect of Interfaces on the Properties of Fiber-Reinforced Ceramics," *J. Am. Ceram. Soc.*, **73**, 1691 (1990).

[6] S.M. Weiderhorn, "Fracture of Sapphire," *J. Am. Ceram. Soc.*, **52**, 485 (1969).

[7] D.H. Roach, S. Lathabai and B.R. Lawn, "Interfacial Layers in Brittle Cracks," *J. Am. Ceram. Soc.*, **71** [2] 97–105 (1988).

[8] S.M. Weiderhorn, *Fracture Mechanics of Ceramics*, (Ed., R.C. Bradt *et al.*) Plenum, NY (1974) Vol. 2, p. 20.

[9] T. Mah, K. Keller, T.A. Parthasarathy and J. Guth, "Fugitive Interface Coating in Oxide-Oxide Composites: A Viability Study," *Ceram. Eng. Sci. Proc.*, **12** [9–10] pp. 1802–15 (1991).

[10] R.W. Rice, "Effects of Inhomogeneous Porosity on Elastic Properties of Ceramics," *J. Am. Ceram. Soc.*, **58** [9–10] 458–59 (1975).

[11] A.G. Evans, F.W. Zok and J.B. Davis, "The Role of Interfaces in Fiber-Reinforced Brittle Matrix Composites," *Composites Science and Technology* **42**, 3–24 (1991).

[12] M. Rühle and A.G. Evans, "Structure and Chemistry of Metal/Ceramic Interfaces," *Mat. Res. Soc. Symp. Proc. Vol. 120*, (1988) MRS

[13] A.G. Evans and B.J. Dalgleish, *Acta Metall. Mater.*, to be published.

[14] J.B. Davis, H.C. Cao, G. Bao and A.G. Evans, "The Fracture Energy of Interfaces: An Elastic Indentation Technique," *Acta Metall. Mater.*, **39** [5] 1019–1024, (1991).

[15] P.G. Charalambides, H.C. Cao, J. Lund and A.G. Evans, "Development of a Test Method for Measuring the Mixed Mode Fracture Resistance of Bimaterial Interfaces," *Mech. Mater.*, **8**, 269–283 (1990).

[16] D.B. Marshall, M.C. Shaw and W.L. Morris, "Measurement of Interfacial Debonding and Sliding Resistance in Fiber Reinforced Intermetallics," *submitted to Acta Metall. Mater.*

[17] M.D. Thouless, O. Sbaizero, L.S. Sigl and A.G. Evans, "Effect of Interface Mechanical Properties on Pullout in a SiC-Fiber-Reinforced Lithium Aluminum Silicate Glass Ceramic," *J. Am. Ceram. Soc.*, **72 [4]** 525–532 (1989).

[18] F.E. Heredia, S.M. Spearing, A.G. Evans, P. Mosher and W. Curtin, *J. Am. Ceram. Soc.*, in press.

[19] W.A. Curtin, "Theory of Mechanical Properties of Ceramic-Matrix Composites," *J. Am. Ceram. Soc.*, **74 [11]** 2837–45 (1991).

[20] D.B. Marshall and W.C. Oliver, "Measurement of Interfacial Mechanical Properties in Fiber-Reinforced Ceramic Composites," *J. Am. Ceram. Soc.*, **70 [8]** 542–48 (1987).

[21] P.D. Jero and R.J. Kerans, "The Contribution of Interfacial Roughness to Sliding Friction of Ceramic Fibers in a Glass Matrix," *Scripta Metall. et Mater.*, **24**, 2315-2318 (1990).

[22] T.J. Mackin and P.D. Warren, 'The Influence of Fiber Roughness on the Sliding Behavior of Sapphire Fibers in TiAl and Glass Matrices," *Acta Metall. Mater.*, to be published.

[23] J.B. Davis, E. Bischoff and A.G. Evans, "Zirconia Coatings for Sapphire Fiber-Reinforced Composites," in Advanced Composite Materials, ed. M.D. Sacks, 631-638 (1991).

[24] K.T. Miller, F.F. Lange and D.B. Marshall, "The Instability of Polycrystalline Thin Films: Experiment and Theory," *Mat. Res. Soc. Proc. Sym. on Ultrastr. Proc.*, **121 [3]** 823–30 (1988) and *J. Mater. Res.*, **1 [5]** 151–60 (1990).

[25] S.S. Cole, Jr. and G. Sommer, "Glass-Migration Mechanism of Ceramic-to-Metal Seal Adherence'" *J. Am. Cer. Soc.*, **44[6]** 265-271 (1961).

[26] E. Samuel and P. Hrma, "MoO_2 Diffusion in Aluminosilicate Glass," *J. Am. Ceram. Soc.*, **72 [6]** 1091-92 (1989).

[27] The Metal Molybdenum, Proceedings of a Symposium sponsored by Office of Naval Research., ed. by Julius Harwood (1958) American Society for Metals.

[28] Ductile Chromium and its Alloys, Proceedings of a Conference sponsored by Office of Ordnance Research, (1957) American Society for Metals.

[29] H.E. Dève, A.G. Evans, G.R. Odette, R. Mehrabian, M.L. Emiliani and R.J. Hecht, "Ductile Reinforcement Toughening of γ-TiAl: Effect of Debonding and Ductility," *Acta Metall. Mater.*, **37**, 853-890 (1989).

[30] M. Rühle, K. Burger, W. Mader and A.G. Evans, "Some Aspects of Structures and Mechanical Properties of Metal/Ceramic Bonded Systems," in Fundamentals of Diffusion Bonding, ed. by Y. Ishida, pp. 43–70, (1987) Elsevier, New York.

[31] K.P. Trumble and M. Rühle, "The Thermodynamics of Spinel Interphase Formation of Diffusion-Bonded Ni/Al_2O_3 Interfaces," *Acta Metall. Mater.*, 39 [8] 1915–24 (1991)

[32] M. Rühle, A. Strecker, D. Waidelich and B. Kraus, "*In Situ* Observations of Stress-Induced Phase Transformations in ZrO_2-Containing Ceramics," *Advances in Ceramics*, Vol. 12, ed. by N. Claussen, M. Rühle and A.H. Heuer, pp. 256–74 (1984) American Ceramic Society, Inc.

[33] H. Tada, P.C. Paris and C.R. Irwin, *The Stress Analysis of Cracks Handbook*, Del Research Corp., Pennsylvania (1973).

FIGURE CAPTIONS

Fig. 1. The approach adopted to identify viable fiber coating concepts for brittle matrix composites consisted of developing testing procedures to evaluate the debonding and sliding propensities of various coatings on sapphire.

Fig. 2. ZrO_2 coating/sapphire interfaces produced by the following diffusion bonding schedules:

a) Sol gel coating diffusion bonded at 1300°C for 12 hours with an applied load ~ 1 MPa

b) Sputtered coating diffusion bonded at 1300°C for 12 hours with an applied load ~ 1 MPa

c) Sputtered coating diffusion bonded at 1300°C for 48 hours with an applied load ~ 3 MPa

Fig. 3. a) Extensive bend contours in the sapphire when unstabilized ZrO_2 sputtered coatings were used. It is believed that the contours result from strain in the fiber due to the $t \rightarrow m$ ZrO_2 phase transformation.

b) The bend contours in the sapphire decrease with coating thickness for the unstabilized sol gel ZrO_2 coating.

c) The extent of bend contours was further reduced when thin stabilized sol gel ZrO_2 coatings were used. The remaining stresses are believed to result from CTE mismatch across the well-bonded interface.

Fig. 4. a) A TEM micrograph shows the discontinuous submicron Mo coating on a sapphire fiber in the high purity Al_2O_3 matrix.

b) TEM micrographs of a diffusion bonded Mo/sapphire interface with the lower purity Al_2O_3. A continuous MoO_2 phase occurs adjacent to the sapphire and an amorphous silicate phase exists within the interfacial pores between Mo and the MoO_2 phase.

Fig. 5. a) Shallow ridges were observed on the sapphire surface of a Mo/Sapphire diffusion couple upon debonding.

b) Pronounced ridges on the debonded sapphire surface when an impure W coating was used. The grain boundary impurity phase is composed of Fe and Cr.

Fig. 6. The Mo coating conforms to the surface features of a high-purity polycrystalline Al_2O_3 substrate during diffusion bonding.

Fig. 7. The Cr/sapphire diffusion bond was found to contain a Cr_2O_3 phase adjacent to the interface.

Fig. 8. a) The relative density of oxide coatings plotted as a function of Γ_i/Γ_f clarifies the role of coating porosity in the debonding process.

b) A summary of the interfacial fracture energy measurements for various coatings on sapphire is presented on a "debond map." Coatings which fall within the fiber debonding regime of the map have some potential for sapphire fibers. However, coatings denoted by (*) were found to chemically react with sapphire, these were precluded from further consideration.

Fig. 9. A porous oxide interface led to fiber pull-out of a few fiber diameters. Oxide particles were observed to sinter to the sapphire fiber and remained attached during pull-out. The fracture mirror on the fiber is also visible.

Fig. 10. Short fiber pull-out lengths were observed when Mo coatings were used.

Fig. 11. The surface morphology of the pushed-out sapphire fibers was found to change when the Mo coating was removed by oxidation: a) as-hot pressed condition b) heat treated condition.

Fig. 12. Long fiber pull-out can result when thick (~ 6 μm) Mo coatings are removed by oxidation.

Fig. 13. Fiber push-out curves reveal that the interfacial sliding resistance was decreased to an acceptable level by removing the submicron thick (0.7 μm) Mo coating from the interface.

Fig. 14. The predicted influence of oxide coatings on the strength of sapphire fiber: ρ is the coating density. It is assumed that the uncoated fibers have a strength, S_o = 2.5 GPa.

Identify Possible Coating Materials

Screening Tests

Composite Performance Evaluation

Interface Property Optimization

Final Coating Selection

Debonding Investigations

Diffusion Bonded Planar Specimens

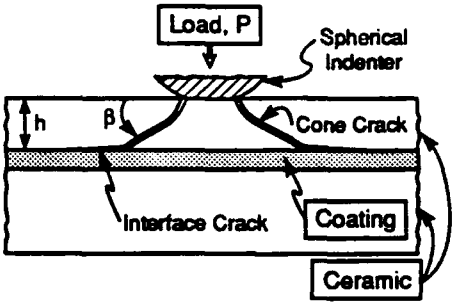

a. Hertzian Indentation Test

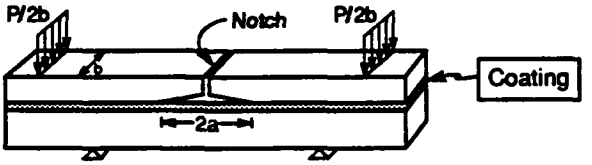

b. Flexure Test

Sliding Resistance Investigations

Hot Pressed Specimens with Fibers

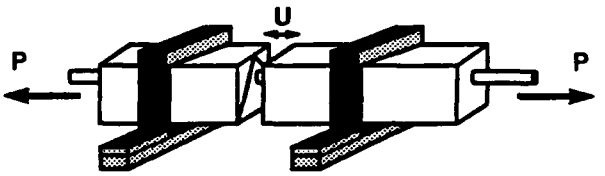

c. Pull-Out Test

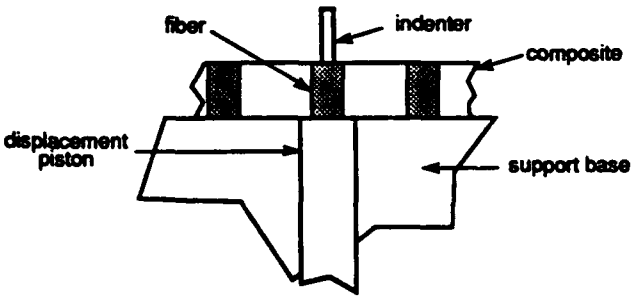

d. Push-Through Test

Figure 1

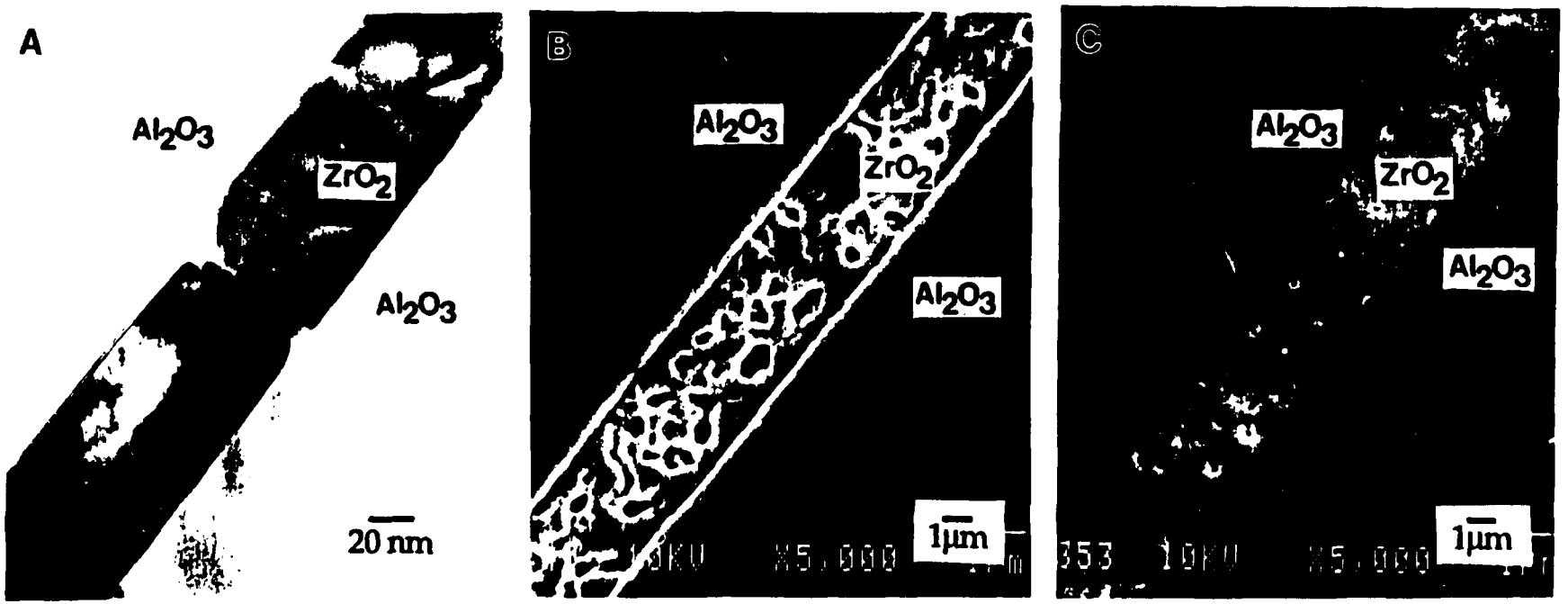
A
Al_2O_3
ZrO_2
Al_2O_3
20 nm
B
Al_2O_3
ZrO_2
Al_2O_3
1μm
C
Al_2O_3
ZrO_2
Al_2O_3
1μm

Figure 2

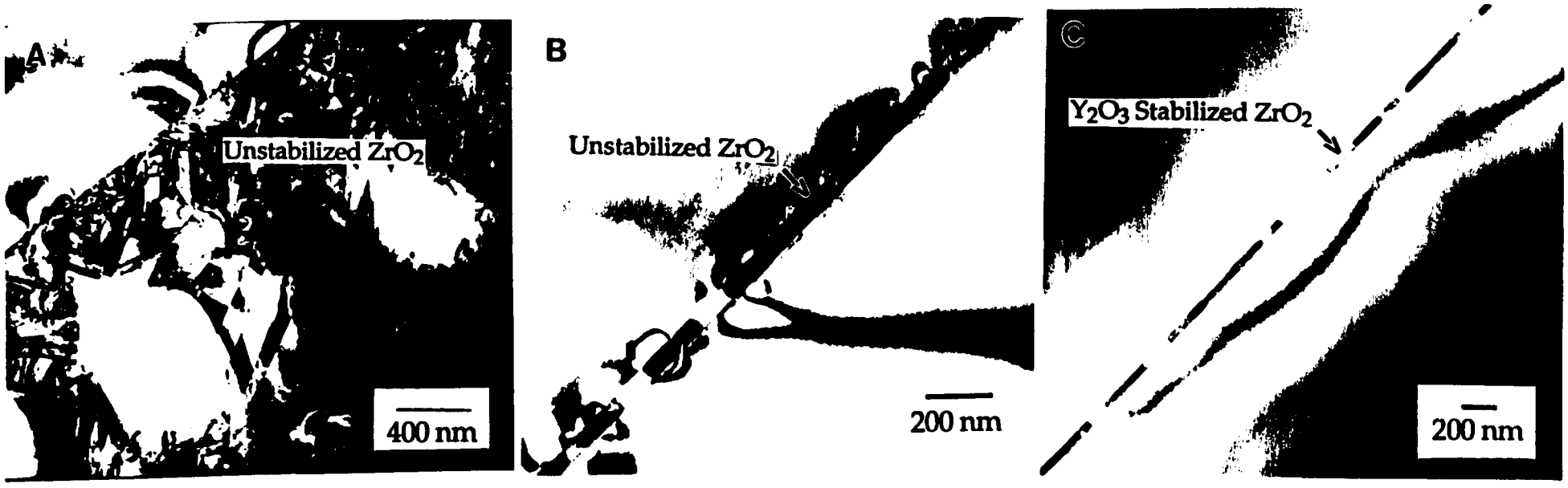
A
Unstabilized ZrO_2
400 nm
B
Unstabilized ZrO_2
200 nm
C
Y_2O_3 Stabilized ZrO_2
200 nm

Figure 3

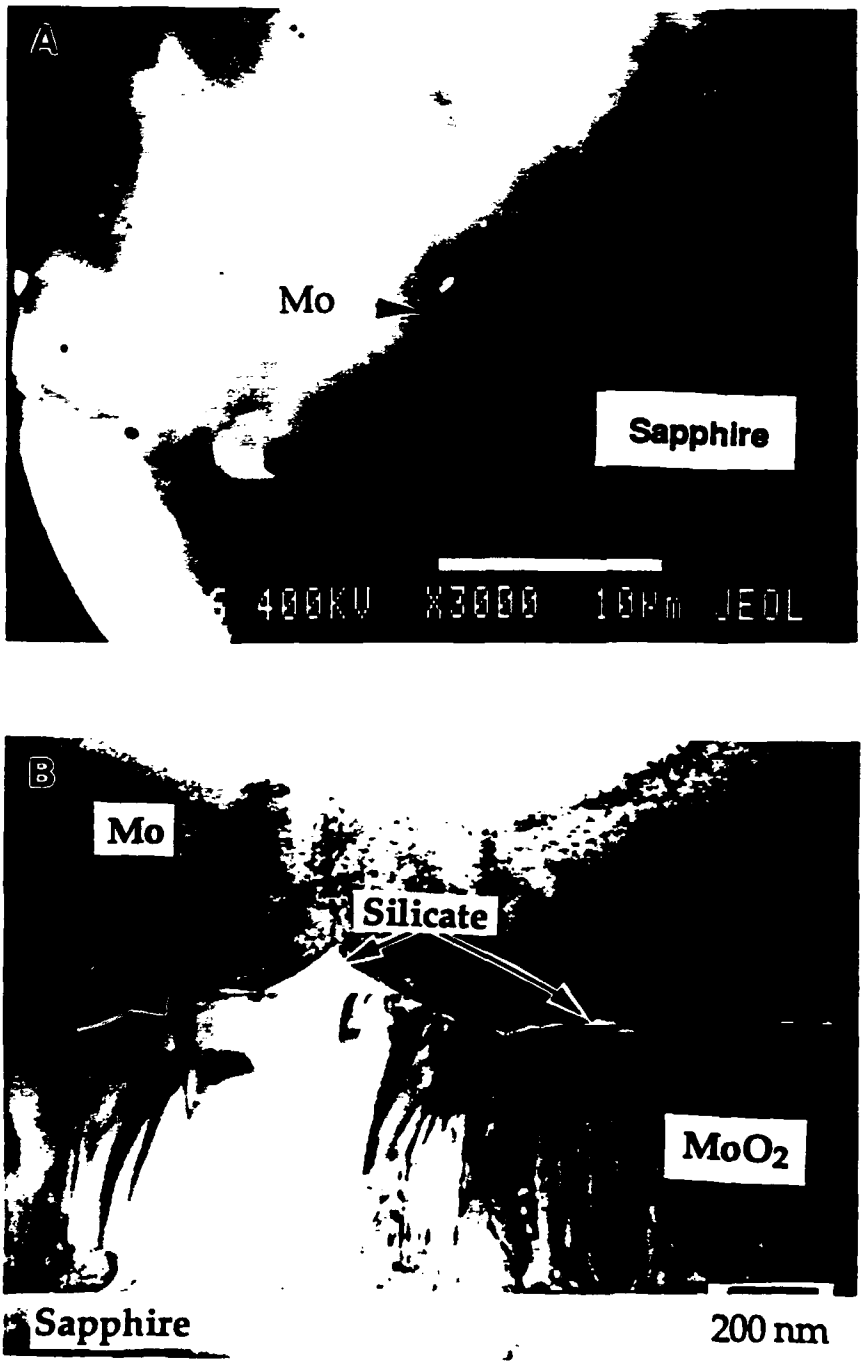
A
Mo
Sapphire
400KV X3000 10Pm JEOL
B
Mo
Silicate
MoO2
Sapphire
200 nm

Figure 4

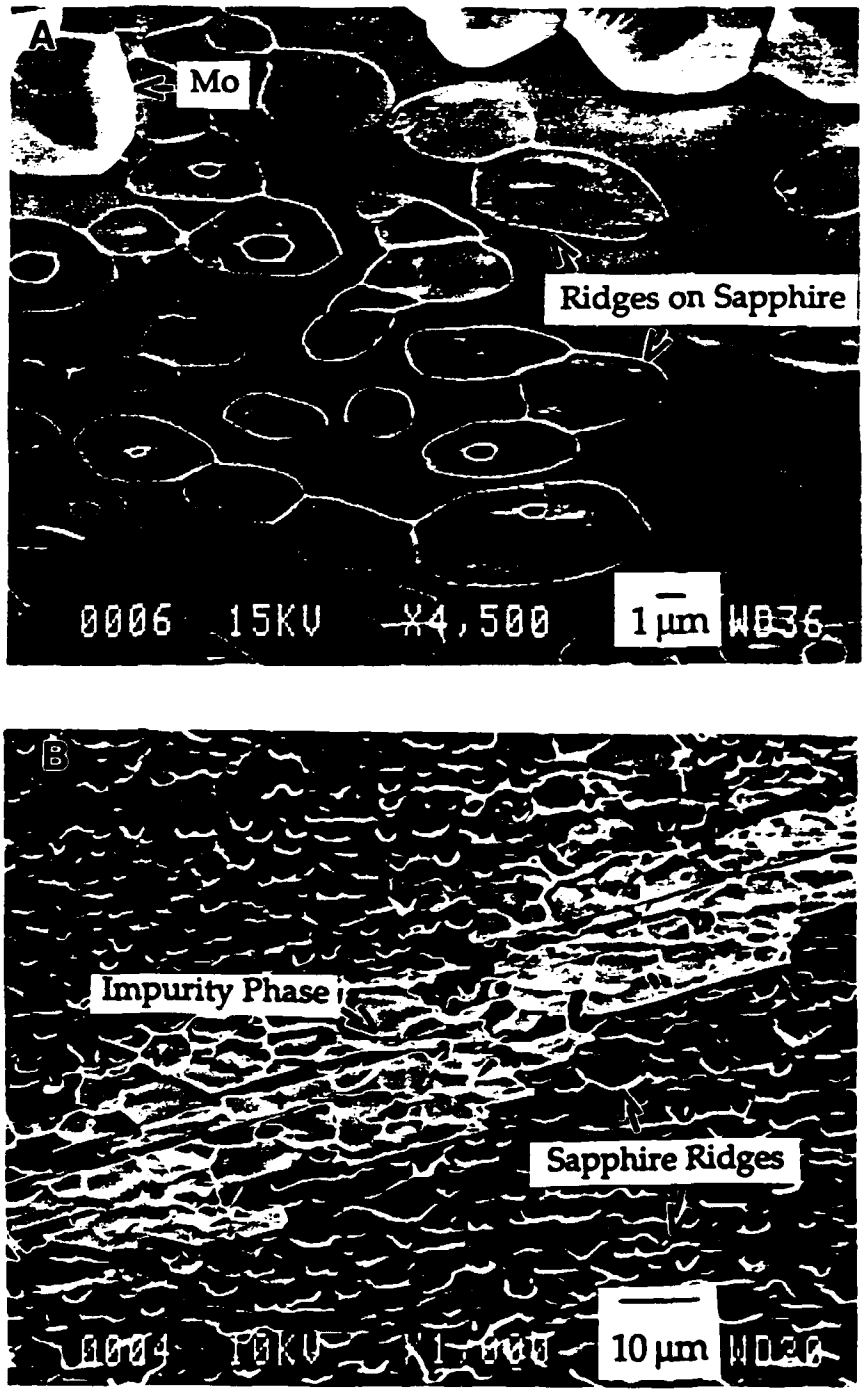
A
Mo
Ridges on Sapphire
0006 15KV X4,500
1 µm
B
Impurity Phase
Sapphire Ridges
10 µm

Figure 5

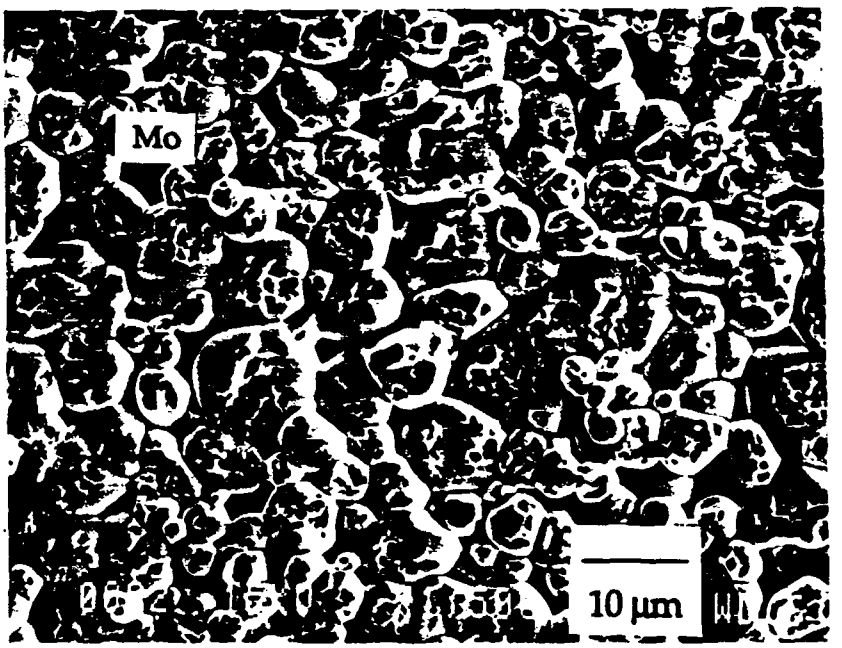

Figure 6

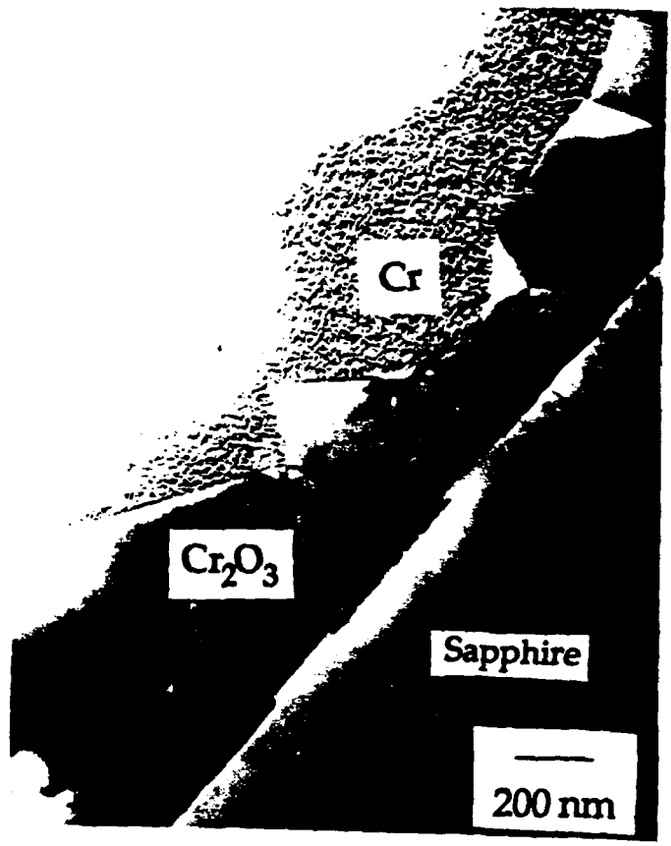

Figure 7

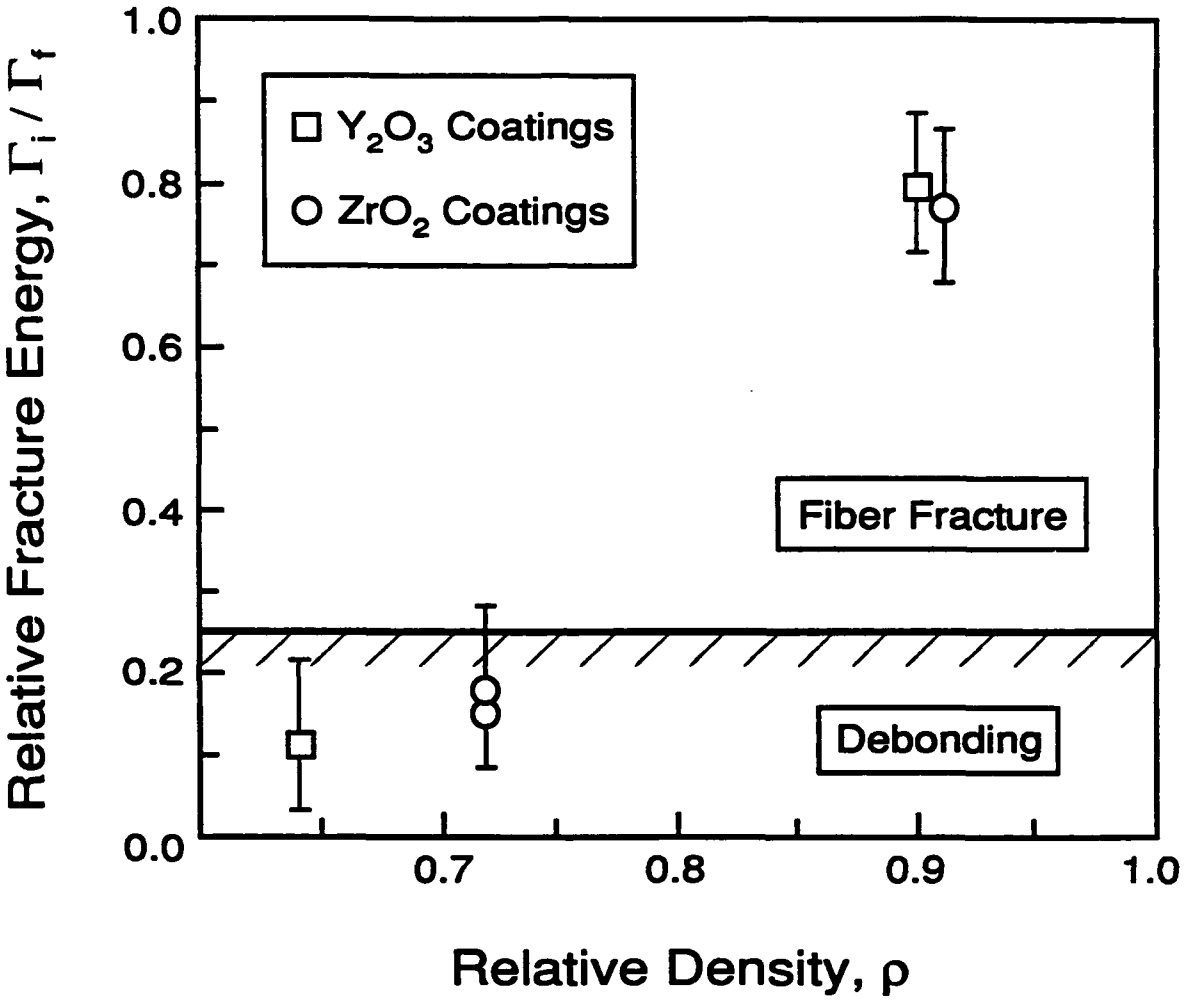
Relative Fracture Energy, Γ_i / Γ_f
1.0
0.8
0.6
0.4
0.2
0.0
0.7
0.8
0.9
1.0
Relative Density, ρ
Y_2O_3 Coatings
ZrO_2 Coatings
Fiber Fracture
Debonding

Figure 8a

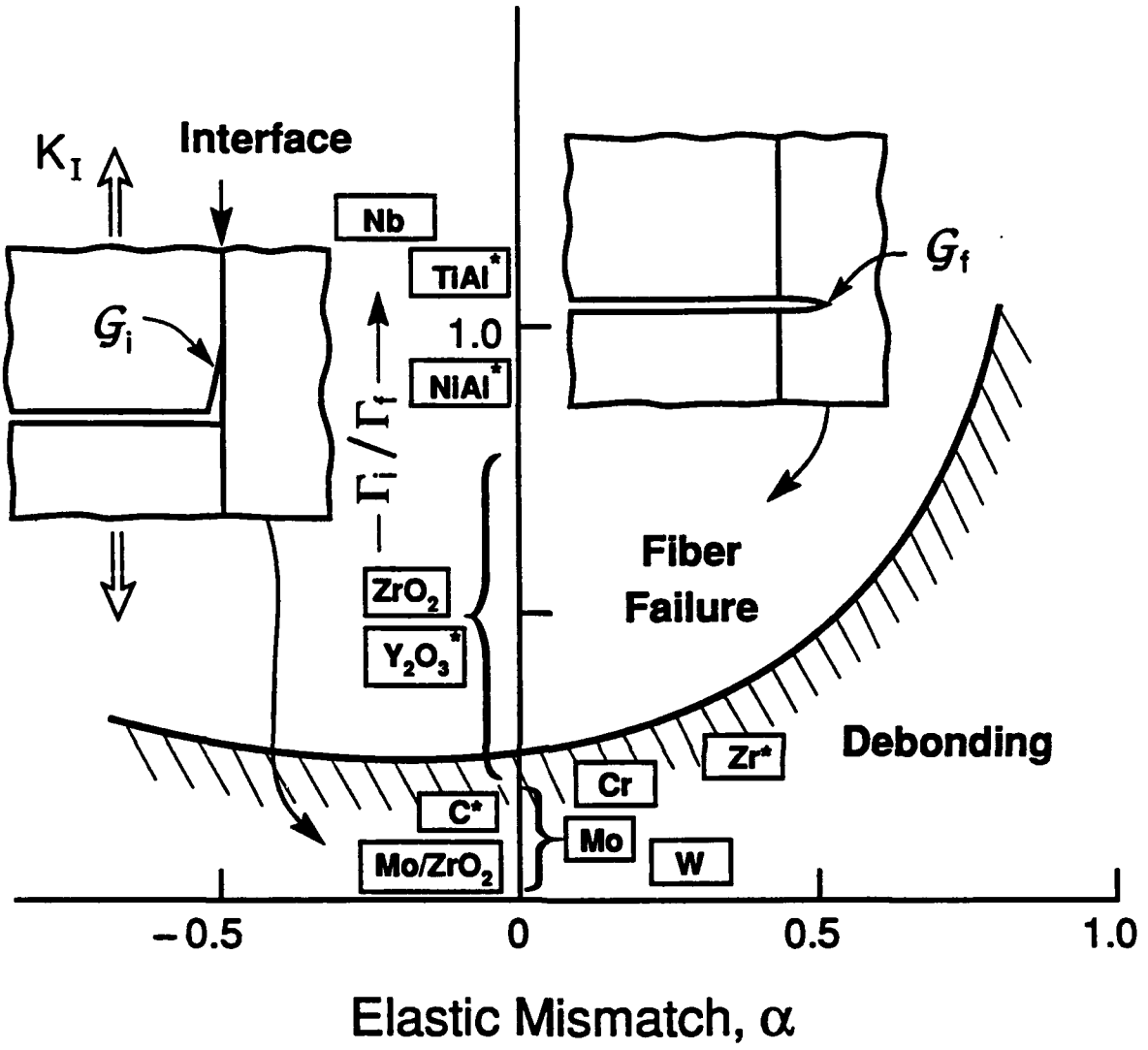
K_I
Interface
Nb
TiAl*
NiAl*
1.0
G_i
G_f
Γ_i / Γ_f
ZrO_2
Y_2O_3*
Fiber
Failure
Debonding
Zr*
Cr
Mo
W
C*
Mo/ZrO_2
−0.5
0
0.5
1.0
Elastic Mismatch, α

Figure 8b

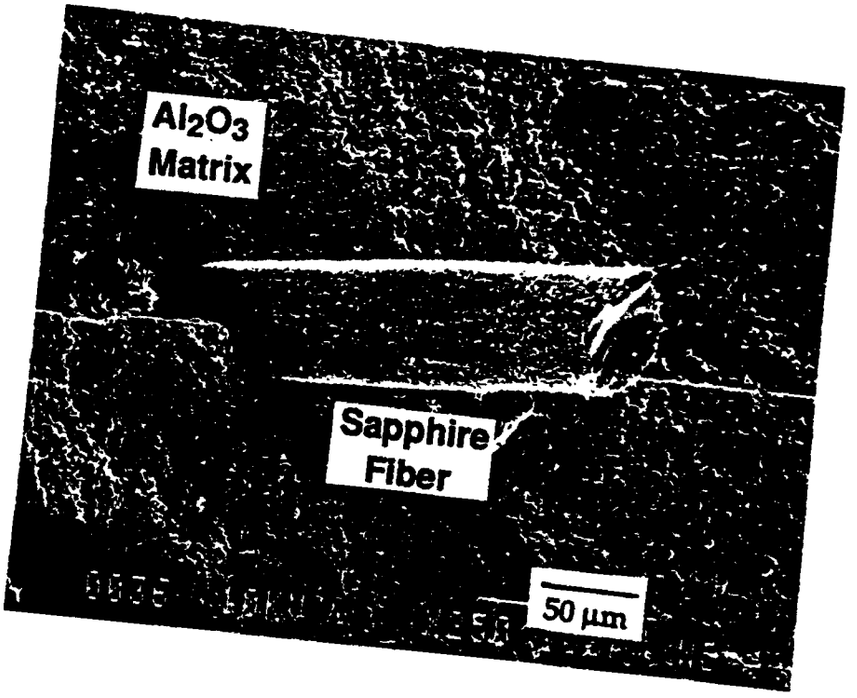

Figure 9

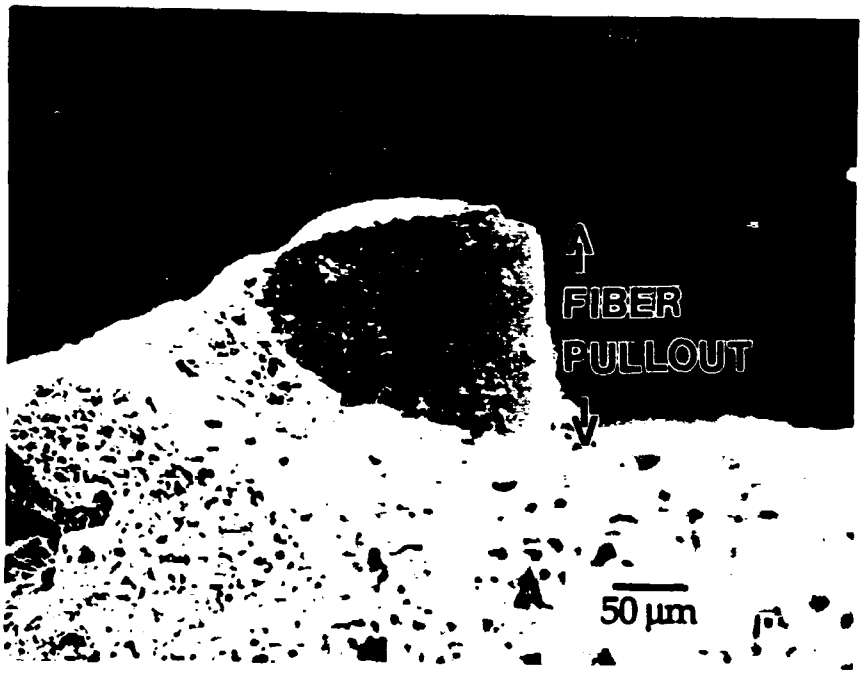

Figure 10

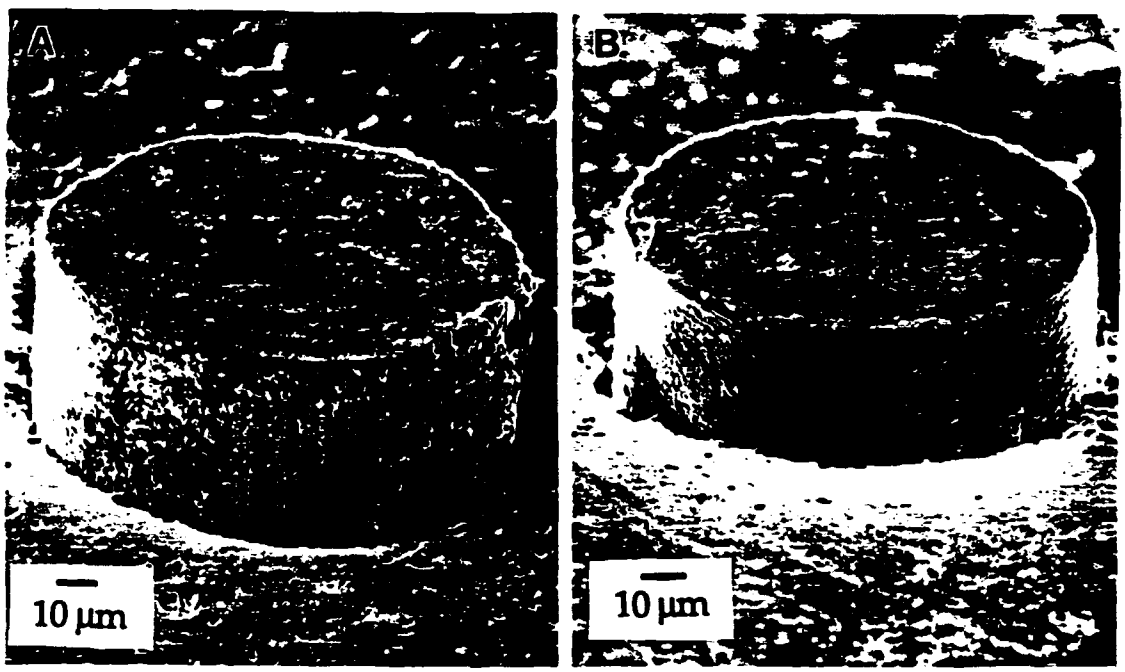

Figure 11

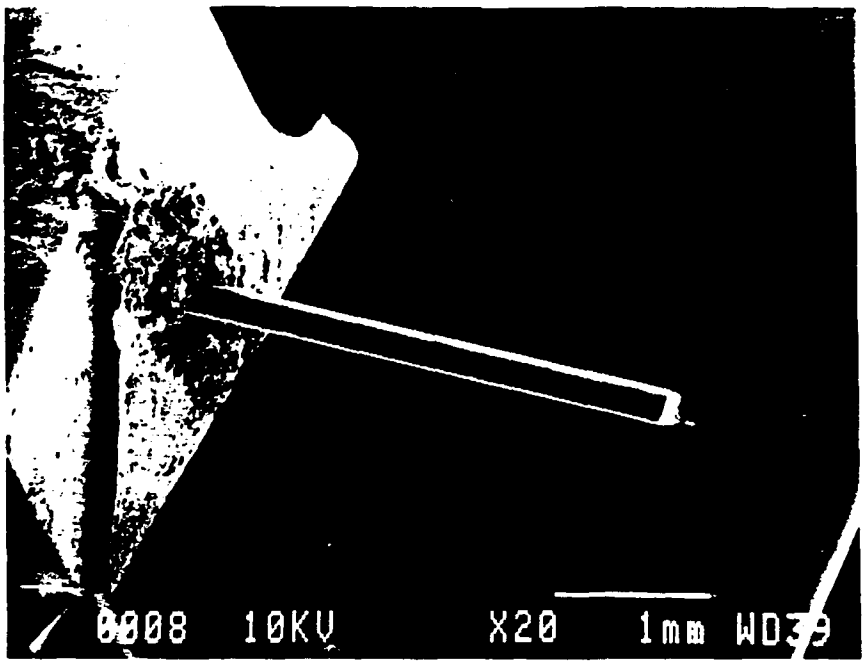

Figure 12

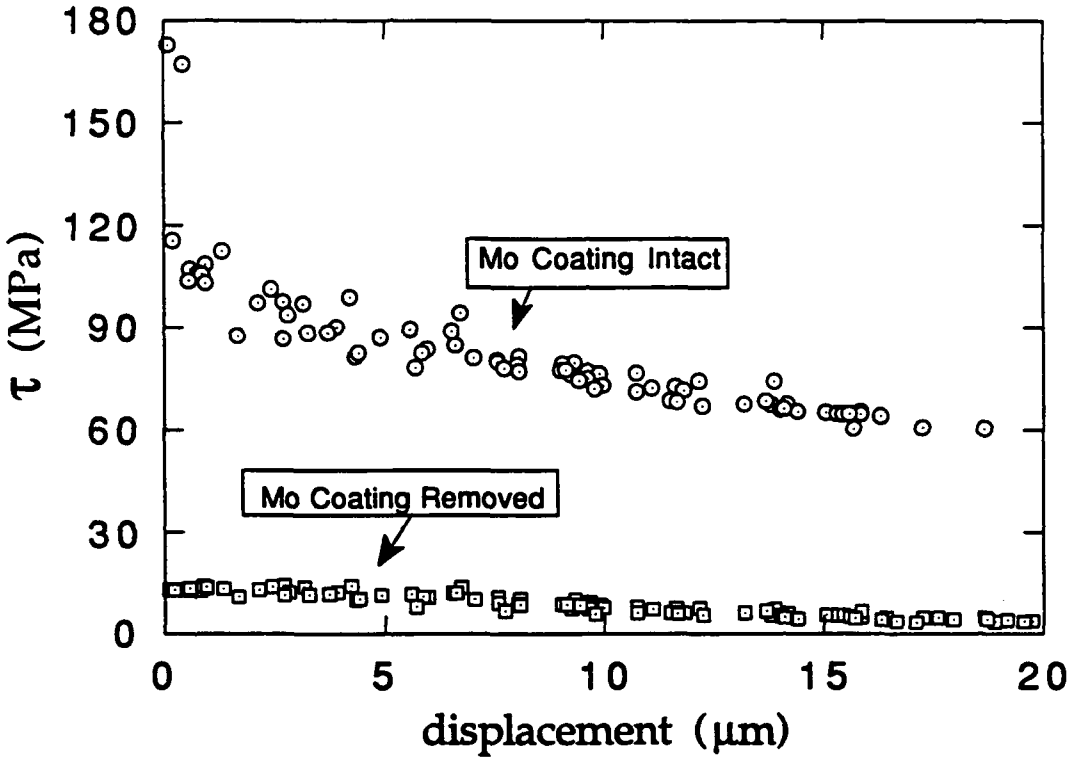
180
150
120
90
60
30
0
τ (MPa)
Mo Coating Intact
Mo Coating Removed
0
5
10
15
20
displacement (μm)

Figure 13

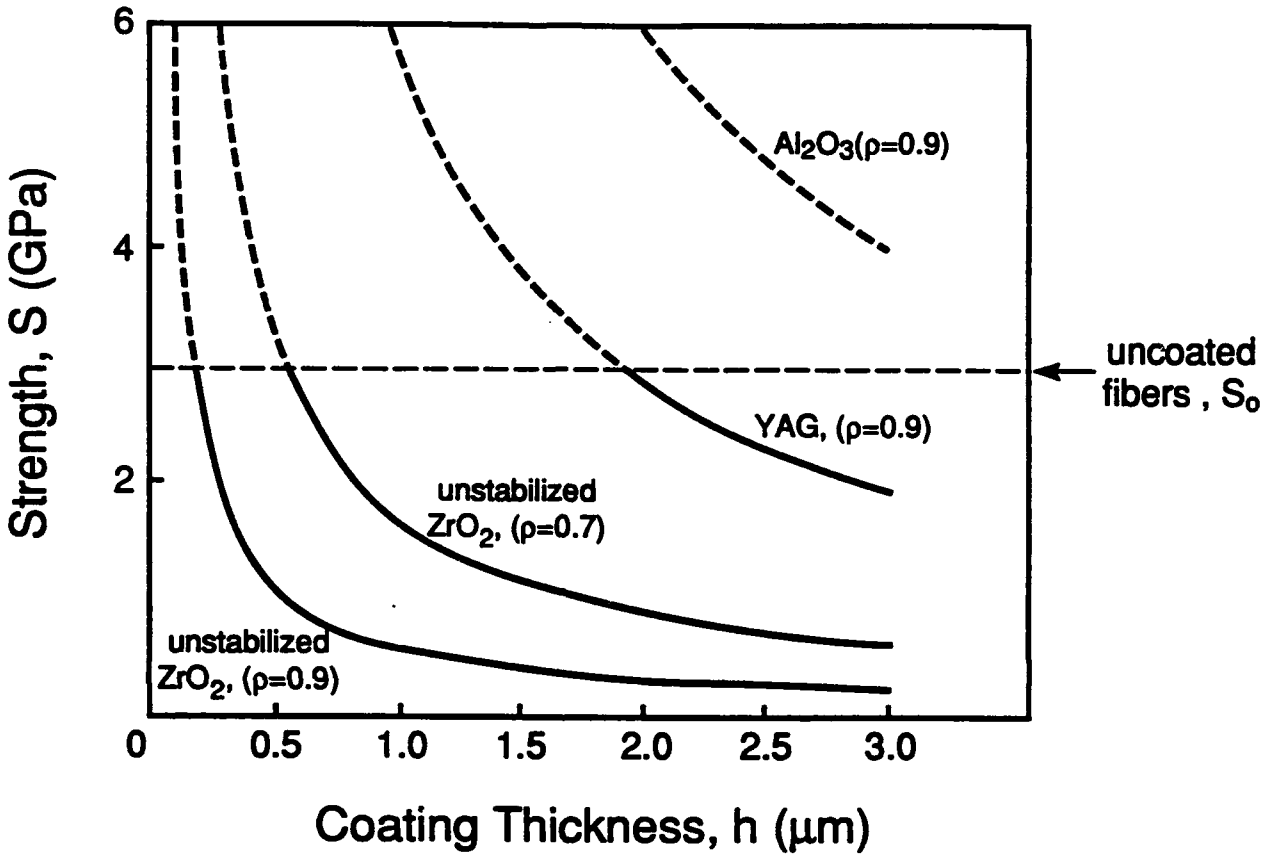
Strength, S (GPa)
6
4
2
0
0.5
1.0
1.5
2.0
2.5
3.0
Coating Thickness, h (μm)
Al2O3(ρ=0.9)
YAG, (ρ=0.9)
unstabilized ZrO2, (ρ=0.7)
unstabilized ZrO2, (ρ=0.9)
uncoated fibers , So

Figure 14

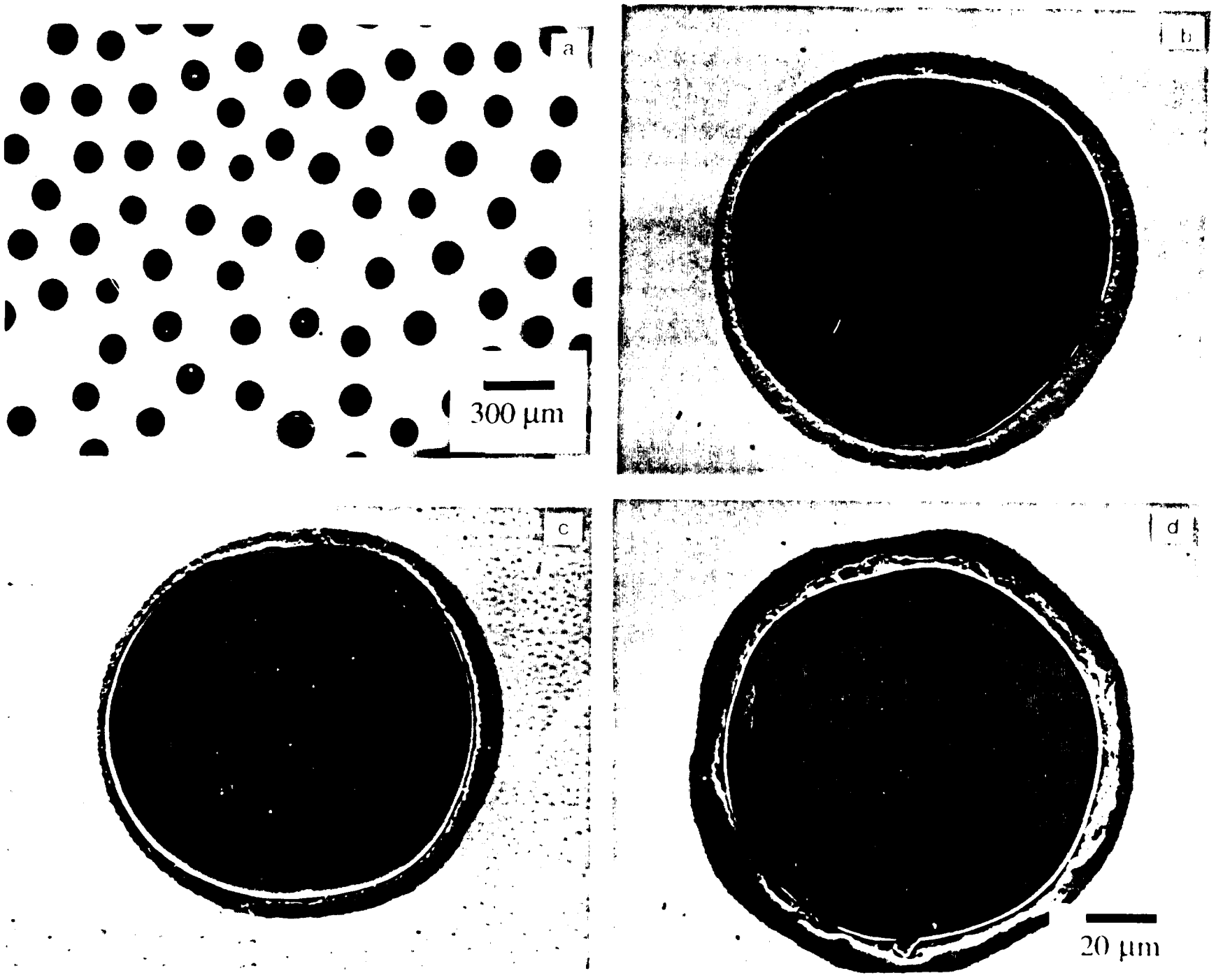
a
300 µm
b
c
d
20 µm

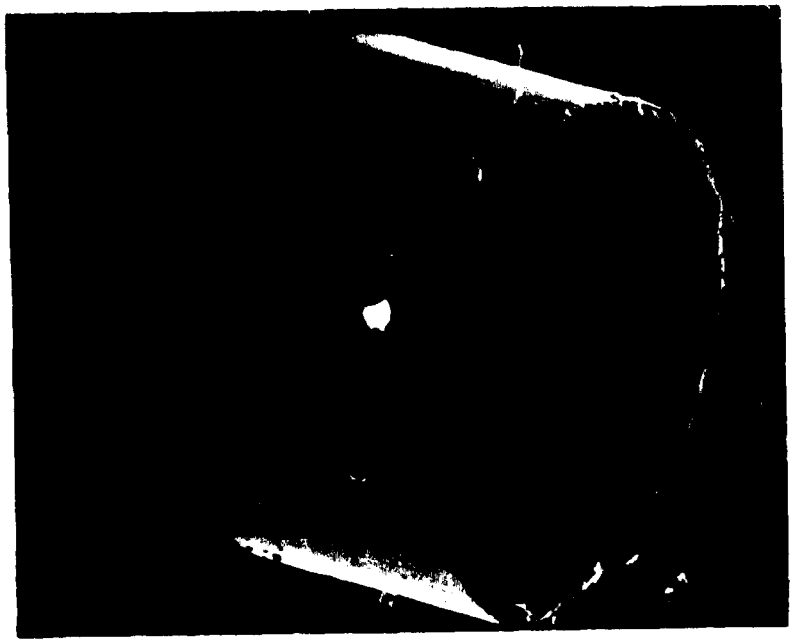

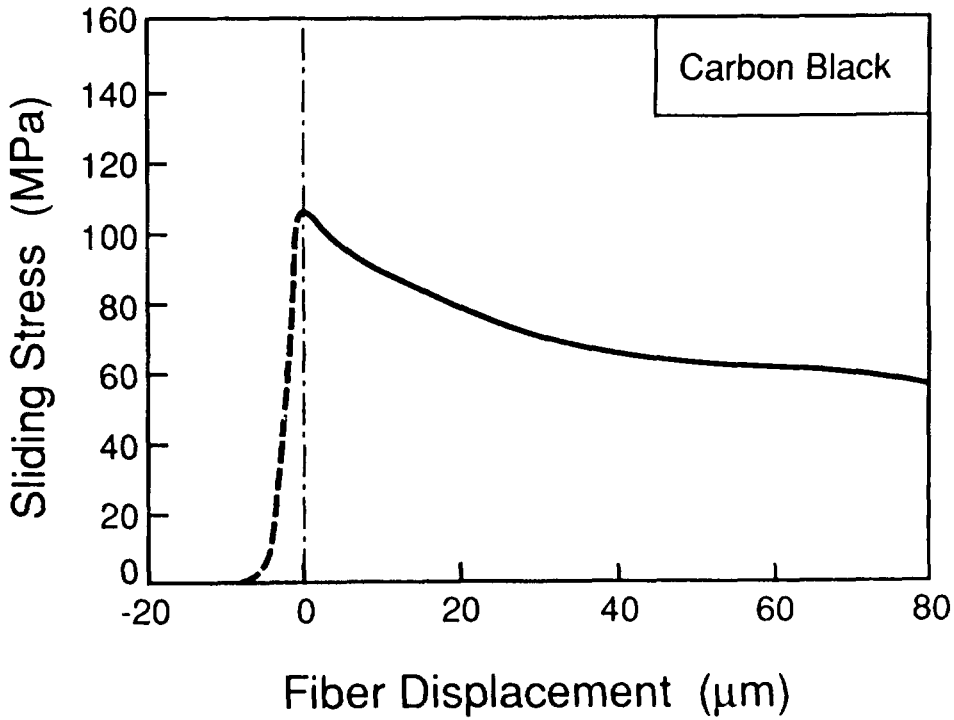
Carbon Black
Sliding Stress (MPa)
160
140
120
100
80
60
40
20
0
-20
0
20
40
60
80
Fiber Displacement (μm)

Figure 3a

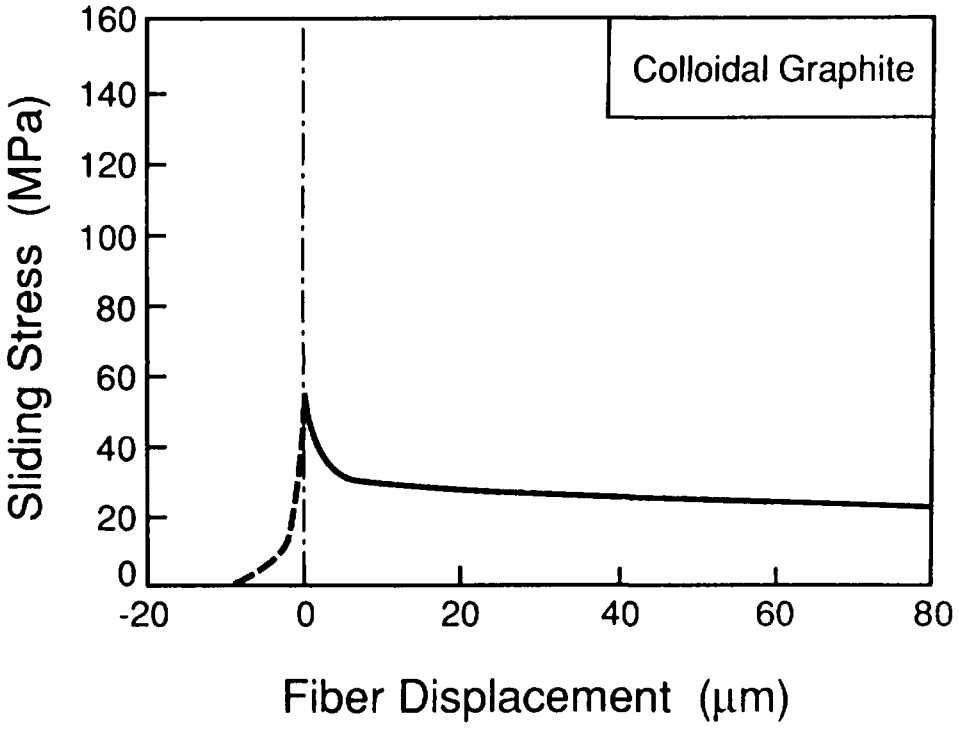
Colloidal Graphite
Sliding Stress (MPa)
160
140
120
100
80
60
40
20
0
-20
0
20
40
60
80
Fiber Displacement (μm)

Figure 3b

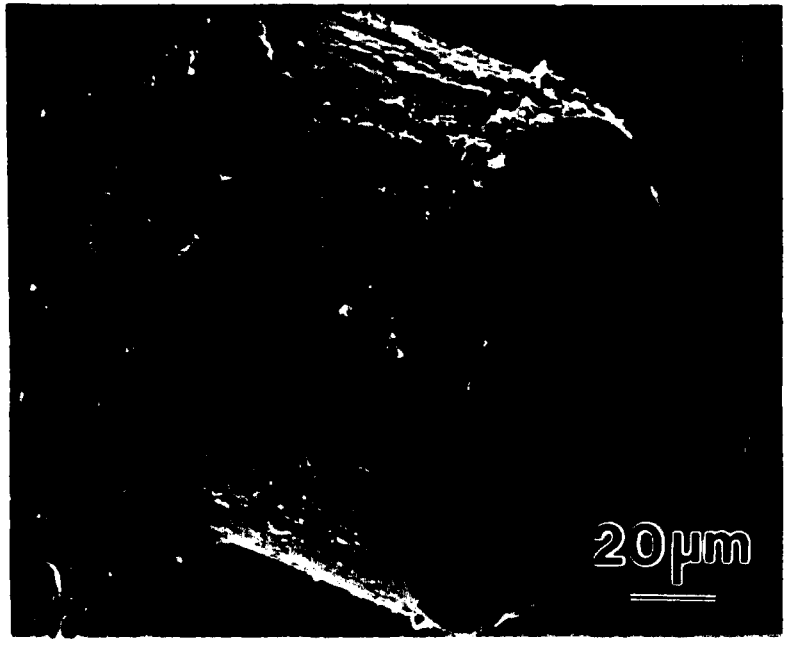
20μm

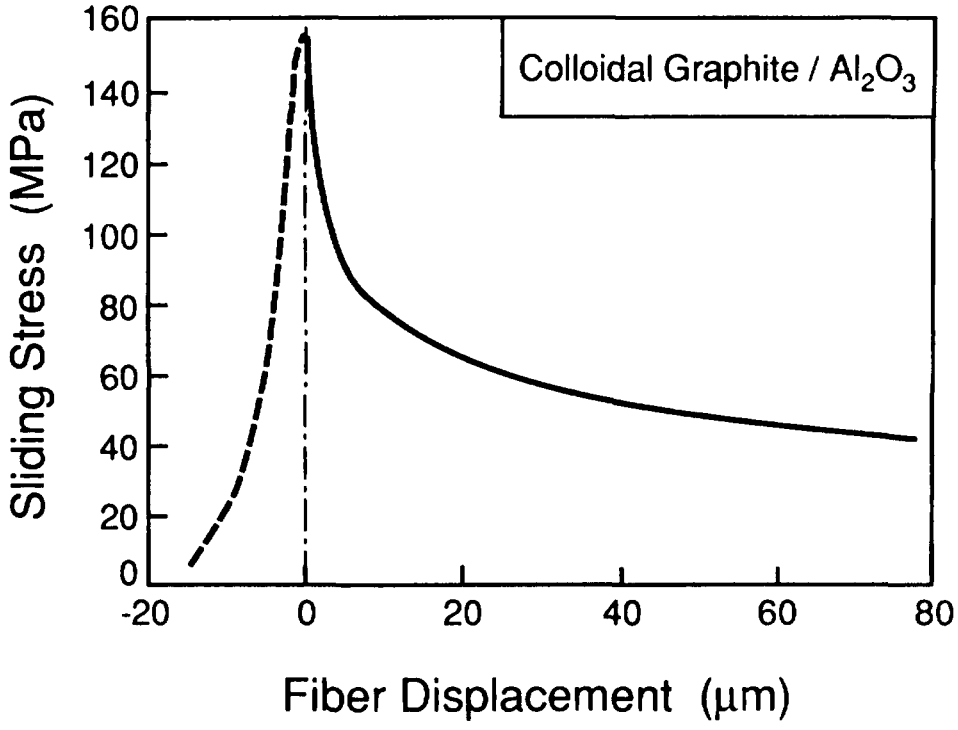
Colloidal Graphite / Al_2O_3
Sliding Stress (MPa)
160
140
120
100
80
60
40
20
0
-20
0
20
40
60
80
Fiber Displacement (μm)

Figure 3c

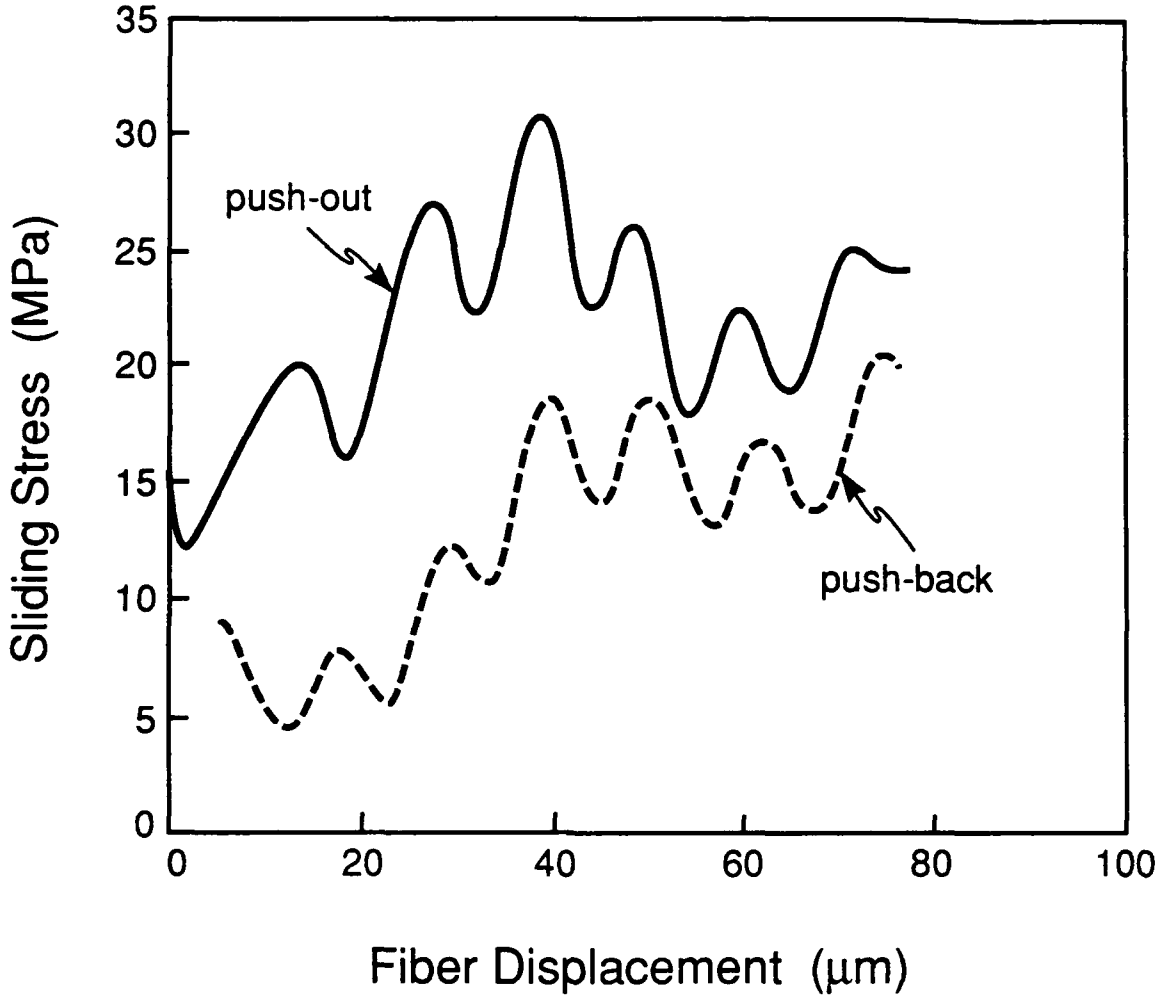
35
30
25
20
15
10
5
0
0
20
40
60
80
100
Sliding Stress (MPa)
Fiber Displacement (μm)
push-out
push-back

Figure 4

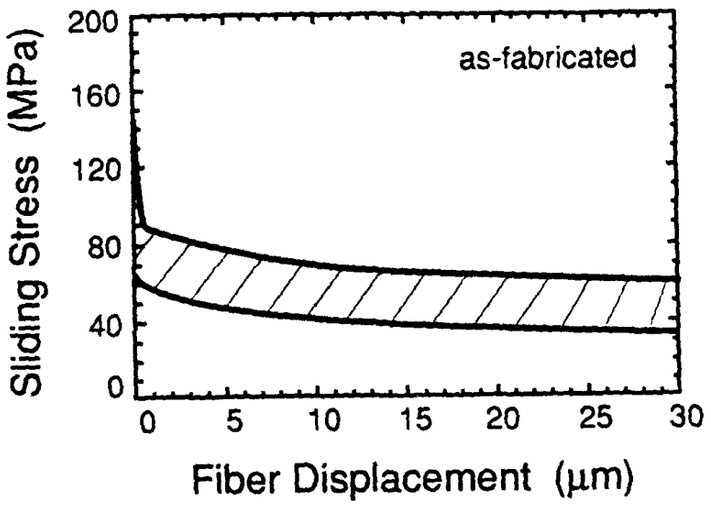

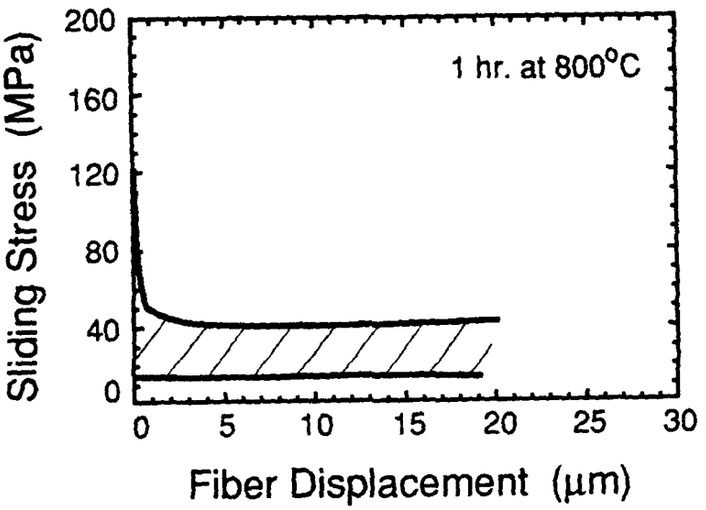

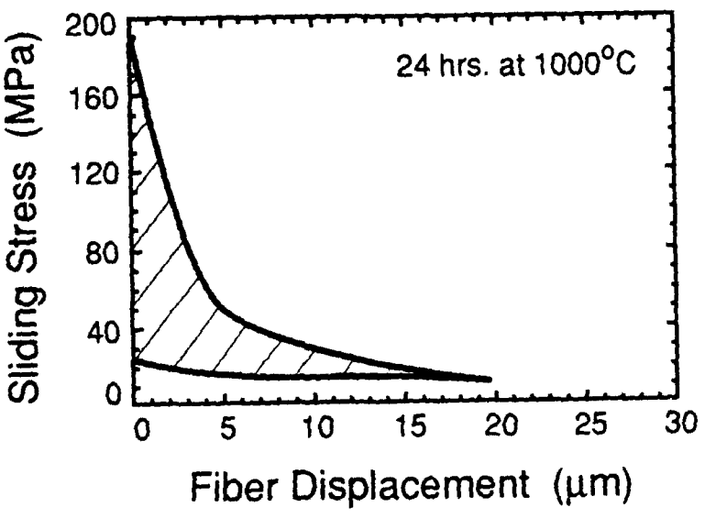

Mackin.DC-6/92-amk-D1#740-9

Figure 5a

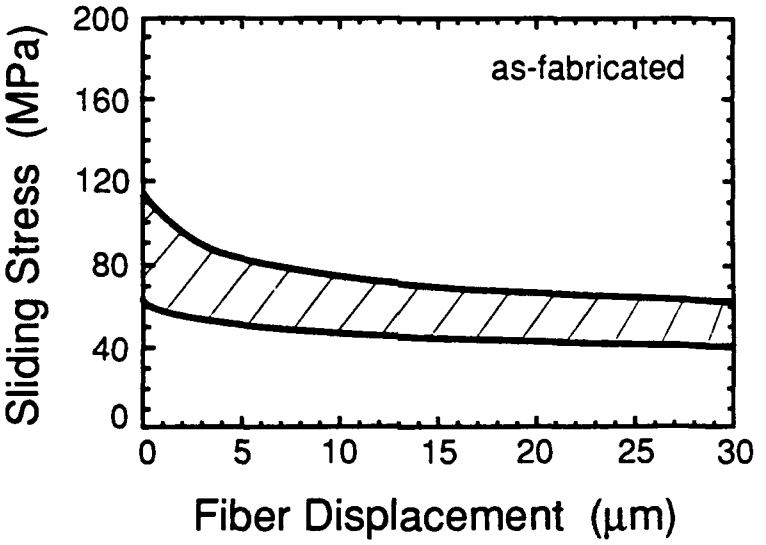
as-fabricated
Sliding Stress (MPa)
200
160
120
80
40
0
0
5
10
15
20
25
30
Fiber Displacement (μm)

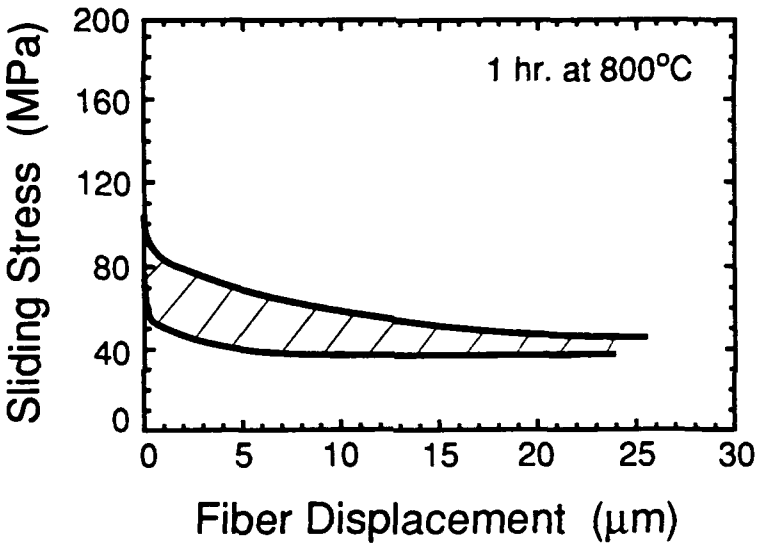
1 hr. at 800°C
Sliding Stress (MPa)
200
160
120
80
40
0
0
5
10
15
20
25
30
Fiber Displacement (μm)

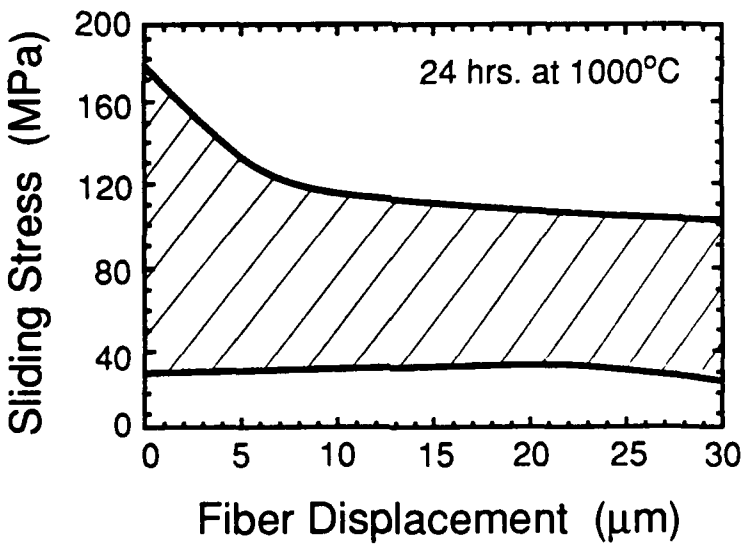
24 hrs. at 1000°C
Sliding Stress (MPa)
200
160
120
80
40
0
0
5
10
15
20
25
30
Fiber Displacement (μm)

Figure 5b

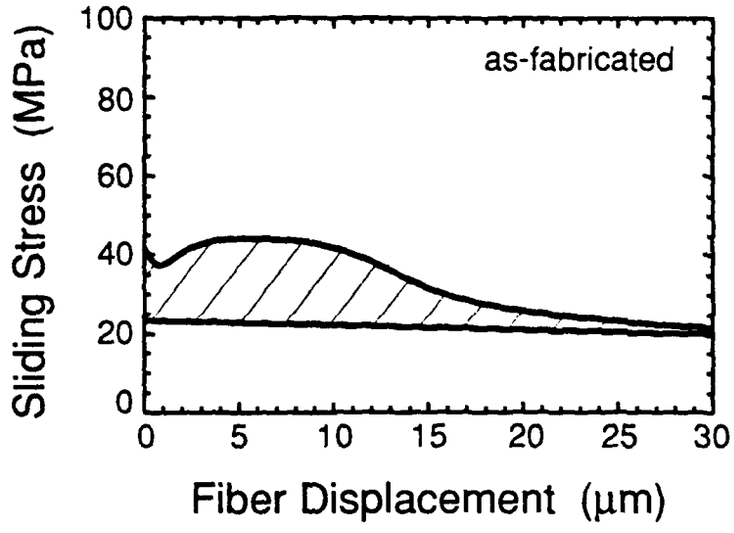

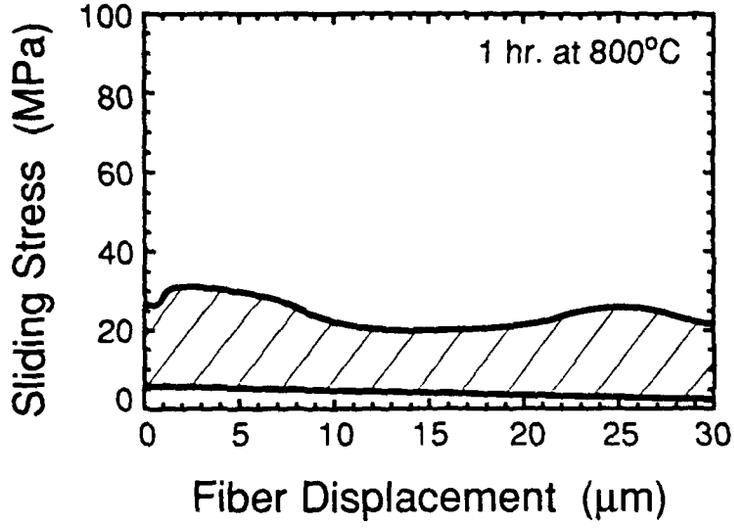

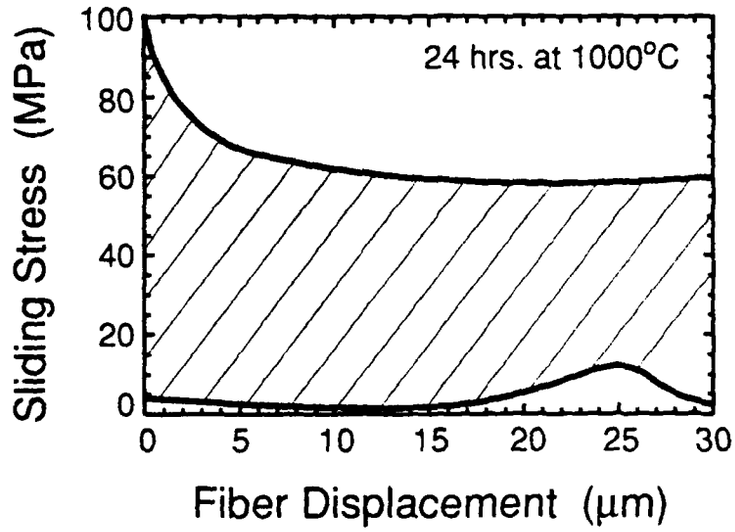

Mackin.DC•6-92•amk•D1#740-1

Figure 5c

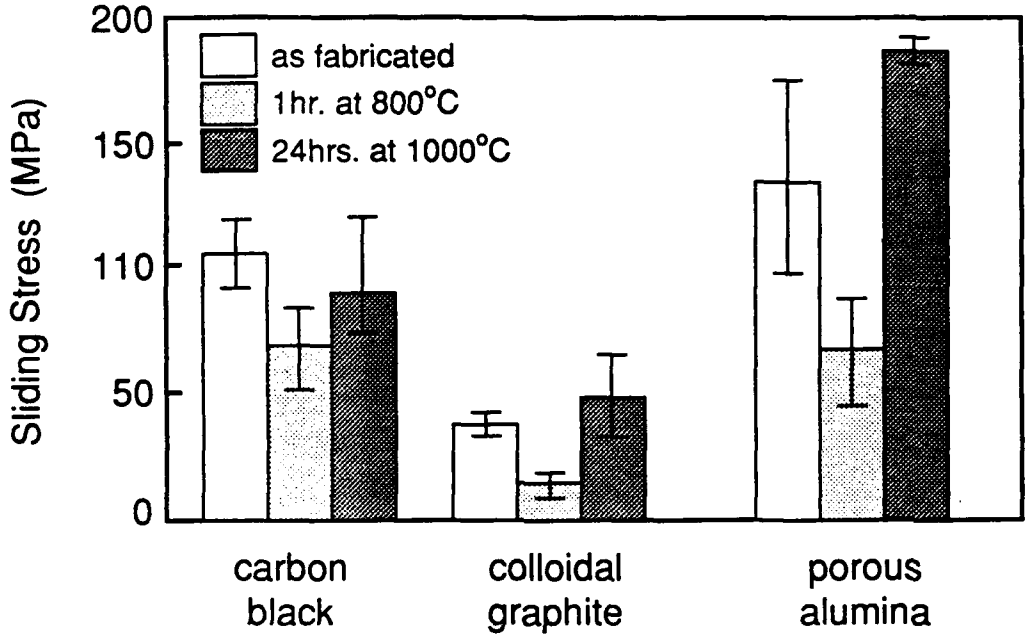

Mackin.Evans.DC•6/92•amk•D1#740-8

Figure

Figure 7

Section 4

MECHANICS OF BRITTLE MATRIX COMPOSITES

Scripta METALLURGICA et MATERIALIA
Vol. 26, pp. 1675-1680, 1992
Printed in the U.S.A.

Deformation of Nanoscale Cermets

by
A.G. Evans
Materials Department, University of California
Santa Barbara, CA 93106-5050

and
J.P. Hirth
Mechanical and Materials Engineering Department
Washington State University
Pullman, WA 99164-2920

(Received March 23, 1992)

Introduction

Cobalt-tungsten carbide cermets are prototypical dual-phase composites wherein the metal is the minor phase (volume fraction, $f_m = 0.1\text{-}0.2$), but is continuous, because of capillarity effects at the interphase interfaces during sintering. The refinement of such composites into the nanometer size scale regime is of interest and indeed, has been achieved [1], with the expectation that nanoscale refinement will enhance such properties as hardness and tensile strength. The role of plastic flow in the metal phase on the stress/strain curve of these composites is addressed in this article. The emphasis of most previous analyses of dual-phase metal/ceramic composites has been on the flow strength of systems with dispersed particles, in the $f_m > 0.5$ range. The results have been interpreted either by using a dislocation pile-up approach [2] or (for $f_m > 0.8$) by considering dislocation loops bowing around particles [3]. Here, we suggest that neither of these models is appropriate for cermets with small metal fraction ($f_m < 0.2$) at size scales in the nanometer regime. Instead, flow in the metal is related to single dislocations moving in the metal channels, controlled by an Orowan-type relation. Furthermore, the constraint of the less deformable WC is shown to provide strong flow strength elevation. The latter effect has previously been evaluated for structures in the micrometer (or greater) regime in terms of a continuum approach [4].

The flow properties are expected to be sensitive to microstructural details, especially the morphology of the metal phase. Two bounds are analyzed (Fig. 1): i) both phases are continuous, with the metal as a cylindrical network along the three-grain interface of the ceramic, ii) only the metal is continuous and thus serves as a "matrix" with embedded ceramic particles. In all cases, it is assumed that the stress is below that at which cracks form in the ceramic, that the interfaces are "strong" (do not debond) and that the ceramic is elastic. Analysis of the latter morphology is approached from two perspectives: one based strictly on continuum plasticity, wherein there are no size effects, and the other using dislocation models. Comparison of these two approaches provides important insight about nanoscale issues.

0036-9748/92 $5.00 + .00

Analysis

Both Phases Continuous

When both the metal and ceramic are continuous, the stress/strain behavior without cracking should be bilinear (Fig. 2a) and essentially the same as that found for either a metal matrix composite with continuous ceramic fibers [5] or a ceramic with a dispersed metal phase [6]. The initial modulus, E_o, is governed by that for the composite E, and the slope, E_t, beyond the "knee" is related to modulus of the composite with *all* of the stress borne by the ceramic. The intermediate behavior around the "knee" is governed by the flow properties of the metal, through the evolution of load shedding to the ceramic. The magnitude of E_t depends on the precise morphology of the metal, analogous to the strong effects of pore shape on the modulus of porous bodies. Two extremes are of interest. When the metal has the morphology of rods aligned along the loading axis, the "rule-of-mixtures" applies, such that

$$E_t/E = (1-f_m) \tag{1a}$$

Conversely, when the metal occurs as an isolated spherical phase

$$E/E_t = 1+[10/(7-5\nu_c)]f_m/(1-f_m) \tag{1b}$$

where ν_c is Poisson's ratio for the ceramic. The corresponding composite Poisson's ratio is

$$\nu_t = (1/2)-E_t(1-2\nu_c)/2E \tag{1c}$$

The location of the "knee" and the behavior in its vicinity are strongly influenced by the highly constrained nature of the plastic flow in the metal. Consequently, there are major effects of morphology and of residual stress caused by thermal expansion misfit. The details are not addressed in this article.

Continuous Metal Phase

Continuum Approach

Some basic continuum results [7,8] are reviewed first. The stress/strain curve for a thin metal layer between elastic plates (Fig. 2b), in the absence of work hardening in the metal, exhibits a non-linear transient with high apparent work hardening of the composite, followed by a limit stress, σ_t, given by;

$$\sigma_t/\sigma_o = (3/4)+(1/4)d/h \tag{2}$$

where σ_o is the uniaxial yield strength of the metal, h is the metal thickness and d the plate width. This limit stress develops after strains in the metal layer of order ϵ_o, where ϵ_o is the uniaxial yield strain. If the metal layer in the composite has uniform width *everywhere*, the initial value of d/h in Eqn. (2) is related to the metal volume fraction, in approximate accordance with

$$f_m = 3h/d. \tag{3a}$$

More generally,

$$f_m = 3\chi h/d \tag{3b}$$

where χ is dependent on the excess metal phase at three- and four-grain interfaces. The simplistic results obtained by inserting Eqn. (3c) into Eqn. (2) have several obvious limitations. The most important problems are concerned with i) the metal phase *morphology*, ii) metal phase *redistribution* and iii) *work hardening* in the metal. Even when the metal is perfectly plastic, σ_t is sensitive to χ, which dictates the metal concentration at which the ceramic phase becomes connected, f_m^*. This effect is illustrated in Fig. 2 for the case of a ceramic phase having nominal "equiaxed" morphology. As expected, $\sigma_t/\sigma_o \to \infty$ as $f_m \to f_m^*$. *Hence the definition of* f_m^* in terms of the metal phase morphology is *critical*. In addition, *conservation of volume* in the metal (assuming no debonding and no cavitation) requires metal redistribution, such that the metal phase thickness h along the transverse interfaces diminishes as the composite deforms. In the limit, h can reach zero, leading to contact of

ceramic grains and a decrease in the effective value of the area fraction f_m in some regions. This effect further elevates the flow strength as the composite deforms and obviates the existence of a limit load. Finally, work hardening in the metal increases the flow strength. Some typical effects for power law hardening with equiaxed particles (when $f_m \approx 0.8$) are illustrated in Fig. 3.

In summary, the dramatic effects of morphology and of work hardening in the metal on the stress/strain curve establish that predictions are only meaningful when complete experimental information is available concerning these factors. Without this information, the utility of the continuum description cannot be evaluated. However, it is emphasized that the continuum approach does not give a particle size effect in the absence of cracking, debonding and cavitation, at least when the morphology is size independent. Clear experimental information that particle size is important, in some cases, indicates the need for a dislocation-based approach to address certain aspects of the flow behavior.

Dislocation Approach

In the nanometer size regime, two issues are important. Dislocations can neither bow around the ceramic particles, because of geometric constraints, nor can they be sustained in a pileup array, because the stress to sustain two dislocations (the minimum size pileup) exceeds that to move a single loop. Instead, loops nucleate and deposit at the interface, as shown in Fig. 4a. The segment of these loops remaining in the metal phase can then move in the z direction as represented in Fig. 4b. In the case depicted, the dislocations in the interface are considered to be edge dislocations and the moving segments screw dislocations. The structure is analogous to that within i) persistent slip bands in fatigued metals [9]; ii) heavily deformed pearlite [10]; and iii) strained multilayer structures (strained superlattices) [11]. When the modulus of the ceramic exceeds that of the metal, the dislocations encounter an image repulsion and stand off a distance y_o from the interface [12,13]. For an extreme case of Al_2O_3/Nb, with a shear modulus ratio of 6, the stand-off distance is $y_o = 0.09h$. Hence, for most cases, this image effect can be neglected.‡

The resolved effective shear stress to move the dislocation segment is

$$\tau = \mu b \cos\phi / h \tag{4}$$

where μ is the shear modulus, b is the Burgers length and ϕ is defined in Fig. 4c. The angle ϕ is dictated by the line energy of the moving (screw) segment,

$$(W_s/L) = (\mu b^2/4\pi)\ln(h/b) \tag{5a}$$

relative to that of the edge segment deposited at the interface

$$W_e/L = [\mu b^2/4\pi(1-\nu)]\ln(\lambda/b) \tag{5b}$$

Here, λ is the mean dislocation spacing in the interface. Usually, as soon as microstrain is imposed on the system, λ decreases with strain to a limiting value , 2-3b [14]. The relation among the above quantities is: $\cos\phi = W_e/W_s$. Consequently, since W_s depends weakly on h, the power dependence of τ on h deviates only slightly from -1 *[15].

The resolved effective shear stress must equal the resolved flow strength, such that,

$$\sigma_{yy} - \sigma_{xx} = \tau/m = \mu b \cos\phi / mh \tag{6}$$

where m is the Schmid factor for the active glide plane. The relationship between σ_{yy} and σ_{xx} depends on the constraint that develops in the thin metal layers. This, in turn, depends on the plastic flow that occurs around the corners of the ceramic particulate, between the transverse and normal layers. If such flow in inhibited, the system behaves in a strictly elastic manner. Conversely, if this process occurs readily, the composite flow strength

‡If it is significant, the effective Orowan segment length becomes $h-2y_o$ instead of h.

*Usually, scatter in data is such that it is difficult to discern deviations from -1 power.

is dictated by a constraint factor, analogous to that for the continuum phenomenon, Eqn. (1). Furthermore, composite flow is controlled by the *transverse layer thickness*, which *decreases* as the composite deforms, leading to geometric hardening. Specifically, since the plastic strain is limited to the metal phase, the transverse plastic strain is

$$\epsilon^p_{xx} = \epsilon^p_{yy}/2 = -\Delta h/2d \tag{7a}$$

whereupon the transverse layer thickness reduces to

$$h/d = (h_o/d)+\epsilon^p_{xx} \tag{7b}$$

where h_o is the initial metal layer thickness. The ratio h_o/d is, in turn, related to the metal volume fraction, subject to the metal phase morphology parameter χ, Eqn. (3b). The plated dislocations in Fig. 4a provide load shedding to the ceramic phase just as in the continuum analysis. Hence, Eqn. (2) applies to this case with $\sigma_0=\tau/m$, Eqn. (6). The limit flow strength for nanoscale structure thus becomes,

$$\sigma_f = \frac{9\cos\phi\chi^2(b/d)\mu}{4m[f_m-(3\chi/2)\epsilon^p_{yy}]^2}\left\{1+\frac{f_m}{\chi}\left[1-\frac{3\chi\epsilon^p_{yy}}{2f_m}\right]\right\} \tag{8a}$$

$$= [9\cos\phi\chi^2(b/d)\mu/4mf_m]\ [1+3\chi\epsilon^p_{yy}/f_m] \tag{8b}$$

Consequently, when f_m is small and the metal phase morphology dictates that $\chi > 1$, *constraint becomes a dominant factor*, leading to linear hardening. Furthermore, there is a nanoscale size effect, associated with the term b/d. Note that the linearity in the hardening is qualitatively similar to the flow behavior expected when the ceramic phase is continuous.

Acknowledgement

The research was supported by the DARPA University Research Initiative at the University of California, Santa Barbara, under ONR contract No. 00014-86-K-0753.

References

1. B.E. Kear, Rutgers University, research in progress.
2. N.P. Louat and M.A. Imam, *Scripta Metall.*, 23, 721, (1989).
3. J.C. Williams and J.P. Hirth, in *Rapid Solidification Processing Principles and Technologies, III*, Ed. R. Mehrabian, National Bureau of Standards, Gaithersburg, MD, 1983, p. 135.
4. T. Christman, A. Needleman and S. Suresh, *Acta Metall. Mater.*, 37, 3029, (1989).
5. G.J. Dvorak and Y.N. Bahei-El-Din, *J. Appl. Mech.* 49, 327, (1982).
6. B. Budiansky, Appendix in L.S. Sigl, P.A. Mataga, R.J. Dalgleish, R.M. McMeeking and A.G. Evans, *Acta Metall.*, 36, 945, (1988).
7. G. Bao, J.W. Hutchinson and R.M. McMeeking, *Acta. Metall. Mater.*, 39, 1871, (1991).
8. R. Hill, Mathematical Theory of Plasticity, Oxford Univ. Press (1961).
9. D. Kuhlmann-Wilsdorf and C. Laird, *Mat. Sci. Eng.*, 27, 137, (1977); 37, 11, (1979).
10. M. Dollar, I.M. Bernstein and A. Thompson, *Acta Metall.*, 36, 311, (1988).
11. R. Hull and J.C. Bean, *J. Vac. Sci. Tech.*, A7, 2580, (1989).
12. J.S. Koehler, *Phys. Rev.*, B2, 547, (1970).
13. S.V. Kamat, J.P. Hirth and B. Carnahan, *Mater. Res. Soc. Symp. Proc.*, 103, 55, (1988).
14. J.P. Hirth and J. Lothe, *Theory of Dislocations*, 2nd edition, Wiley, New York, 1982.
15. M.F. Ashby, *Acta Metall.*, 14, 679, (1966).

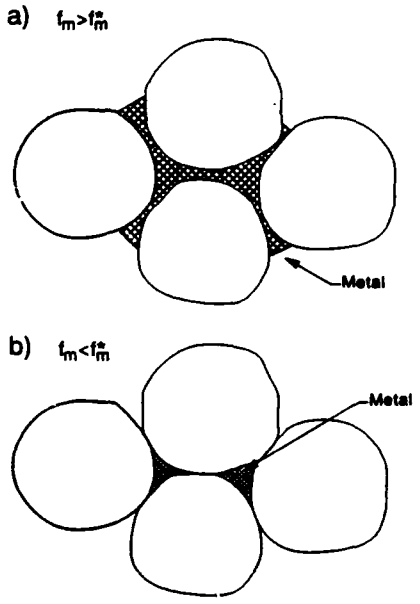

Fig.1. Ceramic-metal composites with (a), the metallic phase continuous and (b), both phases continuous.

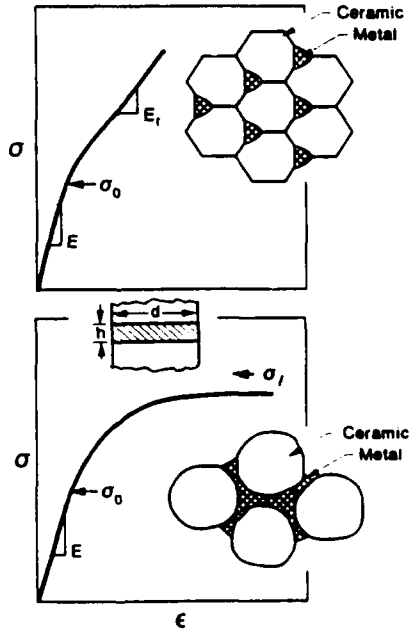

Fig. 2. Typical stress-strain curves for ceramic-metal composites with (a), both phases continuous and (b), the metallic phase continuous

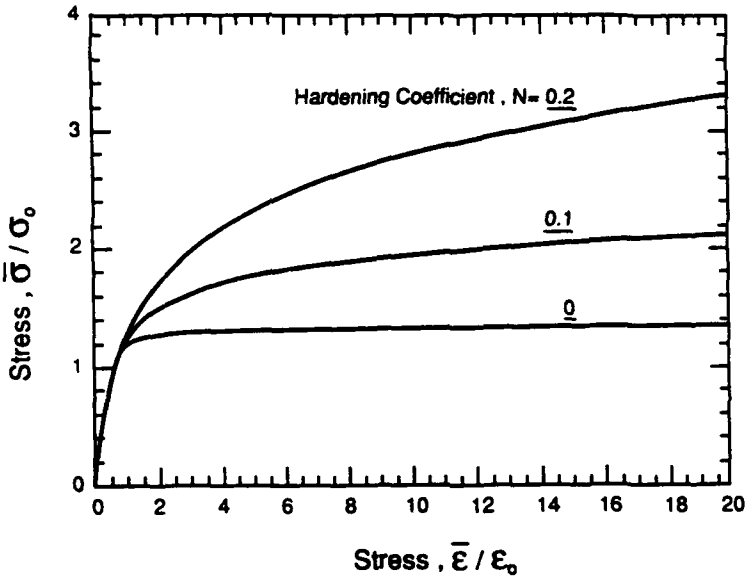

Fig. 3. Effect of power law hardening exponent N on the stress-strain behavior of a metal matrix-equiaxed ceramic particulate composite with f_m = 0.8 [7].

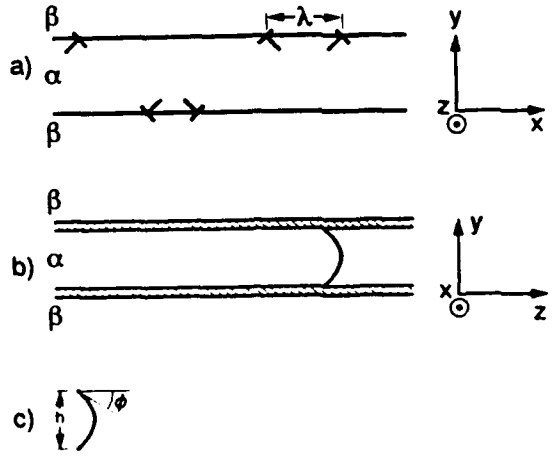

Fig. 4. Dislocations formed in α phase and (a), deposited at or near interface (view along dislocation line), (b), bowing out and moving (view perpendicular to (a). (c) shows the geometry of the bowed segment.

Mechanics of Materials 13 (1992) 59–66
Elsevier

Mixed mode delamination cracking in brittle matrix composites

G. Bao, B. Fan and A.G. Evans

Materials Department, College of Engineering, University of California, Santa Barbara, CA 93106-5050, USA

Received 30 March 1990; first revision 6 November 1990 and second revision 26 September 1991

The growth of delamination cracks from holes and notches in laminated brittle matrix composites is addressed. It is demonstrated that the behavior is strongly influenced by tractions on the delamination crack faces, caused either by intact matrix ligaments or by bridging fibers. These tractions cause the phase angle of loading ψ associated with delamination to increase appreciably as the crack extends, causing mode I to be suppressed. This effect can lead to increased resistance to delamination as the crack extends, whenever the fracture mechanism along the delamination plane has a ψ dependent fracture energy. Trends in resistance curves are predicted.

1. Introduction

Mixed mode cracking is an important damage mechanism in laminated brittle matrix composites, such as ceramic matrix, carbon–carbon, and epoxy matrix systems (Sbaizero et al., 1990; Wang, 1979; Trewetthey et al., 1988; O'Brien, 1982) and in wood (Ashby et al., 1985). Such damage is manifest as delaminations which occur from edges and from either notches (Fig. 1) or holes and as interlaminar cracks which are formed in regions of high in-plane shear stresses. Many of the important modes are manifest upon the flexural and tensile testing of notched beams and plates. While the damage can have some beneficial influences on performance in special loading situations, generally these mechanisms are detrimental and should be suppressed to achieve acceptable structural performance.

Preliminary studies of delamination crack growth resistance have indicated that cracking is strongly resisted by fibers that cross-over the crack

Fig. 1. A delamination crack propagating from a notch in a laminated ceramic matrix composite.

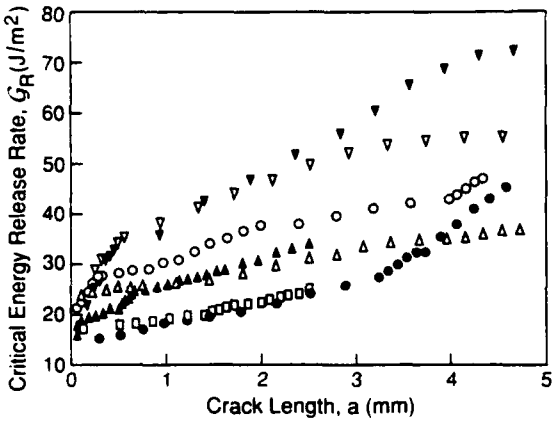

Fig. 2. A series of resistance curves evaluated for delamination crack growth in a laminated ceramic matrix composite when fibers bridge the crack surfaces.

plane leading to a resistance curve (Sbaizero et al., 1990; Bordia et al., 1991) (Fig. 2). An important issue thus appears to be the presence and magnitude of forces normal to the crack, induced either by intact reinforcements or by matrix ligaments. Understanding of this problem also assists in the prediction of effects on mixed mode cracking of a small volume fraction of reinforcements normal to the crack plane, in accordance with 3-D reinforcing schemes. Toward this objective, the present study encompasses calculations of delamination cracks subject to crack surface tractions. Some approximate analytical results are presented first to provide the relevant background. Then, finite element results are generated and used to establish the major trends in the delamination resistance.

2. Some basic mechanics

An assessment of the effects of normal tractions on delamination cracking is obtained (Fig. 3a) by applying an axial stress σ to the composite causing a delamination crack to extend from an edge notch, depth h. The delamination crack is also subject to surface tractions, magnitude p. For the problem posed in this manner, the body is strictly linear and consequently, the stress intensity factors induced by σ and by p can be added together to give the net magnitudes.

Some important background is provided by solutions for a layer on a substrate with net section width H subjected to an end force P and a moment M (Fig. 3b). Rigorous analytical solutions exist for the steady-state situation wherein the crack length a is long compared with the layer thickness, $h(a/h \gtrsim 3)$. For the elastically homogeneous case, the solution has the form (Suo and Huchinson, 1989)

$$K_I = \frac{P}{\sqrt{2hA}} \cos\omega + \frac{M}{\sqrt{2h^3 I}} \sin(\omega+\gamma),$$
$$K_{II} = \frac{P}{\sqrt{2hA}} \sin\omega - \frac{M}{\sqrt{2h^3 I}} \cos(\omega+\gamma), \quad (1)$$

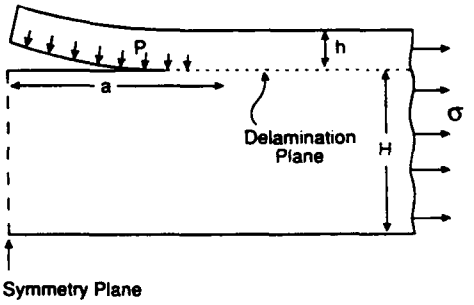

a) Specimen Configuration

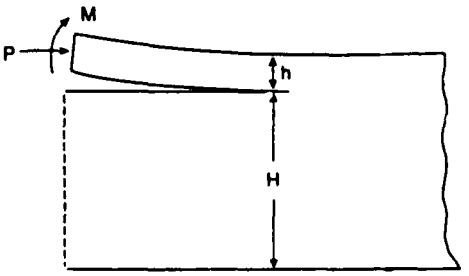

b) Equivalent Configuration

Fig. 3. (a) A schematic of the delamination crack configuration used for the analysis. (b) A layer subject to an end load P and moment M and the equivalence with the problem posed in (a).

where K_I and K_{II} are the mode I and mode II stress intensity factors, respectively, and A and I are geometric factors given by

$$\frac{1}{A} = 1 + 4\eta + 6\eta^2 + 3\eta^3, \qquad \frac{1}{I} = 12(1+\eta^3),$$
$$\text{with, } \frac{\sin\gamma}{\sqrt{AI}} = 6\eta^2(1+\eta), \qquad \eta = \frac{h}{H}. \tag{2}$$

Note the important effect of the relative notch depth, h/H, on the contribution caused by the end load, P.

The effect of the stress σ in the present problem is directly analogous to that of an end force, with

$$P = \sigma h, \tag{3}$$

because the stress in the body below the notch does not contribute to the stress intensities on the delamination crack. Consequently, the effects of σ are given in steady-state by

$$\frac{K_I}{\sigma\sqrt{h}} = \frac{\cos\omega}{\sqrt{2A}}, \qquad \frac{K_{II}}{\sigma\sqrt{h}} = \frac{\sin\omega}{\sqrt{2A}}. \tag{4}$$

An appreciable influence of the relative notch depth, h/H, is apparent. The energy release rate $\mathcal{G}$ and the phase angle of loading ψ can be derived from Eq. (4) using

$$\frac{E\mathcal{G}}{1-\nu^2} = K_I^2 + K_{II}^2 \tag{5a}$$

and

$$\psi = \tan^{-1}(K_{II}/K_I). \tag{5b}$$

The magnitudes are

$$\frac{E\mathcal{G}}{\sigma^2 h(1-\nu^2)} = \frac{1}{2A} \tag{6a}$$

and

$$\psi \equiv \omega = 52.1^\circ - 3\eta^\circ. \tag{6b}$$

The stress p on the crack face imposes a moment M per unit length on the layer. When p is uniform and acts over the entire length of the crack (Fig. 3a), M is given by

$$M = -\tfrac{1}{2}pa^2. \tag{7}$$

In addition to this moment, shear deformations exist in the beam above the crack, which are likely to have an important influence on the stress intensities, except when a/H is large. Inserting Eq. (4) into Eq. (1) thus gives approximate results for the steady-state stress intensities

$$\frac{K_I}{p\sqrt{h}} = -\frac{\sin(\omega+\gamma)}{2\sqrt{2I}}\left(\frac{a}{h}\right)^2,$$
$$\frac{K_{II}}{p\sqrt{h}} = \frac{\cos(\omega+\gamma)}{2\sqrt{2I}}\left(\frac{a}{h}\right)^2. \tag{8}$$

Combining the contributions to K from σ and p, the tip "steady-state" stress intensities are

$$\frac{K_I^t}{\sigma\sqrt{h}} = \frac{\cos\omega}{\sqrt{2A}} - \frac{1}{2}\left(\frac{p}{\sigma}\right)\left(\frac{a}{h}\right)^2\frac{\sin(\omega+\gamma)}{\sqrt{2I}},$$
$$\frac{K_{II}^t}{\sigma\sqrt{h}} = \frac{\sin\omega}{\sqrt{2A}} + \frac{1}{2}\left(\frac{p}{\sigma}\right)\left(\frac{a}{h}\right)^2\frac{\cos(\omega+\gamma)}{\sqrt{2I}}. \tag{9}$$

An important preliminary feature of the solution is the recognition that the mode I tip stress intensity diminishes as the crack extends whereas the mode II component *increases*, because of the dominant effect of the moment contribution caused by p. Furthermore K_I^t becomes zero at a *critical crack length* a_c given by

$$\left(\frac{a_c}{h}\right)^2 = 2\left(\frac{\sigma}{p}\right)\sqrt{\frac{I}{A}}\,\frac{\cos\omega}{\sin(\omega+\gamma)}. \tag{10}$$

A small stress p relative to σ is thus sufficient to close the delamination crack at lengths of order a few times the notch depth, h.

The interpretation of experimental results is facilitated by obtaining the tip energy release rate $\mathcal{G}^t$ and the phase angle of loading ψ^t as a function of delamination crack length. Hence, from Eq. (9)

$$\frac{E\mathcal{G}^t}{\sigma^2 h(1-\nu^2)} = \frac{1}{2A} + \frac{1}{8I}\left(\frac{p}{\sigma}\right)^2\left(\frac{a}{h}\right)^4 - \frac{\sin\gamma}{2\sqrt{AI}}\,\frac{p}{\sigma}\left(\frac{a}{h}\right)^2 \tag{11a}$$

and

$$\psi^{\mathrm{t}} = \omega + \phi, \tag{11b}$$

where

$$\tan\phi = \frac{1}{2}\sqrt{\frac{A}{I}}\,\frac{p}{\sigma}\left(\frac{a}{h}\right)^2 \cos\gamma \times\left[1 - \frac{1}{2}\sqrt{\frac{A}{I}}\,\frac{p}{\sigma}\left(\frac{a}{h}\right)^2 \sin\gamma\right]^{-1}. \tag{11c}$$

Note that in general $\mathcal{G}^{\mathrm{t}}$ is larger than $\mathcal{G}$ in Eq. (6a). When $\eta = h/H \ll 1$, the value of $\mathcal{G}^{\mathrm{t}}/\mathcal{G}$ at $a = a_c$ is

$$\mathcal{G}^{\mathrm{t}}/\mathcal{G} = 1 + \cos^2\omega \approx 1.6. \tag{12}$$

Consequently, the somewhat unexpected result emerges that the tractions *do not* shield the crack tip. *Other features are needed to explain the experimental observation that $\mathcal{G}_R$ increases as the crack extends* (Sbaizero et al., 1990; Bordia et al., 1991).

The above behavior is modified when the stress p acts over a definite length l rather than the entire crack length. For that case, a in Eq. (11) is replaced by l, whereupon $\mathcal{G}^{\mathrm{t}}$ and ψ^{t} are independent of the delamination crack length when a is large compared with h and l. Then, provided that the crack does not arrest before a exceeds l, the delamination will continue to propagate subject to steady-state values of $\mathcal{G}^{\mathrm{t}}$ and ψ^{t}.

3. Numerical solutions

3.1. The finite element method

Stress intensity factors and energy release rates are determined with the finite element code, ABAQUS. Symmetry about the midsection of the beam, depicted in Fig. 3a, allows the requisite solutions to be obtained by considering one half of the beam. The finite element mesh used in the calculation is shown in Fig. 4. To ensure the accuracy of the "steady-state" result, the beam length L/h is chosen to be 15 (Fig. 4). Since the problem is linear, calculations are carried out separately for the axial loading σ and for the surface tractions p.

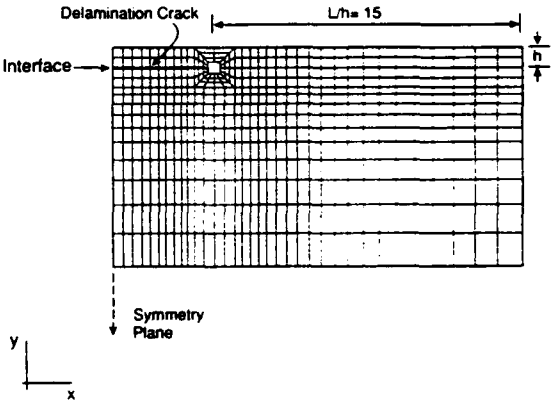

Fig. 4. Finite element mesh used for the calculations.

Stress intensities K_{I} and K_{II} are calculated from nodal displacement Δu_x and Δu_y in the crack tip region, using (Rice, 1968)

$$\Delta u_x = \frac{\kappa + 1}{2\mu}\sqrt{\frac{r}{2\pi}}\,K_{\mathrm{II}}$$

and

$$\Delta u_y = \frac{\kappa + 1}{2\mu}\sqrt{\frac{r}{2\pi}}\,K_{\mathrm{I}}, \tag{13}$$

where $\kappa = 3 - 4\nu$ and μ is the shear modulus. The values of K thus computed are then used to obtain $\mathcal{G}$ which, in turn, is compared with the value of the J-integral given in the finite element calculation, to assess consistency.

3.2. Results

Solutions for K and $\mathcal{G}$ have been evaluated separately for the applied stress, σ, and the crack surface traction, p. The effect of σ obtained for $h/H = 0.1$ are plotted in Fig. 5, using the nondimensional parameters $K/\sigma\sqrt{h}$ and $E\mathcal{G}/\sigma^2 h(1-\nu^2)$. Also indicated on the figure are analytical results for steady-state crack extension. Two aspects of the results are noteworthy. The steady-state values of $K/\sigma\sqrt{h}$ and $E\mathcal{G}/\sigma^2 h(1-\nu^2)$ are in close agreement with the analytical solutions (Eq. (4)). Furthermore, steady-state conditions for mode I develop even when $a/h < 1$, but only occur for mode II when $a/h \approx 2$. In addition, there is an appreciable decrease in the energy

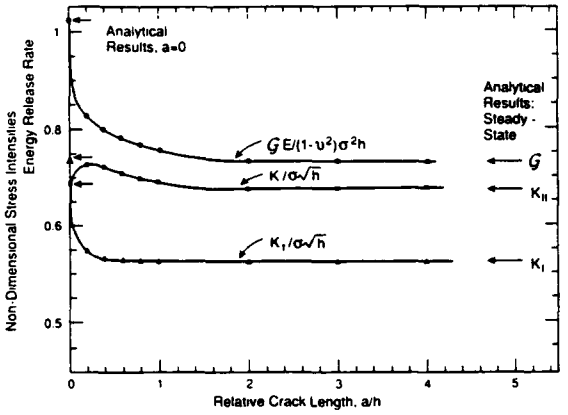

Fig. 5. Nondimensional stress intensities and energy release rate as a function of relative delamination crack length for an applied stress, σ.

release rate between $0 \leq a/h \lesssim 2$, indicative of a region of stable crack extension.

The stress intensities caused by p acting along the entire crack surface are presented using the normalization suggested by Eq. (8): $K(h/a)^2/p\sqrt{h}$. The results, plotted in Fig. 6, reveal that the nondimensional K_{II} attains "steady-state" at $a/h = 1$ and furthermore, the steady-state value is comparable to the beam theory prediction from Eq. (8). However, the nondimensional K_I does not attain "steady-state," even for $a/h = 5$. In addition, K_I is larger than the beam theory prediction (Eq. (8)). The difference is attributed to effects of shear deformation. The net influence of this deformation is a stronger effect of the tractions p on $\mathcal{G}$ than anticipated by the analytical results (Eq. (11a)).

4. Resistance curves

The delamination fracture resistance can be ascertained from the preceding results by adopting a *crack extension criterion*. This criterion requires that the tip energy release rate $\mathcal{G}^t$ attains the fracture energy $\Gamma_i(\psi)$ of the material along the delamination plane. The fracture energy typically has the form (Jensen et al., 1991)

$$\Gamma_i(\psi) = \Gamma_0\left[1 - (1 - \lambda_2)\sin^2\psi\right]^{-1}, \tag{14}$$

where Γ_0 is the fracture energy at $\psi = 0$ and λ_2 is a material dependent coefficient, typically in the range 0.1 to 0.3.

Letting $\mathcal{G}$ in Eq. (6a) become the measured energy release rate $\mathcal{G}_R$, the following result is obtained

$$\frac{P}{\sigma} = \sqrt{\frac{\Gamma_0}{\mathcal{G}_R}}\sqrt{\frac{\Sigma}{A}}. \tag{15}$$

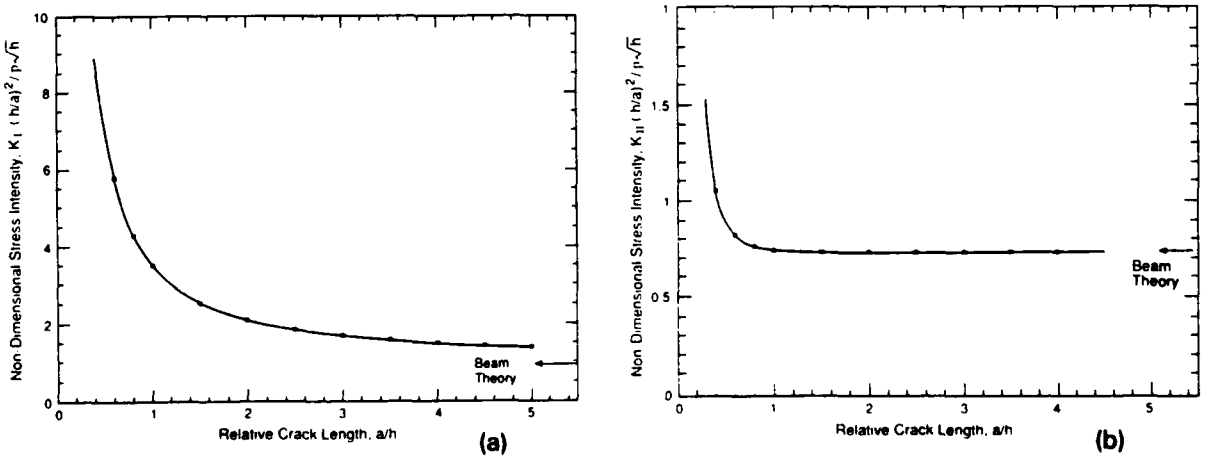

Fig. 6. Nondimensional stress intensity as a function of relative delamination crack length for crack surface tractions, p (a) K_I and (b) K_{II}.

where Σ is a nondimensional parameter representing the effect of p,

$$\Sigma = \frac{p^2 h(1-\nu^2)}{2E\Gamma_0}. \tag{16}$$

Furthermore, equating $\mathcal{G}^{\mathrm{t}}$ to Γ_i and using Eq. (15), the normalized energy release rate $\mathcal{G}_{\mathrm{R}}/\Gamma_0$ for "steady-state" is determined by the following set of parametric equations

$$\frac{\Gamma_0}{\mathcal{G}_{\mathrm{R}}}\left[1-(1-\lambda_2)\sin^2\psi^{\mathrm{t}}\right]^{-1} = 1 + \frac{\Gamma_0}{\mathcal{G}_{\mathrm{R}}}(l_{\mathrm{d}})^4 - 2\sin\gamma\sqrt{\frac{\Gamma_0}{\mathcal{G}_{\mathrm{R}}}}(l_{\mathrm{d}})^2 \tag{17a}$$

and

$$\psi^{\mathrm{t}} = \omega + \phi \tag{17b}$$

and

$$\tan\phi = \sqrt{\frac{\Gamma_0}{\mathcal{G}_{\mathrm{R}}}}(l_{\mathrm{d}})^2\cos\gamma \times\left[1-\sqrt{\frac{\Gamma_0}{\mathcal{G}_{\mathrm{R}}}}(l_{\mathrm{d}})^2\sin\gamma\right]^{-1}, \tag{17c}$$

where l_{d} is a characteristic delamination crack length

$$l_{\mathrm{d}} = \left(\frac{\Sigma}{4I}\right)^{1/4}\left(\frac{a}{h}\right). \tag{18}$$

It is readily apparent from Eqs. (17) and (18) that $\mathcal{G}_{\mathrm{R}}/\Gamma_0$ depends on Σ only through l_{d}. The trends in $\mathcal{G}_{\mathrm{R}}/\Gamma_0$ as a function of l_{d} are plotted in Fig. 7 for different values of λ_2. *Resistance curve behavior is predicted.* Each resistance curve in Fig. 7 terminates at a critical value of l_{d} at which the phase angle ψ^{t} becomes $\pi/2$. In addition, it is apparent that the value of λ_2 has a strong effect on the predicted resistance behavior. *Indeed, when $\lambda_2 = 1$, the resistance $\mathcal{G}_R$ decreases, because, as already noted, the tractions p induce an appreciable K_{II}, having the same sign as the contribution from σ.*

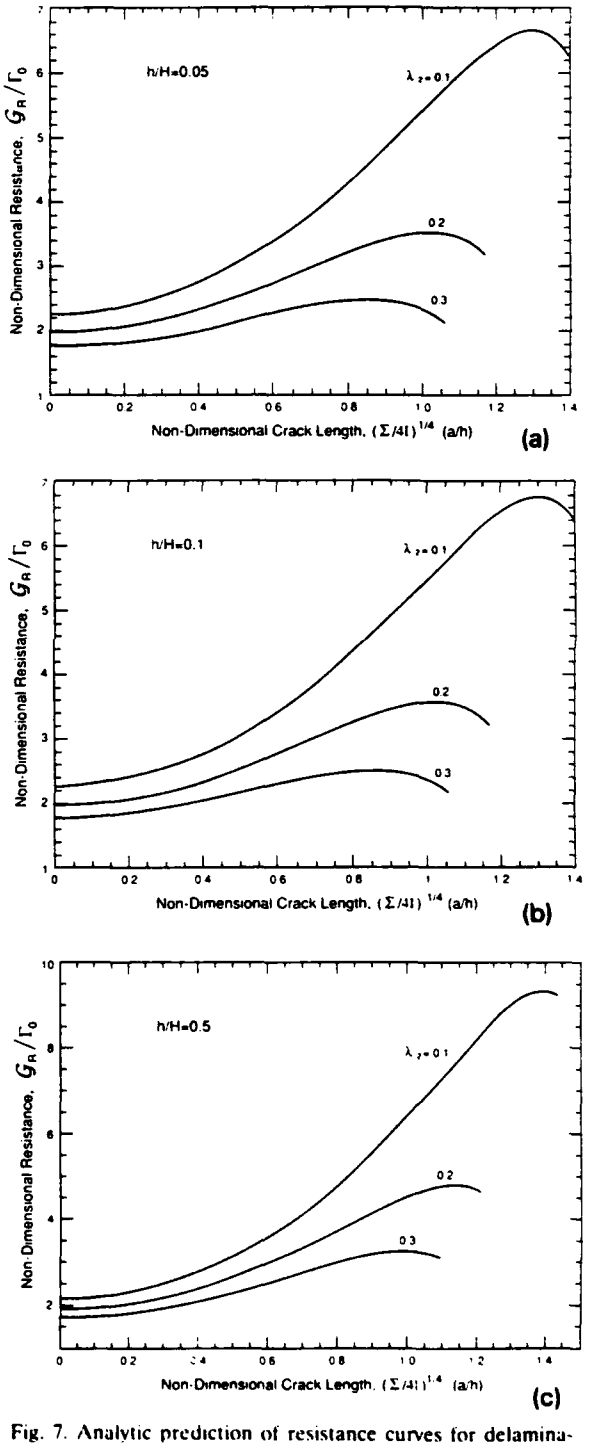

Fig. 7. Analytic prediction of resistance curves for delamination cracking for various λ_2: (a) $h/H = 0.05$; (b) $h/H = 0.1$ and (c) $h/H = 0.5$.

The preceding results neglect effects of the shear deformation, which provide a contribution to K_1^t. The resistance curve behavior in the transient region at small a/h is also neglected. To assess these effects, the finite element results are used to establish the trends in delamination resistance. For this purpose, it is noted that, for each crack length a/h, the following nondimensional quantities apply,

$$E_1 = \frac{K_{\sigma I}}{\sigma\sqrt{h}}, \qquad E_2 = \frac{K_{\sigma II}}{\sigma\sqrt{h}},$$
$$F_1 = \frac{K_{pI}}{p\sqrt{h}}, \qquad F_2 = \frac{K_{pII}}{p\sqrt{h}}, \tag{19}$$

where K_σ and K_p are stress intensities caused by σ and p, respectively. Then the normalized delamination energy release rate $\mathcal{G}_R/\Gamma_0$ can be determined from the following set of parametric equations

$$\frac{\Gamma_0}{\mathcal{G}_R}\left[1-(1-\lambda_2)\sin^2\psi^t\right]^{-1} = \left[(E_1-\zeta F_1)^2+(E_2+\zeta F_2)^2\right]/(E_1^2+E_2^2) \tag{20a}$$

and

$$\tan\psi^t = (E_2+\zeta F_2)/(E_1-\zeta F_1), \tag{20b}$$

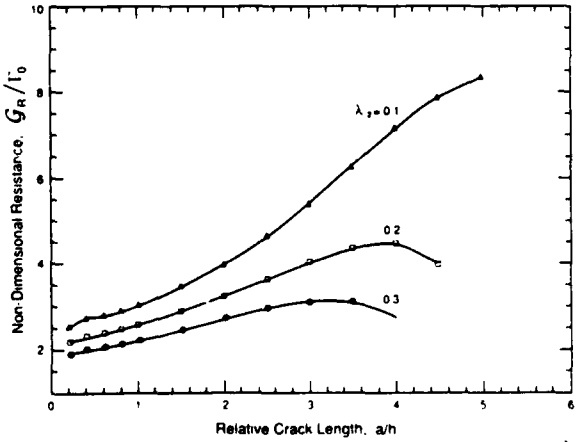

Fig. 8. Numerical prediction of resistance curves for $\Sigma = 10^{-3}$ and $h/H = 0.1$.

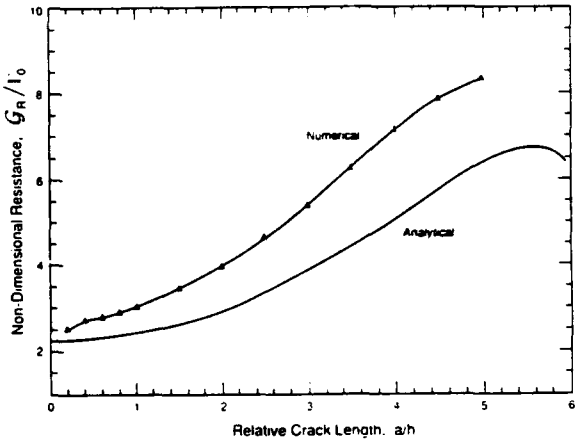

Fig. 9. A comparison of the analytical and numerical resistance curves for the case $\Sigma = 10^{-3}$, $h/H = 0.1$ and $\lambda_2 = 0.1$.

where

$$\zeta = 2\Sigma(E_1^2+E_2^2)\frac{\Gamma_0}{\mathcal{G}_R}. \tag{21}$$

Trends in $\mathcal{G}_R/\Gamma_0$ as a function of a/h are plotted in Fig. 8 for $\Sigma = 0.001$, $h/H = 0.1$ and for different values of λ_2. The resistance curves obtained from the finite element calculation are similar to those apparent from the steady-state analysis (Fig. 9) except that the $\mathcal{G}_R/\Gamma_0$ are slightly higher.

5. Concluding remarks

The predicted resistance curves $\mathcal{G}_R$ (Figs. 7 and 8) have the same features as the curves measured for ceramic matrix composites (Fig. 2). An influence of bridging fibers and/or ligaments thus appears to provide a plausible rationale for resistance curve behavior in delamination cracking, with the tractions p apparently governed by the sliding resistance along the fiber/matrix interface (Bordia et al., 1991). However, one important finding of the calculations is that the slope of the resistance curve is a strong function of the matrix fracture mechanism. Notably, a material with shear insensitive matrix fracture energy would be susceptible to unstable delamination

cracking, *because $\mathcal{G}_R$ decreases with crack extension*. Conversely, when the matrix fracture energy increases appreciably with increase in phase angle, $\mathcal{G}_R$ rises with crack extension and delamination cracking occurs stably, subject to increasing applied loads. *A basic understanding of the matrix fracture process is thus needed to predict and interpret delamination cracking.*

Acknowledgements

One of the authors (GB) wishes to thank Professor R.M. McMeeking for his encouragement and comments on the paper. Discussions with Professor Z. Suo were very helpful.

References

Ashby, M.F., K.E. Easterling, R. Harryson and S.K. Maiti (1985), *Proc. Roy. Soc. A398*, 24.

Bordia, R.J., B.J. Dalgleish, P.G. Charalambides and A.G. Evans (1991), *J. Am. Ceram. Soc.*, November, in press.

Jensen, H., J.W. Hutchinson and K.S. Kim (1990), *Int. J. Solids Struct. 26*, 1099.

O'Brien, T.K. (1982), *ASTM STP 775*, 140–167.

Rice, J.R. (1968), in: H. Liebowitz, ed., *Fracture*, Vol. 2, Academic Press, New York, pp. 191–311.

Sbaizero, O., P.G. Charalambides and A.G. Evans (1990), *J. Am. Ceram. Soc. 73*, 1936.

Suo, Z. and J.W. Hutchinson (1989), *Int. J. Solids Struct. 25*, 1337.

Trewetthey, B.R., J.R. Gillespie and L.A. Carlsson (1988), *J. Compos. Mater. 22*, 459.

Wang, S.S. (1979), in: S.W. Tsai, ed., *Composite Materials, Testing and Design*, ASTM, Philadelphia, ASTM STP 674, pp. 662–663.

Acta metall. mater. Vol. 39, No. 12, pp. 2997–3005, 1991
Printed in Great Britain.

0956-7151 91 $3.00 + 0.00

ON CRACK EXTENSION IN DUCTILE/BRITTLE LAMINATES

H. C. CAO and A. G. EVANS

Materials Department, College of Engineering, University of California, Santa Barbara, CA 93106, U.S.A.

(Received 10 January 1991; in revised form 24 May 1991)

Abstract—The problem of crack progression in a laminate consisting of alternate brittle and ductile layers has been addressed. A finite element analysis has been used to calculate stresses in the vicinity of a crack and the results rationalized on the basis of low and high stress bounds associated, respectively, with small-scale yielding and with a shear lag at the interface. Preliminary experiments conducted on Al_2O_3/Al laminates have been used to assess the crack extension criterion, upon comparison with the stress analysis. Implications for the strength and toughness of laminates are briefly presented.

Résumé—On a soulevé le problème de la progression des fissures dans un matériau laminaire constitué de couches fragiles et ductiles alternées. Une analyse par éléments finis a été utilisée pour calculer les contraintes au voisinage d'une fissure, et les résultats ont été rationalisés à partir de limites de faible et de forte contraintes associées respectivement à une plasticité à petite échelle et à un retard du cisaillement à l'interface. Des expériences préliminaires menées sur des matériaux laminaires Al_2O_3/Al ont permis d'établir un critère d'allongement des fissures, par comparaison avec l'analyse des contraintes. On présente brièvement ce qui en découle pour la résistance mécanique et la dureté des matériaux laminaires.

Zusammenfassung—Die Frage der Rißausbreitung in einem aus alternierend spröden und duktilen Schichten bestehendem Laminat wird behandelt. Mit einer Finit-Element-Analyse werden die Spannungen in der Nähe des Risses berechnet; die Ergebnisse werden auf der Grundlage von Bindungen mit kleiner Spannung, die mit Fließen in kleinem Maßstab zusammenhängen, und mit großer Spannung, die mit einem Scherungsverzug an der Grenzfläche zusammenhängen, erklärt. Vorläufiige, an Al_2O_3/Al-Laminaten durchgeführte Experimente ermöglichen, das Rißausbreitungskriterium nach Vergleich mit der Spannungsanalyse abzuschätzen. Die Bedeutung der Festigkeit und der Zähigkeit der Laminate wird kurz behandelt.

1. INTRODUCTION

Several composite reinforcement concepts involve material combinations consisting of one brittle and one ductile constituent. Examples include metal matrix composites reinforced with ceramic fibers and laminated composites comprised of alternate layers of either ceramics or intermetallics with metals [1, 2]. Failure propagation in such composites involves the transmission of cracks from one brittle layer into the adjacent brittle layers, across the intervening ductile material [1–3], as schematically indicated on Fig. 1. This crack propagation process may be characterized by a resistance curve [3], wherein the nominal stress intensity factor increases with crack extension (Fig. 1). The intent of the present study is to explore criteria for the propagation of cracks in such systems.

To motivate analysis of this phenomenon, experiments are conducted on laminated test specimens. The materials used consist of a high-purity polycrystalline Al_2O_3 and Al. In this system, the interface has a sufficiently high fracture energy [1, 4] that crack propagation occurs without debonding. The additional complexity introduced by debonding is thus avoided.

2. EXPERIMENTS

2.1. Procedures

Two types of specimen geometries have been used: an asymmetric ceramic/metal/ceramic sandwich and a laminate consisting of alternate layers of ceramic and metal. The specimens were made by solid-state diffusion bonding at a temperature close to the melting point of the metal, and subject to a small applied pressure (~ 5 MPa). Test beams for sandwich specimens were cut from the bonded plates and surfaces ground using a resin-bonded diamond wheel. The overall dimensions were $3 \times 4 \times 25$ mm, the outer alumina layer was 1 mm and the aluminum layer was 100 μm. The side faces were metallographically polished to facilitate observations of cracking in the Al_2O_3 and a slip in the alloy, and to control edge flaws. Laminate specimens having dimensions of $\sim 5 \times 10 \times 45$ mm were prepared in a similar fashion. The thickness of the alumina layers was ~ 1 mm, while the aluminum layers varied in thickness between 50 and 100 μm. The volume fraction of metal was $f \approx 0.05$–0.1. The beams were tested in three-point flexure with an outer span of either 20 or 40 mm, in the orientations depicted in Figs 2 and 3. In some cases, Knoop indentations were placed into

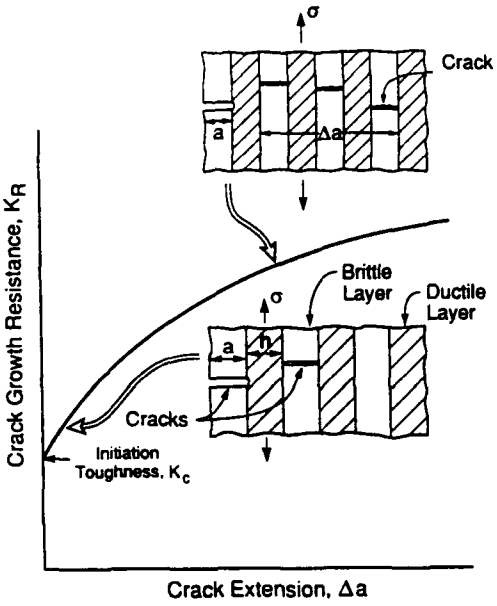

Fig. 1. A schematic indicating crack transmission across ductile layers and associated resistance curve characteristics.

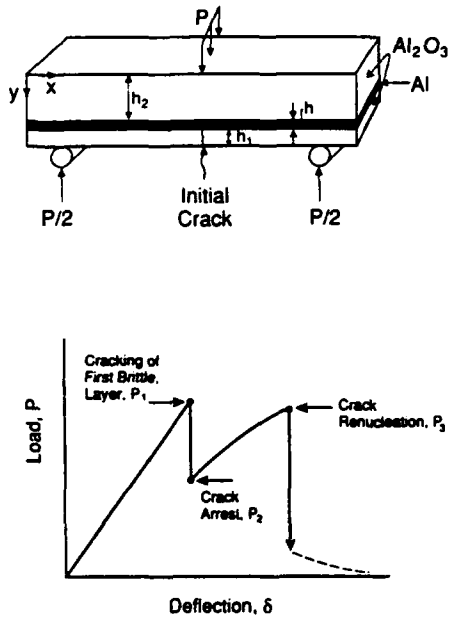

Fig. 2. A schematic of the sandwich test geometry and a typical load/deflection curve, indicating the characteristic loads.

the tensile surface prior to testing in order to extend cracks stably up to the interface. The first type of specimen geometry is used to address the crack extension criterion and the second to study the toughness of laminated composites.

2.2. *Mechanical properties*

The load/defection response of sandwich specimens is characteristic of the behavior reported in a previous publication [1]. An initial load drop, which initiates at P_1, coincides with cracking of the outer tensile layer (Fig. 2). The lower load P_2 is the load sustained by the crack arrested at the first interface. Further deflection of the beam causes the load to increase non-linearly to a load at which another crack nucleates in the second Al_2O_3 layer and the load drops. The sequence of events between crack arrest, plastic deformation and crack transmission are vividly revealed in Fig. 3. The plastic zone initiates at the tip and then extends preferentially along the interface. The sequence of events observed in laminate specimens is similar: the crack continues to arrest and renucleate at each metal/ceramic interface (Fig. 4). Additionally, the crack is bridged by intact metal layers across the crack surfaces. The nominal resistance associated with this process is presented in Fig. 5.

In some cases, multiple cracking of the brittle layers occurred, whereupon the crack front and the fracture zone became diffuse. For material that

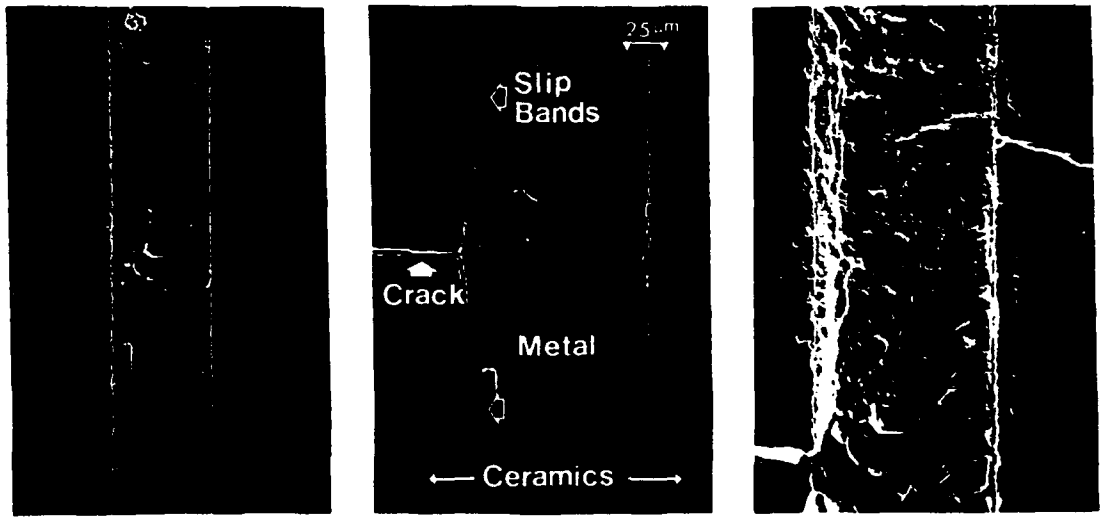

Fig. 3. Observations of cracking and the formation of the plastic zone near the crack tip.

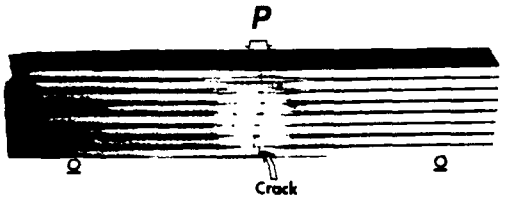

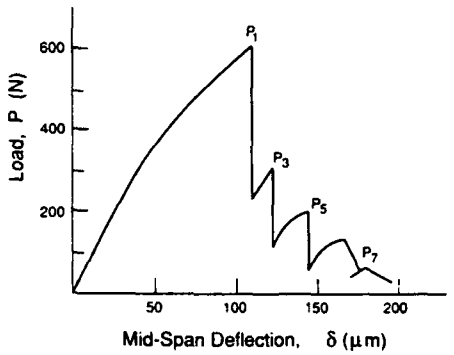

Fig. 4. A laminate specimen and the corresponding load/deflection curve. The load peaks refer to extension across successive brittle layers, while the minima represent arrest at the metal layers. Note the dark regions in the metal intercepting the crack. These occur because the metal is drawn from the surface due to plastic deformation.

exhibits such behavior, analysis of the fracture process involves considerations additional to those discussed in the present study. Multiple cracking becomes more prevalent as either the strength or thickness of the brittle layers increases. For example, this mode can be induced by careful polishing of the specimen side surfaces to eliminate edge flaws in the ceramic layer.

The above experimental information has established several characteristics that motivate the following analyses: (i) cracks can be transmitted between brittle layers without failing either the ductile layer or the interface; (ii) the crack propagation load diminishes as the crack extends, resulting in a nominal resistance to crack extension, $K_R = 10$–$15\ \mathrm{MPa}\sqrt{\mathrm{m}}$, substantially higher than the cracking resistance of the brittle layers [1] ($\sim 3\ \mathrm{MPa}\sqrt{\mathrm{m}}$); (iii) cracks arrested at the interface exhibit plastic blunting, accompanied by the formation of a plastic zone within the metal layer.

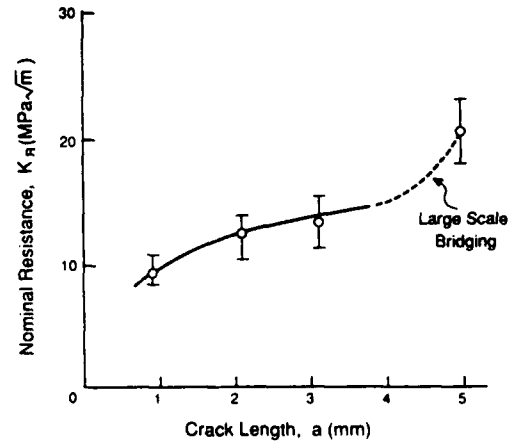

Fig. 5. A nominal resistance curve obtained from Fig. 4.

3. STRESS FIELDS

3.1. Some basic results

A simplified overview of the salient mechanics provides a background for the more detailed finite element calculations. Two limits seemingly characterize the stress distribution in the next brittle layer ahead of a crack arrested at a brittle/ductile interface. The limits can be expressed in terms of two nondimensional quantities: ℓ/a, the ratio of the plastic zone size to the crack length and σ/σ_0, the ratio of the imposed stress to the uniaxial yield strength of the ductile material (Fig. 6). For small values of both parameters ($\ell/a < 1$, $\sigma/\sigma_0 < 1$), a *small-scale yielding* (S.S.Y.) limit applies, wherein $\ell/a \sim (\sigma/\sigma_0)^2$. For large values of both parameters, a *shear lag* (S. L.)

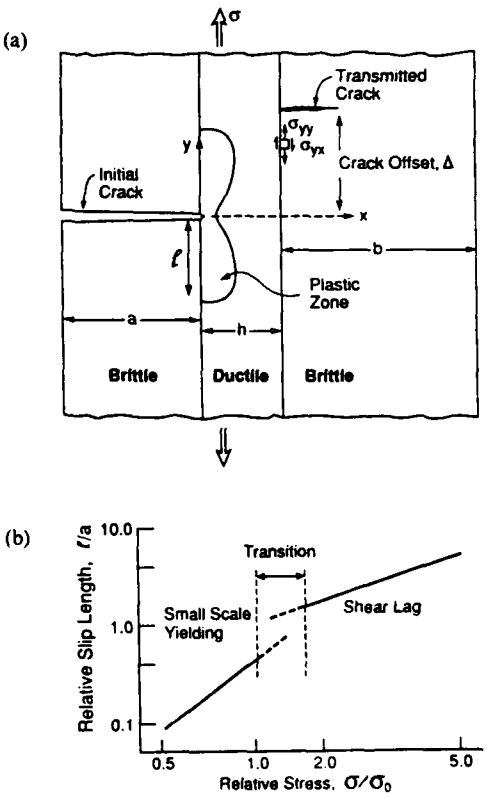

Fig. 6. (a) A schematic showing the plastic zone width, ℓ. (b) Schematic of trends in plastic zone size. At small stresses, the results are conveniently normalized using small-scale yielding $\ell/a \sim (\sigma/\sigma_0)^2$, while at larger stresses, a shear lag scaling is used, $\ell/a \sim (\sigma/\sigma_0)$.

limit obtains with, $\ell/a \sim \sigma/\sigma_0$. An elementary appreciation for these limits can be gained from standard S.S.Y. and S.L. solutions. For an elastically homogeneous material in S.S.Y., the stress σ_{yy} in the elastic zone on the plane ahead of the crack is

$$\sigma_{yy} \approx K_I/\sqrt{2\pi x} \tag{1}$$

where

$$K_I = \sigma\sqrt{\pi a}$$

and x is the distance ahead of the crack. Consequently, at a distance h ahead of the crack, within the elastic zone,

$$\sigma_{yy} \approx \frac{\sigma}{\sqrt{2}}\sqrt{\frac{a}{h}}. \tag{2}$$

The corresponding width of the plastic zone is [5]

$$\ell/a = 0.817(\sigma/\sigma_0)^2 \tag{3}$$

The results for σ_{yy} and ℓ given by equations (1) and (3), respectively, will be shown to have wide applicability in the S.S.Y. limit, even when the plastic zone size ℓ is large compared with the ductile layer thickness, h, and when the elastic mismatch is substantial.

In the shear lag limit, slip in the ductile layer near the interface (Fig. 5) extends several multiples of the crack length. Then, with the shear stress on the interface given by the shear yield strength $\sigma_0/\sqrt{3}$, force equilibrium governs the simple result,

$$\ell/a = \sqrt{3}(\sigma/\sigma_0). \tag{4}$$

To estimate the σ_{yy} stress, some simple premises are made, and later justified by the finite element calculations. By regarding that tractions $\sigma_0/\sqrt{3}$ be imposed on the intact brittle layer over the slip length, l, the σ_{yy} stress on the plane ahead of the crack for an elastically homogeneous system has the approximate form, [6]

$$\sigma_{yy} - \sigma \approx \frac{(3+\upsilon)}{2\pi\sqrt{3}}\sigma_0 \int_h^\ell dy/y. \tag{5}$$

The lower integration limit ($y = h$) has been used because $\sigma_{xy} = 0$ at the crack plane and only attains the shear yield strength $\sigma_0/\sqrt{3}$ at a distance, $y \approx h$ from the crack plane. Integration of equation (5) gives,

$$\sigma_{yy} - \sigma \approx \frac{(3+\upsilon)}{2\pi\sqrt{3}}\sigma_0 \ln(\ell/h). \tag{6}$$

The following numerical results will be shown to have broad consistency with the simple estimation of σ_{yy} and ℓ represented by equations (6) and (4).

The S.S.Y. and S.L. limiting solutions are both important because they relate to separate events in the failure sequence. The S.L. limit is most likely to apply upon tensile loading when disconnected cracks first form in the brittle layers. The S.S.Y. limit is more applicable to long cracks and hence, for characterizing the crack extension resistance.

3.2. Numerical procedure

A finite element program ABAQUS has been used to generate numerical elastic/plastic solutions. Two basic plane strain geometries have been used. In the first instance, the S.S.Y. limit is addressed by having a thin metal layer contained in an infinite body with a semi-infinite crack. Displacement boundary conditions are used, characterized by the remote K, in accordance with the homogeneous elastic field

$$u_i = \frac{K}{2\mu_c}\sqrt{\frac{x}{2\pi}}\tilde{u}_i(\theta) \tag{7}$$

where u_i is the displacement, (r, θ) are the coordinates with respect to the crack tip, μ_c is the shear modulus of the cermic and $\tilde{u}_i(\theta)$ is a non-dimensional coefficient [6]. The boundary conditions are imposed along a circular contour having radius many times (> 100) both the metal layer thickness h and the plastic zone size, ℓ. The geometry is discretized by using 4-noded quadra-lateral isoparametric elements in association with a full integration scheme. The ratio between the layer thickness and the outer boundary radius is 1/2000. The size of the smallest element is $h/50$ (Fig. 7). A small circular region is removed from the crack tip at the front metal/ceramic

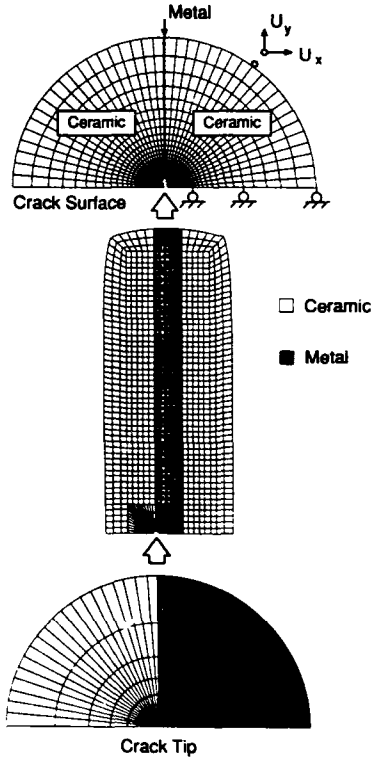

Fig. 7. Finite element mesh used for small-scale yielding calculations.

Table 1. Material properties

Young's Modulus, E	
	$E_c(Al_2O_3) = 420$ GPa
	$E_m(Al) = 70$ GPa
	$\alpha = (\bar{E}_c - \bar{E}_m)/(\bar{E}_c + \bar{E}_m) = -0.7$†
Poisson's ratio, υ	
	$\upsilon_c(Al_2O_3) = 0.2$
	$\upsilon_m(Al) = 0.3$
Yield strength, σ_0	
	Al = 70 MPa

†$\bar{E}$ indicates the plane strain tensile modulus as defined by $\bar{E} = E/(1-\nu^2)$.

interfaces to exclude aspects of the problem associated with the large plastic strain at the crack tip. The region is also taken to be $h/50$. The metal is represented by a power hardening, Osgood–Ramberg, law with isotropic hardening and a hardening coefficient, $N = 20$, characteristic of Al. An elastic mismatch characteristic of Al/Al_2O_3 [8] (Dundurs' elastic mismatch parameter $\alpha = -0.7$, Table 1) is also used.† The crack plane $y = 0$ is a symmetry plane. The same mesh is used to investigate the effect of elastic constant mismatch by suppressing the plastic deformation in the metal and varying the α elastic mismatch parameter for fixed $\beta = \alpha/3$.

The second geometry examines the S. L. limit and the transition range. It consists of three finite layers: two elastic layers on the outside and an elastic/plastic layer on the inside (Fig. 8). Periodic boundary conditions are used and thus, the results refer to a periodic linear array of cracks in a laminated composite. The lower boundary $y = 0$ is a symmetry plane and the upper boundary is kinetically constrained to move along the y-axis with no rotation and with zero shear traction.

3.3. Stresses

In all cases, the elastic/plastic calculations confirm that, for elastic mismatch represented by $\alpha = -0.7$, the plastic zone develops preferentially along that interface intersecting the crack front (Fig. 9) and subsequently extends across the metal layer. Trends in the plastic zone size with stress obtained using finite geometries are plotted on Fig. 10. The S.S.Y. and S.L. limits are apparent: S.S.Y. at $\ell/a \lesssim 1$ and S.L. at $\ell/a \gtrsim 1$. The slight non-linearity at large ℓ/a may be attributed to the use of periodic boundary conditions, which cause interactions between plastic zones. The interface shear stress remain essentially constant within the plastic zone and somewhat larger

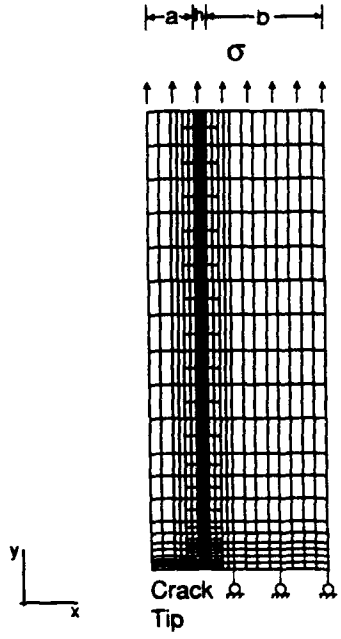

Fig. 8. Finite element mesh for three-layer system ($a/b = 2/5$, $h/a = 1/4$).

than $\sigma_0/\sqrt{3}$ because of work hardening (Fig. 11). This feature is the basis for the shear lag limit.

A summary of the S.S.Y. calculations is presented in Fig. 12. The results emphasize the σ_{yy} stresses in the brittle layer, at $x = h$, and are normalized by the stresses expected at the same location in a homogeneous elastic body. The major conclusion for present purposes is that the σ_{yy} stresses are almost the same as those applicable to a homogeneous elastic body (within 10%), even when the plastic

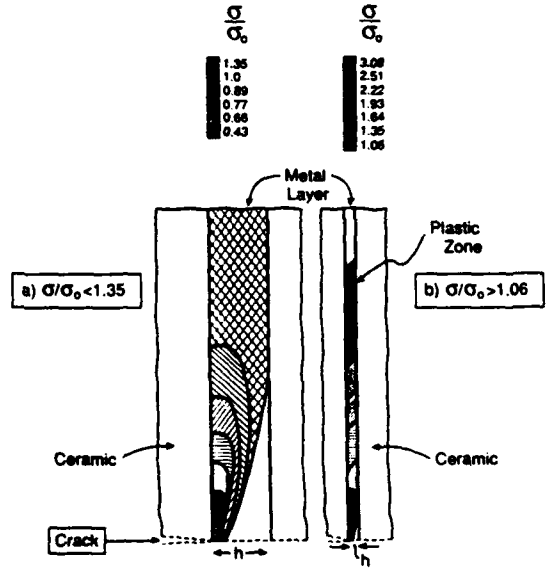

Fig. 9. Calculated evolution of plastic zone. The hatched areas define the zone size at different stresses σ/σ_0, (a) $\sigma/\sigma_0 < 1.35$, (b) $\sigma/\sigma_0 > 1.06$.

†The Dundurs' parameters for bimaterial combinations are defined by

$$\alpha = \frac{E_c(1-\upsilon_m) - E_m(1-\upsilon_c)}{E_c(1-\upsilon_m) + E_m(1-\upsilon_c)}$$

$$\beta = \frac{E_c(1-2\upsilon_m) - E_m(1-2\upsilon_c)}{E_c(1-\upsilon_m) + E_m(1-\upsilon_c)}$$

where E is the Young's modulus and υ is Poisson's ratio. The subscripts c and m refer to ceramic and metal, respectively.

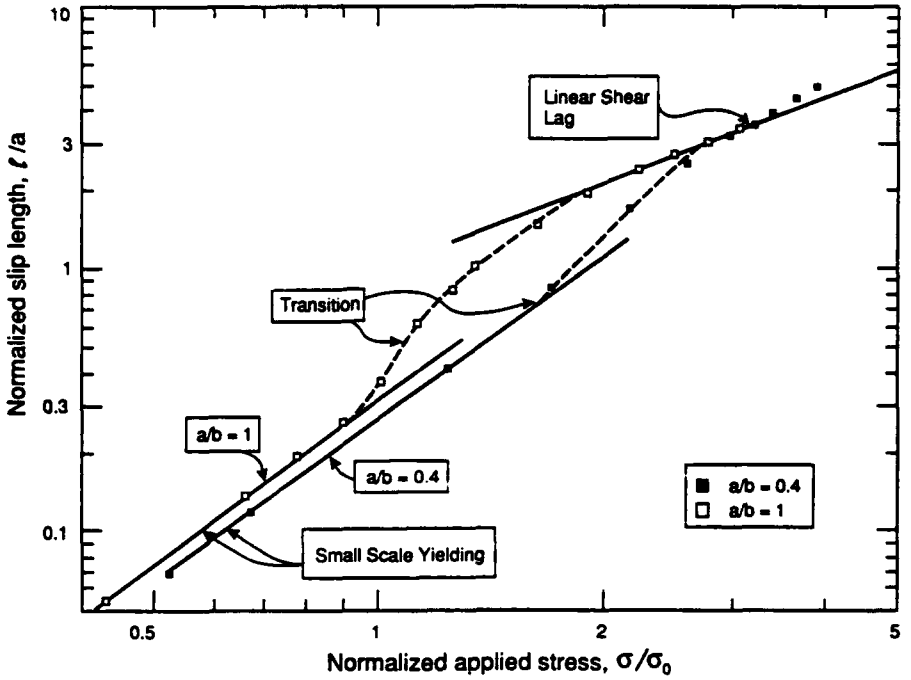

Fig. 10. Calculated trends in non-dimensional slip length ℓ/a with relative applied stress. Also shown are the analytical small-scale yielding and shear lag predictions.

zone size ℓ is several times the metal layer thickness [Fig. 12(a)]. These stresses have a maximum σ_{max} represented by

$$\frac{\sigma_{max}\sqrt{h}}{K_I} \approx 1/\sqrt{2\pi}. \quad (8)$$

A similar conclusion obtains upon varying the elastic mismatch between the metal and the ceramic [Fig. 12(b)].

For analysis of the laminate geometry, the σ_{yy} stresses are normalized by the nominal applied stress, σ, defined as,

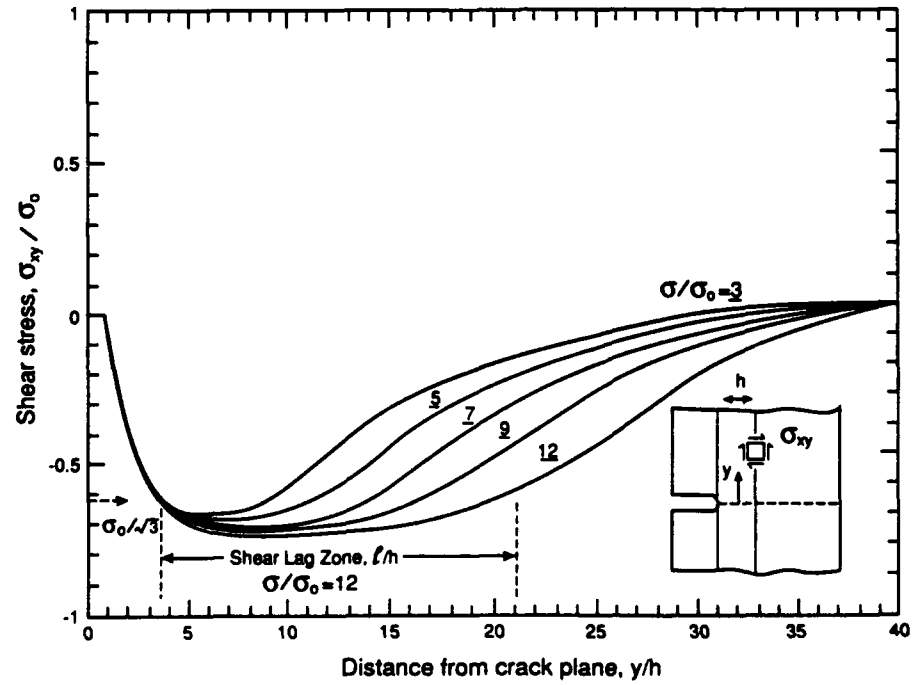

Fig. 11. Interface shear stresses for various applied stress levels: also indicated is the extent of the shear lag zone at the largest applied stress.

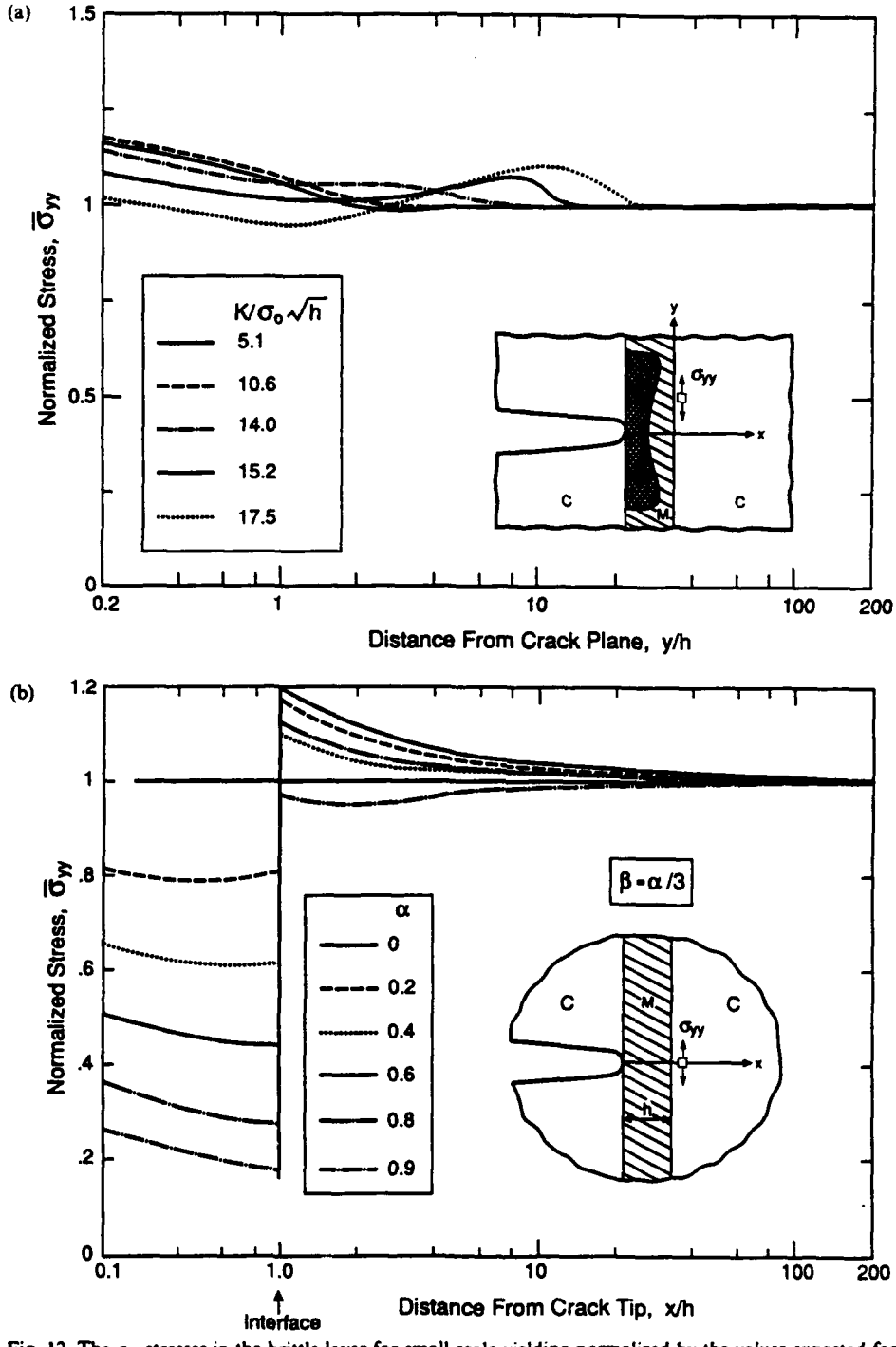

Fig. 12. The σ_{yy} stresses in the brittle layer for small-scale yielding normalized by the values expected for a homogeneous elastic body. (a) Effect of limited plasticity in metal layers. (b) Effect of elastic mismatch.

$$\sigma = P/[a + b + E_m h/E_c] \quad (9)$$

where P is the imposed load per unit width.

Based on the values of ℓ summarized in Fig. 11, the σ_{yy} stresses are plotted in Fig. 13 in accordance with the logarithmic formulism suggested by equation (6). It is apparent that at applied stresses sufficiently high for the shear lag to be most applicable, *all of the results* have about the same magnitude *at small* y/ℓ when normalized in accordance with the logarithmic form

$$\left(\frac{b}{a}\right)\left[\frac{\sigma_{yy}}{\sigma} - 1\right]\ln(\ell/h) \equiv 5.8 \quad (10)$$

where σ is the applied stress, with a, b, ℓ and h defined in Fig. 6(a). Consequently, equation (10) encompasses

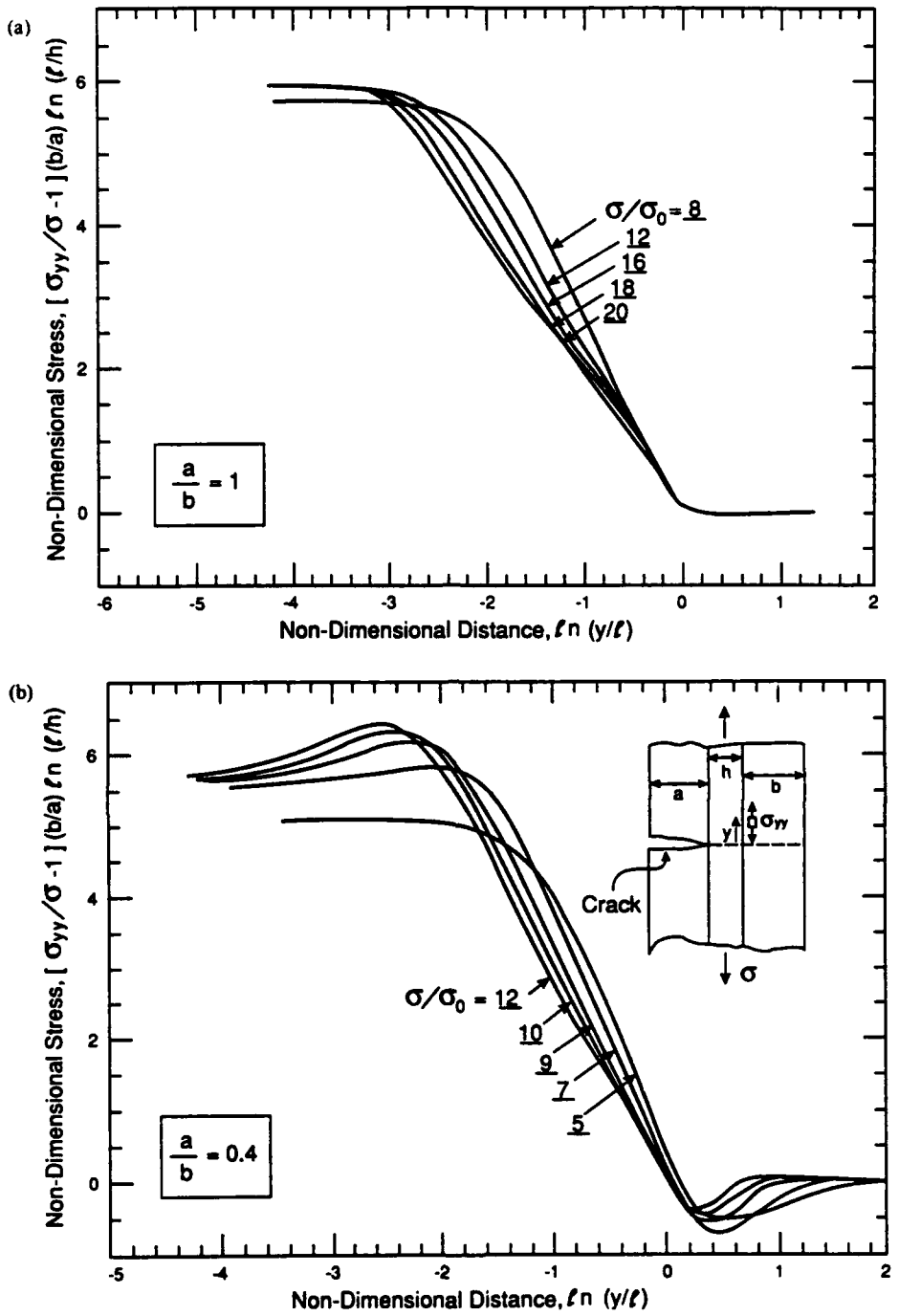

Fig. 13. Variation in the non-dimensional stress in the shear lag range with non-dimensional distance, y/ℓ. (a) $a/b = 1$, (b) $a/b = 0.4$.

all of the effects of geometry, applied stress and yield strength: furthermore, this parameter is relatively constant for $\ln(y/\ell)$ up to ≈ -3. At *intermediate* y/ℓ, the stresses exhibit the approximate form

$$\left(\frac{b}{a}\right)\left[\frac{\sigma_{yy}}{\sigma} - 1\right]\ln(\ell/h) \approx -5.8\,Q\ln(y/\ell) \qquad (11)$$

where Q is a coefficient that ranges between $-1/2$ and $-1/3$ for different geometries.

4. CRACK PROGRESSION

Most of the experimental information presented in Section 2 refers to crack progression wherein $\ell/a < 1$, whereupon S.S.Y. conditions should apply. Consequently, equating K_I in equation (8) to the measured resistance and also inserting the metal layer thickness ($h = 100\,\mu$m), then the maximum σ_{yy} stress in the Al_2O_3 upon crack extension is predicted to be

~400 MPa. This stress is similar to the reported strength S of this Al_2O_3 [1]. Hence, a plausible criterion for crack extension is that $\sigma_{max} \approx S$, leading to a critical value of the nominal stress intensity factor, K_{I0}, given by

$$K_{I0} = S\sqrt{2\pi h}. \tag{12}$$

The implied influence of the metal layer thickness, as well as the insensitivity to the yield strength σ_0, are clearly amenable to further experimental assessment.

The consequences of this criterion for short cracks, when the shear lag limit obtains, is deduced from equation (10) by equating σ_{max} to S, leading to an implicit expression for the cracking stress, σ_c, given by,

$$\sigma_c = \frac{h\sigma_0}{a}\exp\left[\frac{5.8a/b}{S/\sigma_c - 1}\right]. \tag{13}$$

In the important limit $a/b \ll 1$,

$$\sigma_c \approx (h\sigma_0/a)(1 - 2.9a/b). \tag{14}$$

This prediction is again amenable to experimental assessment.

5. CONCLUDING REMARKS

A key feature of the analysis has been the demonstration that the stresses of interest can be rationalized on the basis of small-scale yielding and shear lag limits. The analysis, coupled with experimental results on laminates, suggests that a stress controlled fracture criterion applies, with crack extension occurring when the peak stress in the ceramic reaches the fracture strength. This criterion predicts that, in both S.S.Y. and S.L. regimes, the crack extension resistance is *enhanced* as the metal layer thickness *increases*. This behavior should be contrasted with the reduction in initial cracking stress for the brittle layers as the thickness increases [1, 9]. The other property predicted to be of importance is the yield strength, σ_0. However, the relative roles of S and σ_0 are strongly influenced by the operative regime, either S.S.Y. or S.L.

Several important features of the crack extension process have not been addressed in the present study and require further research. A more complete understanding of the transition between the S.S.Y. and S.L. regimes is needed, as well as of interactions between plastic zones in the latter. The criterion for crack extension should be extended to involve a ceramic cracking process governed by *weakest link statistics*. Finally, crack bridging effects on the resistance require consideration in order to provide a complete description of the fracture behavior.

REFERENCES

1. B. J. Dalgleish, K. P. Trumble and A. G. Evans, *Acta metall.* **37**, 1923 (1989).
2. H. E. Dève, A. G. Evans and R. Mehrabian, *Mater. Res. Soc.* **170**, 33 (1990).
3. G. R. Odette, W. Shekerd and G. E. Lucas. To be published.
4. Y. Klipfel, M. Y. He, R. M. McMeeking, R. Mehrabian and A. G. Evans, *Acta metall.* **38**, 1063 (1990).
5. G. P. Charepanov, *Mechanics of Brittle Fracture*. McGraw-Hill, New York (1979).
6. S. Timoshenko and J. N. Goodier, *Theory of Elasticity*, p. 147. McGraw-Hill, New York (1959).
7. P. Paris and G. C. Sih, *ASTM STP* 381 (1965).
8. J. W. Hutchinson, *Metal/Ceramic Interfaces* (edited by M. Rühle *et al.*), pp. 295–307. Pergamon Press, Oxford (1990).
9. M. S. Hu and A. G. Evans, *Acta metall.* **37**, 917 (1989).

MATERIALS

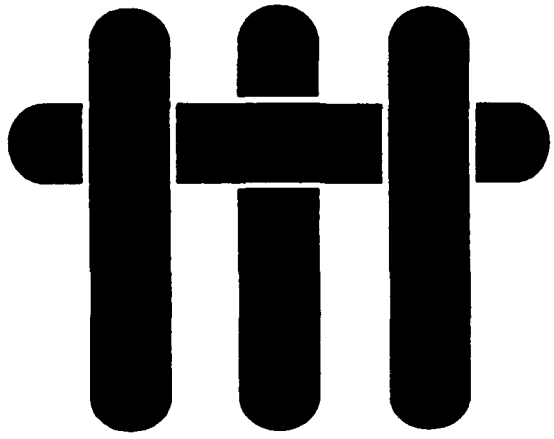

THE FRACTURE RESISTANCE OF DIRECTIONALLY SOLIDIFIED DUAL-PHASE NiAl REINFORCED WITH REFRACTORY METALS

by

F.E. Heredia, M.Y. He, G.E. Lucas, A.G. Evans
Materials Department
College of Engineering
University of California
Santa Barbara, California 93106–5050

H.E. Dève
3M Corporation
St. Paul, Minnesota

and

D. Konitzer
General Electric, Engine Division
Cincinnati, Ohio

Submitted to Acta Metallurgica et Materialia, May 1992

ABSTRACT

The fracture resistance of two directionally-solidified, NiAl refractory metal systems has been measured and analyzed. One system, NiAl/Mo, has a microstructure consisting of Mo rods. The second system, NiAl/Cr(Mo), has a layered microstructure. Both materials are found to have an appreciably higher initiation toughness than NiAl, followed by a rising resistance, with the layered microstructure giving the superior properties. The results have been rationalized by available models based on the following three mechanisms: crack trapping, crack renucleation and ductile phase bridging.

1. INTRODUCTION

The fracture resistance characteristics of dual-phase intermetallics with a second phase consisting of a ductile refractory metal have been broadly documented.[1-6] Present understanding indicates important effects of the flow strength and ductility of the refractory metal, its morphology and dimensions, as well as the interface debond resistance.[4-9] There are two main morphological classes of dual-phase material:[10-12] i) Type I materials with a continuous intermetallic phase, wherein the refractory metal is configured as either a network or as aligned rods. ii) Type II materials with a layered structure comprising alternate layers of intermetallic and metal. The key differences in these morphologies are sketched in Fig. 1. For type I microstructures, the crack has unimpaired access to the brittle material; whereas, for the type II layered microstructure, a crack that first forms in a brittle layer must *renucleate* in the next brittle layer.[13] These differences are reflected in the initiation toughness. The subsequent *rise in the resistance* with crack extension is expected to be similar for both microstructures.[7,8]

In the present study, the two morphological classes of refractory reinforcement are investigated for the same NiAl matrix, using materials produced by directional solidification;[10-12] i) NiAl/Mo is used to provide a type I system with a continuous NiAl matrix, plus *aligned rods* of Mo reinforcement. ii) NiAl/Cr(Mo) is used to create a type II system with *alternating layers* of NiAl and Cr(Mo). The fracture resistance of these materials is measured and related to microstructure, through crack growth models.

2. MATERIALS

The materials studied (Table I) were produced by directional solidification at a growth rate of 10 cm per hour, using procedures described elsewhere.[12] The NiAl/Mo

material has the type I microstructure shown in Fig. 2. Polished cross-sections examined in the scanning electron microscope (SEM) indicate that this material consists of aligned Mo rods with radius, R ≈ 0.6 μm, and a volume fraction, f_m ≈ 0.12. Comparable examinations of the NiAl/Cr(Mo) material indicate a type II layered microstructure (Fig. 3). The NiAl layers have an average thickness h_1 ≈ 0.75 μm, and the Cr(Mo) layers have a thickness, h_2 ≈ 0.35 μm, corresponding to a volume fraction of refractory metal, f_m ≈ 0.3. The layers are essentially continuous in the growth direction. However, some discontinuities exist.

3. EXPERIMENTAL PROCEDURES

Specimens were made by EDM with the dimensions specified in Fig. 4. A narrow straight 3 mm-deep notch was introduced, also by EDM. The specimens were loaded in flexure upon a 20 mm span, in a servohydraulic machine, with a displacement gauge in contact with the specimen. Loads were imposed using displacement control on the actual specimen. This technique allowed precracks to be introduced from the notch. Subsequent to precracking, loads and displacements were recorded subject to constant displacement rates and the crack length was monitored using a high-resolution optical microscope. Resistance curves were generated using this approach.

Subsequent to testing, fracture surfaces were examined in the scanning electron microscope (SEM) and quantitative measurements made of the plastic stretch of the refractory metal. Other morphological features were characterized, as appropriate.

4. MEASUREMENTS AND OBSERVATIONS

Crack growth resistances measured on the two refractory metal reinforced materials, as well as NiAl, are summarized in Fig. 5. The corresponding load, displacement

responses are plotted on Fig. 6. It is apparent that there are major contrasts in behavior. i) The NiAl has an initiation resistance, $K_o \approx 6\ MPa\sqrt{m}$, with no resistance enhancement upon crack extension. ii) The NiAl/Mo type I material has a somewhat higher initiation resistance, $K_o = 10\ MPa\sqrt{m}$. Furthermore, the resistance then rises to a level $K_s \approx 15\ MPa\sqrt{m}$, after a crack extension, $\Delta a \approx 300\ \mu m$. At this stage, the crack extends *unstably* across the specimen. iii) The NiAl/Cr(Mo) type II material has a much larger initiation resistance, $K_o \approx 17\ MPa\sqrt{m}$, followed by a rising resistance that reaches $K_s \approx 22\ MPa\sqrt{m}$, at a crack extension $\Delta a \approx 500\ \mu m$. In this material, crack growth is *stable*. Furthermore, the load/displacement curve (Fig. 6) is reminiscent of that found for ductile/brittle laminates, comprising successive load drops as the crack extends across the brittle layers.[13]

In the NiAl/Mo type I material, plastic stretching of the Mo is evident from inspection of the side surfaces‡ (Fig. 7a). Corroborating evidence that the Mo is ductile is obtained from fracture surfaces (Fig. 8). It is also evident from Fig. 8 that the Mo/NiAl interface is susceptible to *debonding*, with a debond length ($d \approx R$) sufficient to achieve a plastic stretch, $u_c \approx 1.5R$. At locations where the crack interacts with the Mo, there are steps in the NiAl, manifest as "trails" emanating from the reinforcements (Fig. 9). These "trails" are typical of those induced by *crack trapping*,[14-17] as the crack front circumvents the reinforcements.

The fracture morphology for the type II layered material is more difficult to specify. A key feature is the intermittent splitting that occurs at the NiAl/refractory metal interface evident both from side views and from fracture surfaces (Fig. 10). The split length can be relatively large, but the majority of the interface decohesions are small, typically 10 μm. The ductility of the refractory metal is evident from the plastic stretch

‡ In regions where the crack extends *unstably*, the Mo does not exhibit significant plastic stretch, indicative of a rate-dependent ductile-to-brittle transition.

exhibited on the fracture surface (Fig. 11), as well as the distortion between adjacent interface decohesions (Fig. 10).

5. SOME BASIC MECHANICS

Interpretation of the preceding measurements and observations is subject to knowledge of the micromechanics associated with each of the observed mechanisms. The most important are: i) ductile phase bridging, ii) crack front trapping, iii) splitting and iv) crack renucleation. The mechanics of each phenomenon is briefly reviewed and the salient results provided.

5.1 Bridging

When crack bridging by ductile reinforcements occurs, it contributes to a geometry insensitive rise in crack growth resistance.[7,8,9,18] The principal characteristics are governed by the flow properties of the refractory metal reinforcement, as well as the extent of interface debonding. The maximum toughening arises when the interface is susceptible to *debonding*. In this case, the following relationships have been found to predict toughening, provided that the refractory metal also has high ductility.[9,18] i) A linear softening traction law governs bridging, with peak stress, σ_c, plastic stretch u_c[18] leading to an elevation of the steady-state fracture energy, $\Delta\Gamma_s$, given by:

$$\Delta\Gamma_s = f_m \sigma_c u_c/2 \qquad (1)$$

The magnitudes of σ_c and u_c depend on the interface, through the extent of debonding. When debonding is extensive,‡ the peak stress $\sigma_c \approx \sigma_o$, the uniaxial yield strength,

‡ Without debonding, constraint causes σ_c to be appreciably above σ_o; typically $\sigma_c \approx 4\sigma_o$.[7]

whereas the plastic stretch, $u_c \approx d$, the debond length.[2,4] ii) Between initiation and steady-state, the enhanced fracture energy $\Delta\Gamma_R$ has the form[9,18]

$$\Delta\Gamma_R \approx \sigma_c f u_c \left[1.6\alpha - 0.1\alpha^2 + 0.5\alpha^3\right]/4$$

with

$$\alpha = \Delta a/L_s \tag{2}$$

where L_s is the crack length at the onset of steady-state, given by[18]

$$L_s = 0.12\pi u_c E/\sigma_c \tag{3}$$

with E being the composite Young's modulus.

5.2 Crack Trapping

Crack trapping effects arise in type I materials with a continuous brittle matrix.[14-17] It occurs when the crack front interacts with higher toughness reinforcements, requiring the crack to penetrate between the reinforcements. The associated perturbation of the crack front requires an increase in the imposed stress intensity factor, corresponding to an increase in crack growth resistance. The important variables affecting the resistance are the volume fraction of reinforcements, f_m, as well as a parameter that provides a combined measure of the reinforcement toughness and the interface integrity. Simulations of this phenomenon have been performed for a range in f_m and reinforcement properties.[15-17] The results are summarized in Fig. 12. It is apparent that, when the reinforcement has a high toughness, substantial trapping effects occur, even at moderate volume fractions.

5.3 Splitting and Renucleation

In materials having a layered type II microstructure, with alternating brittle and ductile layers, crack extension is impeded at the interface.[13,19] The impediment occurs either by plastic blunting, when the interface has good integrity (as found in Al_2O_3/Al),[13,19] or by splitting, when the interface decoheres (as found in TiAl/Nb).[1] In both cases, the intervening ductile layer modifies the stress ahead of the crack front.[20,21] The stress modification caused by *yielding* with a well-bonded interface only becomes significant when the yield strength σ_o is much lower than fracture strength of the intermetallic,[20] such that the slip length, L, is larger (Fig. 13). Nevertheless, the mere existence of this ductile layer displaces the next brittle layer to a location that experiences diminished stress. Consequently, a crack renucleation phenomenon must occur (at this reduced stress level) before crack growth can proceed. The stress in the brittle layer, σ_{yy}, that dictates the renucleation event has magnitude (Fig. 13)[13,19,20]

$$\sigma_{yy}\sqrt{h_m}/K_{tip} \approx 1/\sqrt{2\pi} \qquad (4)$$

where K_{tip} is the crack tip stress intensity factor dictated by the applied load, plus crack face tractions caused by bridging, etc. In order to predict the critical applied K, a renucleation criterion is needed in conjunction with (Eqn. 4), as discussed below.

Conversely, the stress σ_{yy} can be substantially modified by *splitting*. The important variables affecting this behavior are expressed by the relation[21]

$$\sigma_{yy}\sqrt{h_m}/K_{tip} \approx F(L/h_m, \ell/h_m) \qquad (5)$$

where L is now the split length, ℓ the crack length and F is the function plotted on Fig. 14. The stress alleviation caused by splitting is pronounced when the split length, as

well as the crack length, are relatively large. However, for short cracks, σ_{yy} *increases* upon initial splitting.

Renucleation occurs when σ_{yy} reaches the critical level needed to form a crack in the next brittle layer. Two bounds govern this criterion, dependent on the intermetallic layer thickness, h_I. When the layer is relatively thick, cracking involves flaws in the intermetallic and a *statistical criterion*, based on the intermetallic tensile strength, is relevant.[13,19] For thin layers, a *tunnel cracking* mechanism occurs, controlled by flaws that propagate through-thickness in steady-state.[22,23] Such behavior is *deterministic* and occurs at a critical stress given by

$$S = \Omega K_m / \sqrt{h_I} \tag{6}$$

where K_m is the critical mode I stress intensity factor for the intermetallic and Ω is a numerical coefficient, of order unity. By equating σ_{yy} in Eqn. (5) to S in Eqn. (6), the renucleation toughness, K_N, becomes

$$K_N = K_m [\Omega/F] \sqrt{h_m/h_I} \tag{7}$$

6. ANALYSIS OF RESULTS

Interpretation of the experimental results is achieved by initially addressing the effects that govern the elevation of the *initiation toughness* above the matrix toughness using the parameters summarized in Table I. The enhanced toughness involves crack trapping in type I material and crack renucleation in type II material. For the type I NiAl/Mo system, the *crack trapping* calculations (Fig. 12), in conjunction with a NiAl matrix toughness of 5-6 MPa$\sqrt{m}$, predict an initiation toughness, $K_o \approx 10$ MPa$\sqrt{m}$

(Fig. 5a). This value of K_o is consistent with the resistance measured at crack extensions up to ~ 100 μm.

For the type II NiAl/Cr(Mo) system, initial crack extension involves renucleation which occurs at a stress intensity K_N given by (Eqn. 7) with the parameters summarized in Table I. The prediction that appears to be consistent with the experimental measurement is that based on the assumption that splitting is ubiquitous.

Following initial crack growth, the increase in resistance $\Delta\Gamma_R$ caused by deformation of the intact refractory metal ligaments is given by Eqns. (1) to (3), based on the parameters indicated on Table I. The corresponding steady-state stress intensity factor K_R is related to $\Delta\Gamma_R$ by,

$$K_R = \sqrt{K_o^2 + E\Delta\Gamma_R} \tag{8}$$

This predicted effect of bridging is superposed on the experimental data (Fig. 5). It is apparent that ductile bridging does *not* fully account for the increase in resistance found experimentally for either material. Such conditions contrast with the dominant effect of ductile bridging found in other ceramic and intermetallic matrix composites.[1,2,4,9]

The extra contribution to the crack growth resistance probably arises from the non-planarity of the fracture. This phenomenon is known to increases the ductile phase bridging contribution to the crack growth resistance,[8] as well as introducing possible frictional contributions when the crack faces are in contact.[24] A quantification of these effects is not attempted.

7. CONCLUDING REMARKS

The formation of refractory metal reinforcements within NiAl by directional solidification has been shown to provide a marked increase in the resistance to fracture.

The most important effects relate to the substantial increase in initiation toughness, which involves interactions of the crack front with the refractory metal. These interactions depend on the reinforcement and matrix morphologies, and involve crack trapping, as well as renucleation phenomena. Existing models of these mechanisms appear to be consistent with the experimental measurements.

Crack trapping represents a substantial contribution to the overall fracture toughness of the NiAl/Mo system. A similarly important role of crack trapping has not been evident from data on related intermetallic and ceramic systems, which have relatively coarse microstructure ($R > 10\ \mu m$) and low modulus reinforcements.[1,9] Crack trapping is predicted to be dependent only on volume fraction and thus be independent of scale. The relatively high modulus of the Mo may thus be critical. Notably, when a crack approaches a bimaterial interface, its motion is retarded by a high modulus layer, because of the diminished crack opening, reflected in a reduced stress intensity factor.[22,23] Consequently, the crack often arrests before reaching the interface. Such a condition would facilitate the crack bowing mechanism that is assumed in the trapping calculation[15-17] and be consistent with the bowing demarcation found in the NiAl/Mo system. This presumed importance of the reinforcement modulus requires additional study.

ACKNOWLEDGEMENTS

The authors wish to acknowledge the Defense Advanced Research Projects Agency (DARPA) for financial support under ONR Grant N00014-86-K-0753.

TABLE I

Property Summary For The Two Composites

	NiAl/Mo	NiAl/Cr(Mo)
E(GPa)	~ 205	~ 210
M_c(μm)	0.45	~ 0.5
σ_c(MPa)	~ 200	~ 210
f	0.12	0.3
K_o (MPa$\sqrt{m}$)	10	17
K_s (MPa$\sqrt{m}$)	~ 15	22
Reinforcement Dimensions (μm)	0.6	0.35

REFERENCES

[1] G.R. Odette, H.E. Dève, C.K. Elliott, A. Hasegawa and G.E. Lucas, *Interfaces in Ceramic Metal Composites* (edited by R.J. Arsenault, R.Y. Lin, G.P. Martins and S.G. Fishman), p. 443, TMS-AIME, Warrendale, PA, USA (1990).

[2] H.E. Dève, A.G. Evans, G.R. Odette, R. Mehrabian, M.L. Emiliani and R.J. Hecht, *Acta Metall. Mater.*, **38**, 1491 (1990).

[3] P.R. Subramanian, M.G. Mendiratta, D.B. Miracle and D.M. Dimiduk, *MRS Symp. Proc.*, **194**, 147 (1990).

[4] H.E. Dève and M. Maloney, *Acta Metall. Mater.*, **39**, 2275 (1991).

[5] T.C. Lu, A.G. Evans, R.J. Hecht and R. Mehrabian, *Acta Metall. Mater.*, **39**, 1853 (1991).

[6] R.M. Nekkanti and D.M. Dimiduk, *MRS Symp. Proc.*, **194**, 175 (1990).

[7] M.F. Ashby, F.J. Blunt and M. Bannister, *Acta Metall. Mater.*, **37**, 1847 (1989).

[8] M. Bannister and M.F. Ashby, *Acta Metall. Mater.*, **39**, 2575 (1991).

[9] B.D. Flinn, C. Lo, F.W. Zok and A.G. Evans, *J. Am. Ceram. Soc.* (1992), in press.

[10] J.L. Walter and H.E. Cline, *Met. Trans.*, **1**, 1221 (1970).

[11] H.E. Cline and J.L. Walter, *Met. Trans.*, **1**, 2907 (1970).

[12] H.E. Cline, J.L. Walter, E. Lifshin and R.R. Russell, *Met. Trans.*, **2**, 189 (1971).

[13] H.-C. Cao and A.G. Evans, *Acta Metall. Mater.*, **39**, 2997 (1991).

[14] F.F. Lange, *Philos. Mag.*, **22**, 983 (1970).

[15a] H. Gao and J.R. Rice, *J. Appl. Mech.*, **56**, 828 (1989).

[15b] N. Fares, *J. Appl. Mech.*, **56**, 837 (1989).

[16] A.F. Bower and M. Ortíz, *J. Mech. Phys. Solids*, **39**, 815 (1991).

[17] A.F. Bower and M. Ortíz, *J. Mech. Phys. Solids* (submitted) (1991).

[18] G. Bao and C.-Y. Hui, *Int. J. Solids Struct.*, **26**, 631 (1990).

[19] M.C. Shaw, D.B. Marshall and A.G. Evans, submitted (*J. Am. Ceram. Soc.*)

[20] K.F. Chan, M.Y. He and J.W. Hutchinson, in preparation.

[21] M.Y. He, F.E. Heredia, D.J. Wissuchek and A.G. Evans, in preparation.

[22] J.W. Hutchinson and Z. Suo, *Advances in Applied Mechanics*, **28**, 63 (1991).

[23] T. Ye, Z. Suo and A.G. Evans, *Int. J. Solids Struct.*, in press.

[24] G. Vekinis, M.F. Ashby and P.W.R. Beaumont, *Acta Metall. Mater.*, **38**, 1151 (1990)

FIGURE CAPTIONS

Fig. 1. A schematic showing the type I and type II microstructures with associated crack growth events and resistance curves.

Fig. 2. Cross section of the NiAl/Mo system examined in the scanning electron microscope a) general view b) aligned rods.

Fig. 3. Cross section of the NiAl/Mo(Cr) system examined in the SEM a) overview b) layers.

Fig. 4. The specimen geometry used for fracture resistance testing.

Fig. 5. Resistance curve results a) NiAl/Mo b) NiAl/Mo(Cr). Also shown are predicted values of the initiation toughness and subsequent propagation resistance.

Fig. 6. Load/displacement curves measured for the two materials.

Fig. 7. SEM views of a crack extending in the NiAl/Mo system, indicating the plastic stretch of the Mo that occurs as the crack extends through the material.

Fig. 8. SEM fractographs of the NiAl/Mo system showing plastic stretch of the Mo and interface debonding.

Fig. 9. Higher-resolution SEM views of the fracture surface of the NiAl/Mo indicating characteristic crack trapping "trails" in the NiAl.

Fig. 10. Periodic splitting evident on both fracture and side surfaces, in some regions of the layered NiAl/Mo(Cr).

Fig. 11. A high-resolution view of a fracture surface showing plastic stretch of the refractory metal to a ridge.

Fig. 12. Predictions of the influence of crack trapping on the initiation fracture toughness.[15-18]

Fig. 13. Effects of slip and splitting on the σ_{yy} stress ahead of a semi-infinite crack in a layered material.[20]

Fig. 14. Effects of splitting on the stress ahead of a finite crack in a layered material.[21]

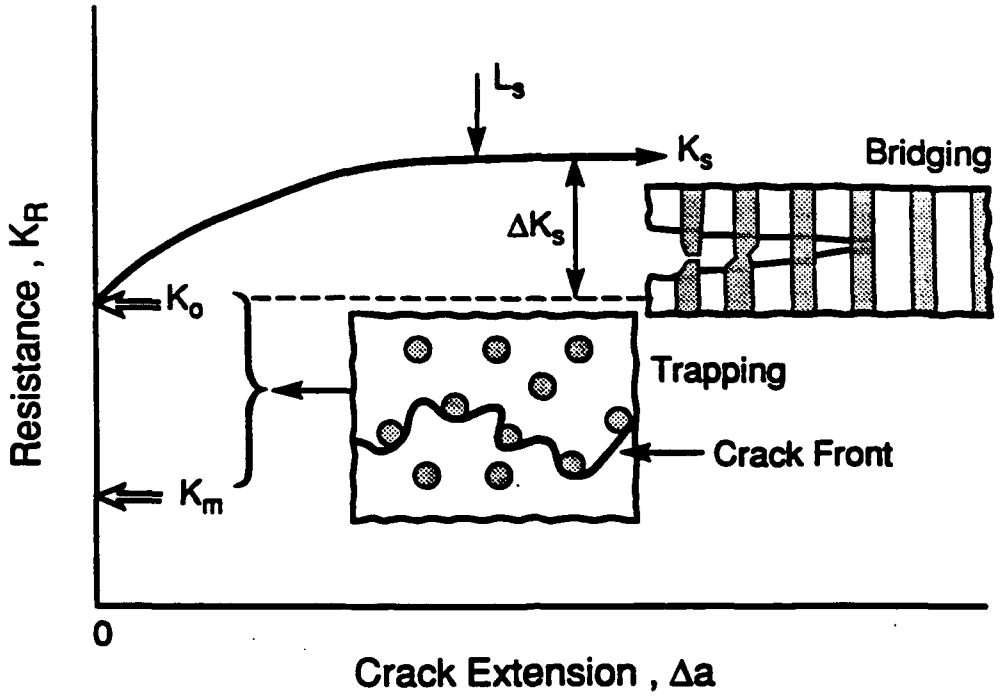

a) Type I Microstructures : Rods

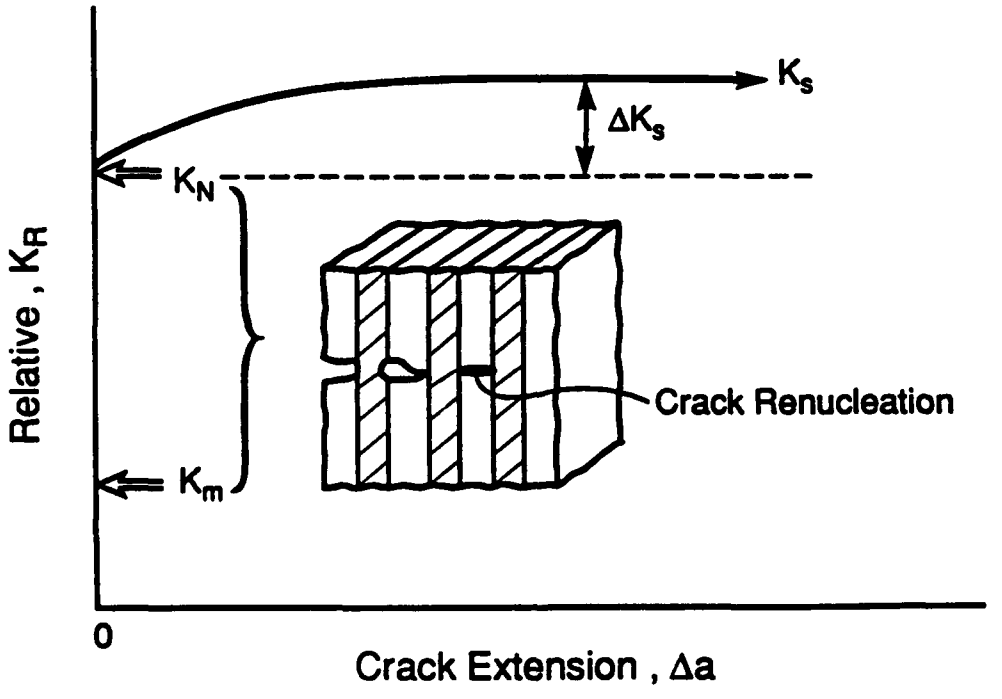

b) Type II Microstructures : Layers

Fig. 1

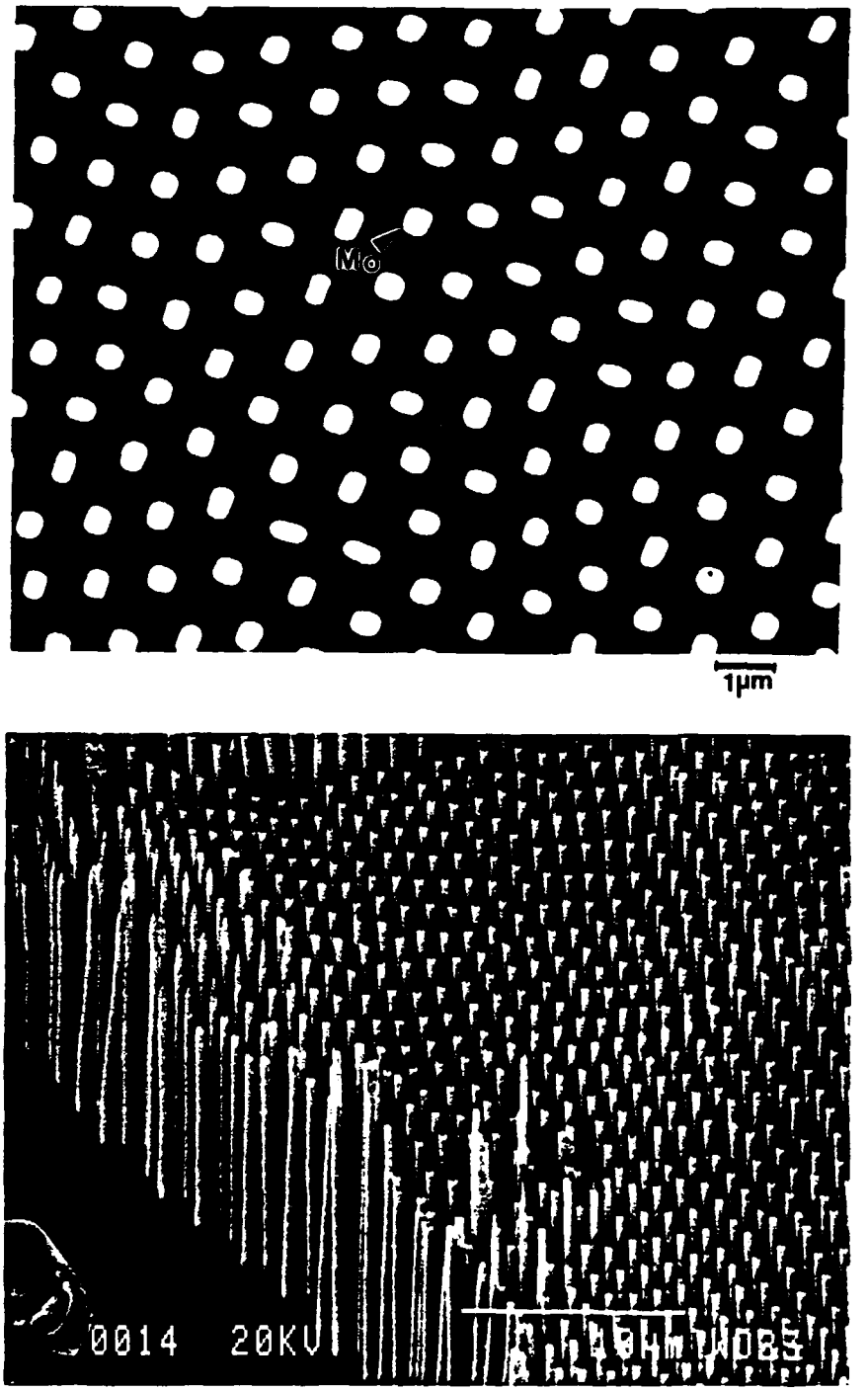

Fig. 2

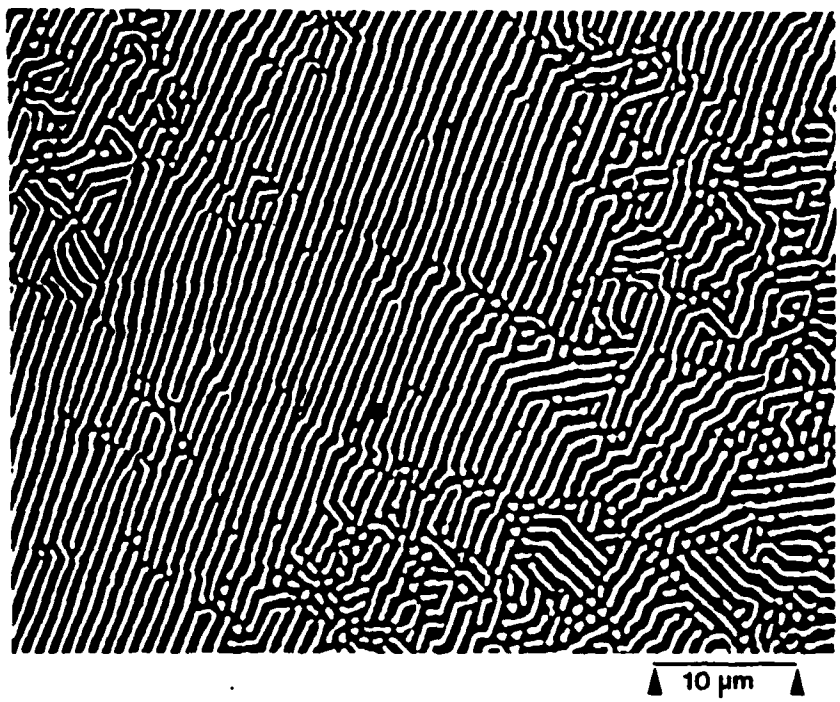

Fig. 3

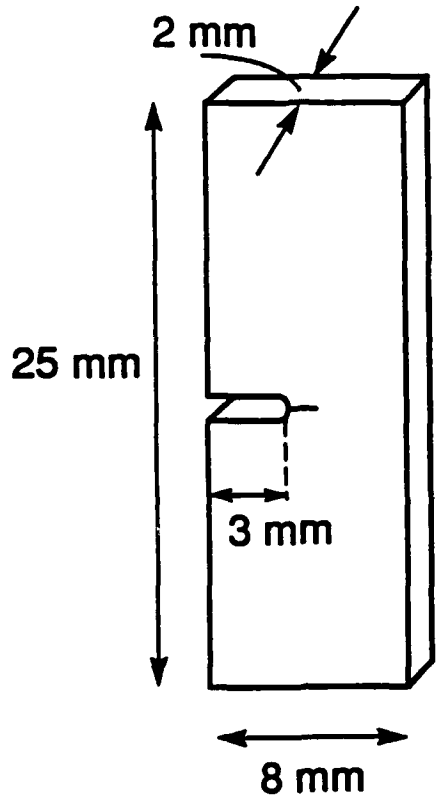

Fig. 4

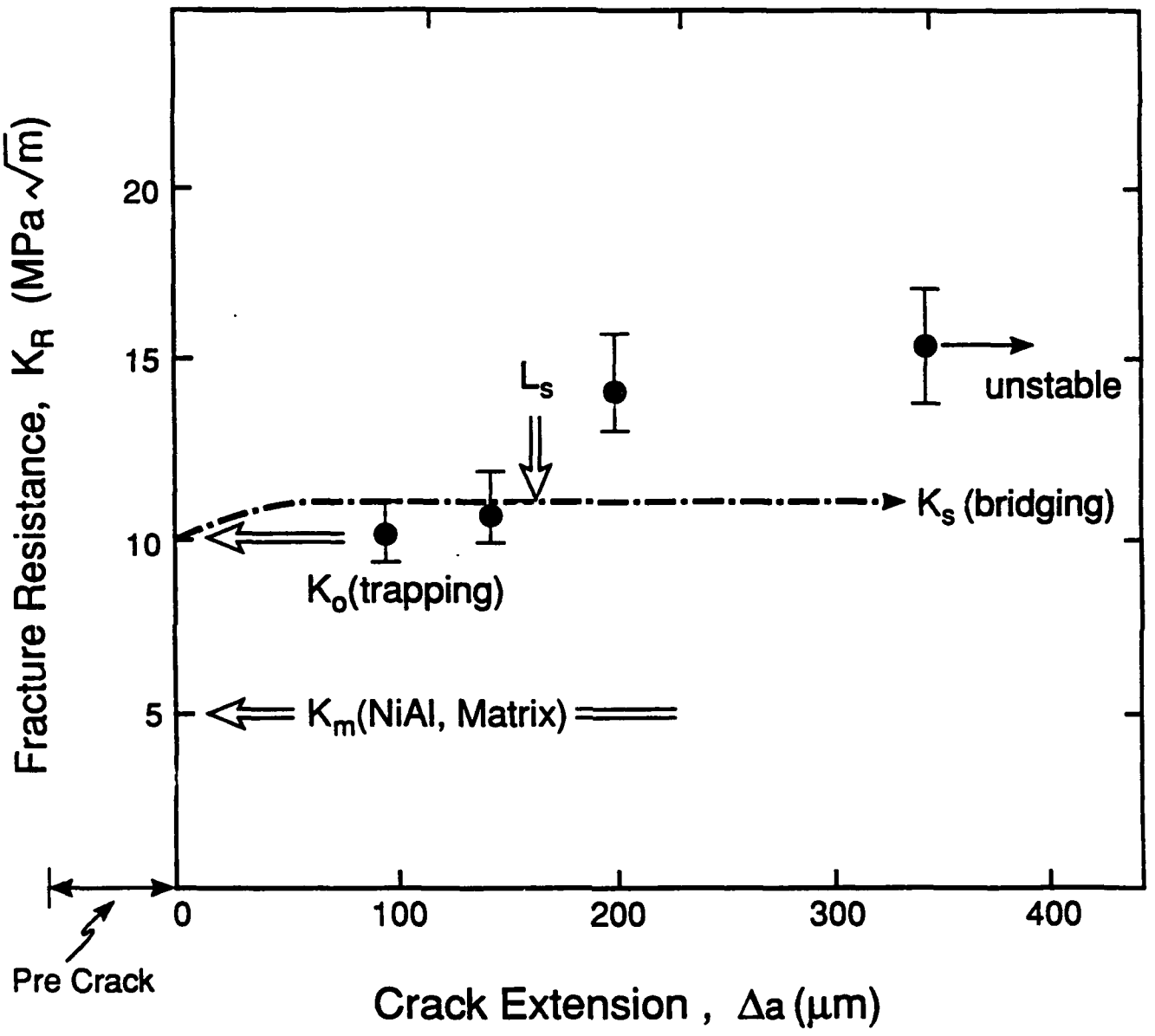
Fracture Resistance, K_R (MPa$\sqrt{m}$)
20
15
10
5
L_s
unstable
K_s (bridging)
K_o(trapping)
K_m(NiAl, Matrix)
0
100
200
300
400
Pre Crack
Crack Extension , Δa (μm)

5a

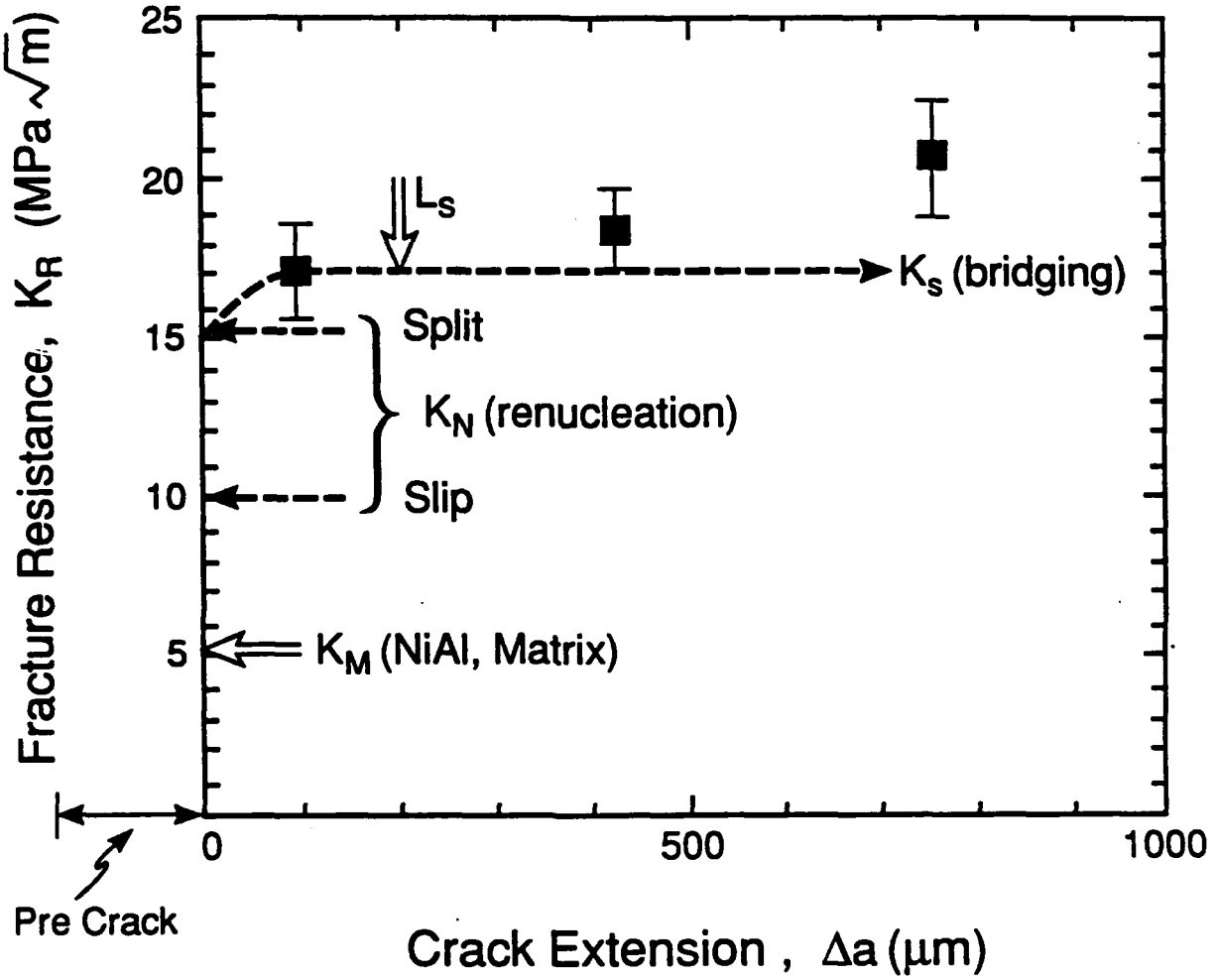
25
20
15
10
5
0
500
1000
Fracture Resistance, K_R (MPa$\sqrt{m}$)
Crack Extension , Δa (μm)
L_S
K_s (bridging)
Split
K_N (renucleation)
Slip
K_M (NiAl, Matrix)
Pre Crack

5b

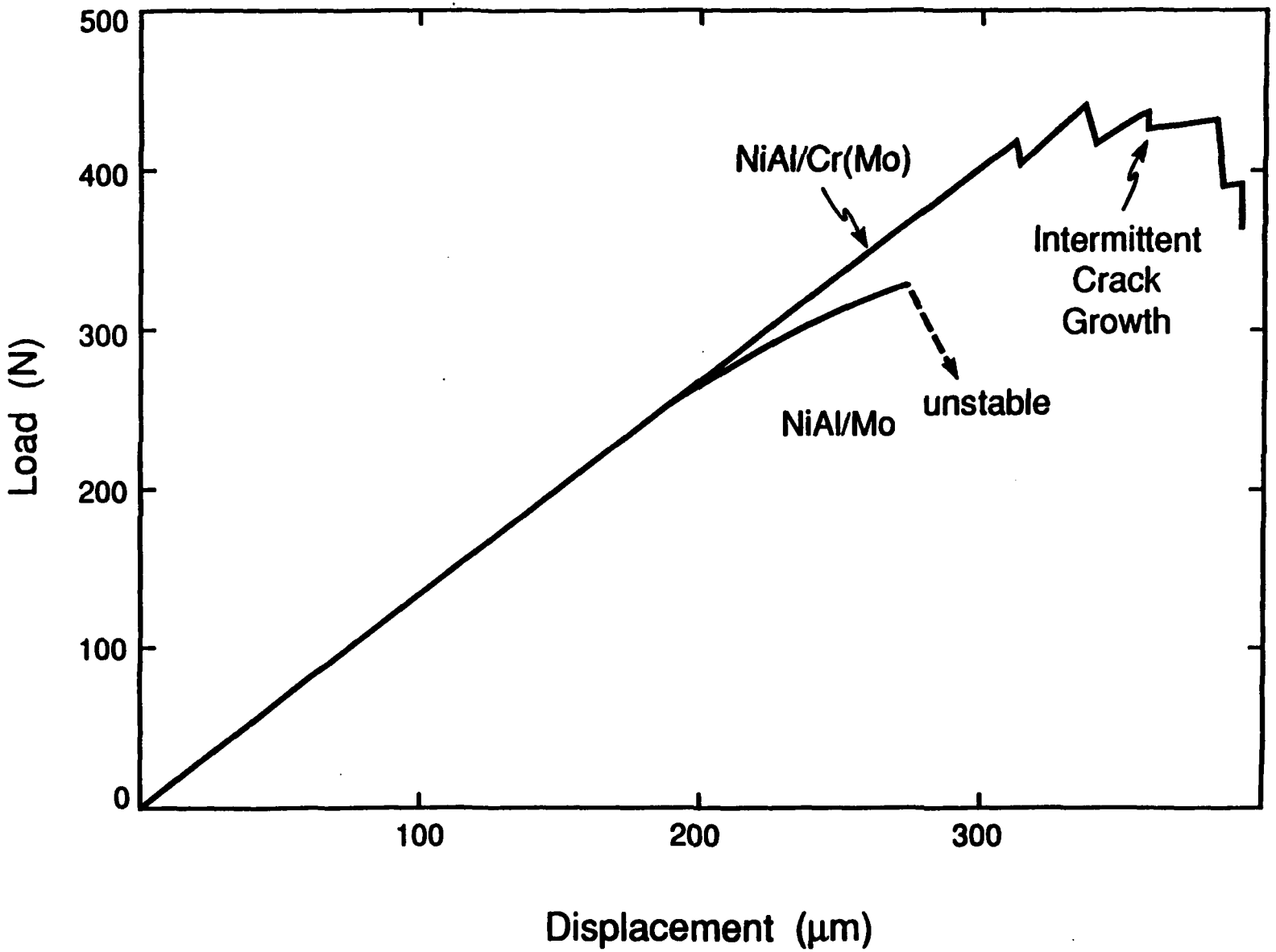
500
400
300
200
100
0
Load (N)
100
200
300
Displacement (μm)
NiAl/Cr(Mo)
Intermittent
Crack
Growth
NiAl/Mo
unstable

Fig. 6

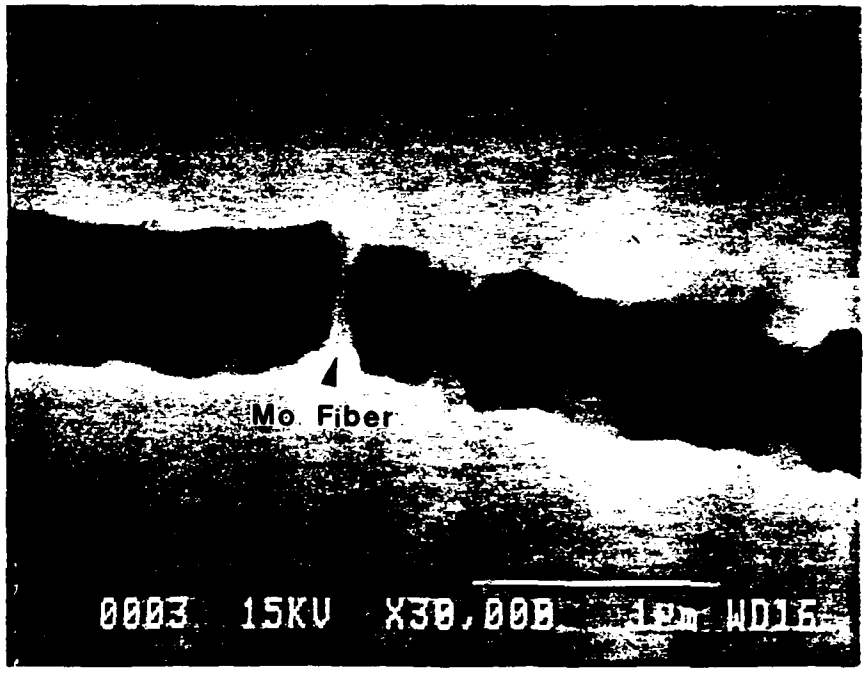

Fig. 7

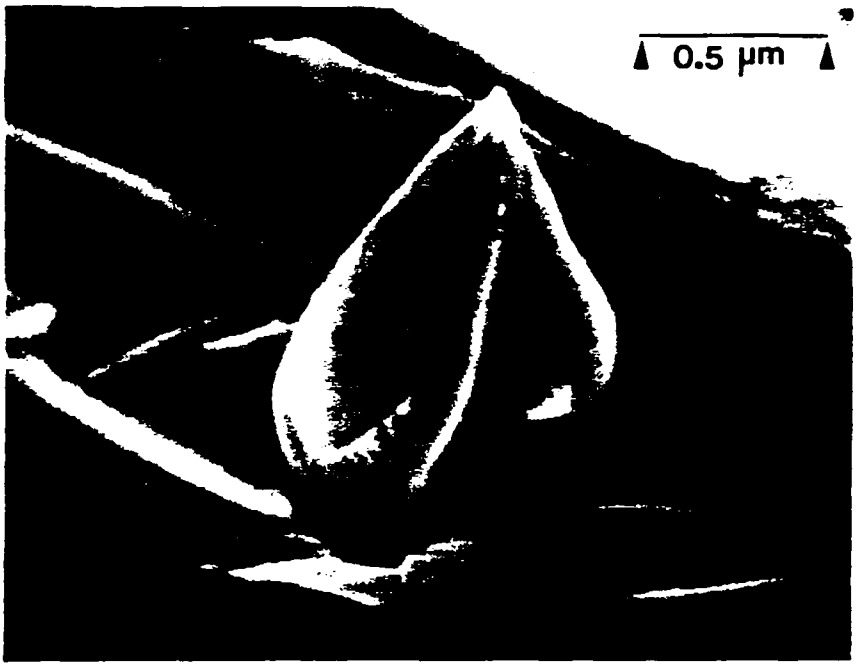

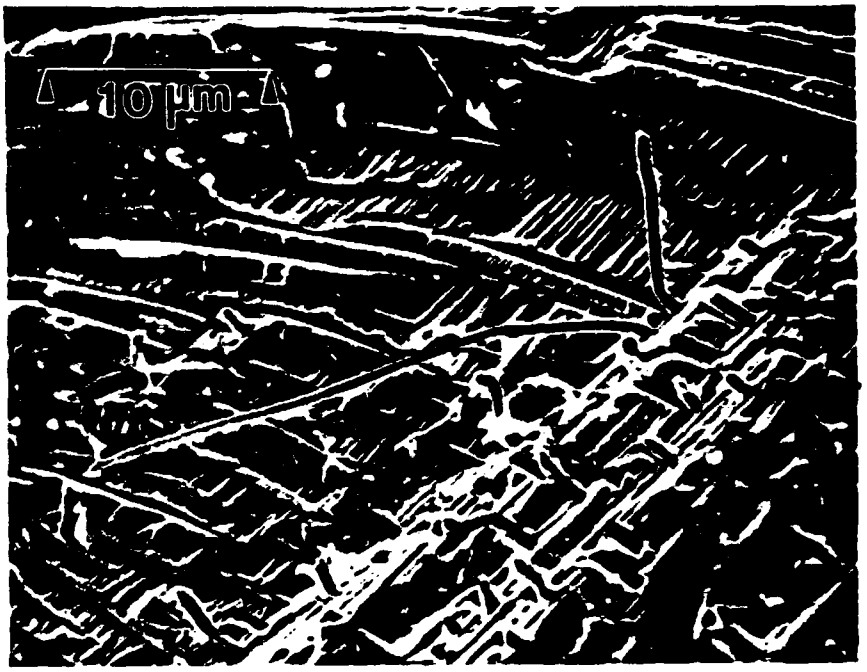

Fig. 8

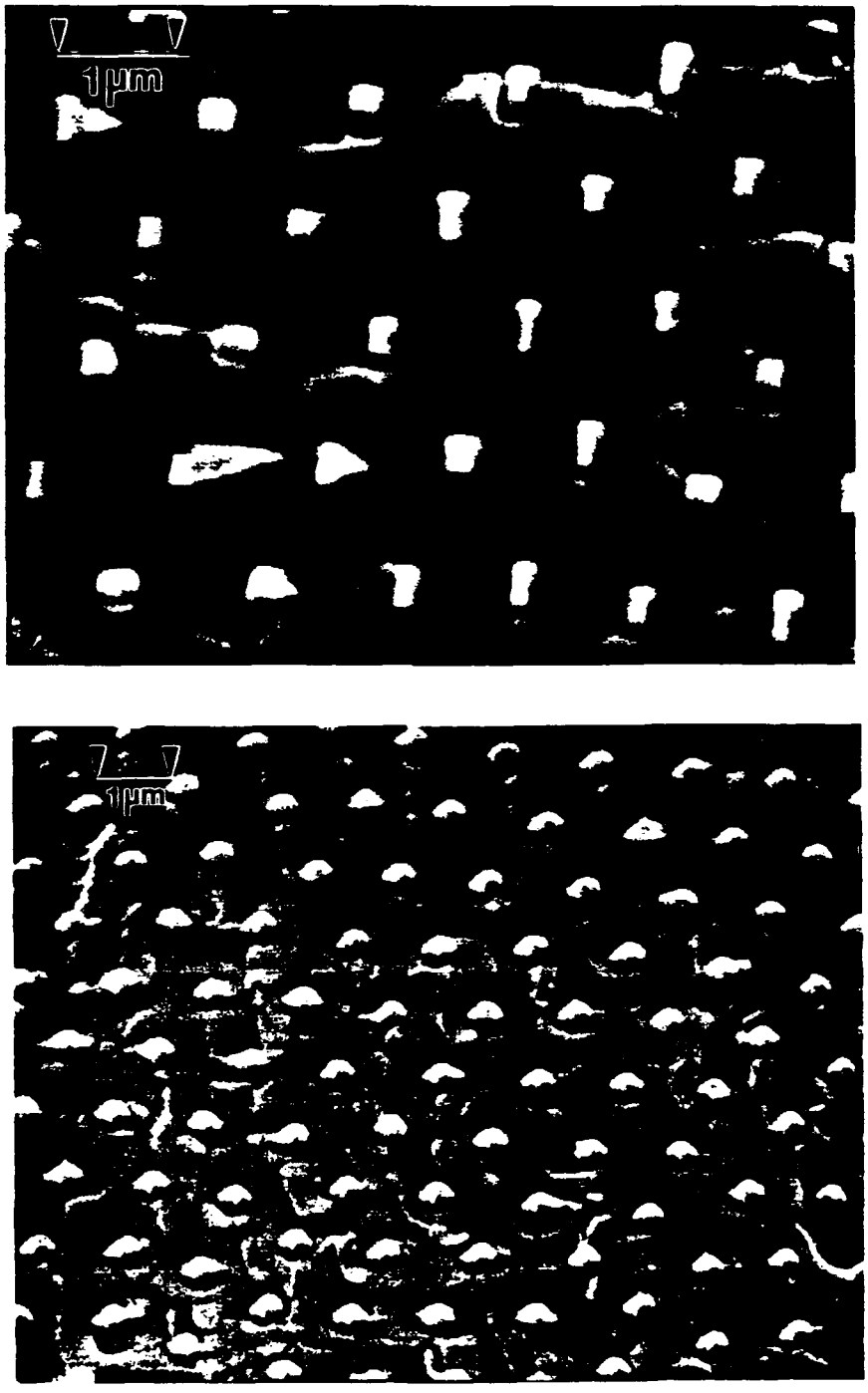

Fig. 9

Fig. 10

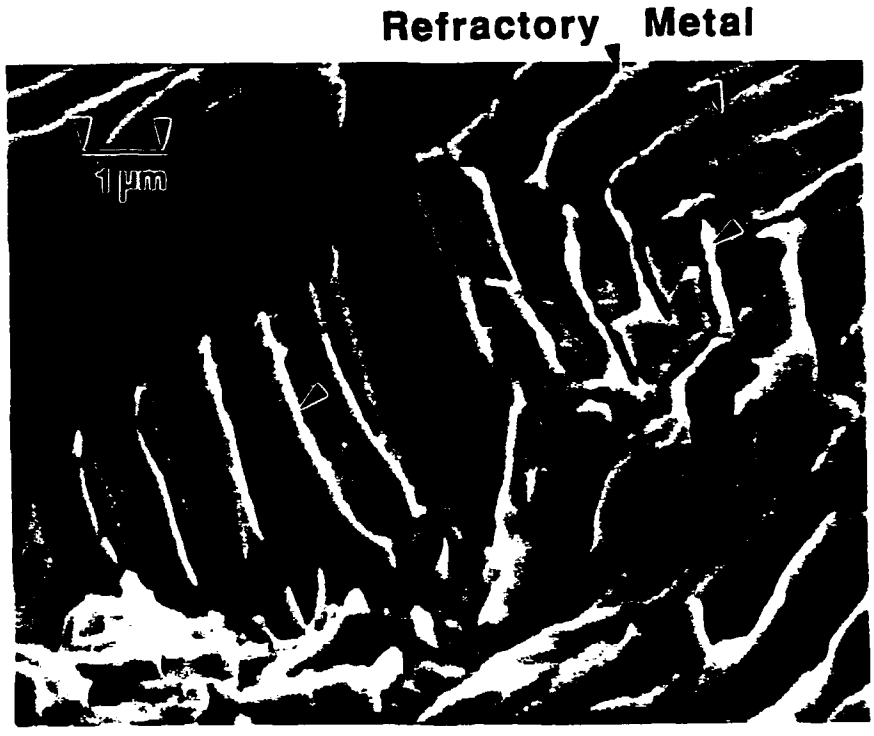

Fig. 11

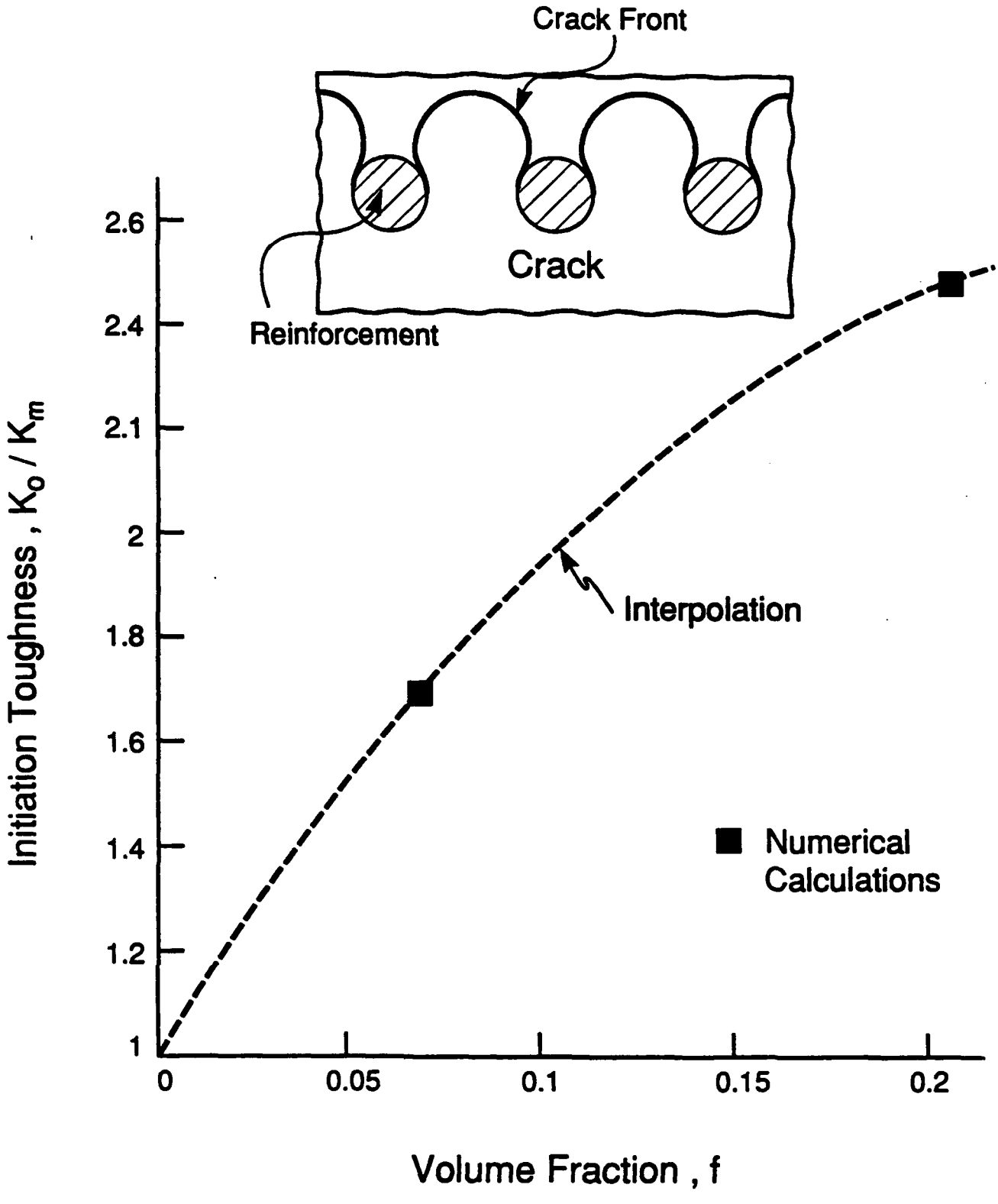
Crack Front
Crack
Reinforcement
Initiation Toughness , K_o / K_m
2.6
2.4
2.1
2
1.8
1.6
1.4
1.2
1
0
0.05
0.1
0.15
0.2
Interpolation
Numerical Calculations
Volume Fraction , f

Fig. 12

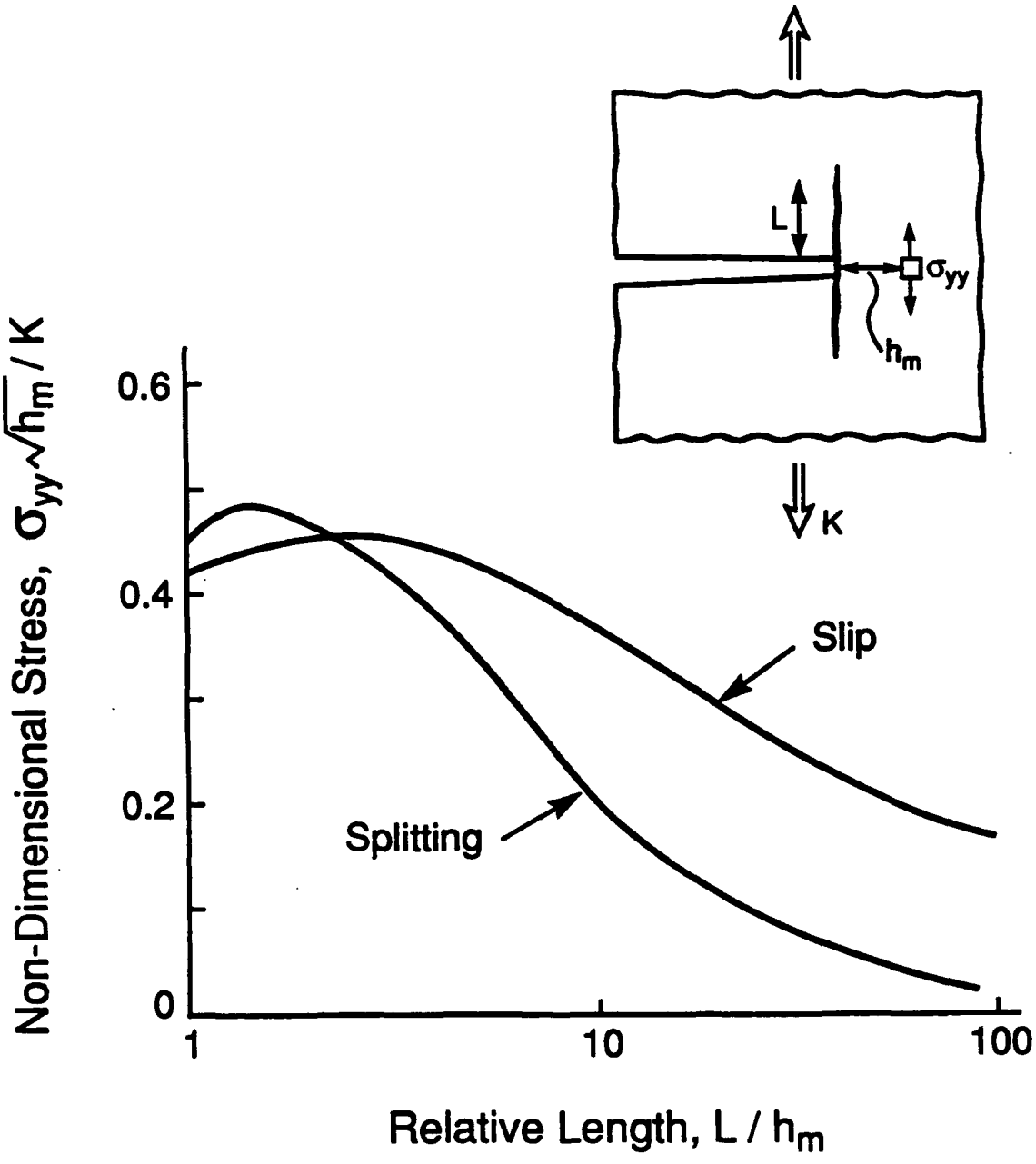
L
σ_{yy}
h_m
K
Non-Dimensional Stress, $\sigma_{yy}\sqrt{h_m}$ / K
0.6
0.4
0.2
0
Slip
Splitting
1
10
100
Relative Length, L / h_m

Fig. 13

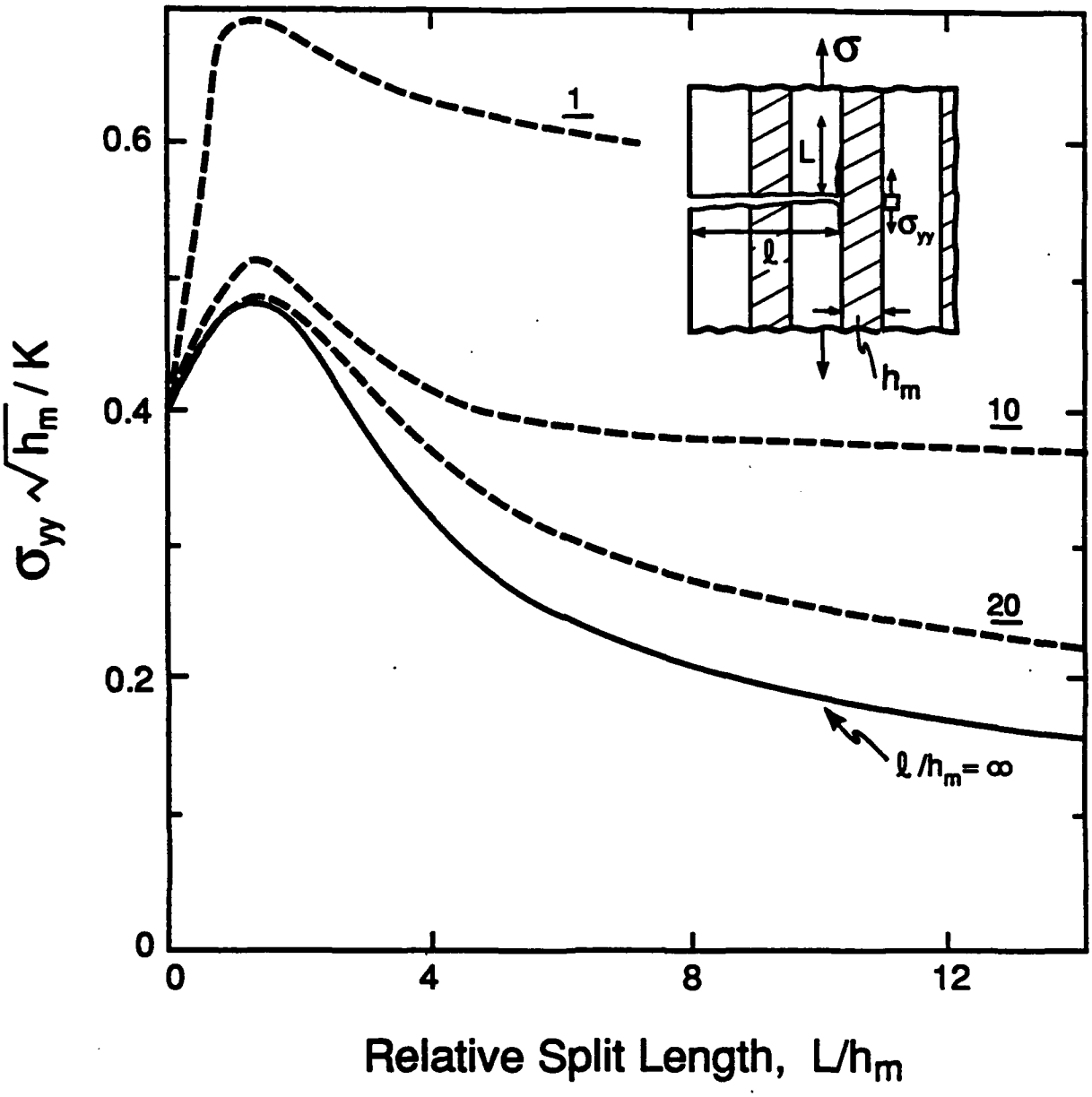
σ
L
σyy
ℓ
hm
1
10
20
ℓ /hm= ∞
0.6
0.4
0.2
0
0
4
8
12
σyy √hm / K
Relative Split Length, L/hm

Fig. 14

M A T E R I A L S

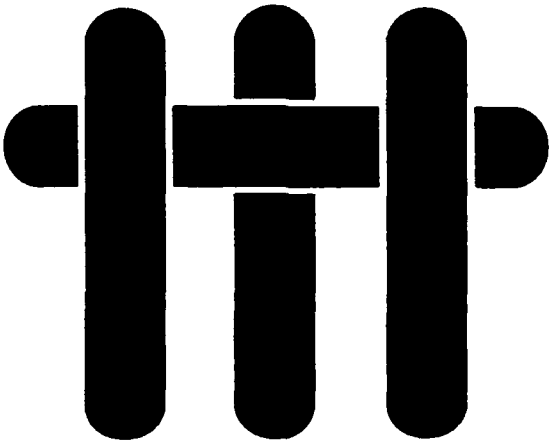

THE MECHANICS OF CRACK GROWTH IN LAYERED MATERIALS

by

M.Y. He, F.E. Heredia, D.J. Wissuchek, M.C. Shaw and A.G. Evans

Materials Department
College of Engineering
University of California
Santa Barbara, California 93106–5050

June 1992

Submitted to *Acta Metallurgica et Materialia*

kjs 6/12/92

ABSTRACT

Layered materials comprised of one brittle and one ductile constituent exhibit crack growth characteristics that depend on the sequential renucleation of cracks in each brittle layer. An analysis of the problem is presented with two different interface responses. One for a well-bonded, slipping interface and the other for an interface that debonds. It is shown that either slip or debonding enhance the fracture resistance, with debonding being the more effective. The analysis is compared with experimental results for several layered systems.

1. INTRODUCTION

Nanoscale and microscale layered materials can exhibit unprecedented mechanical property profiles: stiffness, tensile strength, notch strength, creep strength, fatigue resistance, etc. Furthermore, possibilities for spatial tailoring exist, especially when the materials are produced by vapor deposition. Alternating layers of brittle and ductile materials have particular interest, because the disparate properties of the constituents provide the ideal opportunity for achieving novel property profiles. Among this group are metal/ceramic and metal/intermetallic systems. Such materials provide a focus for the present article.

A substantial theoretical and experimental background relevant to layered systems of this type exists in the following fields i) pearlite,[1] ii) ceramic fiber-reinforced metals,[2,3] iii) metal-toughened ceramics[4,5] and intermetallics.[6-9] However, some unique *crack growth features expected* in layered systems are emphasized in this study. The objective is to provide a *mechanics framework* for predicting the crack growth resistance of ductile/brittle layered materials, in terms of constituent material properties (including the interfaces), as well as the layer thicknesses. Two predominant interface responses are considered. a) A well-bonded interface subject to slip by plastic flow in the metal. b) An interface that debonds and splits in a controlled manner.

2. EXPERIMENTAL BACKGROUND

Experimental results on crack growth have been presented for layered metal/ceramic and metal intermetallic systems produced using a variety of processing techniques: diffusion bonding (DB),[10,11] directional solidification (DS),[12] thermal processing (TP)[13] and physical vapor deposition (PVD).[14] However, different length scales are involved. Diffusion bonded systems have layer thickness, $h \gtrsim 20$ μm: DS

materials have h ≈ 1 μm, TP materials have h ≈ 0.1 μm and PVD materials have h ≈ 0.01 – 1 μm. Experimental studies conducted on these systems have identified the existence of a major fracture mechanism transition. The two fracture mechanisms are:[10] i) Class I behavior dominated by a single crack. ii) Class II behavior involving multiple microcracking. The conditions that dictate the transition between these mechanisms have not yet been explicitly delineated. Nevertheless, it is apparent from the experiments that Class I behavior is most likely when both the metal content is relatively low and the layers are relatively thick.[10] This behavior is emphasized in the present article (Fig. 1).

When the metal layers retain good ductility through processing, plastic stretch of the metal layers accompanies crack growth, resulting in a fracture surface morphology having the characteristics depicted in Fig. 2. Notably, the metal layers rupture along a *ridge*.[10] When this occurs, without interface debonding, crack growth is subject to a resistance curve having the characteristics indicated on Fig. 3: i) An initiation resistance, K_N, exceeding that of the brittle layer, K_B, followed by a rising resistance. ii) When the metal layers are thin ($h_m < 1$ μm, where h_m is the metal layer thickness), a *steady-state fracture resistance*, K_s, is reached. iii) Thicker metal layers ($h_m > 10$ μm) may result in a continuously rising resistance caused by large-scale bridging (LSB).[15-17] Generally, both K_N and K_s increase as h_m increases (Fig. 4):[10] K_s also increases as the metal yield strength σ_o and the metal volume fraction, f_m, increase.

Interface *debonding* and/or misaligned layers result in resistance curves having the same qualitative features, but subject to quantitative differences. Usually, *interface decohesion elevates* both K_N and K_s, but the fracture morphology is more intricate[12] (Fig. 5). *Misalignment* introduces an additional level of complexity though effects on crack path, on crack trapping, ligament formation, etc.[13,18,19] (Fig. 6). Notably, a crack may extend along a low fracture energy plane, within a colony, having layers oriented *normal* to the loading axis. It then encounters a colony with obliquely oriented layer

planes. At this encounter, the crack is arrested and induces a series of decohesion and deformation events that dictate the subsequent behavior.[13,18,19]

3. THE MECHANICS OF LAYERED MATERIALS

Some basic, analytical results for cracks normal to the interfaces in elastically homogeneous bodies are reviewed, before presenting numerical results that address specific issues. Asymptotic solutions for semi-infinite cracks arrested at an interface provide the information summarized in Fig. 7.[20] The normal stresses, σ^*, in the brittle layers *ahead* of the crack front are important, since these layers are susceptible to the events that result in macroscopic crack growth. The calculations show that yielding in the metal layer at the crack front has minimal effect on σ^*, except for very low values of yield strength, σ_o (Fig. 7a). The essential non-dimensional parameter is

$$\Omega = h_m(\sigma_o/K)^2 \tag{1}$$

where K is the stress intensity factor. Notably, reduced values of σ^* only arise when $\Omega < 0.02$; moreover, when Ω is small, the following limit must obtain: $\sigma^* \to 0$ as $\sigma_o \to 0$.

When the *interfaces* decohere, the normal stress, σ^* ahead of the crack can be dramatically *reduced*[20] (Fig. 7b). In particular, there is a strong influence of the decohesion length L on σ^*, when L/h_m exceeds ~ 3. Indeed, when $L/h_m = 10$, σ^* is about half the value that obtains without splitting. Furthermore, $\sigma^* \to 0$ when $L/h \to \infty$, and is negligibly small, (< 0.01) when $L/h_m > 30$. Consequently, splitting has a considerably larger effect on σ^* than slip.

To address effects of *crack size* on crack growth, numerical results for both splitting and slip have been obtained using finite element procedures with elastic homogeneity assumed. The finite element mesh is depicted in Fig. 8. For calculations with splitting,

the split length L is prescribed. When slip occurs, the shear stress σ_{xy} on the interface is not allowed to exceed the shear strength, $\tau = \sigma_o/\sqrt{3}$. This model approximates the effect of yielding in the metal layers. The numerical results obtained for both mechanisms (Fig. 9) reveal appreciable effects of crack size. The trend is for σ^* to increase as the crack size *decreases*.

In some cases, the crack does not extend. Instead, splitting occurs *ahead of the crack* (Fig. 6), resulting in ligament formation. This process is governed by the σ_{xx} stress. Variations in this stress with distance from the crack front (Fig. 10) indicate a maximum. This maximum occurs at a distance ahead of the crack $\approx$ 2L.

4. CRACK GROWTH PREDICTION

The preceding mechanics must be coupled with a crack growth criterion in order to predict the crack growth resistance. It has been proposed that the RKR criterion[21] is most appropriate when layer cracking is the operative mechanism. This criterion states that fracture proceeds when σ^* attains the fracture strength S of the brittle layers.† The magnitude of the tensile stress at which cracking occurs in the brittle layer is subject to a *mechanism transition*. When the layers are sufficiently *thick* that the fracture flaws are smaller than the layer thickness, the layer strength, S, is *flaw controlled*.[10] In this case, S is related to the tensile strength of the material (as qualified by statistical issues associated with the stress gradient and the layer thickness). When the layers are *thin*, relative to the flaw size, the layer strength is controlled by *tunnel cracking*.[22] For this cracking mode, the *fracture toughness* and the layer *thickness* have a dominant influence on S (Fig. 11). The strength controlled by tunnel cracking is given by,

---

† Consistent with the behaviors found for Fe/Fe_3C materials.[1,21]

$$S = \Sigma\left(K_B/\sqrt{h_b}\right) \qquad (2)$$

where h_b is the thickness of the brittle material and Σ is a non-dimensional parameter of order unity that depends in the extent of debonding and sliding.[23]

5. COMPARISON WITH EXPERIMENTS

The preceding calculations can be compared with experiments in which explicit measurements have been made of the toughness of the brittle constituents and the initiation toughness of the layered system. Such results exist for the three systems summarized in Table I, as illustrated in Fig. 3. In other layered materials, inelastic behavior in the more brittle constituent (e.g., twinning in TiAl)[13,24] invalidates direct comparison with the present calculations.

Inspection of the results reveals that the initiation toughness K_N is relatively larger for systems that exhibit interface splitting (NiAl and TiAl), in qualitative accordance with the calculations. Furthermore, explicit comparisons can be made for each material. i) In Al_2O_3/Al and Al_2O_3/Cu, there is no interface debonding[10,25] (Fig. 2). Moreover, for the systems tested, the Al_2O_3 layers are relatively thick and have fracture properties in the flaw controlled regime. Using independently measured value of the ceramic tensile strength,[10] S, and metal yield strength, σ_o, a comparison of the predicted and measured values of initiation toughness is shown in Fig. 4, for a range of metal thicknesses and volume fractions.[10] The good correlation validates the strength-based (RKR) approach,[21] at least when the interface is strongly bonded. ii) The NiAl/Cr(Mo) system exhibits profuse interface splitting (Fig. 5).[12] However, not all interfaces are susceptible to splitting. When splitting occurs, the split lengths are appreciably larger than the layer thickness ($L/h \approx 10$). Moreover, the thin intermetallic layer thickness dictates that fracture proceed by *tunnel cracking*, such that (Eqn. 2) applies. Predictions

are made both with and without splitting, as indicated on Fig. 12. The correlation with experiment is indicative of a predominant role of split interfaces. iii) For the TiAl/Nb system, the TiAl is relatively thick and is expected to be in the flaw controlled regime.[6,17] Interface splitting is also evident in this system ($L/h \approx 2$). However, independent measurements of tensile strength for TiAl are not available.

The calculations assist in the interpretation of a splitting phenomenon found in TiAl/Ti_3Al with a lamellar or layered colony microstructure[13,18,19] (Fig. 6). In this material, periodic splits occur where the crack encounters a colony with the layers oriented normal to the crack plane. There is no coplanar cracking of the TiAl layers. The splitting is attributed to the σ_{xx} stress and indeed, occurs where this stress has a maximum, at $x/L \approx 2$ (Fig. 10). However, a criterion for predicting the onset of periodic split cracking would require an in-plane strength property for the TiAl layers (or the TiAl/Ti_3Al interface), yet to be identified.

6. IMPLICATIONS

The above connections between experimental results and the analysis allow some implications to be made about crack growth in layered materials. The first important result is that materials with *thin layers* and *well-bonded* interfaces have an initiation toughness exceeding that of the brittle constituent, but only by, $\sqrt{2\pi f_m}/(1-f_m)$. Substantially higher values of initiation toughness require either *thicker layers* or interfaces that exhibit extensive *debonding* and/or sliding. Control of the interface has greater appeal, because the advantages of thick layers are only manifest at thicknesses in the 10–100 μm range. Interface debonding is not yet predictable from fundamental principles, but some empirical guidelines exist that provide useful insight.[26]

While interface slip is not as effective as debonding in enhancing toughness (Fig. 7), slip may still be more attractive, when reasonable transverse properties are required. An

interesting option in this regard is suggested by an experimental observation that a ductile interface layer can lead to high toughness.[17] Notably, a thin *interface layer* with *low yield strength* should provide high initiation toughness, by enabling the slip length to become large compared with the layer thickness. Such a thin layer should not degrade the propagation toughness associated with ductile phase bridging.

7. CONCLUSION

An analysis has been presented that predicts the initiation toughness for layered materials with one brittle constituent. The analysis appears to be consistent with experimental results for several ceramic/metal and intermetallic/metal systems produced by either diffusion bonding or directional solidification. Two important implications have been addressed. i) Thin layer bimaterial systems with well-bonded interfaces *are not* conducive to substantial toughening. ii) Higher initiation toughness can be achieved with thick layers. But, a more attractive approach is to introduce thin *interface layers* that allow extensive (but controlled) inelastic deformation, either by slip or debonding. Among these two options, slipping interfaces are preferred (where possible), because they provide superior transverse cracking resistance. These layers can be produced either by reaction between the bimaterial constituents or by using physical vapor deposition to produce the multilayers.

The analysis may also be used to rationalize behaviors found in lamellar microstructures, such as periodic splitting. These splitting effects are, in turn, fundamental to the high toughness exhibited by these materials. Further study of such phenomena may lead to a fundamental understanding of the fracture properties of lamellar systems.

Finally, it is recognized that new effects may emerge in nanoscale systems, wherein the deformation of the metal layers is governed by the threading of individual

dislocations. However, the expectation is that the associated enhancement in the resistance to plastic flow would lead to *lower* levels of initiation toughness than those addressed by the present analysis.

ACKNOWLEDGEMENT

The authors wish to thank Dr. D.B. Marshall for his technical support and for valuable discussions. This work was supported by the Office of Naval Research through contract N00014–90–J–1300. Provision of the ABAQUS finite element code by Hibbitt, Karlsson and Sorensen, Inc. of Providence, Rhode Island is gratefully acknowledged.

TABLE I

Material Systems Investigated

SYSTEM	LAYER THICKNESS (μm)		$K_B(MPa\sqrt{m})$
	BRITTLE	DUCTILE	
Al_2O_3/Al	45–680	8–250	3.5
NiAl/Cr(Mo)	0.75	0.35	5
TiAl/Nb	100–200	50	6–8

REFERENCES

[1] J.J. Lewandowski and W.W. Thompson, *Met. Trans.*, **17A** (1986) 1769.

[2] S. Ochiani and K. Osanuru, *Met. Trans.*, **21A** (1991) 971.

[3] M.S. Hu, H.-C. Cao, J. Yang and A.G. Evans, *Acta Metall. Mater.*, in press.

[4] L.S. Sigl, P.A. Mataga, B.J. Dalgleish, R.M. McMeeking and A.G. Evans, *Acta Metall.*, **36** (1988) 945.

[5] B.D. Flinn, C. Lo, F.W. Zok and A.G. Evans, *J. Am. Ceram. Soc.*, in press.

[6] C.K. Elliott, G.R. Odette, G.E. Lucas and J.W. Sheckard, *Mater. Res. Soc. Proc.*, **120** (1988) 95.

[7] P.R. Subramanian, M.G. Mendiratta, P.B. Miracle and D.M. Dimiduk, *MRS Symp. Proc.*, **194** (1990) 147.

[8] M.F. Ashby, F.J. Blunt and M.K. Bannister, *Acta Metall.*, **37** (1989) 1947.

[9] M.K. Bannister and M.F. Ashby, *Acta Metall. Mater.*, **39** (1991) 2575.

[10] M.C. Shaw, D.B. Marshall, M.S. Dadkhah and A.G. Evans, *J. Am. Ceram. Soc.*, to be published.

[11] H.-C. Cao and A.G. Evans, *Acta Metall. Mater.*, **39** (1991) 2997.

[12] F.E. Heredia, M.Y. He, G.E. Lucas, A.G. Evans, H.E. Dève and D. Konitzer, *Acta Metall. Mater.*, to be published.

[13] H.E. Dève, A.G. Evans and D.S. Shih, *Acta Metall. Mater.*, in press.

[14] G.R. Rowe, *Mat. Res. Soc. Proc.*, **273** (1992) in press.

[15] F.W. Zok and C. Hom, *Acta Metall. Mater.*, **38** (1990) 1895.

[16] B.N. Cox and C.S. Lo, *Acta Metall. Mater.*, **40** (1992) 69.

[17] G.R. Odette, B.L. Chao, J.W. Sheckard and G.E. Lucas, *Acta Metall. Mater.*, in press.

[18] D.J. Wissuchek and G.E. Lucas, to be published.

[19] K.S. Chan, *Met. Trans.*, **A22** (1992) 2021.

[20] K.S. Chan, M.Y. He and J.W. Hutchinson, to be published.

[21] R.O. Ritchie, J. Knott and J.R. Rice, *J. Mech. Phys. Solids*, **21** (1973) 395.

[22] J.W. Hutchinson and Z. Suo, *Advances in Appl. Mech.*, **29** (1992) 63.

[23] T. Ye, Z. Suo and A.G. Evans, *Intl. Jnl. Solids Structures*, in press.

[24] H.E. Dève and A.G. Evans, *Acta Metall. Mater.*, **39** (1991) 1171.

[25] B.J. Dalgleish, K.P. Trumble, and A.G. Evans, *Acta Metall.*, **37** (1989) 1923.

[26] A.G. Evans and B.J. Dalgleish, *Acta Metall. Mater.*, in press.

FIGURE CAPTIONS

Fig. 1. A schematic of crack growth in a layered material with associated resistance curve.

Fig. 2. A scanning electron fractograph of a diffusion-bonded Al_2O_3/Al material indicating plastic stretch of the Al to a ridge.

Fig. 3. Resistance curves for three layered materials a) Al_2O_3/Al with $h_m \approx 100\ \mu m$, b) NiAl/Cr(Mo) with $h_m \approx 1\ \mu m$, c) TiAl/Nb with $h_m \approx 50\ \mu m$.

Fig. 4. Measurements of K_N as a function of metal layer thickness for the Al_2O_3/Al and Al_2O_3/Cu systems. The predictions are also shown.

Fig. 5. The fracture surface for a NiAl/Cr(Mo) layered material indicating splitting, as well as plastic distortion.

Fig. 6. A crack within a layered, colony structure exhibited by the system, $TiAl/Ti_3Al$.

Fig. 7. Asymptotic solutions for the effects of slip and splitting on the stress, σ^*.
   a) The normal stress ahead of the crack as a function of relative distance from the crack with a slip.
   b) The normal stress ahead of the crack as a function of the relative slip or splitting length.

Fig. 8. Finite element mesh used to evaluate effects of slip and splitting.

Fig. 9. Effect of crack size on the stress ahead of a crack subject to a) splitting or b) slip.

Fig. 10. The in-plane, σ_{xx} stress ahead of a crack with a split.

Fig. 11. A schematic of the trend in strength with brittle layer thickness.

Fig. 12. Predictions of initiation toughness for weakly bonded layered systems with and without splitting and comparison with results for NiAl/Cr(Mo).

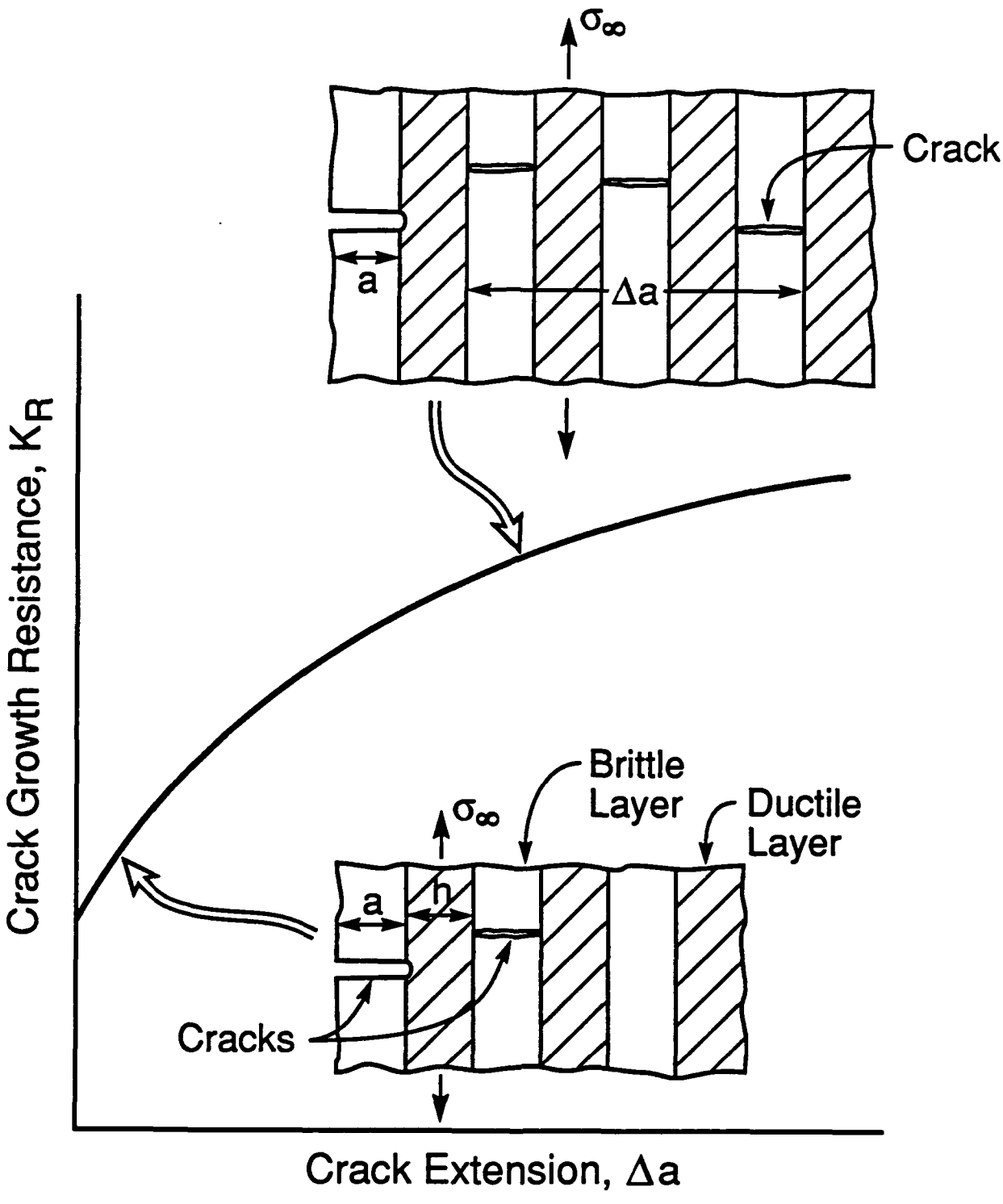
σ_∞
Crack
a
Δa
Crack Growth Resistance, K_R
σ_∞
Brittle Layer
Ductile Layer
a
h
Cracks
Crack Extension, Δa

Figure 1

Al/Al_2O_3

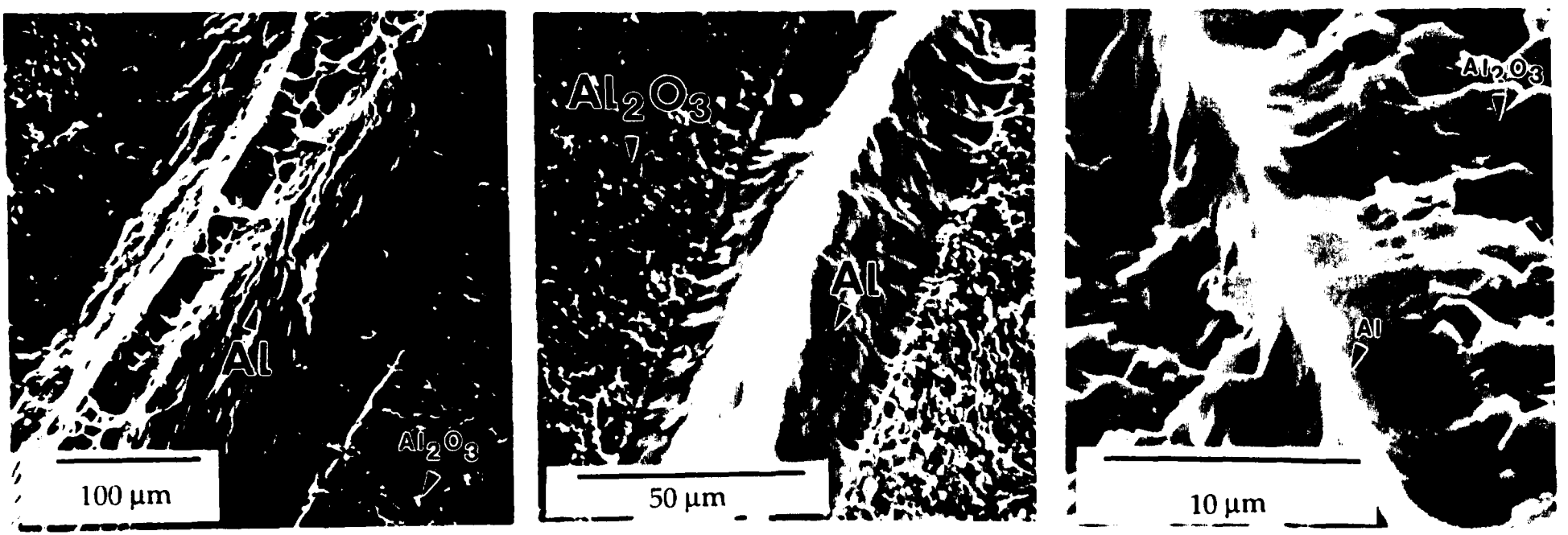

$h_m = 250\ \mu m$ $h_m = 50\ \mu m$ $h_m = 8\ \mu m$

Fig. 2

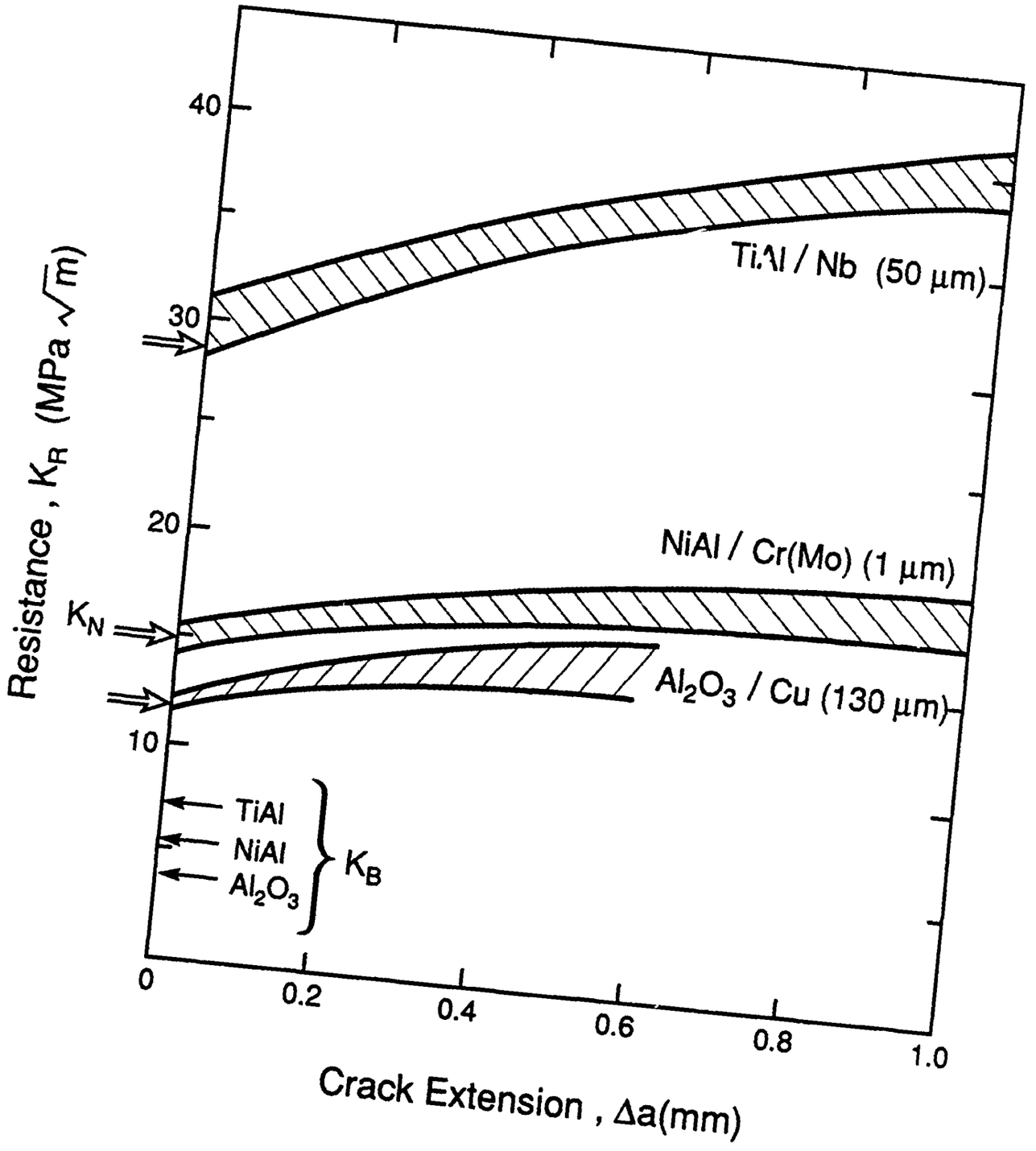
Resistance , K_R (MPa $\sqrt{m}$)
40
30
20
10
K_N
Ti.Al / Nb (50 μm)
NiAl / Cr(Mo) (1 μm)
Al_2O_3 / Cu (130 μm)
TiAl
NiAl
Al_2O_3
K_B
0
0.2
0.4
0.6
0.8
1.0
Crack Extension , Δa(mm)

Figure 3

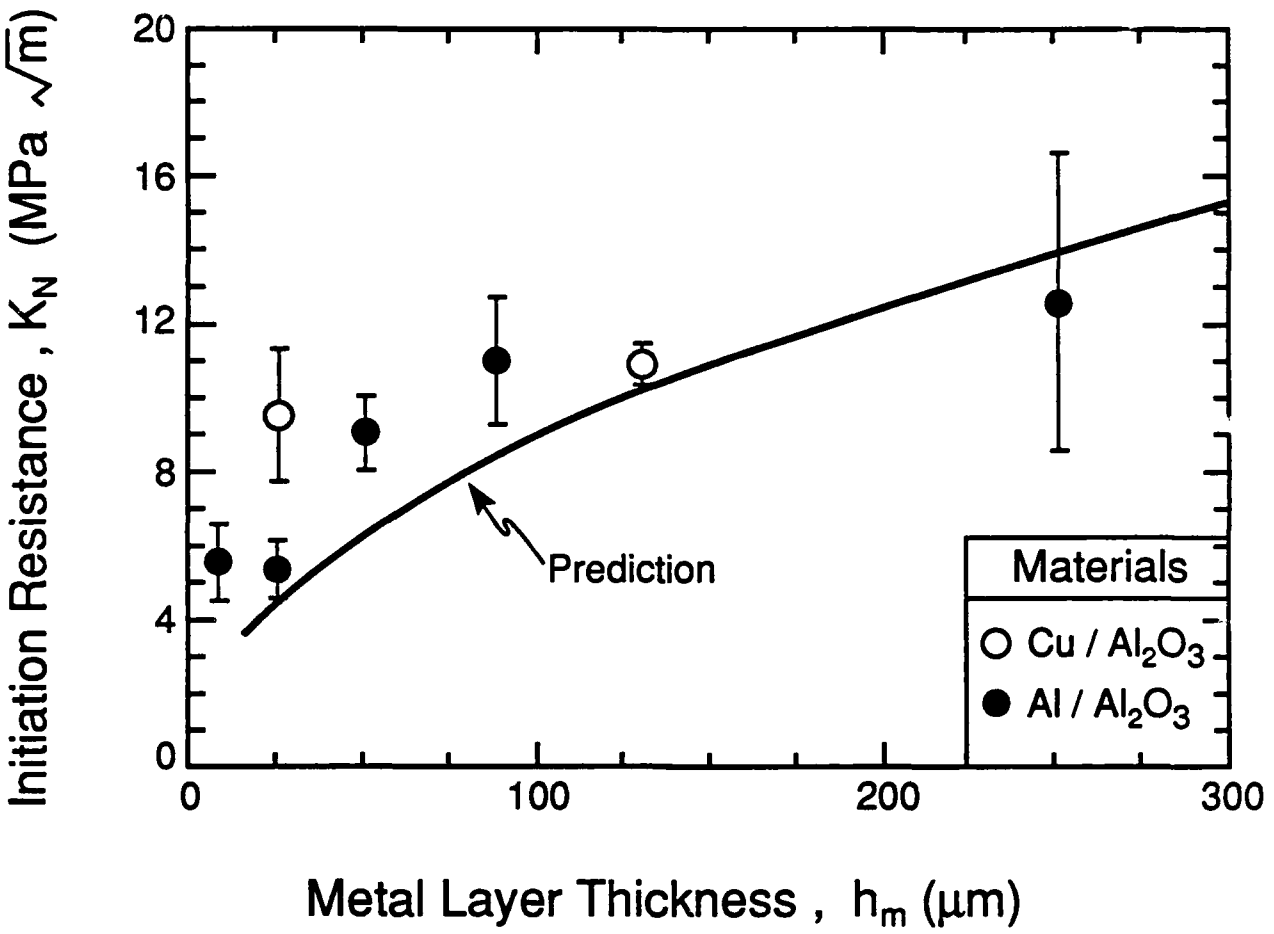
Initiation Resistance , K_N (MPa $\sqrt{m}$)
20
16
12
8
4
0
0
100
200
300
Metal Layer Thickness , h_m (μm)
Prediction
Materials
Cu / Al_2O_3
Al / Al_2O_3

Figure 4

NiAl/Cr(Mo)

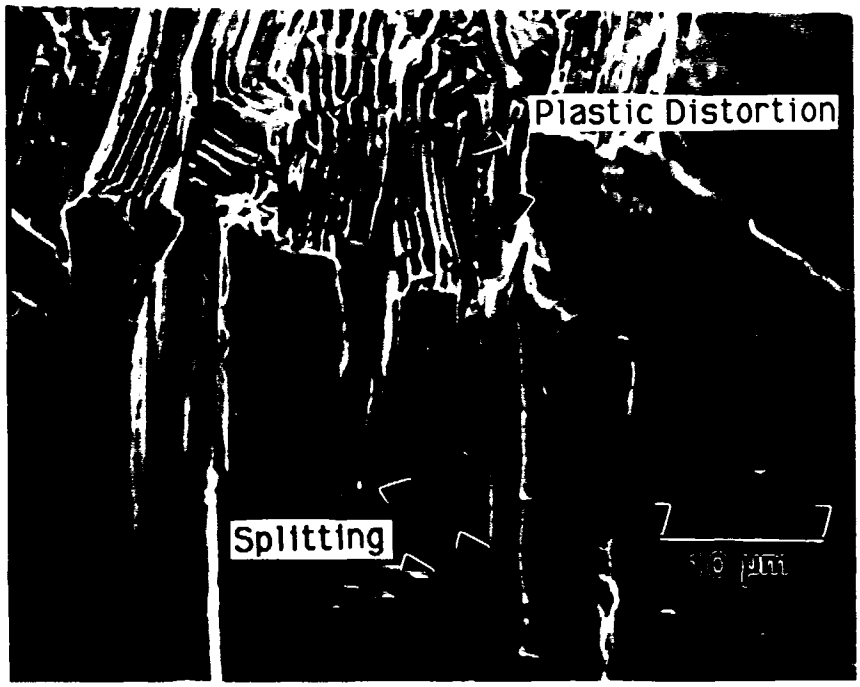

Fig. 5

$TiAl/Ti_3Al$

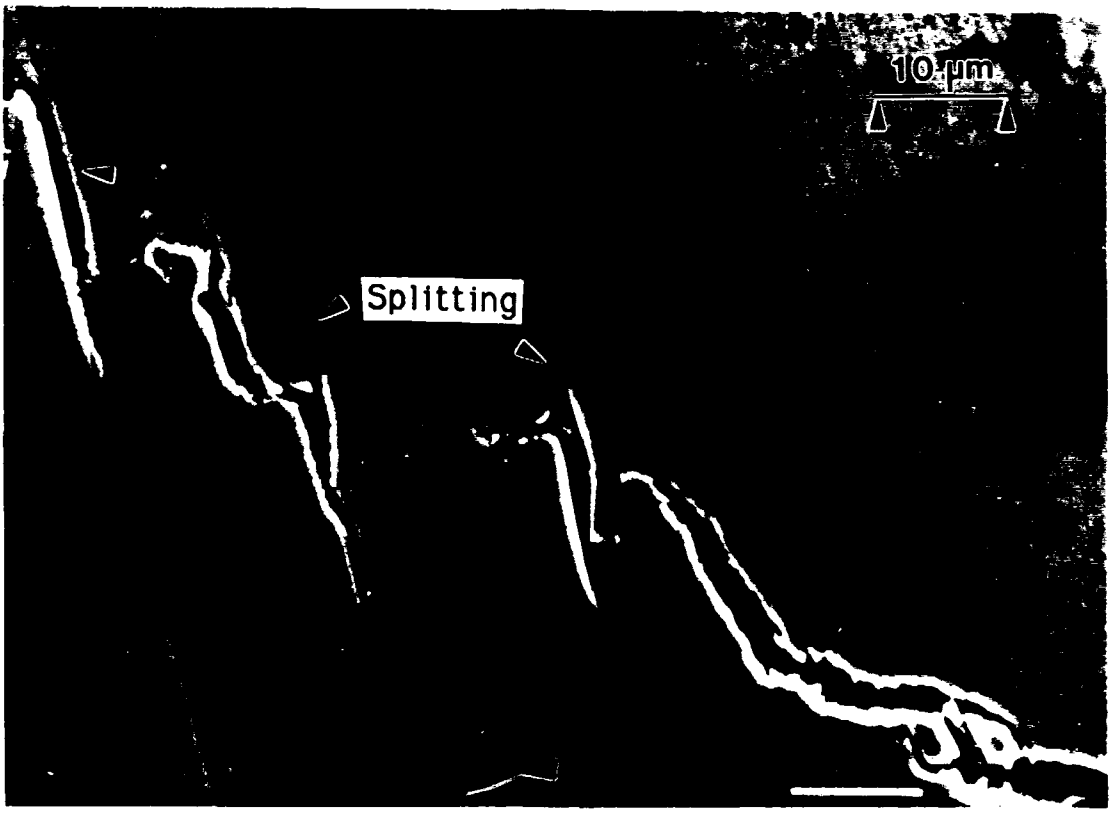

Fig. 6

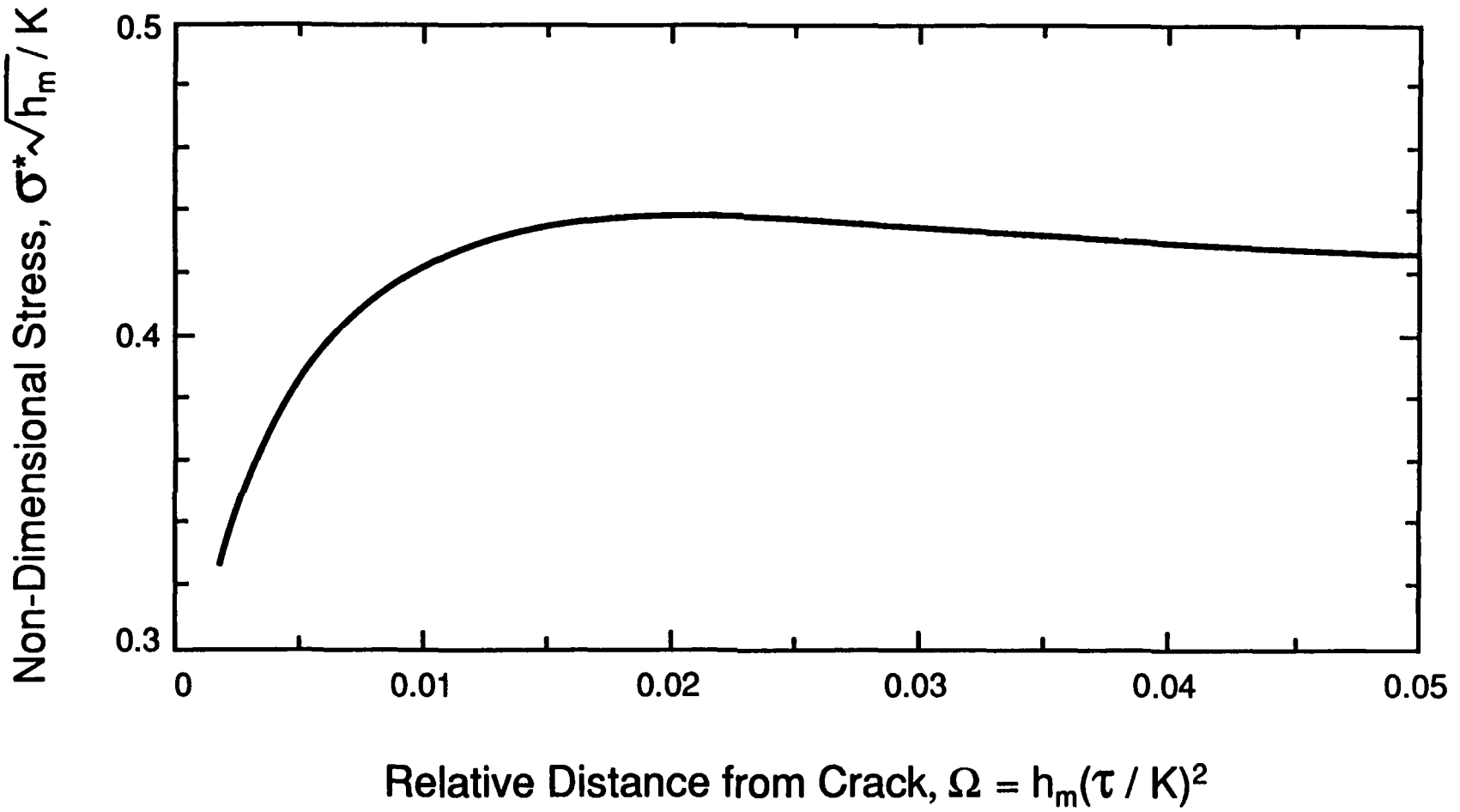
Non-Dimensional Stress, $\sigma^*\sqrt{h_m}$ / K
0.5
0.4
0.3
0
0.01
0.02
0.03
0.04
0.05
Relative Distance from Crack, $\Omega = h_m(\tau / K)^2$

Figure 7a

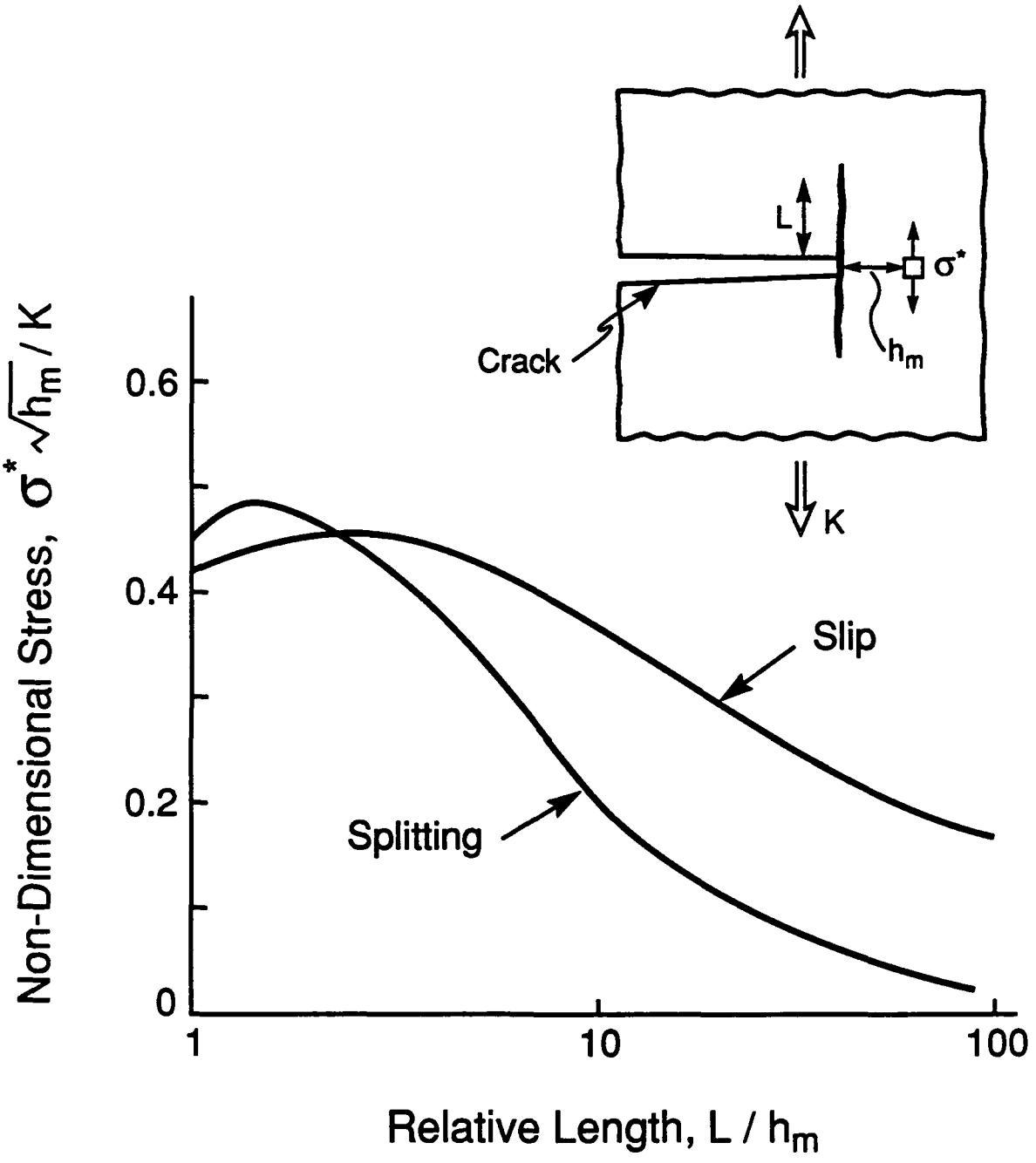
L
σ*
Crack
h_m
K
Non-Dimensional Stress, σ* √h_m / K
0.6
0.4
0.2
0
Slip
Splitting
1
10
100
Relative Length, L / h_m

Figure 7b

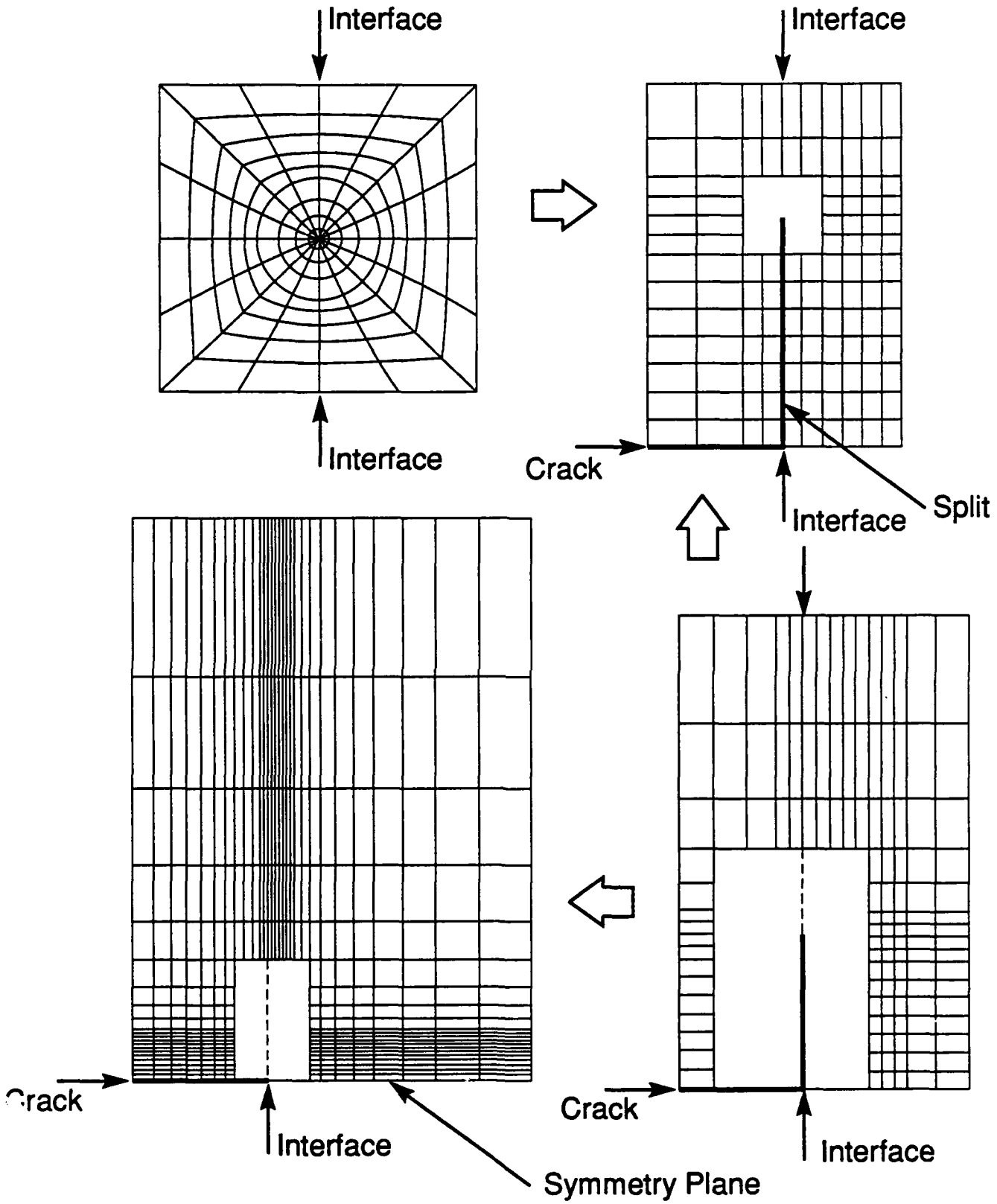
Interface
Interface
Interface
Crack
Interface
Split
Crack
Interface
Crack
Interface
Symmetry Plane

Figure 8

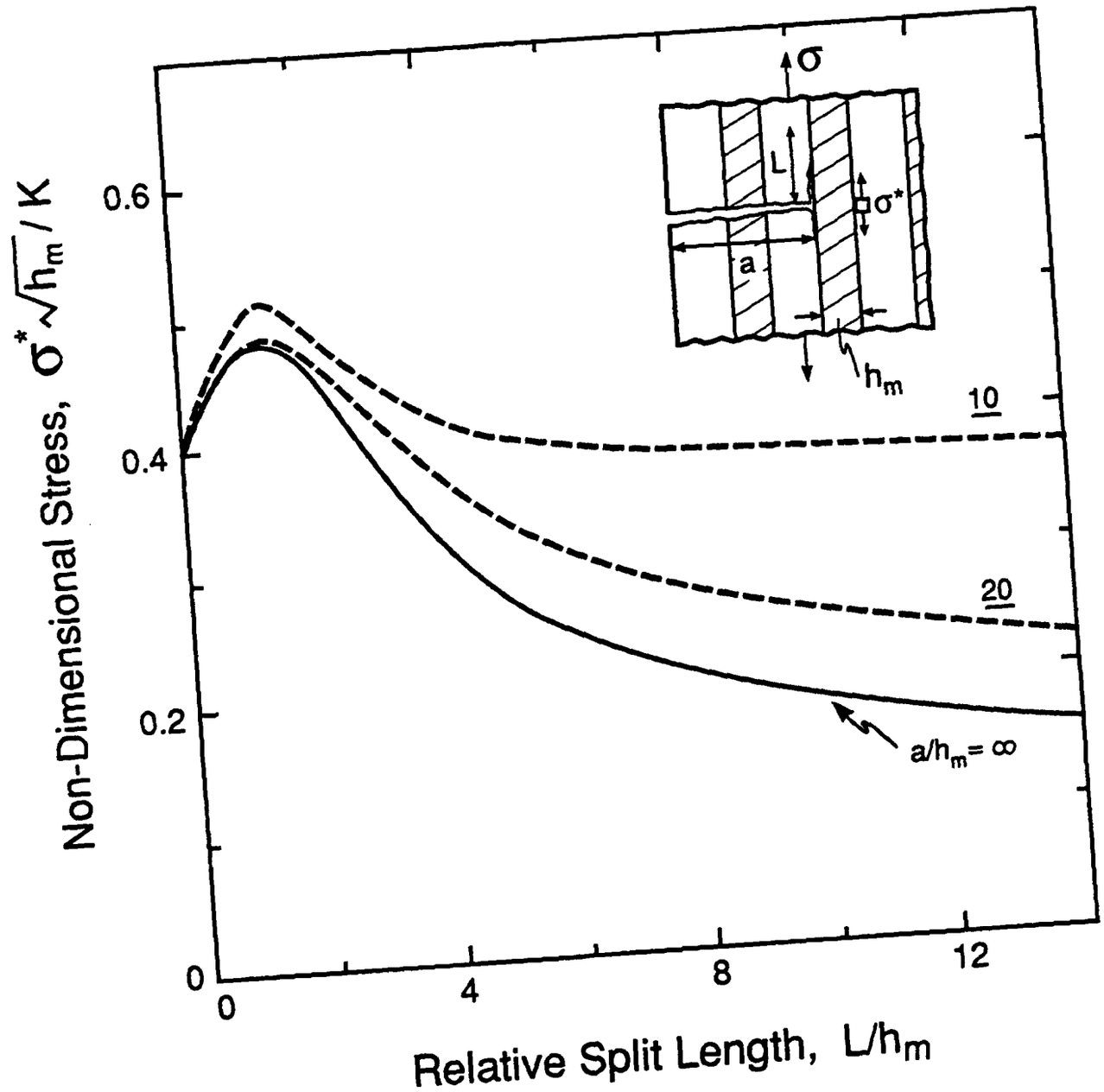
σ
L
σ*
a
h_m
10
20
$a/h_m = \infty$
Non-Dimensional Stress, $\sigma^*\sqrt{h_m}$ / K
0.6
0.4
0.2
0
0
4
8
12
Relative Split Length, L/h_m

Figure 9a

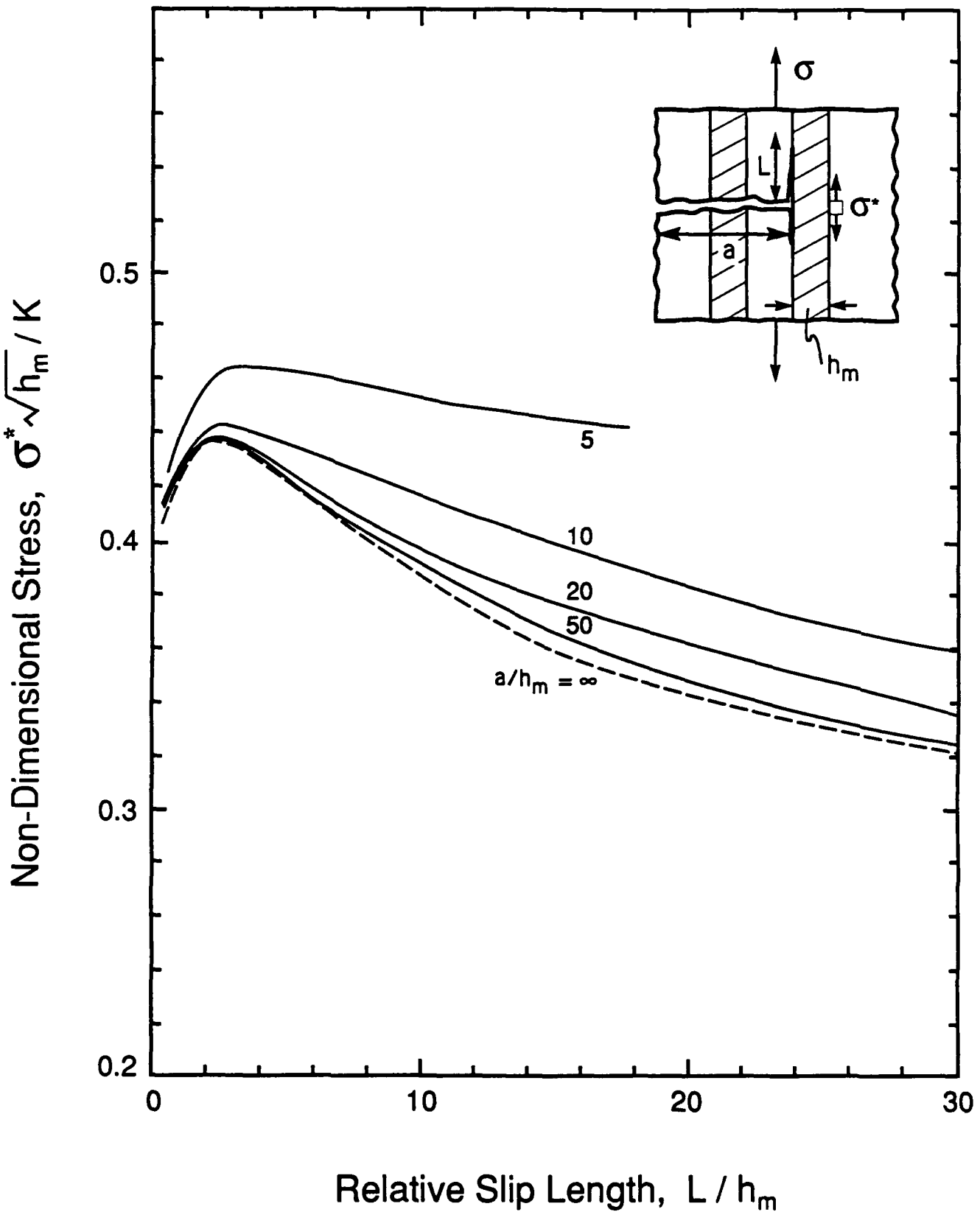
σ
L
σ*
a
h_m
5
10
20
50
$a/h_m = \infty$
0.5
0.4
0.3
0.2
0
10
20
30
Non-Dimensional Stress, $\sigma^* \sqrt{h_m} / K$
Relative Slip Length, L / h_m

Figure 9b

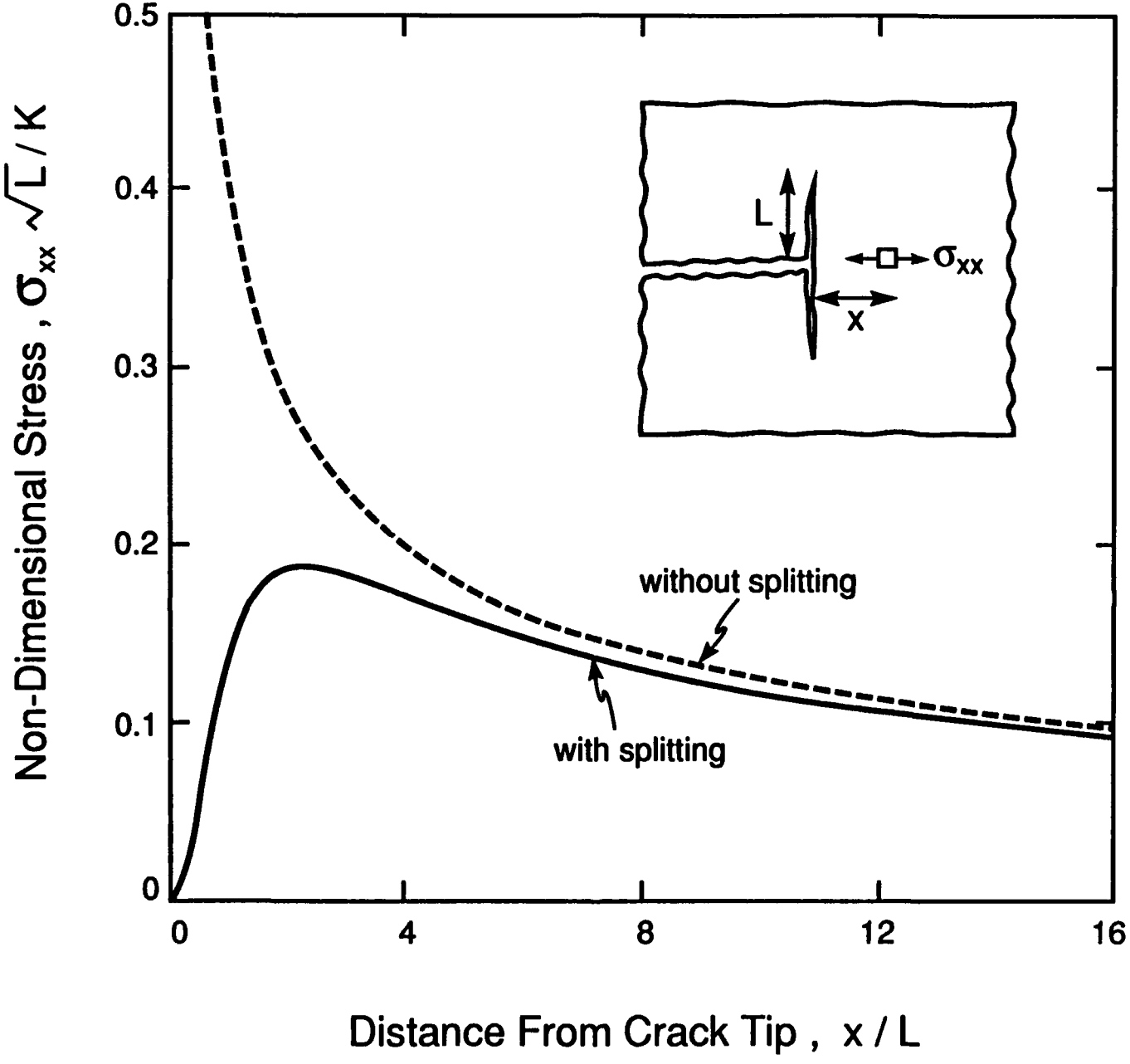
0.5
0.4
0.3
0.2
0.1
0
0
4
8
12
16
Non-Dimensional Stress , $\sigma_{xx}\sqrt{L}$ / K
Distance From Crack Tip , x / L
L
σ_{xx}
x
without splitting
with splitting

Figure 10

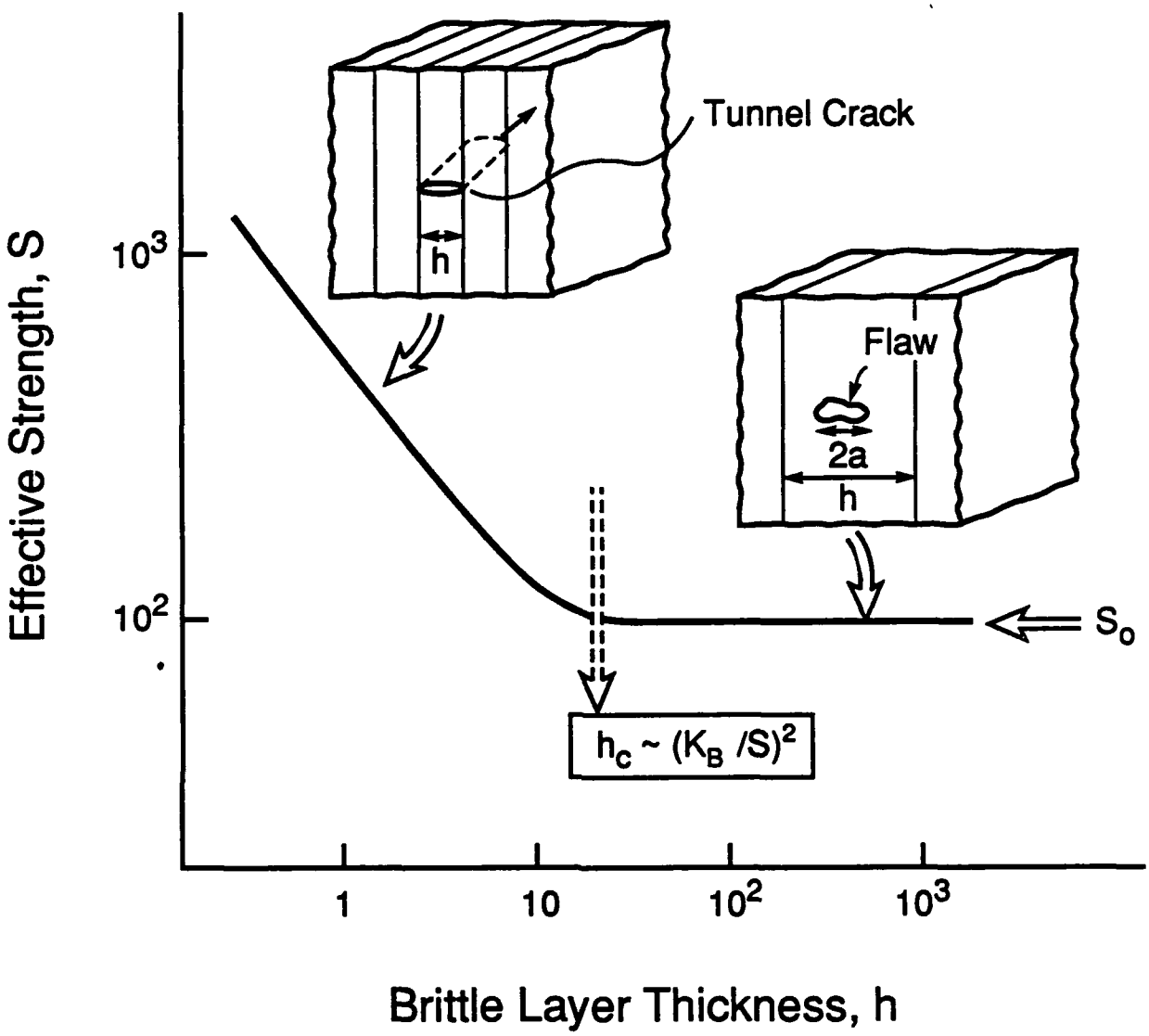
Tunnel Crack
h
Flaw
2a
h
10^3
10^2
S_o
$h_c \sim (K_B/S)^2$
Effective Strength, S
1
10
10^2
10^3
Brittle Layer Thickness, h

Figure 11

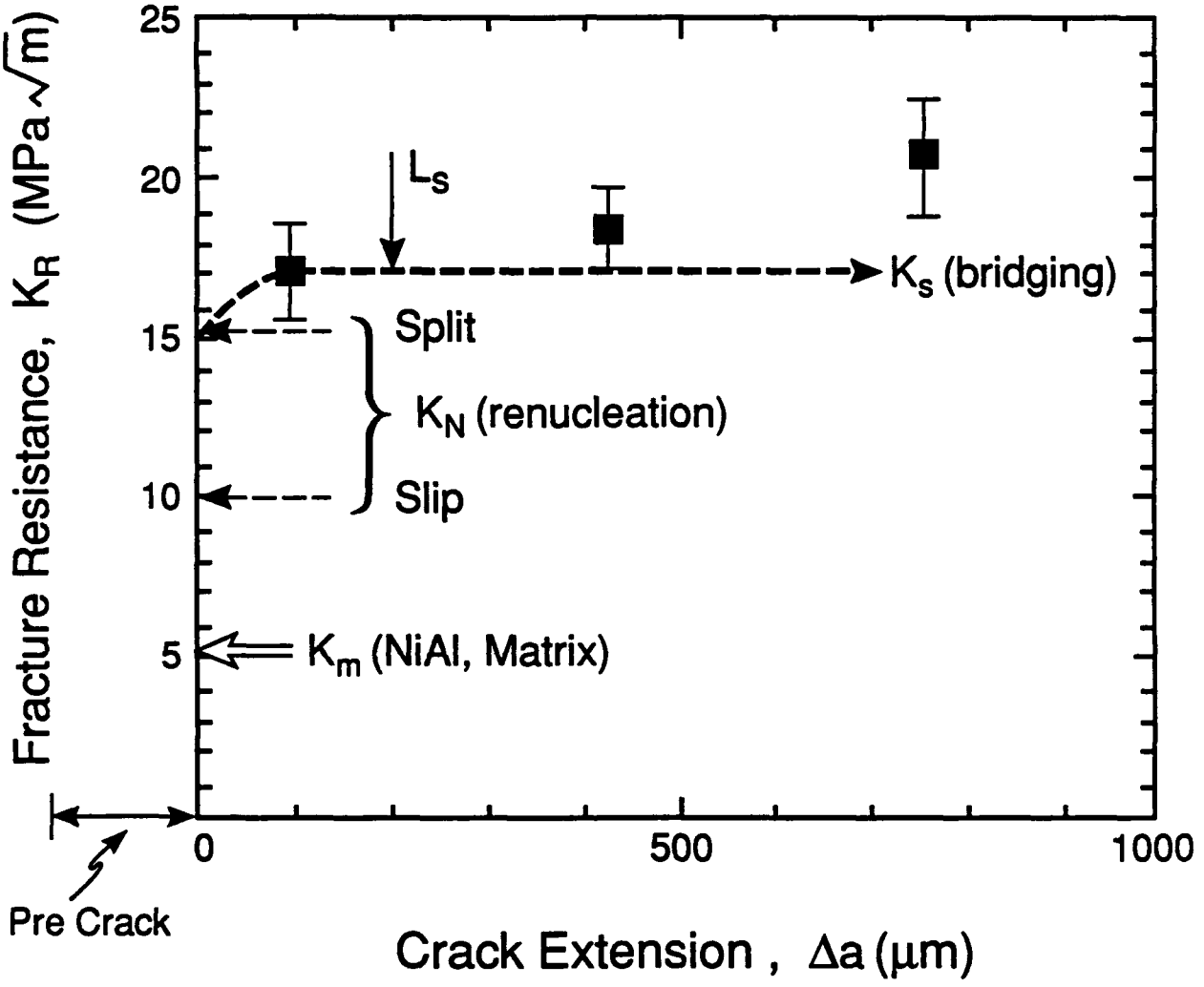
25
20
15
10
5
0
500
1000
Fracture Resistance, K_R (MPa$\sqrt{m}$)
Crack Extension , Δa (μm)
L_s
K_s (bridging)
Split
K_N (renucleation)
Slip
K_m (NiAl, Matrix)
Pre Crack

Figure 12